

Quasi-Optical Design and Analysis of Bolometric Interferometers for Cosmic Microwave Background Experiments

Presented by
Gareth Stanley Curran, M.Sc.

A thesis submitted for the degree of
Doctor of Philosophy



NUI MAYNOOTH

Ollscoil na hÉireann Má Nuad

**Department of Experimental Physics,
National University of Ireland, Maynooth,
Maynooth, Co. Kildare, Ireland.**

December 2010

Head of Department
Prof. J. Anthony Murphy

Research Supervisor
Dr. Crídhe O'Sullivan

To my family

Table of Contents

Abstract	v
-----------------------	----------

Acknowledgements	vi
-------------------------------	-----------

Chapter 1 Introduction	1
-------------------------------------	----------

1.1	Introduction	1
1.2	The Electromagnetic Spectrum	1
1.2.1	Overview of the Electromagnetic Spectrum	1
1.2.2	Terahertz Radiation and Astronomy	2
1.3	The Cosmic Microwave Background (CMB)	6
1.3.1	The Big Bang and the CMB	7
1.3.2	Past, Present and Future CMB Experiments	19
1.3.3	Other Applications of Terahertz Imaging	29
1.4	Interference and Polarisation	30
1.4.1	Interference and the Interferometer	30
1.4.2	The Fizeau Interferometer	37
1.4.3	Polarisation.....	39
1.4.4	The Stokes Parameters	44
1.5	Imaging versus Interferometry	47
1.6	The Millimetre-Wave Bolometric Interferometer.....	50
1.6.1	Overview of the MBI Project.....	50
1.6.2	Science with MBI.....	51
1.7	The QU Bolometric Interferometer for Cosmology.....	54
1.7.1	Overview of the BRAIN and QUBIC Projects	54
1.7.2	Science and Challenges with QUBIC	55
1.8	Synopsis and Thesis Outline	56

Chapter 2 Analytical Tools for Modelling Quasi-Optical Systems	59
---	-----------

2.1	Introduction	59
2.2	Ray Tracing Analysis	60
2.2.1	Background	60

2.2.2	Ray Tracing Through an On-Axis Cassegrain System	61
2.3	Fresnel Diffraction Analysis	64
2.3.1	Background	64
2.3.2	The Fresnel Integral	65
2.4	Gaussian Beam Mode Analysis	69
2.4.1	Background	69
2.4.2	Derivation of Gaussian Beam Modes	70
2.4.3	Propagation of Gaussian Beam Modes	76
2.4.4	Multi-Moded Gaussian Beams.....	78
2.4.5	ABCD Matrices.....	80
2.4.6	GBM Analysis of a Two-Slit Interferometer	84
2.5	Physical Optics Analysis.....	87
2.5.1	Background	87
2.5.2	Physical Optics Analysis of an Aperture with Stop.....	91
2.6	Description of Modelling Software.....	92
2.7	Conclusions	108
 Chapter 3 The Millimetre-Wave Bolometric Interferometer		110
3.1	Introduction	110
3.2	The Instrumentation of the MBI-4 System	111
3.2.1	Observing Strategy and Telescope Mount	112
3.2.2	Interference	113
3.2.3	Detectors and Signal Processing	115
3.2.4	Cryogenics	117
3.2.5	The Optical System.....	118
3.3	Design of the MBI-4 Optical Beam Combiner	122
3.3.1	The Design of the Optical System	123
3.3.2	A First Approximation Using Geometrical Optics	123
3.3.3	Diffraction Analysis	129
 Chapter 4 Electromagnetic Modeling of Horn Antennas and Waveguides		152
4.1	Introduction	152
4.2	Smooth-Walled and Corrugated Horn Antennas	153
4.2.1	Smooth-Walled Conical Horns	153

4.2.2	The Implementation of Smooth-Walled Horns in MODAL.....	157
4.2.3	MBI-4 Phase Flattening Lenses	158
4.2.4	Corrugated Conical Horns.....	166
4.3	Scatter Matrix Analysis of Quasi-Optical Systems.....	170
4.3.1	Scatter Matrix Methods.....	171
4.3.2	MBI-4 Back-To-Back Horn Antennas	175
4.3.3	Truncation by MBI-4 Windows	181
4.3.4	Singular Value Decomposition Analysis	184
4.4	Mode Scattering at Rectangular-Circular Junctions	194
4.4.1	Rectangular Waveguide Modes	195
4.4.2	Circular Waveguide Modes.....	201
4.4.3	Scattering at a Rectangular-Circular Discontinuity	211
4.5	Beam Distortion in Closely Packed Waveguide Arrays	216
4.5.1	Circular Waveguide Arrays.....	216
4.5.2	Rectangular Waveguide Arrays	223
Chapter 5 Quasi-Optical Analysis of MBI-4		233
5.1	Analysis of the Fizeau Optical System Using MODAL	233
5.1.1	Defining the System in MODAL	233
5.1.2	Evaluation of Propagation Techniques	238
5.1.3	Calculating the System Scattering Matrix.....	244
5.1.4	The Effects of Truncation on the System.....	256
5.1.5	Mechanical Tolerances in MBI-4.....	261
5.1.6	Frequency Dependence of the Instrument.....	281
5.1.7	Simulating Lab Measurements.....	284
5.2	Conclusions	289
Chapter 6 Quasi-Optical Design and Analysis of QUBIC.....		291
6.1	Introduction	291
6.2	Science and Challenges with QUBIC	292
6.3	The QUBIC Instrument.....	293
6.4	Design and Analysis of the Beam Combiner	294
6.4.1	Optical System Design Constraints	294
6.4.2	Physical Optics Analysis of the Mirror Configurations.....	295

6.4.3	The Implementation of Lenses.....	308
6.5	Conclusions and Future Work.....	311
Chapter 7 Summary and Conclusions		314
References		320
Appendix A Scatter Matrix Elements		A1
Appendix B Beam Power Profiles.....		A2
Appendix C Mechanical Tolerance Data		A9
Appendix D Frequency Dependence Data		A22

Abstract

The main topic of this thesis is the quasi-optical analysis of optical systems for experiments used to measure the polarisation anisotropies of the cosmic microwave background. The polarisation signal is so low and difficult to measure that very accurate modelling and a deep understanding and characterisation of the instruments used to make such measurements is essential.

The two instruments investigated in this thesis are the Millimetre-Wave Bolometric Interferometer (MBI) and the Q and U Bolometric Interferometer for Cosmology (QUBIC), both of which are collaborations between institutes in Europe and the United States. A prototype of MBI called MBI-4 has already been built and has been used for experimental observations. The main aim of this prototype has been to prove the concept of bolometric interferometry for measurements of the CMB. In this thesis the optical combiner of MBI-4 is designed and modelled in detail, taking into account mechanical tolerances and truncations effects, amongst others. The QUBIC instrument is currently in the design stage, having evolved from both MBI-4 and BRAIN, an experiment located in Antarctica as a test for a more elaborate instrument. The optical design of QUBIC is also analysed, including a physical optics analysis of lenses, although not in the same detail as MBI-4.

A number of techniques are used in this analysis, including Gaussian beam modes and physical optics, to allow for a complete model of the optical systems to be obtained. As part of this modelling, a mode-matching technique is applied to predict the beam patterns of horn antennas. In this thesis, the technique is extended to include a transition from rectangular to circular waveguide geometries as such a junction occurs in the MBI back-to-back horns.

The results obtained in this thesis give a useful insight into the power and usefulness of various optical design and analysis techniques as well as criteria for the successful design of current and future interferometry experiments.

Acknowledgements

I would firstly like to offer a warm and sincere thanks to my supervisor Dr. Cr  idhe O’Sullivan for her help throughout this work. Her advice and guidance is very much appreciated and I thank her for sharing her enthusiasm and knowledge in this area.

I would like to thank Prof. Anthony Murphy, Head of the Experimental Physics Department, for the use of the facilities at NUI Maynooth.

For financial support throughout this project I thank both the Institute of Technology Blanchardstown and the Experimental Physics Department at NUI Maynooth.

Also, thanks to all the staff and postgraduates of the Experimental Physics Department. In particular I’d like to thank: Grainne Roche for all her help and advice over the years; Dr. Marcin Gradziel for his extensive help with MODAL and who was kind enough to share his office with me for the first two years of my Ph.D.; Dr. Neil Trappe for sharing his knowledge in this area; Mr. Tully Peacocke for his advice and assistance with running the cluster; Mr. John Kelly and Mr. Derek Gleeson for all things technical; David Bennett with whom I worked closely on QUBIC; Stephen Doherty for the many discussions on CST; Donnacha and Dan, with whom I shared an office for the last year. It is thanks to you and the rest of the department that have made my time here so enjoyable.

To the MBI and QUBIC collaborations, I thank you for allowing me be part of these great projects and I look forward to continuing to work with you all in the future.

To Mam, Dad and Nicola, for your constant love and support throughout this work, and always. As usual you’ve all been wonderful. My parents have taught me almost everything I know and even after studying physics for over fourteen years my Dad is still teaching me new things, most recently the meaning and significance of Archimedes Principle with the aid of a swimming pool and some *Tinto de Verano*...thanks Dad!

Finally, I'd like to thank Núa and Rubén, both of whom have been amazing. Núa has been my rock throughout this project and her patience and love have made this possible. On the days when things were not going as planned, Rubén's smiling face cheered me up no matter how hard or long the day seemed. The final year of a Ph.D. and the first year of your new baby's life are not very compatible, but I was lucky, while I spent a lot of the time carrying out research Núa was doing the real work at home. Now it's my turn!

Chapter 1

Introduction

1.1 Introduction

In this Chapter we look at an overview of the electromagnetic spectrum and in particular the astronomy carried out by observing in the THz region. This is followed by an introduction to the Big Bang theory and the cosmic microwave background radiation that remained after this event occurred.

The cosmic microwave background is of such significance in cosmology that its discovery has led to extensive efforts to measure it as accurately as possible using a series of ground-based, balloon borne and satellite experiments. Here we outline these experiments, and in particular introduce the Millimetre-Wave Bolometric Interferometer (MBI) and the Q U Bolometric Interferometer for Cosmology (QUBIC). The astronomy carried out at THz frequencies is examined with a particular emphasis on the cosmic microwave background and the advantages and disadvantages of both interferometers and imaging systems for such measurements are discussed.

This thesis investigates the operation of bolometric interferometers, MBI and QUBIC, which will be used to measure the polarisation of the cosmic microwave background. With this in mind we look at both interference and polarisation of electromagnetic radiation with a particular focus on the Stokes parameters. Finally, a summary of the remainder of the thesis is given. We start by taking a brief look at the electromagnetic spectrum.

1.2 The Electromagnetic Spectrum

1.2.1 Overview of the Electromagnetic Spectrum

Astronomical objects emit radiation in all parts of the spectrum (Table 1.1), however, the Earth's atmosphere limits what we can actually detect. Ultraviolet and

shorter wavelengths are blocked whereas visible light can pass through. The atmosphere is also transparent to some infrared wavelengths and radio waves, giving rise to two main transmission windows.

Until relatively recently, astronomers could only observe and gather information in the visible part of the electromagnetic spectrum due to the lack of detector technology. In the middle of the 20th century the radio part of the spectrum opened up thanks to advancements in radar technology that had taken place during World War II. In more recent times developments in detector technology, in particular at THz frequencies, has provided an opportunity for astronomers and scientists to explore new areas of astronomy.

The Electromagnetic Spectrum		
Region	Wavelength	Frequency (Hz)
Radio	>1mm	$<3 \times 10^{11}$
Infrared	700nm – 1mm	$3 \times 10^{11} - 4.3 \times 10^{14}$
Visible	400nm – 700nm	$4.3 \times 10^{14} - 7.5 \times 10^{14}$
Ultraviolet	10nm – 400nm	$7.5 \times 10^{14} - 3 \times 10^{16}$
X-ray	0.1nm – 10nm	$3 \times 10^{16} - 3 \times 10^{18}$
Gamma-ray	<0.1nm	$>3 \times 10^{18}$

Table 1.1 The different regions of the electromagnetic spectrum and their corresponding wavelengths and frequencies.

1.2.2 Terahertz Radiation and Astronomy

In 1932, Karl Jansky detected radio emissions from our own galaxy, the Milky Way (Verschuur and Kellermann, 1988). This new phenomenon of observing non-visible radiation from space created a new branch of astronomy. Previously unseen objects in the universe could now be observed. In the last few decades the techniques of radio astronomy have been vastly improved and the wavelengths that can be detected have been getting shorter, something that is technically more difficult. At the same time in optical astronomy the observable wavelengths have

been getting longer, extending well into the infrared. It is only in the past twenty years however, that astronomers have focused on the area between these wavelengths, the submillimetre region, and it is now possible to observe these wavelengths as well. This region of the electromagnetic spectrum (Figure 1.1) is referred to as the far infrared, the submillimetre or the terahertz region.

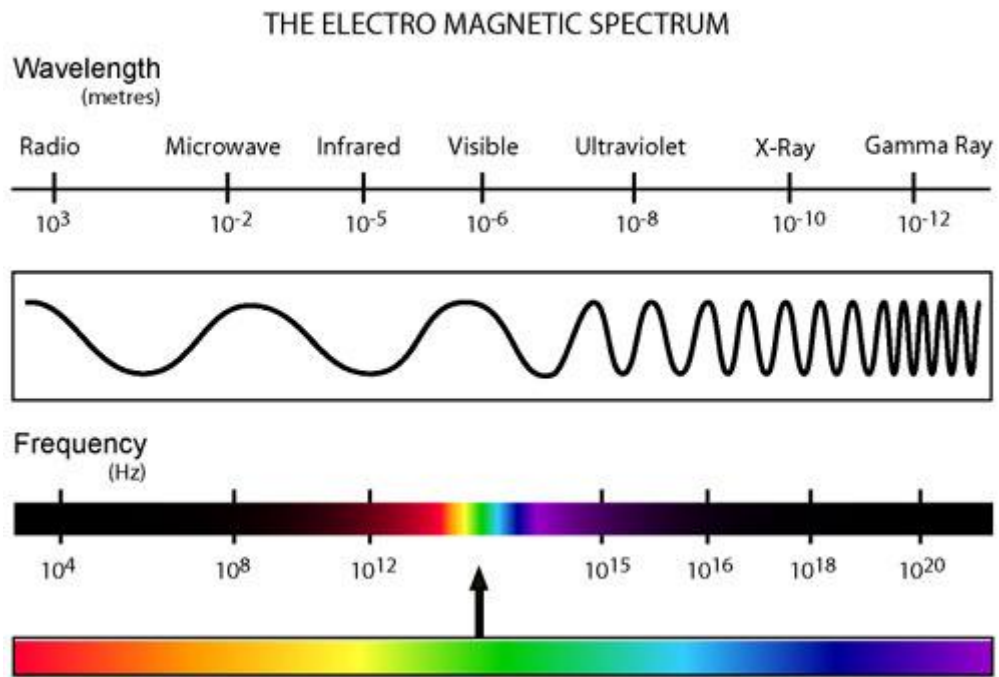


Figure 1.1 The electromagnetic spectrum illustrating waves of different wavelength and frequency.

This part of the spectrum, corresponding to the frequency range 0.1–10 THz, was one of the last electromagnetic wavebands to be exploited, hence the other name, “THz gap”. Until recently, the availability of sources and detectors for radiation in this particular range of frequencies was very limited. Significant progress has been achieved in the last decade, for the most part driven by the potential applications of THz radiation (often now referred to as T-rays) in medical imaging and security. THz frequencies have always been important in the fields of atmospheric physics and astronomy.

THz or submillimetre-wave astronomy is, as its name implies, concerned with making observations of the sky in the very far-infrared region of the electromagnetic spectrum. Several features of this waveband make it of vital

importance for astronomy. There is a great deal of dust and gas in the interstellar medium (ISM) of our Galaxy and like many other cool objects, they emit most of their radiation in the far infrared. The continuum emission from dust clouds in the ISM has quite a broadband spectrum, characteristic of blackbody radiation. From Wien's displacement law, $\lambda_{\text{max}} T = 0.2898 \times 10^{-2} \text{ mK}$, the intensity of emission of these clouds at temperatures from 10K to 100K peaks in the submillimetre region (Holliday, 1999). As an example, Figure 1.2 shows the continuum emission spectrum of 2 ultra-compact HII regions (Caltech Astronomy Department website).

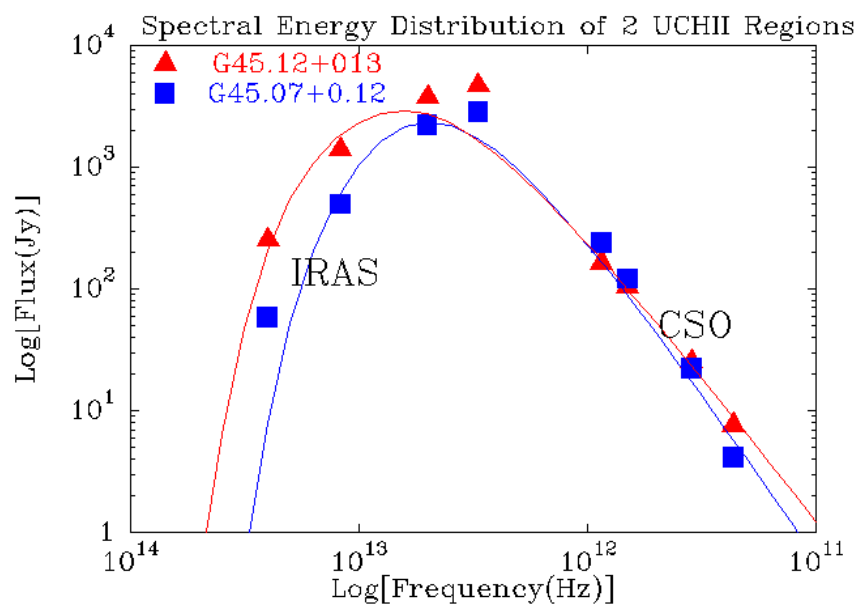


Figure 1.2 The continuum emission spectrum of 2 G45 Ultra-compact HII regions (Caltech Astronomy Department website).

Dust clouds are of great interest to astronomers as it is from these that stars and planets are formed when self-gravity overcomes thermal, turbulent and magnetic pressures causing them to collapse (Ray and Beckwith, 1992). When observing at submillimetre wavelengths dust grains in these clouds become transparent making it possible to look deep inside regions that are obscured at optical wavelengths, allowing astronomers to investigate and further develop theories on the very early stages of star birth, a process not yet fully understood. The continuum emission is most sensitively detected using bolometers, which are devices that simply absorb incident radiation and warm up. This changes their resistance so that when fed with a constant bias current a change in voltage is produced across the device (Ray and

Beckwith, 1992). Bolometric detectors are usually held in a liquid helium cryostat at the focus of a large reflector to improve sensitivity to the levels required for doing useful astronomy.

Besides the continuum, interstellar dust and gas clouds likely emit some 40,000 individual spectral lines, only a few thousand of which have been resolved and many of these have not yet been identified. Much of the terahertz band has yet to be mapped with sufficient resolution to avoid signal masking from spectral line clutter. Some THz bands are obscured by atmospheric absorption making ground based observations impossible (White, 2006). Results (Hauser *et al.*, 1998) from the NASA Cosmic Background Explorer (COBE) Diffuse Infrared Background Experiment (DIRBE) and from examining the spectral energy distributions in observable galaxies, indicate that approximately one-half of the total luminosity and 98% of the photons emitted since the 'Big Bang' fall into the submillimetre and far infrared, i.e. the THz band. Much of this energy is being radiated by cool interstellar dust. Older galaxies like the Milky Way have a much greater abundance of dust making submillimetre detectors true probes of the universe.

Synchrotron radiation is yet another form of radiation observed at submillimetre wavelengths. It is caused by streams of particles moving at relativistic speeds through a magnetic field. Matter spiralling towards a black hole generates such emissions as does our own Sun when charged particles are ejected outward through its magnetic field.

THz observations also offer the best opportunity yet to probe the universe as it was not long after its creation in the Big Bang, about 14 billion years ago. The universe was much hotter and denser in the past but the relic radiation, the cosmic microwave background has since cooled to just below 3K and now its blackbody power spectrum peaks at millimetre wavelengths (Siegel, 2002). Since this thesis is concerned with the optical design of instruments whose aim is to observe the cosmic microwave background radiation it is discussed in more detail in the next section.

1.3 The Cosmic Microwave Background (CMB)

Georges Lemaître, professor of physics and astronomer at the Catholic University of Leuven, Belgium, first pointed out that if the universe is expanding, there must have been an era in the past when it was much more dense than it is now. During this hot, dense era, approximately 14 billion years ago, a massive expansion occurred creating not only subatomic particles and matter but also space and time, and the universe has been expanding ever since. This event was named the *Big Bang* by Fred Hoyle, a steady-state cosmologist, in an attempt to ridicule the theory. However, the theory survived the ridicule, the name remained and we now refer to all cosmological models with an evolving universe as *big bang cosmologies*. There are several different theoretical models that attempt to describe the universe as we know it today and only a detailed study of the remnant radiation from the big bang, known as the cosmic microwave background (CMB) radiation, will distinguish between these theories and put further constraints on the cosmological model.

Two physicists at the Bell Telephone Laboratories in Holmdel, New Jersey, Arno Penzias and Robert Wilson, accidentally detected this radiation while using a very sensitive radio telescope for both communication and radio astronomy, and reported their findings in 1965 (Penzias and Wilson, 1965). To have accurately calibrated results they had to understand all sources of noise in their system. There was an unaccounted for signal at a very low level that appeared to be from either the system itself or everywhere in the sky. After careful analysis they were confident that it was the latter, however they only had measurements at one wavelength and so could not confirm the shape of the spectrum but found that the intensity corresponded to a blackbody at a temperature of approximately 3K. It was clear that Penzias and Wilson had found the CMB radiation and further confirmation came when a group at Princeton carried out similar observations at a different wavelength and found that the radiation was present and that the spectrum was indeed consistent with that of a blackbody. For their painstaking work in detecting this signal, Penzias and Wilson were awarded the Nobel Prize in Physics in 1977.

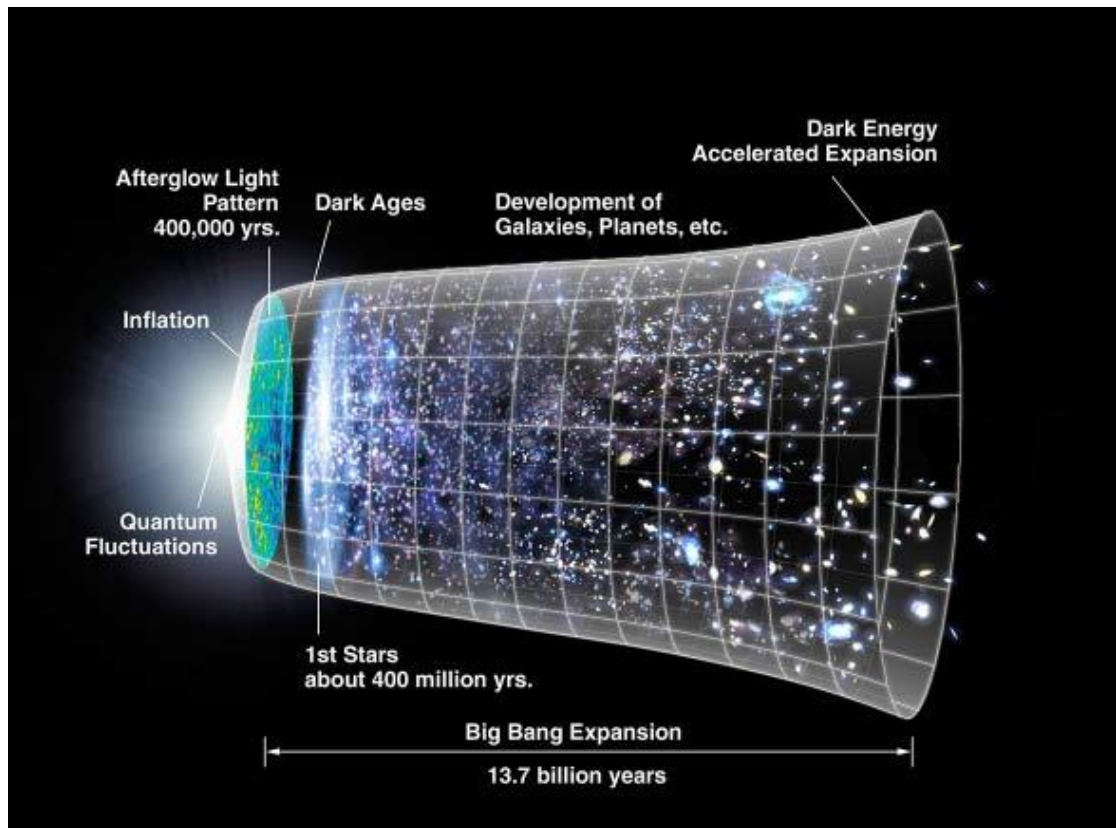


Figure 1.3 Schematic diagram of the Big Bang theory (Lawrence Berkley National Laboratory website).

1.3.1 The Big Bang and the CMB

The field of observational cosmology is a growing one and a combination of theory and observations will increase our understanding of what happened in the very early universe. In theoretical models it is assumed on the largest scales that at any instant the general properties, such as density and composition, are the same everywhere and that the universe appears the same in all directions, that is, that the universe is both homogeneous and isotropic. Until the early 1970's there were vigorous debates about whether or not the universe was the same at all times, a so-called steady-state universe. However a long chain of observational evidence has been amassed against the steady-state theory, including the discovery of the remnant CMB radiation in 1965, and few hold it today with evolving theories, or big bang cosmologies, taking the upper hand.

Following from Lemaître's idea of a hot dense universe, George Gamow, a Russian physicist, suggested in 1946 that when the universe was less than about 200 seconds old the temperature was greater than one billion Kelvin, hot enough for nuclear reactions to proceed rapidly. In 1948, Ralph Alpher, Hans Bethe and Gamow showed that these nuclear reactions might be able to explain the current abundance of helium in the universe (Alpher *et al.*, 1948). In a more thorough analysis of the problem, Alpher and Robert Herman found that the early universe should have been filled with radiation and that its remnant should be detectable as a low intensity background of microwaves throughout the sky (Alpher and Herman, 1975), CMB radiation.

The CMB radiation itself was released approximately 380,000 years after the Big Bang (Bennett *et al.*, 2003a). Before this, when the universe was young enough to have its temperature higher than 4000K, the hydrogen atoms were ionised and the universe was a plasma of ions and electrons coupled strongly to the photon field (photon-baryon fluid). The large Thompson scattering cross-section of the electrons resulted in a short mean free path for the photons and hence an opaque universe in thermal equilibrium. Because of these multiple reflections the spectrum of the photons was that of a blackbody with a temperature the same as that of the matter. The COBE satellite measured this predicted blackbody profile to within 1% accuracy (Mather *et al.*, 1990) as outlined in section 1.3.2. As the universe expanded its density decreased and the temperature dropped below 4000K, at which point the electrons and protons could combine to form neutral elements (hydrogen) in a process known as recombination (Turner, 1996; Lineweaver, 1999). The photons, as they interact very weakly with neutral atoms, decoupled from the matter and the universe became transparent to the radiation. Since the matter was now free from radiation pressure the denser areas coalesced under the influence of gravity to form stars and galaxies, and in fact the one in 100,000 variations observed in the CMB are exactly the right amplitude to form the large scale structures we see today (Hu and White, 2004).

The universe is constantly expanding and the temperature of the CMB radiation has subsequently cooled to approximately 2.73K with the peak wavelength of the radiation lying in the THz region of the electromagnetic spectrum. The CMB

photons that are detected today were last scattered at the time of decoupling and therefore cosmologists studying this radiation are effectively looking through the universe back at a time when it was opaque. The apparent source of the photons, when the universe became transparent for the first time, is referred to as the ‘surface of last scattering’.

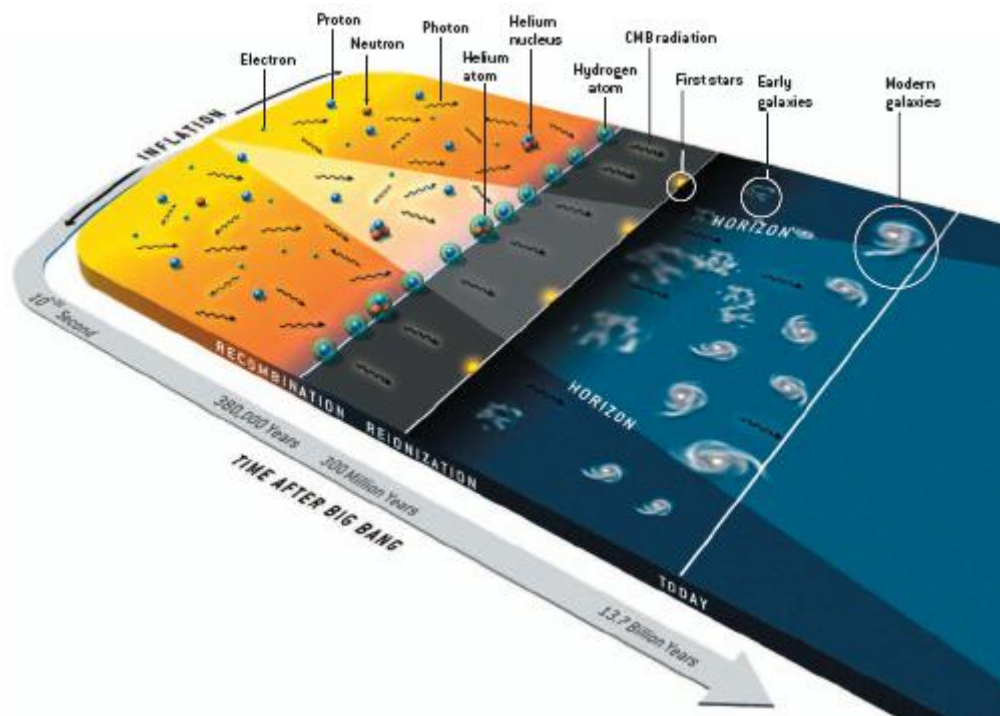


Figure 1.4 The timeline of the universe showing the radius and particle horizon (Hu and White, 2004).

Measurements of the blackbody spectrum of the CMB have made the big bang theory the most widely accepted model of the early universe (Spergel *et al.*, 2003). However, this model alone does not explain all observed phenomena of the CMB and additions have had to be made to the original model. In 1981, Alan Guth developed the theory of inflation as an explanation for the large scale uniformity of the universe (Guth, 1981). Alexei Starobinski had developed a similar theory the year before (Starobinski 1980), however Guth modified this to allow for a graceful exit from inflation, a modification independently made by Andrei Linde (Linde, 1982) and by Andreas Albrecht and Paul Steinhardt (Albrecht and Steinhardt, 1982). The theory of cosmological inflation postulates that at the end of the grand

unification epoch, 10^{-36} seconds after the big bang, the universe underwent a period of exponential expansion or '*inflation*' for approximately 10^{-32} seconds (Prantzos, 2000). During this time the energy density of the universe was dominated by a vacuum energy or '*cosmological constant*'. When the nature of this vacuum changed the universe underwent a phase change, resulting in the rapid expansion. The large scale properties of the universe, widely separated parts of which were in casual contact before inflation, were preserved by this event (Figure 1.4). Since Guth's early work, each of these observations has received further confirmation, most impressively by the observations of the CMB made by the WMAP satellite (NASA's WMAP website).

Temperature Anisotropies

Although the COBE satellite measured the temperature of the CMB blackbody spectrum to great accuracy this result was perhaps overshadowed by its detection of variations at the level of one part in 100,000 in the temperature of the CBM (Smoot *et al.*, 1992). If the temperature was completely uniform this would have indicated that matter was distributed evenly at the surface of last scattering and concentrations of matter such as galaxies and galaxy clusters would not exist in today's universe. Since the COBE experiment, WMAP has made more sophisticated measurements (Bennett *et al.*, 2003a) and revealed that the characteristic sizes of the CMB temperature variations follow the distinctive pattern predicted by cosmological theory. Figure 1.5 shows an all-sky map of temperature anisotropies from the 2003 data release of the WMAP satellite. Scientists have used this information to precisely estimate the age, composition and geometry of the universe.

The exponential expansion of the early universe provides a physical mechanism for triggering the primordial sound waves by means of quantum fluctuations (Guth and Pi, 1982) and it also solves the horizon problem, an issue which involves the rate of expansion and the speed at which information can travel.

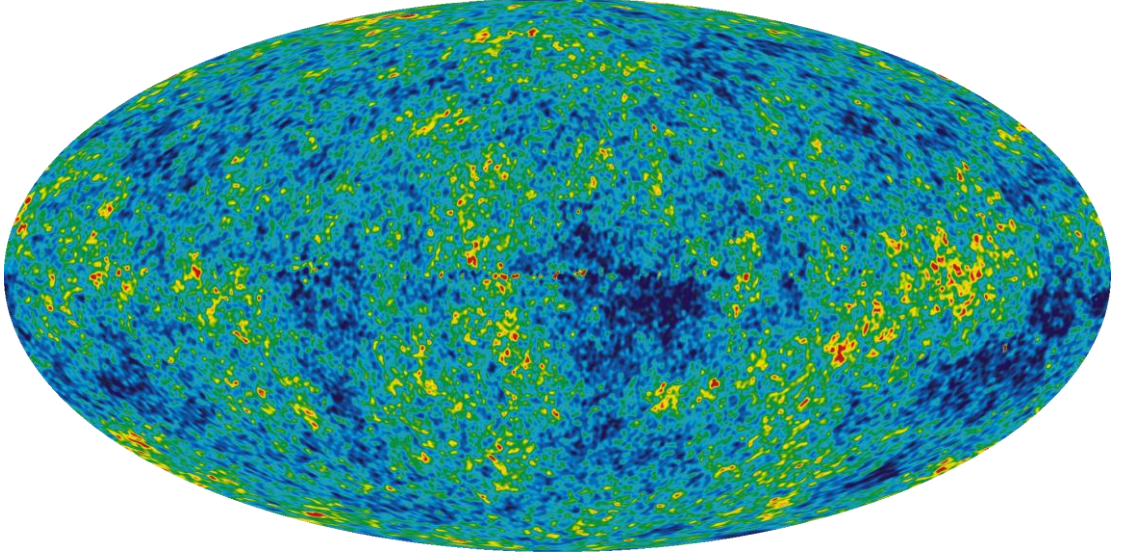


Figure 1.5 Full sky temperature anisotropy map from WMAP results released in 2003 (NASA's WMAP website).

The CMB temperature fluctuations can be represented by a sum of spherical harmonics (Smoot and Scott, 1998) as,

$$\frac{\Delta T}{T}(\theta, \phi) = \sum_{l=2}^{\infty} \sum_{m=-l}^l a_{lm} Y_{lm}(\theta, \phi) \quad (1.1)$$

where θ and ϕ represent spherical angles and l is the Legendre multipole ($\approx \pi/\theta$, where θ is the angular separation between two points on the sky). The $l=1$ dipole term is omitted because the intrinsic CMB dipole is obscured by the apparent dipole resulting from the Earth's motion with respect to the reference frame defined by the CMB. It is convenient to represent the spectrum of angular scale sizes of the CMB temperature fluctuations, ΔT , as a plot of power, $l(l+1)C_l/2\pi$, where $C_l = \langle |a_{lm}|^2 \rangle$ (Coles and Lucchin 1995), as a function of multipole, l (Figure 1.6). Up to now it has been the aim of CMB experiments to measure the magnitude of the various multipole amplitudes, C_l , as accurately as possible for comparison with the predictions of theoretical models.

The early universe contained sound waves generated from small disturbances in gas density caused by scattering of photons off electrons. The compressions of

the sound waves heated the gas while the rarefactions cooled it, giving rise to temperature fluctuations. At recombination, when the photons were released, those emitted from hotter, denser regions were more energetic than those emitted from rarefied regions and so the pattern of hot and cold spots induced by the sound waves was frozen into the CMB. In Figure 1.6 it can be seen that the regions with the greatest variations subtend about one degree across the sky, representing the fundamental acoustic mode that just had time to complete one compression/rarefaction cycle before decoupling. Other peaks in temperature contrast represent the different harmonic modes that end in compression or rarefaction.

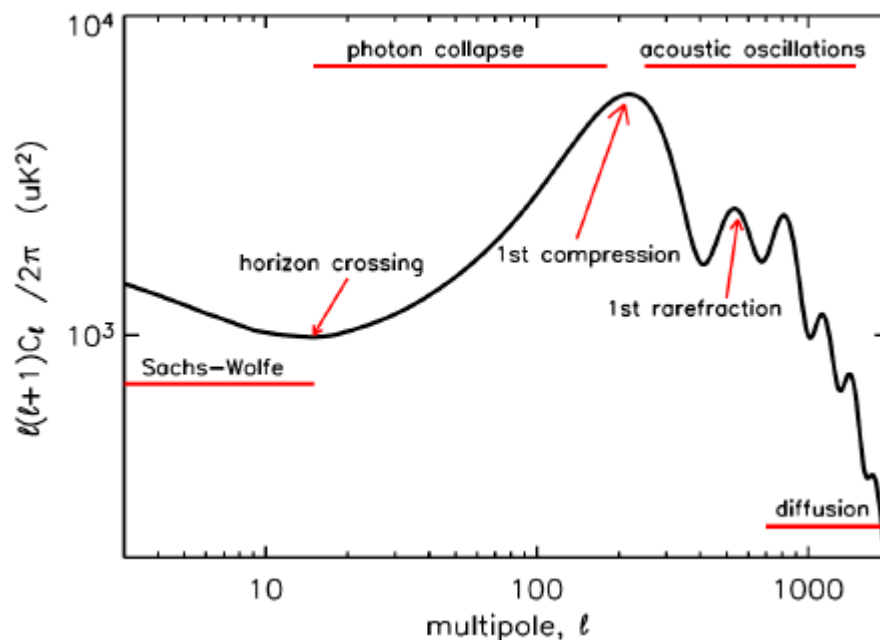


Figure 1.6 An example of the CMB temperature power spectrum with the key features labelled.

The flat region at low multipoles corresponds to angles greater than the horizon size at recombination and is known as the Sachs-Wolfe plateau (White and Cohn, 2002). The fluctuations at these angular scales are due to both scalar perturbations, which are longitudinal waves resulting in density fluctuations, and tensor perturbations, or gravitational waves, predicted by Einstein in 1918 in his Theory of General Relativity. Since tensor fluctuations or primordial gravitational waves are stretched during inflation they are negligible on sub-horizon angular

scales and the temperature fluctuations on these scales are caused by scalar perturbations only.

The importance of the CMB power spectrum is in its shape and in particular the location and relative heights of the acoustic peaks. The location of the first peak in l -space probes the horizon size at decoupling, measuring the geometry of the universe on the largest scale possible leading directly to constraints on Ω_0 , the total energy density of the universe in units of critical density. Other cosmological parameters that are constrained by power spectrum are h - the Hubble constant in units of 100km/s/Mpc, Ω_b - the fractional density of baryonic matter in the universe, Ω_m - the fractional density of matter, including baryonic and dark, and Ω_Λ - the fractional density of dark energy, where $\Omega_\Lambda + \Omega_m = \Omega_0$.

While measuring the temperature anisotropies of the CMB has placed constraints on the cosmological parameters outlined above, degeneracies between some combinations of parameters still exist. Therefore a detailed study of not only the temperature variations but also the polarisation properties of the CMB is required to conclusively distinguish between current theories and accurately constrain cosmological parameters. It is now the goal of CMB experiments to measure the polarisation anisotropies.

CMB Polarisation

The cosmic microwave background has three measurable properties: its frequency spectrum, which has been confirmed to be that of a blackbody at 2.73K; the temperature anisotropies discussed above which have been measured in detail by WMAP; and also anisotropies in polarisation resulting from the temperature fluctuations at recombination. If the temperature anisotropies we observe are the result of primordial fluctuations then their presence at the surface of last scattering would polarise the CMB anisotropies themselves. The verification of this polarisation on small scales would therefore represent a fundamental check on our basic assumptions about the behaviour of fluctuations in the universe and would help

in reconstructing the model of the fluctuations from the observed power spectrum. Also, since the polarisation probes the era of last scattering directly, as opposed to the temperature fluctuations which may evolve over time, the localisation in time provides a powerful constraint for reconstructing the sources of anisotropy.

The degree of linear polarisation of the CMB is related to the quadrupole temperature anisotropy at last scattering (Figure 1.7). In general, if an incident unpolarised photon scatters off an electron, the photon becomes polarised in the plane perpendicular to the incoming direction (Figure 1.8). However, the number of free electrons in universe before recombination meant that photons could only travel relatively short distances before scattering. The temperature of the photons remained uniform over these distances and therefore polarisation was not achieved via Thompson scattering because of the isotropic radiation field. After recombination the mean free path of photons became much greater and it was possible for the scattering of two photons from parts of the sky at different temperatures to scatter off the same electron. In such a case where there is a quadrupole anisotropy (Figure 1.7) in temperature between the photons, polarisation is obtained via anisotropic Thompson scattering. If we consider Figure 1.8, hot radiation is incident on the scattering electron from the above and below, and cooler radiation is incident from the left and right. The result is a wave linearly polarised in the same direction as the hotter photon, that is, in the direction of travel of the cooler photon.

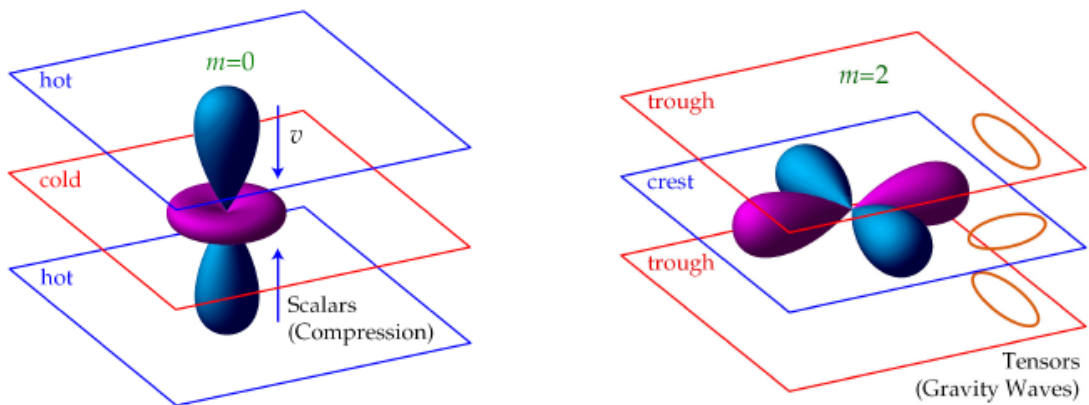


Figure 1.7 Left: An $m=0$ pattern arising from a scalar perturbation. Right: An $m=2$ pattern arising from a tensor perturbation, (Hu and White, 1997).

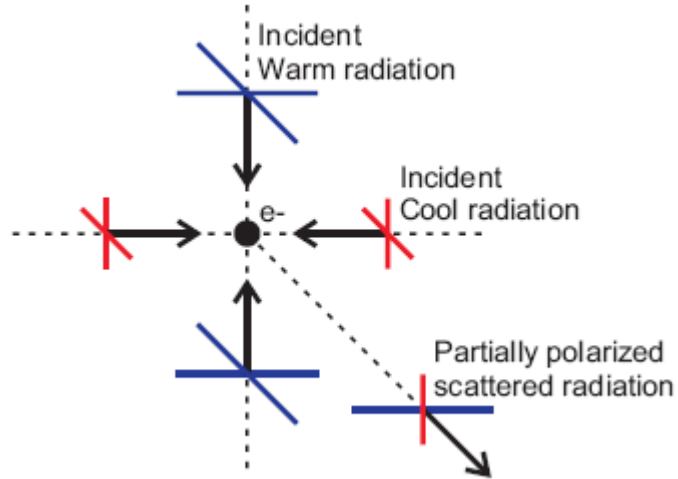


Figure 1.8 Warm radiation is incident from the top and bottom while cooler radiation is incident from the left and right, corresponding to a quadrupole anisotropy in the local temperature distribution. The electron does not scatter radiation polarised along the line of sight (the polarisation must be perpendicular to the outgoing wavevector) leading to a partially polarised outgoing wave (Hinderks, 2005).

The total intensity, I , of the CMB radiation can be decomposed into polarised and unpolarised components, I_p and I_{up} , such that

$$I = I_p + I_{up} \quad (1.2)$$

and the degree of polarisation, p , is defined by the ratio of the polarised intensity to the total intensity

$$p = \frac{I_p}{I}. \quad (1.3)$$

The polarisation pattern of the CMB is generally decomposed into two components. The two linear Stokes parameters Q and U (described in more detail in section 1.4.4) combine on the spherical sky as a tensor which can be decomposed into a scalar field, usually referred to the E mode of polarisation, and a pseudo-scalar field, referred to as the B mode of polarisation (where the V Stokes parameter, which quantifies the degree of circular polarisation present, is expected to be zero for the

CMB). The E and B definitions are chosen by analogy to electric and magnetic fields since B modes have curl and E modes are free from curl (Rusholme *et al.*, 2002). In Figure 1.9 we see the orientation of both polarisations, the B modes being the same as E modes having undergone a 45 degree rotation. Figure 1.10 shows E and B hot spots formed from the superposition of eight properly phased plane waves of the form shown in Figure 1.9 evenly distributed in angle. The handedness of the B modes is apparent, unlike the E modes which are invariant under reflection.

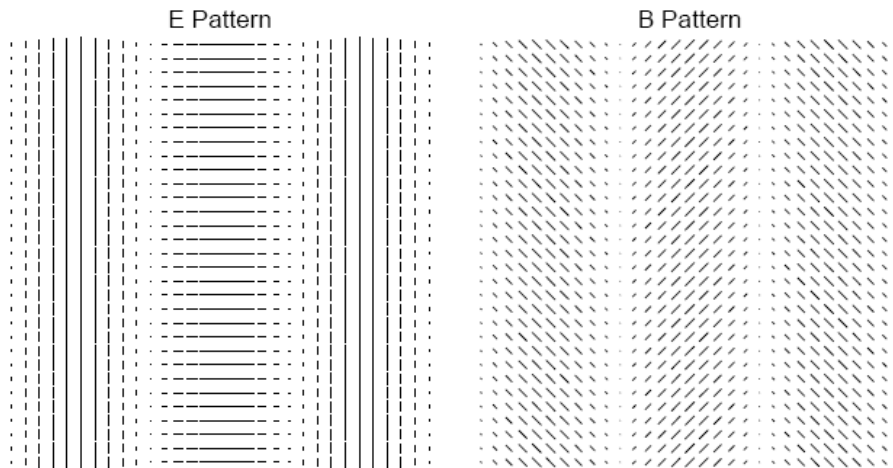


Figure 1.9 Example of E (left) and B (right) plane wave modes (Hinderks, 2005).

This particular decomposition into E and B modes (rather than Q and U) is also physically useful. Scalar perturbations only produce E mode polarisation (Zaldarriaga, 2001) and therefore the E mode signal is dominated by contributions from the density fluctuations in the primordial plasma that are in turn the dominant source of the temperature anisotropy signal. Vector and tensor perturbations result in both E and B mode polarisations (White and Cohn, 2002), but since inflationary models do not support vector perturbations we expect the B mode polarisation to be due to the intrinsic polarisation of gravitational waves, or tensor modes that result in a mixture of Stokes Q and U on the sky (Hu and White, 1997). In fact, the B mode signal has two separate sources, the first being the relic gravitational wave radiation generated in the early universe by inflation and the second being the gravitational lensing of E mode polarisation by intervening foreground structures in the universe. This lensing effect mixes some of the polarised power between E and B modes and

occurs at smaller angular scales where it dominates the expected B mode signal. This sets a limit of approximately 10^{-4} on the values of the tensor to scalar ratio that could be measured even with a perfect instrument (Knox and Song, 2002). If the relic tensor modes lie below this level they cannot be measured from the CMB.

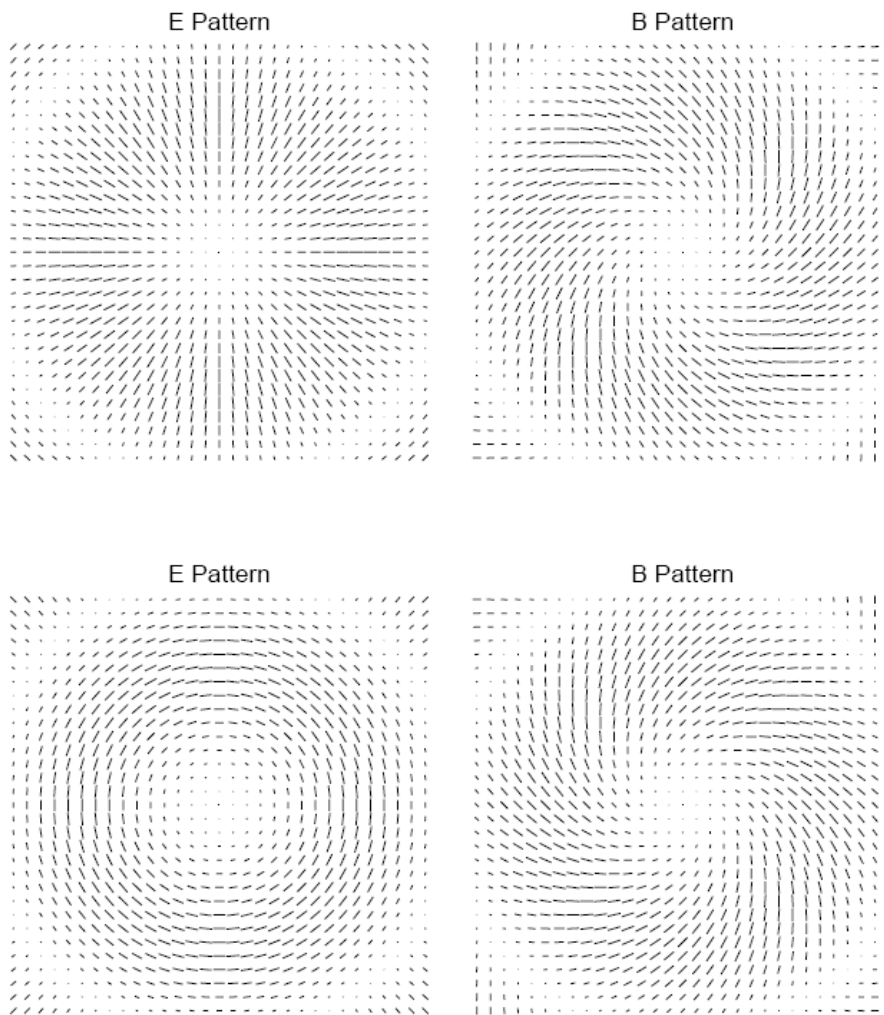


Figure 1.10 E and B hot spots formed from the superposition of plane waves. The handedness of B modes is apparent while the E modes are invariant under reflection (Hinderks, 2005).

The observed polarisation on the sky arises from the superposition of signals from many different scalar and tensor modes with randomly orientated wave vectors and therefore the sky pattern will contain both Stokes Q and U components. These parameters do not allow for easy separation of the contributions from scalar and tensor modes and therefore we use the E - B decomposition mentioned above to

overcome this. This decomposition results in a set of coefficients for the multipole expansion of the polarisation field, E_{lm} and B_{lm} , analogous to the a_{lm} term in Equation 1.1 for the temperature field, from which six power spectra can be formed: C_l^{TT} , C_l^{TE} , C_l^{EE} , C_l^{BB} , C_l^{TB} and C_l^{EB} . The last two of these vanish since the B field has opposite parity to the T and E fields and the remaining four spectra completely describe the two-point statistics of the CMB (Hinderks, 2005). Figure 1.11 shows simulated spectra where it is clearly seen that the E -mode spectrum, which is dominated by scalar perturbations, lies more than an order of magnitude below the temperature spectrum, and as with the temperature spectrum, acoustic oscillations lead to peaks in the E -mode spectrum.

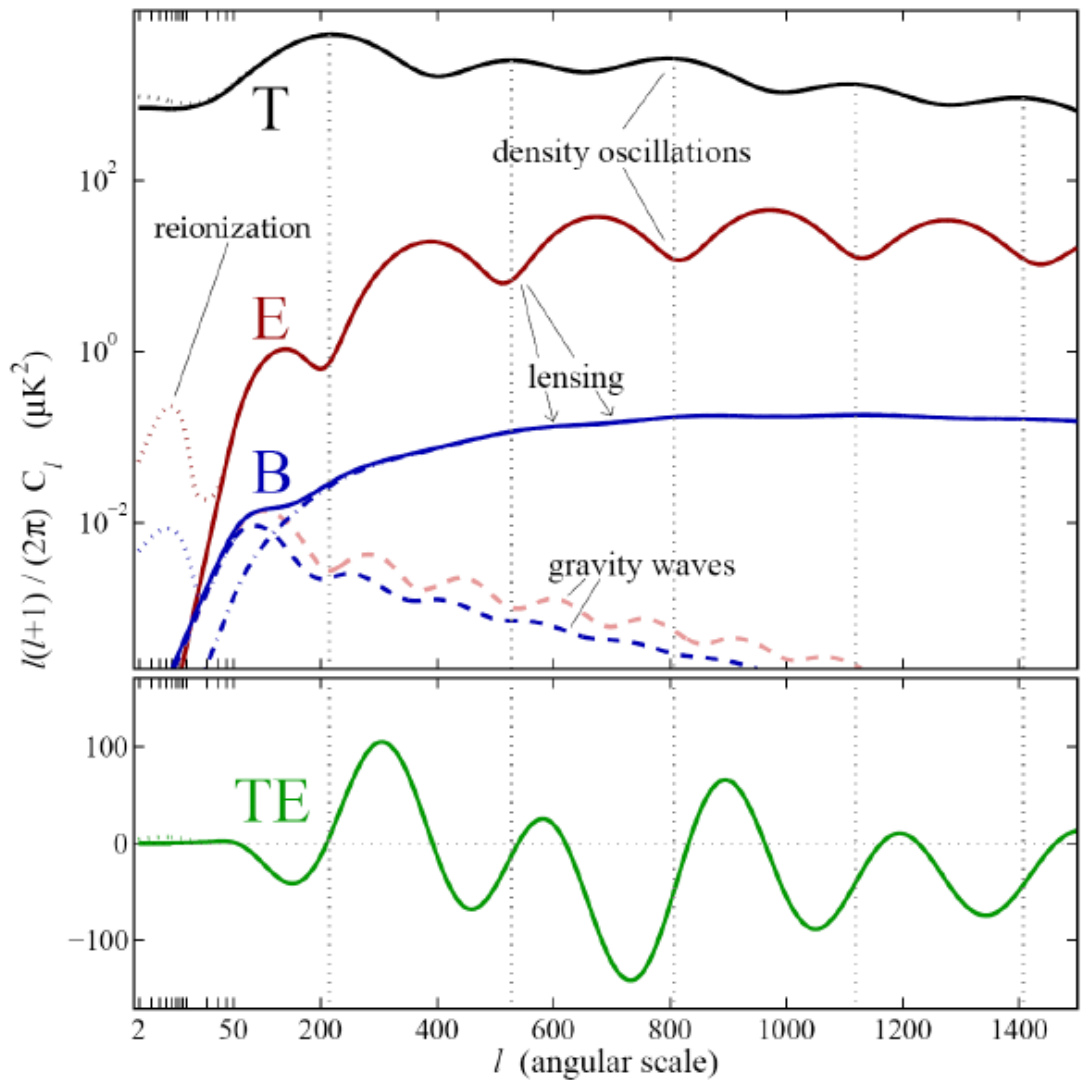


Figure 1.11 The four CMB power spectra for the standard cosmological model. The dashed line shows the gravitational wave contribution to the E and B spectra assuming a value of $r=0.1$. Figure taken from Carlstrom *et al.* (2003).

Since only photons that scattered in an optically thin region near last scattering could have had a quadrupole anisotropy, only a small percentage of the CMB radiation is polarised. The amount of polarisation was predicted to be at a level 10% lower than the temperature anisotropy (Hu and White, 1997), a prediction confirmed by the first polarisation measurements made by DASI (Kovac *et al.*, 2002). While detection of *B* mode polarisation due to gravitational lensing would be a significant achievement in both technology and science, it is the *B* mode polarisation due to gravitational waves that will tell us more about the theory of inflation and is currently the holy grail of cosmology.

In the past 20 years CMB experiments have provided scientists with data which corroborates the theories that have been developed in this area, for example the detection of the peaks in the power spectrum is consistent with the standard cosmological model. However, to conduct further investigation into inflation and dark energy, Figure 1.11 makes it clear that researchers need a new generation of CMB telescopes that can observe the radiation with even greater sensitivity and resolution. In the next section we look at some past, present and future experiments dedicated to characterising the CMB.

1.3.2 Past, Present and Future CMB Experiments

On the 18th November 1989, the Cosmic Background Explorer (COBE) (Figure 1.12) was launched, only the second satellite experiment dedicated to measuring the CMB radiation (the first space experiment was the Relikt on board the Prognoz 9 satellite launched in the 1st of July 1983). There were three instruments on board, a Diffuse Infrared Background Experiment (DIRBE) to search for the cosmic infrared background radiation, a Differential Microwave Radiometer (DMR) to map structure in the cosmic radiation and a Far Infrared Absolute Spectrophotometer (FIRAS) to compare the spectrum of the cosmic microwave background radiation with a precise blackbody.



Figure 1.12 An artist's impression of the Cosmic Background Explorer, COBE (Lawrence Berkley National Laboratory website).

The DMR instrument consisted of six differential microwave radiometers made up of two channels that operated at 31.5GHz, 53GHz and 90GHz (Bennett *et al.*, 1992). Multi-frequency data is required to separate the CMB from foreground signals. Each differential radiometer measured the difference in power received from two directions in the sky separated by 60 degrees using a pair of horn antennas with a 7 degree FWHM beam. The FIRAS instrument was a polarising Michelson interferometer operated differentially with an internal reference blackbody and calibrated by an external blackbody having an estimated emissivity of 0.9999 (Mather *et al.*, 1999). It covered the wavelength range from 0.1 to 10mm in two spectral channels separated at 0.5mm and had approximately 5% spectral resolution.

Each COBE instrument yielded a major cosmological discovery but it was the DMR experiment that found the intrinsic temperature anisotropies of the CMB (Figure 1.13) for the first time at a level of $\Delta T/T = 10^{-5}$. FIRAS also confirmed that the CMB spectrum is that of a nearly perfect blackbody (Figure 1.14) with a temperature of $2.725 \pm 0.002\text{K}$ (Mather *et al.*, 1994), an observation which matches the predictions of the Big Bang theory extremely well.

Almost a decade after the launch of COBE, in 1998 the balloon borne experiment BOOMERanG (Balloon Observations Of Millimetric Extragalactic Radiation ANd Geophysics) (see Figure 1.15) made its first long duration flight over Antarctica. The telescope contained a 1.2m off-axis primary mirror and was flown at an altitude of 120,000ft. The detector system consisted of a bolometric array that was cryogenically cooled to 0.28K and operated at 90GHz, 150GHz, 240GHz and 400GHz. The instrument performed extremely well and mapped 3% of the sky with an angular resolution of 10', forty times finer than COBE (Netterfield *et al.*, 2002). A second flight of 14 days duration made in 2003 in which the instrument was modified to be polarisation sensitive resulted in a statistical detection of the polarisation anisotropies of the CMB.

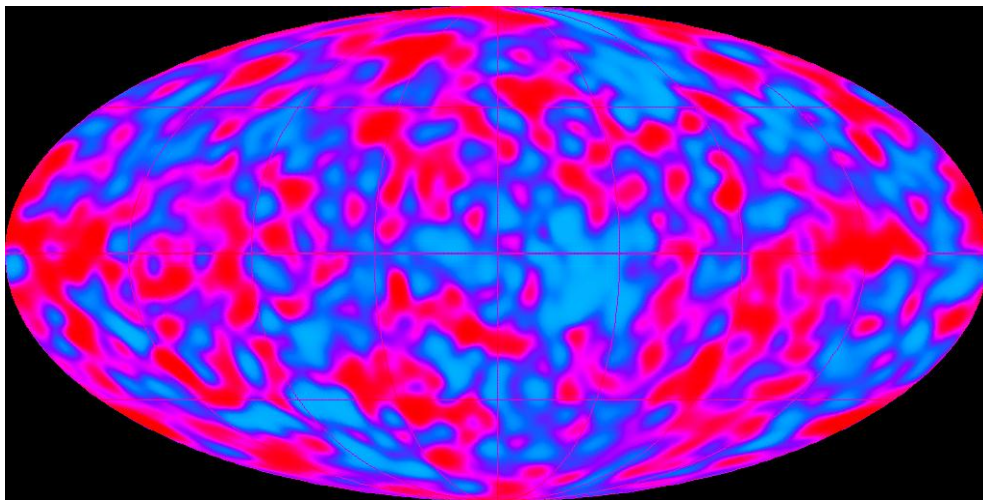


Figure 1.13 The temperature anisotropies in the cosmic microwave background as measured by the Differential Microwave Radiometer (DMR) on board the COBE satellite. The temperature fluctuations are extremely small, only one part in 100,000 compared to the 2.73K average temperature of the radiation field (NASA's Legacy Archive for Microwave Background Data Analysis website).

The next significant satellite experiment after COBE was the Wilkinson Microwave Anisotropy Probe (WMAP) (Figure 1.16), a NASA Explorer mission which was launched on the 6th January 2001. The mission was designed to determine the geometry, content and evolution of the universe via a 13arcminute-FWHM resolution full sky map of the temperature anisotropies of the cosmic microwave background radiation. The WMAP optics consisted of two back-to-back off-axis Gregorian telescopes with 1.4m x 1.6m primary reflectors and 0.9m x 1.0m

secondary reflectors. The radiometric system contained differential polarisation sensitive receivers with HEMT amplifiers used for detection. With its small angular resolution and the ability to measure polarisation anisotropies in the CMB, WMAP has generated full sky maps and discovered that the universe was re-ionised earlier than previously believed. The first results from this experiment were released in February 2003 (Bennett *et al.*, 2003a) and the data derived from the WMAP sky maps has 45 times the sensitivity and 33 times the angular resolution of the COBE DMR mission.

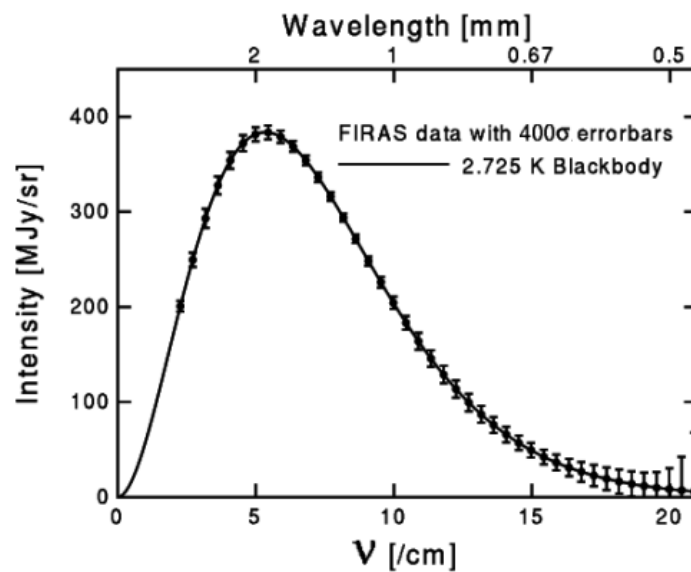


Figure 1.14 The spectrum measured by the FIRAS experiment on board the COBE satellite compared to the theoretical blackbody spectrum for a temperature of 2.725K (Institute for Astronomy at the University of Hawaii website).

Although both the BOOMERanG experiment and WMAP detected the polarisation of the CMB, it was a ground based experiment called DASI (Degree Angular Scale Interferometer) that first detected this small signal during measurements taken in the South Pole winter of 2001 and 2002 (Kovac *et al.*, 2002). DASI was a 13-element interferometer designed to measure the temperature and polarization anisotropy of the CMB over a large range of scales with high sensitivity. The instrument used cooled HEMT amplifiers running between 26GHz-36GHz, in

10 1-GHz channels and operated from the US National Science Foundation's Amundsen-Scott South Pole station.

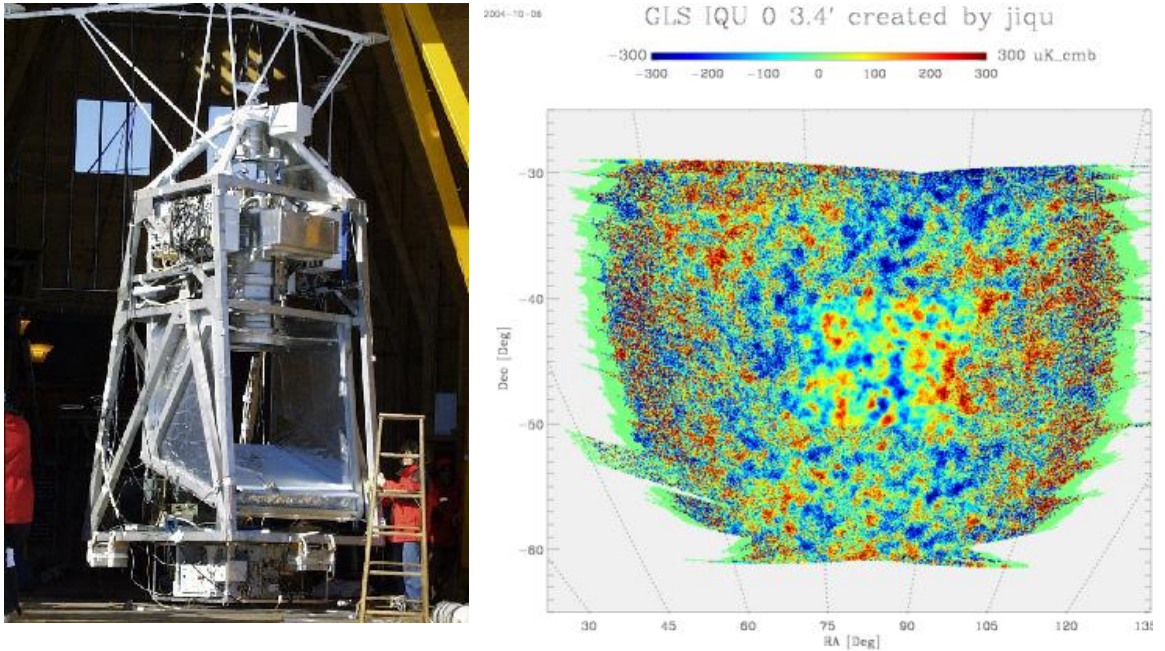


Figure 1.15 Left: The receiver from the BOOMERanG Experiment (Hallym University Dept of Physics website). Right: The polarisation anisotropies of the CMB at 145GHz as measured by BOOMERanG (Caltech Astronomy Department website).

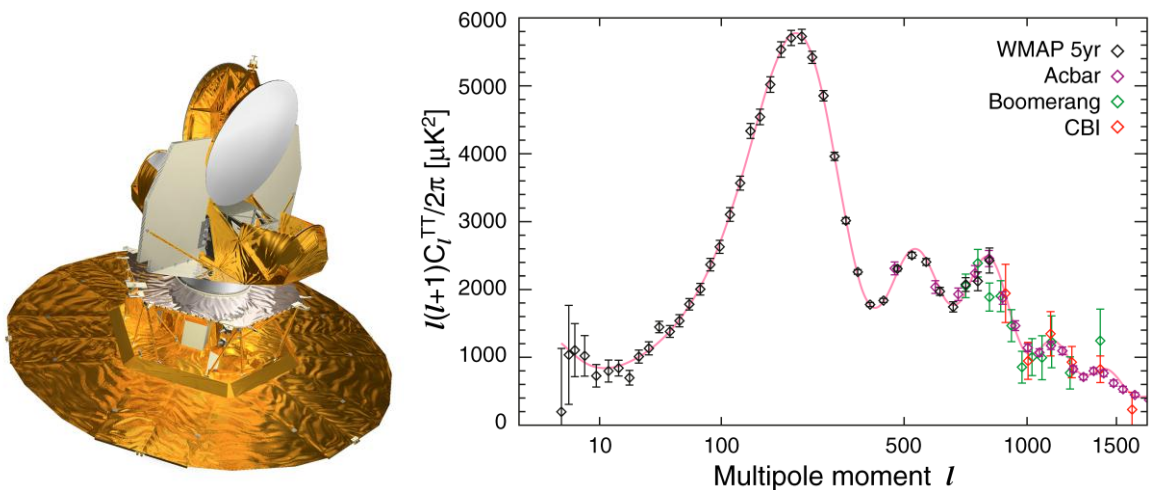


Figure 1.16 Left: An artist's impression of the WMAP satellite (NASA's WMAP website). Right: The WMAP 5-year TT power spectrum along with recent results from the ACBAR (Reichardt *et al.*, 2009, purple), Boomerang (Jones *et al.*, 2006, green), and CBI (Readhead *et al.*, 2004a, red) experiments. The curve is the best-fit Λ CDM model to the WMAP data (Nolta *et al.*, 2009).



Figure 1.17 The Degree Angular Scale Interferometer (DASI) located at the US National Science Foundation's Admunsen-Scott South Pole station (Chicago University Department of Astronomy and Astrophysics website).

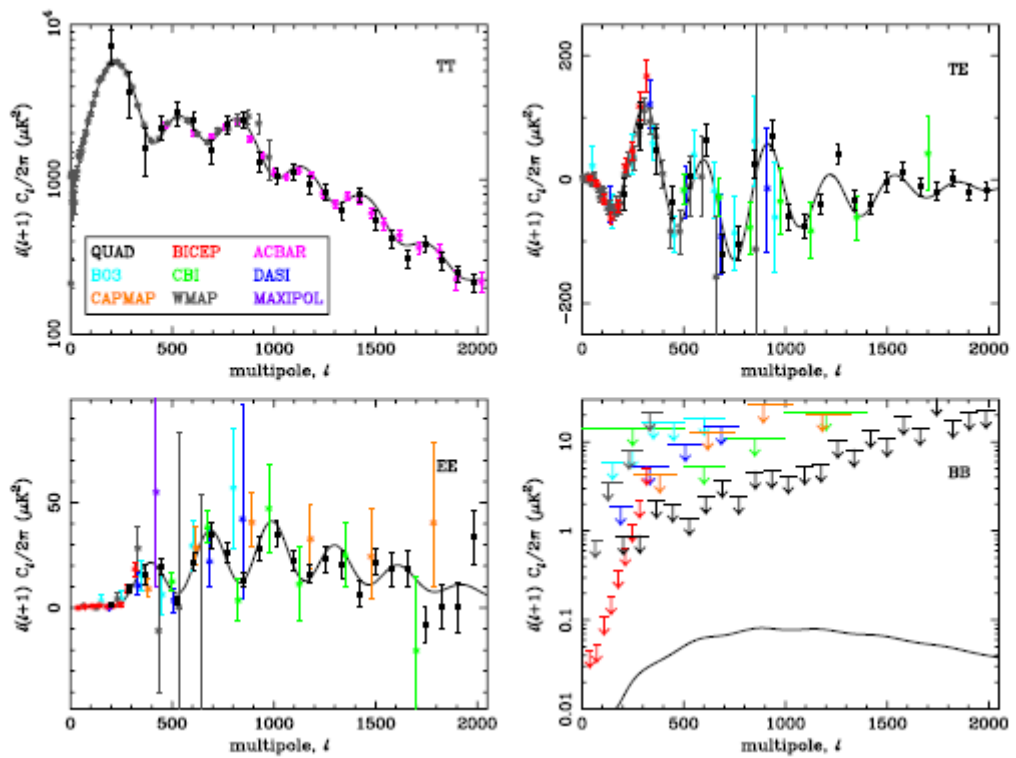


Figure 1.18 QUaD measurements of the TT , TE , EE , and BB power spectra compared to results from the WMAP, ACBAR, BICEP, B03, CBI, CAPMAP, MAXIPOL, and DASI experiments (Brown *et al.*, 2009). The BB measurements are plotted as 95% upper limits. The smooth black curves in each panel are the power spectra expected in the best-fit Λ CDM model to the WMAP 5-year data.

Even more sensitive instruments have been deployed in the last number of years. Between 2005 and 2007 the QUaD (Quest at DASI) experiment (see Figure 1.17), also situated at the US National Science Foundation's Admunsen-Scott South Pole station and which the research group at NUI Maynooth were heavily involved (O'Sullivan *et al.*, 2008), has made high precision measurements of the E-mode polarisation of the CMB radiation. QUaD is a bolometer-based polarimeter optimized for CMB polarization measurements. It uses an on-axis Cassegrain design with an under-illuminated 2.6m primary mirror for an angular resolution of 4.6arcmin at 150GHz. The focal plane consisted of thirty-one corrugated feed horns, each feeding a polarisation-sensitive bolometer (PSB) pair which measures the intensity of the radiation in orthogonal linear polarisations as the telescope scans across the sky. These signals are then processed into a map of the polarisation pattern on the sky. The results obtained by QUaD (Figures 1.18 and 1.19) agree well with the predictions made by the standard cosmological model in which the content of the universe is dominated by dark matter (Stanford University QUaD website).

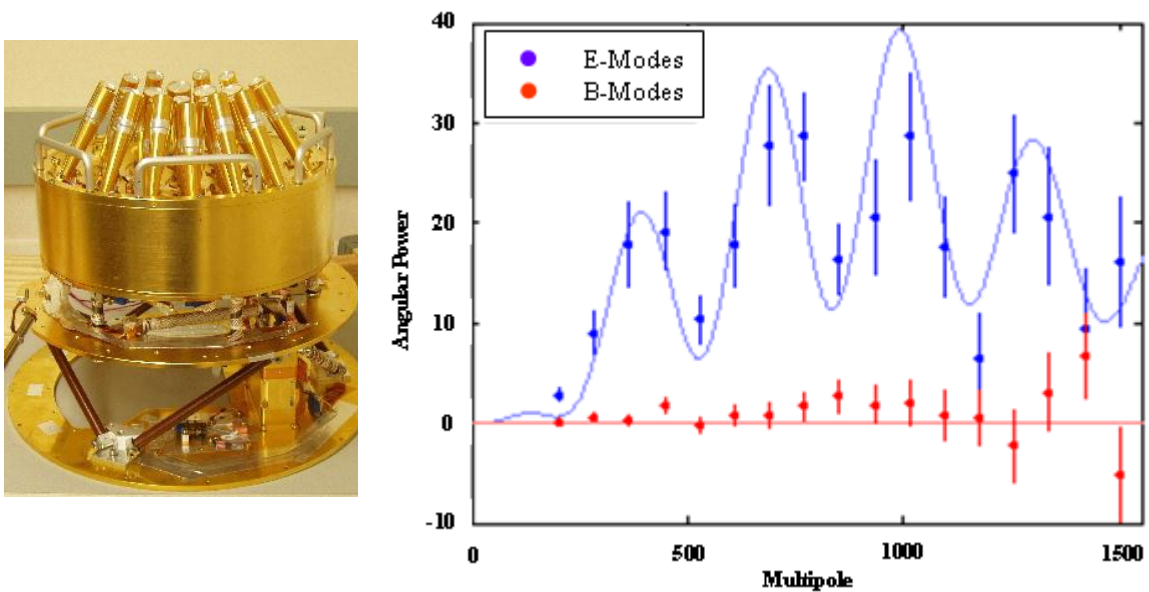


Figure 1.19 Left: The focal plane of the QUaD telescope with 31 corrugated feed horn antennas (Stanford University QUaD website). Right: The process of the gravitational collapse of clumps while the universe is very hot sets up certain resonances in the matter that causes the polarization patterns to be particularly strong for clumps of a particular size. These resonances can be seen in the graph, which shows the polarization strength as a function of the angular size of the clump on the sky. The solid line shows the predictions of the standard cosmological model, and the points show the QUaD measurements (Stanford University QUaD website).

Further to this, the PLANCK Surveyor satellite (Figure 1.20) was launched on the 14th May 2009 having been selected as the third Medium-Sized Mission (M3) of ESA's Horizon 2000 Program and is today part of its Cosmic Vision Program. It is designed to image both the temperature and polarisation anisotropies of the cosmic microwave background radiation over the whole sky with unprecedented sensitivity and angular resolution (5') over a wide frequency range (Tauber, 2005) and will provide more information than any other CMB experiment to date.

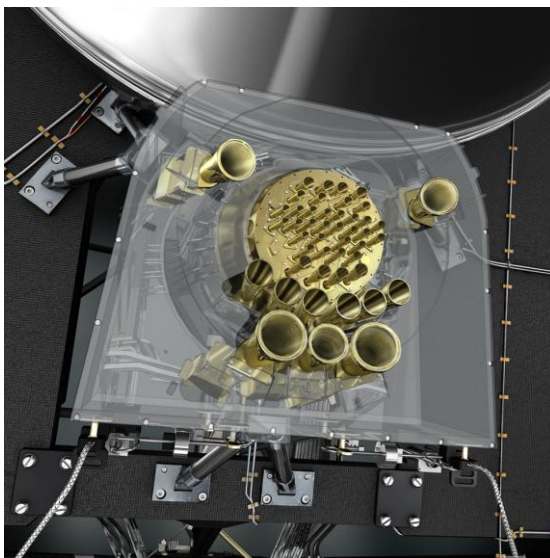


Figure 1.20 Left: Artist's impression of the PLANCK focal plane which is located directly below the telescope primary mirror (visible at the top). It comprises the HFI bolometric detector array (small feed horns on golden circular base) and the LFI radio receiver array (larger feed horns around the HFI). The box holding the feed horns is made transparent in this view, to also show the elements inside and behind it (ESA's PLANCK website). Right: The satellite just after mating with the Ariane 5 ECA launcher (ESA's PLANCK website).

The PLANCK experiment has ten times the sensitivity and more than fifty times the angular resolution (5' for most channels) of the COBE satellite. There are two instruments on board: the High Frequency Instrument (HFI) and the Low Frequency Instrument (LFI), which are fed by a 1.5m Gregorian telescope system with an optical configuration that minimises off-axis distortions. LFI consists of an

array of radio receivers cooled to 20K by a scorpion cooler and sensitive to radiation in the frequency range of 30 to 70GHz. Its best angular resolution is 10' and its temperature sensitivity is 12mK. This array forms a ring around the HFI detectors as shown in Figure 1.20. HFI consists of an array of thirty-six back-to-back horn antennas, sixteen of which are coupled to polarisation sensitive bolometric detectors. The HFI detectors are split into six channels centred on the following frequencies: 100GHz, 143GHz, 217GHz, 353GHz, 545GHz and 857GHz, each with a 33% bandwidth (some of the higher frequencies are not sensitive to polarisation), and were chosen so that contaminating foregrounds can be determined to provide accurate measurements of the CMB radiation. Although PLANCK will essentially extract all the scientific information possible from temperature anisotropies it will not do this for polarisation and is very unlikely to measure *B*-modes (it will however provide much information on polarised foregrounds). The research group at NUI Maynooth was heavily involved in the design of the corrugated horn antennas for all channels of the HFI instrument on board the PLANCK Surveyor (Gleeson, 2004).

Considerable progress in the field of observational cosmology has clearly been made over the last 20 years and the push is now on to commission a new generation of still more sensitive instruments to detect and measure the *B*-modes. To achieve this sensitivity new techniques are being tested and this thesis describes two experiments that use one promising technique: bolometric interferometry. The two instruments making use of this novel approach to measuring CMB polarisation characteristics are the Millimetre-Wave Bolometric Interferometer (MBI) and the Q U Bolometric Interferometer for Cosmology (QUBIC). MBI is acting as a pathfinder for the EPIC mission, a concept formed as part of NASA's Physics of the Cosmos program, formerly the Beyond Einstein program. The QUBIC instrument is a joint venture between Europe and the United States and it is hoped that a first module will see light in the summer of 2011. A detailed discussion on both of these instruments is given in Chapters 3 to 6.

This is a summary of a selection of past and present instruments dedicated to measuring the temperature and polarisation anisotropies of the cosmic microwave background radiation. Although only a few experiments are outlined here it provides

Name	Year Deployed	Frequency (GHz)	Angular Scale (l)	Detection Type	Measured Quantity (T=Temperature, P=Polarisation)
Ground-Based Experiments					
CAT	1994	13.5-16.5	300-500	Interferometer	T
ACBAR	2001	150-274	200-3000	Bolometer	T
DASI	2001	26-36	100-900	Interferometer	T and P
CAPMAP	2002	40, 90	1800-3000	MMIC/HEMT	T and P
CBI	2002	26-36	300-3500(T) 400-4250(P)	Interferometer	T and P
VSA	2002	26-36	150-1800	Interferometer	T
QUEST	2005	100-150	25-2500	Bolometer	P
AMiBA	2007	86-102	800-8000	Interferometer	T and P
SPT	2007	150	11000	Bolometer	T and P
ACT	2008	148-277	8000	Bolometer	T
AMI	Future	12-18	1080-22000	Interferometer	T
QUIET	Future	40-90	180-1800	HEMT	T and P
SZA	Future	26-115	>1500	Interferometer	T
Balloon-Borne Experiments					
MAXIMA	1995	150-420	36-1080	Bolometer	T
QMAP	1996	30-140	900	HEMT/SIS	T
BOOMERanG	1997	90-410	25-1200	Bolometer	T
Archeops	1999	143-545	10-1000	Bolometer	T and P
BOOMERanG03	2003	145-345	25-1800	Bolometer	P
EBEX	Future	150-450	1350	Bolometer	T and P
SPIDER	Future	90-210	180	Bolometer	P
Satellite Experiments					
RELIKT	1983	37	33	Radiometer	T
COBE	1989	31.5-90	2-30	Radiometer	T
WMAP	2001	23-94	2-9000	Radiometer	T and P
PLANCK	2009	30-857	2-2000	Bolometer	T and P

Table 1.2 A sample of past, present and future experiments to measure the cosmic microwave background radiation.

a clear illustration of the importance of these measurements and the improvements in technology that have been made over the last two decades. With such improvements

instruments are becoming much more sensitive to signals with smaller amplitudes, not least from the reduced cost of making detectors and components due to the evolution in manufacturing technologies, something which will be necessary if the elusive B modes are to be measured in full. Table 1.2 provides a more comprehensive list of CMB experiments and it can be clearly seen that significant progress has been made and will hopefully continue to be made moving into the future with advancements in technology and a better understanding of the cosmological model.

1.3.3 Other Applications of Terahertz Imaging

Applications of THz radiation are also being implemented in a wide range of fields outside the traditional niches of space science and molecular line spectroscopy. These include biomedical imaging, defence and security, and the detection of narcotics. A summary of some of these applications, which is given by White (White, 2006), is outlined below and shows the importance of exploring this region of the spectrum further. The results of work in this thesis will be useful for the design of THz optical system in general.

THz radiation is non-ionizing and not highly scattered in tissues, therefore making it attractive for use in biomedical applications such as Terahertz Pulsed Imaging or TPI (Pickwell and Wallace, 2006). TPI is a novel, noninvasive, imaging modality that uses pulses of electromagnetic radiation in the frequency range of 0.1 to 10THz (Mogensen and Jemec, 2007) and has been used to image a variety of human tissues such as teeth, skin and breast. The sensitivity of THz absorption to water content of a sample as a means of extracting medically useful information has been investigated by the THz Optics group at NUI Maynooth (McAuley *et al.*, 2006) and the development in the last few years of practical methods to generate and detect broadband pulses of THz radiation that can be contained within portable systems suitable for clinical studies has led to its use in the detection of skin and breast cancers (Fitzgerald *et al.*, 2006). In a study to compare THz images with results from standard histological examinations to determine the feasibility of this technique

in diagnosing colon cancer results showed, for the first time, that images generated with radiation in the THz range can reliably distinguish between normal colon, tumour, and even dysplastic tissue in excised tissue samples.

Other areas making use of radiation at THz frequencies are the identification of explosive and biological materials using THz reflective time domain spectroscopy (THz-RTDS) (Wang *et al.*, 2009) and the detection of concealed weapons using stand-off imaging system (Luukanen, 2010).

1.4 Interference and Polarisation

Radiation at THz frequencies experiences the same interference and polarisation phenomena as other forms of electromagnetic radiation. If we are to understand the polarisation characteristics of the cosmic microwave background and the bolometric interferometers that are being designed to make measurements of such characteristics then it is important to understand both interference and polarisation effects. In the next few sections we look at interference and the operation of an interferometer as well as polarisation and the Stokes parameters that the interferometer can measure.

1.4.1 Interference and the Interferometer

Interference is the combining of two or more waves that meet in one point in space. When two harmonic waves of the same frequency and wavelength but differing in phase combine, the resultant wave is also harmonic and its amplitude depends on the phase difference. The phase difference $\delta\phi$ between the two waves is often the result of a difference in path length Δr , where in general

$$\delta\phi = \frac{\Delta r}{\lambda} 2\pi. \quad (1.4)$$

The superposition of beams of strictly monochromatic light always gives rise to interference, however, light produced from a real physical source is never strictly monochromatic. The amplitude and phase undergo irregular fluctuations which are much too fast for the eye or a physical detector to follow (Born and Wolf, 1999). If the two beams originate from the same source, the fluctuations are in general correlated and the beams are said to be completely or partially coherent, depending on whether the correlation is complete or partial. If the beams originate from different sources then the fluctuations are completely uncorrelated and the beams are said to be mutually incoherent and so no interference is observed.

The superposition principle states that if the function Ψ_1 and Ψ_2 are separate solutions to the wave equation,

$$\frac{\partial^2 \Psi}{\partial x^2} = \frac{1}{v^2} \frac{\partial^2 \Psi}{\partial t^2}, \quad (1.5)$$

where v is the speed of the wave, then the sum of these functions ($\Psi_1 + \Psi_2$) is also a solution. In accordance with this, the electric field \mathbf{E} at a point in space arising from separate fields $\mathbf{E}_1, \mathbf{E}_2, \dots$ of various contributing sources is given by

$$\mathbf{E} = \mathbf{E}_1 + \mathbf{E}_2 + \dots \quad (1.6)$$

Since the field \mathbf{E} varies in time extremely quickly it is very difficult to detect its phase. However, the irradiance or intensity can be measured using physical sensors such as photocells or bolometers. This intensity of light is defined as the time average (T) of the amount of energy which crosses in unit time a unit area perpendicular to the direction of energy flow (Born and Wolf, 1999) and is proportional to the square of the amplitude of the electric field (Hecht, 1998),

$$I = \varepsilon_0 c \langle \mathbf{E}^2 \rangle_T. \quad (1.7)$$

Within a linear, homogeneous, isotropic dielectric, this expression for the intensity becomes

$$I = \epsilon v \langle \mathbf{E}^2 \rangle_T. \quad (1.8)$$

Consider the case of two monochromatic waves of the same frequency propagating in a homogeneous medium. The separation a between the sources (S_1 and S_2) of these waves is much greater than the wavelength λ and the point of observation P is sufficiently far from the sources so that at that point the wavefronts will be planar as shown in Figures 1.21 and 1.22. We will consider only linearly polarised waves of the form

$$\mathbf{E}_1(\mathbf{r}, t) = \mathbf{E}_{01} \cos(\mathbf{k}_1 \cdot \mathbf{r} - \omega t + \epsilon_1) \quad (1.9)$$

and

$$\mathbf{E}_2(\mathbf{r}, t) = \mathbf{E}_{02} \cos(\mathbf{k}_2 \cdot \mathbf{r} - \omega t + \epsilon_2). \quad (1.10)$$

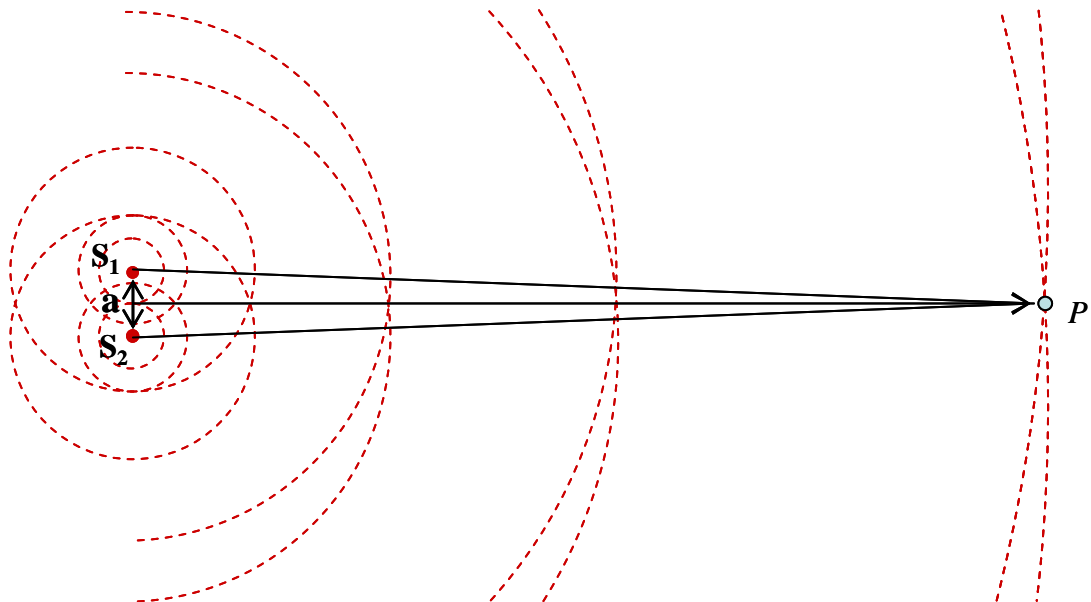


Figure 1.21 Waves from two point sources create approximately plane waves at the point P some large distance away.

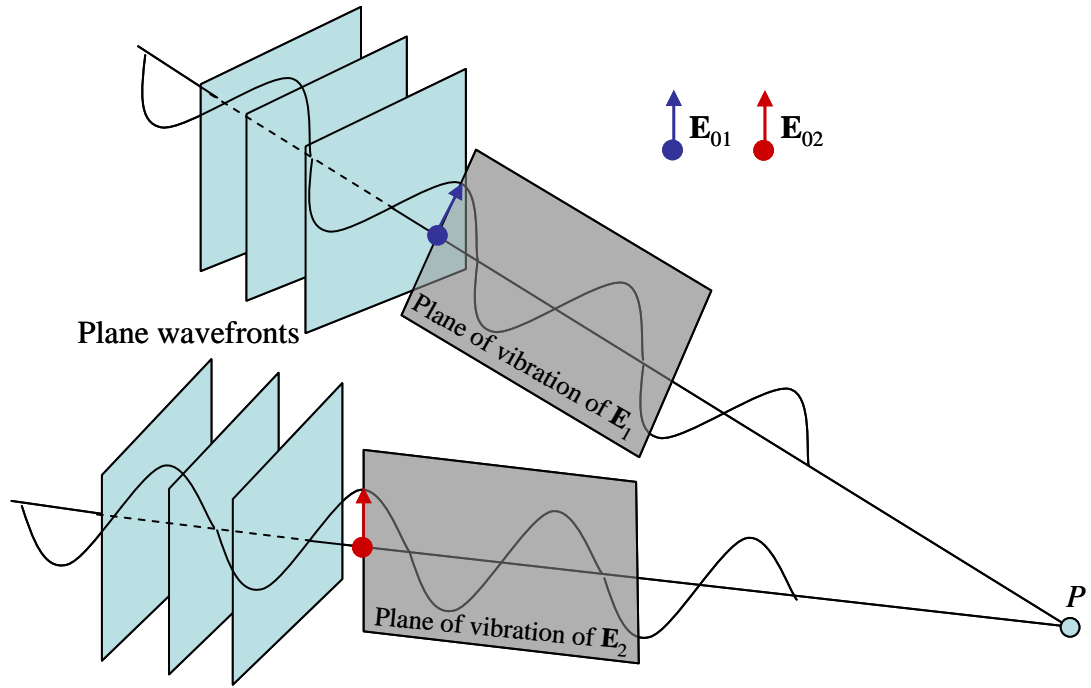


Figure 1.22 Plane wavefronts approaching point P with \mathbf{E}_{01} and \mathbf{E}_{02} depicting polarisation directions.

Since we are concerned only with relative irradiances or intensities within the same medium, we can neglect the constants in Equation 1.8 and write

$$I = \langle \mathbf{E}^2 \rangle_T \quad (1.11)$$

where

$$\mathbf{E}^2 = \mathbf{E} \cdot \mathbf{E} \quad (1.12)$$

or in this case

$$\mathbf{E}^2 = (\mathbf{E}_1 + \mathbf{E}_2) \cdot (\mathbf{E}_1 + \mathbf{E}_2) \quad (1.13)$$

and consequently

$$\mathbf{E}^2 = \mathbf{E}_1^2 + \mathbf{E}_2^2 + 2\mathbf{E}_1 \cdot \mathbf{E}_2. \quad (1.14)$$

Taking the time average of both sides yields

$$\langle \mathbf{E}^2 \rangle = \langle \mathbf{E}_1^2 \rangle + \langle \mathbf{E}_2^2 \rangle + 2\langle \mathbf{E}_1 \cdot \mathbf{E}_2 \rangle \quad \text{or} \quad I = I_1 + I_2 + I_{12} \quad (1.15)$$

where $I_{12} = 2\langle \mathbf{E}_1 \cdot \mathbf{E}_2 \rangle$ is known as the *interference term* (Born and Wolf, 1999). To evaluate this term we start by writing

$$\mathbf{E}_1 \cdot \mathbf{E}_2 = \mathbf{E}_{01} \cdot \mathbf{E}_{02} \cos(\mathbf{k}_1 \cdot \mathbf{r} - \omega t + \varepsilon_1) \times \cos(\mathbf{k}_2 \cdot \mathbf{r} - \omega t + \varepsilon_2) \quad (1.16)$$

or equivalently

$$\begin{aligned} \mathbf{E}_1 \cdot \mathbf{E}_2 = & \mathbf{E}_{01} \cdot \mathbf{E}_{02} [\cos(\mathbf{k}_1 \cdot \mathbf{r} + \varepsilon_1) \times \cos(\omega t) + \sin(\mathbf{k}_1 \cdot \mathbf{r} + \varepsilon_1) \\ & \times \sin(\omega t)] \times [\cos(\mathbf{k}_2 \cdot \mathbf{r} + \varepsilon_2) \times \cos(\omega t) + \sin(\mathbf{k}_2 \cdot \mathbf{r} + \varepsilon_2) \times \sin(\omega t)] \end{aligned} \quad (1.17)$$

The time average of some function $f(t)$ taken over an interval T is given by

$$\langle f(t) \rangle = \frac{1}{T} \int_t^{t+T} f(t') dt' . \quad (1.18)$$

The period, τ , of the harmonic functions is $2\pi/\omega$ and we assume $T \gg \tau$. In this case the $1/T$ coefficient in front of the integral has a dominant effect. If we also assume that $\langle \cos^2 \omega t \rangle_T = \frac{1}{2}$, $\langle \sin^2 \omega t \rangle_T = \frac{1}{2}$ and $\langle \cos \omega t \sin \omega t \rangle_T = 0$ we can use these to multiply out and average Equation 1.17 to give

$$\langle \mathbf{E}_1 \cdot \mathbf{E}_2 \rangle_T = \frac{1}{2} \mathbf{E}_{01} \cdot \mathbf{E}_{02} \cos(\mathbf{k}_1 \cdot \mathbf{r} + \varepsilon_1 - \mathbf{k}_2 \cdot \mathbf{r} - \varepsilon_2). \quad (1.19)$$

The interference term is then

$$I_{12} = \mathbf{E}_{01} \cdot \mathbf{E}_{02} \cos \delta \quad (1.20)$$

where δ is equal to $(\mathbf{k}_1 \cdot \mathbf{r} + \varepsilon_1 - \mathbf{k}_2 \cdot \mathbf{r} - \varepsilon_2)$ and represents the phase difference arising from the combined path length and initial phase angle difference.

If we consider the situation where \mathbf{E}_{01} and \mathbf{E}_{02} are parallel the irradiance can be reduced to a scalar expression given by

$$I_{12} = E_{01} \cdot E_{02} \cos \delta. \quad (1.21)$$

We can also write

$$I_1 = \langle \mathbf{E}_1^2 \rangle_T = \frac{E_{01}^2}{2} \quad \text{and} \quad I_2 = \langle \mathbf{E}_2^2 \rangle_T = \frac{E_{02}^2}{2} \quad (1.22)$$

and therefore the interference term becomes

$$I_{12} = 2\sqrt{I_1 I_2} \cos \delta \quad \text{and} \quad I_2 = \langle \mathbf{E}_2^2 \rangle_T = \frac{E_{02}^2}{2} \quad (1.23)$$

whereby the total irradiance is

$$I = I_1 + I_2 + 2\sqrt{I_1 I_2} \cos \delta. \quad (1.24)$$

At various points in space the total irradiance can be greater than, less than or equal to $I_1 + I_2$, depending on the interference term, or more appropriately the phase difference δ . A maximum irradiance is obtained when $\cos \delta = 1$, which occurs when $\delta = 0, \pm 2\pi, \pm 4\pi, \dots$, in other words the waves are in phase which results in total constructive interference. A minimum irradiance is obtained when the waves are 180° out of phase, that is, when $\delta = \pm\pi, \pm 3\pi, \pm 5\pi, \dots$ and this is referred to as total destructive interference.

The observation of such interference between electromagnetic waves experimentally requires the use of an interferometer. As mentioned above, the two beams experiencing the interference need to be derived from the same source and there are two ways of doing this. The first method is to divide the wavefront of a beam from a single source into separate sources, as in Young's double-slit

experiment (see section 1.4.2) or as is done by using a diffraction grating. This method is known as *division of wavefront* and is carried out by a wavefront-splitting interferometer. The second technique is called *division of amplitude* and involves dividing the amplitude of the single incident beam onto the amplitude-splitting interferometer by means of partial reflection, obtaining identical wavefronts that can be brought together by different paths. Amplitude-splitting interferometers include the Michelson spectral interferometer and the Fabry-Perot interferometer while wavefront-splitting interferometers include the Rayleigh and Fizeau interferometers.

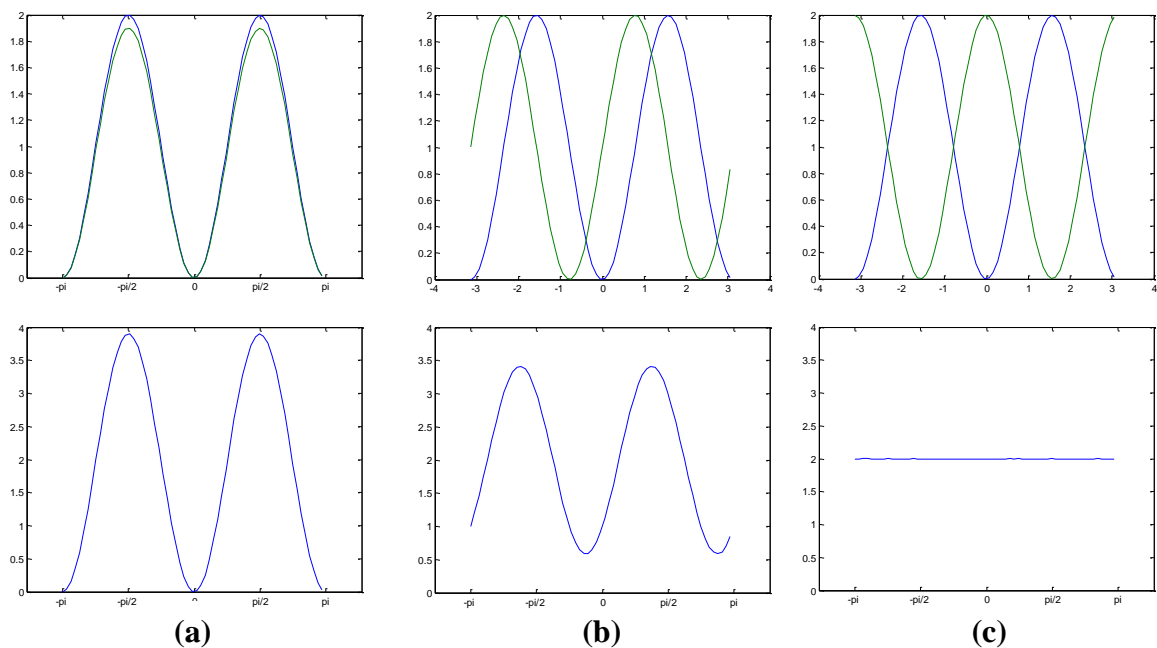


Figure 1.23 The fringe pattern formed (bottom) when two separate fringe patterns (top) from individual sources are superimposed. Part (a) shows the peaks coinciding while parts (b) and (c) show the peaks at different degrees of displacement. The off-axis distance is given on the x -axis of each plot while the intensity is shown on the y -axis.

Armand Fizeau (1819–1896) carried out an experiment in 1868 which was developed further by Michelson twenty years later (Tolansky, 1973). Fizeau considered what would happen if the light from two separate sources, for example two stars close to each other, were observed at a single wavelength. As mentioned earlier there would be no coherence between two such sources and therefore no interference would occur. However, it is possible to produce interference fringes from each source separately and superpose the two systems. Assuming the two sources are of similar intensity then one system can be moved relative to the other

and the fringes will experience constructive or destructive interference as shown in Figure 1.23. In part (a) the peaks of the two systems coincide and clear bright fringes are produced. Part (b) shows that if the systems are displaced by approximately one quarter of a fringe then a broadened pattern occurs, and finally a one-half fringe displacement as in part (c) results in uniform illumination and the fringes disappear.

We have so far seen that the creation of a fringe pattern from the interference of two or more sources of light can be achieved through the use of various types of interferometer. In the next section we discuss the Fizeau interferometer in more detail since it is this type of device that is used as a beam combiner in MBI-4.

1.4.2 The Fizeau Interferometer

In an interferometer with an array of $N > 2$ antennas the signals are combined in such a way that interference fringes are measured for all possible baselines ($N(N-1)/2$ antenna pairs). This beam combination can occur in two different ways: *pairwise* combination or *all-in-one* combination (Zmuidzinas, 2003). In the first method the power from each of the N antennas in the array is split $N-1$ ways, adding the signals in a pairwise fashion, squaring the signals and extracting the interference term. This disadvantage of this method lies in the fact that it produces extremely low signal levels at each of the required $N(N-1)/2$ detectors (Timbie and Tucker, 2008).

In the case of the all-in-one method of combination, the signals from each antenna are split and combined in such a way that linear combinations of all the antennas signals are formed at each of the outputs of the beam combiner (Figure 1.24). This method avoids the problem of large numbers of detectors and the low signal levels that are evident in the pairwise scheme. Orthomode transducers (OMT's) are inserted after the antennas to allow the Stokes parameters to be determined simultaneously.

A Fizeau interferometer uses the all-in-one method of combining beams where the signals from redundant baselines can be added together to improve the signal-to-noise ratio at each bolometer compared to the pairwise combination method (Charlassier *et al.*, 2008). The signals reaching each bolometer are multiplexed in such a way that a portion of the visibility of each baseline appears at each bolometer. When the signals are combined the resultant sensitivity is comparable to that of a filled-dish with an array of bolometers coupled to the same number of modes (N) on the sky (Zmuidzinas, 2003). All-in-one systems process antenna signals in two different ways. In the first mode of operation the signals from different antennas are interfered to measure the visibility for each baseline, where each visibility selects a narrow range of l (multipole) values and has no response to very low multiples. The second mode is used to measure large spatial frequencies (low l) and involves combining signals from each antenna with other signals from the same antenna (autocorrelation).

In MBI-4 the Fizeau beam combiner is essentially a Cassegrain telescope where all the signals from feed horn antennas illuminate the primary mirror and are correlated on an array of detectors at the focal plane.

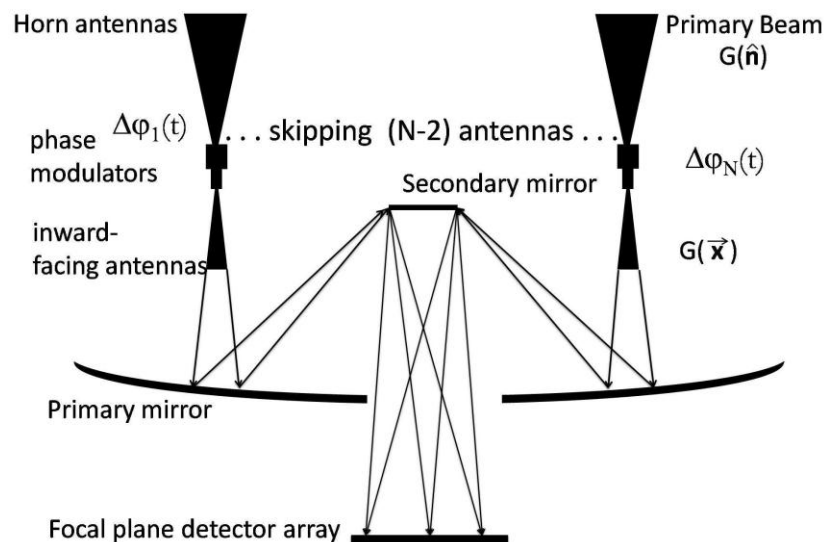


Figure 1.24 A schematic diagram of a Fizeau adding interferometer with $N > 2$ where the top triangles represent corrugated conical horn antennas (Malu and Timbie, 2010).

1.4.3 Polarisation

Light propagates as a transverse electromagnetic wave and the polarisation of this wave is a description of the behaviour of the electric field vector \mathbf{E} in the plane (generally called the xy plane) that is perpendicular to the direction of propagation, generally z (Smith and King, 2000). The plane of polarisation is defined as the plane containing the ray, i.e. the z -axis, and the electric field vector. If the vector \mathbf{E} remains in a fixed direction the wave is said to be linearly or plane polarised, if it changes randomly in time then the wave is randomly polarised or unpolarised. The vector \mathbf{E} can also rotate uniformly in the xy -plane giving rise to circular polarisation, either right or left-handed, depending on the direction of rotation, and a combination of plane and circular polarisations results in elliptical polarisation.

Let us first consider linear polarisation and let two orthogonal optical disturbances be represented by,

$$\mathbf{E}_x(z, t) = \hat{\mathbf{i}}E_{ox} \cos(kz - \omega t) \quad (1.25)$$

and

$$\mathbf{E}_y(z, t) = \hat{\mathbf{j}}E_{oy} \cos(kz - \omega t + \varepsilon) \quad (1.26)$$

where ε is the relative phase difference between the waves meaning E_y lags E_x when $\varepsilon > 0$ and E_y leads E_x when $\varepsilon < 0$. The resultant field is the vector sum of the individual waves,

$$\mathbf{E}(z, t) = \mathbf{E}_x(z, t) + \mathbf{E}_y(z, t) \quad (1.27)$$

or in the case where both waves are in phase Equation 1.27 can be written as

$$\mathbf{E} = (\hat{\mathbf{i}}E_{ox} + \hat{\mathbf{j}}E_{oy}) \cos(kz - \omega t). \quad (1.28)$$

From this we can see that the resultant wave has a fixed amplitude given by $|\hat{\mathbf{i}}E_{ox} + \hat{\mathbf{j}}E_{oy}|$ which means that this wave is also linearly polarised as shown in Figure 1.25.

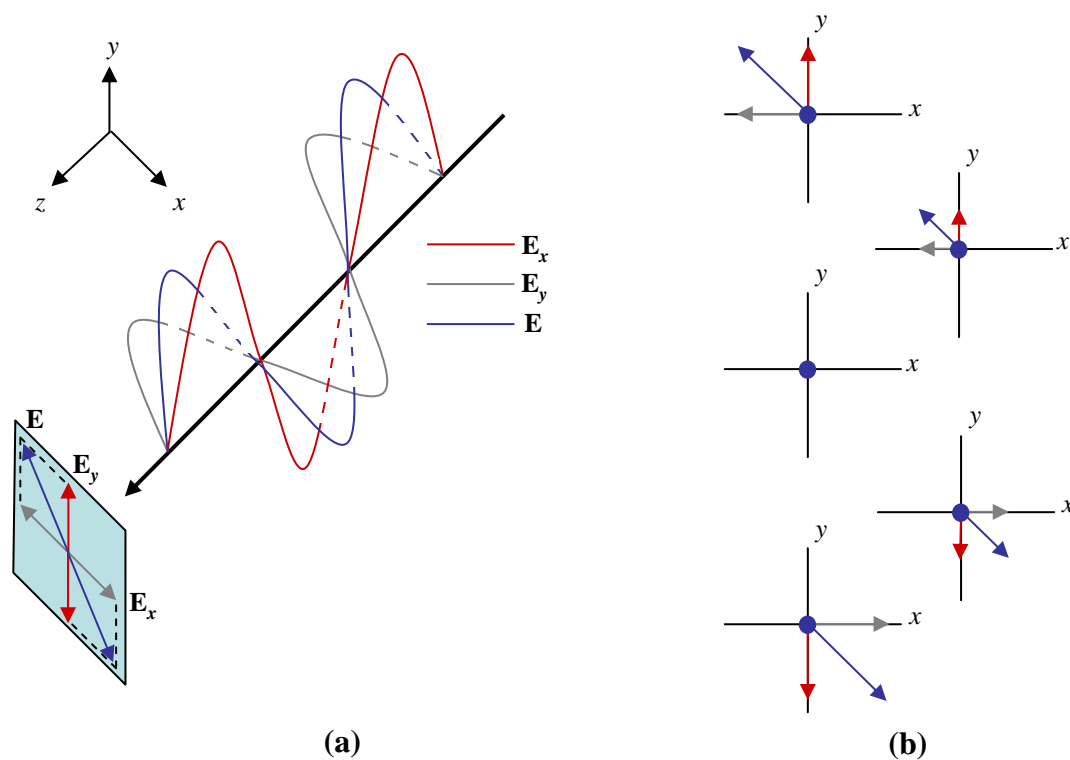


Figure 1.25 In part (a) the E -field is shown to be linearly polarised in the second and fourth quadrants. A portion of the same field is shown looking along the z -axis in part (b).

If we consider the case where $E_{ox} = E_{oy} = E_o$, in other words both constituent amplitudes are equal, and the phase difference $\varepsilon = -\pi/2 + 2m\pi$ where $m = 0, \pm 1, \pm 2, \dots$, the resultant wave is said to be circularly polarised. In this case,

$$\mathbf{E}_x(z, t) = \hat{\mathbf{i}}E_o \cos(kz - \omega t) \quad (1.29)$$

and

$$\mathbf{E}_y(z, t) = \hat{\mathbf{j}}E_o \sin(kz - \omega t) \quad (1.30)$$

and the resultant wave is given by

$$\mathbf{E} = E_o [\hat{\mathbf{i}} \cos(kz - \omega t) + \hat{\mathbf{j}} \sin(kz - \omega t)] \quad (1.31)$$

and is right circularly polarised (see Figure 1.26). The electric field vector makes one complete rotation as the wave propagates a distance of one wavelength. In comparison, if $\varepsilon = \pi/2 + 2m\pi$ where again $m = 0, \pm 1, \pm 2, \dots$, then the resultant wave,

$$\mathbf{E} = E_o [\hat{\mathbf{i}} \cos(kz - \omega t) - \hat{\mathbf{j}} \sin(kz - \omega t)] \quad (1.32)$$

rotates anticlockwise and is left circularly polarised.

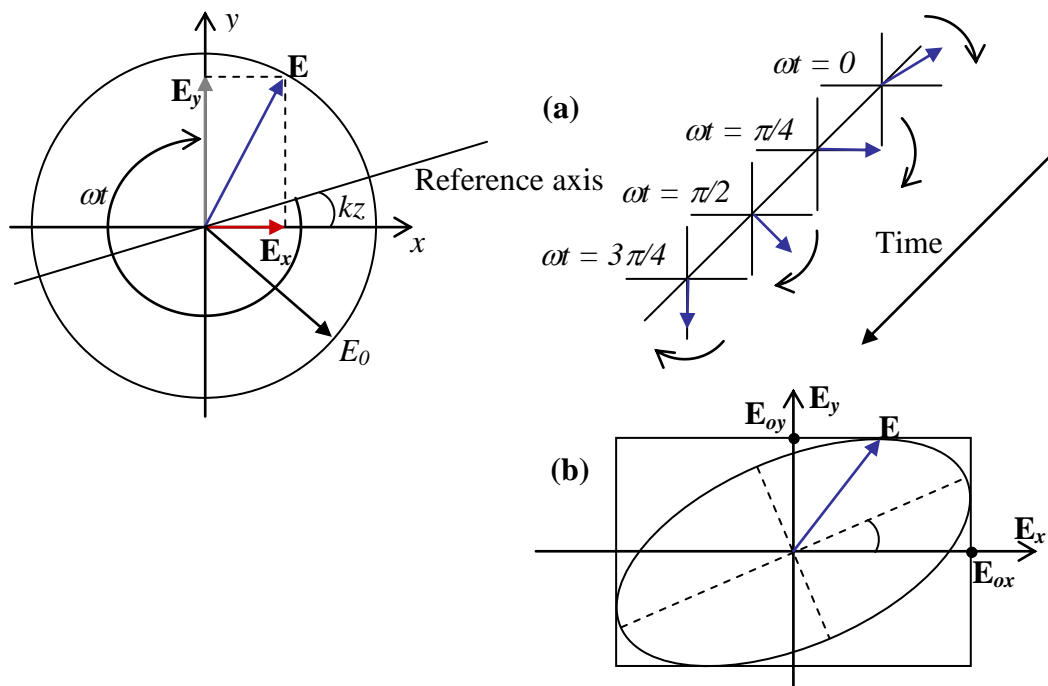


Figure 1.26 Part (a) shows right-circular polarisation at some arbitrary point along the axis of propagation while part (b) shows elliptical polarisation.

Finally, elliptically polarised radiation, of which linear and circular polarisations are special cases, results when the electric field vector \mathbf{E} both rotates and changes in magnitude as it does so. If we recall that

$$E_x = E_{ox} \cos(kz - \omega t) \quad (1.33)$$

and

$$E_y = E_{oy} \cos(kz - \omega t + \varepsilon) \quad (1.34)$$

following Hecht (1998) we can derive an expression for the curve traced out by the tip of \mathbf{E} . Since the equation of the curve should not be a function of either position or time we can eliminate the $(kz - \omega t)$ dependence starting with the expansion of the expression for E_y into

$$\frac{E_y}{E_{oy}} = \cos(kz - \omega t) \cos \varepsilon - \sin(kz - \omega t) \sin \varepsilon \quad (1.35)$$

and combining it with E_x/E_{ox} from Equation 1.33 to give

$$\frac{E_y}{E_{oy}} - \frac{E_x}{E_{ox}} \cos \varepsilon = -\sin(kz - \omega t) \sin \varepsilon. \quad (1.36)$$

It then follows from Equation 1.33 that

$$\sin(kz - \omega t) = \left[1 - \left(\frac{E_x}{E_{ox}} \right)^2 \right]^{\frac{1}{2}} \quad (1.37)$$

and so Equation 1.36 leads to

$$\left(\frac{E_y}{E_{oy}} - \frac{E_x}{E_{ox}} \cos \varepsilon \right)^2 = \left[1 - \left(\frac{E_x}{E_{ox}} \right)^2 \right] \sin^2 \varepsilon. \quad (1.38)$$

Finally, rearranging the terms yields

$$\left(\frac{E_y}{E_{oy}}\right)^2 + \left(\frac{E_x}{E_{ox}}\right)^2 - 2\left(\frac{E_x}{E_{ox}}\right)\left(\frac{E_y}{E_{oy}}\right)\cos \varepsilon = \sin^2 \varepsilon \quad (1.39)$$

which is the equation for an ellipse making an angle α with the $E_x E_y$ -coordinate system (see Figure 1.26) such that

$$\tan 2\alpha = \frac{2E_{ox}E_{oy}\cos \varepsilon}{E_{ox}^2 - E_{oy}^2}. \quad (1.40)$$

If we set $\alpha = 0$ or equivalently $\varepsilon = \pm\pi/2, \pm3\pi/2, \pm5\pi/2, \dots$, then Equation 1.39 may be reduced to

$$\frac{E_y^2}{E_{oy}^2} + \frac{E_x^2}{E_{ox}^2} = 1 \quad (1.41)$$

where the principle axis of the ellipse is aligned with the coordinate axis. Figure 1.27 shows various polarisation configurations where at $\pi/2$ or $3\pi/2$ the light would be circularly polarised if $E_{ox} = E_{oy}$, however, in this example $E_{oy} > E_{ox}$.

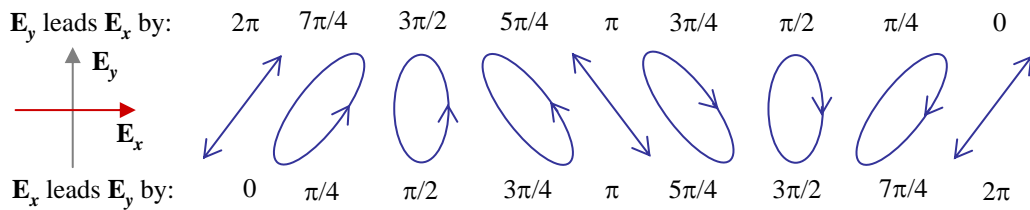


Figure 1.27 Various polarisation configurations.

We can also now refer to a particular electromagnetic wave in terms of its specific state of polarisation using the convention that linearly or plane polarised light is said to be in a P-state, right or left-circularly polarised light is in and R or L-

state respectively and elliptical light is said to be in an E-state. We will refer to these polarisation states further on.

1.4.4 The Stokes Parameters

So far we have considered the parameters of light in terms of the electric field vector \mathbf{E} with the most general case being light that is elliptically polarised. The endpoint of \mathbf{E} was envisioned as continuously sweeping out an ellipse over a period equal to that of the propagating wave. This time period is far too short to be detected and therefore in practice, average measurements are made over comparatively long time intervals. This more modern representation of polarised light has its origins in 1852 with the invention of the Stokes Vector by the physicist G. G. Stokes as a method of predicting the result of adding two incoherent beams (Shurcliff and Ballard, 1964). He introduced four quantities that are only functions of observables of the electromagnetic wave and are called the Stokes Polarisation Parameters (e.g. Collett, 2005).

To define these parameters we consider a system of four filters which each transmit half the light incident on them with the other half being discarded. The first filter is isotropic and hence passes all polarisation states equally. The second and third are linear polarisers whose transmission axes are horizontal and at $\pm 45^\circ$ respectively and the last polariser is a circular one which is opaque to L-states. The transmission intensity of each of the filters is given by I_0 , I_1 , I_2 and I_3 and from these the Stokes parameters are defined as

$$I = 2I_0 \tag{1.42}$$

$$Q = 2I_1 - 2I_0 \tag{1.43}$$

$$U = 2I_2 - 2I_0 \tag{1.44}$$

$$V = 2I_3 - 2I_0 \tag{1.45}$$

where I is simply the incident irradiance on the system, and Q , U and V specify the state of polarisation. The second parameter, Q , describes the tendency to obtain either a horizontal ($Q > 0$) or a vertical ($Q < 0$) P-state polarisation. If the beam displays no preferential orientation with respect to the axis ($Q = 0$), it may be elliptical at $\pm 45^\circ$, circular or unpolarised. In a similar manner U implies a tendency for a P-state polarisation orientated at $\pm 45^\circ$ when $U > 0$ and $U < 0$ respectively or neither when $U = 0$ and finally V describes the preponderance of right-handedness ($V > 0$), left-handedness ($V < 0$) or neither ($V = 0$) (Collett, 2005).

If we have the expression

$$\mathbf{E}_x(t) = \hat{\mathbf{i}}E_{ox}(t)\cos\left[\left(\bar{k}z - \bar{\omega}t\right) - \varepsilon_x(t)\right] \quad (1.46)$$

and

$$\mathbf{E}_y(t) = \hat{\mathbf{j}}E_{oy}(t)\cos\left[\left(\bar{k}z - \bar{\omega}t\right) - \varepsilon_y(t)\right] \quad (1.47)$$

with

$$\mathbf{E}(t) = \mathbf{E}_x(t) + \mathbf{E}_y(t) \quad (1.48)$$

we can rewrite the Stokes parameters as (Hecht, 1970)

$$I = \langle E_{0x}^2 \rangle_T + \langle E_{0y}^2 \rangle_T \quad (1.49)$$

$$Q = \langle E_{0x}^2 \rangle_T - \langle E_{0y}^2 \rangle_T \quad (1.50)$$

$$U = \langle 2E_{0x}E_{0y}\cos\varepsilon \rangle_T \quad (1.51)$$

$$V = \langle 2E_{0x}E_{0y}\sin\varepsilon \rangle_T \quad (1.52)$$

where $\varepsilon = \varepsilon_y - \varepsilon_x$. If the beam is unpolarised then $\langle E_{ox}^2 \rangle_T = \langle E_{oy}^2 \rangle_T$, neither averaging to zero because the amplitude squared is always positive. In this case

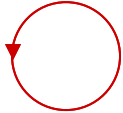
Polarisation State	Stokes Parameters	Schematic Diagram
Horizontal P-state	(1, 1, 0, 0)	
Vertical P-state	(1, -1, 0, 0)	
P-state at +45°	(1, 0, 1, 0)	
P-state at -45°	(1, 0, -1, 0)	
R-state	(1, 0, 0, 1)	
L-state	(1, 0, 0, -1)	

Table 1.3 The normalised representation of the Stokes parameters for various polarisation states.

$I = \langle E_{0x}^2 \rangle_T + \langle E_{0y}^2 \rangle_T$ but Q , U and V all equal zero, the latter two because both $\cos \varepsilon$ and $\sin \varepsilon$ average zero independently of the amplitudes. In some instances it may be convenient to normalise these parameters by dividing each one by I and hence using an incident beam of unit intensity. The set of Stokes parameters for natural light using this normalised representation is given by (1, 0, 0, 0). If the light is

horizontally polarised it has no vertical component and the parameters are $(1, 1, 0, 0)$ and similarly for vertical polarisation we have $(1, -1, 0, 0)$. Table 1.3 shows examples of sets of Stokes parameters for different polarisation states.

1.5 Imaging versus Interferometry

The CMB E -mode polarisation signal is small and the B mode polarisation signal is even smaller. The B mode signal will be at most $\sim 0.1\mu\text{K}$, so control and minimisation of systematic effects is essential (Hamilton *et al.*, 2008; Tucker and Timbie, 2008). The choice of using an interferometer over a traditional imaging system for cosmic microwave background measurements lies mainly in the potential control of these systematic effects, which in certain circumstances are more manageable in interferometers. In the past, interferometers have proven to be powerful tools for CMB observations with instruments such as CAT (Baker *et al.*, 1999), VSA (Dickinson *et al.*, 2004), DASI (Halverson *et al.*, 2002) and CBI (Readhead *et al.*, 2004a) making measurements of the temperature anisotropies at centimetre wavelengths. DASI was also the first instrument to detect the CMB polarisation (Kovac *et al.*, 2002, Leitch *et al.*, 2005) and CBI has done the same at smaller angular scales (Readhead *et al.*, 2004b, Cartwright *et al.*, 2005).

The simplicity of an interferometric optical system eliminates numerous systematic problems that plague imaging optical systems. For example, instead of a single reflector antenna the interferometers discussed in this thesis use arrays of corrugated horn antennas which have extremely low sidelobes and easily calculable, symmetric beam patterns. The lack of reflections from optical surfaces (in front of the horns) means a reduction in the spurious instrumental polarisation that is unavoidably induced by imaging optical systems. There are a number of additional factors that must also be taken into account when choosing which system best suits the particular requirements of an instrument; angular resolution is one of these factors. For a monolithic dish with a diameter equal to the length of a two-element interferometer baseline, the interferometer has an angular resolution approximately twice that of the monolithic dish (Ali *et al.*, 2003). The reason for this is due to the

fact that for acceptable sidelobe performance, the edge illumination of the monolithic dish must be tapered considerably, which reduces the effective aperture diameter. The effective edge taper of the interferometer is much smaller and so the effective diameter is almost equal to the length of the baseline, and so a higher resolution is obtained.

Single dish imaging systems also require some form of *chopping* by either steering the primary mirror or nutating the secondary mirror (Timbie and Tucker, 2008), however, interferometers do not require this rapid chopping and therefore the time constant of the bolometers used can be relatively long. Interferometers also provide direct 2D imaging and do not need the rapid scanning of the beam on the sky as imagers do and therefore, for ground-based experiments, the signal from an interferometer is significantly less affected by the atmosphere (Church, 1995).

If we consider an interferometer with n apertures there are $n(n-1)/2$ baselines (i.e. the n beams can be combined in $n(n-1)/2$ pairs). However, the n beams can also be combined into a single beam, which results in a multiplexing advantage and therefore, since the photon signal-to-noise ratio is increased, detectors with a lower sensitivity can be used. Also, by having all the beams traverse symmetric paths, unmeasured path changes in the optics due to temperature variations for example, are minimised. In order to accomplish multiplexing, each pair of telescope beams must be modulated at a unique frequency so the signal from the telescope pairs can be recovered. With an array of N_D detectors, there is also an increase in observation speed since there are now effectively many interferometers operating simultaneously.

Hu *et al.* (2003) have studied systematic effects in imaging polarisation experiments, something which Bunn (2007) has extended as well as performing similar calculations for interferometers. Table 1.4 outlines a variety of systematic errors and how they are managed in imaging and interferometric instruments. The relative importance of these effects in interferometric systems differs from imaging systems with some sources of error in imaging systems being dramatically reduced in interferometers (Timbie and Tucker, 2008).

A Comparison of Systematic Effects		
Systematic Effect	Imaging System Solution	Interferometer Solution
Cross-polar beam response	Instrument rotation and correction in analysis	Instrument rotation and non-reflective optics
Beam ellipticity	Instrument rotation and small beam width	No T to E and B leakage from beams; instrument rotation
Polarised sidelobes	Correction in analysis	Correction in analysis
Instrumental polarisation	Rotation of instrument and correction in analysis	Clean non-reflective optics
Polarisation angle	Construction and characterisation	No T to E and B leakage from beams; construction and characterisation
Relative pointing	Rotation of instrument and dual polarisation pixels	No T to E and B leakage from beams; instrument rotation
Relative calibration	Measure calibration using temperature anisotropies	Detector comparison not required for mapping or measuring Q and U
Relative calibration drift	Control scan-synchronous drift to 10^{-9} level	All signals on all detectors
Optics temperature drifts	Cool optics to $\sim 3\text{K}$ and stabilise to $< \mu\text{K}$	No reflective optics
$1/f$ noise in detectors	Scanning strategy and phase modulation/lock-in	Instant measurement of power spectrum without scanning
Astrophysical foregrounds	Multiple frequency bands	Multiple frequency bands

Table 1.4 A comparison of systematic effects and the method used to overcome them using both an imager and an interferometer (Tucker and Timbie, 2009).

For example, interferometry solves many of the problems (see Table 1.4) related to mismatched beams and pointing errors raised by Hu et al. (Hu *et al.*, 2003) since the Stokes parameters are measured directly without differencing the signal from separate detectors. An interferometer measures the Stokes parameters by correlating the component of the electric field captured by each antenna with the component from all of the other antennas as outlined in sections 1.4.1. and 1.4.4. Differential pointing errors and different beam shapes for different antennas do not cause leakage from T into E- and B -modes (Tucker and Timbie, 2009). Antenna pattern differences do cause distortion of the observed polarisation field so errors in

modelling beam shapes and pointing causes mixing between E and B . Coupling between intensity and polarisation will also arise if the beams have cross-polar contributions. Therefore, beam mismatches are less of a worry than cross-polarisation, the reverse of which is true for an imaging system. An interferometer is inherently less sensitive to beam ellipticity and in its imaging mode, the very symmetric patterns of the corrugated conical feed horns also minimises the effect (Kaplan and Delabrouille, 2002).

A significant challenge in CMB polarisation measurements is the separation of the very weak B -modes from the much stronger E -modes. Unless a full-sky map is made with infinite angular resolution, the two modes leak into each other (Lewis *et al.*, 2002, Bunn, 2003). However, it has been shown (Park *et al.*, 2003, Park and Ng, 2004) that an interferometer can separate the E - and B -modes more cleanly than an imaging system, although realistic calculations and simulations remain to be done (Timbie and Tucker, 2008). Separation of these modes requires precise knowledge of the orientation of the polarisation and errors in this angle will mix Q into U and therefore E -modes into B -modes. To keep this mixing below the 0.003% level the error in angle must be kept below 0.003 radians or 0.2 degrees, something which is feasible by careful construction and characterisation of the system (Tucker and Timbie, 2008). Also, like imaging systems, foregrounds also pose a problem for interferometers, however, the removal of these signals can be done in visibility space, something which has been studied by Bunn (2003).

1.6 The Millimetre-Wave Bolometric Interferometer

1.6.1 Overview of the MBI Project

The Millimetre-Wave Bolometric Interferometer (MBI) is a project in which the THz Optics Research Group at NUI Maynooth are involved in collaboration with the National Aeronautics and Space Administration (NASA), Lawrence Livermore National Laboratories, Brown University, Cardiff University, Northwestern

University, the University of California at San Diego, the University of Richmond and the University of Wisconsin-Madison. While it was envisaged that a 64-element instrument would eventually be built once the concept of bolometric interferometry was proved with a 4-element prototype, a new instrument called the Q U Bolometric Interferometer for Cosmology (QUBIC) is now being designed. This instrument will combine the techniques used by both MBI-4 and BRAIN (section 1.7.1) with the first module expected to be built by the summer of 2011.

A number of multiple-aperture optical telescopes are now operating or are under construction including CHARA, a six telescope interferometric array, and the Palomar Testbed Interferometer (PTI), a 110m baseline stellar interferometer. These ground based telescopes have served as demonstrations of the technologies needed to build NASA's Space Interferometry Mission (Boker and Allen, 1999), which will accurately determine the positions and distances of stars. However, relatively few demonstrations of the relevant technologies have occurred in the far-infrared and none have been carried out at millimetre and submillimetre wavelengths even though imaging interferometry forms the basis for several planned and proposed NASA and ESA missions. For example, the Terrestrial Planet Finder (TPF) will detect nearby stars using infrared interferometry and ESA is planning a similar mission called DARWIN (Darwin website) to be launched in 2015. Two other interferometer missions are under consideration by NASA, the Submillimetre Probe of the Evolution of Cosmic Structure (SPECS) and a possible predecessor to SPECS called the Space Infrared Interferometric Telescope (SPIRIT).

1.6.2 Science with MBI

CMB Polarisation

Cosmology is now a data-rich, high precision area of astrophysics with a standard model that has been well constrained by a variety of observations such as those by COBE (Smoot *et al.*, 1992) and WMAP (Spergel *et al.*, 2008), and many more ground-based and balloon-borne experiments in between (section 1.3.2).

Current telescopes such as PLANK and QUIET will also provide data to help constrain the cosmological model even further. Together with measurements of the temperature anisotropy and spectral information of the CMB, observations of the polarisation are now beginning to rule out some models of inflation and measurements of the low energy CMB are probing physics at the highest energies ever studied. Future polarisation measurements will bring into sharper focus our understanding of the early universe (Tucker and Timbie, 2009). As described in section 1.3.1, *E*- and *B*-mode polarisation components probe different physical phenomena with the search for *B*-mode polarisation being a direct search for primordial gravitational waves produced during an inflationary epoch. If this tensor *B*-component is detected we will have a direct probe of the universe at far earlier times than any other method can provide. The ration of tensor to scalar perturbations is denoted by the quantity T/S .

Other than the signature of the primordial tensor perturbations which were imprinted on the CMB at the time of last scattering and are a relic of the extremely early universe, the dominant source of *B* polarisation in the CMB is expected to be gravitational lensing of *E* modes by large scale structure, a contribution produced at a much later time.

Initial measurements of the *E*-type polarisation have already been made (Brown *et al.*, 2009) and upper limits on *B*-type polarisation have been established. The angular resolution and observing strategy of MBI are chosen to study CMB polarisation at l values from ~ 2 to 500. The ultimate goal is to measure three features expected in the *B*-mode power spectrum: the peak at $l \sim 5$ caused by reionisation, the peak near $l \sim 100$ that arises from the last scattering surface and the low l shoulder of the gravitational lensing signal which peaks near $l \sim 1000$.

Galactic Studies

It is envisaged that MBI will also be used to carry out galactic observations, for example mapping magnetic fields in dense regions of star formation by measuring the wavelength-dependant polarisation properties of dust. Observations

of the thermal component of the dust radiation have revealed that the wavelength-dependence of the polarisation is quite strong. There is only a small amount of data which focuses specifically on molecular cloud envelopes but it provides a consistent picture of a degree of polarisation that falls with wavelength in the far-infrared and then begins to rise in the submillimetre, near $350\mu\text{m}$ in wavelength. These results have been explained using a model in which the efficiency of grain alignment is correlated with exposure to radiation from both embedded stars and external sources (Hildebrand *et al.*, 1999). The importance of understanding the properties of grain alignment lies in the fact that studies of polarised dust emission provide one of the few methods of mapping the magnetic fields mentioned above. Without the physical understanding it is difficult to determine, for any given line-of-sight, which specific regions are being sampled, within an extended, heterogeneous and complex molecular cloud (Ali *et al.*, 2003).

Summary

MBI-4 is a prototype instrument to demonstrate and prove the concept of using a bolometric interferometer to measure the polarisation of the CMB. However, if the large MBI-type instrument (such as MBI-64 or QUBIC) with a baseline of approximately 6m as described by Ali *et al.* (2003) is constructed it should be possible to address the following scientific goals:

- Characterise the polarization of the CMB. The instrument would simultaneously measure the temperature and polarisation anisotropy of the CMB at angular scales from $30'$ to $40''$.
- Characterise clustering in the far-infrared background (FIRB).
- Measure and map magnetic fields near the centre of the galaxy by measuring the Faraday rotation of synchrotron radiation.
- Measure the wavelength-dependant properties of dust polarisation.
- Image the Sunyaev-Zeldovich (SZ) effect in clusters of galaxies.
- Spectrally separate the kinetic and thermal SZ effects.
- Search for CMB and point source foregrounds.

MBI will serve as a test-bed for a possible future space-based interferometer mission to measure the polarisation of the CMB. NASA has identified measuring the polarisation of the CMB as a high-priority goal. Several members of the MBI team are leading one of the mission-concept studies for the Beyond Einstein Inflation Probe, for which MBI is serving as a pathfinder. The characterisation of polarised foregrounds at millimetre wavelengths is essential to the planning of the Beyond Einstein Inflation Probe as indicated by NASA, the US National Science Foundation (NSF) and the US Department of Energy (DOE) task force planning for the next generation CMB polarisation mission.

1.7 The QU Bolometric Interferometer for Cosmology

1.7.1 Overview of the BRAIN and QUBIC Projects

BRAIN (Background RAdiation INterferometer) is another bolometric interferometer project run by a consortium from Europe and the US. To reduce the impact of atmospheric emission (Hanany and Rosenkranz, 2003) the Concordia station in Dome-C was chosen as the best site for observations. This station is a French–Italian base placed on the Antarctic plateau at ~1100Km from both Mario Zucchelli and Dumont D’Urville stations where low humidity and absence of wind create the best conditions for astrophysical observations (Polenta *et al.*, 2007). A pathfinder for the instrument was built and brought to the observation site with the aim of testing the cryogenic system. Short observations of the atmospheric emission were made for a few elevations and the acquired data fit very well the secant law as expected for atmospherical emission, however, measurements repeated at different azimuth and during different days would be needed to obtain a statistically significant estimation of the transparency of the atmosphere at 145 GHz. The BRAIN pathfinder proved the concept of cryogenics needed for measurements of the CMB at Dome C, much the same as the MBI-4 instrument was built as prototype to test the concept of bolometric interferometry. It was decided by both groups, the MBI team and the BRAIN team, to collaborate on a project, one that would use the

findings of both MBI-4 and the BRAIN pathfinder to design and create one state-of-the-art bolometric interferometer known as the Q U Bolometric Interferometer for Cosmology (QUBIC). Further details of the instrument and the design and analysis of its optical system are given in Chapter 4.

1.7.2 Science and Challenges with QUBIC

The scientific objective of the QUBIC instrument is very similar to that of MBI and BRAIN, that is, to generate a complete polarisation map of the cosmic microwave background (in a small section of sky), and in particular to measure the *B*-type polarisation generated by gravitational wave perturbations. Although detection of the lensing signal would not have the same revolutionary importance as detection of the tensor signal, it may provide powerful corroborative evidence of our understanding of the physics of CMB polarisation, and would be a valuable discovery in itself.

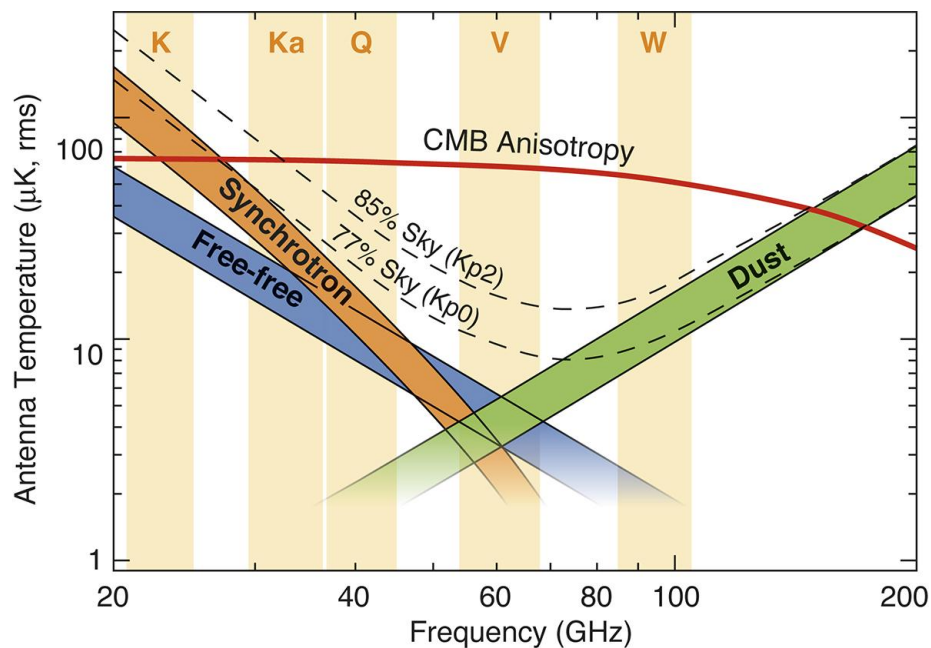


Figure 1.28 This figure, from Bennett *et al.*, (2003b) shows the rms anisotropy as a function of frequency from the CMB (red line) and three known sources of foreground emission: synchrotron, free-free, and thermal dust emission. The composite galactic emission for two sky cuts, retaining 77% and 85% of the sky respectively, are shown as dashed lines. The five WMAP radiometer bands are indicated in the background.

Due to the extremely small amplitude of the B mode signal its detection will pose formidable although not insurmountable challenges. The sensitivity required should be achievable by observing for approximately one year with around 10^3 detectors, however foregrounds (see Figure 1.28) and systematic effects will prove to be the most difficult challenges. With regards to foregrounds, known sources of polarised foreground emission such as galactic dust and synchrotron radiation are expected to be larger than the cosmological signal. However, the experience of past experiments such as WMAP suggest that with multi-frequency data it will be possible to characterise and remove these unwanted foreground signals from the data. The result from the PLANCK satellite will be very important for background removal.

Systematic errors are the other chief challenge and any experiment hoping to characterise the CMB B -mode polarisation will require unprecedented control of systematic effects. In the past, interferometry has proved to be a powerful technique for reducing systematic errors in CMB experiments and the QUBIC team believe that the potential for improved control of the systematics in a bolometric interferometer is one of the main reasons for exploring this option for characterising the CMB B -modes.

With such sensitivity and characterisation of systematic effects required it is essential that the system as a whole is fully understood. The THz Optics group at NUI Maynooth were involved in the design and modelling of the optical system which plays a vital role in the successful operation of the instrument. Chapter 6 describes the instrument in more detail and analyses a number of possible optical system for the beam combiner.

1.8 Synopsis and Thesis Outline

In this chapter I have given an introductory overview of the theory of the CMB, its origin and the importance of making accurate measurements of the extremely faint polarisation properties. I have described some of the best known

experiments to date and outlined the measurements that are yet to be made. Since this thesis is concerned with bolometric interferometers that will be used to measure the polarisation of the CMB I have also outlined the basic formalism of interferometry and polarisation. This was followed by a look at imaging versus interferometry and the systematic effects that can occur with these instruments. I have described the MBI-4 and QUBIC experiments, the optics of which I have been involved in analysing. The difficulty and importance of measuring CMB modes is the motivation behind the accurate optical characterisation that forms the basis for much of the rest of this thesis.

Chapter 2 introduces the analytical tools used throughout this thesis for modelling spatially coherent beam propagation in quasi-optical systems. We begin by looking at ray tracing, a technique in which diffraction effects are neglected but which proves to be very useful in the initial design of an optical system. This is followed by a discussion on Fresnel diffraction analysis and Gaussian beam mode analysis, both of which assume scalar representations of the field and take diffraction into account. In the case of the Fresnel approach, an example consisting of a circular aperture with a stop is provided, while for Gaussian beam modes a double-slit interferometer is considered. The final technique discussed in Chapter 2 is physical optics. Unlike the previous techniques, this method of analysis considers the full vector description of the field and provides a very accurate tool for modelling optical systems. Chapter 2 finishes with a description of the software used to carry out the work in this thesis. I introduce MODAL, a software package developed at NUIM and which was used most extensively throughout this work.

In Chapter 3 we consider the Millimetre-Wave Bolometric Interferometer (MBI) and the work done on the optical design of the beam combiner. We begin by looking at the MBI-4 instrumentation before examining in detail the design of the optical system. A first approximation using geometrical optics is presented before a preliminary investigation of the diffraction effects that take place in the beam combiner.

Chapter 4 discusses the electromagnetic modelling of horn antennas and waveguides. We begin by looking at smooth-walled horn antennas and their

implementation as detector horns in MBI-4. This is followed by an analysis of the phase-flattening lenses used within the MBI-4 instrument and the effect of using these lenses with different horn designs. Corrugated conical horn antennas are also considered in this chapter where their beam patterns are analysed and compared to those of the smooth-walled horn. A scattering matrix approach to analysing quasi-optical system is discussed and used to investigate the performance of the back-to-back corrugated horns of MBI-4. The concept of extending the mode-matching code to include rectangular-to-circular transitions is investigated with an example given. Finally, this chapter looks at the effects of waveguide arrays on the individual beam patterns of elements within those arrays. This is important in terms of MBI and QUBIC where the focal plane will contain many detector elements.

Chapter 5 investigates the MBI-4 instrument in more detail. A full scattering matrix describing the beam combiner is calculated using physical optics and mechanical tolerances are analysed. The frequency dependency of the instrument is also considered. Finally, Chapter 5 simulates lab measurements that were taken with the MBI-4 instrument in 2010.

Chapter 6 is concerned with the Q and U Bolometric Interferometer for Cosmology (QUBIC), an evolution of the MBI-4 project. We begin by looking at the science that QUBIC will carry out and the challenges it will face. This is followed by a description of the instrument and an analysis of the optical beam combiner. Three designs for the beam combiner are considered, two of which contain mirrors while the third is composed of lenses. In all three cases a physical optics analysis is carried out and the fringe patterns at the image plane examined. Commercial physical optics packages do not yet include the option of lenses and so extensive use was made of the in-house software MODAL.

Chapter 7 looks at the overall conclusions drawn from the work in this thesis. The most significant results are highlighted and possible future work in both the analysis of optical systems and software is discussed.

Chapter 2

Analytical Tools for Modelling Quasi-Optical Systems

2.1 Introduction

This chapter is concerned with a detailed description of the techniques that are appropriate for modelling spatially coherent beam propagation in quasi-optical systems. Some examples of the applications of these techniques to analyses performed as part of the project work for this thesis will also be described. To begin with, it is appropriate to give a brief explanation as to what *quasi-optics* or long wavelength optics analysis actually entails.

Quasi-optics deals with the propagation of a beam of radiation that is reasonably well collimated but has relatively small extent, in wavelengths, in the direction transverse to the axis of propagation (Goldsmith, 1982). It spans the middle ground between geometrical optics, where the wavelength is assumed to be zero, and diffraction-dominated propagation, where at some plane along the optical axis the beam width is approximately equal to the wavelength. Quasi-optics therefore includes the situation of a beam of radiation whose diameter is only moderately large when measured in wavelengths (approximately 10 to 100).

For different regions of the electromagnetic spectrum, different specialised approaches to understanding the physics involved in propagation are appropriate. Metallic conducting and dielectric waveguides are often used at microwave frequencies to guide an electromagnetic beam, but these structures become lossy at high frequencies because of the materials involved. The power loss per unit length of dielectric materials generally increases at least as fast as linearly with frequency, but loss proportional to the square of frequency is found in the millimetre and submillimetre range (Goldsmith, 1982). For a rectangular metallic waveguide the loss increases with frequency to the power of 1.5. This is where quasi-optics provides a low-loss beam guide solution by taking advantage of the essentially lossless nature of propagation in free space. Lenses and mirrors are still used for

focusing the propagating beam, but they are relatively well separated from each other and are quite thin so that the loss per unit length over which the beam travels is greatly reduced.

Four optical analytical techniques were employed in the work described in this thesis, these being: geometrical optics (ray tracing), Fresnel diffraction, Gaussian beam modes and physical optics (electromagnetics). In the next section we begin by looking at ray tracing.

2.2 Ray Tracing Analysis

2.2.1 Background

In his famous book, *Opticks* (Newton, 1979), first published in 1704, Isaac Newton described light as a stream of particles or corpuscles called a ray. This satisfactorily explained rectilinear propagation and allowed him to develop theories of reflection and refraction. Huygens also had ideas of how light could be represented by a ray. He postulated that light is propagated as a wavefront and that at any instant, every point on the wavefront is a source of secondary wavelets, which propagate outwards as spherical waves. These secondary wavelets then combine to form a new wavefront (see for example, Smith and King, 2000). A ray can then be drawn as the normal to the wavefront (see Figure 2.1).

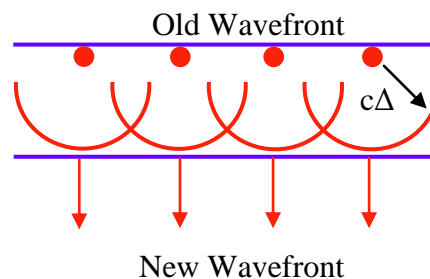
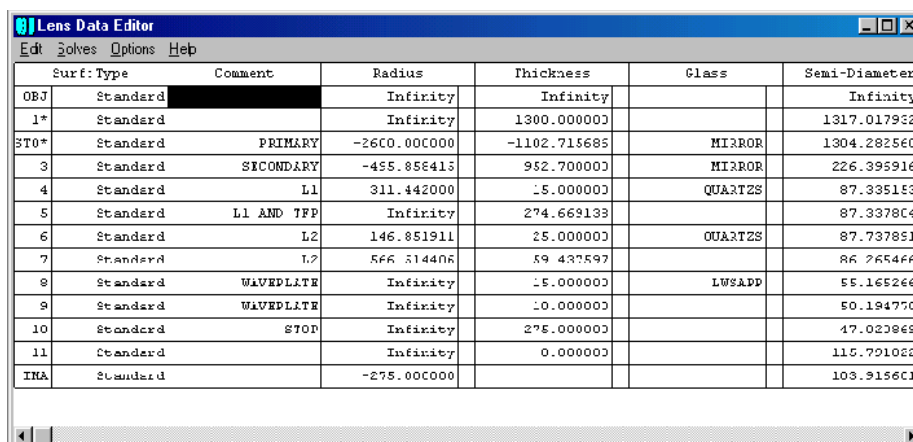


Figure 2.1 Every point on the old wavefront becomes a source of Huygens' wavelets. These then recombine to form the new wavefront. The ray can then be drawn as the normal to the wavefront.

We can also use Huygens' wavelets to understand the processes of reflection and refraction, both of which allow us to analyse almost any optical system. The ray tracing in this thesis was carried out using a program called ZEMAX (see section 2.6), which enables a quick and accurate analysis using both of the above properties of radiation. The technique does not take diffraction into account. However, ray tracing is very useful if the wavelength is much less than the size of the components in the optical system, particularly in the initial design stages and ZEMAX (one of the industry standards for ray tracing) has a well developed optimisation facility.

2.2.2 Ray Tracing Through an On-Axis Cassegrain System

The purpose of this section is to present an example of how ZEMAX may be used to analyse an optical system. The example given is one of the QUaD (Q and U Extra-galactic Sub-mm Telescope) Cassegrain telescope system (e.g. O'Sullivan *et al.*, 2008). It consists of a primary collecting mirror, a secondary mirror, two focusing lenses and a waveplate (Piccirillo *et al.*, 2001). It is the layout of the primary and secondary mirrors that defines the system as being Cassegrain. QUaD was used for measuring the polarisation properties of the CMB. This type of system is implemented in many astronomical optical telescopes, including MBI. The radius of curvature, thickness and type of material was entered into the Lens Data Editor of ZEMAX (see section 2.6) for each surface contained in the system as shown in Figure 2.2.



Surf	Type	Comment	Radius	Thickness	Class	Semi-Diameter
OBJ	Standard		Infinity	Infinity		Infinity
1*	Standard		Infinity	1300.000000		1317.017952
STO*	Standard	PRIMARY	-2600.000000	-1102.715685	MIRROR	1304.282560
3	Standard	SECONDARY	-455.856415	952.700000	MIRROR	226.395916
4	Standard	L1	311.442000	15.000000	QUARTZ	87.335153
5	Standard	L1 AND TFP	Infinity	274.669133		87.337804
6	Standard	L2	146.851911	25.000000	QUARTZ	87.737851
7	Standard	L2	566.514406	59.437597		86.265466
8	Standard	WAVEPLATE	Infinity	15.000000	LOSSAPP	55.165266
9	Standard	WAVEPLATE	Infinity	10.000000		50.184750
10	Standard	STOP	Infinity	275.000000		47.023849
11	Standard		Infinity	0.000000		115.791022
IMA	Standard		-275.000000			103.915601

Figure 2.2 Lens Data editor of ZEMAX. This window contains the data about each surface in the Cassegrain system.

The apodisation of the primary mirror was selected (in this case it is uniformly illuminated) and then the rays were propagated. They travelled from infinity to the primary mirror where they were reflected onto the secondary mirror. The light then passed through the two lenses, followed by a waveplate and on to the image plane. The refractive index of both lenses was taken to be 2.2, while for the waveplate (present in the initial design) the refractive index was assumed to be 1.6.

The hyperbolic convex secondary mirror has one focus coincident with the focus of the coaxial concave primary mirror. It is often convenient to arrange the second focus to lie at the pole of the primary mirror. The rays pass through an aperture at this focus point where the light can be viewed or recorded. The diagram below (Figure 2.3) shows the layout of the QUaD Cassegrain system complete with the rays, which appear to be incident from infinity. The image is then obtained at the image plane.

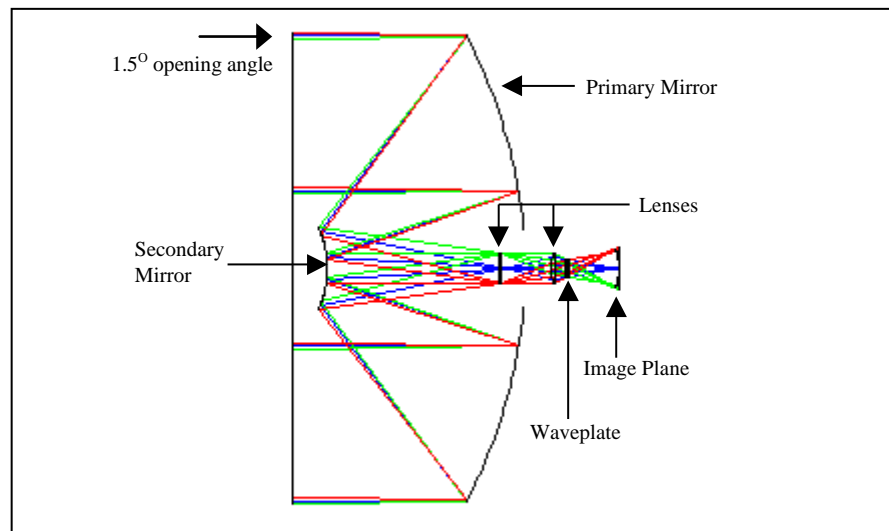


Figure 2.3 A two-dimensional layout of the Cassegrain system as produced by ZEMAX. The rays can be seen striking the primary mirror from infinity before being reflected from the secondary. They then pass through the aperture at the pole of the primary where image can be viewed.

ZEMAX also allows the generation of a point-spread function at the image plane as shown in Figure 2.4 and the viewing of a three-dimensional model of the system (Figure 2.5).

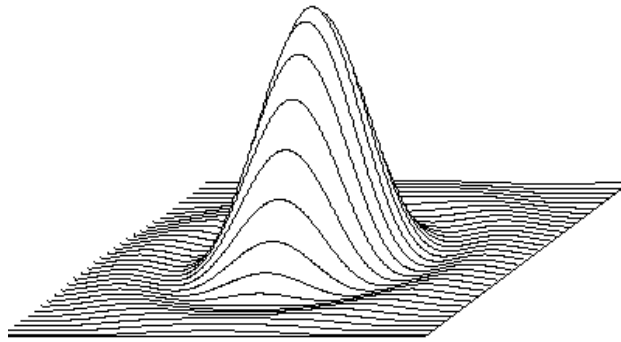


Figure 2.4 Point-spread function at the image plane of the Cassegrain system above.

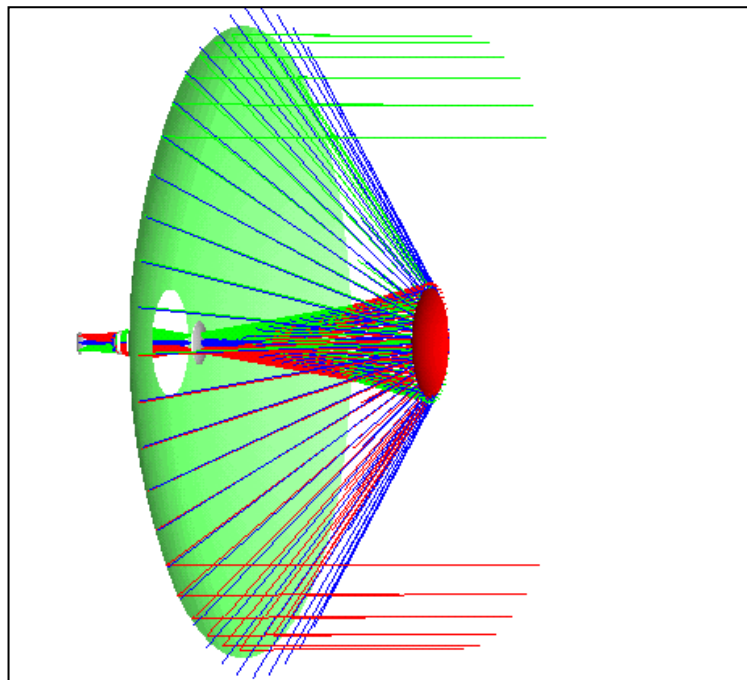


Figure 2.5 A 3D model of the Cassegrain telescope as generated in ZEMAX.

This example has shown the relative ease with which ray tracing can be done and also the power of ray tracing when designing and analysing optical systems. The question of whether the optical components are aligned and positioned correctly is solved immediately, and the focal points of the system can be found. It is therefore useful as a visual aid when designing quasi-optical systems but for long

wavelength diffraction-limited systems, it must be used in conjunction with other analysis techniques such as Gaussian beam modes or Fresnel diffraction, which will be the topic of the following section.

2.3 Fresnel Diffraction Analysis

2.3.1 Background

Augustin Jean Fresnel (1788-1827) introduced an ad-hoc theory to deal with diffraction in the near field region of a propagating beam (Smith and King, 2000). This region extends right up to the diffracting element itself and is known as the *Huygens-Fresnel Principle*. According to the simple Huygens' Principle as discussed in section 2.2.1, at any instant every point on a primary wavefront is a continuous emitter of secondary wavelets radiated uniformly in all directions. Experimentally however, there was no wave found travelling back towards the source. Therefore, the theoretical model had to be modified to change the radiation pattern of the secondary emitters, which invoked an obliquity factor given by,

$$K(\theta) = \frac{1}{2}(1 + \cos \theta). \quad (2.1)$$

This expression was actually derived theoretically by Kirchhoff, Fresnel simply conjectured about its form (Hecht, 1998). The obliquity factor has its maximum value, $K(0) = 1$, in the forward direction and also dispenses with the backward wave, since $K(\pi) = 0$. Having solved the problem of the secondary wavelets travelling backwards towards the source, the *Fresnel Integral*, described next, (combined with the obliquity factor) is the most commonly used approach to analysing Fresnel diffraction of optical components in quasi-optical systems.

2.3.2 The Fresnel Integral

With reference to the co-ordinate system shown in Figure 2.6, consider an aperture in an opaque screen that is illuminated by monochromatic light of wavelength λ . The observation plane is positioned at a distance z along the axis normal to the aperture. From the Huygens-Fresnel principle, the field amplitude at the point (x_1, y_1) may be described by (Goodman, 1968),

$$U(x_1, y_1) = \iint_{S_0} \frac{1}{j\lambda} U(x_0, y_0) \frac{\exp(jkr_{01})}{r_{01}} (1 + \cos\theta) dx_0 dy_0 \quad (2.2)$$

where $(1 + \cos\theta)$ is the obliquity factor with θ being the angle between the unit vector perpendicular to the aperture, $\hat{\mathbf{n}}$, and the unit vector parallel to the vector \mathbf{r}_{01} , $\hat{\mathbf{r}}_{01}$. The value of the obliquity factor lies between zero and one, which implies that there is no backward wave motion, and causes the amplitude per unit area to decrease as the viewing angle increases. $U(x, y)$ is a scalar function at the point (x, y) representing one of the field components at that point assuming all other components can be treated in the same manner (Goodman, 1968).

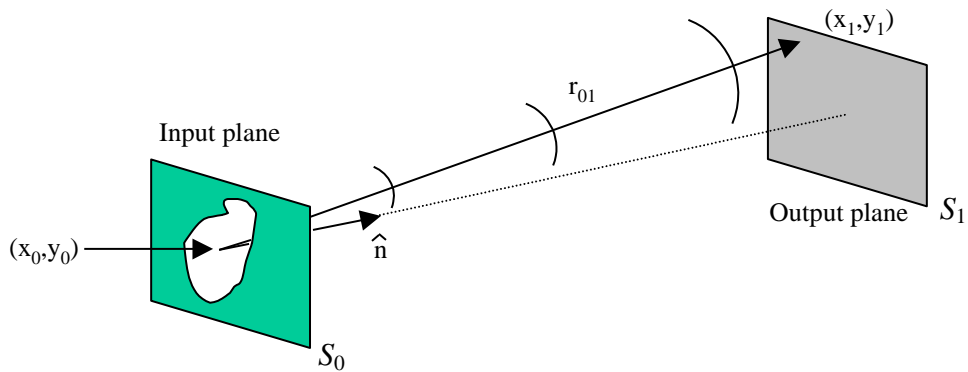


Figure 2.6 Co-ordinate system for the definition of the Fresnel integral.

As described earlier, Equation 2.2 is derived from the fact that each point on the aperture plane is a source of Huygens' wavelets. Each source of spherical waves, (x_0, y_0) , is weighted with the field associated with that point, $U(x_0, y_0)$. At the

observation plane, if analysis is restricted to an area close to the z -axis and it is assumed that z is much greater than the maximum linear dimension of the aperture, then two approximations may be assumed. The first is that r_{01} is approximately equal to z and the second is that $\cos \theta$ is approximately equal to one. Taking these into account, the field distribution at the observation plane can be re-expressed as,

$$U(x_1, y_1) = \iint_{s_0} \frac{1}{j\lambda} U(x_0, y_0) \frac{\exp(jkr_{01})}{z} dx_0 dy_0. \quad (2.3)$$

We see that the r_{01} term in the exponential is not replaced with z , since the resulting errors will be multiplied by a large number k ($= 2\pi/\lambda$) and consequently phase errors much greater than one radian may be generated. The famous Fresnel assumption describes how the phase term in Equation 2.3 may be approximated in relation to the distance z between the observer plane and the input plane. The distance r_{01} between a point $P_0(x_0, y_0, z_0)$, on the input plane and a point $P_1(x_1, y_1, z_1)$, on the output plane is given by,

$$r_{01} = \sqrt{z^2 + (x_0 - x_1)^2 + (y_0 - y_1)^2} = z \sqrt{1 + \left(\frac{x_0 - x_1}{z}\right)^2 + \left(\frac{y_0 - y_1}{z}\right)^2} \quad (2.4)$$

on setting $z_0 = 0$ at the aperture plane and $z_1 = z$. Expanding r_{01} using the binomial expansion yields to first order that,

$$r_{01} = z \left[1 + \frac{1}{2} \left(\frac{x_0 - x_1}{z}\right)^2 + \frac{1}{2} \left(\frac{y_0 - y_1}{z}\right)^2 \right]. \quad (2.5)$$

When the distance z is sufficiently large for this approximation to be an accurate one (i.e. $z > 2a^2/\lambda$), the observer is said to be in a region of Fresnel diffraction, which results in the well-known Fresnel approximation for the field distribution,

$$U(x_1, y_1) = \frac{\exp(jkz)}{jkz} \iint_{s_0} U(x_0, y_0) \exp\left\{j \frac{k}{2z} [(x_0 - x_1)^2 + (y_0 - y_1)^2]\right\} dx_0 dy_0. \quad (2.6)$$

However, as z becomes larger, the higher order terms in the binomial expansion can no longer be neglected (Goubau, 1969) and the Fresnel integral breaks down. In that case, Equation 2.6 is then best re-expressed in terms of a spherical co-ordinate system.

When using Fresnel integrals to analyse a full quasi-optical system, a double integral must be performed numerically at each optical phase transforming component to evaluate the field at the next component. This can prove very time-consuming computationally and it is therefore usually the case that Fresnel integrals are only used in the analysis of a single component of the system. This will provide a complete description of the field at this component. As an example, a uniformly illuminated circular aperture with a stop at its centre (see Figure 2.7) was analysed using Fresnel integrals. This is a simple model of a Cassegrain telescope illuminated by a far field source on the axis of the telescope. Since MBI is a Cassegrain system this example was carried out as part of the work for this thesis.

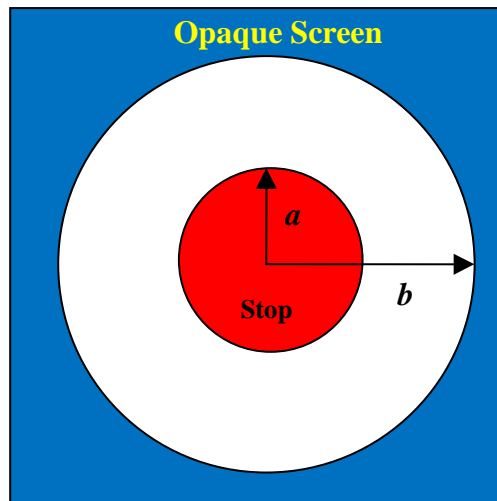


Figure 2.7 Opaque screen with a circular aperture and a stop at its centre.

The graphs shown in Figures 2.8, 2.9 and 2.10 are reconstructions of the field where $\lambda = 1\text{mm}$, the circular aperture had a radius of 10mm and the stop a radius of 2mm. Figure 2.8 shows the field at the plane of the aperture, Figure 2.9 shows the

field after being propagated a distance of 20mm (20λ) and Figure 2.10 is the far field pattern, with a propagation distance of 200mm (200λ), which is seen to have an approximate airy pattern as expected (although without deep nulls and higher sidelobe (diffraction ring) levels). The fields are similar to those obtained using a Gaussian beam mode analysis of the same system as carried out by Curran (2002).

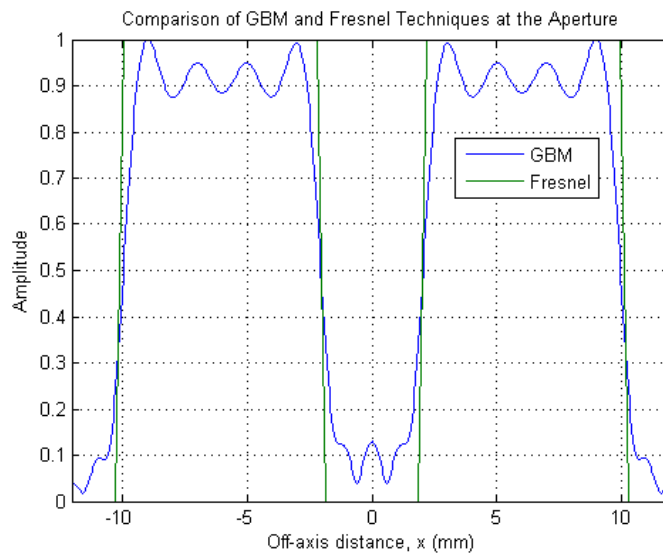


Figure 2.8 The amplitude of the field at the plane of the aperture and stop. The Fresnel field is the field assumed at the plane of the aperture while the field constructed using Gaussian beam modes, discussed in section 2.4, is shown for comparison.

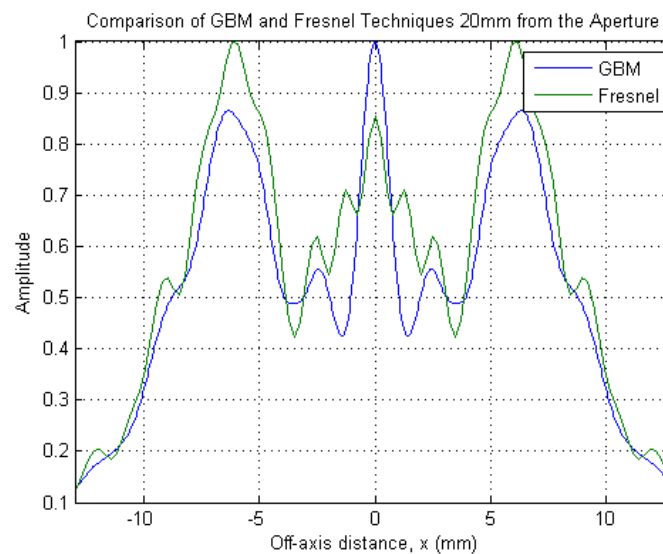


Figure 2.9 The amplitude of the field 20mm from the plane of the aperture and stop as generated using Fresnel integrals. The field generated using Gaussian beam modes (section 2.4) is shown for comparison.

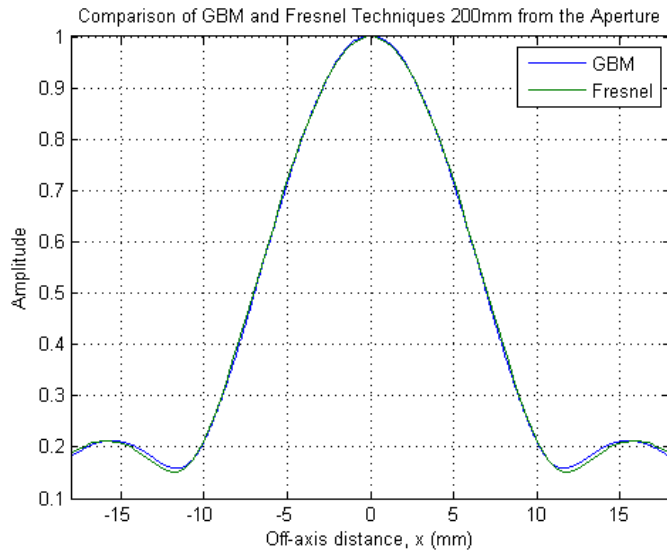


Figure 2.10 The amplitude of the field 200mm from the plane of the aperture and stop as generated using Fresnel integrals. The field generated using Gaussian beam modes (section 2.4) is shown for comparison.

2.4 Gaussian Beam Mode Analysis

2.4.1 Background

Gaussian beam mode theory, which was developed for the analysis of laser cavities in the 1960's, was found to be both conceptually and computationally superior to diffraction integral techniques, such as the Fresnel Integral described in the previous section, in the analysis of millimetre/submillimetre-wave quasi-optical systems (Siegman, 1986). Consider a monochromatic spatially coherent beam represented by the complex scalar field $E(x, y, z)$. This beam can be considered to be composed of a linear sum of independently propagating complex modes represented by $\Psi_i(x, y, z)$:

$$E(x, y, z) = \sum_0^{\infty} A_i \Psi_i(x, y, z) \quad (2.7)$$

where A_i are the mode coefficients and each mode has a transverse amplitude distribution whose envelope is a Gaussian function (Lesurf, 1993). These modes are solutions to the wave equation appropriate to quasi-optical propagation and so retain their form as they propagate. In the next section I discuss the Gaussian beam mode sets most commonly used and show how they can be used in a computationally efficient method for modelling the propagation of diffracting free-space beams.

2.4.2 Derivation of Gaussian Beam Modes

In the derivation of Gaussian beam modes (here I follow that of Siegman, 1986) two important assumptions are made. Firstly, the radiation is assumed to be moving as a paraxial beam whose cross-sectional size is not so large that it can be treated as an infinite plane parallel wave. By ‘*paraxial*’ we mean that the beam is essentially moving along a given axis but with some diffraction taking place, so the beam spreads out into a small opening angle. Secondly, we assume the radiation can be represented as a scalar field.

The Gaussian beam modes are derived by finding modal solutions to the electric and magnetic wave equations in free space appropriate to paraxial propagation. It is always true that (Martin and Lesurf, 1978),

$$\nabla^2 \mathbf{E} = -\frac{1}{c^2} \frac{\partial^2 \mathbf{E}}{\partial t^2} \quad (2.8)$$

$$\nabla^2 \mathbf{B} = -\frac{1}{c^2} \frac{\partial^2 \mathbf{B}}{\partial t^2} \quad (2.9)$$

and if the source of the radiation is monochromatic, then the wave equation for the case of the electric field reduces to the Helmholtz equation,

$$\nabla^2 \mathbf{E} - k^2 \mathbf{E} = 0 \quad (2.10)$$

where, $k = 2\pi/\lambda$. Assuming the electric field may be written in terms of independent scalar distributions $E(x, y, z)$, the three components of the electric field may be treated as separate scalar solutions of the wave equation and therefore Equation 1.8 may be written in the general form,

$$\nabla^2 E + k^2 E = 0 \quad (2.11)$$

where now E represents some typical component of the field. If a wave is propagating in the z -direction then a solution of the form,

$$E = \Psi(x, y, z) \exp(-jkz) \quad (2.12)$$

is appropriate, where $\Psi(x, y, z)$ is a slowly varying function with respect to z . If we substitute this into Equation 2.11 we obtain,

$$\frac{\partial^2 \Psi}{\partial x^2} + \frac{\partial^2 \Psi}{\partial y^2} - 2jk \frac{\partial \Psi}{\partial z} = 0, \quad (2.13)$$

or in polar co-ordinates,

$$\frac{1}{r} \frac{\partial}{\partial r} \left(r \frac{\partial \Psi}{\partial r} \right) + \frac{1}{r^2} \left(\frac{\partial^2 \Psi}{\partial \theta^2} \right) - 2jk \frac{\partial \Psi}{\partial z} = 0 \quad (2.14)$$

where Ψ varies so slowly with respect to z that its second derivative can be neglected (paraxial approximation). The solutions to these equations are a set of modes analogous to the set of modes that characterise the propagation of radiation in a metallic waveguide. The precise nature of the modal solutions clearly depends on the co-ordinate system chosen.

For a system described in terms of cylindrical polar co-ordinates, the solution to the wave equation can be written in terms of a set of modes called Laguerre-Gaussian modes, which are given by,

$$\Psi_{n\alpha}^c(r, \vartheta, z) = \sqrt{\frac{2(2-\delta_{0\alpha})n!}{W(z)^2 \pi(n+\alpha)!}} \left(\frac{2r^2}{W(z)^2}\right)^{\frac{\alpha}{2}} L_n^\alpha\left(\frac{2r^2}{W(z)^2}\right) \times \cos(\alpha\vartheta) \exp\left(-\frac{r^2}{W(z)^2}\right) \exp\left(-\frac{jkr^2}{2R(z)}\right) \exp(j\phi_{n\alpha}) \quad (2.15)$$

and

$$\Psi_{n\alpha}^s(r, \vartheta, z) = \sqrt{\frac{2(2-\delta_{0\alpha})n!}{W(z)^2 \pi(n+\alpha)!}} \left(\frac{2r^2}{W(z)^2}\right)^{\frac{\alpha}{2}} L_n^\alpha\left(\frac{2r^2}{W(z)^2}\right) \times \sin(\alpha\vartheta) \exp\left(-\frac{r^2}{W(z)^2}\right) \exp\left(-\frac{jkr^2}{2R(z)}\right) \exp(j\phi_{n\alpha}) \quad (2.16)$$

with $L_n^\alpha(\varepsilon)$ being an associated Laguerre polynomial of order n and degree α in ε (Gradshteyn and Ryzhik, 1980). In this case the full set of $\Psi_{n\alpha}^c$ and $\Psi_{n\alpha}^s$ are orthonormal.

For a cylindrically symmetric system the Laguerre-Gaussian mode-set can be written as,

$$\Psi_n(r, z) = \frac{1}{W(z)} \sqrt{\frac{2}{\pi}} L_n^0\left(\frac{2r^2}{W(z)^2}\right) \exp\left(-\frac{r^2}{W(z)^2}\right) \exp\left(-\frac{jkr^2}{2R(z)}\right) \exp(j\phi_n) \quad (2.17)$$

where $\phi_n = \phi_{n0}$ and $L_n^0(\gamma)$ is a normalised zeroth order Laguerre polynomial of degree n . R , the phase radius of curvature, and W , the beam radius, are slowly varying functions of z and their evolution with z will be discussed in the next section. $\phi_{n\alpha}$ is called the ‘‘phase slippage’’. It is mode dependent and is given by the equation,

$$\phi_{n\alpha} = (2n + \alpha + 1) \tan^{-1}\left(\frac{\lambda z}{\pi W_o^2}\right) \quad (2.18)$$

where z is the distance from the waist (where the beam is narrowest) along the axis of propagation. Figure 2.11 shows the amplitude distributions of the lower order modes given by Equation 2.17. The zeroth order mode has simply a Gaussian profile while the increasing complexity of the higher order modes is apparent. As Equation 2.17 is the symmetric subset of the associated Laguerre-Gaussian beam mode set there is only variation in the amplitude along r , the radial distance from the axis, with the electric field reversing directions in successive annular rings. The more complicated structure of the associated Laguerre-Gaussian of Equation 2.16 means the modes also vary with \mathcal{G} ; the annular rings have azimuthal nulls as \mathcal{G} varies between 0 and 2π . Examples of associated Laguerre-Gaussian modes where the Laguerre polynomials L_n^α of higher degrees (α) and orders (n) are used are shown in Figure 2.12. As the degree and order of the polynomial increases, more nulls and increasing complexity in the structure is introduced. Note that it is the $\cos(m\mathcal{G})$ term which modulates the field and the effect of choosing the $\sin(m\mathcal{G})$ mode instead of the cosine term is just to change the orientation of the field by $\pi/2m$.

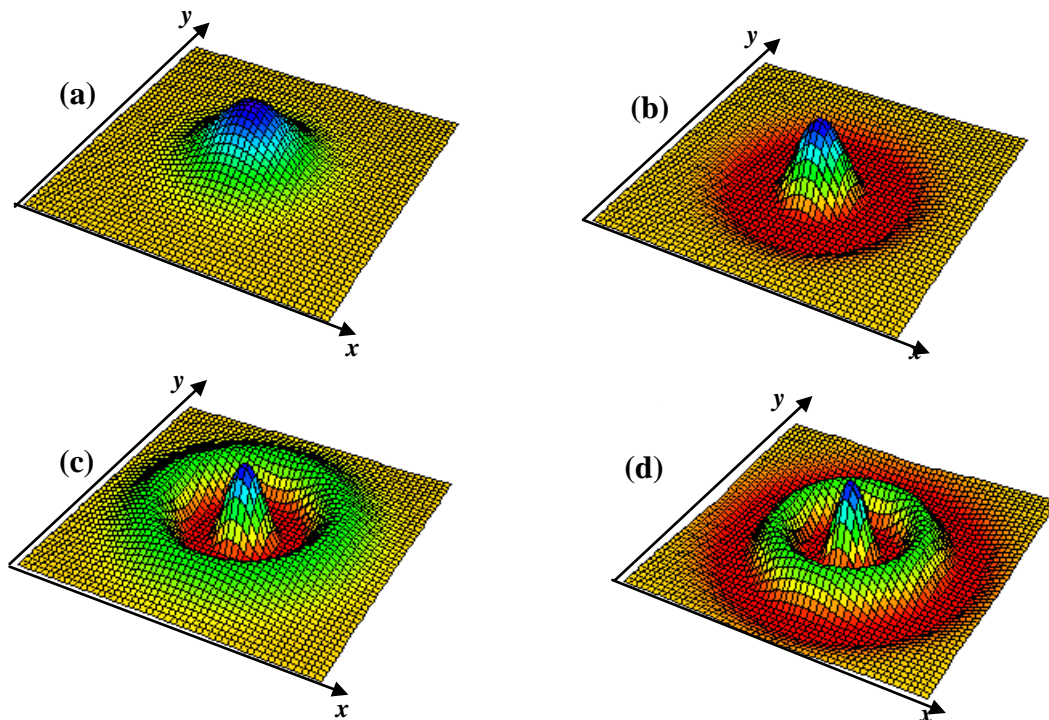


Figure 2.11 Laguerre modes of orders 0, 1, 2, 3 showing field amplitudes at the mode waist: (a) L_0^0 , (b) L_1^0 , (c) L_2^0 and (d) L_3^0 (Trappe, 2002).

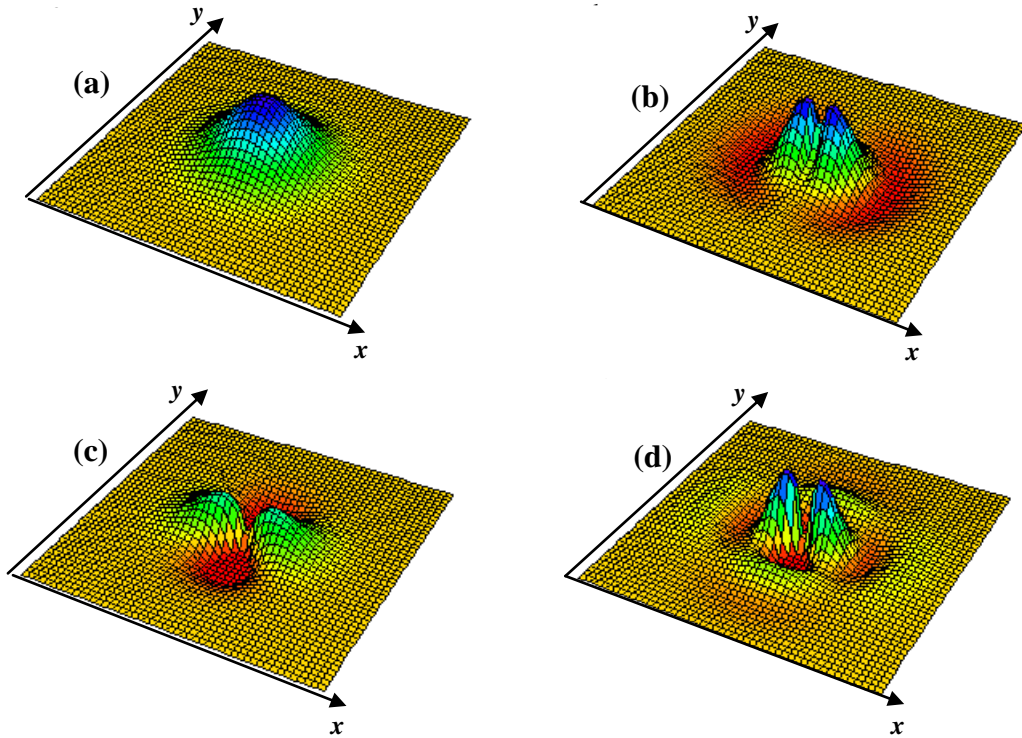


Figure 2.12 The associated Laguerre-Gaussian modes at a waist position for the case of (a) L_0^0 , (b) L_1^1 , (c) L_2^2 and (d) L_2^0 (Trappe, 2002).

The expression for the Laguerre-Gaussian modes, Equation 2.17 for example,

$$\Psi_n(r, z) = \underbrace{\frac{1}{W(z)}}_1 \underbrace{\sqrt{\frac{2}{\pi}} L_n^0 \left(\frac{2r^2}{W(z)^2} \right)}_2 \underbrace{\exp\left(-\frac{r^2}{W(z)^2}\right)}_3 \underbrace{\exp\left(-\frac{jk r^2}{2R(z)}\right) \exp(j\phi_n)}_4$$

may be broken down into a number of components which can be described and understood separately (components 1 to 4 above) in terms of the contribution each makes to the physical evolution of the beam as it propagates through free space (Trappe, 2002). Component (1) normalises the generalised power in the beam so that the integral $\iint |\Psi_n(r, z)| 2\pi r dr$ over any plane perpendicular to the beam is unity. Component 2 describes the amplitude variation of the mode across a cross-sectional plane. This is a Gaussian function modulated by the Laguerre polynomial of order n .

The scale size of the amplitude pattern is a function of the propagation distance through the z dependence of the beam width parameter $W(z)$. This expanding scale of the modal field distribution as it propagates away from the waist is the diffractive spreading of the beam discussed by Martin and Bowen (Martin and Bowen, 1993). Component 3 describes the variation of the phase of the beam-mode field over a cross sectional plane relative to the on-axis value. This term has the format of a parabolic approximation to a spherical phase front that is correct within the limits of the paraxial approximation in the near field. Finally, component 4 is the on-axis phase slippage, ϕ_n , dependent on the individual mode number n , and is relative to the plane wave phase shift e^{-ikz} . The phase slippage term has important consequences for the evolution of the form of an arbitrary beam as it propagates.

In Cartesian co-ordinates, the solution to the wave equation is given by a set of modes called Hermite-Gaussian modes, which are generally written as,

$$\Psi(x, y) = h_m \left(\frac{\sqrt{2}x}{W(z)} \right) h_n \left(\frac{\sqrt{2}y}{W(z)} \right) \exp \left(\frac{-jk(x^2 + y^2)}{2R(z)} \right) \exp(\phi_{mn}(z)) \quad (2.19)$$

where m and n are transverse mode numbers and r is the radial off-axis distance from the beam centre (i.e. $r^2 = x^2 + y^2$). As with the Laguerre-Gaussian mode-set we must take into account the phase slippage, which can be written as,

$$\phi_{mn}(z) = (m + n + 1) \tan^{-1} \left(\frac{\lambda z}{\pi W_0^2} \right) \quad (2.20)$$

where W_0 is the beam waist radius and z is the distance away from the beam waist (where the beam is narrowest) along the axis of propagation. The normalised Hermite-Gaussian function is defined by

$$h_m(x) = \frac{1}{\sqrt{2^{m-0.5} m! \sqrt{\pi W(z)^2}}} H_m \left(\frac{\sqrt{2}x}{W(z)} \right) \exp \left(\frac{-x^2}{W(z)^2} \right) \quad (2.21)$$

where $H_m(\gamma)$ is a Hermite polynomial of order m in γ (as defined in Gradshteyn and Ryzhik, 1980). The Hermite-Gaussian beam modes are orthonormal in the sense that,

$$\iint \Psi_{mn} \Psi_{m'n'} dx dy = \delta_{mm'} \delta_{nn'}. \quad (2.22)$$

Figure 2.13 shows the different order Hermite-Gaussian functions and illustrates the increasing complexity of the higher order mode fields.

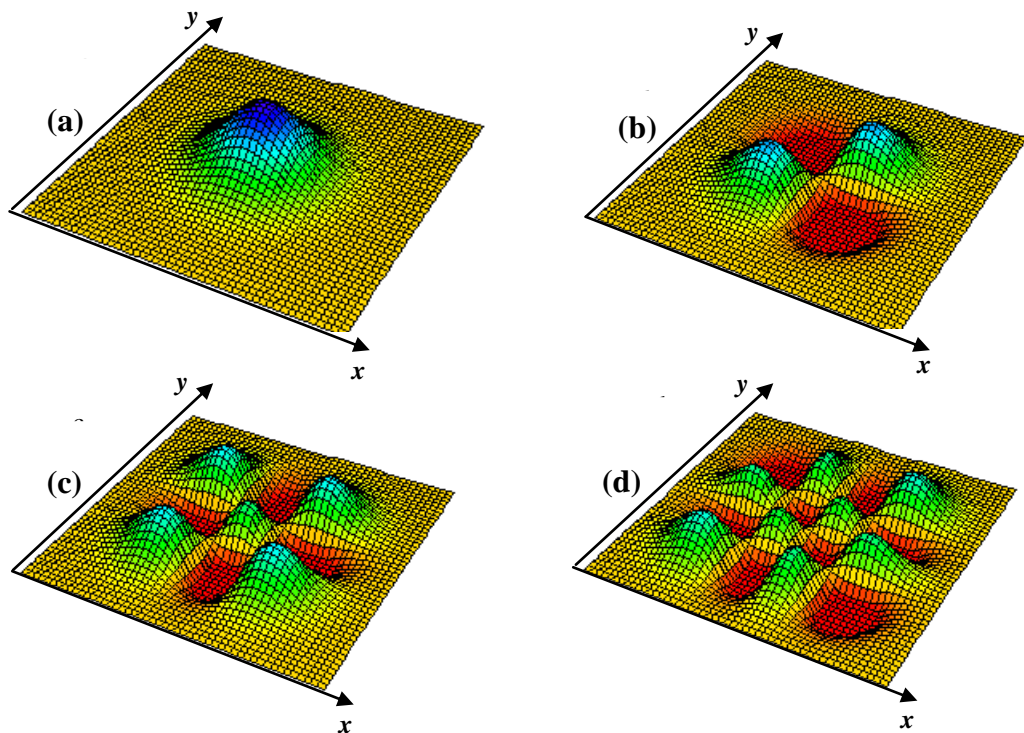


Figure 2.13 The Hermite-Gaussian field distributions of (a) h_{00} , (b) h_{11} , (c) h_{22} and (d) h_{33} at a waist position (e.g. Trappe, 2002).

2.4.3 Propagation of Gaussian Beam Modes

Consider the fundamental mode of a Gaussian mode set. It has a Gaussian profile and is the simplest mathematical solution to the Helmholtz equation. This mode is given by,

$$\Psi_0(x, y) = \frac{1}{W} \sqrt{\frac{2}{\pi}} \exp\left(-\frac{(x^2 + y^2)}{W(z)^2}\right) \exp\left(-\frac{jk(x^2 + y^2)}{2R(z)}\right) \quad (2.23)$$

and represents a Gaussian beam propagating in the z -direction, whose intensity profile does not change as it propagates except for a re-scaling factor as shown in Figure 2.14. The off-axis distance at which the amplitude is equal to $1/e$ times its on-axis value is given by the beam width parameter, W . This parameter varies as the beam propagates along the z -axis and at some distance z away from the waist is given by (Goldsmith, 1998),

$$W^2(z) = W_o^2 \left[1 + \left(\frac{\lambda z}{\pi W_o^2} \right)^2 \right] \quad (2.24)$$

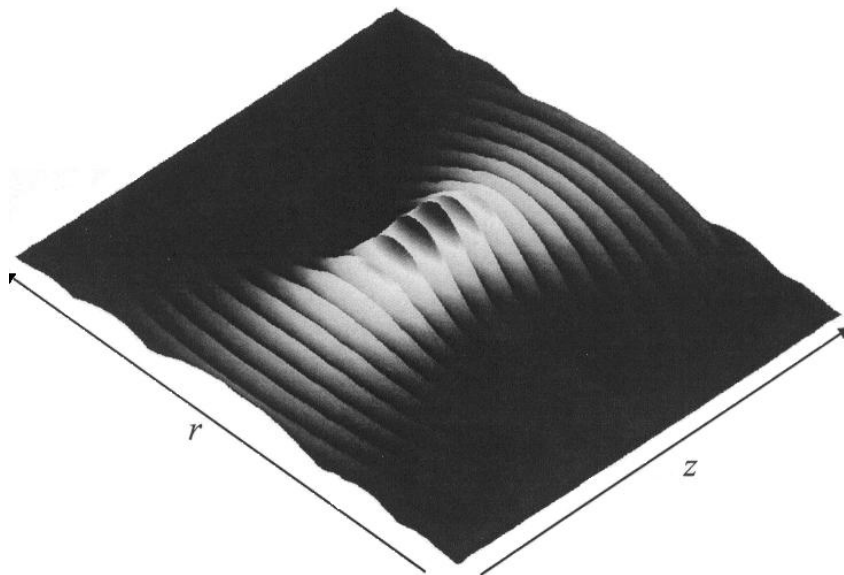


Figure 2.14 Propagating fundamental Gaussian beam mode showing both the change in width and the radius of curvature.

where W_o is the beam radius at the waist (where W is a minimum). W_o is known as the beam waist radius.

Another property of the beam that varies as it propagates is called the *phase front radius of curvature*, R , which describes the curvature of the equiphase surface of the beam. R varies with propagation distance z according to (Goldsmith, 1996)

$$R(z) = z \left[1 + \left(\frac{\pi W_o^2}{\lambda z} \right)^2 \right]. \quad (2.25)$$

At the beam waist, the phase radius of curvature is infinite and the beam is similar to a plane wave (Figure 2.14), while at a large distance from the waist, the radius of curvature is just equal to that distance so that the beam looks like a spherical wave spreading from a point source at the waist. Equations 2.24 and 2.25 can be used to model the propagation of Gaussian beams in free space. Furthermore, by using this method, the input plane does not necessarily have to be at a waist, that is, all that has to be known are the values of W and R locally and from this, expressions for the output waist and radius of curvature may be obtained.

2.4.4 Multi-Moded Gaussian Beams

A propagating beam of finite extent from a quasi-optical antenna, such as a horn or a lens, can often be approximated by a simple Gaussian profile (the fundamental mode). By using only the fundamental mode, the gross properties of the beam can be easily obtained and the analysis of the optical system in question is greatly simplified. For this reason, propagating the fundamental mode is used as a first order analysis. For a more detailed evaluation of the beam properties (for non-Gaussian beams), a multi-moded beam analysis must be used. In this case, the field of the beam, E , is regarded as a linear combination of Gaussian beam modes, as in Equation 2.7 (typically most of the power in the beam is carried by the fundamental). Although the beam width W , and the phase front radius of curvature R , are mode independent, the phase slippage depends on the mode.

It is this phase slippage (see Equation 2.18) term that essentially determines how the amplitude profile changes as the beam diffracts, because different modes have different phase velocities. If a field is not a pure mode, but rather consists of a sum of modes, the relative phase between different component modes varies along the axis of propagation since the phase slippage terms are functions of z , and are mode dependent. Therefore, at any point along the propagating axis the field may be calculated by summing the individual Gaussian modes from which the beam is comprised with the correct phase slippages (Murphy and Egan, 1993). Writing the field as a sum of Hermite-Gaussian modes, for example, yields the following equation,

$$E = \sum_{\substack{n=0 \\ m=0}}^{\infty} A_{mn} \Psi_{mn} \quad (2.26)$$

where A_{mn} are the appropriate double indexed amplitudes. In general A_{mn} values may also be complex. The phase slippage may be incorporated into these amplitude coefficients as follows,

$$A_{mn} \Psi_{mn} \rightarrow (A_{mn} \exp(j\phi_{mn})) (\Psi_{mn} \exp(-j\phi_{mn})) \rightarrow A'_{mn} \Psi'_{mn} \quad (2.27)$$

in which case the mode amplitudes actually evolve in phase as the beam propagates (effectively rotating in phase space, while maintaining a constant modulus) and Ψ' does not now contain the phase slippage term. It is usually more convenient to adopt such a convention. We know that the modes are orthonormal, and from Equation 2.22 we can write,

$$\int_{-\infty}^{\infty} h_m(x) h_{m'}(x) dx = \delta_{mm'} \quad (2.28)$$

for the one-dimensional case. Therefore, in terms of computing the A_m values for this one-dimensional case, we can write, over some transverse plane for which z is constant and the field $E = f(x, z)$ is known,

$$A_m = \int_0^{\infty} f(x, z) h_m(x, z) \exp\left(\frac{jkx^2}{2R(z)}\right) dx \quad (2.29)$$

since

$$\int_{-\infty}^{\infty} \left(\sum_m A_m h_m \exp\left(\frac{-jkx^2}{2R(z)}\right) h_m \exp\left(\frac{jkx^2}{2R(z)}\right) \right) dx = \sum_m A_m \int_{-\infty}^{\infty} h_m h_m^* dx = A_m. \quad (2.30)$$

Figure 2.8 shows a Gaussian beam mode reconstruction of the field across an aperture with a central stop. Figures 2.9 and 2.10 show this field as it propagates from the aperture. Equation 2.29 can be extended to the two-dimensional case to give,

$$A_{mn} = \int_{-\infty}^{\infty} \int_{-\infty}^{\infty} f(x, y, z) h_m(x, z) h_n(y, z) \exp\left(\frac{jk(x^2 + y^2)}{2R(z)}\right) dx dy. \quad (2.31)$$

It is possible to reconstruct the field using these mode coefficients at any point along the axis of propagation. Also, if the mode set is orthonormal, then the sum,

$$P = \sum_0^{\infty} |A_i|^2 \quad (2.32)$$

is a measure of how good a fit a synthesised beam is to the beam being analysed (Heanue, 1995).

2.4.5 ABCD Matrices

For an optical system containing mirrors and lenses to collimate and focus the beam, a convenient method for keeping track of the beam characteristics is by using the *ABCD* matrix formulation. This method is actually based on paraxial ray

propagation. If a ray defined by the parameters γ_{in} (off-axis angle) and x_{in} (off-axis displacement) as shown in Figure 2.15, passes through some optical system S , and emerges with the parameters γ_{out} and x_{out} , then these parameters may be related by,

$$\begin{bmatrix} x_{out} \\ \gamma_{out} \end{bmatrix} = \begin{bmatrix} A & B \\ C & D \end{bmatrix} \begin{bmatrix} x_{in} \\ \gamma_{in} \end{bmatrix} \quad (2.33)$$

where the elements of the ABCD matrix characterise the optical system.

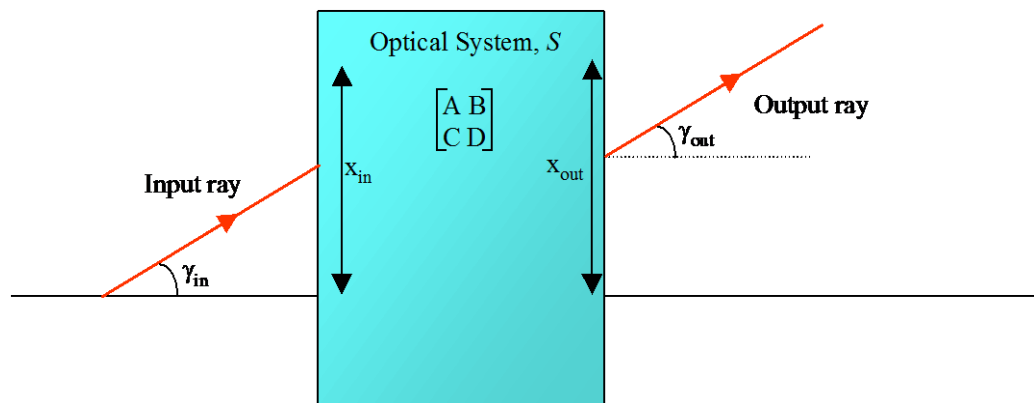


Figure 2.15 Optical system defined by ABCD matrix with input and output rays described by γ_{in} and x_{in} , and γ_{out} and x_{out} .

According to Goldsmith (1998), and Siegman (1986), a Gaussian beam may be viewed as a spherical wave expanding from a complex valued point source, to which we may attribute a ‘complex radius of curvature’, q , defined as,

$$\frac{1}{q} = \frac{1}{R} - j \frac{\lambda}{\pi W^2} \quad (2.34)$$

or

$$q = \frac{j\pi w_o^2}{\lambda} + z. \quad (2.35)$$

We can also write (Siegman, 1986),

$$q_{out} = \frac{Aq_{in} + B}{Cq_{in} + D} \quad (2.36)$$

where $\frac{1}{q_{in}} = \frac{1}{R_{in}} - j\frac{\lambda}{\pi W_{in}^2}$ and $\frac{1}{q_{out}} = \frac{1}{R_{out}} - j\frac{\lambda}{\pi W_{out}^2}$. Thus the ABCD matrix formulation allows us to determine not just R_{out} , but W_{out} also, since from Equation 2.36 we clearly obtain,

$$\frac{1}{R_{out}} = \text{Re} \left[\frac{C + \frac{D}{R_{in}} - j\frac{D\lambda}{\pi W_{in}^2}}{A + \frac{B}{R_{in}} - j\frac{B\lambda}{\pi W_{in}^2}} \right] \quad (2.37)$$

and

$$W_{out}^2 = \frac{-\lambda}{\pi \text{Im} \left[\frac{C + \frac{D}{R_{in}} - j\frac{D\lambda}{\pi W_{in}^2}}{A + \frac{B}{R_{in}} - j\frac{B\lambda}{\pi W_{in}^2}} \right]}. \quad (2.38)$$

To calculate these values, all that must be known is the ABCD matrix that describes the optical system. This matrix defines the effect of the system on the individual Gaussian beam modes as the beam propagates through it. For free space propagation, the ABCD matrix is given by (Goldsmith, 1998),

$$\begin{bmatrix} A & B \\ C & D \end{bmatrix} = \begin{bmatrix} 1 & L \\ 0 & 1 \end{bmatrix} \quad (2.39)$$

where L is the propagation distance. For the case of a thin lens, the amplitude distribution of the beam modes remains unchanged as usual, as does the beam width, W . However, the phase-front radius of curvature, R , changes from R_{in} to R_{out} , which is equivalent to saying that the lens acts as a phase transformer. To determine how much R changes, we use the appropriate ABCD matrix, which characterises the beam passing through a thin lens of focal length f . This matrix is given by (Siegman, 1986),

$$\begin{bmatrix} A & B \\ C & D \end{bmatrix} = \begin{bmatrix} 1 & 0 \\ -\frac{1}{f} & 1 \end{bmatrix}. \quad (2.40)$$

The elements of the matrix can be used to write R_{out} in terms of R_{in} , and W_{out} in terms of W_{in} , as in Equation 2.37 and Equation 2.38 respectively. This yields,

$$W_{out} = W_{in} \quad (2.41)$$

and

$$\frac{1}{R_{out}} = \frac{1}{R_{in}} - \frac{1}{f}. \quad (2.42)$$

In this thin lens system matrix, the propagation through the finite distance between the surfaces of the lens is not taken into account. Furthermore, it is assumed that all the power in the beam passes through the lens, that is, there is no truncation by the lens. The table below (Table 2.1) shows some ABCD matrices for different optical systems. Note also that the phase slippage term is given by (Martin and Bowen, 1993),

$$\phi_{out} - \phi_{in} = -\left[\text{Arg} \left(A + B \left(\frac{1}{q_{in}} \right) \right) \right]. \quad (2.43)$$

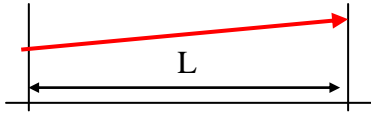
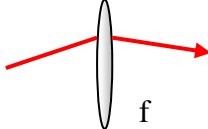
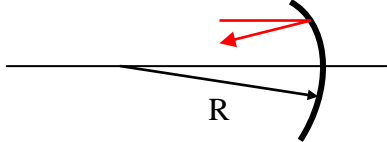
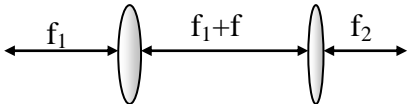
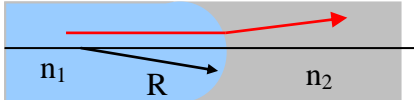
ABCD Matrix	Physical Description
Free space propagation $\begin{bmatrix} 1 & L \\ 0 & 1 \end{bmatrix}$	
Thin lens, focal length f $\begin{bmatrix} 1 & 0 \\ -1/f & 1 \end{bmatrix}$	
Curved mirror, normal incidence $\begin{bmatrix} 1 & 0 \\ 2/R & 1 \end{bmatrix}$	
Gaussian beam telescope $\begin{bmatrix} -f_2/f_1 & f_1 + f_2 \\ 0 & -f_1/f_2 \end{bmatrix}$	
Curved dielectric interface, normal incidence $\begin{bmatrix} 1 & 0 \\ (n_2 - n_1)/R & 1 \end{bmatrix}$	

Table 2.1 ABCD matrices for a variety of optical systems.

2.4.6 GBM Analysis of a Two-Slit Interferometer

Since this thesis is concerned with interferometers another example provided here is the Gaussian beam modes analysis of a two-slit interferometer. The system is described in terms of Cartesian coordinates and therefore the field can be written as a sum of Hermite-Gaussian modes,

$$E = \sum_m A_m \Psi_m \quad (2.44)$$

where Ψ_m are the Hermite-Gaussian modes given in Equation 2.21 and A_m are the appropriate mode amplitudes can be calculated by

$$A_m = \int_{-\frac{d}{2}-a}^{-\frac{d}{2}+a} \Psi_{in} \Psi_m^* dx + \int_{\frac{d}{2}-b}^{\frac{d}{2}+b} \Psi_{in} \Psi_m^* dx \quad (2.45)$$

where Ψ_{in} is the field incident on the plane of the double-slit which is centred on the origin, a is the half width of the first slit, b is the half width of the second slit and d is the separation between the slit centres. In this example the incident field was assumed to be a plane wave of amplitude 1, the slits each had a width of 50mm and the separation between their centres was 200mm. This is very similar to the MBI-4 beam combiner model used in Chapter 3. The field at the plane of the double slits was reconstructed using

$$E(x, z) = \sum_m A_m h_m(x, W(z)) \exp \left[-jk \left(z + \frac{x^2}{2R(z)} \right) \right] \quad (2.46)$$

where z was assumed to be 0. The results of this are given in Figure 2.16. The ringing in the field is due to the finite number of modes being used in the reconstruction of the beam. The far field interference pattern was also reconstructed and can be seen in Figure 2.17. The 200mm baseline modelled here represents the longest of the MBI-4 baselines. However, the 90mm shortest baseline was also modelled and as can be seen from the plot (Figure 2.17) the smaller baseline produces the widest fringes as expected from the theory of interferometry.

In conclusion, the example analysed above demonstrates how Gaussian beam mode analysis proves to be very useful for analysis of diffraction effects. We can easily switch between Cartesian co-ordinates, as in the case of the double-slit, to polar co-ordinates for systems with circular symmetry. It is also possible to include focussing optical components such as curved mirrors and lenses in the analysis of a complete optical system. Although the example here possesses a high degree of symmetry, it is also possible to analyse systems that are asymmetric, in which case a

greater number of modes are typically required for adequate representations. The Gaussian beam mode (GBM) analysis work in this thesis was carried out using both MODAL and in-house software written by the author.

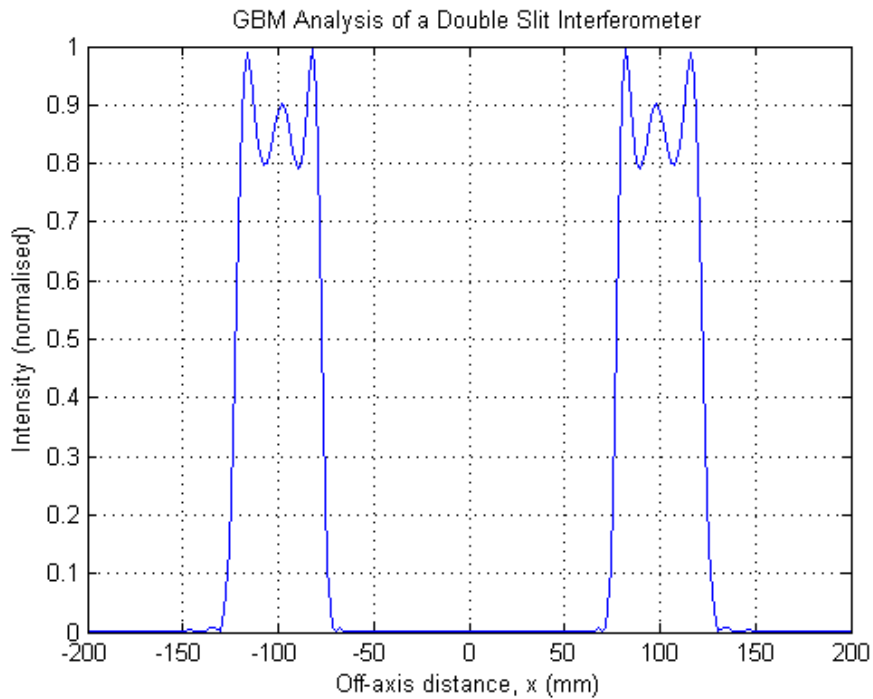


Figure 2.16 Reconstruction of the field at the plane of the surface containing the two slits.

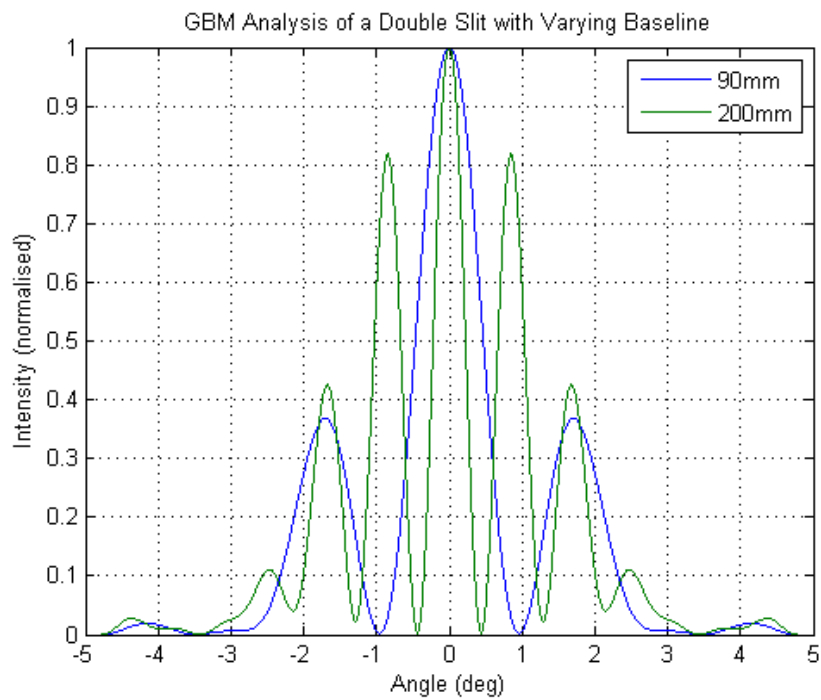


Figure 2.17 Reconstruction of the far field interference pattern produced from both a 90mm and 200mm baseline.

2.5 Physical Optics Analysis

2.5.1 Background

In section 2.2, it was shown how geometrical optics could be used to analyse optical systems. By this method, the radiation is treated as rays of light and diffraction effects are not taken into account. Diffraction is taken into account in the case of Fresnel diffraction and Gaussian beam mode analysis, but electric fields are represented only by a scalar function and beams are assumed to be paraxial. With physical optics, the topic of this section, the amplitude and phase of the true vector fields are included in the analysis and the paraxial approximation is not made.

In physical optics, the field radiated by a scattering element (such as a reflector) is calculated using an approximate surface current distribution. To calculate this field, two things must be known: the geometry and reflective properties of the reflector and the incident electric field. If the surface of the reflector is perfectly conducting then the scattered field is generated by the currents induced on its surface from the incident field can then be found from the relation,

$$\mathbf{E} = \mathbf{E}_i + \mathbf{E}_s \quad (2.47)$$

where \mathbf{E} is the total field, \mathbf{E}_i is the incident field and \mathbf{E}_s is the scattered field. The first step in this process is to calculate the induced currents on the scattering surface. To do this extremely accurately involves techniques such as the Method of Moments (Harrington, 1967; Harrington, 1993) that become very time-consuming for large elements. However, physical optics provides an easier method in which the surface currents are approximated, assuming that the surface of the scattering element is perfectly conducting and large in terms of wavelengths. In the region where the incident field does not directly illuminate the surface the currents are assumed to be zero. Calculating the field radiated by these currents involves no further approximations since the integral of the surface currents can be done with numerical integration with high precision. If the scattering surface is not perfectly conducting

but the reflection and transmission coefficients are known, then the physical optics method can be used to approximate the equivalent electric and magnetic surface currents.

When calculating the surface currents the approximation made by physical optics is in the assumption that the surface current at a specific point on a curved but perfectly conducting scattering element is the same as the surface current on an infinite planar surface which is tangent to the scattering surface at that point. Because of this assumption physical optics does not do as well as other techniques (such as the Method of Moments and the Physical Theory of Diffraction (Keller, 1958)) in predicting the currents at surface edges or on very curved surfaces.

The induced surface currents (which are induced by the incident magnetic field) on a perfectly conducting infinite planar surface with an arbitrary incident field are given by (Collin and Zucker, 1969),

$$\mathbf{J}_e = 2\hat{\mathbf{n}} \times \mathbf{H}_i \quad (2.48)$$

and

$$\mathbf{J}_m = 2\hat{\mathbf{n}} \times \mathbf{E}_i \quad (2.49)$$

where \mathbf{J}_e is the induced electric current, \mathbf{J}_m is the induced magnetic current, $\hat{\mathbf{n}}$ is the normal to the unit surface (pointing away from the illuminated surface), \mathbf{H}_i is the incident magnetic field and \mathbf{E}_i is the incident electric field. The radiated fields resulting from the induced surface currents are found from (Collin and Zucker, 1969),

$$\mathbf{A}_e = \frac{\mu}{4\pi} \iint_S \mathbf{J}_e(\mathbf{r}') \frac{e^{-jkR}}{R} dS \quad (2.50)$$

$$\mathbf{A}_m = \frac{\varepsilon}{4\pi} \iint_S \mathbf{J}_m(\mathbf{r}') \frac{e^{-jkR}}{R} dS \quad (2.51)$$

$$\mathbf{E} = -j\omega \left[\mathbf{A}_e + \frac{1}{k^2} \nabla(\nabla \cdot \mathbf{A}_e) \right] - \frac{1}{\varepsilon} \nabla \times \mathbf{A}_m \quad (2.52)$$

$$\mathbf{H} = \frac{1}{\mu} \nabla \times \mathbf{A}_e - j\omega \left[\mathbf{A}_m + \frac{1}{k^2} \nabla(\nabla \cdot \mathbf{A}_m) \right] \quad (2.53)$$

where \mathbf{A}_e is the electric vector potential, \mathbf{A}_m is the magnetic vector potential, R is the distance given by $R = |\mathbf{r} - \mathbf{r}'|$ where \mathbf{r} is the observation point and \mathbf{r}' is the integration variable, and S is the surface of the scattering surface. The radiated electric and magnetic fields are then found by applying the differential operators in Equations 2.52 and 2.53 respectively to give,

$$\begin{aligned} \mathbf{E}(\mathbf{r}) = & \frac{z}{4\pi} \iint_S \left[\mathbf{J}_e \left(-\frac{j}{kR} - \frac{1}{k^2 R^2} + \frac{j}{k^3 R^3} \right) + \right. \\ & \left. (\mathbf{J}_e \cdot \hat{\mathbf{R}}) \hat{\mathbf{R}} \left(\frac{j}{kR} + \frac{3}{k^2 R^2} - \frac{3j}{k^3 R^3} \right) \right] e^{-jkR} k^2 dS \\ & - \frac{1}{4\pi} \iint_S \mathbf{J}_m \times \hat{\mathbf{R}} \frac{1}{k^2 R^2} (1 + jkR) e^{-jkR} k^2 dS \end{aligned} \quad (2.54)$$

and

$$\begin{aligned} \mathbf{H}(\mathbf{r}) = & \frac{1}{4\pi} \iint_S \mathbf{J}_e \times \hat{\mathbf{R}} \frac{1}{k^2 R^2} (1 + jkR) e^{-jkR} k^2 dS \\ & + \frac{1}{4\pi z} \iint_S \left[\mathbf{J}_m \left(-\frac{j}{kR} - \frac{1}{k^2 R^2} + \frac{j}{k^3 R^3} \right) + \right. \\ & \left. (\mathbf{J}_m \cdot \hat{\mathbf{R}}) \hat{\mathbf{R}} \left(\frac{j}{kR} + \frac{3}{k^2 R^2} - \frac{3j}{k^3 R^3} \right) \right] e^{-jkR} k^2 dS \end{aligned} \quad (2.55)$$

where $\hat{\mathbf{R}} = \mathbf{R}/R = \mathbf{r} - \mathbf{r}'/|\mathbf{r} - \mathbf{r}'|$ and z is the free space impedance ($z = \sqrt{\mu/\varepsilon}$). To obtain expressions for the far field electric and magnetic fields we multiply equations 2.54 and 2.55 by a factor kre^{jkr} in the limit where r ($=|\mathbf{r}|$) goes to infinity to give,

$$\mathbf{E}_{ff} = \frac{jz}{4\pi} \iint_S [\mathbf{J}_e - (\mathbf{J}_e \cdot \hat{\mathbf{r}})\hat{\mathbf{r}}] e^{-jk\mathbf{r}' \cdot \hat{\mathbf{r}}} k^2 dS + \frac{j}{4\pi} \hat{\mathbf{r}} \times \iint_S \mathbf{J}_m e^{-jk\mathbf{r}' \cdot \hat{\mathbf{r}}} k^2 dS \quad (2.56)$$

$$\mathbf{H}_{ff} = -\frac{j}{4\pi z} \hat{\mathbf{r}} \times \iint_S \mathbf{J}_e e^{-jk\mathbf{r}' \cdot \hat{\mathbf{r}}} k^2 dS - \frac{j}{4\pi z} \iint_S [\mathbf{J}_m - (\mathbf{J}_m \cdot \hat{\mathbf{r}})\hat{\mathbf{r}}] e^{-jk\mathbf{r}' \cdot \hat{\mathbf{r}}} k^2 dS \quad (2.57)$$

where $\hat{\mathbf{r}}$ is the far field direction $\hat{\mathbf{r}} = \mathbf{r}/|\mathbf{r}|$.

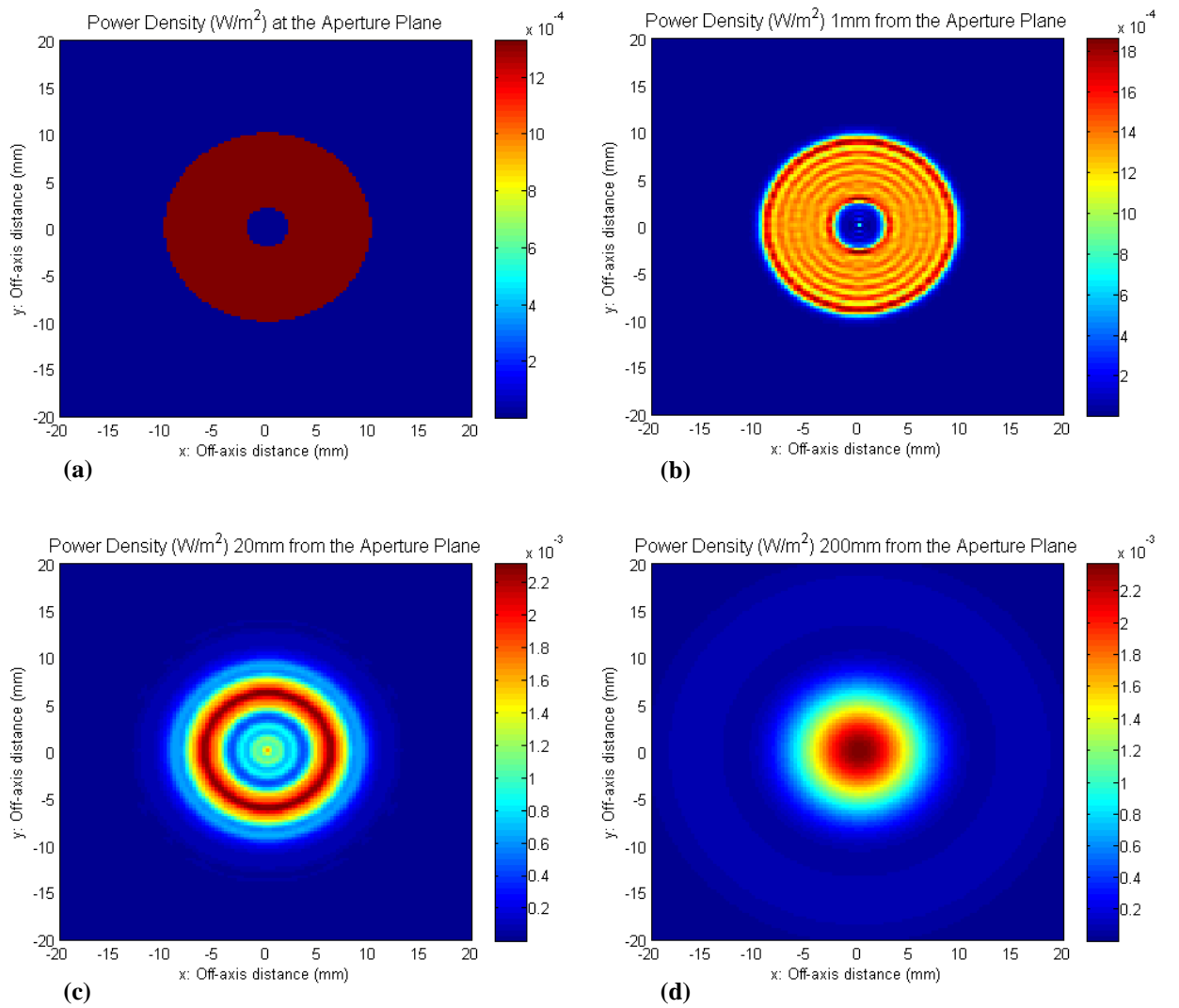


Figure 2.18 Power density of the field at (a) the plane of the circular aperture with a stop, (b) 1mm from the aperture plane, (c) 20mm from the aperture plane and (d) 200mm from the aperture plane.

The physical optics analysis carried out in this thesis, in particular in chapters 5 and 6 where the beam combiners of both MBI and QUBIC are modelled, was carried out using MODAL, a software package developed at NUIM and discussed in more detail in section 2.6. In the next section we look at an example of the application of physical optics to a simple system.

2.5.2 Physical Optics Analysis of an Aperture with Stop

Presented in this section is an example of a physical optics analysis applied to a system comprising a circular aperture with a stop at its centre. The circular aperture had a diameter of 20mm and the stop a diameter of 4mm, that is, the same system as that analysed in section 2.3.2 using the Fresnel integral method (and GBM). The aperture was illuminated with a plane wave which had a wavelength of 1mm and zero initial phase.

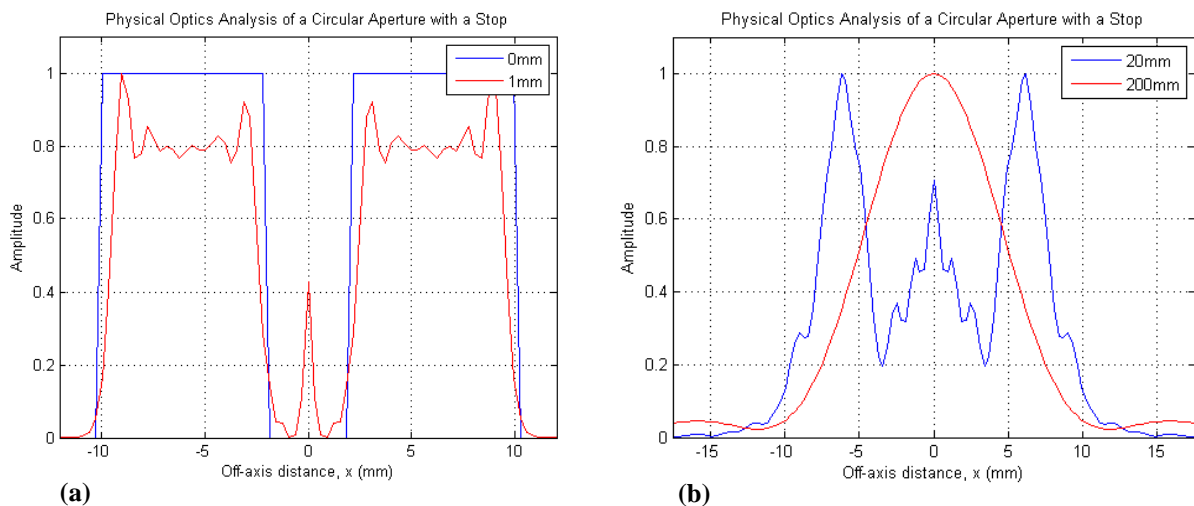


Figure 2.19 A cut through the field at (a) the plane of the circular aperture with a stop and 1mm from this plane, and (b) 20mm and 200mm from the aperture plane.

Figure 2.18 shows the power density of the field at the aperture and at the image plane, which was placed at three different distances from the aperture: 1mm, 20mm and 200mm. A cut across the centre of these fields is shown in Figure 2.19

where in part (a) the Poisson spot can be clearly seen. This is also visible in Figure 2.18 (b). In Figure 2.20 it can be seen that both the GBM method and the Fresnel diffraction method presented in section 2.3.2 for the same system are in relatively good agreement with the physical optics results presented here. However, although the general structure of the fields are the same it is clear that the assumptions made by both the GBM and Fresnel methods do have an effect on the resulting beam patterns.

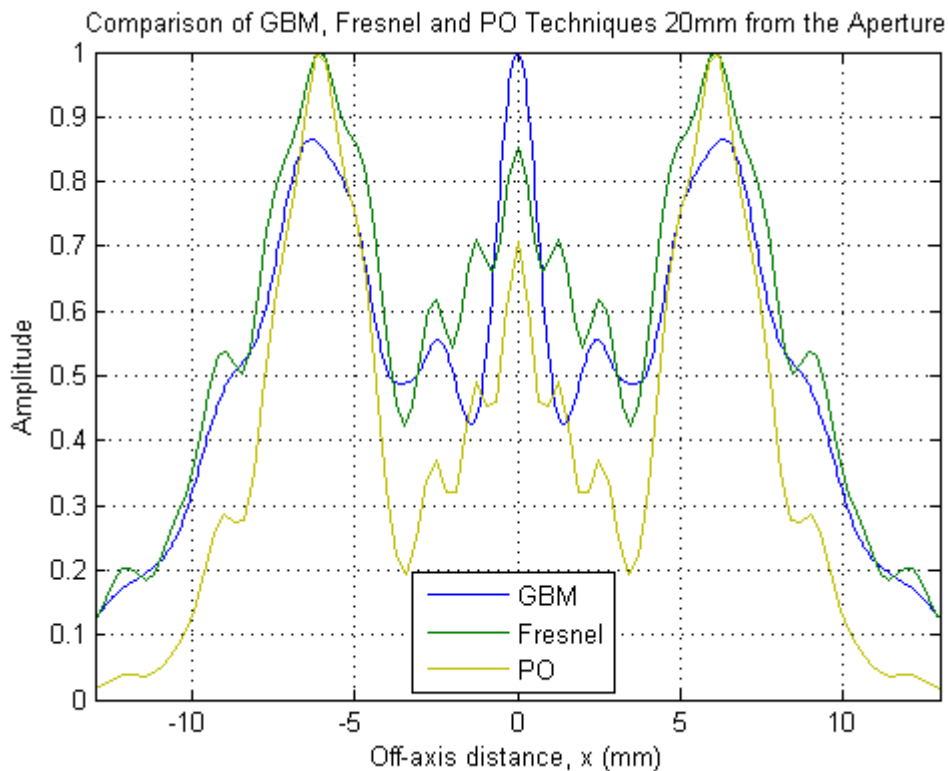


Figure 2.20 A cut through the field at (a) the plane of the circular aperture with a stop and 1mm from this plane, and (b) 20mm and 200mm from the aperture plane.

2.6 Description of Modelling Software

Throughout the work carried out for this thesis a number of software packages were used to model both the components of quasi optical systems and the overall systems themselves. The use of several methods of analysis serves as a verification tool for the results obtained and also aids in the design process by allowing simple models, such as that achieved through geometrical optics, to be built

upon when creating more complex models. In this section a brief outline of each of the software packages used will be given, starting with MODAL, the one that was used most extensively.

MODAL

MODAL (Maynooth Optical Design and Analysis Laboratory) (Gradziel *et al.*, 2008) is a software package being developed by Dr. Marcin Gradziel under a Science Foundation Ireland (SFI) investigator grant. The title of the SFI project is “The Development of an Integrated Quasi-Optical and Electromagnetic Numerical Simulator for the Computer Aided Design and Analysis of Novel Terahertz Systems” and the principle investigator is Prof. J.A. Murphy of NUIM.

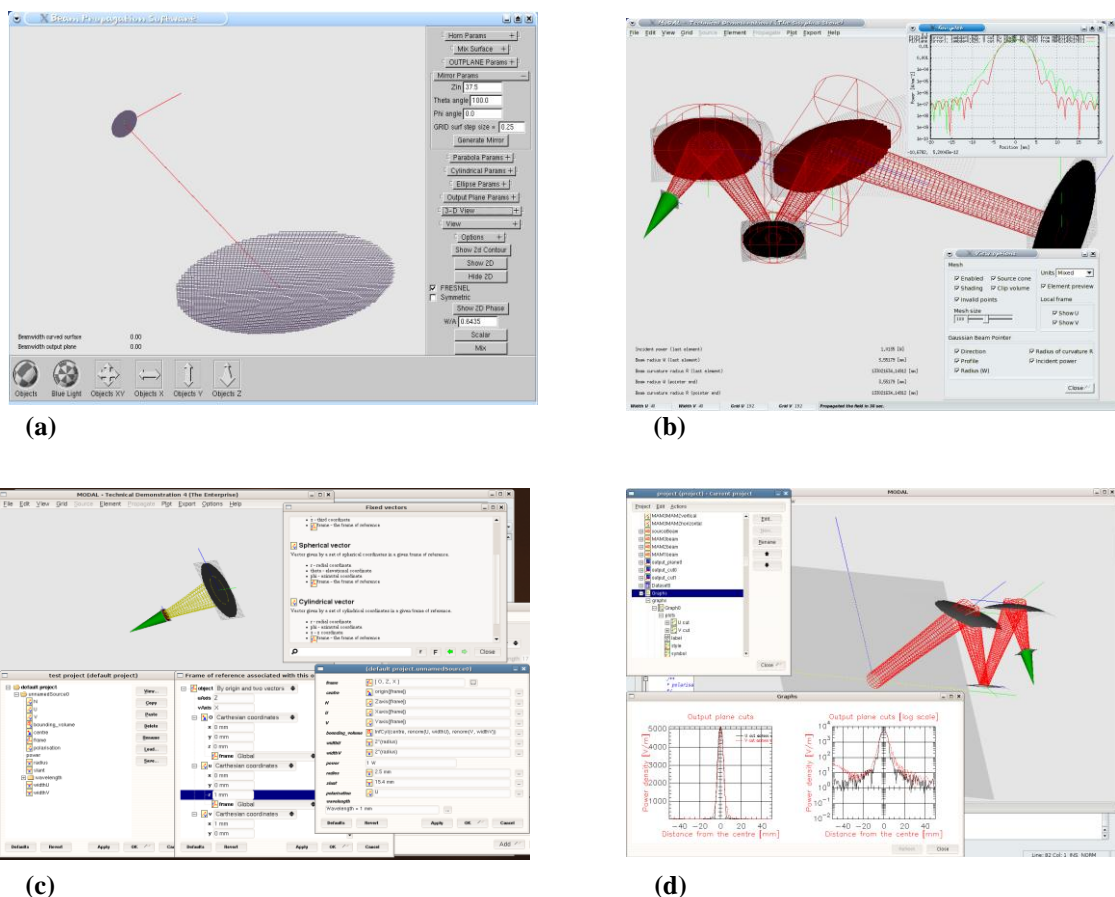


Figure 2.21 Screenshots showing the evolutions of MODAL. Part (a) shows the MODAL prototype software from 2003 (White, 2006), part (b) shows MODAL in 2003 where a linear workflow has been implemented, part (c) shows the MODAL property editor available in 2005 and part (d) shows MODAL as being project based with integrating plotting, developed in 2006.

The initial idea for the software was to allow the quick design of an optical system in a real-time 3D environment in a user-friendly manner through the use of a flexible approach to system definition. Also, users would be able to view the system from different camera angles in the 3D environment as well as view cuts and 3D contour plots of the field at any given plane. The software was also being specifically designed to target the millimetre-wave/THz region of the spectrum with its unique propagation characteristics. Commercially available packages perform best either in the RF/microwave, or IR domains, and a gap still remains between these two modalities in the THz band. It was envisaged that the power of the software would arise from a wide range of analysis techniques (Fresnel diffraction, Gaussian beam modes and physical optics) combined with parallel processing (clusters or multiprocessor machines) where possible. Unlike commercial software such as GRASP, we can update and modify MODAL to suit the systems we investigate at NUIM. The author has work with Dr. Gradziel to tailor the software for the analysis of MBI.

A prototype for the software was originally developed by Dr. David White (White, 2006), however further development has occurred over a number of years (see Figure 2.21) and the current version of MODAL (version 9.1r15) is in a beta development stage. It was developed using C++ as a cross-platform application and can be operated under Linux 32 and 64 bit and Windows 32 bit. The development of MODAL is a complex software project with Subversion being used to manage source code revisions and CMake for program building. It makes use of a number of libraries such as FLTK/FLU for the user interface, OpenGL for 3D visualization of the system, PVM/PPVM for parallel processing, fltkPlot for graphing and XMLWrapp/libxml2 for XML input and output. In the current version of MODAL (not including external libraries) there are approximately 959 files containing a total of 90,000 lines of code. This code based on templates with the equivalent C-code being bigger by a factor of 3 to 5. Such a project would be unmanageable for one developer.

In terms of the high level design of MODAL there are several classes of complex objects representing both physical objects and abstractions. In the current version the fundamental components are:

- Project** The project is viewed through the project window (Figure 2.22) and contains all the components required for defining and analysing an optical system by means of a user-defined set of objects and properties. The project allows the user to add or remove objects, edit existing objects, save the project file or load an existing MODAL project. The open project is visualised in real-time in a separate window where the viewing properties such as camera angle and magnification properties can be adjusted.

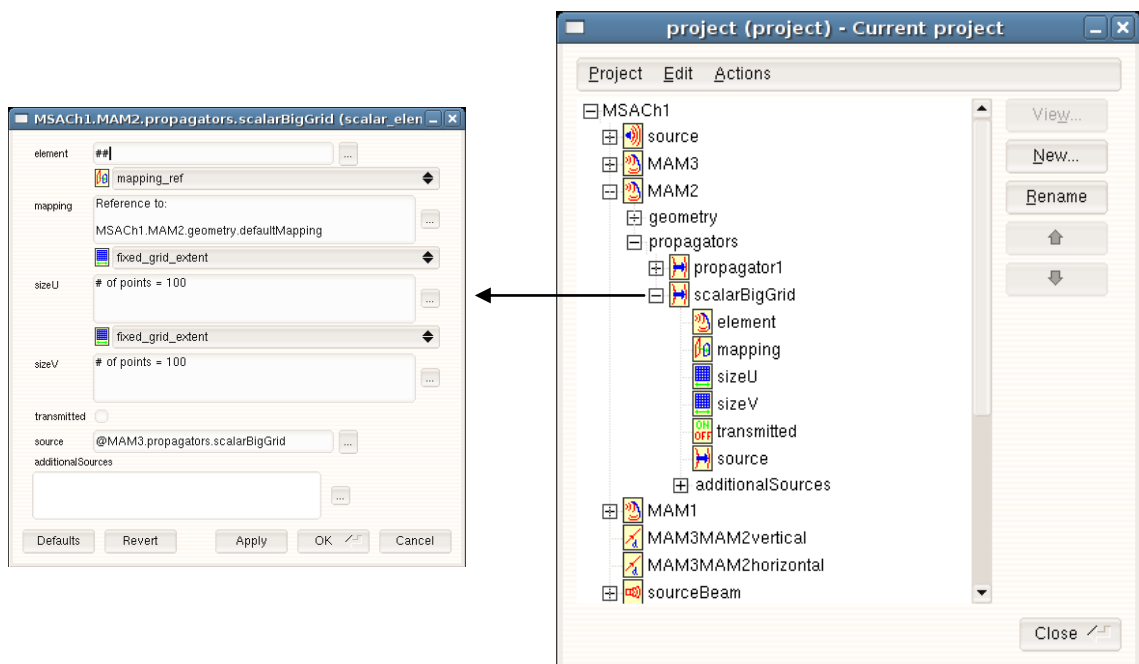


Figure 2.22 An example of a MODAL project window and property editor.

- Elements** Elements represent optical elements within the system being defined, for example sources, detectors, lenses, mirrors and output planes. The source elements are active sources of electromagnetic fields and there are a number of types to choose from such as a plane wave, a Hermite-Gaussian mode or a corrugated conical horn antenna. MODAL has also been designed to implement the SCATTER antenna modelling code (see details of the SCATTER program further on in this section) and allows horn antenna “geometry files” to be imported. More recently smooth-walled conical horns have also been added as a source option.

In terms of detectors, they are similar to the source elements but have a set of field modes that the incident field can couple to. Also, the output planes allow the field to be evaluated at any defined plane within the system.

All elements have certain standard properties such as a local frame of reference, which is defined in terms of its origin and three axes. For sources there are other properties that need to be defined such as the geometry of the source (e.g. radius of a corrugated horn antenna), and also the properties of the field produced by the source (e.g. initial phase, radius of curvature, polarisation direction, frequency and power). For elements such as mirrors and lenses the geometrical surface must also be defined. The mirror surface is described in different ways, depending on the type of conic section required. For example, a parabolic mirror is defined by a frame (whose centre can be at any point on the surface), the focal point and the direction from the focal point to the vertex, while both hyperbolic and ellipsoidal mirrors are defined again by the appropriate frame, but also by the two focal points. When the surface is defined a bounding volume is used to select the section of the surface needed. This is a geometrical solid, for example a cylinder, which cuts through the geometrical surface of the mirrors and therefore specifies the section of the mirror and its edges. Lenses are defined by specifying the diameter of the lens, the centre thickness, the radius of curvature and conic constant of each of its surfaces, and the refractive index of the medium from which the lens is constructed. The lenses do not have to be spherical in shape and if required data files describing more complex lens surfaces can be implemented.

- **Mapping** Before propagating any electromagnetic fields a mapping is used to create an array of sample points on the surface of each element (see Figure 2.23). This is also required for visualisation of the system and establishes a relationship between a pair of indices (U and V) and the point on the surface. MODAL uses ray tracing to achieve this whereby the mapping procedure generates a matrix of rays that are then cast onto the surface of the element to calculate points of intersection and surface normal. The calculations are done by means of the surface geometry described above. There are three forms of mapping available in MODAL at present: isometric mapping, perspective mapping and uniform far

field mapping. In isometric mapping the rays are launched from a 2D grid of points in a given direction. The position of the grid can be defined by the user. Perspective mapping also makes use of a 2D grid, however, the rays are launched from a point source through each of the points on the user-defined 2D grid. The uniform far field mapping option launches a cone of rays from an arbitrary point. Each mapping can be used with a varying number of sample points in the U and V directions.

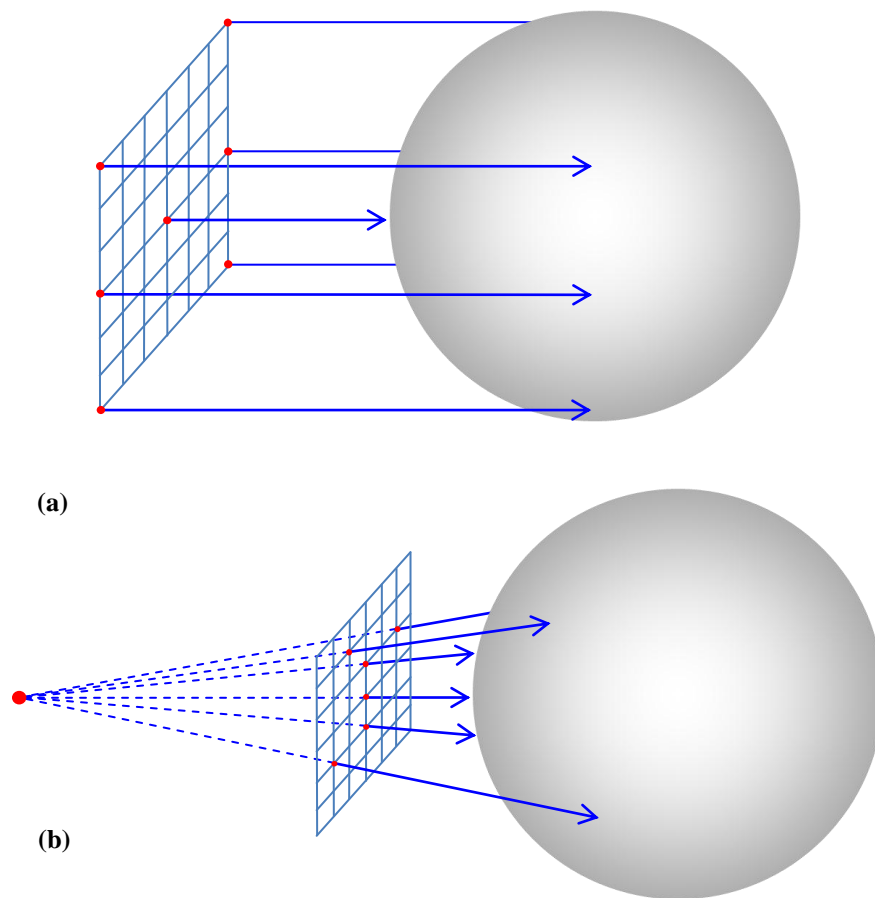


Figure 2.23 Mapping of elements in MODAL is done using either (a) an isometric method or (b) a perspective method. In the isometric method the rays originate from points on a grid while in the perspective method the rays are passed through the points on a grid but originate from a point source.

- **Propagator** To calculate a field representation at a certain element with the defined system a propagator is used. There are currently three classes of propagator in MODAL, these are source propagator, element propagator and far field propagator. The source propagator calculates the field produced from a

source. The element propagator calculates the reflected or transmitted field at an element by propagating the field from other propagators to (and possible through) the element. The far field propagator calculates the far field for a given near field. Each element propagator requires a source, which is in general a pointer to some other propagator.

There are a number of different field representations and propagation techniques available to the user. For the near field, defined on some surface, the user can choose from a scalar electric field or vector electric and magnetic fields. In the case of a scalar field, the calculations are done using either Fresnel diffraction integrals, as discussed in detail in section 2.3, or Gaussian beam mode analysis, as presented in section 2.4. MODAL also makes use of singular value decomposition analysis (SVD), which is discussed in more detail in Chapter 4. In the case of a vector field representation, physical optics (section 2.5) is used to calculate the required fields. Far fields can also be expressed in terms of scalar or vector fields.

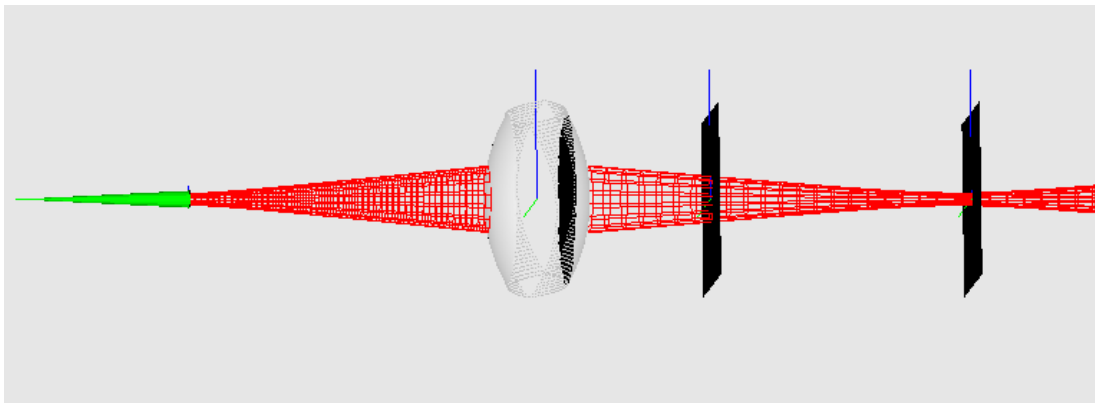


Figure 2.24 Beam propagation through a simple biconvex lens. The refractive index of the lens material is $n=1.5$ and both surfaces are spherical with radii of curvature $R=100\text{mm}$. The centre thickness of the lens is 60mm and its diameter is 100mm . The front surface of the lens is 200mm from the horn. The wavelength is $\lambda=1\text{mm}$, the corrugated horn source has an aperture radius $a=5\text{mm}$ and a slant $R=100\text{mm}$ (Gradziel *et al.*, 2008). The red lines show the equivalent Gaussian beam width and is used for visualization purposes only.

When a lens is present within a system, as in Figure 2.24, it is modelled by considering the two lens surfaces as dielectric interfaces and only a physical

optics analysis can be used (Gradziel *et al.*, 2008). In this approach the incident field (see Figure 2.25) is decomposed into transmitted and reflected components, $L(0)$ and $R(0)$ respectively, by treating the field as a locally spherically wave. The angle of incidence is calculated from the local direction of the Poynting vector and the surface normal, and the orientation and complex amplitude of the transmitted and reflected fields are determined using the standard Fresnel relationships (Hecht, 1998). At this point the transmitted field is propagated to the back surface where again it is decomposed in to transmitted, $T(1)$, and reflected, $L(1)$, components. This process is repeated between the front and back surfaces until the power in the lens field is below a predefined threshold or a certain number of iterations is reached, both of which are defined within the code and at present are not accessible to the user. The contributions from all the iterations are summed to give the total transmitted and reflected fields for the lens. It is important that the sampling rate at the surface is sufficiently dense to ensure the convergence of the physical optics propagation steps between the two lens surfaces (Gradziel *et al.*, 2008).

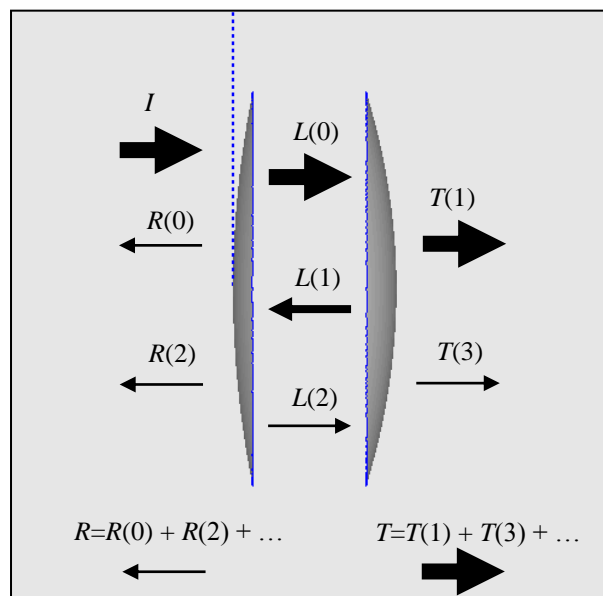


Figure 2.25 Physical optics propagation through a dielectric lens modeled in MODAL. I is the incident field, $T(n)$ and $R(n)$ are the transmitted and reflected components respectively and $L(n)$ represents the wave propagating through the lens (Gradziel *et al.*, 2008).

- **Beams** Having defined the optical system and its relevant propagators the beams propagating from one element to the next can be visualised. This is achieved by specifying the element, the distance of propagation and the source propagator. The beam is then displayed where the width has been calculated using a simple ABCD matrix approach as discussed in section 2.4.5 (see Figure 2.24).
- **Dataset/Metric** While propagators are used to calculate the fields at sources and elements within the system, to get access to this data the user must create a dataset. A dataset is a structured set of user-defined columns containing numerical data. Each column is inserted into the dataset manually with a range of options available, for example, a dataset may contain an x column, containing the x -coordinates of the field points from a certain propagator, a y column, containing the y -coordinates of the field points, and an E_x column, containing the magnitude of the x -component of the electric field. Each column can represent 1D or 2D matrices, as long as all columns do the same, and can be customised to suit the user's needs. If we consider a column containing a vector field value, the user can define the following:
 - Propagator (the source of the field)
 - Wavelength (spectral component of the field)
 - Component of the field (electric field, magnetic field, Poynting vector etc.)
 - Cartesian component of interest (x or y , in a given frame of reference)
 - Complex number component (real, imaginary, magnitude or phase)
 - Units for values (must be consistent with selected component).

Therefore the user could, for example, easily select the real value of the x -component of the Poynting vector in a defined frame in W/m^2 .

Another option that is available in MODAL allows the user to calculate a metric. Currently these include field power (calculates the total power in the field), field power fraction (calculates the fractional power given two fields), GBM mode-set parameters (provides the parameters of the mode-set used to describe the field),

scalar field coupling (calculates the coupling coefficient between a scalar field and a detector mode) and vector field coupling (calculates the coupling coefficient between a scalar field and a detector mode). These can be obtained for any propagator within the system and therefore at any plane where an output has been defined. In terms of coupling, a detector and incident propagator are defined by the user. MODAL has been extended recently to allow a dataset or metric be calculated as a function of a changing property value (for example the coupling coefficient as a function of detector position).

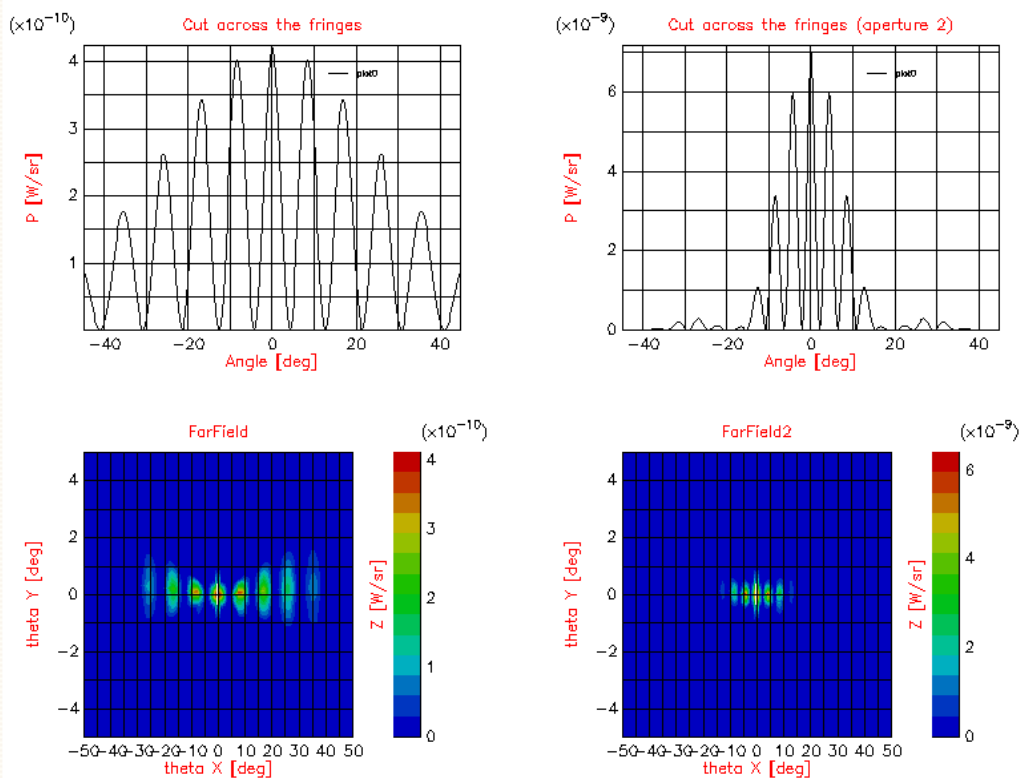


Figure 2.26 An example of xy and contour plots produced in MODAL for a double-slit interferometer. Two different system are shown.

- **Dataset Exporter** The datasets described above can be exported as a text file using a dataset exporter. The user can specify the filename, a header and footer, the separator to be used within the structure of the file and whether or not to export column labels and units.
- **Graph** As well as exporting data MODAL also allows the user to plot a variety of graphs (Figure 2.26) within the software, including xy graphs, contour graphs

and metric graphs. The data for these plots is taken directly from the datasets or metrics the plots are highly customisable through the user interface.

To enable the above components of MODAL to be implemented in a user-friendly manner three modules are required, a physical units module, a geometry module and a properties module. The physical units module knows about various physical quantities and handles the inputting and outputting of these with consistency. MODAL knows about different quantities and their units and through a dimensional analysis provides a bridge between the user input and internal computational routines. The user input can be done in the most convenient units while internally the same system of units (SI) is used consistently.

The geometry module handles geometrical objects such as scalars, points, directions, surfaces, solids, frames and transformations. The module allows the user to define objects in terms of other relevant objects, for example a vector can be expressed in terms of two points, or a frame can be defined in terms of another frame and some transformation. Within MODAL the same hierarchical editor is used for all objects and each class of object has its own set of operations. New object types and classes can therefore be added without significant changes to the code.

The properties module allows all higher level objects to have structure, for example, each property has its own unique name in a project (e.g. `Mirror1.geometry.frame`) and these properties can refer to each other by absolute or relative name. It allows objects to have dynamic dependencies, such as a graph depending on a particular dataset, and when the dataset changes the graph will be informed of this change. This can be propagated down many levels to the most primitive of object (e.g. points) within the project.

While the main components of MODAL have been described above the program is easily extendable due to its modular nature and layered structure (see Figure 2.27). Sources can be added by writing the code for the new source and adding it to the central object factory, the existing field representation does not have to be rewritten. In a similar way, new propagation techniques can be added to work with existing field representations. While more difficult, new field representations

can also be included, however, low-level field objects, sources and propagators, data extractors (dataset columns) and possibly new sources and elements would need to be added to the existing code. An example of this would be the inclusion of a dual polarisation scalar field. On an even higher level would be additional functionality, such as the ability to carry out optimisations.

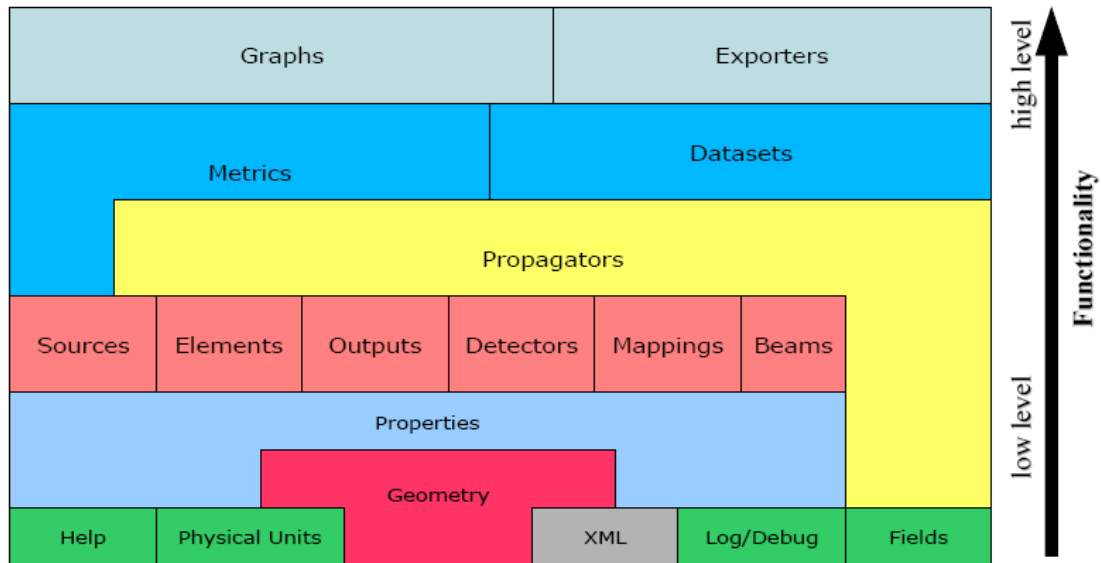


Figure 2.27 Schematic diagram showing the layered structure of MODAL and its functionality levels.

SCATTER

The mode-matching scattering-matrix software package SCATTER was originally developed by Ruth Colgan (Colgan, 2001) of the Terahertz Optics Group at NUI Maynooth. At the time, it was designed to fill the void in software availability for producing the electromagnetic beam patterns of corrugated horn antennas. In 2004, the program was further developed and extended by Emily Gleeson (Gleeson, 2004) and several extensions to the original software were included.

Line 1	Frequency (GHz)	Max. azimuthal order, n	Number of horn sections, N
Line 2 to Line $N+1$	Horn segment lengths, l (mm)		
Line $N+2$ to Line $2N+1$	Radius of horn segments, r (mm)	Number of real and evanescent modes	

Table 2.2 Layout of the SCATTER geometry file.

The current version of the SCATTER software reads in a “geometry file” that describes the horn antenna in terms of the radius, r , and length, l , of each corrugation (see Figure 2.28) and the frequency of operation, as shown in Table 2.2. The specification of the geometry file is achieved through a user interface, which also displays the aperture field pattern and the far field pattern for the given horn. It is generally assumed that the horn is excited equally by all modes, but this can be easily modified. Mode-matching is a very powerful technique and was extensively used as part of the overall analysis of complete optical systems in which horn antennas were used. The SCATTER code was extended by the author to include rectangular-to-circular junctions as part of the analysis of the horn antennas in the MBI project, as described in Chapter 4.

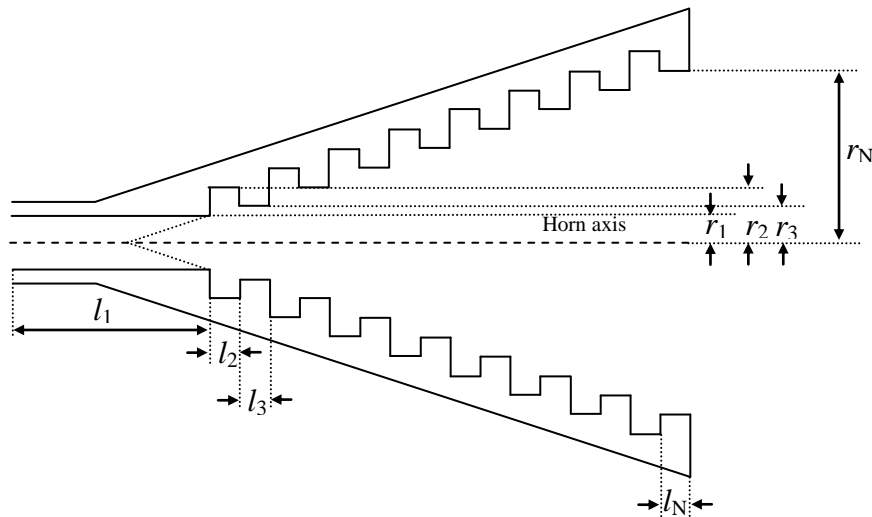


Figure 2.28 Corrugated horn antenna with grooves oriented perpendicular to the horn axis (left) and perpendicular to the horn surface (right).

ZEMAX

ZEMAX software (ZEMAX website) is a powerful ray tracing software package that can model, analyse and allow the design of optical systems to be optimised. The interface has been designed to be simple to use and with a little practice it allows very rapid interactive design.

There are six different *Editor Windows*, the Lens Data editor, the Merit Function editor, the Multi-Configuration editor, the Tolerance editor, the Extra Data editor and the Non-Sequential Components editor, each serving a different and useful purpose. For a simple optical system in which the user simply wants to view the layout and rays, details about each surface between the object and the image plane, for example the thickness of a lens and its radius of curvature, can be entered into the Lens Data editor (see Figure 2.2). For media other than air, the substance name, which can be obtained from the built-in glass catalogue, must also be entered. If the material needed does not appear in this catalogue, the user may define their own material refractive index as a function of wavelength.

Apodisation of the entrance pupil of the system enables the user to illuminate this aperture either uniformly or non-uniformly. The apodisation factor determines the rate of variation in amplitude (number of rays) across the pupil. By default, the system will have uniform illumination, but Gaussian and tangential may also be chosen. Gaussian apodisation imparts an amplitude variation over the pupil that is Gaussian in form, while tangential apodisation simulates the intensity fall off characteristic of a point source illuminating a flat plane. Once the source is defined the user is in a position to ray trace through the optical system. The wavelength of the radiation must be entered (in microns) and then a two-dimensional layout of the optical components may be viewed, complete with rays. The number of rays traced through the system can be varied and vignetting may be switched on or off.

ZEMAX also contains a tool called Physical Optics Propagation (POP) which uses diffraction calculations to propagate the beam through the optical system surface by surface. When using POP the beam is modelled using an array of points containing the complex field amplitude. ZEMAX then chooses between Fresnel

diffraction propagation or angular spectrum propagation, depending on which provides the highest numerical accuracy. The accuracy of the results from using POP are approximately equal to propagation using the Gaussian beam mode or Fresnel integral methods with ray tracing still being used for propagation through dielectrics.

GRASP

GRASP (TICRA's GRASP website) is a software package that provides the user with a set of tools for analysing general reflector antennas. A pre-processor allows the user to define the geometry of the antenna or system being modelled and provides a means of visualising the system, while the post-processor contains several plotting facilities for calculated beam patterns.

The software has been developed using Fortran 90 and makes extensive use of object-orientated programming techniques so that the reflector surfaces and antenna feeds within the system are described in terms of their particular class. Throughout the process of defining the system the user may visualise the system or generate a file containing geometrical information which can be imported into CAD packages. In defining the system the user can select from a number of reflector surface, rim definitions, feed types and reflector materials before choosing analysis methods such as physical optics, geometrical optics and geometrical theory of diffraction. With such capabilities GRASP has become the industry standard for modelling reflector antenna systems.

CST

The CST Studio Suit 2009 is a commercially available software package, which makes use of finite integration techniques (FIT) to carry out electromagnetic simulations. Unlike most numerical methods, FIT discretises the integral form of Maxwell's equations rather than the differential ones. To solve these numerically

one must define a finite calculation domain. To that end a mesh system is implemented to split up the domain into many grid cells.

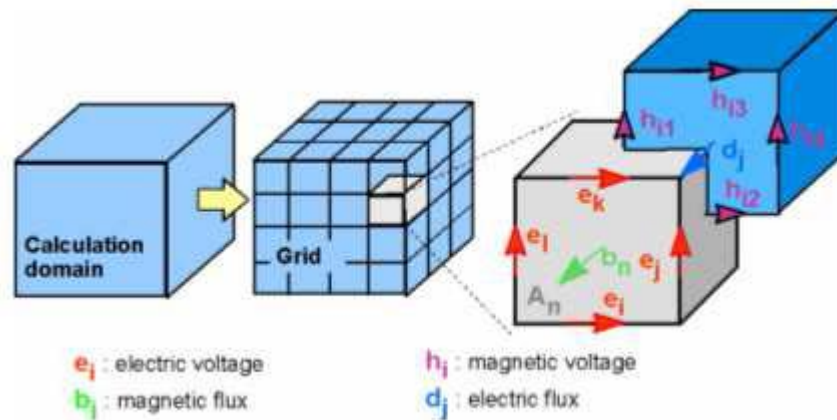


Figure 2.29 An image of the CST mesh system (CST Documentation Centre).

The primary mesh can be visualised in CST using Mesh View, however, internally a second or dual mesh is set up orthogonal to the first one (see Figure 2.29). The spatial discretisation of Maxwell's equations is performed on these two orthogonal grid systems with Maxwell's equations being formulated for each of the cell facets separately.

A noteworthy point of the FIT technique is that the properties of the continuous gradient, curl and divergence operators are maintained in grid space. In addition to orthogonal hexahedral grids, FIT can also be applied to more general mesh types such as topologically irregular grids and tetrahedral grids.

Although FIT simulations and CST Microwave Studio are proven and reliable it has the drawback of requiring significant computational power and lengthy simulation times when considering detailed structures in the mm-range.

Other Software

Along with the software mentioned above, the author has also made extensive use of both Mathematica (Wolfram Mathematica website) and Matlab

(MathWorks Matlab website) throughout this project. These have been used to develop programs to act as verification tools, for example, in the Gaussian beam mode analysis of optical systems and also to develop many data handling and analysis programs.

2.7 Conclusions

In this section the techniques used in the quasi-optical analysis work in this thesis were presented. The simplest approach examined was geometrical optics or ray tracing. It treats the radiation as having a negligible wavelength and is very useful in the initial design stages of a system. Focal points can be instantly recognised and it becomes obvious whether the beam intercepts the optical components or not. However, rays effectively represent infinite plane waves and therefore fail to adequately deal with diffraction effects associated with coherent fields and components of scale sizes of 1 to 100λ . The industry standard program ZEMAX was used in the work outlined in this thesis to perform a ray tracing geometrical optics analysis of the various optical systems considered.

To account for diffraction effects the Fresnel Integral was considered. Fresnel diffraction refers to propagation over a finite distance and therefore is also sometimes referred to as near-field diffraction. This method is quite efficient when applied to single elements within optical systems, however, it becomes inefficient when analysing a complete system due to the number of the integrals required. Fresnel integrals can be used to propagate radiation through free-space, taking into account apertures and stops. This integral method is also powerful in analysing diffraction at mirrors, which appear in most optical systems. The method assumes a paraxial beam and does not take into account the vector nature of the field. In the work presented in this thesis Fresnel diffraction analysis is carried out using MODAL.

In a Gaussian beam modes analysis, a more efficient alternative, a monochromatic spatially coherent beam is represented by a complex scalar field

considered to be made up of a linear sum of complex independently propagating modes. These modes are solutions to the wave equation and maintain the same amplitude profile as they diffract. The Gaussian beam mode method takes into account the changing width of the beam as it propagates, along with the evolution of its phase-front radius of curvature. While this method is equivalent in accuracy to Fresnel integral method, the disadvantage of using the Fresnel approach directly is that the transformation (often involving computationally intensive integrals) has to be applied at each optical component in the system. Gaussian beam mode analysis has the advantage that as long as the modes themselves are not scattered (by truncation or aberrational effects), the propagation through focussing systems is very simply taken care of by the evolution of a common phase curvature term. Fresnel transformations are therefore only more efficient for the analysis of systems with significant truncation and aberrational effects. In the absence of such effects, in which case only one set of integrals have to be performed at the input plane to determine the mode coefficients, Gaussian beam mode analysis can be very efficient as a quasi-optical technique. Fresnel and Gaussian beam mode diffraction assume both paraxial propagation and that the field can be represented by a scalar function.

The final, more accurate approach presented in this chapter and relevant to the work carried out in this thesis is physical optics. Physical optics treats the radiation as an electromagnetic wave whose sources are currents that flow in the surfaces of reflectors (or other scattering elements) and in the bulk of dielectric materials. MODAL is most widely used to analyse optical systems using physical optics as presented in this thesis.

To summarise, four methods used for quasi-optical analysis in this research were presented: geometrical optics, Fresnel transformations, Gaussian beam mode analysis, and physical optics. Each has its own advantages and disadvantages, depending on the application, but used together they form a powerful set of tools for analysing different properties of quasi-optical systems. By applying them to the same system and comparing their predictions, a very powerful high-confidence approach to analysing quasi-optical systems can be developed. Chapters 3 to 6 will show how these techniques of quasi-optical analysis were put to use in the design and analysis of the both the MBI and QUBIC instruments.

Chapter 3

The Millimetre-Wave Bolometric Interferometer

3.1 Introduction

This chapter presents the work done on the optical design of the beam combiner for the Millimeter-Wave Bolometric Interferometer (MBI), a ground based instrument designed to measure the polarization anisotropies of the Cosmic Microwave Background (CMB) at a central frequency of 90GHz. Interferometry has never before been used to carry out such measurements at this frequency, nor using incoherent bolometers as detectors. MBI will therefore act as a prototype for this type of system and must be modelled in detail to ensure that its operation is fully understood.

The telescope contains a number of quasi-optical components, including a complex back-to-back system of corrugated feed horn antennas. Knowledge of the optical performance and beam patterns of such a system is critical for understanding systematic effects in the reliable extraction of feasible polarization signals. To model the system accurately we have employed a variety of both commercial and in-house software packages. MODAL (section 2.6) (Gradziel *et al.*, 2008), an optical design and analysis package developed at NUI Maynooth and targeting the millimetre and sub-millimetre region of the electromagnetic spectrum was used most widely. This not only allows the initial design and preliminary analysis of the multi-element optical system to be carried out in a computationally efficient manner using quasi-optical techniques but also enables a complete electromagnetic characterisation using physical optics. We describe the techniques used, their predictions and the performance of the telescope as calculated to-date.

MBI is a Fizeau interferometer that combines the advantages of interferometry for control of systematic effects with the high sensitivity and frequency coverage possessed by bolometers (Korotkov *et al.*, 2006). It is the first

bolometric interferometer of its kind which results in a novel instrument with capabilities that would be difficult to achieve using more traditional techniques and will allow MBI and instruments based on its technology to explore a wide range of angular scales and wavelengths. Unlike a single-dish imaging telescope, an interferometer instantaneously performs a differential measurement with the effective beam pattern of each individual baseline being a set of fringes that sample the sky with positive and negative weights. This differencing removes the need for mechanical chopping or rapid scanning.

The prototype MBI instrument has four interferometer apertures and uses nineteen cooled spider-web bolometers. This prototype is called MBI-4 and also operates at a central frequency of 90GHz. The configuration used in this system may be expanded to an $N=8$ instrument with eight apertures and it was proposed to ultimately design and build a 64-element interferometer or $N=64$ configuration (MBI-64), however, this might be superseded by the QUBIC instrument as discussed in Chapter 6. MBI-64 will operate as either eight $N=8$ interferometers in parallel or as one $N=64$ system. As a prelude to MBI-4, both a room temperature and a cryogenic interferometer called the MBI Test Bed (MTB) were demonstrated and successfully produced interference fringes as desired. MBI-4 has also undergone demonstration and test observations at Pine Bluff Observatory, Cross Plains, Wisconsin before being used for full scale scientific observations and measurements.

3.2 The Instrumentation of the MBI-4 System

In this section we look at the components of the MBI-4 instrument (discussed in more detail by Hyland (Hyland, 2008)) and how they are used to measure the interference pattern created by the optical beam combiner. We begin by looking at the structure of the telescope mount and how this is operated to allow the implementation of the desired observing strategy.

3.2.1 Observing Strategy and Telescope Mount

MBI-4 will be deployed at Pine Bluff Observatory, Wisconsin, the same location as that used for test measurements outside the lab. This site was chosen because of its proximity to the University of Wisconsin-Madison, the reasonable viewing it provides and the existing infrastructure, as well as the ease of finding calibration targets such as guide stars in the dark night skies.



Figure 3.1 MBI-4 at the Pine Bluff Observatory site.

The observing strategy requires that MBI can observe any point on the sky and be able to rotate around the line of sight to allow the measurement of either the Q or U Stokes parameters. This is accomplished with a standard altitude-azimuth design for pointing with an added rotation axis. Due to the importance of levelling the system the base of the telescope mount is a tripod, with each corner containing a wheel for ease of movement and a jack-screw to allow alteration of the height. Sitting above the tripod base is a 1-inch thick aluminium driving disk with a diameter of 53 inches, surrounded by a stainless steel ring. This one-eighth inch thick

ring provides support to the disk and acts as a driving surface which turns the mount on its azimuth axis.

The frame and the z -axis (rotation) bearing that sits on top of the base was recycled from the COMPASS experiment (Farese *et al.*, 2004) with an extra plate added to the bottom surface to prevent buckling. Elevation is achieved by means of an arm and pivot and allows the telescope to be positioned at angles between 0 and 90 degrees. In summary, the MBI pointing platform consists of a fully steerable altitude-azimuth mount on which the entire cryostat can be rotated around the optical (z) axis. Tracking of the sky occurs under computer control using feedback from 17-bit absolute optical encoders on each of the three axes: azimuth, elevation, and z . Absolute pointing is achieved using a bore-sighted optical telescope (Tucker *et al.*, 2008).

3.2.2 Interference

In a simple two-element interferometer, signals from two telescopes pointing at the same point in the sky are correlated so that the sky temperature is sampled with an interference pattern with a single spatial frequency. The output of such an interferometer is the visibility, $V(\vec{u}) \propto \int G(\hat{x}) \Delta T(\hat{x}) e^{i2\vec{u} \cdot \hat{x}} d\hat{x}$, where \hat{x} is a unit 3-vector in the direction of the point on the sky, $G(\hat{x})$ is the beam pattern of each antenna (assumed to be identical) and $\Delta T(\hat{x})$ is the map temperature fluctuations on the sky we are trying to measure. The vector \vec{u} has length B/λ , where B is the length of the baseline, and is orientated along the baseline. To recover the full phase information complex correlators are used to simultaneously measure both the in-phase and quadrature phase components of the visibility (Tucker and Timbie, 2009). This type of interferometer is called a *multiplying* interferometer.

An alternative approach to interferometry is to use an *adding* interferometer, in which incoherent detectors are used, such as in MBI, and the electric fields from two telescopes are added and then squared at the detector (e.g. Rohlfs and Wilson,

1996). The result is an interference term and a constant term proportional to the intensity (Figure 3.2), which is an offset that is removed by phase modulating one of the signals. Synchronous detection at the modulation frequency recovers the interference term and reduces susceptibility to low frequency drifts ($1/f$ noise) in the bolometer and readout electronics. The adding interferometer recovers the same visibility as the multiplying interferometer.

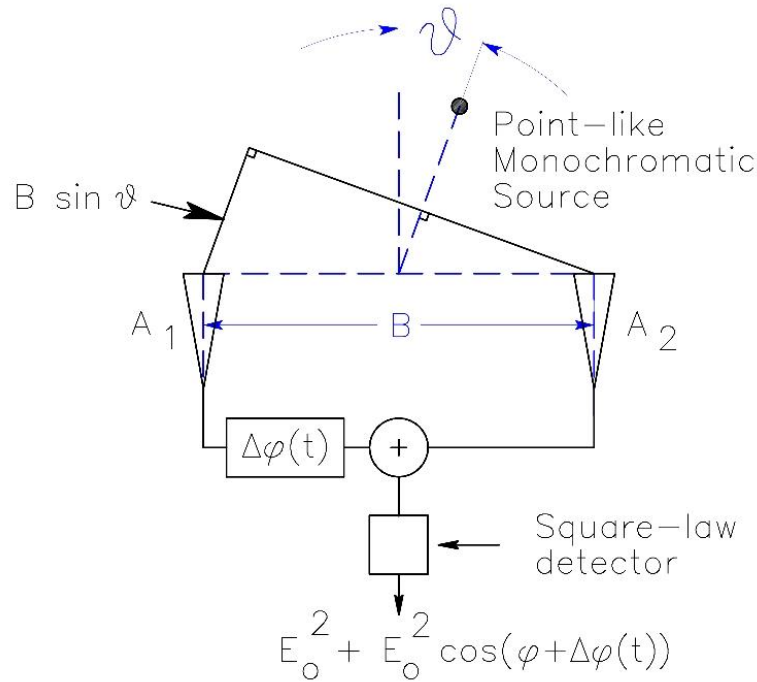


Figure 3.2 Schematic diagram of an adding interferometer where $\phi = (2\pi B/\lambda)\sin\theta$ (Tucker *et al.*, 2008).

The polarisation of radiation is completely characterised by the Stokes parameters, I , Q , U , and V . If the incoming wave is expressed as $\vec{E} = E_x\hat{i} + E_y\hat{j}e^{i\phi}$, then the linear polarisation Stokes parameters are $U = \langle 2E_xE_y \cos\phi \rangle$ and $Q = \langle E_x^2 - E_y^2 \rangle$, the circular polarisation parameter is $V = \langle 2E_xE_y \sin\phi \rangle$ and the intensity $I = \langle E_x^2 + E_y^2 \rangle$, where the angle brackets denote the time average. Stokes Q and U are related to each other by a rotation and therefore an instrument that measures U can be rotated by 45° to measure Q , and vice-versa.

As discussed by Tucker *et al.* (2008), an interferometer measures the Stokes parameters directly, without differencing the signal from separate detectors and correlates the components of the electric field captured by each antenna with the components from all the other antennas. On the baseline formed by two of these antennas, say 1 and 2, the interferometer's correlators measure $\langle E_{1x}, E_{2x} \rangle$, $\langle E_{1y}, E_{2y} \rangle$, $\langle E_{1x}, E_{2y} \rangle$ and $\langle E_{1y}, E_{2x} \rangle$, with the first two being used to measure I and the second two, U . Rotating the instrument allows the measurement of Q . The Stokes V parameter can be recovered in a similar manner but is expected to be zero for the CMB and will not be measured by MBI.

3.2.3 Detectors and Signal Processing

The detectors used in MBI are spiderweb bolometers that were designed for the ACBAR (Arcminute Cosmology Bolometer Array Receiver) experiment (Reichardt, 2009) and are not sensitive to polarisation. They are voltage biased and arranged in a resistance bridge with other resistors. If the bolometers resistance changes then the percentage of the overall resistance that it represents will change and therefore the voltage drop across it will vary. The resistance of the bolometers increases as they are cooled and so to establish the voltage the temperature across them is measured. The voltage bias is modulated in the form of a sine-wave with a frequency of 208Hz, which is expected to be faster than the rate of change of temperature in the bolometric detectors.

A lock-in amplifier is used to measure the signal and the output is proportional to the amplitude or inversely proportional to the temperature of the bolometers. This in turn is inversely proportional to the power received by the detectors. The lock-in amplifier integrates out random thermal and electrical noise, therefore only slowly varying signals are considered.

The signals to be detected from the CMB are extremely small and therefore signal processing is vitally important if fidelity between the final reading and the

signal is to be maintained. The sinusoidal voltage bias board is a copy of the BLAST (Balloon-borne Large-Aperture Submillimeter Telescope) (BLAST website) bias board and sits at the base of the telescope mount. A single bias line is fed into the cryostat with all the bolometers being biased with the same signal at 208Hz. Twelve digital lines control the amplitude of the bias signal between 0 and 16 volts peak to peak and the frequency is set using an external reference signal provided by one of two National Instruments Field Programmable Gate Array (FPGA) boards. These boards are also used in the acquisition chain to lock-in to the bias signal, an arrangement that minimises spurious signals due to small differences in clocks.



Figure 3.3 A spiderweb bolometer (ESA's Planck Satellite website).

The voltage across the bolometers is amplified by a JFET module which is located on the 77K shield of the cryostat but generally operates at 120K to 130K, with the extra heat being provided through the wires connecting it to a 300K connector. An optimal operating temperature of 120K will minimise the noise in the JFET module. A shielded cable connects the module to a readout board which uses a band pass filter centred on 208Hz to filter out noise before amplifying the signal by a factor of 196. The output passes to the analogue inputs of FPGA boards which

perform a lock-in detection, including phase information, before being recorded by a data acquisition program. This is performed approximately three times per second and the program also records the states of the phase modulators.

3.2.4 Cryogenics

The MBI cryostat (Figure 3.4) consists of two cryogen tanks, an outer tank for liquid nitrogen and an inner tank for liquid helium, with the final cooling being done using a series of refrigerators. The refrigeration unit is composed of a ^4He and two ^3He refrigerators operating at a cold head temperature of 260mK. Such a system was chosen based on the cooling requirements of the detectors and the overall performance of the system.

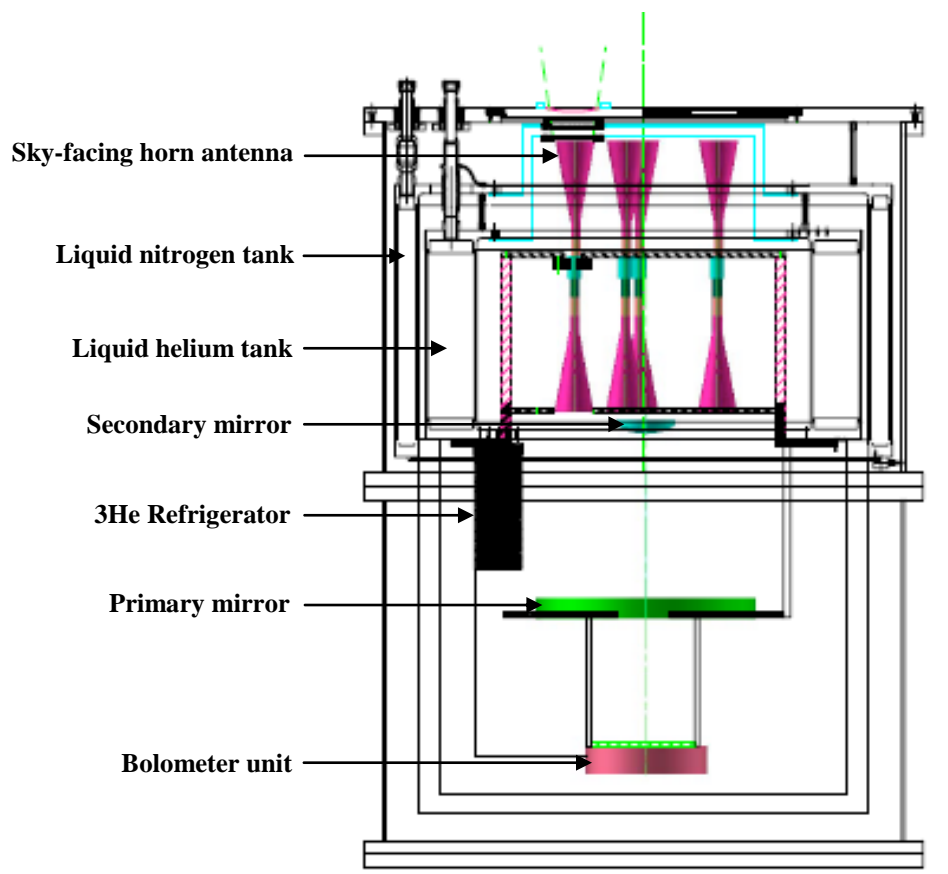


Figure 3.4 Schematic diagram of the MBI-4 cryostat.

The cold plate of the first ^3He fridge is thermally linked to the bolometer readout wiring at a preliminary stage that is thermally isolated from the focal plane. This is done to intercept heat flowing down the wires from the hot stages before it makes it to the bolometers. The first ^3He stage is used because it has more cooling power and a higher temperature than the second or final ^3He stage. The bolometer focal plane is connected to the final ^3He stage through a similar arrangement and the phase shifters are cooled separately to 4.2K due to the fact their large operational thermal load makes it impractical to cool them with the ^4He and ^3He refrigerators while they are in use.

The cryostat for MBI was constructed by A. S. Scientific Ltd. and has a cold time of 96 hours without any thermal load. It is cylindrical in shape with a length of 1m and a diameter of 0.7m.

3.2.5 The Optical System

The sensitivity of a receiver to broadband signals increases as the square root of the bandwidth. The bandwidth of MBI was chosen to make the instrument sensitive to polarisation B-modes of approximately 1° ($l = 150 - 270$). This bandwidth placed constraints on the design of the optical system, since for interferometers bandwidth restricts the angular range, θ , over which fringes are detected (Thompson *et al.*, 1998; Boker and Allen, 1999). If it is assumed that the path lengths (through both arms of an interferometer) for a source at the centre of the field of view (FOV) are equal, then the path length difference for a source at an angle θ from the centre along the baseline axis is θB , where B is the baseline distance. If the path length difference is small compared to the coherence length of the radiation, $\lambda^2 / \Delta\lambda$, then the fringe contrast is not affected. Therefore the FOV is determined by $\theta_{FOV} \leq (\lambda / \Delta\lambda)(\lambda / B)$, which indicates that for angles of the order of the product of the spectral resolution times the angular resolution, the fringe smearing is important. This relation imposes restrictions on the ratio between the

maximum baseline achievable by the interferometer and the spectral bandwidth of the receiver. For MBI-4 the bandwidth is 15%, which sets the maximum baseline to approximately six times the diameter of each antenna.

A flow chart and schematic diagram of the MBI optical chain is shown in Figures 3.5 and 3.6 respectively, starting with the vacuum windows and filters for each of the four sky horn antennas. These are circular corrugated horn antennas and are analysed in some detail in 4.3.2. Radiation from the sky horns is propagated through the circular waveguide section at the back of the horn which is followed by a circular-to-rectangular waveguide transition, which selects a single polarisation direction. Two of the horns are set to select an x -polarisation while the other two are orientated perpendicular to this to select polarisation in the y -direction. Although the relative alignment of these directions is critical they are initially set by eye and then fine-tuned using micro screws. By setting the polarisation directions in this way it enables interference between E_x and E_x , E_y and E_y , and E_x and E_y , which allows for the recovery of the Stokes Q and U parameters.

The ferrite phase modulators make use of the Faraday Effect, a magneto-optical phenomenon, to rotate the linear polarisation that passes through them. They are operated so that they shift the polarisation by either plus or minus 90° from its original orientation. By controlling the direction of rotation, the phase of the radiation emitted is changed between two states which have a 180° phase difference. A 45° waveguide twist then forces the polarisation direction to be changed by either $+45^\circ$ or -45° , maintaining the 90° difference between each of the baseline horns before connecting to a rectangular-to-circular waveguide transition followed by the inward facing horn, which has exactly the same structure as the sky horn.

The radiation emitted into the cryostat from the inward-facing horns is reflected off a parabolic primary mirror followed by a hyperbolic secondary mirror arranged in a Cassegrain configuration. This is the beam combiner section of MBI. The position and curvature of the mirrors has been optimised by NUI Maynooth for the internal geometry of the cryostat, something which is explained in more detail in section 3.3.



Figure 3.5 Flow-chart describing the MBI optical chain.

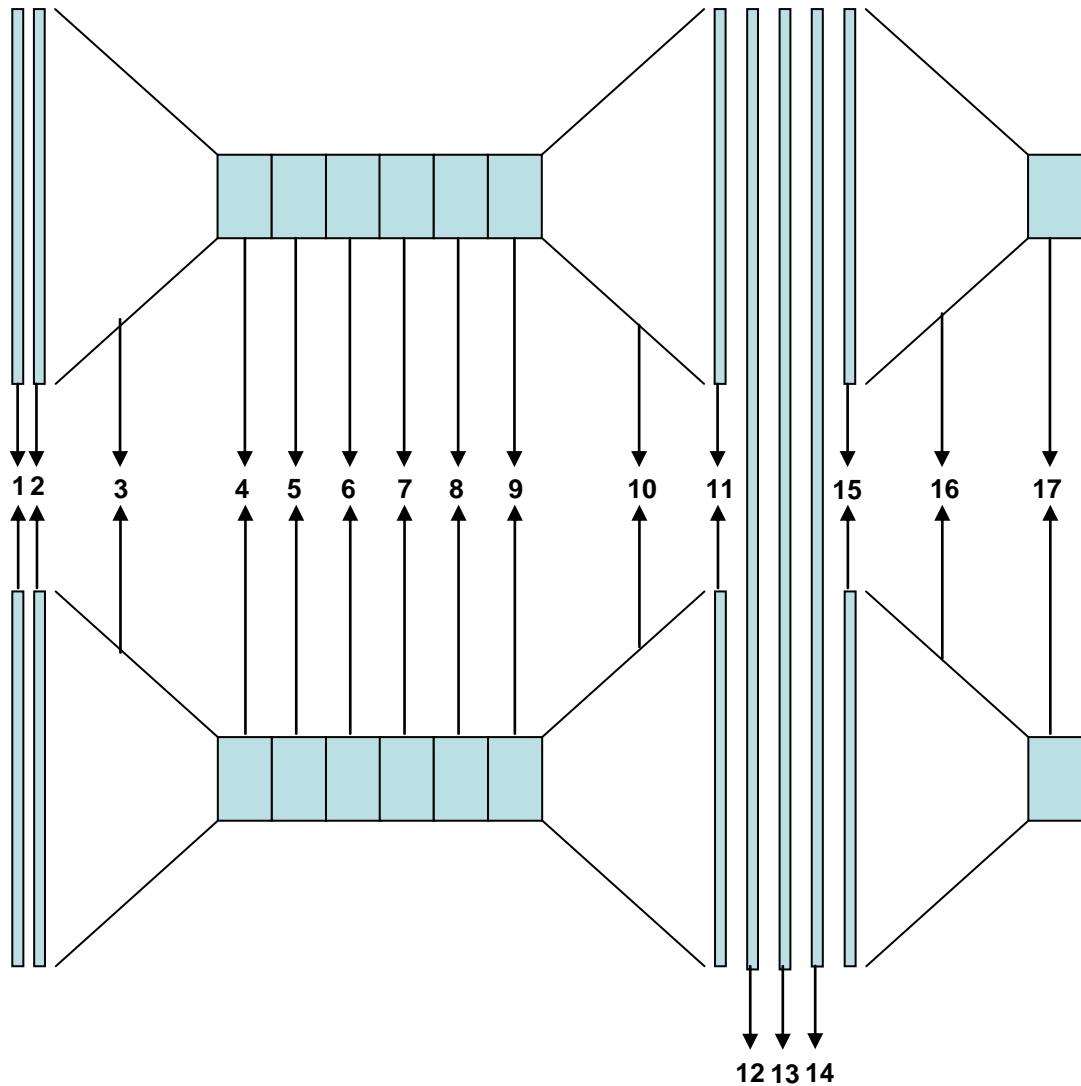


Figure 3.6 Schematic diagram of the MBI optical chain showing the position of (1) vacuum window, (2) warm filter, (3) sky-facing corrugated horn antenna, (4) circular waveguide, (5) circular-to-rectangular waveguide transition, (6) 45 degree waveguide twist, (7) phase modulator, (8) rectangular-to-circular waveguide transition, (9) circular waveguide, (10) inward-facing corrugated horn antenna, (11) phase-flattening lens, (12) secondary mirror, (13) primary mirror, (14) cold filter, (15) phase-flattening lens, (16) detector horn and (17) bolometer for a single baseline.

After reflection from the secondary mirror the radiation is focused into the focal plane which is covered with two layers of metal mesh filters at 400mK. The focal plane is a solid block of copper which has had nineteen smooth-walled conical feed horns (see section 4.2) machined into it with the excess material removed to reduce the thermal load on the cryogenics (Figure 3.8). A corrugated polyethylene lens is attached to the mouth of each horn to help flatten the phase of the incoming

radiation across the aperture. The horns feed the radiation to an array of spiderweb bolometers as discussed in section 3.2.3.

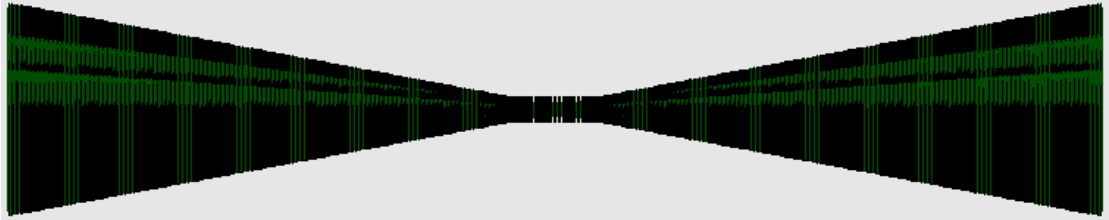


Figure 3.7 Back-to-back horn corrugated horn antenna with no circular waveguide extension between the horns.

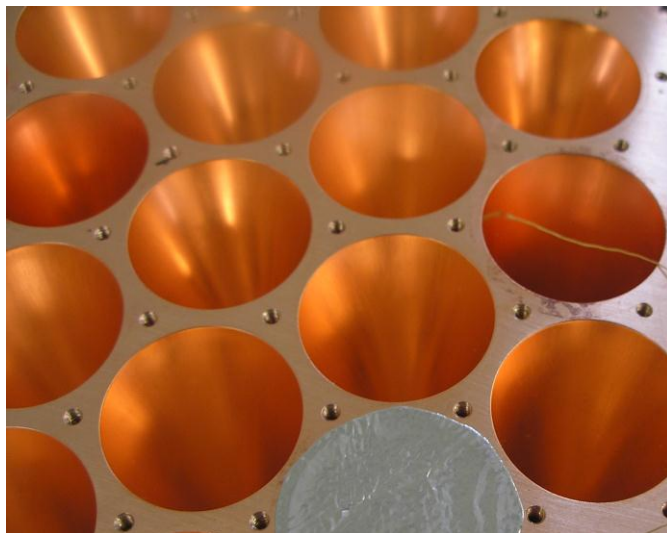


Figure 3.8 Detector horn antennas milled from a copper block.

3.3 Design of the MBI-4 Optical Beam Combiner

There are a number of ways in which beams can be combined to form an interference pattern, a Butler combiner (a guided-wave structure consisting of waveguides or microstrip transmission lines), for example, however for scalability reasons (scaling up to 64 horn antennas) an optical beam combiner was chosen for MBI. The design of the optical beam combiner for MBI-4 was carried out at NUI

Maynooth using a combination of geometrical optics and a diffraction analysis. The following sections outline the design process and provide details on the parameters calculated for different possible mirror configurations within the physical constraints of the cryostat and the type of detectors used.

3.3.1 The Design of the Optical System

The optical beam combiner was designed around a number of constraints that were already in place, including the physical size of the cryostat, the size and arrangement of the detector horn array, the size and position of the back to back horn system feeding the telescope (as described in section 4.3.2) and the focal plane sampling required for the instrument. With this in mind a Cassegrain configuration was chosen, a diagram of which is shown in Figure 3.9.

A Cassegrain reflector (named after Laurent Cassegrain after a design for a reflecting telescope was published in the *Journal des Sçavans* on the 25th April, 1972 (Baranne, 1997)), is a combination of a concave primary mirror and a convex secondary mirror, which in a symmetrical system are aligned along the optical axis. In the classical Cassegrain configuration the primary mirror is parabolic while the secondary is hyperbolic, as is the case for MBI-4 (Figure 3.9).

3.3.2 A First Approximation Using Geometrical Optics

Consider the Cassegrain system shown in Figure 3.10. In MBI-4 the values that were fixed before the optical system was considered were the aperture radius of the inward facing corrugated conical horn antennas ($\sim 25\text{mm}$), the aperture radius of the smooth-walled conical detector horn antennas ($\sim 12.5\text{mm}$) and the resolution required ($\sim 1^\circ$). Since resolution $\approx \lambda/D$, the longest baseline, D , was also fixed at 200mm.

It was necessary when designing the system to ensure that each fringe was sampled at least twice (Nyquist criterion), which, given the size of the detector horns, meant a fringe spacing of at least 50mm. If we consider the equivalent system shown in Figure 3.11, for small angles $f \approx XD/\lambda$ giving an equivalent focal length of $f = 3000\text{mm}$ and an $f/15$ ($f/\# = f/D = 3000/200$) beam at the output plane.

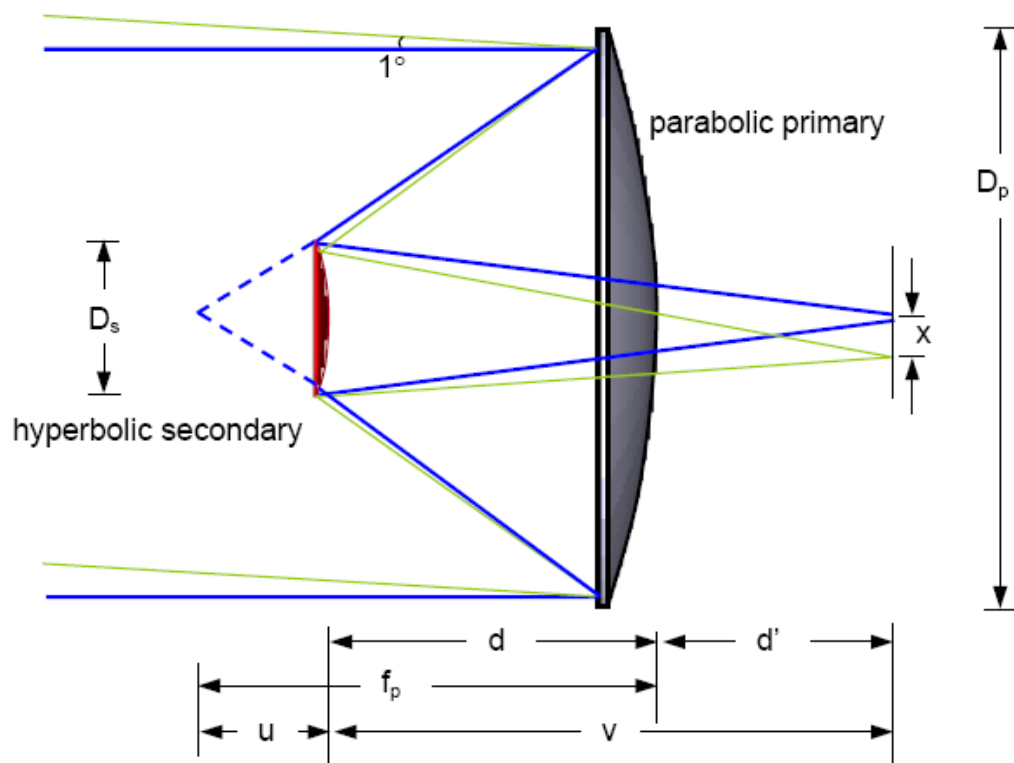


Figure 3.9 Schematic diagram of a classical Cassegrain system. D_p = diameter of primary mirror, D_s = diameter of secondary mirror, d = distance between mirrors, d' = distance of image plane behind primary, f_p = focal length of primary mirror.

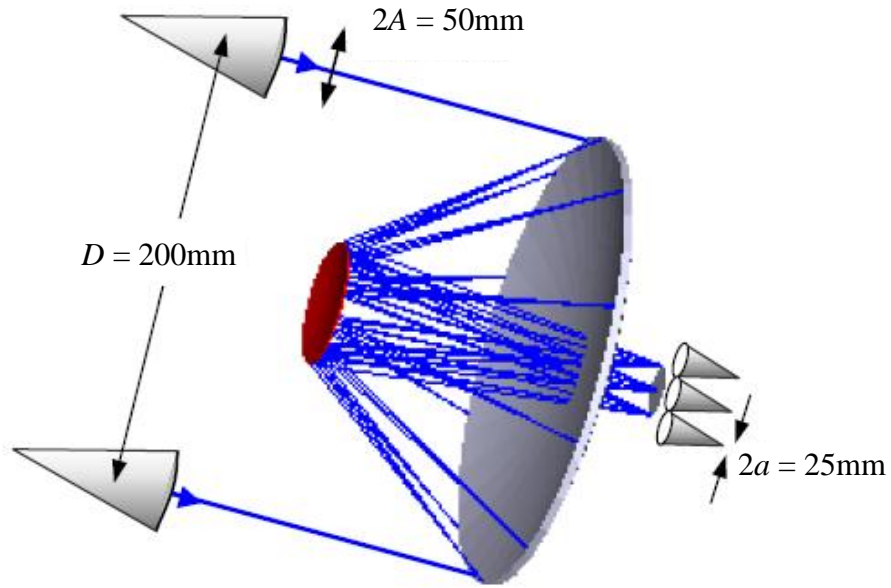


Figure 3.10 MBI-4 Cassegrain system showing one long baseline with fixed horn antenna radii. A is the radius of the inward-facing horn antenna while a is the radius of the detector horn antenna.

With regards to the mirrors in the system, the parabolic primary with focal length f_p and the hyperbolic secondary with focal length f_s , separated by a distance d , must combine to give a focal length f as,

$$\frac{1}{f} = \frac{1}{f_p} + \frac{1}{f_s} - \frac{d}{f_p f_s} \quad (3.1)$$

As long as this condition was met we were free to choose f_p , f_s and d . It was also important to keep the diameter of the secondary mirror relatively small compared to that of the primary mirror to prevent as much blockage as possible.

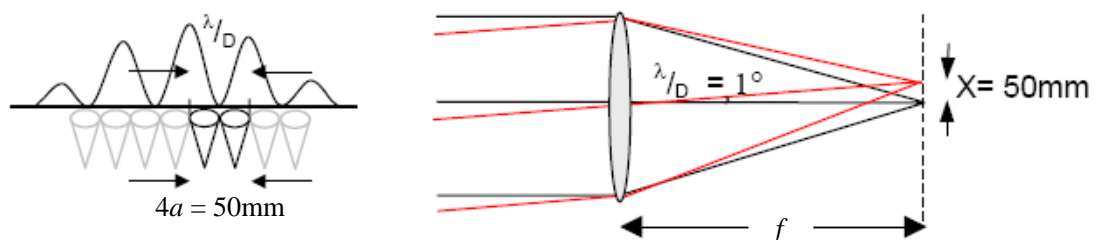


Figure 3.11 The Cassegrain system with the mirrors replaced by an equivalent bi-convex lens.

As an initial step, the ratio of the diameter of the secondary mirror to that of the primary was set at 1/4 (i.e. $D_s/D_p = 1/4$). From Euclid's theorem on similar triangles this meant that the mirror separation $d = (3/4)f_p$. As an example, a value of 500mm was chosen for d , giving a primary focal length $f_p = 666.67$ mm and from Equation 3.1 a secondary focal length $f_s = -214.3$ mm (following the sign convention that concave mirrors have a positive focal length while convex mirrors have a negative focal length). In a classical Cassegrain system the near focal point of the hyperbolic secondary mirror (u) is coincident with the focus of the primary mirror, so again by means of similar triangles $u = f_p/4$. The image distance $v = D_s \times f / \# = 750$ mm, meaning that focal plane is a distance of $v - d = 250$ mm behind the primary as shown in Figure 3.12.

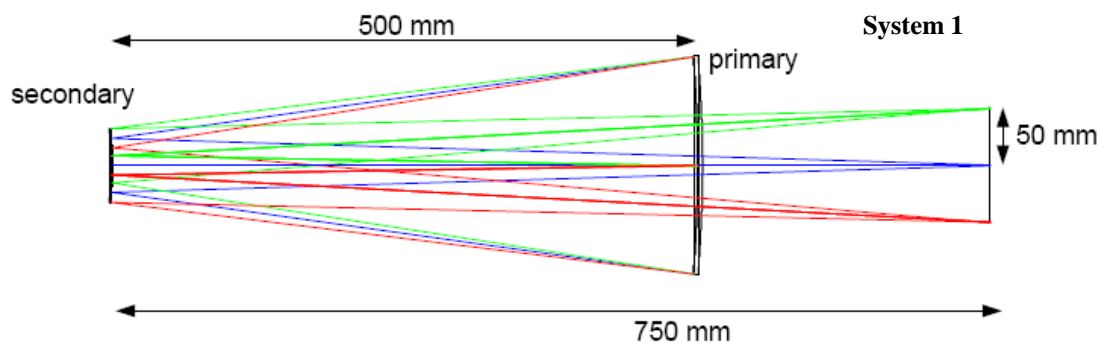


Figure 3.12 Cassegrain design concept with a mirror separation of 500mm.

If d had been set to 750mm and the same criteria applied then $f_p = 1000$ mm, $f_s = -375$ mm, $u = 250$ mm and $v = 750$ mm, meaning that the focal plane would lie at the same location as the primary mirror (Figure 3.13 (a)). On the other hand, if d was set to 1500mm, then $f_p = 2000$ mm, $f_s = -1500$ mm, $u = 500$ mm and $v = 750$ mm, placing the focal plane half way between the primary and secondary mirrors (Figure 3.13 (b)). In this case D_s would almost need to be doubled in diameter to accommodate off-axis rays. The particular system that was eventually chosen (see Table 3.8) depended on the physical restrictions imposed by the existing cryostat.

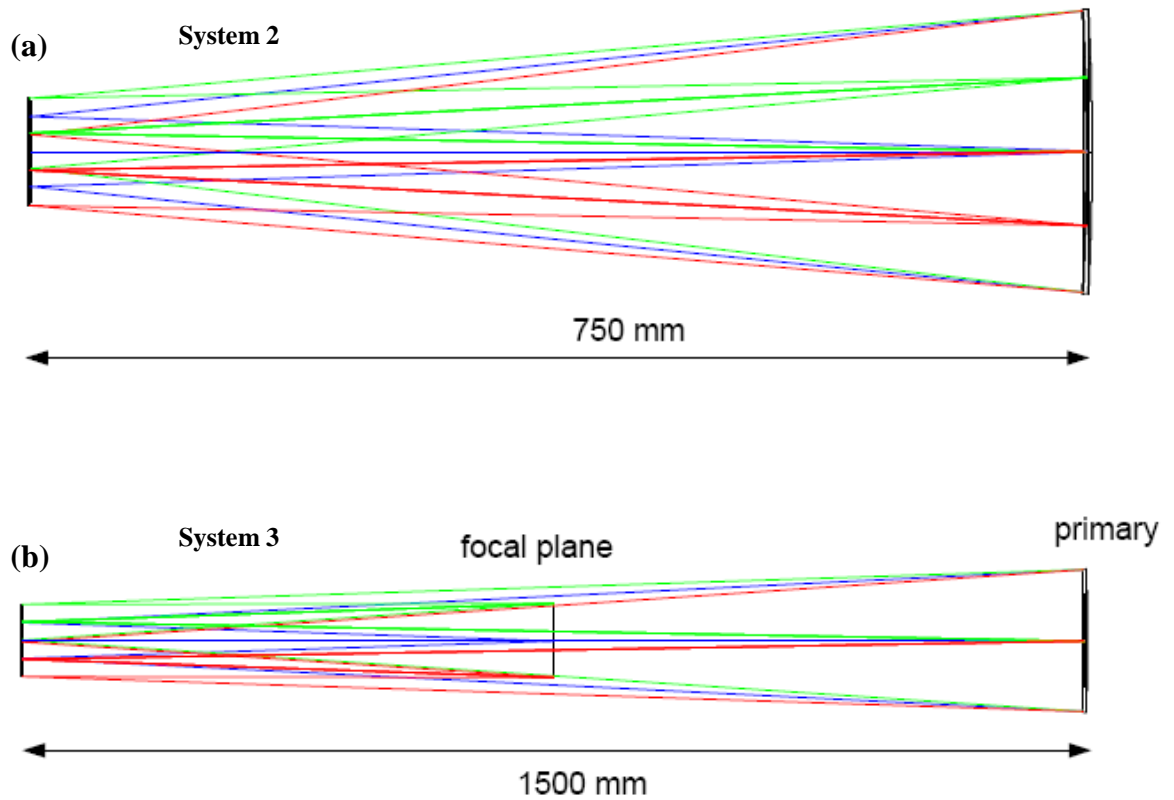


Figure 3.13 Cassegrain design concept with a mirror separation of (a) 750mm and (b) 1500mm. In part (a) the focal plane coincides with the plane of the primary mirror while in part (b) it is located half way between both mirrors.

If the restriction on the detector horn size was removed and they were replaced with bare waveguide for example, then a more typical $f/3$ beam at the output plane might be chosen. This would allow a more compact system in which again we could choose $D_s = (1/4)D_p = 50$ mm so that $d = (3/4)f_p$ and $u = (1/4)f_p$. If $f_p = 150$ mm, then $u = 37.5$ mm, and since the output beam is $f/3$ then $v = 3 \times D_s = 150$ mm and the mirror separation is $d = 112.5$ mm. The image plane would be located 37.5 mm behind the primary mirror. A schematic diagram of such a system is shown in Figure 3.14 and the details are summarised in Table 3.1. Again, due to the restriction on the detector horn antennas such a system would not be applicable to the current version of MBI-4 but may be implemented in future instruments. To decide on the best option for the MBI-4 beam combiner a diffraction analysis was required.

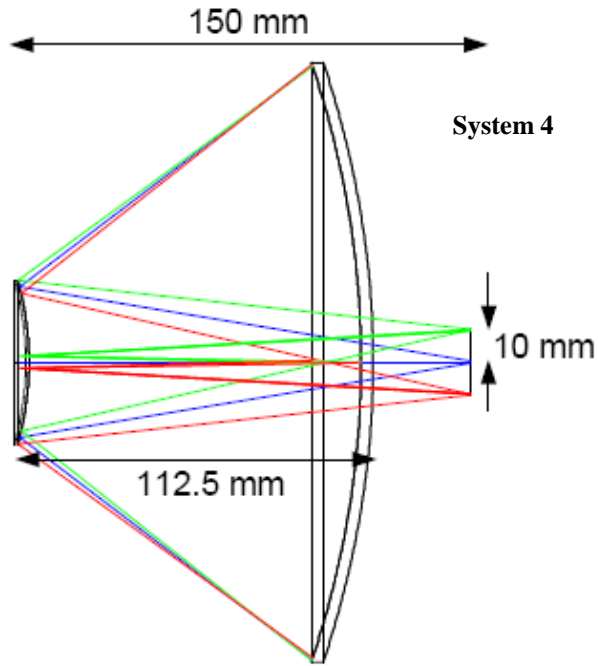


Figure 3.14 Schematic diagram of a more compact optical system with an $f/3$ beam at the output plane.

Parameters of Initial Designs Considered for the MBI-4 Optical System				
	System 1	System 2	System 3	System 4
$f/\#$ at image	15	15	15	3
Equivalent focal length, f (mm)	3000	3000	3000	300
D_s/D_p ratio	0.25	0.25	0.25	0.25
Mirror separation, d (mm)	500	750	1500	112.5
Secondary Diameter, D_s (mm)	50	50	50	50
Primary focal length, f_p (mm)	666.67	1000	2000	150
Secondary focal length, f_s (mm)	-214.29	-375	-1500	-75
Object distance, u (mm)	166.67	250	500	37.5
Image distance, v (mm)	750	750	750	150
Primary to image, d' (mm)	250	0	-750	37.5

Table 3.1 Parameters of the Cassegrain optical designs considered for the MBI-4 optical beam combiner.

3.3.3 Diffraction Analysis

We will now consider the diffraction effects that occur in the beam combiner system and examine the beam width and radius of curvature at different planes. The beam width at the output or focal plane is given by,

$$w(d_{out} = f) = \frac{\lambda f}{\pi w_{in}} \quad (3.2)$$

where f is the focal length of the system and w_{in} is the input beam waist radius. Considering the MBI corrugated horn in Figure 3.15 with an aperture diameter of $2a = 50$ mm and an axial length of 130mm, the waist radius of the beam is given by (Goldsmith, 1998),

$$w_o = \frac{0.6435a}{\left(1 + \frac{\pi(0.6435a)^2}{\lambda R}\right)^{0.5}} \quad (3.3)$$

where R is the slant length of the horn giving a value of $w_o = 7.67$ mm (the beam radius at the aperture is given by $w_a = 0.6435a = 16.1$ mm).

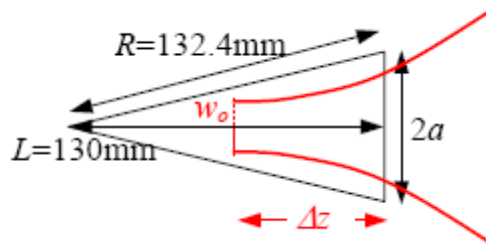


Figure 3.15 Schematic diagram of a corrugated horn antenna showing the position of the waist behind the aperture of the horn.

The distance from this waist position to the aperture of the horn is given by

$$\Delta z = \frac{R}{1 + \left(\frac{\lambda R}{\pi(0.6435a)^2} \right)} \quad (3.4)$$

and therefore $\Delta z = 102.3\text{mm}$. Remembering that the equivalent focal length of the system is $f = 3000\text{mm}$, the beam width at the focal plane is given by Equation 3.2, resulting in a value of 414.6mm from an input beam width of 7.67mm . The fringe pattern for this system is shown in Figure 3.16 with oversized mirrors (primary mirror diameter = 300mm , secondary mirror diameter = 100mm) used in ZEMAX, to prevent truncation. The fringes were obtained using Zemax's physical optics option (see section 2.6) with a fundamental Gaussian source.

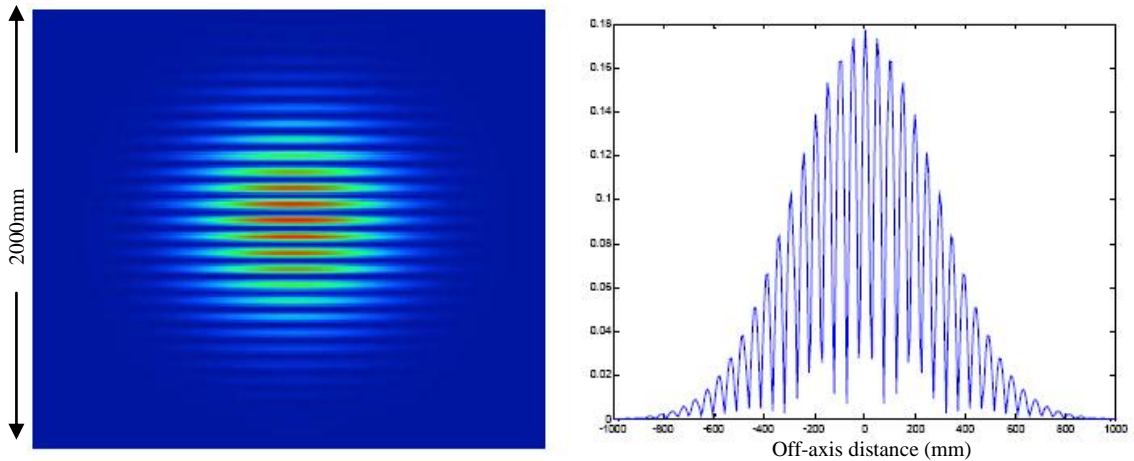


Figure 3.16 Fringe pattern at the image plane taking into account the phase front radius of curvature of the beam at the aperture of the corrugated horn antenna. These plots were obtained using Zemax's physical optics option (see section 2.6) with a fundamental Gaussian source.

If we consider the layout of the system and assume for example that the phase centre of the horn is located 100mm in front of the secondary mirror, the distance x in Figure 3.17, then lengthwise the system of Figure 3.12 will fit inside the cryostat as shown in Figure 3.20. The beam width at each component was calculated using ABCD matrices and the complex beam parameter, as in Equation 2.36 ($q_{out} = (Aq_{in} + B)/(Cq_{in} + D)$). Since the beam width at different planes was required the system was described in three different ways: one ABCD matrix

containing everything up to and including the primary mirror, one ABCD matrix containing everything up to and including the secondary mirror and one ABCD matrix containing everything up to the image plane. The complex beam parameters were computed and the beam width values were then calculated using,

$$w = \left[\frac{\lambda}{\pi \operatorname{Im}(-1/q)} \right]^{0.5} \quad (3.5)$$

where w is the beam width at the output of the system described by the ABCD matrix.

Table 3.2 shows the parameters of the system and the calculated beam width values. These parameters are also shown as Configuration 1 in Figure 3.18. Considering the width of the beam at the secondary mirror, which would have to fit between the horn antennas and therefore have a diameter of 150mm or less, there would be significant truncation effects in the system. Figure 3.19 shows the interference pattern on the image plane and also the field produced from a single source. Figure 3.20 illustrates how the system could be fit into the MBI cryostat.

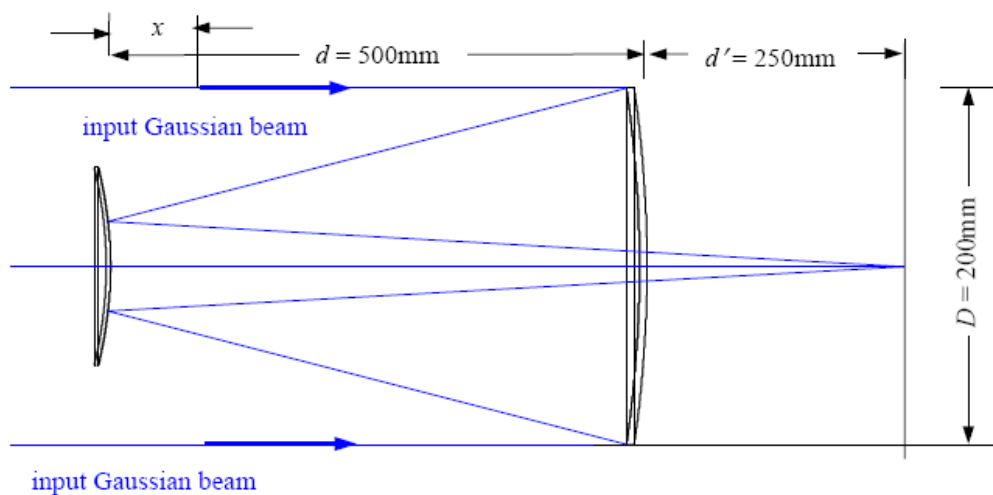


Figure 3.17 Schematic diagram of the Cassegrain optical system showing the variable distance x from the secondary mirror to the beam waist position.

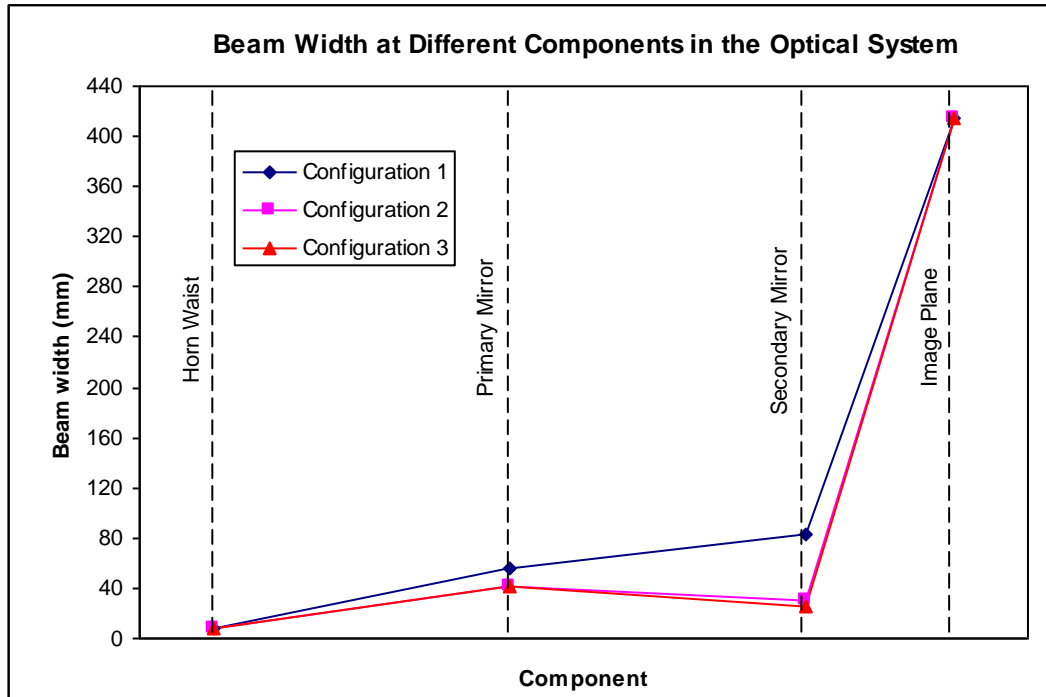


Figure 3.18 Beam width at different components in the optical system for three different configurations described in the text.

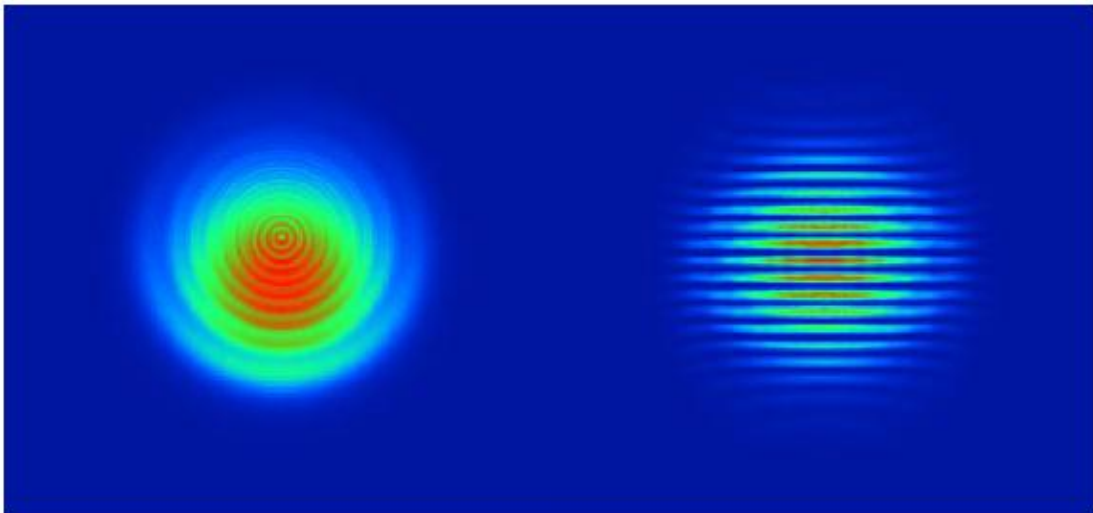


Figure 3.19 Field produced on the image plane by a single source and the interference fringes on the image plane produced by two sources 200mm apart (same system as Figure 3.16 but with truncation effects taken into account).

In order to reduce the size of the beam on the secondary mirror the distance between the primary and secondary mirrors could be shortened to 150mm for

example as shown in Figure 3.21, with the beam waist 150mm behind the secondary. This would require mirrors with a greater curvature and hence a shorter focal length but would indeed reduce the beam widths as the results in Table 3.3 indicate (see also Configuration 2 in Figure 3.18). Figure 3.22 shows both the field from a single source and the interference pattern on the image plane. While truncation is reduced, in order to use a system such as this one the cryostat length would have to be increased by approximately 250mm.

To reduce the distance from the secondary mirror to the image plane in an attempt to fit the system into the cryostat, the angle between the primary and the secondary could be steepened, perhaps using a $D_s / D_p \approx 1/8$ model. This would require mirrors with an even higher degree of curvature than those in the previous system and would also produce a beam at the image plane with a smaller phase front radius of curvature. Figures 3.23 and 3.24 show a ray tracing diagram of such a system and the fields at the image plane, respectively, while the system parameters and beam widths are given in Table 3.4 and compared with the previous configurations in Figure 3.18 (Configuration 3). As can be seen in Figure 3.25, this optical configuration does fit within the physical constraints of the cryostat (although it was not the final system chosen, as discussed later in this section).

The narrow beam waist produced by the horn antenna causes the beam to diffract significantly (the angular divergence of a beam is given by $\theta = \lambda / \pi w_0$). Another approach was to consider moving the beam waist location to the aperture of the horn antenna (thereby increasing it to $0.6435a$) by flattening the phase front radius of curvature using lenses. If we consider *System 1* described in the previous section (see Table 3.1) with the mirrors separated by a distance $d = 500\text{mm}$ and the distance from the beam waist to the secondary mirror $x = 100\text{mm}$ as shown in Figure 3.26, then the fringe pattern in Figure 3.27 is obtained where the size of the mirrors was extended in ZEMAX to prevent truncation.

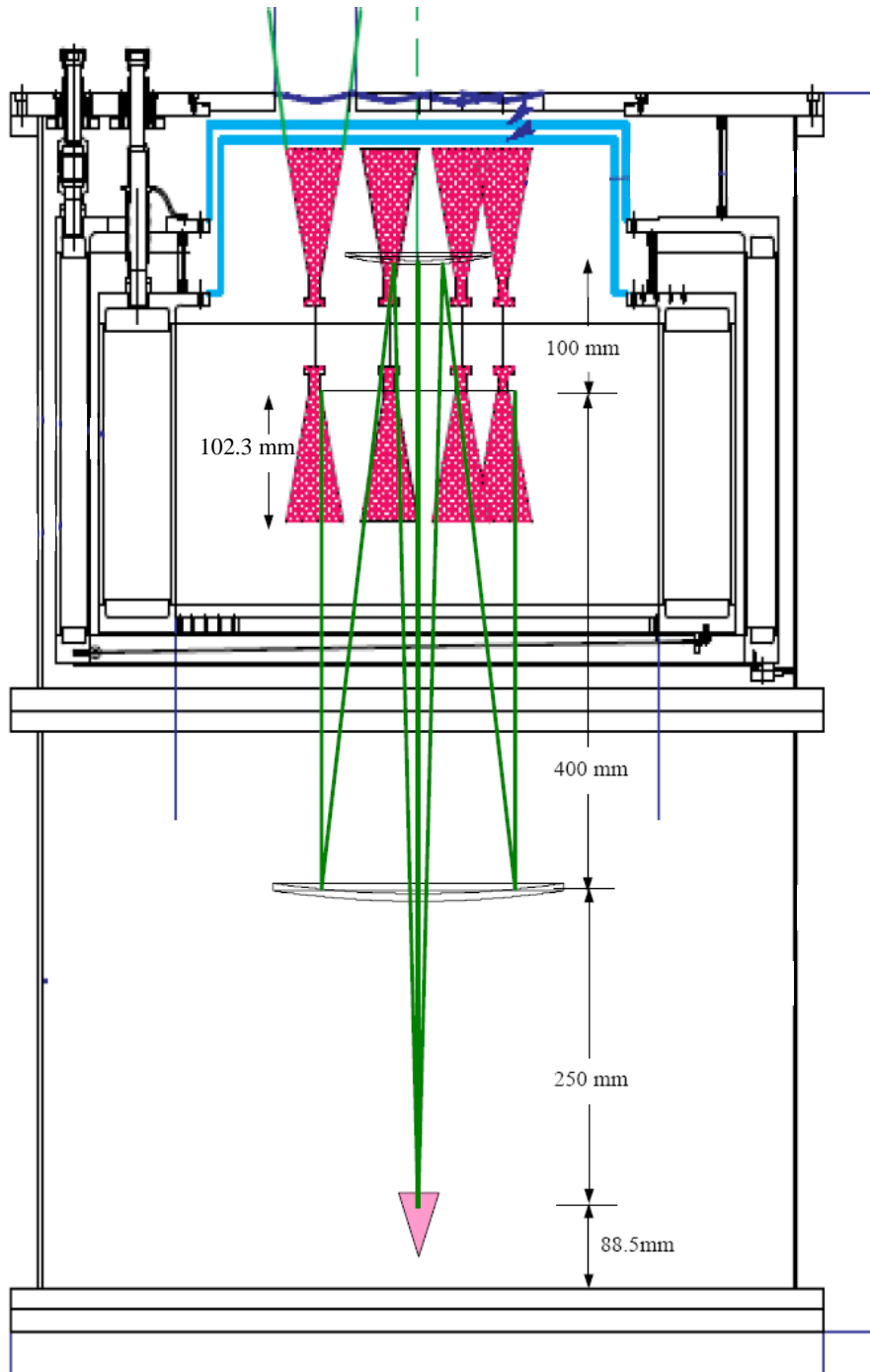


Figure 3.20 The optical system in the cryostat with the waist position of the horn antennas a distance of 100mm in front of the secondary mirror.

Optical System Parameters and Beam Widths			
System Parameters		Beam Widths (w)	
Distance from w_o to Primary (mm)	400	Beam Waist, w_o (mm)	7.7
Distance from Prim. to Sec. (mm)	500	w at Primary (mm)	56
Distance from Sec. to Image (mm)	750	w at Secondary (mm)	83
f_p (mm)	666.67	w at Image (mm)	415
f_s (mm)	-214.29		

Table 3.2 Optical system parameters and beam widths at different components for a beam waist located 100mm in front of the secondary mirror and a mirror separation of 500mm.

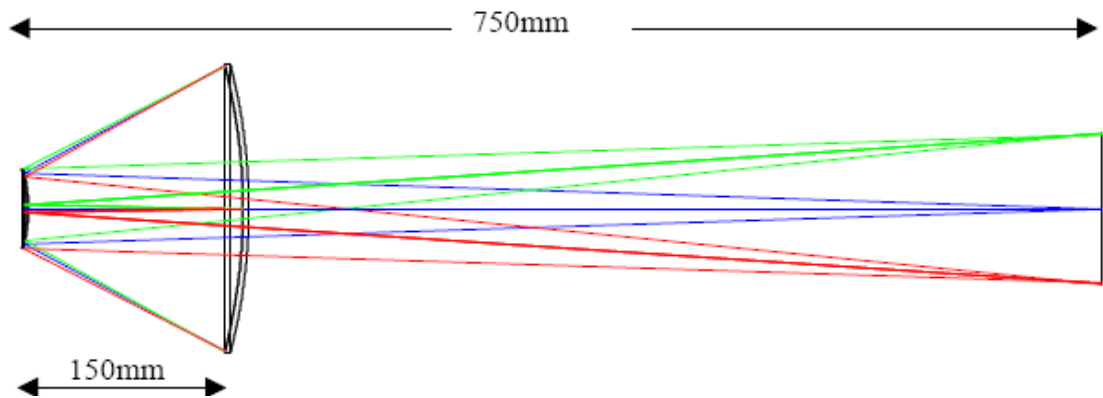


Figure 3.21 Ray tracing diagram with the primary and secondary mirrors separated by a distance of 150mm with the initial beam waist position 150mm behind the secondary mirror.

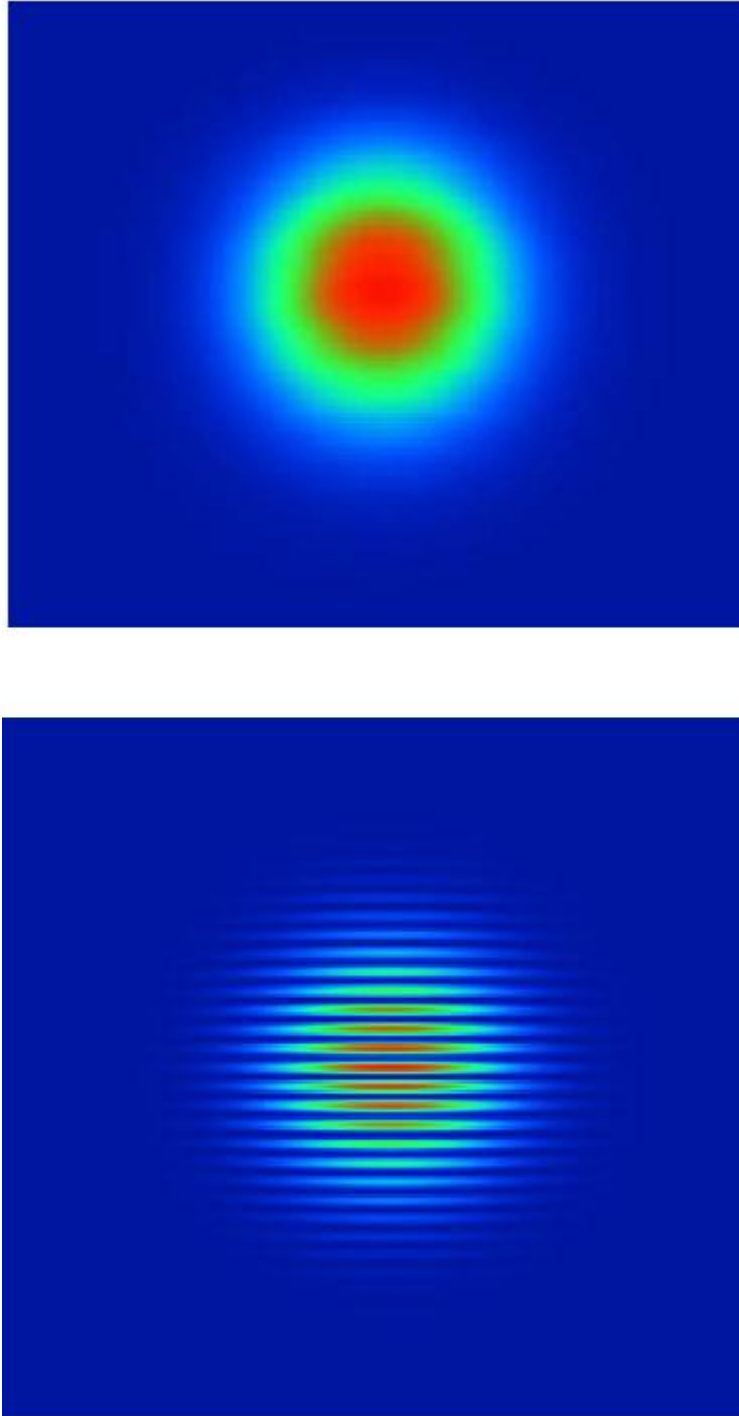


Figure 3.22 The top image shows the field produced on the image plane by a single source located 150mm behind the secondary mirror for a mirror separation of 150mm. The bottom image shows the interference fringes produced by the system. The beam waist radius at the image plane is 415mm.

Optical System Parameters and Beam Widths			
System Parameters		Beam Widths (w)	
w_o to Primary (mm)	300	Beam Waist, w_o (mm)	7.7
Prim. to Sec. (mm)	150	w at Primary (mm)	42
Sec. to Image (mm)	750	w at Secondary (mm)	31
f_p (mm)	200	w at Image (mm)	415
f_s (mm)	-53.57		

Table 3.3 Optical system parameters and beam widths at different components for a beam waist located 150mm behind the secondary mirror and a mirror separation of 150mm. $D_s/D_p=1/4$.

Optical System Parameters and Beam Widths			
System Parameters		Beam Widths (w)	
w_o to Primary (mm)	300	Beam Waist, w_o (mm)	7.7
Prim. to Sec. (mm)	150	w at Primary (mm)	42
Sec. to Image (mm)	375	w at Secondary (mm)	26
f_p (mm)	171.43	w at Image (mm)	415
f_s (mm)	-22.73		

Table 3.4 Optical system parameters and beam widths at different components for a beam waist located 150mm behind the secondary mirror in a compact system (Fig. 3.23). $D_s/D_p=1/8$.

Since the best possible coupling between the telescope field and the detector horn antenna is achieved when the phases of the two fields are matched, in an ideal situation the image plane would coincide with a beam waist and therefore the field at this point would have a flat phase front radius of curvature (it was shown by Lavelle (2008) that having a flat phase telescope beam would increase the coupling by a factor of 1.4). The actual curvature of the phase at the image plane was calculated for an aperture waist located at different distances from the primary mirror using ABCD matrices. In this case the system is defined by five matrices, each one representing either a free space propagation or a thin lens (see Table 2.1) since again the optical system can be analysed in terms of lenses rather than mirrors for convenience. The ABCD matrix representing the overall system is then obtained by

multiplying the individual matrices with the leftmost matrix representing the last element in the system encountered by the beam, that is,

$$\begin{bmatrix} 1 & L_3 \\ 0 & 1 \end{bmatrix} \times \begin{bmatrix} 1 & 0 \\ -1/f_s & 1 \end{bmatrix} \times \begin{bmatrix} 1 & L_2 \\ 0 & 1 \end{bmatrix} \times \begin{bmatrix} 1 & 0 \\ -1/f_p & 1 \end{bmatrix} \times \begin{bmatrix} 1 & L_1 \\ 0 & 1 \end{bmatrix} \quad (3.6)$$

where L_1 is the distance from the source to the primary mirror ($= x + d$), L_2 is the distance from the primary mirror to the secondary mirror ($= d$), L_3 is the distance from the secondary mirror to the image plane ($= d + d'$), f_p is the focal distance of the primary mirror and f_s is the focal distance of the secondary mirror.

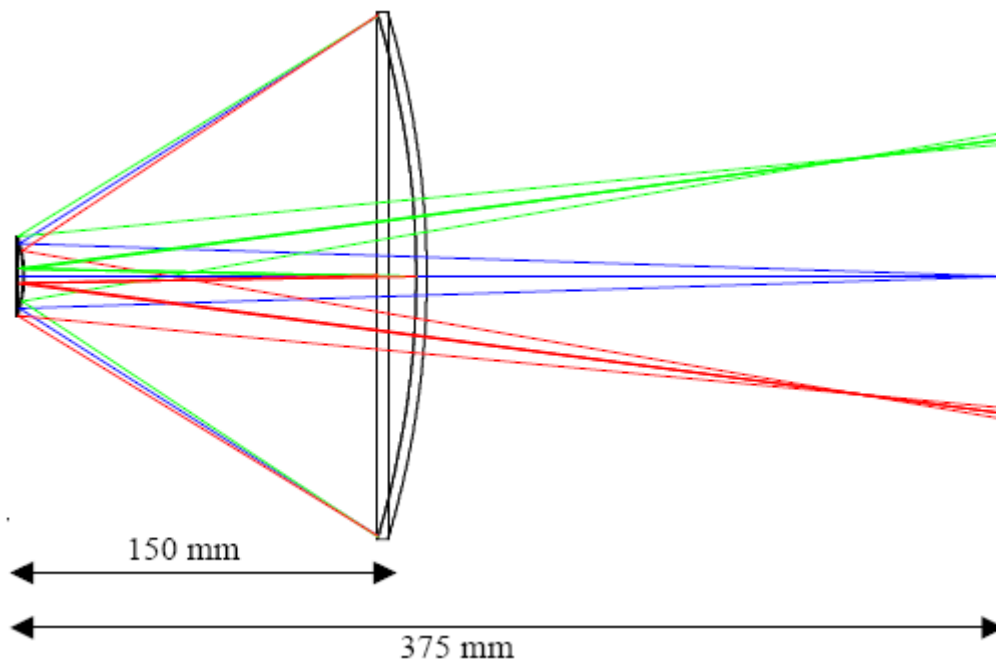


Figure 3.23 Ray tracing diagram of the system containing mirrors with a higher degree of curvature and a steep angle between the primary and secondary.

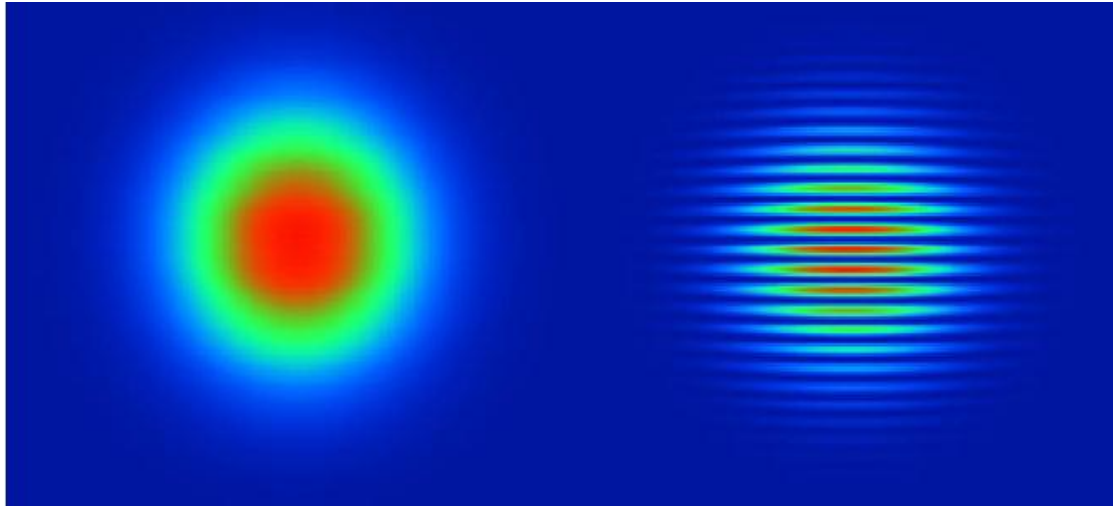


Figure 3.24 The image from a single source and the interference pattern at the image plane of a system with a mirror separation of 150mm and a secondary mirror to image plane distance of 375mm.

From these matrices the complex beam parameters were obtained and the radius of curvature calculated using the equation (Goldsmith, 1998),

$$R = \left[\operatorname{Re} \left(\frac{1}{q} \right) \right]^{-1} . \quad (3.7)$$

The results of this analysis can be seen in Table 3.5, where it is clear that to achieve a waist at the output plane, the input waist would have to be ~10,000mm from the primary mirror. However, if the input waist is moved closer to the plane of the mirror the output radius of curvature is still large.

Although the radius of curvature is an important factor it is also important to note that if the input beam waist position is located too far from the primary mirror the diameter of this mirror would have to be quite large to avoid significant truncation effects ($\text{diameter} \geq 4w$). With this in mind the beam width at different components in the system was calculated for an initial waist location at various distances from the secondary mirror, or varying values of x in Figure 3.26. Similar to calculating the radius of curvature, the beam width was calculated as before using

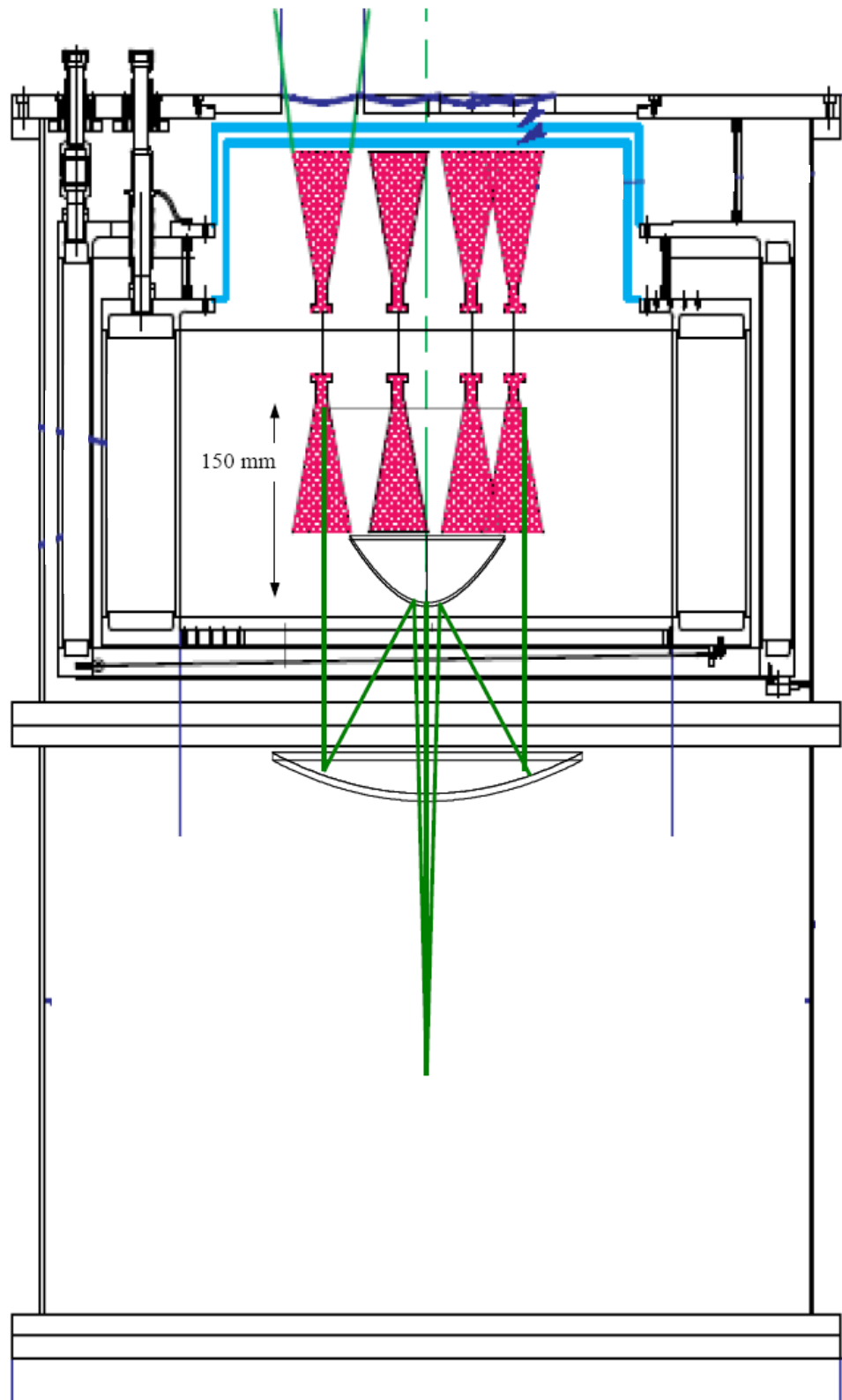


Figure 3.25 The optical system in the cryostat with the waist position of the horn antennas a distance of 150mm behind the secondary mirror and a secondary mirror to image plane distance of 375mm.

ABCD matrices and the complex beam parameter with $z=0$ corresponding to the initial beam waist position. From the ABCD matrices three different corresponding complex beam parameters, q_{out} , were obtained and for each one of these the beam width was calculated using Equation 3.5.

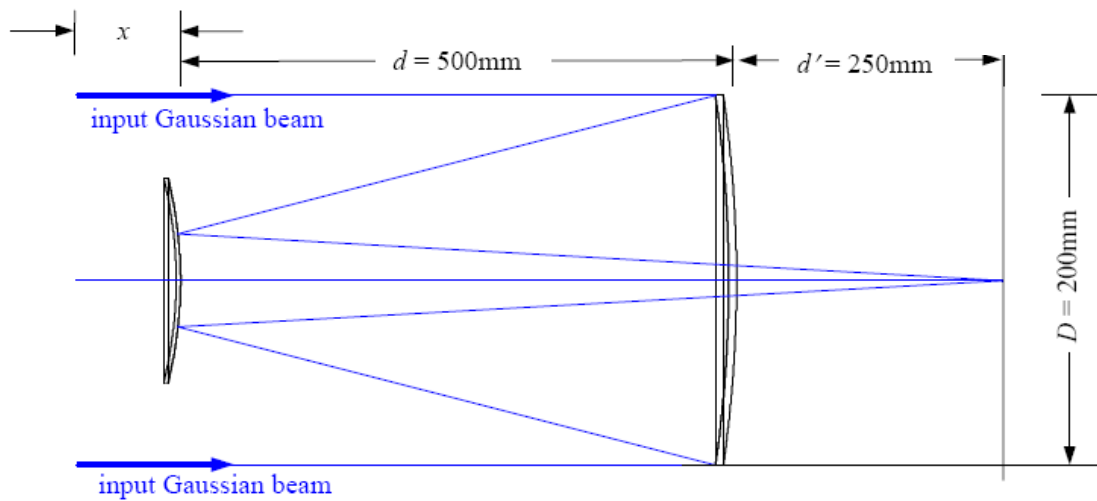


Figure 3.26 Schematic diagram of a Cassegrain system with varying beam waist to secondary mirror distance, x .

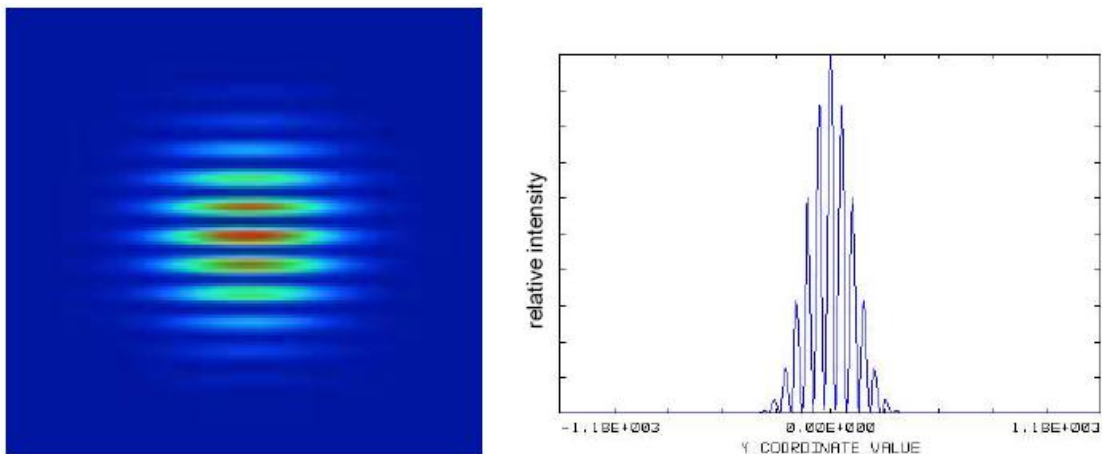


Figure 3.27 Fringe pattern generated with the beam waist position located 100mm from the secondary mirror and a mirror separation of 500mm. In this example a waist of 16.1mm was used.

Phase Curvature as a Function of Beam Waist to Primary Mirror Distance	
Distance from Beam Waist to Primary Mirror (mm)	Phase Front Radius of Curvature at the Focal Plane (mm)
10,000	∞
9,000	9.0×10^3
8,000	4.5×10^3
1,000	1.0×10^3
300	9.3×10^2
100	9.1×10^2

Table 3.5 Phase front radius of curvature of the beam at the image plane calculated with the beam waist at different distances from the primary mirror.

Beam Width at Different Components in the Optical System			
Distance from Waist to Secondary (mm)	Beam width at Primary Mirror (mm)	Beam width at Secondary Mirror (mm)	Beam width at Image Plane (mm)
0	36.65	41.34	197.50
100	42.66	42.98	197.50
200	48.82	44.62	197.50
300	55.08	46.26	197.50
400	61.40	47.90	197.50
500	67.78	49.54	197.50

Table 3.6 Beam width at different components in the optical system with the beam waist (16.1mm) located at different distances from the secondary mirror.

Table 3.6 shows the results of this analysis depicted in the graph in Figure 3.28. While the beam width at the image plane remains constant for all values of x , there is significant variation at the primary mirror and to a lesser extent at the secondary mirror, which is important when considering truncation of the beam.

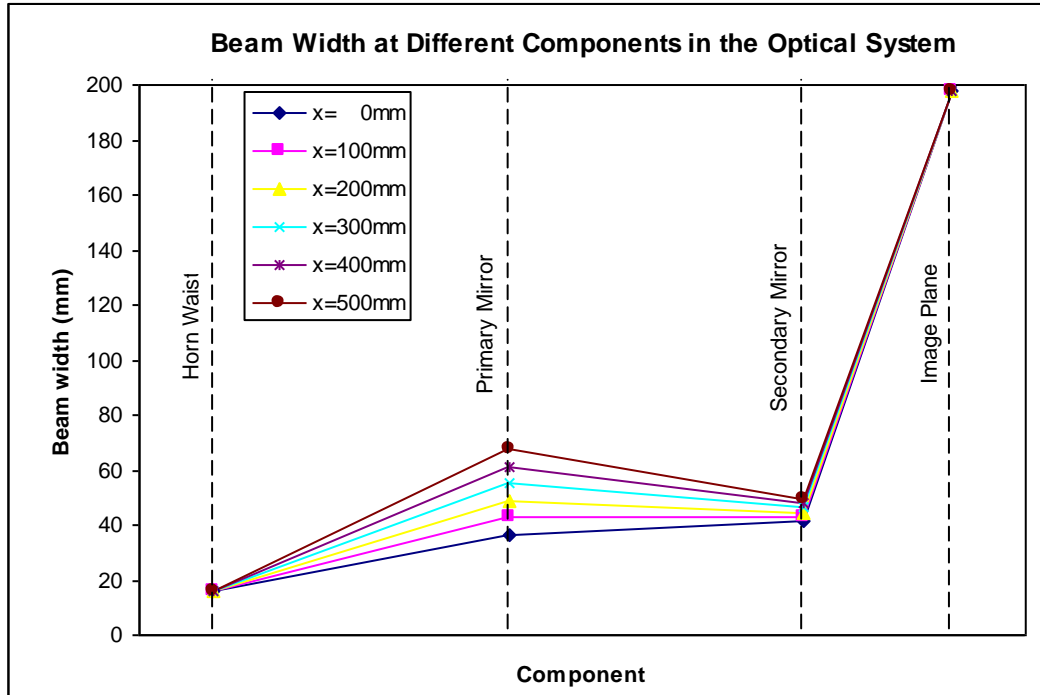


Figure 3.28 Beam width at different components in the optical system with the beam waist (16.1mm) located at different distances from the secondary mirror.

Optical System Parameters and Beam Widths			
System Parameters		Beam Widths (w)	
w_o to Primary (mm)	250	Beam Waist, w_o (mm)	16.1
Prim. to Sec. (mm)	200	w at Primary (mm)	23
Sec. to Image (mm)	375	w at Secondary (mm)	15
f_p (mm)	228.57	w at Image (mm)	197.5
f_s (mm)	-30.93		

Table 3.7 Optical system parameters and beam widths at different components for a beam waist located at the horn aperture located 50mm behind the secondary mirror.

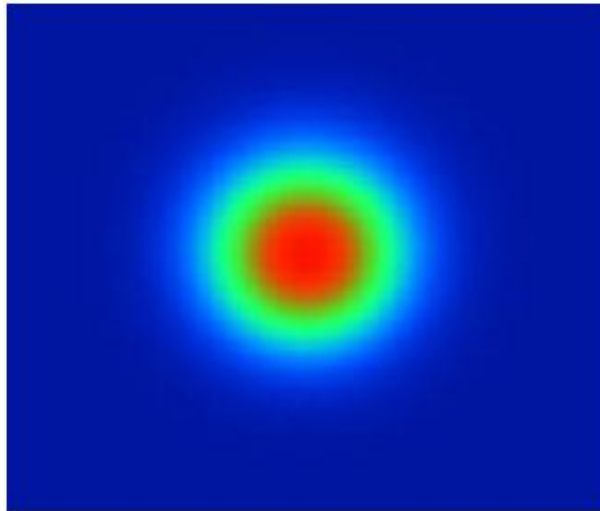


Figure 3.29 The intensity of the field from a single source on the image plane, located 425 mm from the horn antenna aperture at which the beam waist is located. Truncation is not accounted for in this analysis.

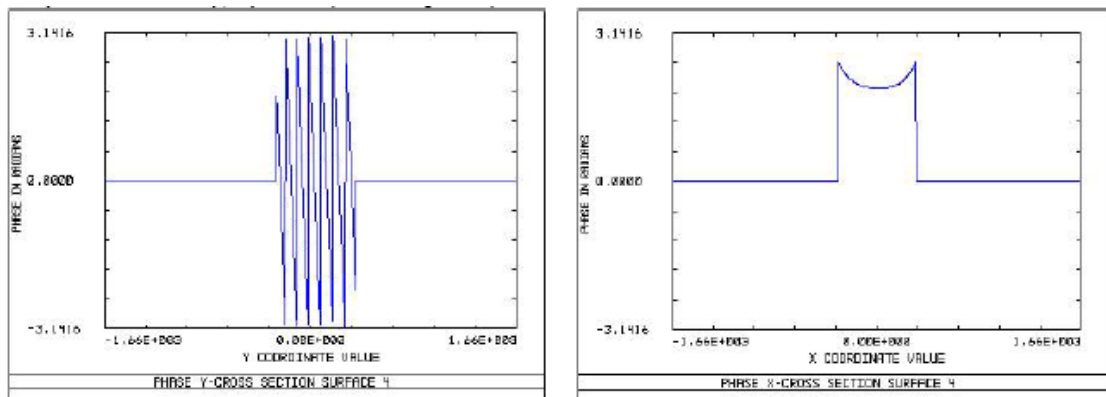


Figure 3.30 The phase of the field from a single source on the image plane, located 425 mm from the horn antenna aperture at which the beam waist is located. Truncation is not accounted for in this analysis.

Taking into account the fact that the distance from the beam waist to the primary mirror affects the phase radius of curvature, and truncation is dependant on the distance from the waist to the secondary mirror we considered a system where the beam waist position (i.e. the horn aperture plane with lenses attached) was placed 50mm behind the secondary mirror with a mirror separation of 200mm. The beam widths at the different components in such a system are shown in Table 3.7. Figures 3.29 and 3.30 show the field intensity and phase on the image plane where the beam radius of curvature is found to be 406mm using ABCD matrices. Figure 3.31 shows

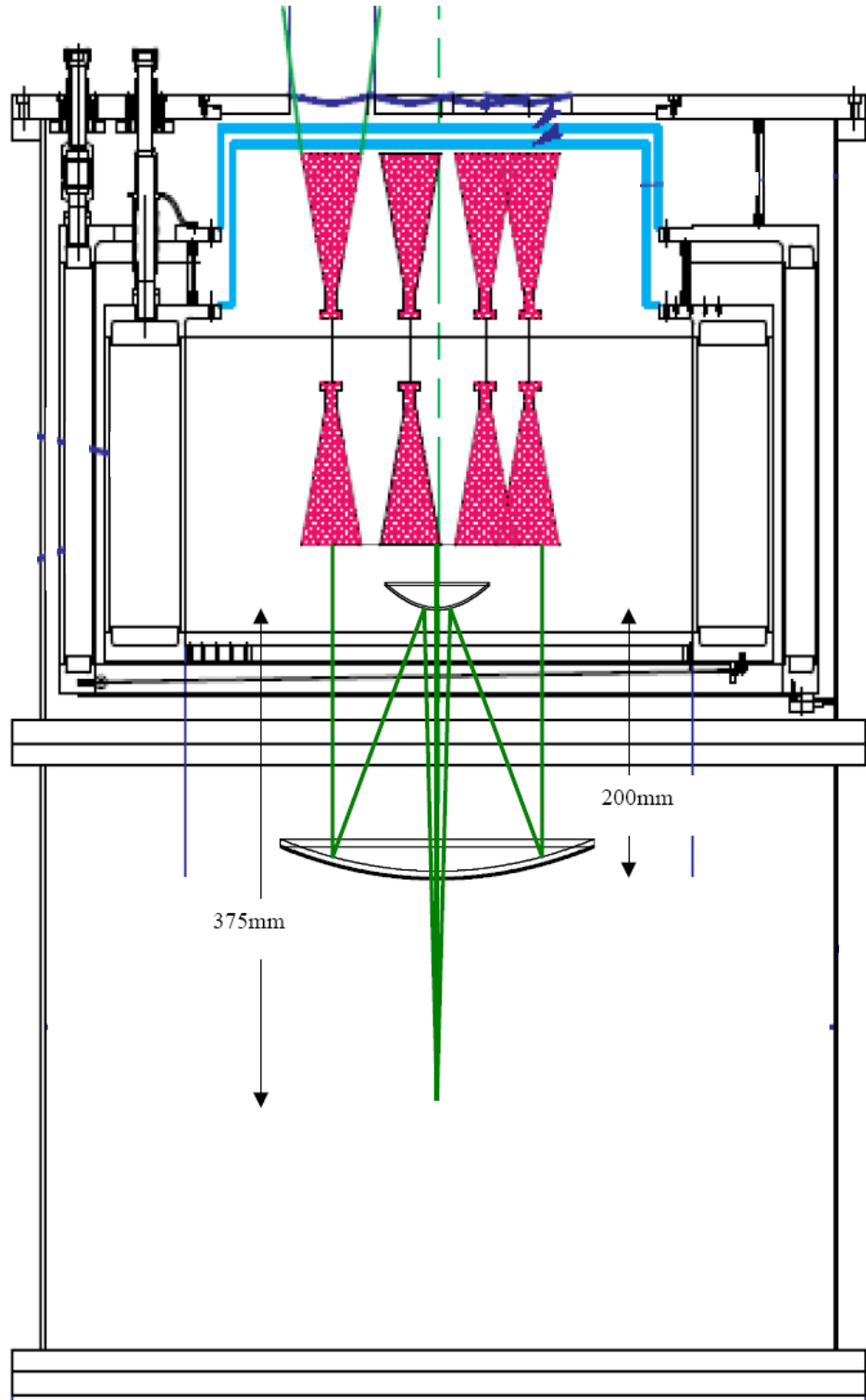


Figure 3.31 The optical system inside the cryostat. The field at the mouth of the horns has been flattened and is placed 50 mm from the secondary mirror.

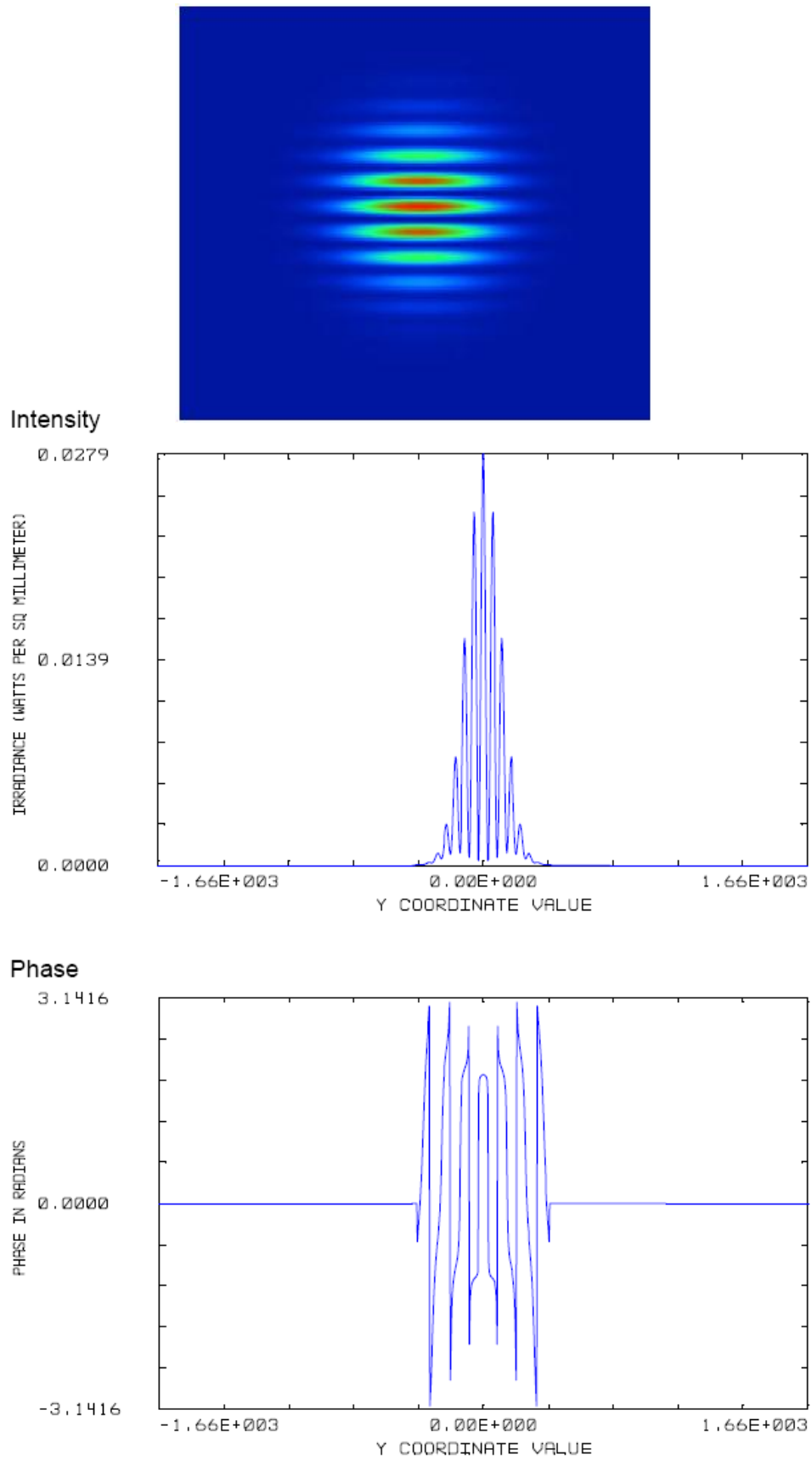


Figure 3.32 The intensity and phase of the interference pattern on the image plane for the system outlined in Table 3.7. Truncation is not accounted for in this analysis.

the system in the cryostat and Figure 3.32 shows the fringes on the image plane where the diameters of the mirrors in ZEMAX were such as to neglect truncation.

In a Cassegrain system blockage of the primary mirror by the secondary is a serious issue (our original design examined the longer baseline but obscuration by the secondary is even more problematic for the shorter baseline) and the 100mm secondary mirror implemented in the last design was thought to be too large, given the separation of the inward facing horns. Two other diameters for the mirror were examined, 64mm and 80mm. This was carried out in ZEMAX by modelling the mirror as an obscuring disk as seen from the input beam since the effect it has is to obscure part of the beam as it propagates towards the primary mirror. While the 80mm diameter mirror (and the resulting beam pattern shown in Figure 3.33) would collect more power from the primary mirror, the 64mm diameter would be more desirable in terms of truncation effects.

Figure 3.34 shows a schematic diagram of such a system where the beam hits the secondary 12.6mm from the centre of the mirror, or $1.26w$, where w is the beam width at that plane, from one edge of the 64mm surface. The power on the image plane from a single source is shown in Figure 3.35 as well as the fringe pattern. A comparison between the fringes produced by the 64mm mirror and those produced by the 100mm mirror described earlier is shown in Figure 3.36, where both sets of fringes have been normalised independently.

The one remaining issue was the aperture in the primary mirror, which given the layout of the inward facing horn antennas shown in Figure 3.37, was designed to be elliptical in shape with a major axis of 164mm and a minor axis of 96mm. This can also be seen in Figure 3.37, which shows a top view (from the sky) of the optics and sky-facing horns.

The initial design of the MBI beam combiner was carried out using a combination of both geometrical optics and diffraction analysis. Having analysed a number of systems a trade-off between having a flat phase front radius of curvature at the image plane and also a low level of truncation by the primary mirror was required. In the final system that was built the waist position (corresponding to the

horn aperture with lenses attached) was placed 50mm behind the hyperbolic secondary mirror (diameter=64mm), a distance large enough to give a relatively large radius of curvature on the focal plane but also small enough to allow for a parabolic primary mirror whose radius (150mm) would allow it to fit within the dimensions of the cryostat. An elliptical hole was chosen for the primary mirror to prevent as much truncation as possible from the four optics-facing horn antennas. This is the system that was implemented in the MBI-4 instrument with the phase flattening lenses being designed at NUI Maynooth (Figure 4.7, (Lavelle, 2008)). In the next Chapter we look in more detail at the different type horn antennas used in the system.

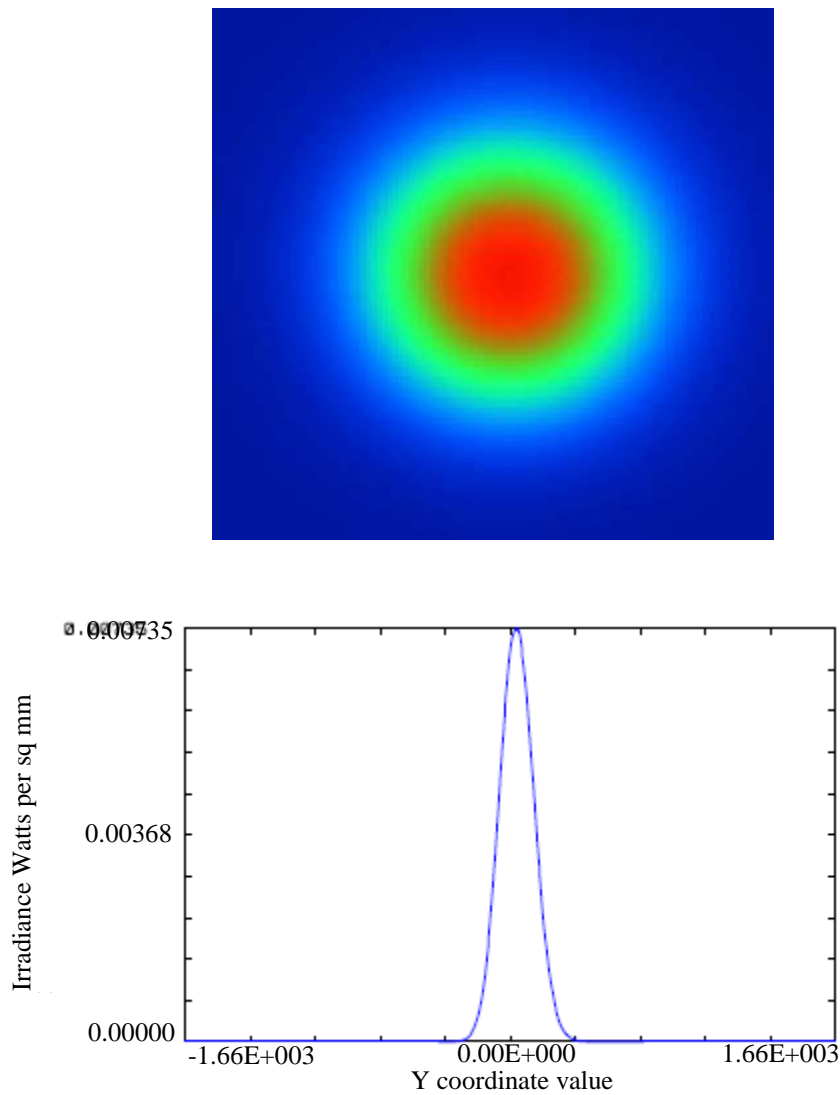


Figure 3.33 The intensity (linear and logarithmic scale) of a single beam at the image plane using an 80 mm secondary mirror.

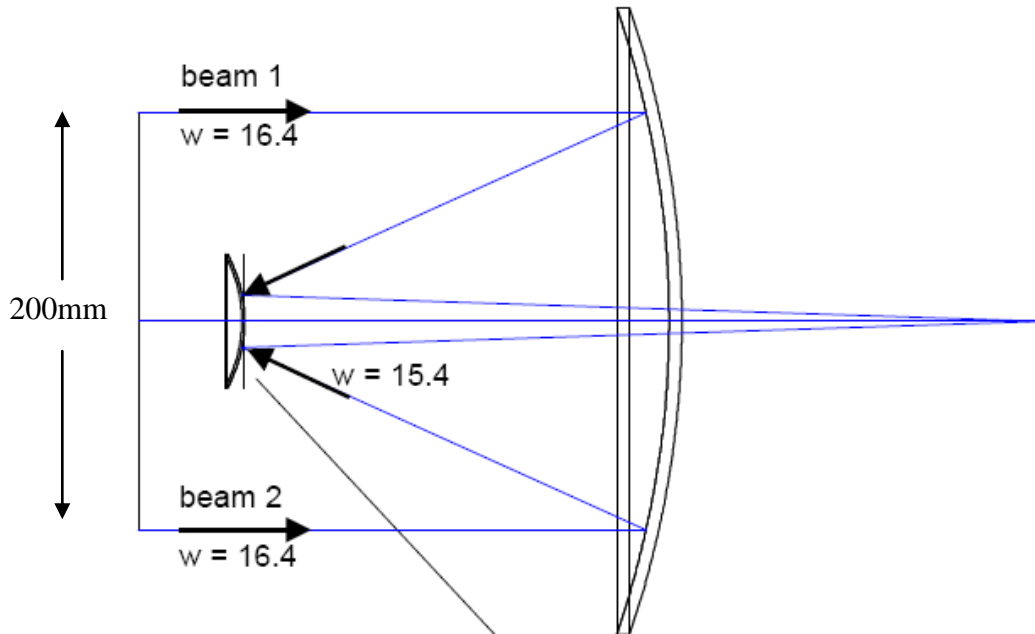


Figure 3.34 Ray tracing of the Cassegrain system with a 64mm secondary mirror.

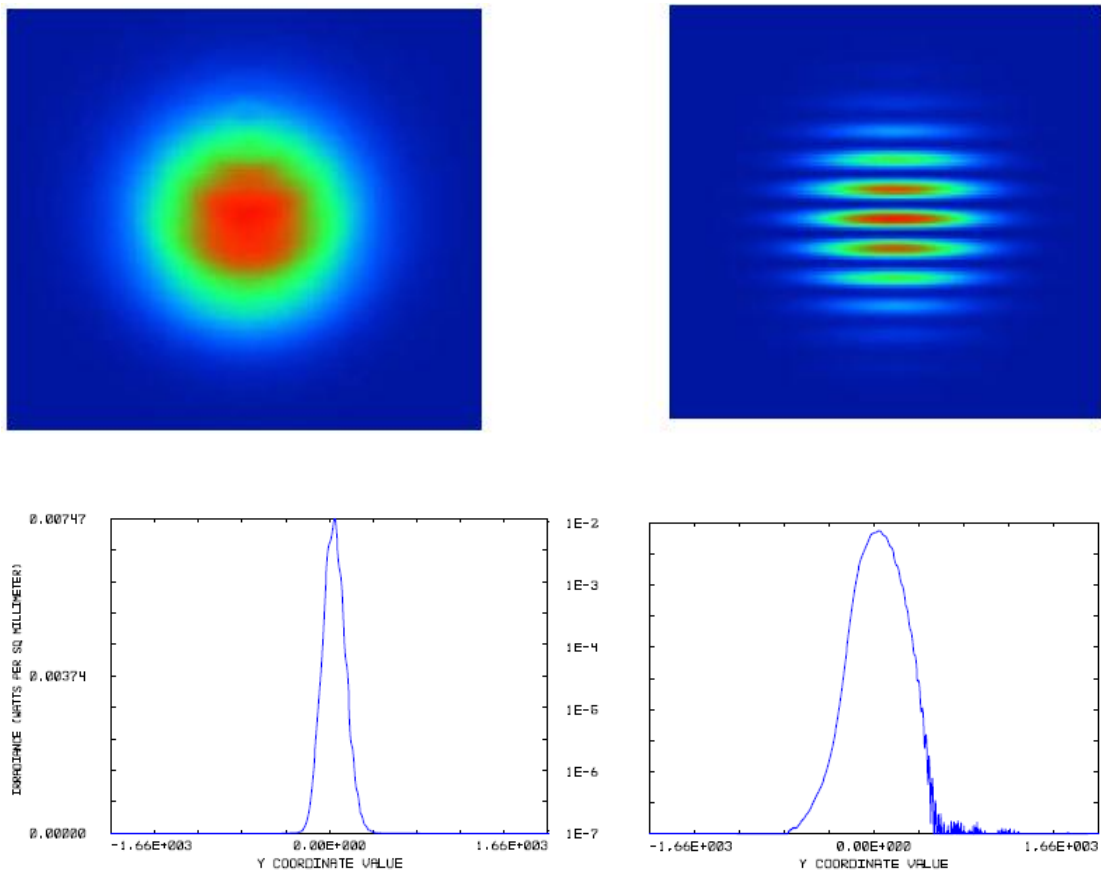


Figure 3.35 *Top left:* The intensity of a single beam using a 64mm secondary mirror. *Top right:* The fringe pattern at the image plane from two sources 200mm apart. *Bottom left:* A linear scale intensity cut through a single beam using a 64mm secondary mirror. *Bottom right:* A dB scale intensity cut through a single beam using a 64mm secondary mirror.

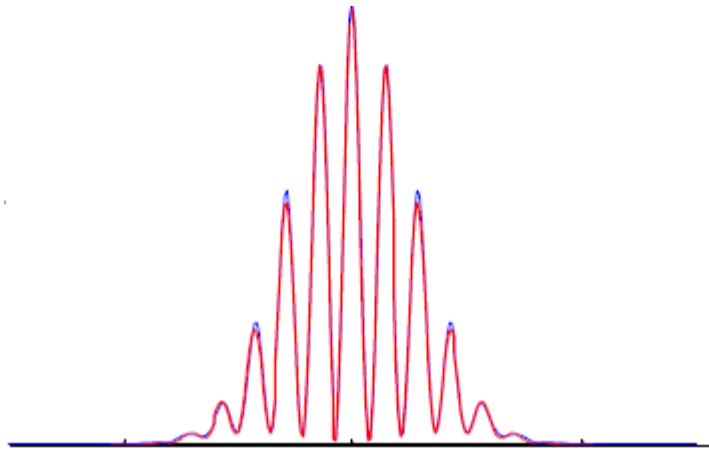


Figure 3.36 A Comparison of the interference fringes produced at the image plane by the long baseline using a 64mm diameter (blue) and a 100mm diameter (red) secondary mirror.

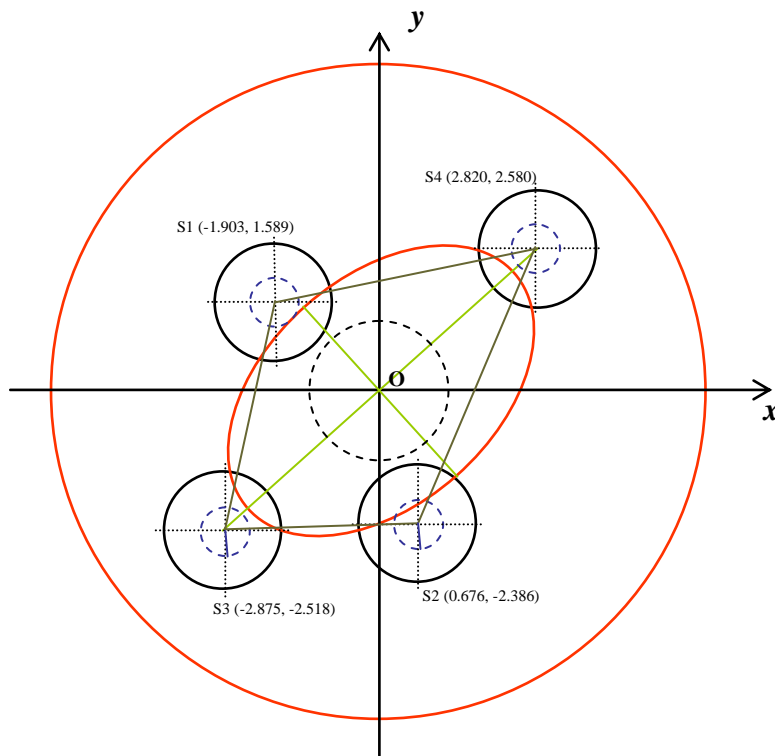


Figure 3.37 Schematic diagram showing the four sky-facing horn antennas along with the primary mirror and elliptical aperture, and the secondary mirror in the centre. This is a view from the sky.

Summary of the Design Parameters of the MBI-4 Optical System			
System Parameter	Primary	Secondary	Image
Distance from waist (mm)	250	50	425
Diameter (mm)	300	64	n/a
Radius of curvature (mm)	457.14	-61.86	n/a
Conic constant (k)	-1	-1.3571	n/a
Focal length (mm)	228.57	-30.93	n/a

Table 3.8 The parameters of the optical system implemented in the MBI-4 instrument. The beam radius values for this system can be seen in Table 3.7.

Chapter 4

Electromagnetic Modeling of Horn Antennas and Waveguides

4.1 Introduction

In this chapter we look at modelling horn antennas and waveguide structures. Both smooth-walled conical horn antennas and corrugated horn antennas are used in MBI-4 to feed the radiation from the sky to the optical system and also as feeds for the bolometric detectors in the focal plane array. To generate a full and accurate model of the complete system for MBI-4, as is done in Chapter 5, it is necessary to have a good understanding of these structures and the aperture fields that they produce.

In terms of corrugated horn antennas we look how a scattering matrix approach is used alongside mode-matching to calculate the intensity distributions for different structures and this method is used to produce the fields from the MBI-4 corrugated horn antennas. A singular value decomposition analysis is also carried out on a full back-to-back horn scattering matrix to find the number of independent modes that can propagate through the full system.

Within the structure of the back-to-back horn antennas in MBI-4 there are rectangular-to-circular transitions. While commercially-available transitions change from one geometry to the other in a gradual way to reduce any power loss that may occur, the effect of a sudden change in the waveguide shape is examined in this chapter (this is also applicable to the SAFARI instrument (a far infrared imaging spectrometer) on board SPICA (SPace Infrared telescope for Cosmology and Astrophysics) mission, for example, which may use a rectangular waveguide to feed a circular integrating cavity (Doherty, submitted to SPIE Photonics West Conference Proceedings 2011)).

Finally we look at the effects of beam distortion from horn antennas in closely packed arrays and what effect this will have on field distributions. In CMB polarisation experiments the sensitivity required is such that a large number of detectors are needed and therefore the focal plane arrays are becoming more and more dense.

4.2 Smooth-Walled and Corrugated Horn Antennas

In this section we look at smooth-walled and corrugated conical horn antennas. We look at the aperture field intensities and how the smooth-walled horn compares to the corrugated horn in terms of sidelobe structure. The techniques for modelling horn antennas are applied to MBI and are described in detail. These are then extended to model rectangular-to-circular waveguide junctions. We begin now by looking at the smooth-walled horn antenna.

4.2.1 Smooth-Walled Conical Horns

The simplest type of horn is the smooth-walled conical horn which is composed of a circular waveguide, supporting the TE_{11} mode, which flares out into a cone shaped antenna. It is relatively easy to fabricate and for this reason is a popular choice of feed at shorter wavelengths ($<1\text{mm}$) where manufacturing difficulties arise with corrugations. Smooth-walled horns are used in MBI to feed the bolometers. In comparison to the corrugated horn which will be discussed later, the radiation performance is noticeably poorer, lacking both the pattern symmetry and polarisation purity of the corrugated horn when coherently fed with the TE_{11} mode. The field at the aperture of the horn is given by (see e.g. Murphy, 1988; Gleeson, 2004)

$$E(x, y) \propto \left(\left(J_0 \left(p'_{1,l} \frac{r}{a} \right) + J_2 \left(p'_{1,l} \frac{r}{a} \right) \cos 2\phi \right) \hat{\mathbf{i}} + \left(J_2 \left(p'_{1,l} \frac{r}{a} \right) \sin 2\phi \right) \hat{\mathbf{j}} \right) \exp \left[\frac{-jkr^2}{2L} \right] \quad (4.1)$$

in mixed Cartesian/cylindrical coordinates where $p'_{1,l}$ represents the l^{th} zero of $dJ_1(z)/dz$, a is the aperture radius of the horn and L is the slant length, as shown in Figure 4.1. The spherical wavefront of the beam is described by the complex exponential term which develops as the field propagates from the horn phase centre located behind the aperture. The field described by Equation 4.1 is not cylindrically symmetric because of the dependence on the azimuthal angle ϕ .

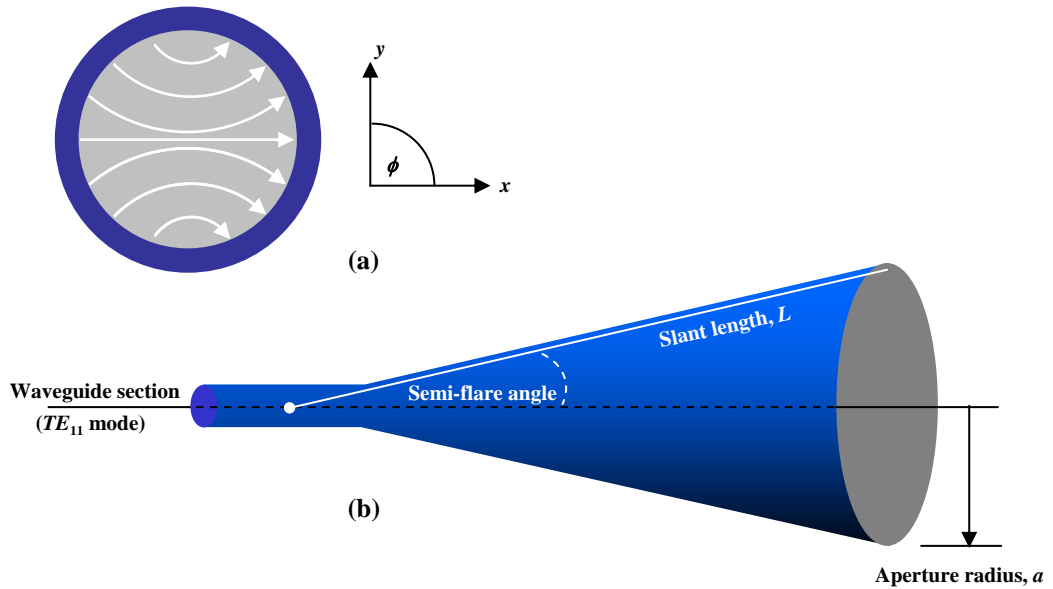


Figure 4.1 Part (a) shows the transverse electric field line configuration of the TE_{11} mode in a circular waveguide. The geometry of a smooth walled conical horn is shown in part (b) where L is the slant length and a is the aperture radius.

The waveguide is assumed to be perfectly conducting and so the boundary conditions mean that the tangential component of E is zero and therefore that the field lines are perpendicular to the walls (Goldsmith, 1998). The transverse electric field must also fall to zero in the H -plane ($\phi = 90^\circ$) and so is highly tapered in that plane. In the E -plane ($\phi = 0^\circ$), the field is less tapered and so does not fall to zero at the horn walls but by a factor of 1.6 from the on-axis value (Colgan, 2001) resulting in quite a different aperture field than that produced in the H -plane as shown in Figure 4.2. It is this relatively sharp edge to the distribution in the E -plane that accounts for higher side lobes compared with the radiation characteristics in the H -plane. The horn used in this example (following Olver *et al.*, 1994) is a smooth

walled conical horn with a diameter of 4λ and a semi-flare angle of 5° operating at 150GHz.

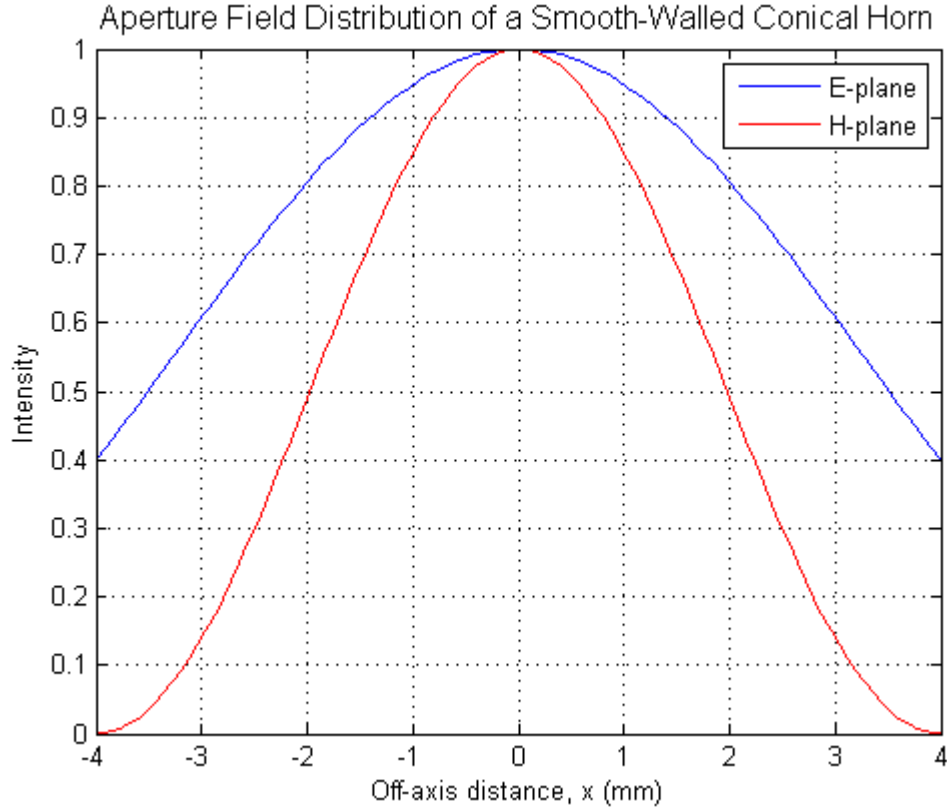


Figure 4.2 E-plane and H-plane intensity distributions at the aperture of a smooth walled conical horn antenna with a diameter of 4λ and a semi-flare angle of 5° operating at 150GHz.

To generate the far field pattern for a horn antenna a Fourier transform of the aperture field components is carried out using the equation (see e.g. Colgan, 2001),

$$E(\theta, \varphi) = \int_{\phi=0}^{2\pi} \int_{r=0}^a E_a(r, \phi) \exp\{jkr \sin \theta \cos(\phi - \varphi)\} \exp\left\{\frac{-jkr^2}{2L}\right\} r dr d\phi. \quad (4.2)$$

An analytical integration can be performed by making use of the equation (Born and Wolf, 1999),

$$\frac{i^{-n}}{2\pi} \int_0^{2\pi} e^{ix \cos \alpha} e^{in\alpha} d\alpha = J_n(x) \quad (4.3)$$

and rewriting the $\sin n\phi$ and $\cos n\phi$ terms associated with each Bessel function in the aperture field description (Equation 4.1) in terms of their corresponding exponential functions to yield for the field in the co-polar direction

$$\begin{aligned} E_x(\theta, \varphi) = & (1 + \cos \theta) \int_{q=0}^1 J_0(ka \sin \theta q) J_0(1.84118q) \exp\left\{\left(\frac{-jkr^2}{2L}\right)q^2\right\} q dq \\ & + (1 + \cos \theta) \cos 2\phi \int_{q=0}^1 J_2(ka \sin \theta q) J_2(1.84118q) \exp\left\{\left(\frac{-jkr^2}{2L}\right)q^2\right\} q dq \end{aligned} \quad (4.4)$$

where $q = r/a$ and a is the aperture radius of the horn. Setting $\varphi = 0^\circ$ gives the E -plane pattern and $\varphi = 90^\circ$ for the H -plane pattern. This integral over q is not possible analytically and therefore must be carried out numerically. The cross-polar field can be obtained in a similar manner giving,

$$E_y(\theta, \varphi) = (1 + \cos \theta) \sin 2\phi \int_{q=0}^1 J_2(ka \sin \theta q) J_2(1.84118q) \exp\left\{\left(\frac{-jkr^2}{2L}\right)q^2\right\} q dq \quad (4.5)$$

Using this Fourier transform method the far field radiation patterns, both co-polar (for $\varphi = 0^\circ$ and $\varphi = 90^\circ$) and cross-polar ($\varphi = 45^\circ$), were calculated for the same horn antenna as used in the calculation of the aperture fields above ($2a = 4\lambda$, semi-flare angle = 5° , $f = 150\text{GHz}$). As shown on the graph below (Figure 4.3), the cross-polar field peaks at approximately -18dB at an angle of 18 degrees off-axis as expected (Olver *et. al.*, 1994).

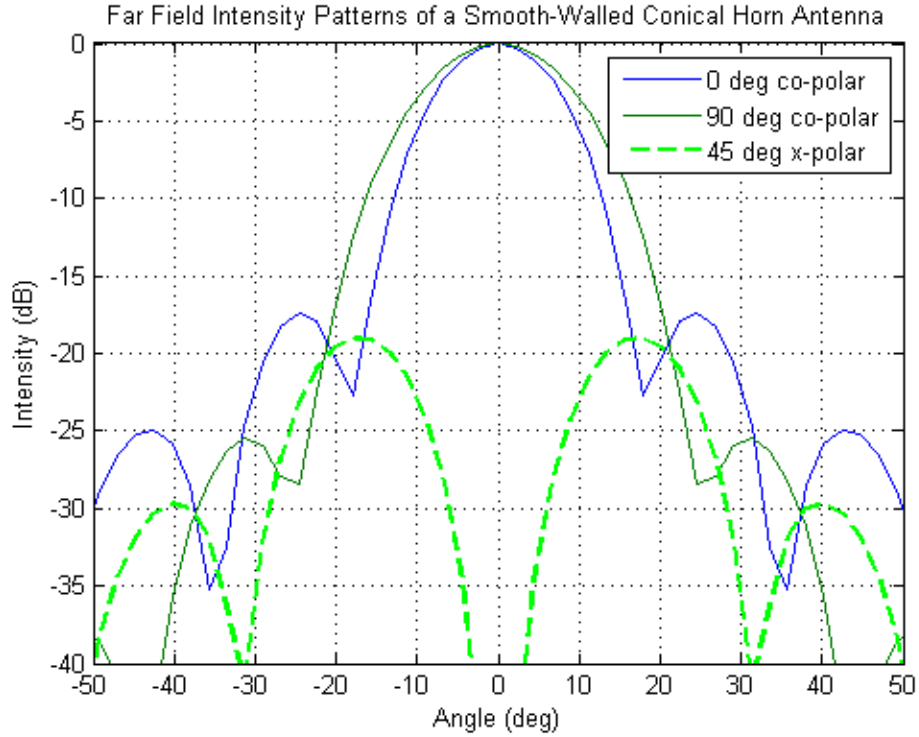


Figure 4.3 Co-polar and crosspolar radiation patterns for a smooth walled conical horn.

4.2.2 The Implementation of Smooth-Walled Horns in MODAL

MODAL, before beginning this work, did not have the ability to model smooth-walled conical horns. To allow for the analysis of the complete MBI system it was therefore necessary to have these structures implemented as an element in the MODAL code.

The intensity distribution for smooth-walled horns, as outlined in the previous section, is given by Equation 4.1. An equivalent form of writing this expression is given by Goldsmith (1998), where the aperture plane field distribution for y-polarised excitation is given by,

$$E_y = \frac{J_1(ur/a)}{ur/a} \sin^2 \phi + J_1'(ur/a) \cos^2 \phi \quad (4.6)$$

$$E_x = \left[\frac{J_1(ur/a)}{ur/a} - J_1'(ur/a) \right] \sin \phi \cos \phi \quad (4.7)$$

where $u = 1.841$, J_1 is a Bessel function of first order and J_1' is its derivative. Again, for a smooth-walled conical horn antenna of slant length, L , Equations 4.6 and 4.7 would be multiplied by a spherical factor of $\exp[-j\pi r^2/\lambda L]$ to account for phase curvature at the aperture. This is the format that was implemented in MODAL.

The fields for two very different smooth-walled horn antennas were generated using the equations above, the first horn being the same as that used in the previous section and presented by Olver *et al.* (1994). The operating frequency was 150GHz with an aperture radius of 2λ and a semi-flare angle of 5° . The second horn antenna modelled was a detector horn from the bolometric array in MBI-4. This horn had an operating frequency of 90GHz, an aperture radius of 12.7mm and a slant length of 54.3mm. Figure 4.4 shows the horn aperture field intensity for the Olver *et al.* (1994) and MBI horns using Equation 4.6 and 4.7 and also that produced by MODAL after the implementation of the smooth-walled conical horn code.

As further verification the far field intensity distributions were calculated for both horns using Equation 4.4 and MODAL. As can be seen from Figure 4.5 both methods produce results which are in excellent agreement, as expected.

4.2.3 MBI-4 Phase Flattening Lenses

In the previous section we calculated the aperture field distribution for the MBI-4 smooth-walled conical horn antennas that are used to feed the radiation onto the bolometric detectors. However, in the instrument itself, lenses are attached to the front of the horns in order to flatten the phase radius of curvature in an attempt to achieve better coupling to the incoming beam from the optical system (as the radius

of curvature is very large). Lenses were also considered to flatten the phase of the beam from the telescope but these were not implemented in the instrument. A coupling analysis carried out by Lavelle (2008) has shown that if such lenses were present it would increase the coupling by a factor of 1.4.

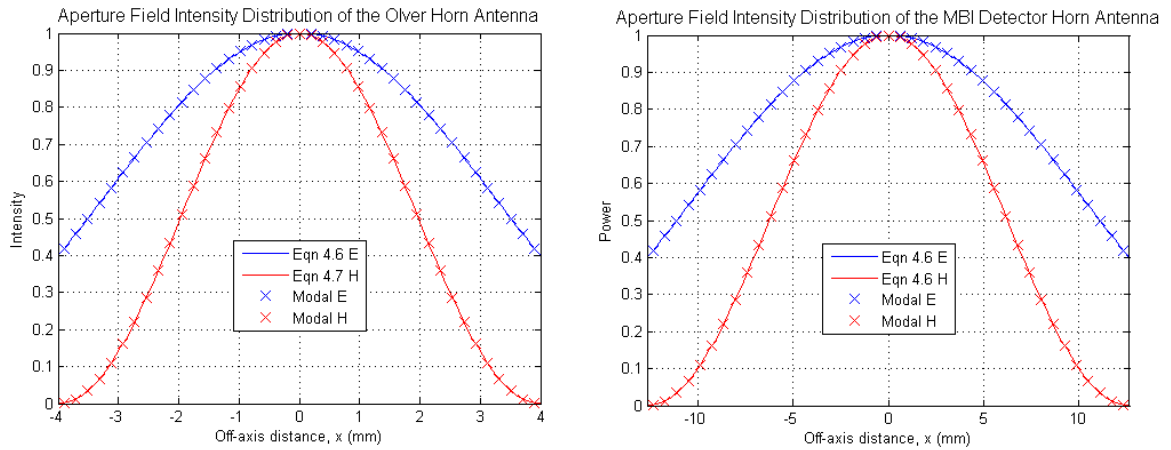


Figure 4.4 Aperture intensity distributions for the Olver *et al.* (1994) horn and MBI-4 detector horn.

Both horns are smooth-walled conical horn antennas whose aperture fields were calculated using Equations 4.6 and 4.7 as outlined in the text. Also, the aperture fields generated after implementation into MODAL are shown.

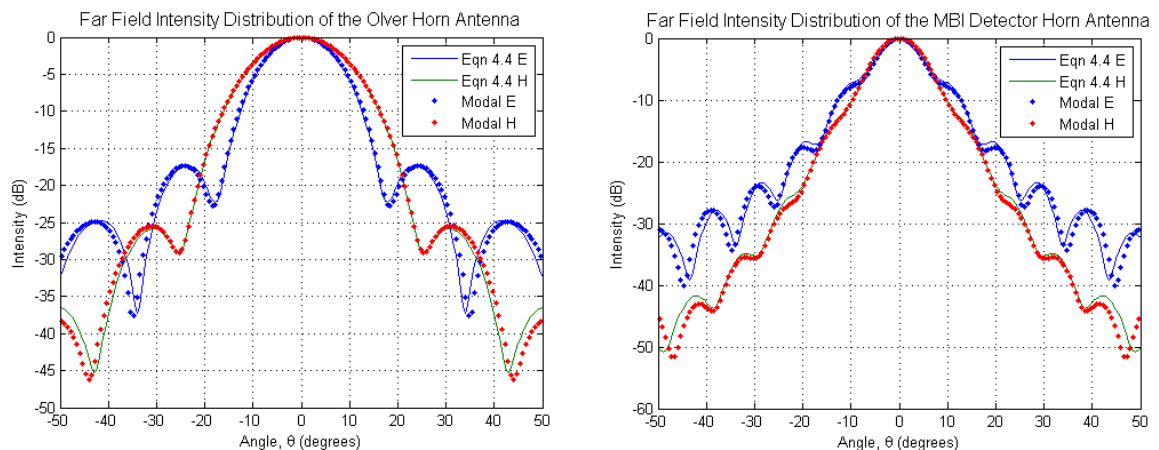


Figure 4.5 The far field intensity patterns of both the Olver *et al.* (1994) horn antenna and the MBI-4 detector horn antenna as generated using Equation 4.4 described in the text and also using MODAL after the implementation of smooth-walled conical horns into the code.

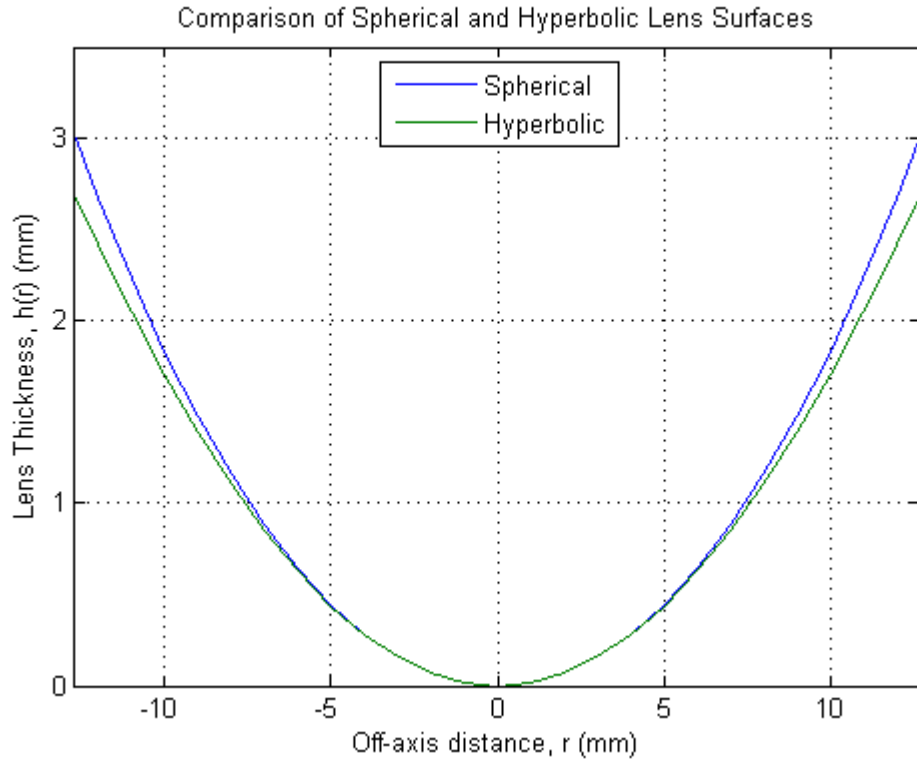


Figure 4.6 A comparison of a hyperbolic surface with its spherical approximation.

In order to match the phases of two fields, and therefore improve the coupling, a lens must have a focal length such that,

$$\frac{1}{R_{out}} = \frac{1}{R_{in}} - \frac{1}{f} \quad (4.8)$$

where R_{in} and R_{out} are the phase radii of curvature for the two fields. In the case of MBI-4 $R_{out} \approx 1 \times 10^3$ m (telescope beam) and R_{in} , the phase radius of curvature of the field from the detector horn, is given by the slant length of the horn as 54.3mm. The focal length of the lens must therefore also be 54.3mm.

The (hyperbolic) surface of a plano-convex lens of refractive index n which has a focal length f is given by

$$h_r(r) = \frac{f \left(\sqrt{\frac{(n+1)r^2}{f^2(n-1)} + 1} - 1 \right)}{n+1} \quad (4.9)$$

where r is the off-axis distance and for ease of manufacturing a spherical approximation to the hyperbolic surface

$$h_r(r) = f(n-1) \left(1 - \sqrt{1 - \frac{r^2}{f^2(n-1)^2}} \right) \quad (4.10)$$

was used in MBI-4. This is a very close approximation to the hyperbolic surface as can be seen in the comparison plot in Figure 4.6. A coupling analysis to investigate the effects of using a spherical lens rather than a hyperbolic lens was carried out by Lavelle (2008), where it was shown that the implications of this are relatively small. The refractive index of HDPE, from which the lens was to be constructed, is $n = 1.52$ and since the radius of the lens is equal to the radius of the horn antenna (12.7mm), the centre thickness was found to be approximately 3mm using Equation 4.10. Due to constraints within the cryostat the lenses were placed inside the horn antennas as shown in Figure 4.7.

To calculate the field coupling coefficient between the incident telescope beam and the beam from the detector horn antenna the following equation, which normalises the power in each beam to be unity, can be used (Goldsmith, 1998),

$$c_{th} = \frac{\int_{A_h} \Psi_t \Psi_h^* dA_h}{\sqrt{\int_{A_t=\infty} \Psi_t \Psi_t^* dA_t} \sqrt{\int_{A_h} \Psi_h \Psi_h^* dA_h}} \quad (4.11)$$

where Ψ_t is the field from the telescope, Ψ_h is the field from the horn antenna and Ψ^* is the complex conjugate of the field. The power coupling can then be calculated as $P_{th} = |c_{th}|^2$. With regards to the area over which the integrals were carried out, the telescope beam is integrated over infinity while the horn beam is

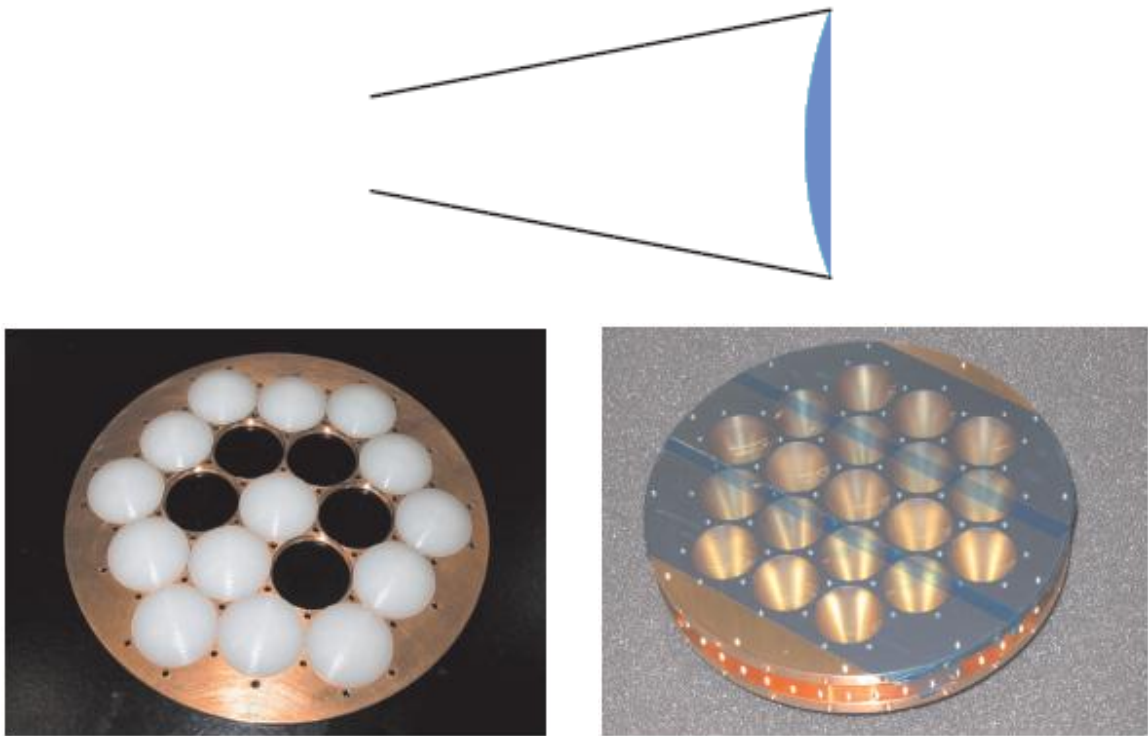


Figure 4.7 *Top:* The spherical lens antenna sitting inside the smooth-walled corrugated horn antenna. *Bottom left:* The spherical lenses held by the holder for the detector horn array. *Bottom right:* The detector horn array (Lavelle, 2008).

Horn Antenna and Spherical Lens Configurations			
Parameter	System 1	System 2	System 3
Horn Aperture Radius, a (mm)	12.7	9.525	9.525
Horn Field Radius, w_h ($=0.76a$) (mm)	9.652	7.239	7.239
Horn Field Phase Radius of Curvature, R_h (mm)	∞	49.3	∞
Lens Shape	Spherical	Spherical	Spherical
Lens Radius (mm)	12.7	12.7	9.525
Lens Thickness	3.02	3.02	2.54
Lens Focal Length, f (mm)	54.3	54.3	36.8
Telescope Field Beam Radius, w_t (mm)	197.5	197.5	197.5
Telescope Field Phase Radius of Curvature, R_t (mm)	∞	∞	∞

Table 4.1 Parameters defining the three lens and horn configurations analysed.

integrated over the area of the horn aperture since the horn field does not exist outside of this. Depending on the location of the detector horn antenna being analysed this may or may not be centred on the telescope beam.

In this analysis three configurations of horn antenna and lens were considered and are summarised in Table 4.1. Firstly, the horn and lens combination used in the current MBI-4 instrument where the horn has a radius of 12.7mm and a slant length of 54.3mm was examined. The lens surface is spherical and its cross-sectional radius is the same as that of the horn, therefore producing a flat phase curvature. It is made of HDPE ($n = 1.52$) and has a focal length of 54.3mm to match the phase curvature of the horn antenna field. In order to estimate the coupling a best fit Gaussian beam given by,

$$\Psi = \exp[-((x^2 + y^2)/w_h^2)] \exp[-jk((x^2 + y^2)/2R)] \quad (4.12)$$

was chosen for the detector with a beam radius of $w_h = 0.76a$ (Goldsmith, 1998) = 9.652mm. The telescope field was also assumed to have a Gaussian distribution with a radius of $w_t = 197.5$ and an infinite phase front radius of curvature. Both the telescope and the horn antenna beams are shown in Figure 4.8. Applying Equation 4.11 and assuming that the detector horn is in the centre of the array we can write,

$$c_{th} = \frac{\int_{\phi=0}^{2\pi} \int_{\rho=0}^a \Psi_t \Psi_h^* \rho d\rho d\phi}{\sqrt{\int_{\phi=0}^{2\pi} \int_{\rho=0}^{\infty} \Psi_t \Psi_t^* \rho d\rho d\phi} \sqrt{\int_{\phi=0}^{2\pi} \int_{\rho=0}^a \Psi_h \Psi_h^* \rho d\rho d\phi}} \quad (4.13)$$

where ρ is the off-axis distance and ϕ is the angle. From this the power coupling was calculated to be 0.66% (this number is so low because a single bolometer only couples to a small part of the full telescope field, see for example Figure 4.8). An alternative approach would be to integrate the telescope field over the area of the horn aperture (as carried out in Chapter 5) since this is the absolute maximum power

that could be absorbed by the horn. If this is done then a coupling value of 84% is obtained for the same on-axis detector horn antenna.

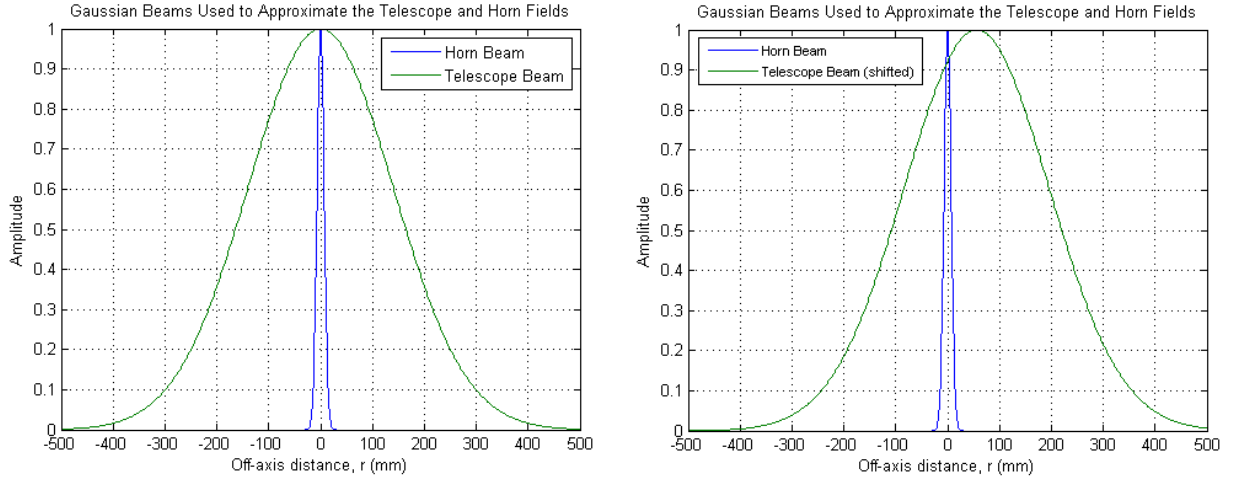


Figure 4.8 *Left:* The telescope and detector horn antenna beams with the horn antenna located at the centre of the array. *Right:* The telescope and detector horn antenna beams with the horn antenna located 55.8mm from the centre representing a horn at the edge of the detector array.

The second system examined here was one that was being considered for use in MBI-4 lab measurements. The horn antenna was smaller and therefore would provide better sampling. It had a radius of 9.525mm and a slant length of 36.8mm. It was essential to know the difference in power coupling between using the previous lens, which was designed for the larger horn, on this new antenna and using a lens specifically designed for the new horn antenna, that is, the third system outlined in Table 4.1. To calculate the power coupling for the 9.525mm radius horn with the 12.7mm lens (whose focal length was 54.3mm) both the surface for the $f = 54.3$ mm and $f = 36.8$ mm lenses were calculated using Equation 4.10 and the difference in curvature found. This can be seen in Figure 4.9. The difference in surface curvature is equivalent to the phase curvature remaining on the horn antenna beam, which is calculated as (Lavelle, 2008),

$$\phi_s = \frac{-2(n-1)\pi(t_c - z_s(r))}{\lambda} \quad (4.14)$$

where $t_c - z_s(r)$ is the surface height, n is the refractive index of the material and λ is the wavelength. The best-fit spherical radius of this curvature was calculated to be $R_h = 49.3\text{mm}$. For the horn antenna with a new lens designed to flatten the phase the radius of curvature of the horn field after propagating through the lens was assumed to be infinite. Using Equation 4.13 the power coupling for systems 2 and 3 as outlined above was calculated to be 0.3% and 0.4% respectively (Table 4.2), indicating a loss of approximately 25% if the larger lens is used with the smaller horn antenna.

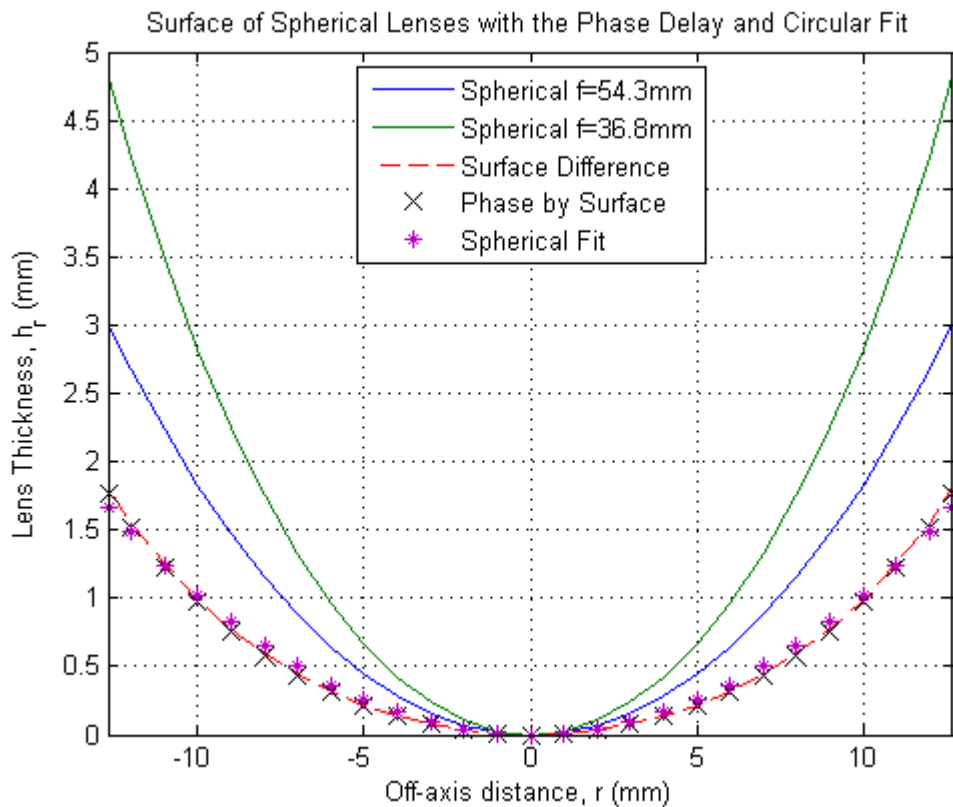


Figure 4.9 A comparison of the surface of the $f = 54.3\text{mm}$ lens and the $f = 36.8\text{mm}$ lens. Also shown is the difference in the surfaces and the phase that this imposes on the beam. The best fit spherical section used to determine the radius of curvature of the phase can also be seen.

The above analysis accounted for a horn antenna placed at the centre of the array which coincided with the centre of the Gaussian beam from the telescope. The power coupling for each of the systems above was recalculated assuming a horn antenna located at the edge of the array with its centre positioned 55.88mm (2.2in) from the centre of the telescope beam (see Figure 4.8). The results of this are given in Table 4.2 where it can be seen that the loss in coupled power between systems 2

and 3 is also approximately 20%. This analysis assumed a flat telescope field, however calculations to include the real radius of curvature showed no difference in coupling for horn antennas at the edge of the array, where the effect of field curvature would be greatest.

The low power coupling values can be explained by the fact that the telescope beam has a radius much greater than that of the detector horn antenna and therefore only a small portion of this beam is collected by the horn. However, a loss of 20% in coupled power occurs when the larger lens is implemented with the smaller horn and therefore must be taken into account when deciding on the appropriate horns and lens combination to be used.

Power Coupling Between Telescope and Detector Horn Antenna Beams		
Configuration	On-axis Detector Horn	Off-axis Detector Horn
System 1	0.66%	0.57%
System 2	0.30%	0.26%
System 3	0.37%	0.32%

Table 4.2 Parameters defining the three lens and horn configurations analysed.

4.2.4 Corrugated Conical Horns

The development of many types of alternative horn feeds took place in the 1960's in response to the need for improved performance for large reflector antennas used in radio astronomy and satellite communications. One such feed was the corrugated horn antenna. It was discovered in 1966 (Simmons and Kay, 1966) that by having grooves or slots of an appropriate depth in the wall of the horn, the boundary conditions would appear the same for both the electric and magnetic fields. The grooves, or corrugations, ensure no axial current can be set up along the walls, since the current travelling down one side of a corrugation, which is usually a quarter-wavelength deep, would be 180° out of phase with the current at the

opposite side of the groove. The effect of the field produced by this opposite current is to oppose the field that initially set up the current. The overall result is that no current can exist at the horn wall and a short circuit at the bottom of the groove is transformed to an open circuit at the top and the fields taper to zero at the horn boundary (Olver *et al.*, 1994). The corrugated conical horn therefore has significant advantages over the smooth-walled conical horn. Spillover efficiency and cross-polarisation losses are reduced while at the same time the aperture efficiency (i.e. coupling to a point source in the far field of the antenna) for a telescope fed by such a horn is increased. With the use of conventional (smooth walled conical / rectangular) horn feeds, efficiency levels of 50 – 60% were attainable, whereas with the use of corrugations, the efficiency level could be increased by as much as 15% to 20% (Balanis, 1997).

Corrugated or scalar horns usually have the form of a corrugated waveguide flared to make a conical section (Goldsmith, 1998) and are generally fed by a smooth-walled circular waveguide (Figure 4.10). The geometry of the circumferential slots usually has one of the two orientations as illustrated in Figure 4.11. They can be perpendicular to either the axis of the horn and hence the direction of propagation, or they can be perpendicular to the horn surface, that is, the outer wall of the horn. The first design is usually chosen as it is the easier of the two to machine.

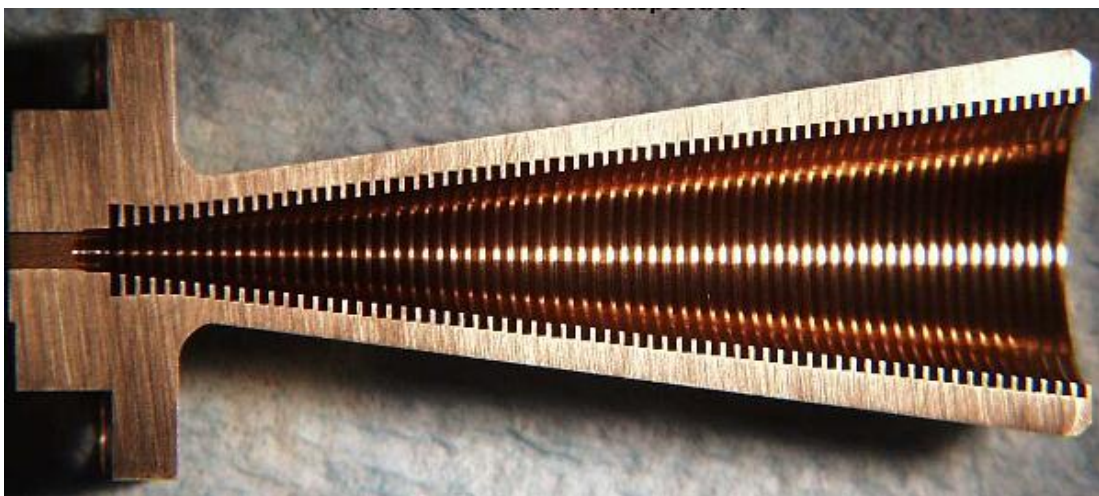


Figure 4.10 A cross-section of a corrugated conical horn antenna showing the circular waveguide feed and the corrugation geometry (ZAX Millimeter Wave Corporation website.)

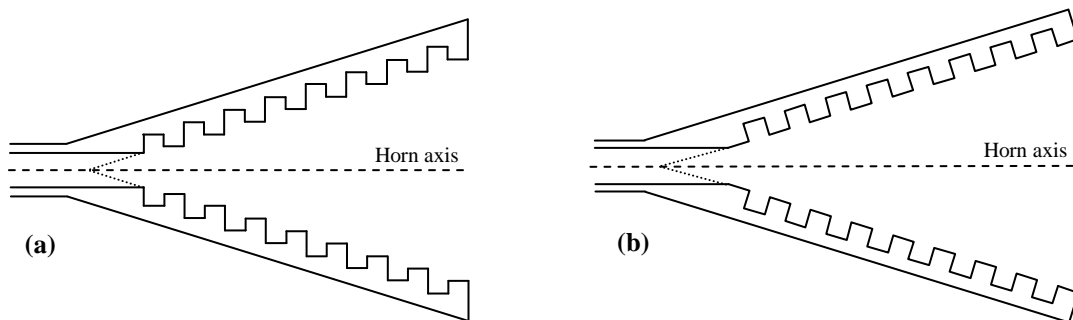


Figure 4.11 Corrugated Horn antenna with grooves orientated perpendicular to (a) the horn axis and (b) the horn wall surface.

For horns of aperture width greater than 2λ the optimum annular groove depth is $\lambda/4$ (Clarricoats & Olver, 1984). This is the resonant depth for which the short circuit at the bottom of the groove is effectively transformed into an open circuit at the corrugation boundary, cutting off the axial current at the ridges. Since the axial current is generated by the azimuthal magnetic field, H_ϕ , this will also be zero. In order to achieve an effective corrugated surface the corrugations are assumed to be infinitely thin, however in reality the theory holds for as few as three corrugations per wavelength (Colgan, 2001). The fact that the azimuthal components of both the electric and magnetic fields vanish at the horn walls forces the field across the aperture to be almost linearly polarised. This linearity implies that the fields are essentially scalar, hence giving rise to the term ‘scalar horn’, and also that neither the pure TE or TM modes can be supported without scattering in the horn, since each of these exhibit significant levels of cross-polarisation. In the case where the horn is fed by either a single-moded smooth-walled or corrugated circular waveguide, the dominant mode is the HE_{11} mode, or hybrid mode, which is a linear combination of the TE_{11} and TM_{11} modes and effectively means that it is neither pure transverse electric nor transverse magnetic (while waveguide modes are discussed later in this chapter, hybrid modes will not be examined in detail). For symmetrical radiation patterns and low cross-polarisation levels, the horn is said to have achieved the ‘balanced hybrid’ condition.

If we consider a corrugated conical horn with its aperture in the x - y plane and its axis defining the z -direction as shown in Figure 4.12, and which is being fed with

a HE₁₁ mode under the balanced hybrid condition as described above, then the field at the horn mouth is given by (Wylde, 1984),

$$E = E_o J_0^T \left(2.405 \frac{r}{a} \right) \exp \left[- \frac{jkr^2}{2L} \right] \hat{\mathbf{i}} \quad (4.15)$$

where E_o is a constant, a is the aperture radius and L is the slant length, which also equals the radius of curvature of the equiphase surface at the front of the horn. The spherical phase factor is contained in the exponential function as was the case with the smooth-walled horn. As an example of this, the aperture field of a corrugated horn antenna was calculated. The horn in question (following Olver *et al.*, 1994 as an example) had a diameter of 4λ , a semi-flare angle of 5° and an operating frequency of 150GHz. The results of this calculation are shown in Figure 4.13. The far field pattern for the corrugated horn is obtained in much the same way as that for the smooth-walled conical horn, that is, by carrying out the ϕ integration of the Fourier transform analytically to give (Olver *et al.*, 1994),

$$E(\theta) \propto (1 + \cos \theta) \int_0^1 J_0(ka \sin \theta q) J_0(2.405q) \exp \left\{ \left(\frac{-jka^2}{2L} \right) q^2 \right\} q dq \quad (4.16)$$

where again $q = r/a$ and the integral can be carried out numerically. Using this integral and the same horn parameters as that described above in the generation of the aperture field, the far field patterns were calculated (Figure 4.13).

Equation 4.16 is valid for standard conical horns (>3 corrugations per wavelength operating under that balanced hybrid condition) but does not take account of the exact shape of the horn (for example if the horn is flared or the corrugation depths vary). This is something that has been researched extensively at NUIM (Murphy, 2001; Gleeson, 2004) and for which dedicated software called SCATTER has been developed (Gleeson, 2004). This program uses a mode-matching scattering matrix method. The scattering matrix method outlined is not only applicable to horn antennas but also to complete optical systems as discussed in more detail in Chapter 5.

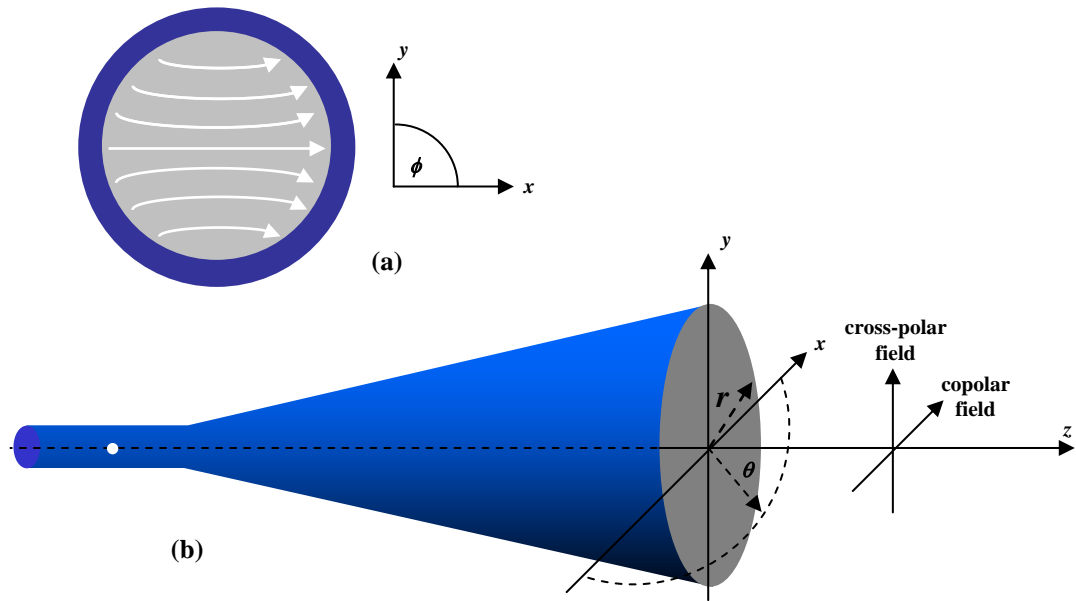


Figure 4.12 Part (a) shows the hybrid electric field line configuration of the HE_{11} mode in a circular waveguide. Part (b) shows a conical horn with its aperture in the x - y plane and the propagation axis along the z direction.

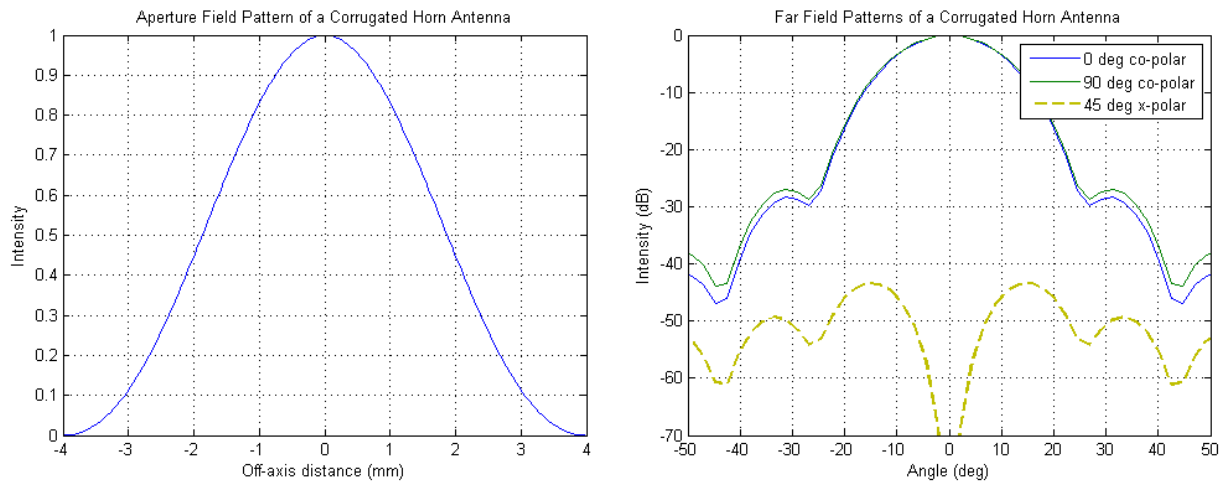


Figure 4.13 Left: The aperture field from a corrugated horn with a diameter of 4λ and a semi-flare angle of 5° operating at 150GHz. Right: The far field pattern for the same corrugated horn antenna.

4.3 Scatter Matrix Analysis of Quasi-Optical Systems

In this section the use of scatter matrices in the analysis of horn antennas is discussed. The techniques presented here may also be applied to complete optical systems such as the optical beam combiner in MBI-4.

4.3.1 Scatter Matrix Methods

This technique for modelling and analysing quasi-optical systems, in this case a horn antenna, divides the overall system into a sequential arrangement of subsystems. The effect of each of these subsystems can be described in terms of transmission and reflection coefficients for the fields propagating both forwards and backwards within that section. The characteristics of this section, that is, the redistribution of power between waveguide modes (or free space modes in the case of free space propagation) is described by a scattering matrix S , while a set of column matrices represent the mode coefficients of the forward and backward travelling fields of the complete system or subsystem.

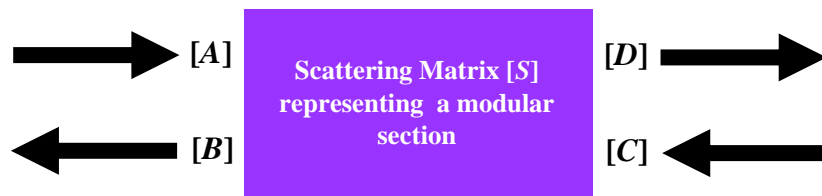


Figure 4.14 The scattering matrix S describes the characteristics of a modular section of a quasi-optical system and relates the coefficients at the input to those at the output.

If $[S]$ is the scatter matrix for the system/subsystem to be analysed, then the mode coefficients are related to one another through the equation

$$\begin{bmatrix} [B] \\ [D] \end{bmatrix} = [S] \begin{bmatrix} [A] \\ [C] \end{bmatrix} \quad (4.17)$$

where column matrices $[A]$ and $[B]$ represent the incident and reflected mode coefficients of the wave respectively as viewed from the input side while $[C]$ and $[D]$ represent the incident and transmitted coefficients on the output side (Figure 4.14). The matrix $[S]$ can be divided into sub-matrix components as in Equation

4.18 which govern the scattering of forward and backward propagating modes at the input and output sides of the optical system,

$$[S] = \begin{bmatrix} [S_{11}] & [S_{12}] \\ [S_{21}] & [S_{22}] \end{bmatrix}. \quad (4.18)$$

In theory the dimension of all these matrices is infinite, however, for the sake of computational analysis this is reduced to a finite number that describe the system sufficiently accurately. In general, the matrices $[A]$ and $[B]$, representing the input side, and $[C]$ and $[D]$, representing the output side, will be square matrices if the same number of mode coefficients are used to describe the field at the input and output planes. We can write

$$\begin{bmatrix} [B] \\ [D] \end{bmatrix} = \begin{bmatrix} [S_{11}] & [S_{12}] \\ [S_{21}] & [S_{22}] \end{bmatrix} \begin{bmatrix} [A] \\ [C] \end{bmatrix} = \begin{bmatrix} [S_{11}][A] + [S_{12}][C] \\ [S_{21}][A] + [S_{22}][C] \end{bmatrix} \quad (4.19)$$

or

$$[B] = [S_{11}][A] + [S_{12}][C], \quad [D] = [S_{21}][A] + [S_{22}][C]. \quad (4.20)$$

If there are the same number of modes on both sides of the system then there are n TE and n TM elements in the $[S]$ matrix with $4n \times 4n$ elements in the sub-matrices. Often it can be assumed that there is no reflection back into the system, for example at the horn aperture, and as a result the column matrix $[C]$ is zero for that system and the reflection and transmission coefficients are given by

$$[B] = [S_{11}][A], \quad [D] = [S_{21}][A] \quad (4.21)$$

where again $[A]$ is the input matrix of coefficients.

In the case of a circular waveguide propagating the fundamental mode (TE₁₁), only other modes of azimuthal order 1 can be excited in a horn fed by the

guide. In such a case the initial input forward propagating matrix of coefficients has one non-zero entry in the TE_{11} mode position (Equation 4.22). The matrix has $2n$ elements which represents the number of modes included at the output (n TE and n TM modes).

$$[A] = \begin{bmatrix} 1 \\ 0 \\ 0 \\ \dots \\ \dots \\ \dots \end{bmatrix} \quad (4.22)$$

The overall transmission and reflection coefficients for a complete optical system are obtained by cascading the scattering matrices of each of the constituent subsystems, which are obtained by analysing each section separately. Let $[S^a]$ and $[S^b]$ be two matrices that describe consecutive sections of an optical system and are of the form

$$[S^a] = \begin{bmatrix} [S_{11}^a] & [S_{12}^a] \\ [S_{21}^a] & [S_{22}^a] \end{bmatrix} \quad [S^b] = \begin{bmatrix} [S_{11}^b] & [S_{12}^b] \\ [S_{21}^b] & [S_{22}^b] \end{bmatrix}. \quad (4.23)$$

The cascaded matrix elements are then of the form

$$[S^c] = \begin{bmatrix} [S_{11}^c] & [S_{12}^c] \\ [S_{21}^c] & [S_{22}^c] \end{bmatrix} \quad (4.24)$$

whose elements are defined as (Olver *et al.*, 1994)

$$[S_{11}^c] = [S_{12}^a] [[I] - [S_{11}^b] [S_{22}^a]]^{-1} [S_{11}^b] [S_{21}^a] + [S_{11}^a] \quad (4.25)$$

$$[S_{12}^c] = [S_{12}^a] [[I] - [S_{11}^b] [S_{22}^a]]^{-1} [S_{12}^b] \quad (4.26)$$

$$[S_{21}^c] = [S_{21}^b] [[I] - [S_{22}^a] [S_{11}^b]]^{-1} [S_{21}^a] \quad (4.27)$$

$$[S_{22}^c] = [S_{21}^b] [[I] - [S_{22}^a][S_{11}^b]]^{-1} [S_{22}^a][S_{12}^b] + [S_{22}^b] \quad (4.28)$$

where $[S^c]$ represents the cascaded matrix, $[I]$ is the identity matrix and $[]^{-1}$ represents the inverse of a matrix. By cascading the scattering matrices for successive sections or discontinuities with the complete scattering matrix describing all previous sections in an iterative process, the complete matrix describing propagation for the overall optical system can be obtained (see Figure 4.15).

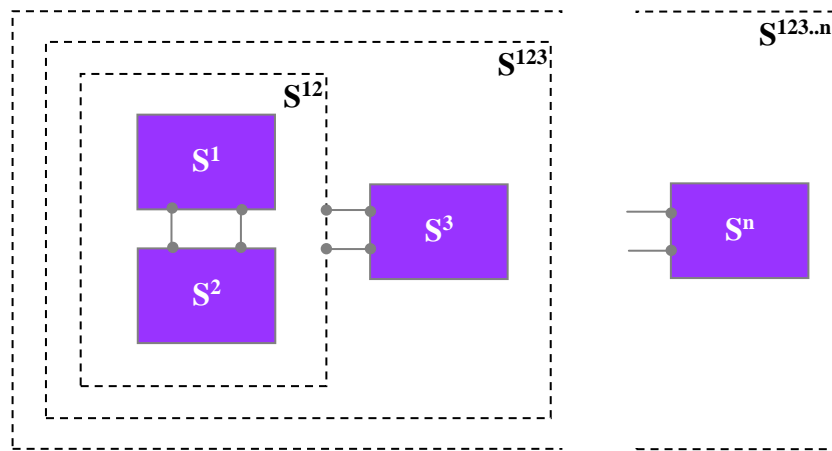


Figure 4.15 The iterative process of cascading adjacent matrices representing a modular section. Matrices representing sections S^1 and S^2 are cascaded together to form a matrix representing S^{12} . This matrix is then cascaded with that from S^3 to form a matrix which represents section S^{123} and so on.

This scattering matrix approach can be applied to both quasi-optical propagation of free space wave modes and the electromagnetic propagation of waveguide modes in a horn antenna. To analyse a horn using this technique the transmission and reflections coefficients at the discontinuities between the waveguide sections must be determined and propagation within the waveguide section must also be taken into account. Figure 4.16 shows how smooth-walled and corrugated horns may be considered as a sequence of waveguide sections. The output from one cylindrical (in this case) section becomes the input for the next. In order to satisfy Maxwell's equations, the electric and magnetic fields across the interface at a particular junction between sections are required to be continuous. As

before, the relationship between the input and output mode coefficients for the junction are expressed in terms of scatter matrices which are cascaded to produce an overall scatter matrix for the horn structure. The field at the mouth of the horn is then represented by a matrix which acts as an operator on the coefficients describing the field at the waveguide input to the horn.

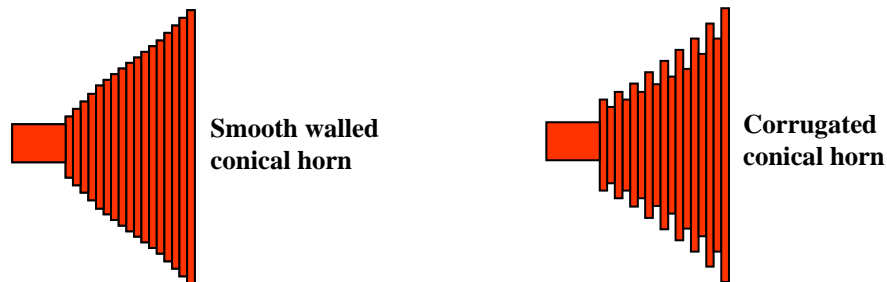


Figure 4.16 The scatter matrix approach assumes that the horn antenna is made up of a series of cylindrical sections of increasing radius.

This principle of cascading matrices representing different sections of a horn antenna, in conjunction with scattering at discontinuities which is discussed later, is used by the SCATTER program and has also been implemented in MODAL to produce the field distributions for corrugated horn antennas analysed in this thesis.

4.3.2 MBI-4 Back-To-Back Horn Antennas

The MBI-4 instrument contains four back-to-back corrugated horn antennas. Both horns in the back-to-back pair are the same with one viewing radiation from the sky while radiation from the other horn is fed to the optical beam combiner. Between the two corrugated structures is a combination of both circular and rectangular waveguides as well as phase shifters.

Since the rectangular waveguide and phase shifters were involved only in the rotation and selection of a single polarisation direction these could be ignored to a first approximation in generating the aperture field intensity of a single horn from the back-to-back system, a diagram of which is shown in Figure 4.17, provided the

output polarisation of the horn was known. The details of the mode launcher given in Table 4.3. For both SCATTER and MODAL a *geometry file* describing the structure of the corrugated horn must be created. This was done for the MBI-4 horn using the information in Figure 4.17. For convenience, the frequency of operation for the system is also stored in the geometry file. Figure 4.18 shows the structure of the horn as produced by MODAL from the geometry file with the resulting aperture intensity distribution shown in Figure 4.19 where the horn has been excited by a single TE₁₁ mode.

It has been shown (Goldsmith, 1998) that the aperture field distribution of a corrugated conical horn antenna can be well approximated by,

$$E_{ap} = J_0\left(\frac{2.405r}{a}\right)\exp\left(\frac{-j\pi r^2}{\lambda L}\right)\hat{y} \quad (4.29)$$

where \hat{y} is the direction of polarisation. The aperture field of the MBI-4 corrugated horn antenna was first estimated in this way and compared to that generated using the scattering matrix method described earlier to see if Equation 4.29 would provide a computationally efficient and accurate way of producing the required fields. The results of this analysis can also be seen in Figure 4.19, where both the Bessel function and true aperture fields are in excellent agreement.

As well as modelling a single horn antenna the complete back-to-back system was also examined in detail. As a first approximation to this a geometry file was generated that described a back-to-back corrugated horn antenna constructed from two of the single horns described above, with one being a mirror image of the other. Again, the dimensions of the throat of the horns and the connecting waveguide were designed for a single-moded system with a single polarisation. The phase shifters were accounted for by selecting the polarisation direction in the model. The resulting horn antenna is shown in Figure 4.20.

Mode Launcher Details of the MBI-4 Corrugated Horn Antenna				
Slot Number	g_i (inches)	t_i (inches)	a_i (inches)	d_i (inches)
1	0.0049	0.0345	0.0628	0.0496
2	0.0070	0.0324	0.0646	0.0478
3	0.0092	0.0302	0.0664	0.0460
4	0.0113	0.0281	0.0682	0.0442
5	0.0135	0.0259	0.0700	0.0424
6	0.0156	0.0238	0.0718	0.0406
7	0.0177	0.0217	0.0736	0.0388
8	0.0199	0.0195	0.0754	0.0370
9	0.0220	0.0174	0.0772	0.0352
10	0.0242	0.0152	0.0790	0.0334
11	0.0263	0.0131	0.0808	0.0316

Table 4.3 Mode launcher details of the MBI-4 corrugated horn antenna. Note that $d_i+a_i=0.1124$ inches and $g_i+t_i=0.0394$ inches.

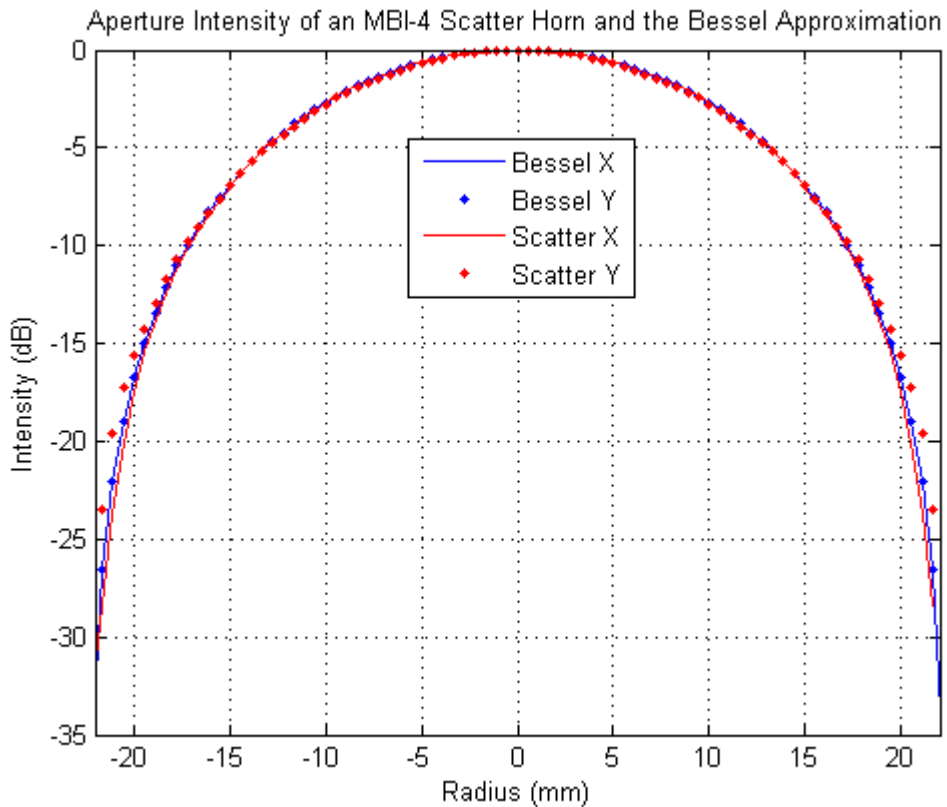


Figure 4.19 The aperture field intensity distribution of a single horn from the back-to-back corrugated horn system used in MBI-4 and the equivalent intensity from a simulated horn of the same dimensions using a Bessel function as in Equation 4.29.

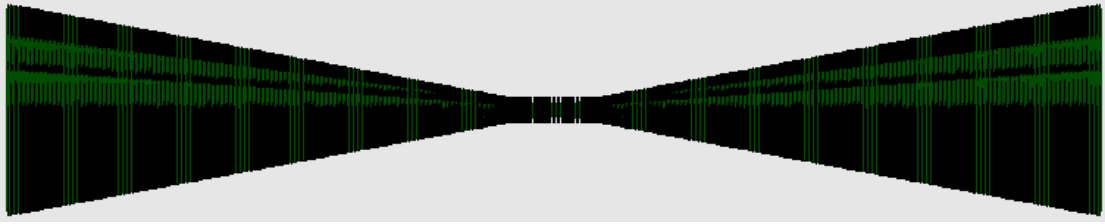


Figure 4.20 Back-to-back horn corrugated horn antenna with no circular waveguide extension between the horns.

To calculate the field at the aperture of the back-to-back horn the input port (port 2) was illuminated by a plane wave at 90GHz. The field was then propagated through the corrugated structure before being analysed at the output port (port 1). The results of the calculation can be seen in Figure 4.21 where the aperture field of the horn antenna is shown. Also, the power at the input of the corrugated horn was calculated and compared to that at the output, resulting in approximately 65% of power being transmitted from port 2 to port 1. It can be seen that the results are very similar to those produced by SCATTER for a single corrugated horn from the back-to-back system.

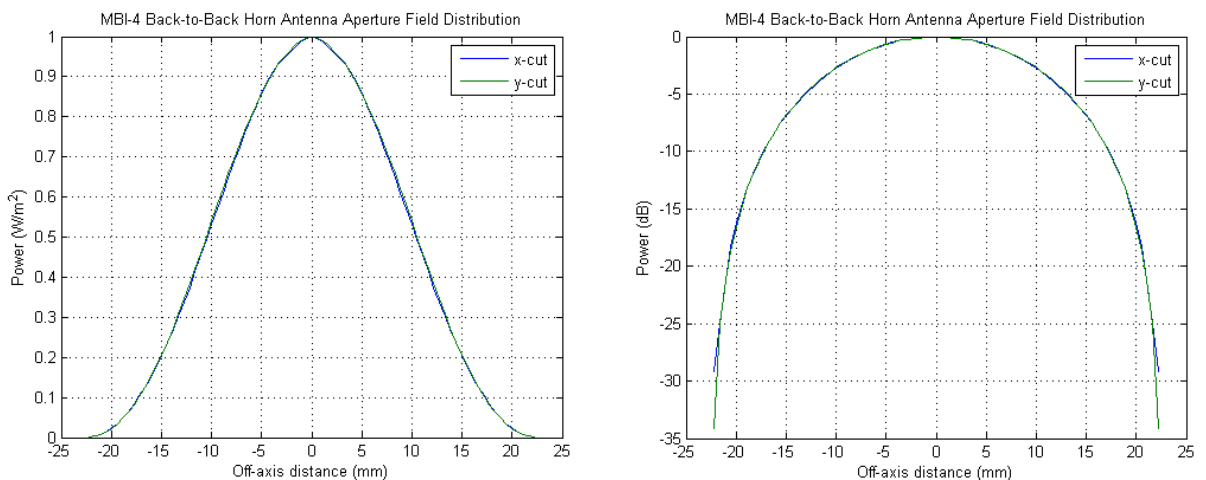


Figure 4.21 Back-to-back horn antenna aperture field on a linear (left) and dB (right) scale.

Further investigation of the back-to-back system was carried out by changing the geometry to include a narrow cylindrical section between the corrugated structures (see Figure 4.22), the radius of which ensured that any higher order modes that might be present were filtered out. This section of cylindrical waveguide had a

radius of approximately 1.55mm and a length that varied from 5mm to 20mm. In all cases the field distribution at the aperture of the output horn remained the same as did the transmitted power (~65%). This provided further verification that the overall structure was single-moded when fed with a plane wave propagating in a direction along the axis of the horn. The radius of the 20mm long cylindrical waveguide was also varied between 1.55mm and 2.15mm in steps of 0.1mm. In the case of the largest radius, 2.15mm, the transmitted power was reduced to approximately 42% at an operating frequency of 90GHz. After the cylindrical waveguide the next horn section has a radius of 2.85mm followed by one of 1.59mm (see Figure 4.23). As the radius of the cylindrical waveguide section is increased it becomes wider than the 1.59mm section of the horn and therefore some of the power is possibly lost due to reflection at this surface, accounting for the reduction in power transmitted from port 2 to port 1. This analysis was also carried out for frequencies of 95GHz and 100GHz, the results of which are shown in Figure 4.24.

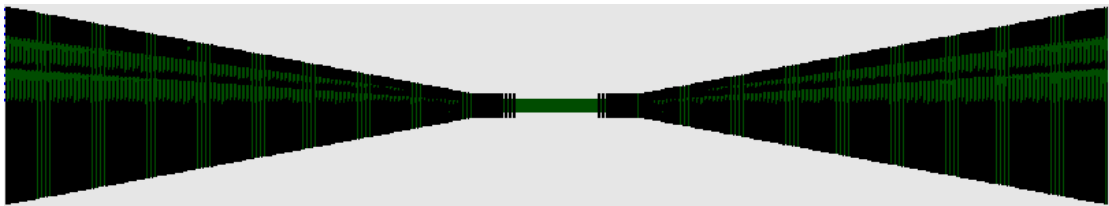


Figure 4.22 Back-to-back horn corrugated horn antenna with a circular waveguide extension between the horns.

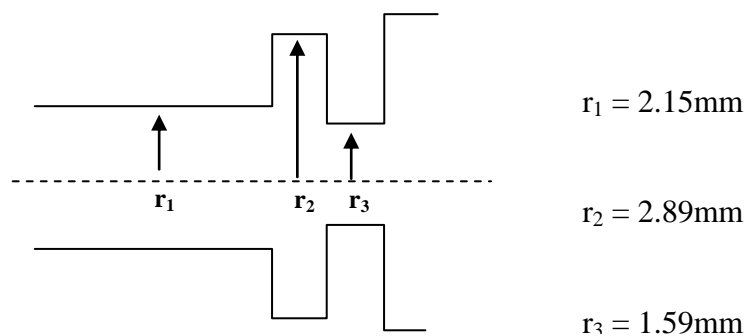


Figure 4.23 Schematic diagram showing a close-up of the cylindrical waveguide section between the back-to-back horns with a radius r_1 , along with the next two sections of the horn antenna with radii r_2 and r_3 respectively (not to scale).

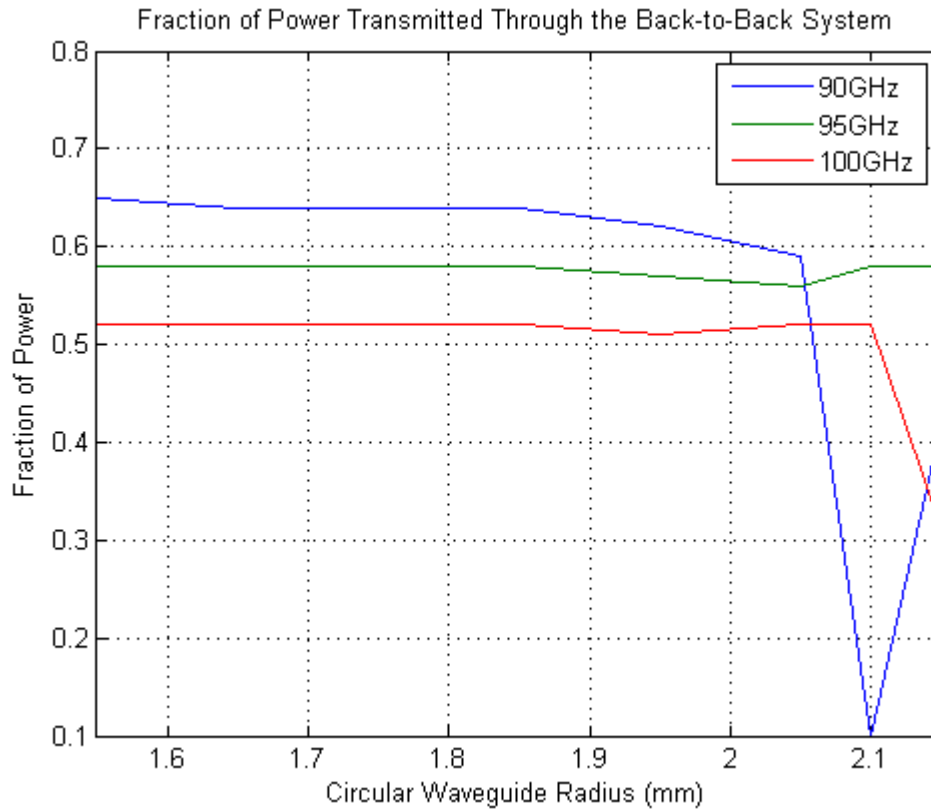


Figure 4.24 The fraction of the power transmitted to the aperture of the horn antenna after propagation through the back-to-back system. This is shown for three different frequencies.

In the next section we consider the aperture field of the horn antenna as described above and how this is affected as it propagates through the windows of the cryostat.

4.3.3 Truncation by MBI-4 Windows

During a pre-opening season research trip to Pine Bluff Observatory at the University of Wisconsin-Madison in January 2009 the author investigated the effect of possible truncation of the beam by the cryostat window. A circular aperture representing the cryostat window was placed in front of the sky-facing horn antenna model (Figure 4.25). The horn model was generated using the technical drawings provided in the previous section and so a full SCATTER model of the horn was

used. The window was defined to have a radius of 22.45mm, the same as that of the horn antenna, and was placed at various distances from the horn aperture and a physical optics analysis of the horn and aperture truncation was carried out.

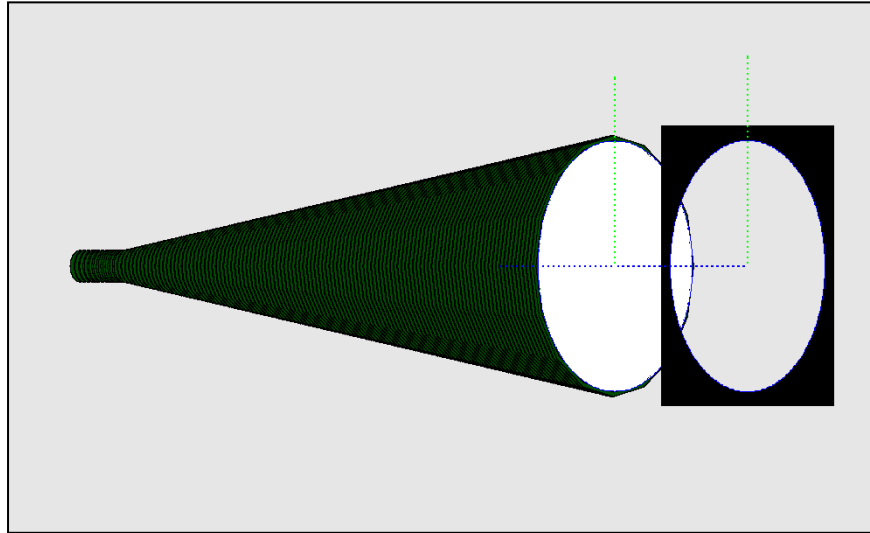


Figure 4.25 A single sky-facing corrugated horn antenna from the MBI-4 back-to-back system with a circular window (aperture) between the horn and the sky.

Figure 4.26 shows the beam patterns after truncation by the window aperture in both the x and y -directions obtained from the analysis where the window was placed a distance of 10mm to 30mm in steps of 5mm from the horn aperture. The horn aperture field is also shown for comparison. The details of the beam edge taper levels can be seen in Table 4.4. A comparison of the far field patterns is shown in Figure 4.27.

In conclusion, truncation of the horn antenna beams by the cryostat windows or filters could be significant, depending on the exact distance from the horn aperture to the truncating surface, particularly in the y -direction, and must be taken into account.

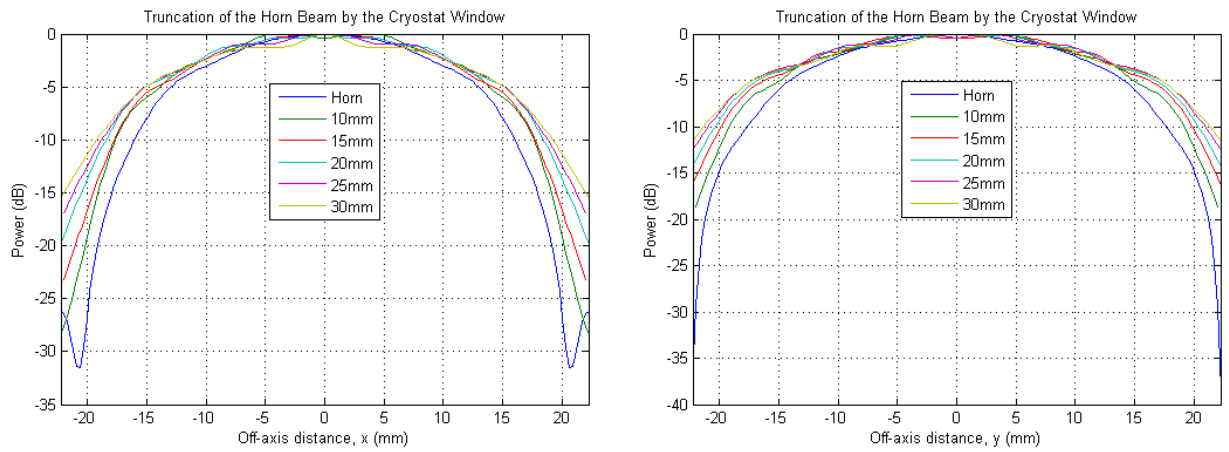


Figure 4.26 The power distribution of the sky-facing corrugated horn antenna after truncation by a window at different distances from the horn aperture. The horn aperture field is also shown for comparison.

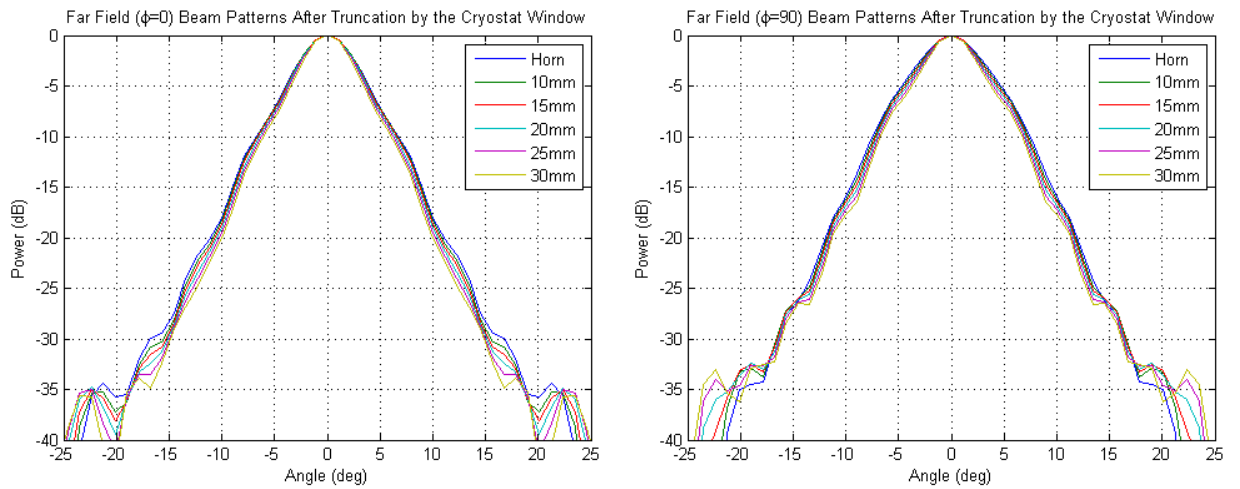


Figure 4.27 The far field beam patterns at $\phi = 0^\circ$ (left) and $\phi = 90^\circ$ (right) after truncation by a window at different distances from the horn aperture. The horn far field is also shown for comparison.

Truncation of the Sky-Facing Horn Beam by the Cryostat Window		
Location	<i>x</i> -Axis Truncation (dB)	<i>y</i> -Axis Truncation (dB)
Window at 10mm	-29	-19
Window at 15mm	-23	-16
Window at 20mm	-20	-14
Window at 25mm	-17	-13
Window at 30mm	-16	-12

Table 4.4 Truncation level of the sky-facing corrugated horn antenna beam by a window at various distances from the horn aperture.

4.3.4 Singular Value Decomposition Analysis

In 2008 the beam patterns on the image plane transmitted independently from back-to-back horn antennas S1 and S4 (see Figure 4.30) were measured by scanning the MBI-4 instrument across a local source (a 100GHz Gunn oscillator feeding a pyramidal horn antenna). The results of these measurements as presented by Hyland (2008) are shown in Figure 4.28, where it can be seen that the beam patterns on the image plane are asymmetric, something that was unexpected from the single-moded back-to-back horn antennas. To understand this, a similar experimental arrangement was modelled in MODAL.

A number of frames were used to set up the model as shown in Figure 4.29 (not to scale). The *Mount Frame* (the local coordinate frame for the MBI telescope) was placed an arbitrary distance of 1m above the *Global Frame* with the option of rotating it around both the *x*- and *y*-axes of the *Global Frame* to give different elevation and azimuth angles respectively. A *Horn Coordinate Frame* was located at the plane of the telescope containing the back-to-back horn antennas (with the apertures of the horns facing the optics located at the $z = 0$ within this plane) and was used to position these antennas as shown in Figure 4.30. The *Horn Coordinate Frame* was then positioned a distance of 0.15m along the $-z$ -axis of the *Mount Frame*, which positioned the telescope such that the centre of the axis of rotation was

roughly half way between the primary and secondary mirrors, as was the case in the real experiment.

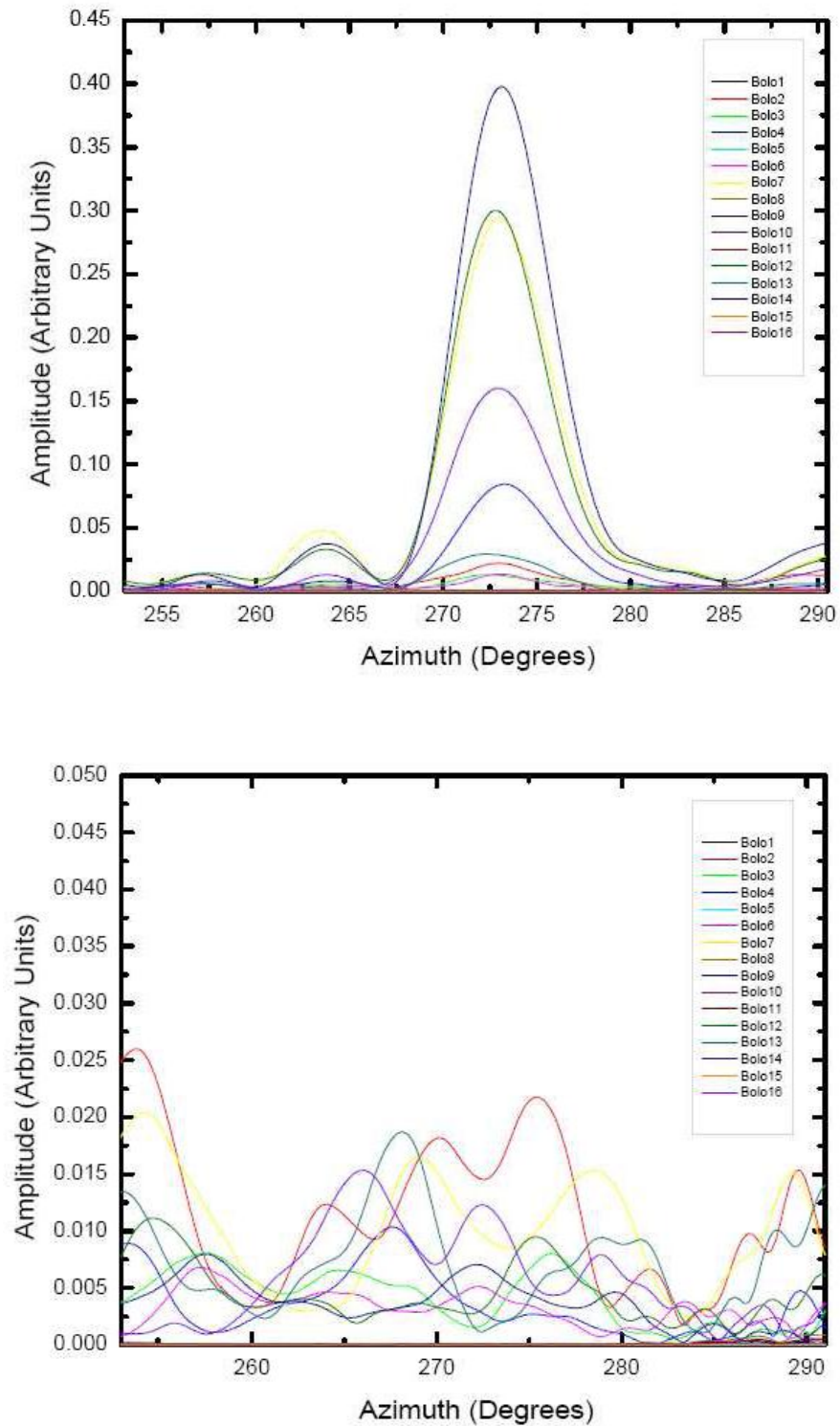


Figure 4.28 Beam pattern measurements taken in 2008 by MBI-4 as presented by Hyland (2008). The two figures represent measurements by two different back-to-back corrugated horn antennas.

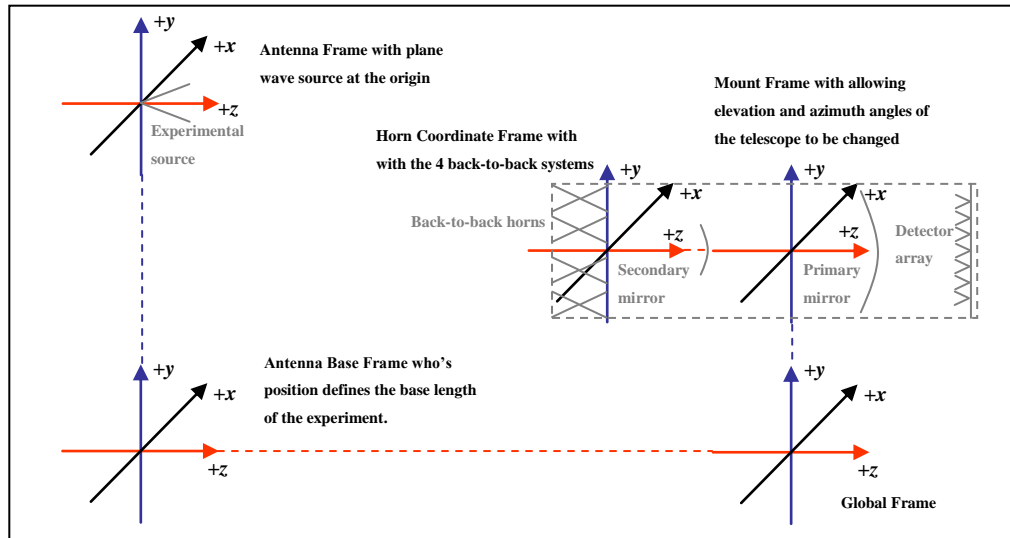


Figure 4.29 Frames used to define the experiment arrangement. The grey lines and text describe the position of MBI-4 within the frames (not to scale).

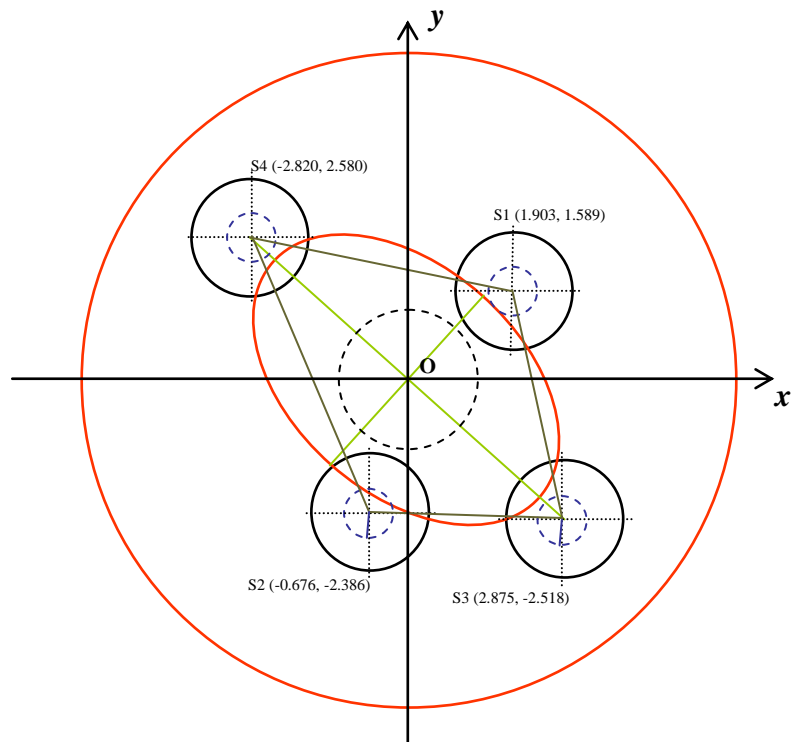


Figure 4.30 Schematic diagram showing the four inward-facing horn antennas and their coordinates as defined in the *Horn Coordinate Frame*. The primary mirror and elliptical aperture are also shown along with the secondary mirror. The view is from the detectors.

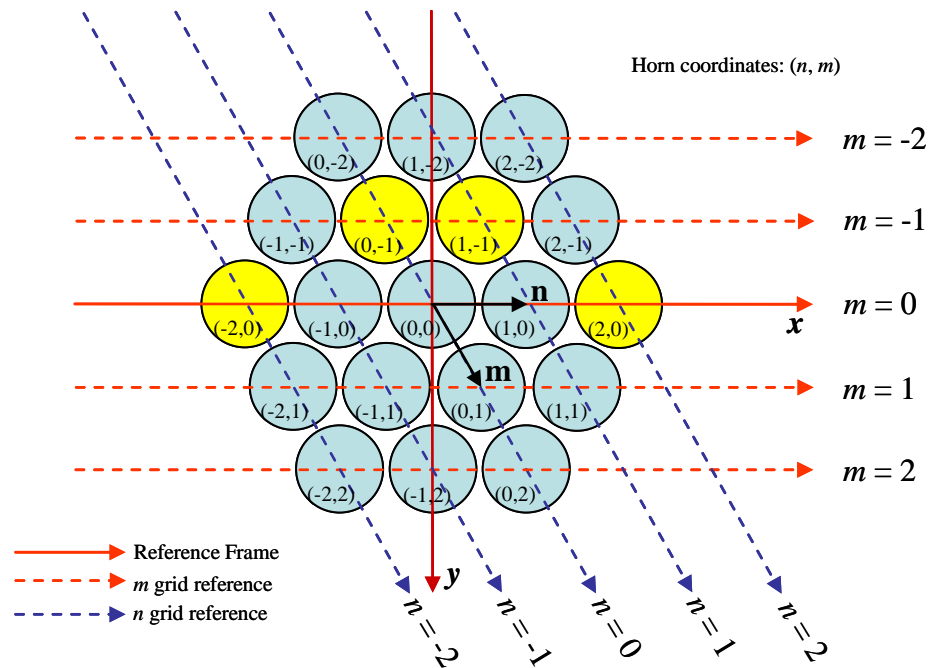


Figure 4.31 The *DetectorReferenceFrame* and grid system used to position and name the detector horn antennas. The x -axis of the frame coincides with the major axis of the elliptical aperture in the primary mirror. The highlighted horn antennas were used to measure the incoming beam.

To set up the source, the *Global Frame* was translated along its $-z$ -axis a distance of 12m to form the *Antenna Base Frame*. In a similar manner to the *Mount Frame*, the *Antenna Frame* was a transformed *Antenna Base Frame* to position it 12m above the ground and with rotation around the x - and y -axis of the *Antenna Base Frame* to allow different elevation and azimuth angles to be set. Since the source used in the measurements was located in the telescope far field the source used in this simulation was a plane wave. The back-to-back horn antenna models were generated as before with a 1.55mm radius mode-filtering cylindrical waveguide section between the two corrugated horn structures. While the source was polarised the back-to-back structures allowed all incident polarisations to propagate.

The detector array was aligned along the axis of the major axis of the elliptical aperture with the centre horn located at the optical centre of the overall system, that is, at the centre of the coordinate frame used to define the positions of

the back-to-back horn antennas above (*Horn Coordinate Frame*). This was also the centre point of both the primary and secondary mirrors. A selection of four horn antennas was used to detect the incoming signal as shown in Figure 4.31.

The system was arranged so that the elevation angles of both the telescope and the plane wave source were 45 degrees, that is, the telescope was looking directly at the source at an azimuth angle of 0 degrees. While keeping the elevation constant the telescope was scanned azimuthally from -15 to 15 degrees in steps of 3 degrees. This analysis was carried out twice, once with S1 (see Figure 4.30) open and all other horns closed, and once with S4 (Figure 4.30) open, again with all remaining horns closed. In each case the field from the plane wave source was passed through the back-to-back horn system by means of a mode matching technique described in section 4.4.7. The output field was then propagated through the beam combining system using physical optics before being coupled with each of 4 selected detector horns antennas outlined above.

The results of this analysis are shown in Figure 4.32 where the beam patterns obtained indicate that the cylindrical section between the back-to-back horns does filter out all higher order modes, as described in the previous section, showing none of the structure that was seen in the experimental measurements. To investigate if the beam passing through the primary aperture before reflection at the secondary could be eliminating the symmetry in the beam patterns this portion of the field was included in the analysis and the same calculations carried out again. However, the results were symmetric beam patterns as before with the instrument scanning across the external source. These can be seen in Figure 4.33.

In the previous section the effect of including the cylindrical waveguide section was investigated and it was found that for illumination by a plane wave propagating in a direction along the axis of the horn antenna the back-to-back structure with no cylindrical waveguide section appeared to be single-moded. However, as the instrument scanned across the source during the measurements the angle at which the plane wave illuminated these horns changed. To establish if this could be the cause of the asymmetry the cylindrical waveguide was removed and the analysis was repeated. As can be seen from Figure 4.34 this did produce asymmetric

beam patterns on the image plane, indicating that the back-to-back structures were no longer single-moded for illumination at off-axis angles.

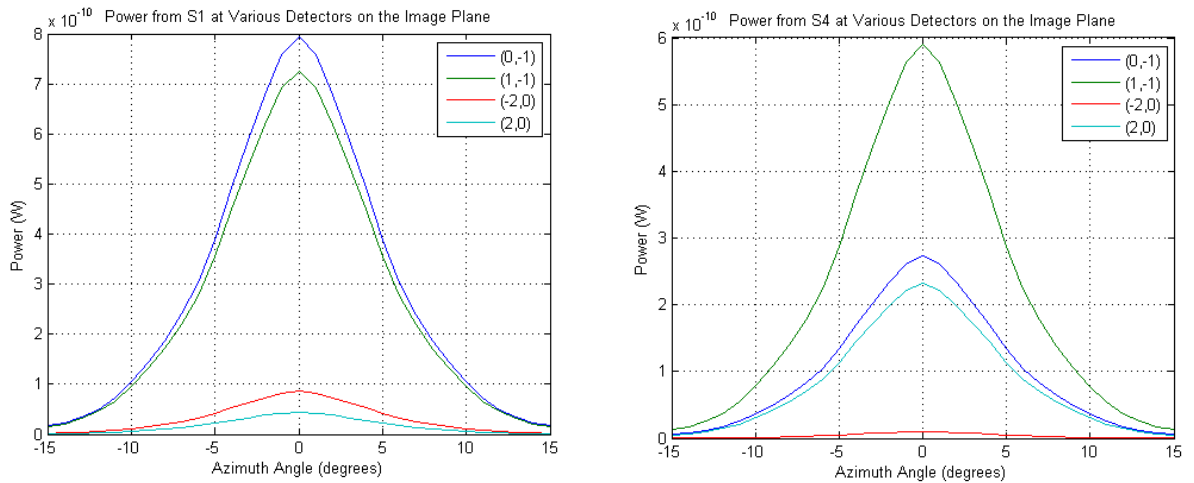


Figure 4.32 Power on the image plane from S1 (left) and S4 (right) with an extended circular waveguide section between the back-to-back horns.

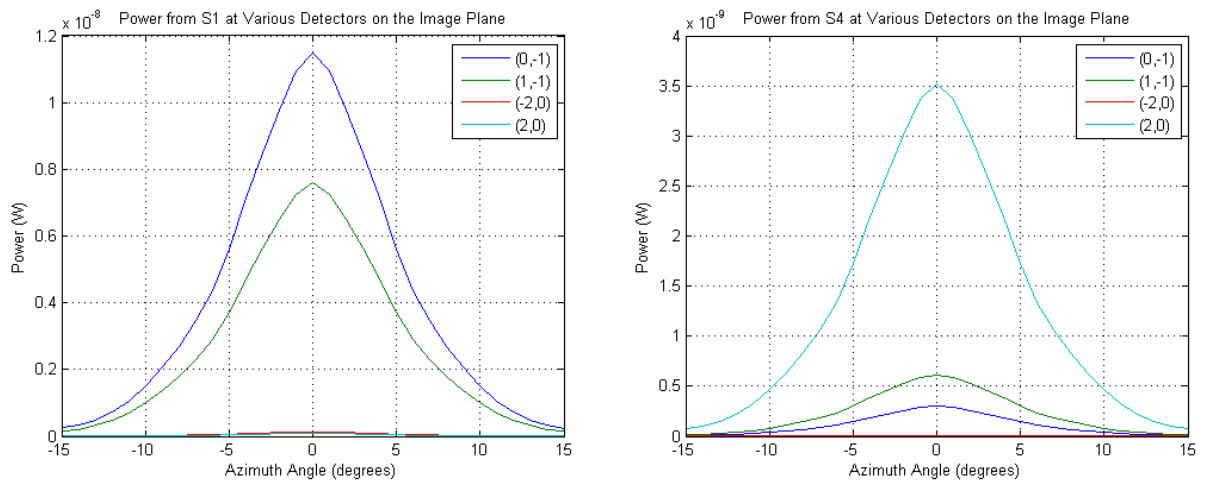


Figure 4.33 Power on the image plane from S1 (left) and S4 (right) with an extended circular waveguide section between the back-to-back horns. In this case the beam that passes through the primary hole before reflection from the secondary is also taken into account.

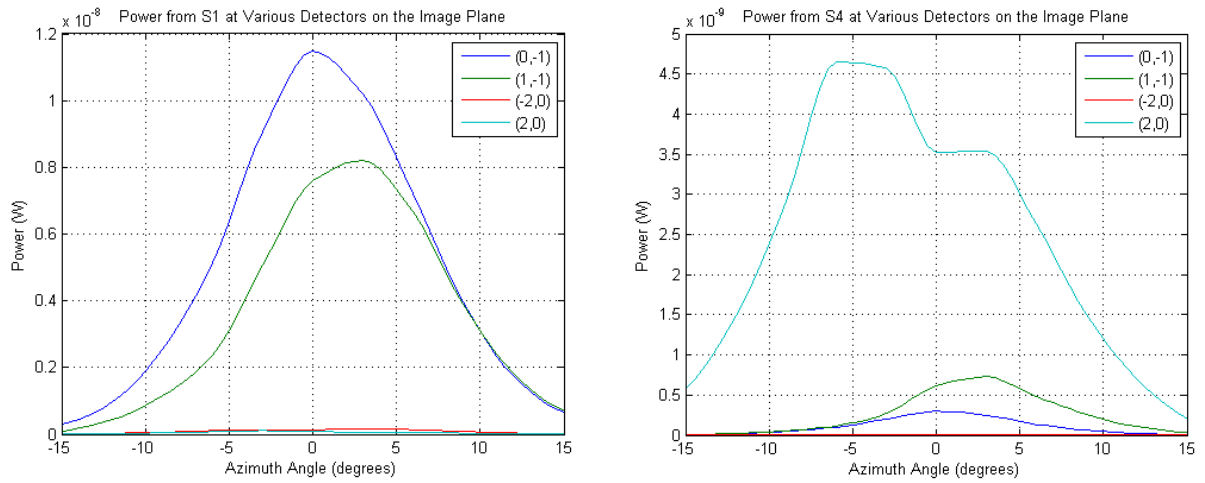


Figure 4.34 Power on the image plane from S1 (left) and S4 (right) with no circular waveguide section between the back-to-back horns. The beam that passes through the primary hole before reflection from the secondary is taken into account.

The asymmetry in the beam is due to the different phase relationship between the hybrid modes that the beam is composed of at different scanning angles. For example, the phase relationship between hybrid modes at -3 degrees is not the same as the phase relationship between the hybrid modes at +3 degrees. This is because the angle is with respect to the centre of rotation of the telescope and not the centre of the horn aperture, and therefore there are asymmetries present due to the layout of the instrument. From the analysis carried out the amplitude and phase of the hybrid modes was extracted and can be seen in Table 4.5.

Amplitude and Phase of the Hybrid Modes at Different Azimuth Angles						
Angle (deg)	Field	Mode 0	Mode 1	Mode 2	Mode 3	Mode 4
-6	Amp	0.000471	0.000101	0.000903	0.000846	0.000159
	Phase	-1.33976	0.191606	0.457431	-1.49784	-0.54169
-3	Amp	0.000367	9.4E-05	0.001264	0.000687	8.97E-05
	Phase	-0.75293	0.556948	0.82101	-0.93484	0.023588
0	Amp	2.53E-13	5.47E-05	0.001472	2.59E-13	2.79E-14
	Phase	0.393511	0.271196	0.534644	-0.07401	-1.41061
3	Amp	0.000367	1.69E-07	0.001268	0.000692	1.3E-05
	Phase	1.17901	-0.30228	-0.38864	0.997089	-1.18294
6	Amp	0.000471	3.35E-05	0.000908	0.00086	3.2E-05
	Phase	-0.59693	0.92945	1.200238	-0.75509	0.207667

Table 4.5 The amplitude and phase of the back-to-back corrugated horn antenna hybrid modes at different azimuth angles.

Each hybrid mode is composed of a combination of TE and TM waveguide modes. To find the exact composition of the field from each of the horns in terms of TE and TM waveguide modes, a Singular Value Decomposition (Björck, 1996) analysis was required. Singular Value Decomposition, or SVD, is based on a linear algebra theorem which states that an $m \times n$ matrix A can be written as the product of three matrices (Golub and Van Loan, 1996):

$$A = UVV^T \quad (4.30)$$

where U is an $m \times m$ orthogonal matrix, V is an $n \times n$ orthogonal matrix and W is an $m \times n$ rectangular matrix with real, non-negative diagonal elements $\sigma_1, \dots, \sigma_\rho$ (where σ_ρ is the minimum value of the matrix, that is all components except the first ρ diagonal elements are zero) representing what are known as the singular values. By convention the diagonal elements of W are arranged in decreasing order, that is,

$$\sigma_1 > \sigma_2 > \sigma_3 > \dots > \sigma_\rho \geq 0. \quad (4.31)$$

An important property of this SVD approach is that it explicitly constructs orthonormal bases for A .

The application of SVD to the back-to-back horn antennas (or any other quasi-optical system) requires the scattering matrix S describing the system. This is found by means of the mode-matching technique mentioned earlier. The relationship between input and output (TE and TM) modes is then described by the equation,

$$Sa = b \quad (4.32)$$

where S is the scattering matrix, a is the matrix of input mode coefficients and b is the matrix of output mode coefficients. If there are n waveguide modes being considered then S will be an $n \times n$ matrix, a will be a $n \times 1$ column matrix and therefore the resulting matrix b will also be a column matrix with n elements. Applying SVD to the S matrix produces three new matrices, U , W and V , such that,

$$S = UWV^T \quad (4.33)$$

where again W is the matrix containing the singular values of S along its diagonal, in decreasing order, and the following relations holds:

$$Sv_i = \sigma_i u_i \quad (4.34)$$

In Equation 4.34, v_i is the basis set for the input hybrid modes, u_i is the basis set for the output hybrid modes and σ_i are the singular values. The v_i and u_i vectors are the column vectors of v and u respectively corresponding to the non-zero singular values σ_i and are composed of a linear combination of TE and TM modes. It is the input modes described by the vectors v_i that are transformed to give the output modes described by u_i .

If there is some arbitrary field Ψ illuminating the back-to-back horn antenna then this must be coupled to each of the input modes, v_i , giving a coupling value α_i . We can now rewrite Equation 4.34 as,

$$\alpha_i S v_i = \alpha_i \sigma_i u_i \quad (4.35)$$

Since σ_i and u_i are known from the singular value decomposition of S and α_i can be obtained from the coupling calculation, the modes that appear at the output of the system can be found by $\alpha_i \sigma_i u_i$. It is important to remember that each input mode v_i and output mode u_i is made from a linear combination of TE and TM waveguide modes.

To analyse the hybrid modes for the MBI-4 back-to-back horn antennas the scattering matrix S describing the system was extracted from MODAL. Since we were interested in the modes that appeared at the output of the horn from illumination by a plane wave at the input it was the S_{12} matrix that was used, which describes the field obtained at port 1 from an input at port 2. This is consistent with

the description of the back-to-back horn antennas given in section 4.3.2. The SVD of this matrix was calculated producing U , W and V as described in Equation 4.33 and it was clear that only the first five singular values (σ_1 to σ_5), found from the diagonal matrix W , were significant with values of 1, 0.9993, 0.9993, 0.9942 and 0.9942 in decreasing order, as is the convention. The hybrid modes of the back-to-back horn that appeared at the output and which would then propagate through the optical system could be found by taking the first five columns of the U matrix. The elements of each column u_i provided information about the amplitude of each TE and TM mode present, the results of which can be seen in Table 4.6, where only the five remaining modes are shown. The power contained in all other modes is approximately zero.

Composition of the Hybridmodes at the Output of the MBI-4 Back-to-Back Horn Antenna									
Mode 0		Mode 1		Mode 2		Mode 3		Mode 4	
Mode	Power	Mode	Power	Mode	Power	Mode	Power	Mode	Power
TM ^c 01	0.0897	TE ^s 11	0.1503	TE ^c 11	0.1503	TE ^s 21	0.1136	TE ^c 21	0.1136
TM ^c 02	0.2240	TM ^s 11	0.0696	TM ^c 11	0.0696	TM ^s 21	0.0675	TM ^c 21	0.0675
TM ^c 03	0.0309	TE ^s 12	0.0369	TE ^c 12	0.0369	TE ^s 22	0.0453	TE ^c 22	0.0453
TM ^c 04	0.0016	TM ^s 12	0.0073	TM ^c 12	0.0073	TM ^s 22	0.0098	TM ^c 22	0.0098
		TE ^s 13	0.0017	TE ^c 13	0.0017	TE ^s 23	0.0025	TE ^c 23	0.0025

Table 4.6 The modal composition of the eigenmodes that propagate through the back-to-back corrugated horn antennas. The superscripts s and c represent the orthogonal sine and cosine modes.

In conclusion, the back-to-back horn structure produced a symmetric beam at the image plane when illuminated by a plane wave propagating parallel to the optical axis of the horn. This was the case both with and without the single-moded cylindrical waveguide section included in the analysis (this section was included in the model, however in reality a more complex structure is present between the horns). However, experimental measurements showed asymmetric beam patterns from each of the measured horn antennas. The experimental arrangement was then modelled taking into account scanning in the azimuth direction. Again, for the case with the cylindrical section included symmetric beams were obtained but without this section the asymmetry found in the experimental measurements was evident,

indicating that at off-axis angles the back-to-back horn antennas became multi-moded. These modes were analysed in terms of their amplitude and phase relative to the scanning angle and their composition in terms of TE and TM waveguide modes was examined by means of SVD.

From the results obtained here it appears as though the real MBI-4 back-to-back horn antennas are not single-moded and are therefore producing asymmetric beams on the image plane. Higher order modes may be removed by including a cylindrical section of appropriate dimensions between the horn structures.

4.4 Mode Scattering at Rectangular-Circular Junctions

In this section the use of scatter matrices in the analysis of horn antennas and waveguide discontinuities is discussed. Originally developed by Wexler (Wexler, 1967) and followed on by Masterman and Clarricoats (Masterman and Clarricoats, 1971), this method of analysis is based on the description of a propagating field within a waveguide taking discontinuities into account and therefore allows an extremely accurate analysis of the horn antenna to be performed.

The original SCATTER mode-matching program generates a matrix which describes the modal scattering at circular to circular transitions and this was later extended to include rectangular waveguide sections. As part of the work for this thesis the author examined the effect of scattering between modes at the junction created by a rectangular and a circular waveguide so in the future MODAL will also be able to do rectangular to rectangular scattering as well as rectangular to circular. It will then be possible to build modular structures containing various transitions and to model these structures accurately in terms of waveguide modes. Such a tool would be useful in modelling systems such as the back-to-back horn antennas in MBI-4 where rectangular waveguides feed the inward-facing corrugated conical horns by means of a circular waveguide (the previous section illustrated the impact this component can have on overall beam patterns). Also, the Safari instrument on

SPICA may also implement arrays of rectangular horns feeding spherical absorber-filled cavities.

In the following two sections we begin by looking at rectangular and then circular waveguide modes. We then examine the details of modal scattering at rectangular to circular waveguide discontinuities.

4.4.1 Rectangular Waveguide Modes

Rectangular waveguides were one of the earliest types of transmission lines used to transport microwave signals and a large variety of components such as couplers, isolators and attenuators remain widely available. While nowadays a lot of microwave circuitry is fabricated using planar transmission lines there is still a need for waveguides in many applications such as high-power and millimetre-wave systems.

The hollow rectangular waveguide has walls made from a conducting material and modes propagate by means of reflection from the internal structure. For this to occur the electric fields must be zero at the points of reflection, therefore giving an integer number of half-wavelengths between reflection points. Each possible number corresponds to a mode that satisfies the boundary conditions of the waveguide. A number of modes may propagate at once.

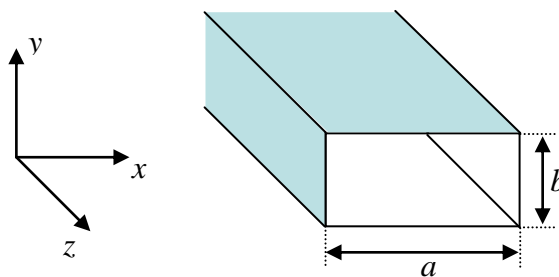


Figure 4.35 Rectangular waveguide where a is the longest side and b is the shortest. Propagation is along the z -direction.

The rectangular waveguide supports both Transverse Electric ($E_z = 0$) and Transverse Magnetic ($H_z = 0$) modes. We consider now a waveguide structure of inner dimensions a and b as in Figure 4.35 with the longest side, a , along the x -axis and b along the y -axis (Marcuvitz, 1993). We assume the guide is filled with a material of permittivity ϵ and permeability μ . The direction of propagation of radiation is along the positive z -axis. The TE modes are characterised by fields with $E_z = 0$, while H_z must satisfy the Cartesian form of the Helmholtz equation,

$$\left(\frac{\partial^2}{\partial x^2} + \frac{\partial^2}{\partial y^2} + k_c^2 \right) h_z(x, y) = 0 \quad (4.36)$$

where $H_z(x, y, z) = h_z(x, y)e^{j(\omega t - \beta z)}$ and $k_c^2 = k^2 - \beta^2$ is the cut-off wavenumber. By using a separation of variables technique and applying the boundary conditions on the electric field components tangential to the waveguide walls, that is,

$$e_x(x, y) = 0 \text{ at } y = 0, b \quad (4.37)$$

$$e_y(x, y) = 0 \text{ at } x = 0, a \quad (4.38)$$

a solution for H_z is found to be (Pozar, 1998)

$$H_{mn,z} = A_{mn} \begin{pmatrix} \cos(m\pi x/a) \cos(n\pi y/b) \\ \sin(m\pi x/a) \sin(n\pi y/b) \end{pmatrix} e^{j(\omega t - \beta z)}. \quad (4.39)$$

The transverse components are then given by,

$$E_{mn,x} = \frac{j\omega\mu n\pi}{k_c^2 b} A_{mn} \begin{pmatrix} \cos(k_x(x+a/2)) \sin(k_y(y+b/2)) \\ -\sin(k_x(x+a/2)) \cos(k_y(y+b/2)) \end{pmatrix} e^{j(\omega t - \beta z)} \quad (4.40)$$

$$E_{mn,y} = \frac{-j\omega\mu m\pi}{k_c^2 a} A_{mn} \begin{pmatrix} \sin(k_x(x+a/2)) \cos(k_y(y+b/2)) \\ -\cos(k_x(x+a/2)) \sin(k_y(y+b/2)) \end{pmatrix} e^{j(\omega t - \beta z)} \quad (4.41)$$

$$H_{mn,x} = \frac{-j\beta m\pi}{k_c^2 a} A_{mn} \begin{pmatrix} \sin(k_x(x+a/2))\cos(k_y(y+b/2)) \\ -\cos(k_x(x+a/2))\sin(k_y(y+b/2)) \end{pmatrix} e^{j(\omega t - \beta z)} \quad (4.42)$$

$$H_{mn,y} = \frac{j\beta n\pi}{k_c^2 b} A_{mn} \begin{pmatrix} \cos(k_x(x+a/2))\sin(k_y(y+b/2)) \\ -\sin(k_x(x+a/2))\cos(k_y(y+b/2)) \end{pmatrix} e^{j(\omega t - \beta z)} \quad (4.43)$$

where $k_x = m\pi/a$ and $k_y = n\pi/b$. The format presented here differs from most texts in that the expressions $k_x(x+a/2)$ and $k_y(y+b/2)$ within the cosine and sine functions assume that the guide is centred on the origin as opposed to the lower left corner of the guide being located there. Similar, for the TM modes we find that

$$E_{mn,z} = A_{mn} \begin{pmatrix} \sin(m\pi x/a)\sin(n\pi y/b) \\ \cos(m\pi x/a)\cos(n\pi y/b) \end{pmatrix} e^{j(\omega t - \beta z)} \quad (4.44)$$

and that the transverse field components are given by,

$$E_{mn,x} = \frac{-j\beta m\pi}{k_c^2 a} B_{mn} \begin{pmatrix} \cos(k_x(x+a/2))\sin(k_y(y+b/2)) \\ -\sin(k_x(x+a/2))\cos(k_y(y+b/2)) \end{pmatrix} e^{j(\omega t - \beta z)} \quad (4.45)$$

$$E_{mn,y} = \frac{-j\beta n\pi}{k_c^2 b} B_{mn} \begin{pmatrix} \sin(k_x(x+a/2))\cos(k_y(y+b/2)) \\ -\cos(k_x(x+a/2))\sin(k_y(y+b/2)) \end{pmatrix} e^{j(\omega t - \beta z)} \quad (4.46)$$

$$H_{mn,x} = \frac{j\omega\epsilon n\pi}{k_c^2 b} B_{mn} \begin{pmatrix} \sin(k_x(x+a/2))\cos(k_y(y+b/2)) \\ -\cos(k_x(x+a/2))\sin(k_y(y+b/2)) \end{pmatrix} e^{j(\omega t - \beta z)} \quad (4.47)$$

$$H_{mn,y} = \frac{-j\omega\epsilon m\pi}{k_c^2 a} B_{mn} \begin{pmatrix} \cos(k_x(x+a/2))\sin(k_y(y+b/2)) \\ -\sin(k_x(x+a/2))\cos(k_y(y+b/2)) \end{pmatrix} e^{j(\omega t - \beta z)}. \quad (4.48)$$

Each expression for the TE and TM modes shows two possible orthogonal polarisations. The propagation constant $\beta = \sqrt{k^2 - k_c^2} = \sqrt{k^2 - \left(\frac{m\pi}{a}\right)^2 - \left(\frac{n\pi}{b}\right)^2}$ is real, corresponding to a propagating mode, when $k > k_c = \sqrt{\left(\frac{m\pi}{a}\right)^2 + \left(\frac{n\pi}{b}\right)^2}$. Each mode therefore has a cutoff frequency given by

$$f_{c,mm} = \frac{k_c}{2\pi\sqrt{\mu\varepsilon}} = \frac{1}{2\pi\sqrt{\mu\varepsilon}} \sqrt{\left(\frac{m\pi}{a}\right)^2 + \left(\frac{n\pi}{b}\right)^2}. \quad (4.49)$$

At a given operating frequency f only those modes having $f_c < f$ will propagate. Modes where $f_c > f$ will have an imaginary propagation constant β , meaning that all field components will decay exponentially away from the source of excitation. Such modes are referred to as evanescent modes (Pozar, 1998). The A_{mn} and B_{mn} terms in the equations are arbitrary amplitude constants and m and n represent the number of sinusoids in the intensity of the field components E_y and E_x respectively over the cross section of the guide (Silver, 1997).

The wave impedance for both TE and TM modes can be expressed as

$$Z_{TE,TM} = \frac{E_x}{H_y} = \frac{-E_y}{H_x} = \frac{k\eta}{\beta} \quad (4.50)$$

where $\eta = \sqrt{\mu/\varepsilon}$ is the intrinsic impedance of the material filling the waveguide. The value of Z is real when β is real representing a propagating mode and imaginary when β is imaginary, representing an evanescent mode. The intensity patterns of some of the lower order TE and TM rectangular modes are shown in Figure 4.36.

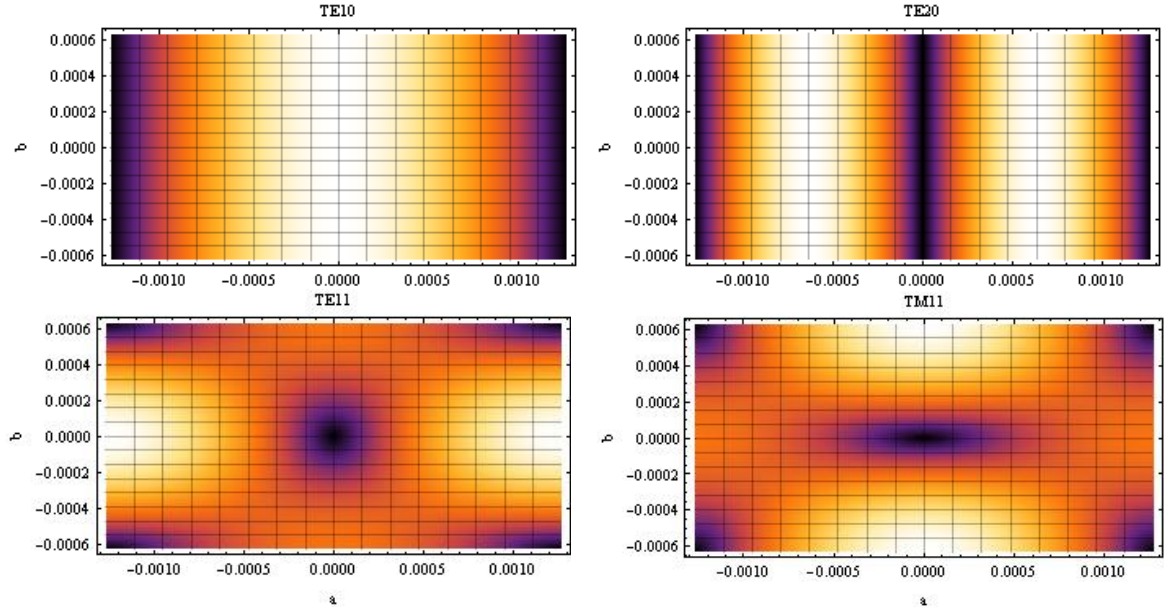


Figure 4.36 Intensity patterns of some lower order TE and TM rectangular waveguide modes. The waveguide used here was 2.54mm in the a -direction and 1.26mm in the b -direction.

In terms of normalisation of the propagating modes, it was convenient to set the total power over any transverse plane to be unity, that is,

$$\int_{-\frac{a}{2}}^{\frac{a}{2}} \int_{-\frac{b}{2}}^{\frac{b}{2}} \left(|e_x|^2 + |e_y|^2 \right) dydx = 1 \quad (4.51)$$

where $\mathbf{E}_{mn} = \mathbf{e}(x, y)e^{j(\alpha x - \beta z)}$ and $\mathbf{H}_{mn} = \mathbf{h}(x, y)e^{j(\alpha x - \beta z)}$, e_x is the x -component of $\mathbf{e}(x, y)$ and taking the waveguide to be centred on the origin $(x, y) = (0, 0)$. Using this normalisation convention, the following expressions for the TE mode amplitudes are found:

$$|A_{mn}|^2 = \frac{1}{\pi^2(\mu\omega)^2} \frac{4ab|k|^4}{(b^2m^2 + a^2n^2)} \quad \text{for } m > 0 \text{ and } n > 0 \quad (4.52)$$

$$|A_{0n}|^2 = \frac{1}{\pi^2(\mu\omega)^2} \frac{2ab|k|^4}{(a^2n^2)} \quad \text{for } m = 0 \text{ and } n > 0 \quad (4.53)$$

$$|A_{m0}|^2 = \frac{1}{\pi^2(\mu\omega)^2} \frac{2ab|k|^4}{(b^2m^2)} \quad \text{for } m > 0 \text{ and } n = 0 \quad (4.54)$$

and similarly for the TM mode amplitudes,

$$|B_{mn}|^2 = \frac{1}{\pi^2|\beta|^2} \frac{4ab|k|^4}{(b^2m^2 + a^2n^2)} \quad \text{for } m > 0 \text{ and } n > 0 \quad (4.55)$$

where the amplitudes of all other modes are zero. The fundamental mode in a waveguide of rectangular cross-section is the TE_{10} mode ($m = 1, n = 0$). By increasing the frequency of the radiation other modes are excited and propagate within the waveguide, at which point the waveguide is said to be over-moded (Pozar, 1998). The order in which the modes begin to propagate depends on the waveguide dimensions. For the usual case where $a = 2b$ the order of the mode cut-on is shown in Table 4.7 (Gleeson, 2004). In this case the TE_{01} and TE_{10} modes are degenerate as are other combinations of mode pairs listed. Although certain modes contain the same energy their field distributions are different as is evident from Equations 4.40 to 4.43 and 4.45 to 4.48 above.

Order of Mode Excitation	
1	TE_{01}, TE_{10}
2	TE_{20}
3	TE_{11}, TM_{11}
4	TE_{21}, TM_{21}
5	TE_{30}
6	TE_{31}, TM_{31}
7	TE_{40}
8	TE_{41}, TM_{41}

Table 4.7 Order of mode excitation with increasing frequency in a rectangular waveguide with $a=2b$.

4.4.2 Circular Waveguide Modes

A circular waveguide is a hollow metal tube of circular cross-section and as with the rectangular guide it supports the propagation of two distinct orthogonal sets of modes, the TE and TM waveguide modes. The number of real propagating modes depends on the inner diameter of the structure, $2a$, and again as with its rectangular counterpart an infinite number of evanescent modes may exist. The coordinate system for circular waveguides is typically defined such that the circular cross-section lies in the xy -plane with radiation propagating in the positive z -direction as shown in Figure 4.37.

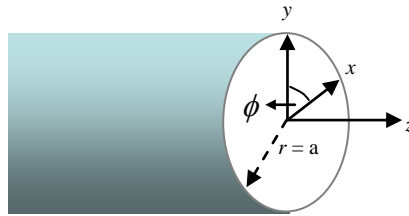


Figure 4.37 Schematic diagram of circular waveguide here...

The transverse field components are found from the longitudinal components as before. In the case of the TE modes these are derived from the expression for the H_z field component while for the TM modes the E_z component is used. Since a cylindrical geometry is involved, it is appropriate to employ cylindrical coordinates.

Transverse Electric (TE) Modes

Considering first the TE modes, the z -component of the H field is given by (Olver, *et. al.*, 1994),

$$H_{nl,z} = A_{nl} J_n(k_c r) \begin{pmatrix} \sin n\phi \\ \cos n\phi \end{pmatrix} e^{j(\alpha x - \beta z)} \quad (4.56)$$

where A_{nl} is an arbitrary constant and J_n is a Bessel function of the first kind and of order n . As can be seen from the expression, there are two possible orthogonal polarisations for each value of n and l , arising from the z -component being either

proportional to $\cos n\phi$ or $\sin n\phi$ (Murphy *et. al.*, 2001), hence the c and s notations seen in some texts. In incoherent systems with no polarisation discrimination both of these degenerate mode sets can propagate. From this expression for H_z the remaining transverse components are derived as (Pozar, 1998),

$$E_{nl,r} = \frac{-j\omega\mu n}{k_c^2 r} A_{nl} J_n(k_c r) \begin{pmatrix} \cos n\phi \\ -\sin n\phi \end{pmatrix} e^{j(\omega t - \beta z)} = C_{nl} \left[\frac{nJ_n(k_c r)}{k_c r} \right] \begin{pmatrix} \cos n\phi \\ -\sin n\phi \end{pmatrix} e^{j(\omega t - \beta z)} \quad (4.57)$$

$$E_{nl,\phi} = \frac{j\omega\mu}{k_c} A_{nl} J'_n(k_c r) \begin{pmatrix} \sin n\phi \\ \cos n\phi \end{pmatrix} e^{j(\omega t - \beta z)} = -C_{nl} J'_n(k_c r) \begin{pmatrix} \sin n\phi \\ \cos n\phi \end{pmatrix} e^{j(\omega t - \beta z)} \quad (4.58)$$

$$H_{nl,r} = \frac{-j\beta}{k_c} A_{nl} J'_n(k_c r) \begin{pmatrix} \sin n\phi \\ \cos n\phi \end{pmatrix} e^{j(\omega t - \beta z)} = \frac{C_{nl}}{Z_{TE}} J'_n(k_c r) \begin{pmatrix} \sin n\phi \\ \cos n\phi \end{pmatrix} e^{j(\omega t - \beta z)} \quad (4.59)$$

$$H_{nl,\phi} = \frac{-j\beta n}{k_c^2 r} A_{nl} J_n(k_c r) \begin{pmatrix} \cos n\phi \\ -\sin n\phi \end{pmatrix} e^{j(\omega t - \beta z)} = \frac{C_{nl}}{Z_{TE}} \left[\frac{nJ_n(k_c r)}{k_c r} \right] \begin{pmatrix} \cos n\phi \\ -\sin n\phi \end{pmatrix} e^{j(\omega t - \beta z)} \quad (4.60)$$

where $C_{nl} = -j\omega\mu A_{nl}/k_c$ and $J'_n(z) = dJ_n(z)/dz$ is the derivative of the Bessel function J_n with respect to its argument. The electric field along the surface of a perfect conductor must be zero and therefore $E_z = E_\phi = 0$ at $r = a$, where a is the radius of the waveguide, meaning that $J'_n(k_c a) = 0$ and hence the argument of the derivative of the Bessel function must be one of its roots. That is,

$$k_c a = \frac{2\pi a}{\lambda_c} = \omega_c \sqrt{\mu\epsilon} a = p'_{nl} \quad (4.61)$$

where p'_{nl} is the l^{th} root of the derivative of the n^{th} order Bessel function J_n , some values of which are given in Table 4.8. The cut-off frequency for any TE circular waveguide mode can then be calculated using $k_c = p'_{nl}/a$. Also, the propagation constant is given by

$$\beta = \sqrt{k^2 - k_c^2} = \sqrt{k^2 - \left(\frac{p'_{nl}}{a}\right)^2} \quad (4.62)$$

and the wave impedance by

$$Z_{TE,nl} = \frac{Z_0}{\sqrt{1 - \left(\frac{p'_{nl}\lambda_0}{2\pi a n_d}\right)^2}} = \frac{Z_0}{\sqrt{1 - \left(\frac{p'_{nl}}{\omega a \sqrt{\mu\varepsilon}}\right)^2}} \quad (4.63)$$

where $n_d = \sqrt{\mu\varepsilon}$ is the refractive index of the waveguide medium with ε being the dielectric constant and μ the relative permeability of the medium. $Z_0 = \sqrt{\mu/\varepsilon} = 1/\omega\varepsilon$ is the characteristic impedance of the waveguide medium.

For consistency with the rectangular modes the circular waveguide modes were normalised so the total power over any transverse plane was unity, as with the rectangular modes, so that

$$\int_0^{2\pi} \int_0^a \left(|e_{nl,r}|^2 + |e_{nl,\phi}|^2 \right) r \, dr d\phi = 1 \quad (4.64)$$

where $\mathbf{E}_{nl} = \mathbf{e}(r, \phi) e^{j(\alpha x - \beta z)}$ and $\mathbf{H}_{nl} = \mathbf{h}(r, \phi) e^{j(\alpha x - \beta z)}$ and, as before, taking the waveguide as centred on the origin ($r = 0$). An expression for C_{nl} can be found by carrying out the integration in Equation 4.64, giving

$$C_{nl} = \sqrt{\frac{2 - \delta_{n0}}{\pi a^2 \left(1 - (n/p'_{nl})^2\right) J_n^2(p'_{nl})}}. \quad (4.65)$$

The transverse components of the field given in Equations 4.57 to 4.60 excluding the exponential term can then be expressed as,

$$e_{nl,r} = \sqrt{\frac{2 - \delta_{n0}}{\pi\alpha^2(1 - (n/p'_{nl})^2)J_n^2(p'_{nl})}} \left[\frac{nJ_n(k_c r)}{k_c r} \right] \begin{pmatrix} \cos n\phi \\ -\sin n\phi \end{pmatrix} \quad (4.66)$$

$$e_{nl,\phi} = -\sqrt{\frac{2 - \delta_{n0}}{\pi\alpha^2(1 - (n/p'_{nl})^2)J_n^2(p'_{nl})}} J'_n(k_c r) \begin{pmatrix} \sin n\phi \\ \cos n\phi \end{pmatrix} \quad (4.67)$$

$$h_{nl,r} = \sqrt{\frac{2 - \delta_{n0}}{Z_{TE}^2 \pi\alpha^2(1 - (n/p'_{nl})^2)J_n^2(p'_{nl})}} J'_n(k_c r) \begin{pmatrix} \sin n\phi \\ \cos n\phi \end{pmatrix} \quad (4.68)$$

$$h_{nl,\phi} = \sqrt{\frac{2 - \delta_{n0}}{Z_{TE}^2 \pi\alpha^2(1 - (n/p'_{nl})^2)J_n^2(p'_{nl})}} \left[\frac{nJ_n(k_c r)}{k_c r} \right] \begin{pmatrix} \cos n\phi \\ -\sin n\phi \end{pmatrix} \quad (4.69)$$

Using the following relationship between cylindrical and rectangular coordinates,

$$\begin{bmatrix} \hat{r} \\ \hat{\phi} \\ \hat{z} \end{bmatrix} = \begin{bmatrix} \cos \phi & \sin \phi & 0 \\ -\sin \phi & \cos \phi & 0 \\ 0 & 0 & 1 \end{bmatrix} \begin{bmatrix} \hat{x} \\ \hat{y} \\ \hat{z} \end{bmatrix} \quad (4.70)$$

where the conversion matrix is orthogonal and therefore its inverse is simply its transpose, and the fact that the derivative of a Bessel function and the Bessel recursion relation are given by:

$$J'_n(z) = \frac{1}{2}(J_{n-1}(z) - J_{n+1}(z)) \quad (4.71)$$

$$J_{n+1}(z) = \frac{2n}{z} J_n(z) - J_{n-1}(z) \quad (4.72)$$

the x and y components of the electric and magnetic field are found as,

$$e_{nl,x} = \sqrt{\frac{2 - \delta_{n0}}{4\pi\alpha^2(1 - (n/p'_{nl})^2)J_n^2(p'_{nl})}} \left[J_{n-1}(k_c a) \begin{pmatrix} \cos(n-1)\phi \\ -\sin(n-1)\phi \end{pmatrix} + J_{n+1}(k_c a) \begin{pmatrix} \cos(n+1)\phi \\ -\sin(n+1)\phi \end{pmatrix} \right] \quad (4.73)$$

$$e_{nl,y} = \sqrt{\frac{2 - \delta_{n0}}{4\pi a^2 (1 - (n/p'_{nl})^2) J_n^2(p'_{nl})}} \left[J_{n-1}(k_c a) \begin{pmatrix} \sin(n-1)\phi \\ \cos(n-1)\phi \end{pmatrix} - J_{n+1}(k_c a) \begin{pmatrix} \sin(n+1)\phi \\ \cos(n+1)\phi \end{pmatrix} \right] \quad (4.74)$$

$$h_{nl,x} = \sqrt{\frac{2 - \delta_{n0}}{4Z_{TE}^2 \pi a^2 (1 - (n/p'_{nl})^2) J_n^2(p'_{nl})}} \left[J_{n-1}(k_c a) \begin{pmatrix} \sin(n-1)\phi \\ \cos(n-1)\phi \end{pmatrix} - J_{n+1}(k_c a) \begin{pmatrix} \sin(n+1)\phi \\ \cos(n+1)\phi \end{pmatrix} \right] \quad (4.75)$$

$$h_{nl,y} = \sqrt{\frac{2 - \delta_{n0}}{4Z_{TE}^2 \pi a^2 (1 - (n/p'_{nl})^2) J_n^2(p'_{nl})}} \left[J_{n-1}(k_c a) \begin{pmatrix} \cos(n-1)\phi \\ -\sin(n-1)\phi \end{pmatrix} - J_{n+1}(k_c a) \begin{pmatrix} \cos(n+1)\phi \\ -\sin(n+1)\phi \end{pmatrix} \right] \quad (4.76)$$

Values of the l^{th} Root of the Derivative of the n^{th} Order Bessel Function J_n						
p'_{nl}	$n=0$	$n=1$	$n=2$	$n=3$	$n=4$	$n=5$
$l=1$	3.83171	1.84118	3.0542	4.20119	5.3175	6.41557
$l=2$	7.01559	5.3314	6.7061	8.01524	9.2824	10.5198
$l=3$	10.1735	8.5363	9.9695	11.3459	12.6810	13.9871
$l=4$	13.3237	11.706	13.1704	14.5858	15.9641	17.3127
$l=5$	16.4706	14.8636	16.3475	17.7887	19.1960	20.5755
$l=6$	19.6159	18.0155	19.5129	20.9725	22.4010	23.8035
$l=7$	22.7601	21.1644	22.6716	24.1449	25.5890	27.0102
$l=8$	25.9037	24.3113	25.8260	27.3101	28.7670	30.2028
$l=9$	29.0468	27.4571	28.9770	30.4703	31.9380	33.3854
$l=10$	32.1897	30.6019	32.1273	33.6270	35.1030	36.5607

Table 4.8 p'_{nl} values where p'_{nl} is the l^{th} root of the derivative of the n^{th} order Bessel function J_n .

Plots of the intensity ($|e_r|^2 + |e_\phi|^2$) of some of the lower order TE circular waveguide modes are shown in Figure 4.38 for a single orthogonal polarisation. If both polarisations are present within the waveguide then the polarisation components should be added in quadrature.

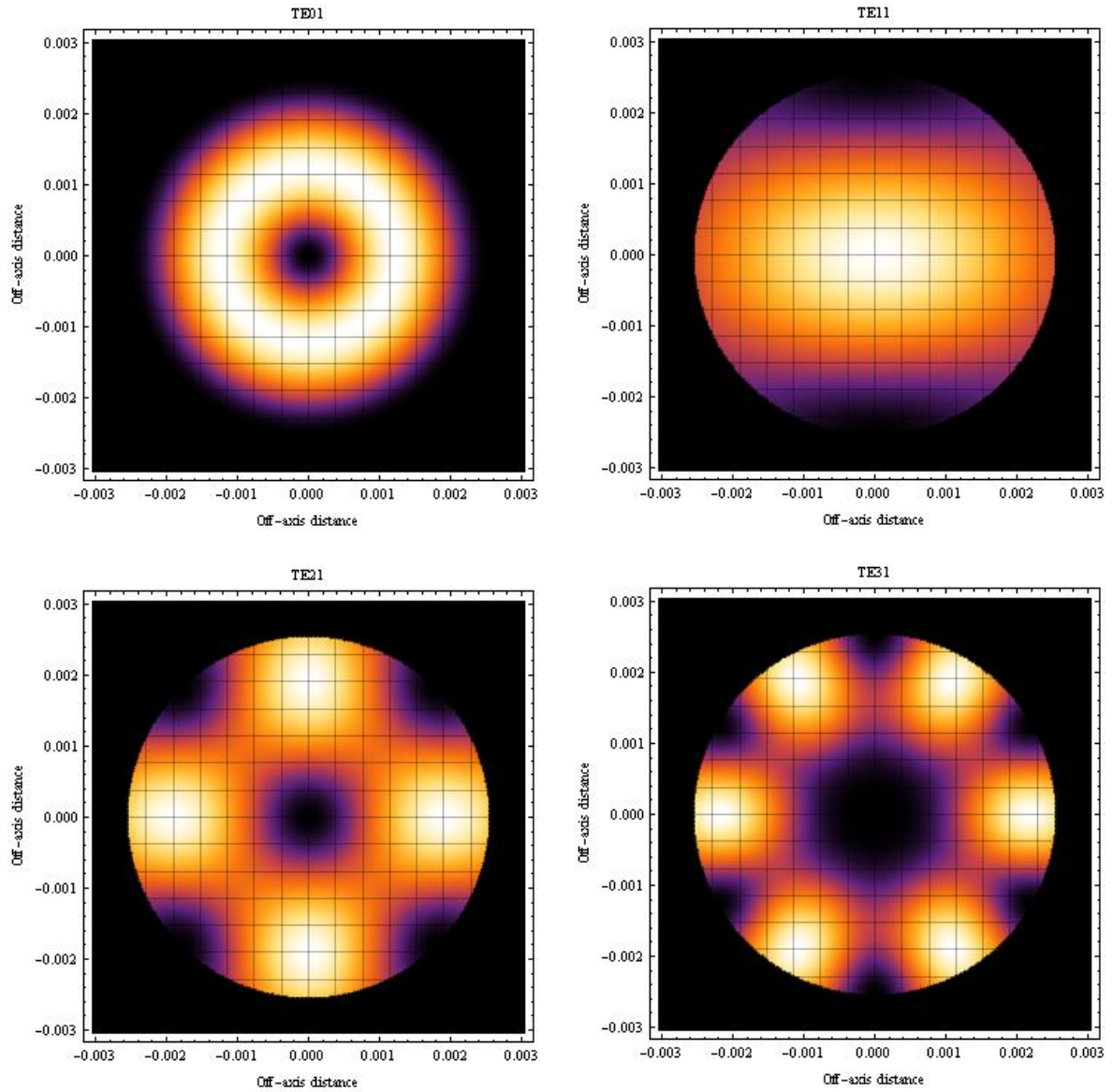


Figure 4.38 Plots of some lower order TE circular waveguide modes. The radius of the waveguide used was 2.54mm.

Transverse Magnetic (TM) Modes

For the TM modes of the circular waveguide we need to solve the wave equation for E_z , giving,

$$E_{nl,z} = B_{nl} J_n(k_c r) \begin{pmatrix} \cos n\phi \\ \sin n\phi \end{pmatrix} e^{j(\omega t - \beta z)}. \quad (4.77)$$

The transverse field components for both orthogonal polarisations can be derived from this and are given by (e.g. Gleeson, 2004),

$$E_{nl,r} = \frac{-j\beta}{k_c} B_{nl} J'_n(k_c r) \begin{pmatrix} \cos n\phi \\ \sin n\phi \end{pmatrix} e^{j(\omega t - \beta z)} = D_{nl} J'_n(k_c r) \begin{pmatrix} \cos n\phi \\ \sin n\phi \end{pmatrix} e^{j(\omega t - \beta z)} \quad (4.78)$$

$$E_{nl,\phi} = \frac{-j\beta n}{k_c^2 r} B_{nl} J_n(k_c r) \begin{pmatrix} -\sin n\phi \\ \cos n\phi \end{pmatrix} e^{j(\omega t - \beta z)} = D_{nl} \left[\frac{n J_n(k_c r)}{k_c r} \right] \begin{pmatrix} -\sin n\phi \\ \cos n\phi \end{pmatrix} e^{j(\omega t - \beta z)} \quad (4.79)$$

$$H_{nl,r} = \frac{j\omega\epsilon n}{k_c^2 r} B_{nl} J_n(k_c r) \begin{pmatrix} -\sin n\phi \\ \cos n\phi \end{pmatrix} e^{j(\omega t - \beta z)} = -\frac{D_{nl}}{Z_{TM}} \left[\frac{n J_n(k_c r)}{k_c r} \right] \begin{pmatrix} -\sin n\phi \\ \cos n\phi \end{pmatrix} e^{j(\omega t - \beta z)} \quad (4.80)$$

$$H_{nl,\phi} = \frac{-j\omega\mu}{k_c} A_{nl} J'_n(k_c r) \begin{pmatrix} \cos n\phi \\ \sin n\phi \end{pmatrix} e^{j(\omega t - \beta z)} = \frac{D_{nl}}{Z_{TM}} J'_n(k_c r) \begin{pmatrix} \cos n\phi \\ \sin n\phi \end{pmatrix} e^{j(\omega t - \beta z)} \quad (4.81)$$

where $D_{nl} = -j\beta B_{nl}/k_c$. As before the electric field along the surface of the conductor must be zero and therefore the boundary condition $E_z = E_\phi = 0$ at $r = a$ holds, so that $J_n(k_c a) = 0$ and the argument of the Bessel function must be one of its roots. That is,

$$k_c a = \frac{2\pi a}{\lambda_c} = \omega_c \sqrt{\mu\epsilon} a = p_{nl} \quad (4.82)$$

where p_{nl} is the l th root of the n th order Bessel function J_n , some values of which are given in Table 4.9. The cut-off frequency for any TM circular waveguide mode is then calculated in a similar way to the TE modes using $k_c = p_{nl}/a$. Also, the propagation constant is given by

$$\beta = \sqrt{k^2 - k_c^2} = \sqrt{k^2 - \left(\frac{p_{nl}}{a}\right)^2} \quad (4.83)$$

and the wave impedance by

$$Z_{TM,nl} = Z_0 \sqrt{1 - \left(\frac{P_{nl} \lambda_0}{2\pi a n_d} \right)^2} = Z_0 \sqrt{1 - \left(\frac{P_{nl}}{\omega a \sqrt{\mu \epsilon}} \right)^2} \quad (4.84)$$

where the variables have the same definitions as before.

The TM modes were normalised in the same as the TE circular modes using Equation 4.64 giving an expression for D_{nl} as,

$$D_{nl} = \sqrt{\frac{2 - \delta_{n0}}{\pi a^2 J_{n+1}^2(p_{nl})}} \quad (4.85)$$

and therefore we can write expressions for the transverse components of the electric and magnetic fields as,

$$e_{nl,r} = \sqrt{\frac{2 - \delta_{n0}}{\pi a^2 J_{n+1}^2(p_{nl})}} J'_n(k_c r) \begin{pmatrix} \cos n\phi \\ \sin n\phi \end{pmatrix} \quad (4.86)$$

$$e_{nl,\phi} = \sqrt{\frac{2 - \delta_{n0}}{\pi a^2 J_{n+1}^2(p_{nl})}} \left[\frac{n J_n(k_c r)}{k_c r} \right] \begin{pmatrix} -\sin n\phi \\ \cos n\phi \end{pmatrix} \quad (4.87)$$

$$h_{nl,r} = -\sqrt{\frac{2 - \delta_{n0}}{Z_{TM}^2 \pi a^2 J_{n+1}^2(p_{nl})}} \left[\frac{n J_n(k_c r)}{k_c r} \right] \begin{pmatrix} -\sin n\phi \\ \cos n\phi \end{pmatrix} \quad (4.88)$$

$$h_{nl,\phi} = \sqrt{\frac{2 - \delta_{n0}}{Z_{TM}^2 \pi a^2 J_{n+1}^2(p_{nl})}} J'_n(k_c r) \begin{pmatrix} \cos n\phi \\ \sin n\phi \end{pmatrix} \quad (4.89)$$

where $\mathbf{E}_{nl} = \mathbf{e}(r, \phi) e^{j(\alpha x - \beta z)}$ and $\mathbf{H}_{nl} = \mathbf{h}(r, \phi) e^{j(\alpha x - \beta z)}$. Using Equation 4.70 and Equations 4.86 to 4.89 the x and y components of the electric and magnetic fields are found to be,

$$e_{nl,x} = \sqrt{\frac{2 - \delta_{n0}}{4\pi\alpha^2 J_{n+1}^2(p_{nl})}} \left[J_{n-1}(k_c a) \begin{pmatrix} \cos(n-1)\phi \\ -\sin(n-1)\phi \end{pmatrix} - J_{n+1}(k_c a) \begin{pmatrix} \cos(n+1)\phi \\ -\sin(n+1)\phi \end{pmatrix} \right] \quad (4.90)$$

$$e_{nl,y} = \sqrt{\frac{2 - \delta_{n0}}{4\pi\alpha^2 J_{n+1}^2(p_{nl})}} \left[J_{n-1}(k_c a) \begin{pmatrix} \sin(n-1)\phi \\ \cos(n-1)\phi \end{pmatrix} + J_{n+1}(k_c a) \begin{pmatrix} \sin(n+1)\phi \\ \cos(n+1)\phi \end{pmatrix} \right] \quad (4.91)$$

$$h_{nl,x} = \sqrt{\frac{2 - \delta_{n0}}{4Z_{TM}^2 \pi\alpha^2 J_{n+1}^2(p_{nl})}} \left[J_{n-1}(k_c a) \begin{pmatrix} \sin(n-1)\phi \\ \cos(n-1)\phi \end{pmatrix} + J_{n+1}(k_c a) \begin{pmatrix} \sin(n+1)\phi \\ \cos(n+1)\phi \end{pmatrix} \right] \quad (4.92)$$

$$h_{nl,y} = \sqrt{\frac{2 - \delta_{n0}}{4Z_{TM}^2 \pi\alpha^2 J_{n+1}^2(p_{nl})}} \left[J_{n-1}(k_c a) \begin{pmatrix} \cos(n-1)\phi \\ -\sin(n-1)\phi \end{pmatrix} - J_{n+1}(k_c a) \begin{pmatrix} \cos(n+1)\phi \\ -\sin(n+1)\phi \end{pmatrix} \right] \quad (4.93)$$

Values of the l^{th} Root of the n^{th} Order Bessel Function J_n						
p_{nl}	$n=0$	$n=1$	$n=2$	$n=3$	$n=4$	$n=5$
$l=1$	2.40483	3.83171	5.13562	6.3801	7.5883	8.77148
$l=2$	5.52008	7.01559	8.41725	9.76102	11.0647	12.3386
$l=3$	8.65373	10.1735	11.6198	13.0152	14.3725	15.7002
$l=4$	11.7915	13.3237	14.7960	16.2235	17.6160	18.9801
$l=5$	14.9309	16.4706	17.9598	19.4094	20.8270	22.2178
$l=6$	18.0711	19.6159	21.1170	22.5827	24.0190	25.4303
$l=7$	21.2116	22.7601	24.2701	25.7482	27.1990	28.6266
$l=8$	24.3525	25.9037	27.4206	28.9084	30.3710	31.8117
$l=9$	27.4935	29.0468	30.5692	32.0640	33.5370	34.9887
$l=10$	30.6346	32.1897	33.7165	35.2187	36.6990	38.1598

Table 4.9 p_{nl} values where p_{nl} is the l^{th} root of the n^{th} order Bessel function J_n .

Plots of the intensity ($|e_r|^2 + |e_\phi|^2$) of some of the lower order TM circular waveguide modes are shown in Figure 4.39 for a single orthogonal polarisation.

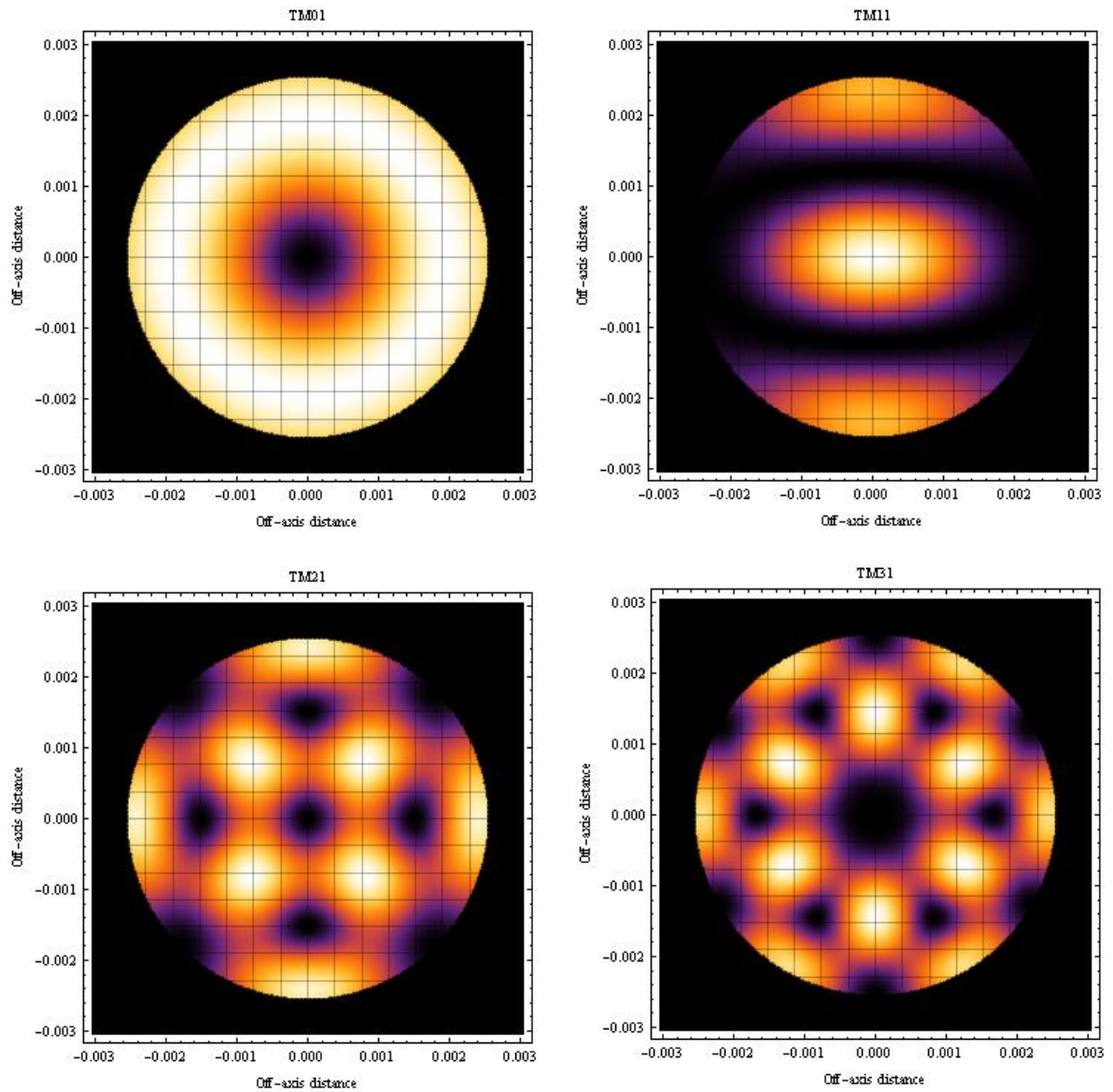


Figure 4.39 Plots of some lower order TM circular waveguide modes. The radius of the waveguide used was 2.54mm.

Having considered both the transverse electric and transverse magnetic modes of the circular waveguide the values of both p'_{nl} and p_{nl} can be examined and therefore the order of excitation of the modes as the operating frequency increases deduced. The results of this can be seen in Table 4.10. It is clear from the data that some modes are degenerate, however, as with the rectangular modes, the field distributions of these modes is quite different.

Mode Cut-On Values	
Mode	$k_c a$
TE ₁₁	1.8412
TM ₀₁	2.4048
TE ₂₁	3.0542
TM ₁₁	3.8317
TE ₀₁	3.8317
TE ₃₁	4.2012
TM ₂₁	5.1356
TE ₄₁	5.3176
TE ₁₂	5.3314
TM ₀₂	5.5201

Table 4.10 Circular waveguide mode cut-on values.

4.4.3 Scattering at a Rectangular-Circular Discontinuity

To calculate the field at a rectangular-circular (or any) discontinuity a mode-matching technique is applied. A comprehensive analysis of smooth-walled and corrugated horn antennas has been carried out at NUIM using this technique and has resulted in the SCATTER software being developed (Colgan, 2001; Gleeson, 2004) as described in Chapter 2. While a complete description of the technique is provided by Colgan (2001) and Gleeson (2004), an outline of the theory is given here to understand the principles involved.

To analyse any discontinuity within a waveguide or horn antenna structure (which can be considered as a series of cascaded uniform cylindrical waveguide sections) the transmission and reflection coefficients must be known for that discontinuity. These arise from the fact that the power from the individual incident modes is scattered between reflected modes in the first waveguide section and transmitted modes in the second waveguide section. In the mode-matching technique, the total transverse field in the two waveguides at the plane of the junction is matched so that the total complex power is conserved and Maxwell's equations are satisfied with the usual boundary conditions applying to the fields at

the conducting walls (Gleeson, 2004). This is assumed at each junction within the waveguide or horn antenna with the output field from one section becoming the input for the next. The relationship between the input and output mode coefficients for the junctions between waveguide sections can be expressed in terms of scattering matrix elements, which are calculated by means of power coupling integrals. Also, a diagonal matrix is used to describe mode propagation (since no power is scattered between modes) in the length of waveguide each side of a junction with the elements representing the phase evolution of the modes ($\exp(-j\beta z)$). In general, a different number of modes can be chosen to represent the field on both sides of the discontinuity.

When the scattering matrix for each junction is calculated they are cascaded together as described in section 4.3.1 so that an overall scattering matrix for the waveguide discontinuity or horn antenna structure is obtained. The scattering matrix operates on the modes at the input of the structure and provides mode amplitudes of the field at the output. For power to be conserved and the fields to match at any particular junction then the following relationships must hold (Olver *et al.*, 1994):

$$[P][[A]+[B]] = [Q][[D]+[C]] \quad (4.94)$$

$$[R][[A]-[B]] = [P]^T [[D]-[C]] \quad (4.95)$$

where A and B are the transmitted and reflected coefficients on the input side and C and D are the transmitted and reflected coefficients on the output side. The matrices $[P]$, $[Q]$ and $[R]$ represent coupling between modes at the junction. If we consider the case of a field propagating from left to right through a waveguide or horn antenna discontinuity then the $[P]$ matrix is a rectangular matrix whose elements are integrals representing mutual coupling between modes on the left and right side of the junction and are given by,

$$P_{n'n} = \int_{S_L} \mathbf{e}_{nL} \times \mathbf{h}_{n'R}^* \cdot d\mathbf{S} \quad (4.96)$$

where n is the mode on the left of the junction and n' is the mode on the right. Also, S_L represents the cross-section surface of the junction on the left-hand side (if this surface is the smaller of the two). The $[Q]$ and $[R]$ matrices represent self-coupling between modes on the right and left of the junction respectively and are given by,

$$Q_{n'n'} = \left(\int_{S_R} \mathbf{e}_{n'R} \times \mathbf{h}_{n'R}^* \cdot d\mathbf{S} \right) \delta_{n'n'} \quad (4.97)$$

and

$$R_{n'n'} = \left(\int_{S_R} \mathbf{e}_{n'R} \times \mathbf{h}_{n'R}^* \cdot d\mathbf{S} \right) \delta_{n'n'} \quad (4.98)$$

All three expressions for the coupled power involve an integral of the form,

$$\int_S \mathbf{e} \times \mathbf{h}^* \cdot d\mathbf{S} = \int_S (E_x H_y^* - E_y H_x^*) dS \quad (4.99)$$

for fields whose components are represented in Cartesian form. $\mathbf{e} \times \mathbf{h}^*$ is the Poynting vector which gives the direction and magnitude of the energy flow density at any point in the waveguide. For both mutual and self-coupling all possible forms of scattering are considered, that is, TE to TE, TE to TM, TM to TE and TM to TM. In SCATTER, the overall form of the matrix describing scattering between modes has the form (Colgan, 2001),

$$P = \begin{bmatrix} P_{TE-TE} & P_{TE-TM} \\ P_{TM-TE} & P_{TM-TM} \end{bmatrix}. \quad (4.100)$$

The elements of a scattering matrix (as in Equation 4.18) for a discontinuity within a waveguide as derived from the power coupling matrices are given by (Olver *et al.*, 1994),

$$[S_{11}] = \left[[R^*] + [P]^+ [Q]^{-1} [P] \right]^{-1} \left[[R^*] - [P]^+ [Q]^{-1} [P] \right] \quad (4.101)$$

$$[S_{12}] = 2 \left[[R^*] + [P]^+ [Q]^{-1} [P] \right]^{-1} [P]^+ \quad (4.102)$$

$$[S_{21}] = 2 \left[[Q] + [P] [R^*]^{-1} [P]^+ \right]^{-1} [P] \quad (4.103)$$

$$[S_{22}] = - \left[\left[[Q] + [P] [R^*]^{-1} [P]^+ \right]^{-1} \left[[Q] - [P] [R^*]^{-1} [P]^+ \right] \right] \quad (4.104)$$

where $[P]^+ = [P^*]^T$ represents the complex conjugate transpose of the matrix P .

In the case of scattering at the junction between a rectangular and circular waveguide it is convenient to use the Cartesian components of both the rectangular modes propagating in the left rectangular waveguide and the circular waveguide modes propagating within the circular waveguide on the right. The equations for these components are given in sections 4.4.5 and 4.4.6 respectively and the elements of the $[P]$, $[Q]$ and $[R]$ matrices are found using Equations 4.96 to 4.98. In this case the mutual coupling between modes on the left of the junctions and those on the right involves coupling rectangular modes with circular modes, however, the same procedure as outlined above is followed.

Transverse Electric (TE) Modes Considered at Discontinuity									
Rectangular Modes on Left of Discontinuity									
m, n	0, 0	1, 0	2, 0	0, 1	1, 1	2, 1	0, 2	1, 2	2, 2
Circular Modes on Right of Discontinuity									
n, l	0, 0	1, 0	2, 0	0, 1	1, 1	2, 1	0, 2	1, 2	2, 2
Transverse Magnetic (TM) Modes Considered at Discontinuity									
Rectangular Modes on Left of Discontinuity									
m, n	0, 0	1, 0	2, 0	0, 1	1, 1	2, 1	0, 2	1, 2	2, 2
Circular Modes on Right of Discontinuity									
n, l	0, 0	1, 0	2, 0	0, 1	1, 1	2, 1	0, 2	1, 2	2, 2

Table 4.11 circular waveguide mode cut-on values here.....

As an example a 10mm long rectangular waveguide with a width $a=2.54\text{mm}$ and a height $b=1.26\text{mm}$ was placed in contact with a circular waveguide of the same

length with a radius of $r=2.5\text{mm}$. It was assumed that both waveguides were centred on the origin. The frequency of the radiation was 150GHz and 18 modes (9 TE and 9 TM) were considered in each of the waveguides as shown in Table 4.11. The power coupling calculations were carried out by means of the integrals above where the cross-sectional area over which the integration was carried out was that of the rectangular waveguide, since this was the smaller of the two and its field did not exist outside of this. From the resulting matrices the elements of the overall scattering matrix for the system were calculated using Equations 4.101 to 4.104. Figure 4.40 shows a cut through the resulting aperture field calculated using the mode-matching technique described above and also that calculated using CST for the same system. While the mode-matching technique shows the overall structure of the field it does not have the same width as the CST model. This is most likely due to the number of modes being used in the mode-matching method, since the higher order modes will ‘fill in’ the field at the edges. (The calculations here are not natural ones for the commercial software packages – in CST, the volume containing the structure is divided into mesh cells and the electromagnetic simulation is carried using a finite integral technique, as outlined in Chapter 2). An overlap integral showed a 93% power coupling between the beam patterns.

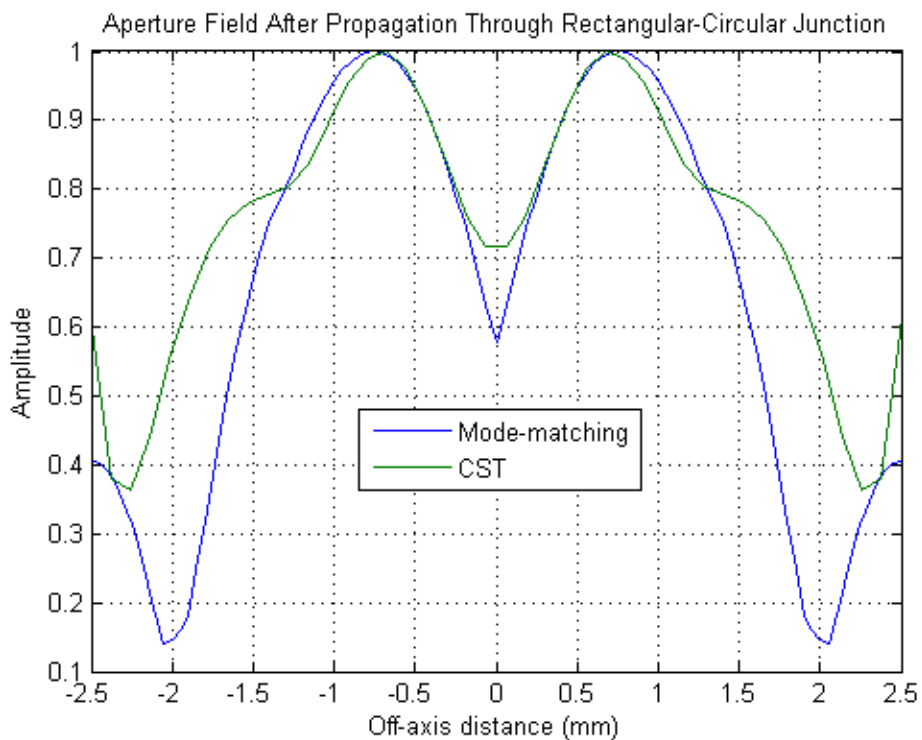


Figure 4.40 Field amplitude at the circular waveguide aperture after propagation through the rectangular waveguide and rectangular-circular discontinuity.

4.5 Beam Distortion in Closely Packed Waveguide Arrays

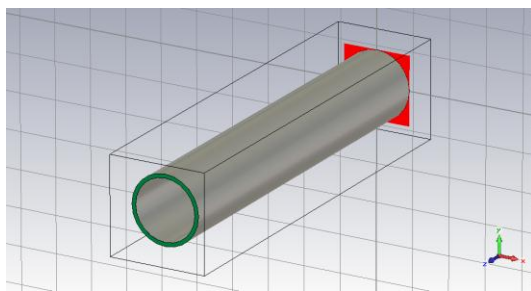
Most new CMB experiments have aspirations of measuring the polarisation (and in particular the B-modes) as well as the temperature anisotropies of the background radiation, something that requires an extremely high level of sensitivity. To achieve this sensitivity the instrument designers are implementing more and more detectors in compact arrays on the focal plane. Depending on the requirements, these detectors vary in their construction. In the following two sections we consider both cylindrical and rectangular waveguides, which may in theory be used to feed radiation onto bolometric detectors, arranged in a variety of ways. In each case the affect of the presence of the neighbouring waveguides on the beam patterns is examined. This analysis is a first approximation in which the waveguides are considered as open-ended hollow cylindrical and rectangular sections. We start by looking at the cylindrical case.

4.5.1 Circular Waveguide Arrays

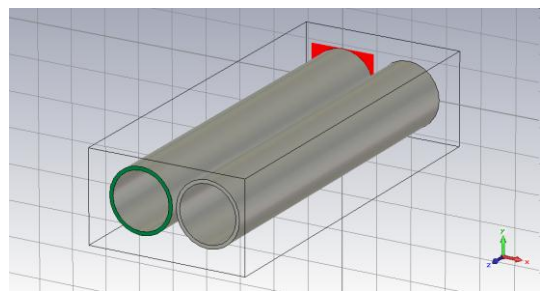
To begin this analysis circular waveguide sections were placed in five different array configurations using CST as shown in Figure 4.41. There are two horizontal configurations and two vertical configurations, along with a single waveguide. The purpose of this was to see if compact arrays of circular waveguides had any effect on individual beam patterns. Each waveguide had an inside radius of 0.8mm and a wall thickness of 0.1mm. They were separated by 0.1mm. The length of each waveguide was 10mm, and the operating frequency was set to 100GHz. It was assumed that the material from which the waveguide wall was constructed was a perfect electrical conductor and that the volume inside the guide was a vacuum.

For each array a single TE_{11} mode was excited at the back of just one circular waveguide, which can be seen as a red area behind that particular guide in Figure 4.41. The field at the aperture was then calculated, taking into account the other waveguide structures in the vicinity. Figure 4.42 shows an x and y -cut of the resulting field magnitudes at the waveguide aperture for the horizontal

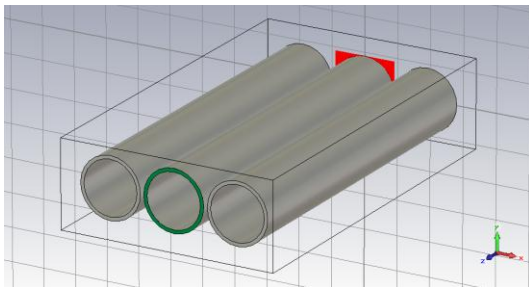
configurations. The far field patterns are also shown. In the case of the vertical configurations, the same results, aperture and far field patterns, are shown in Figure 4.43. As can be seen from the graphs the effect of having other waveguides in the vicinity is small, although visible in the far field pattern. Also, the ringing in the beam is significantly higher in the far field at $\phi = 90^\circ$ due to the severe truncation of the beam in the y -direction by the wall of the waveguide.



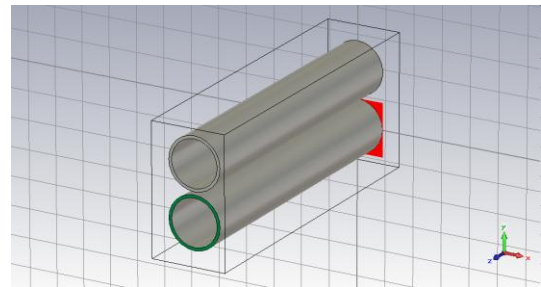
1WG



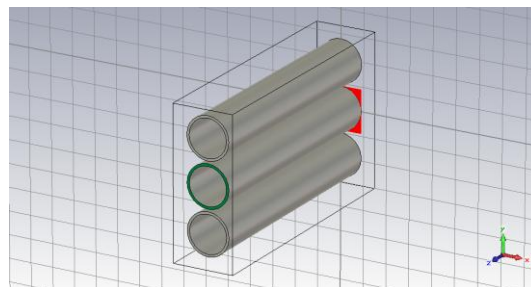
2WG-H



3WG-H



2WG-V



3WG-V

Figure 4.41 Circular waveguide array configurations analysed using CST.

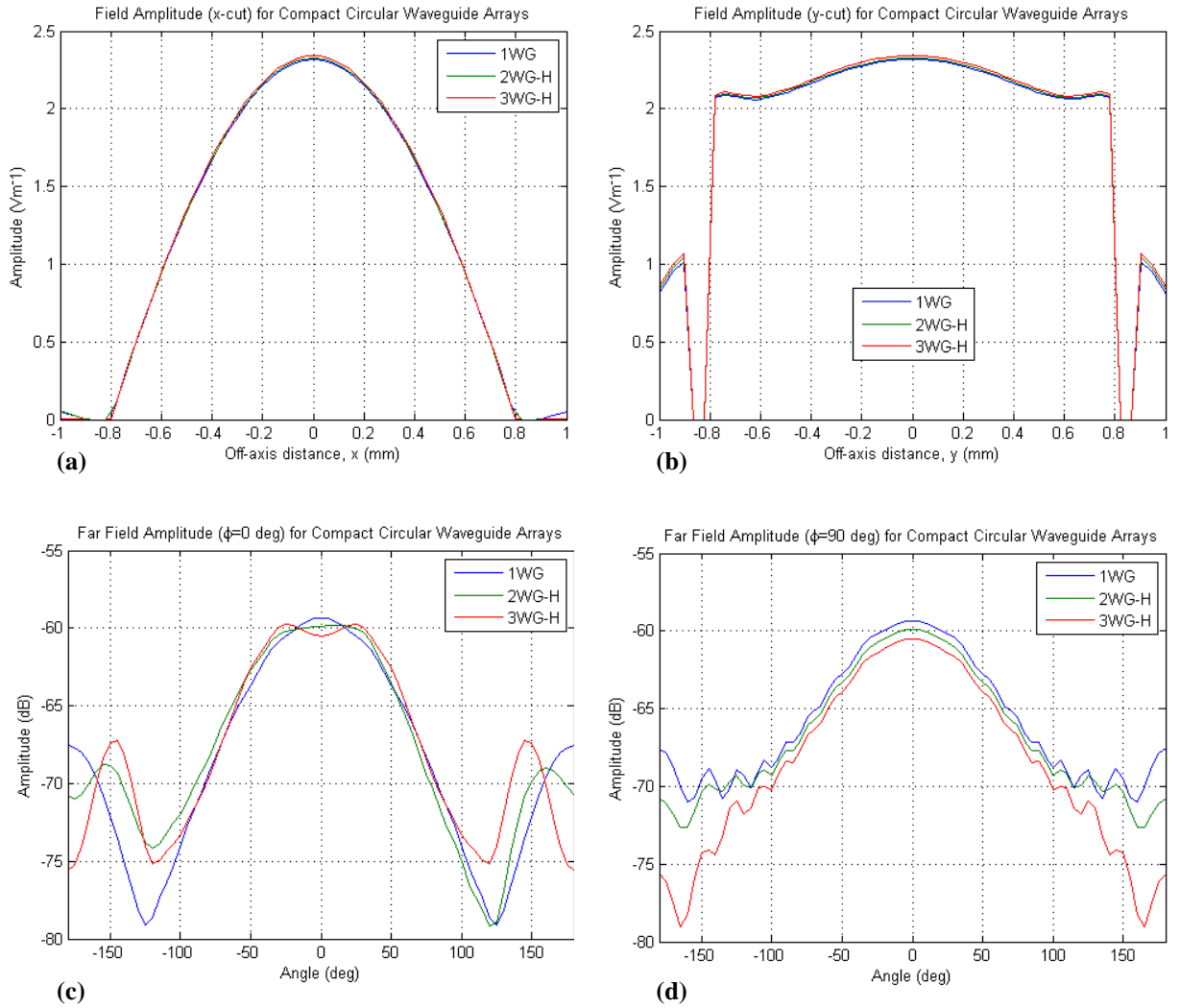


Figure 4.42 (a) Aperture field x-cut, (b) Aperture field y-cut, (c) Far field $\phi = 0^\circ$, and (d) Far field $\phi = 90^\circ$ for the circular waveguide horizontal configurations (Figure 4.41).

To further investigate the effect of close-packed arrays, a reflection coefficient was calculated, again for each configuration with the same single waveguide excited as above. The results of this are shown in Figure 4.44 where the magnitude of the S_{11} parameter, the scattering matrix that describes reflection back to port 1 having been reflected at the aperture of the guide due to impedance mismatch, is plotted for each case. The fact that the S-parameters are so alike confirms the very small effect that was seen in the power at the aperture and far field patterns.

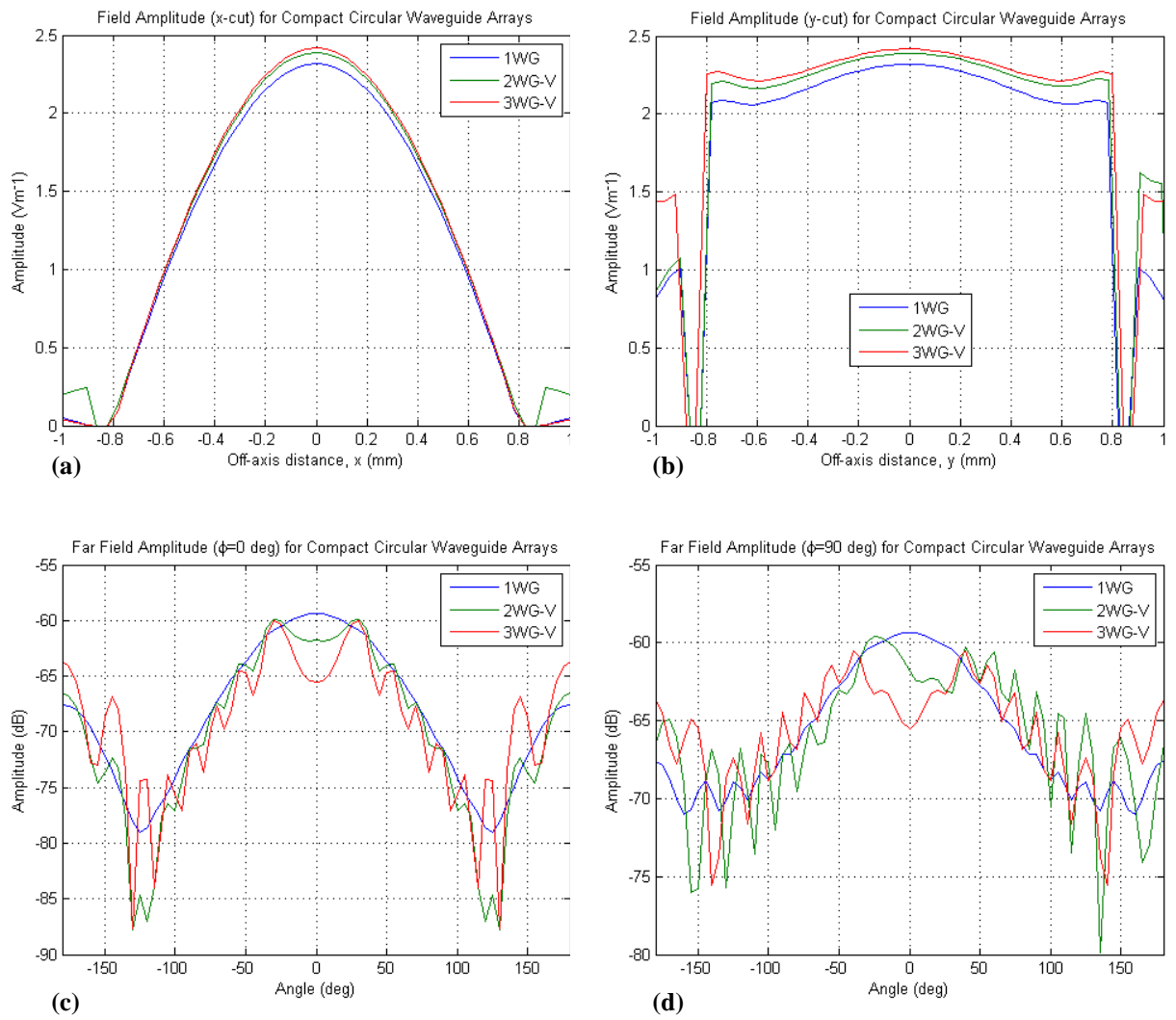


Figure 4.43 (a) Aperture field x -cut, (b) Aperture field y -cut, (c) Far field $\phi = 0^\circ$, and (d) Far field $\phi = 90^\circ$ for the circular waveguide vertical configurations.

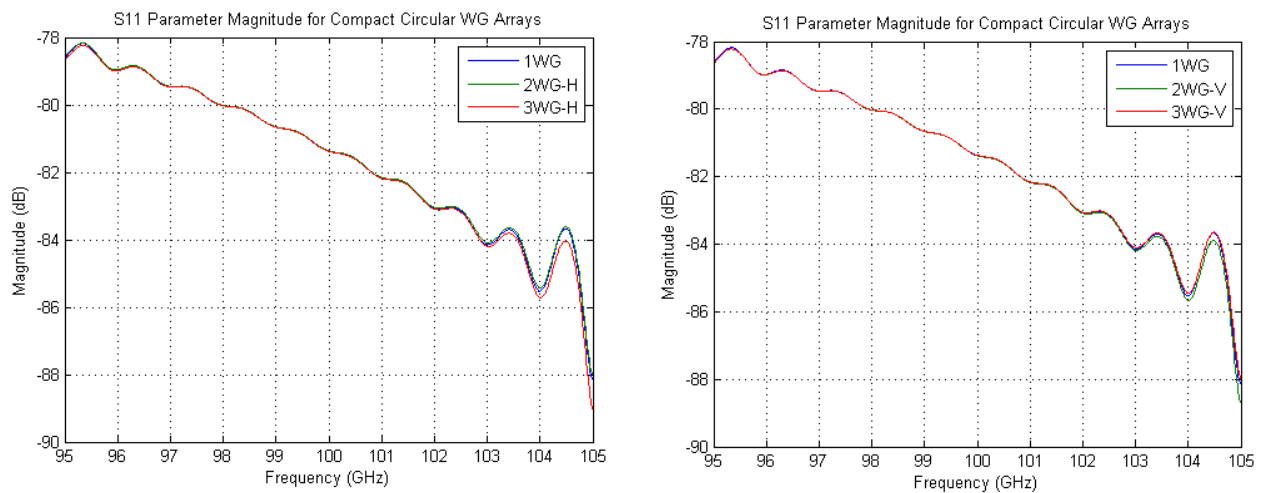


Figure 4.44 Magnitude of the S_{11} parameter for the different horizontal (left) and vertical (right) waveguide configurations.

Another interesting feature of the data lies in the fact that for the 2WG-H configuration the beam is skewed slightly to the left, with its peak being shifted to the right towards the adjacent waveguide. With this in mind a new configuration was set up with the dormant waveguide to the left (rather than to the right as in the 2WG-H case) of the excited one to establish whether or not this would skew the far field pattern in the opposite direction. Both configurations are shown in Figure 4.45 and as expected the far field calculations did show that the beam was skewed in the opposite direction as in Figure 4.46.

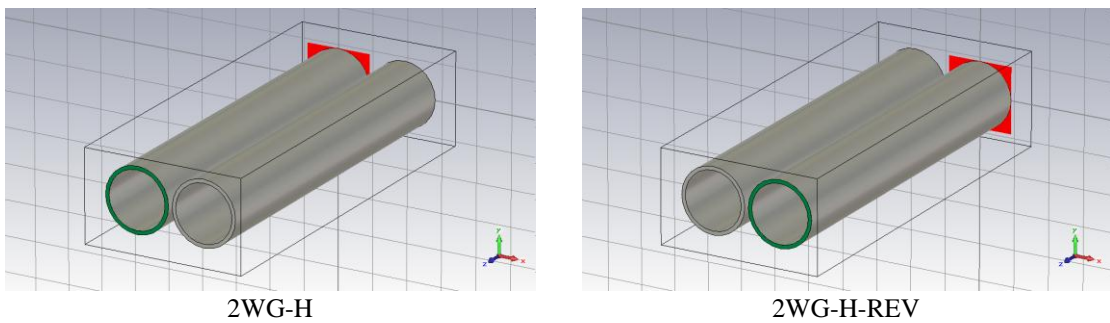


Figure 4.45 Configurations with two waveguides side by side. In the left image the waveguide on the left is excited while in the right image it is the waveguide on the right that is excited.

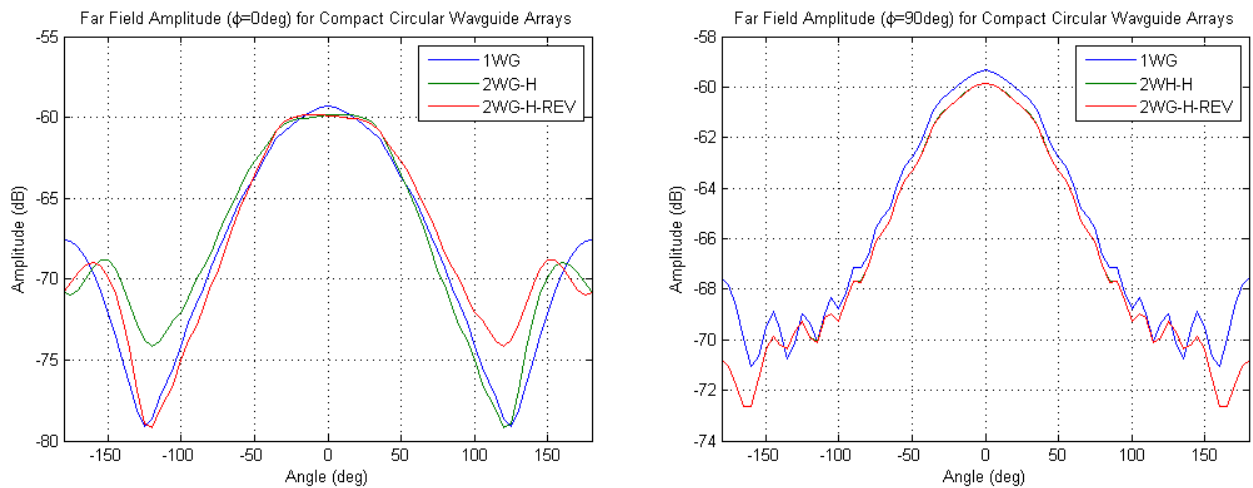


Figure 4.46 Far fields from the waveguide configurations shown in Figure 4.45. The far field of a single circular waveguide (1WG) is also shown.

The reason for the shifting of the field is most likely due to the currents being induced on the surface of the adjacent waveguide. Since these currents are caused by the same source as those in the excited waveguide the fields will be in phase and

therefore add coherently at the aperture plane. The currents in the adjacent waveguide are small compared to those in the excited guide and therefore the overall effect is quite small and can be seen as a slight skewing of the beam. Also, terminating the adjacent waveguides shows no change in these effects. While it appears this effect is not problematic for waveguides in the centre of an array since there are adjacent guides on both sides to counteract the skewing, it is an issue for the waveguides at the array boundary. Also, if this beam distortion is caused by having other waveguides present then it would be expected that the effect should be removed by increasing the distance between the guides. To test this, a model similar to the 2WG-H configuration was set up in which the separation distance was increased and it can be seen in Figure 4.47 that as the waveguides are separated the beam pattern becomes more like that of a single waveguide.

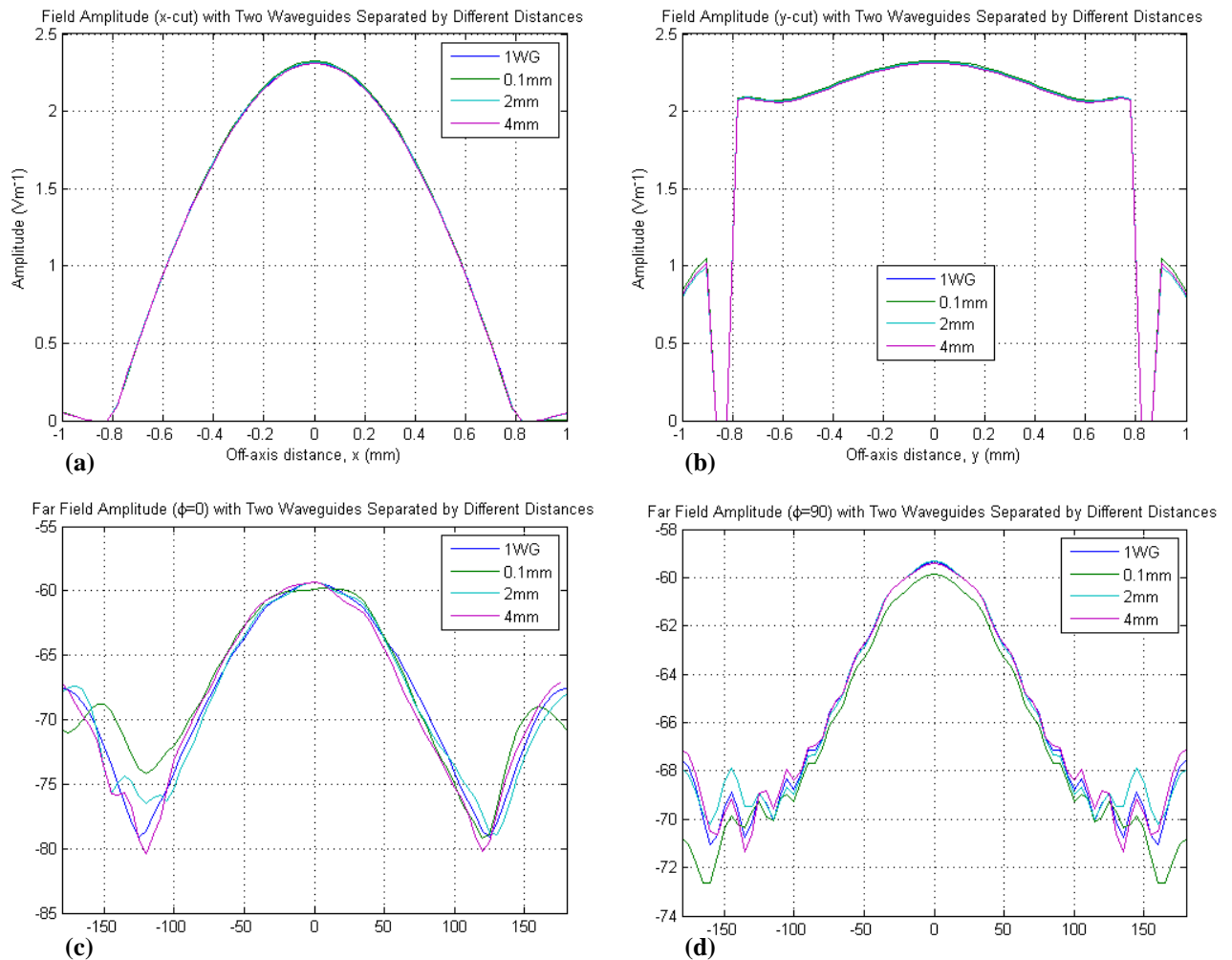


Figure 4.47 (a) Aperture field x-cut, (b) Aperture field y-cut, (c) Far field $\phi = 0^\circ$, and (d) Far field $\phi = 90^\circ$ for the circular waveguide arranged in a horizontal configuration (2WG-H) separated by different distances.

Another problem that can exist in waveguide arrays is crosstalk, where the field from one waveguide is coupled to an adjacent waveguide. To look at the effect of this two adjacent waveguides were modelled with each having a port at the back. In Figure 4.48, port 1 is that at the rear of the waveguide on the left while port 2 is at the rear of the one on the right. To estimate the crosstalk the magnitude of the S_{21} matrix was calculated and is shown in Figure 4.49. The S_{21} matrix describes the power that appears at port 2 having originated at port 1 and it is shown that in this case the crosstalk is extremely small at approximately 2.5×10^{-8} for an operating frequency of 100GHz.

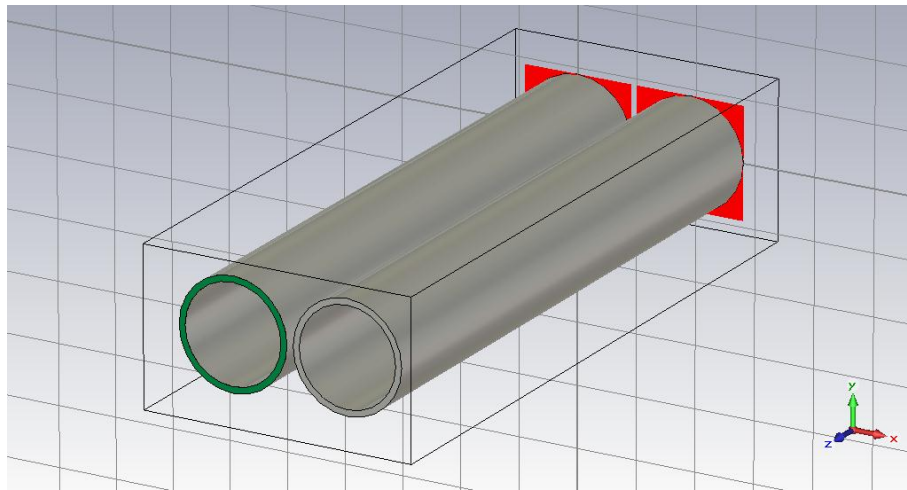


Figure 4.48 Waveguide and port arrangement used to measure cross-talk between the circular waveguides by means of the S_{21} parameter. The waveguide on the left is excited at its port (port 1) while the waveguide port on the right (port 2) is not excited

Having considered both beam distortion and crosstalk between circular waveguides in closely packed formations it is clear that the effects of both are quite small, however they should be considered when designing detector arrays. It was shown that the waveguides which had adjacent guides on both side behaved almost as if they were just single elements, however when a waveguide had an adjacent guide on only one side the beam was pulled to one side. This is the case for waveguides located at the edge of the array. With regards to crosstalk, an extremely small percentage of the power from port 1 was transferred to port 2. This power is

unwanted and although it is quite small the level of sensitivity required for CMB polarisation experiments is such that it may be significant and therefore must be accounted for.

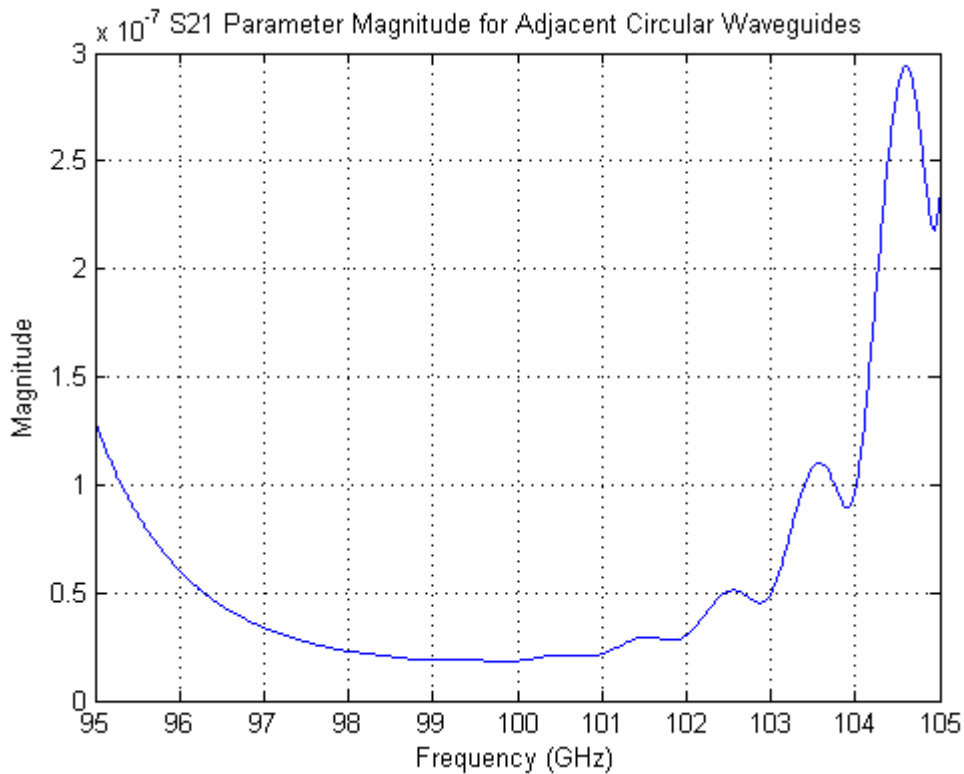


Figure 4.49 The magnitude of the S21 parameter for two adjacent waveguides with only one port (port 1) excited.

4.5.2 Rectangular Waveguide Arrays

A similar analysis to that carried out for circular waveguides in the previous section was also done for rectangular waveguides with a series of configurations modelled as shown in Figure 4.50 . The waveguides used in the analysis had a width of 2.54mm and a height of 1.27mm (standard WR10 waveguide dimensions). The wall thickness was 0.1mm with a separation of 0.1mm between adjacent waveguides. An operating frequency of 100GHz was used throughout the analysis and a single TE₁₀ mode was excited at the input port (see Figure 4.50) as shown in Figure 4.51.

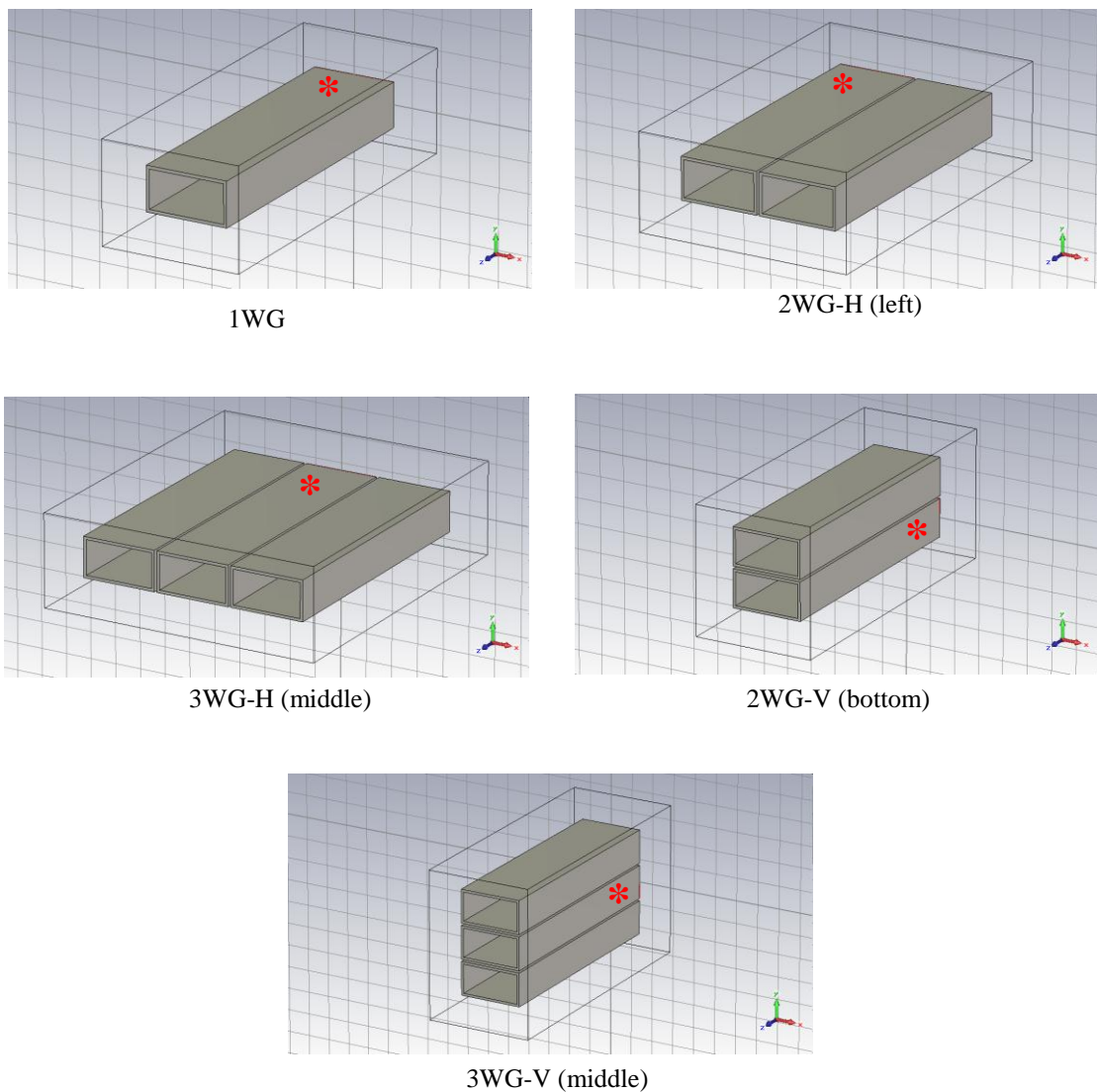


Figure 4.50 Rectangular waveguide array configurations analysed using CST. The waveguide with the excited input port (marked with a red star) is shown in brackets.

Firstly, to get an idea of the effect that the other waveguides had on the single element the aperture and far field amplitude was calculated for each configuration and can be seen in Figures 4.52 and 4.53 for both the horizontal and vertical arrangements respectively. Considering the horizontal configurations first it can be seen that for the case of two waveguides placed side by side (2WG-H) the field in the x -direction is asymmetric. This is more apparent in the $\phi = 0^\circ$ far field pattern. However, when another waveguide is added to the opposite side (3WG-H) the field becomes symmetric again, as was the case with the circular waveguide arrangements. The y -cuts for the horizontal configurations are all symmetric but the

far field exhibit higher levels of ringing due to the more severe truncation of the aperture field. To examine the asymmetry further the 2WG-H configuration was reversed so the excited waveguide was on the right hand side. The results showed that the asymmetry at $\phi = 0^\circ$ was also reversed as expected which can be seen in Figure 4.54. The field at $\phi = 90^\circ$ remained the same.

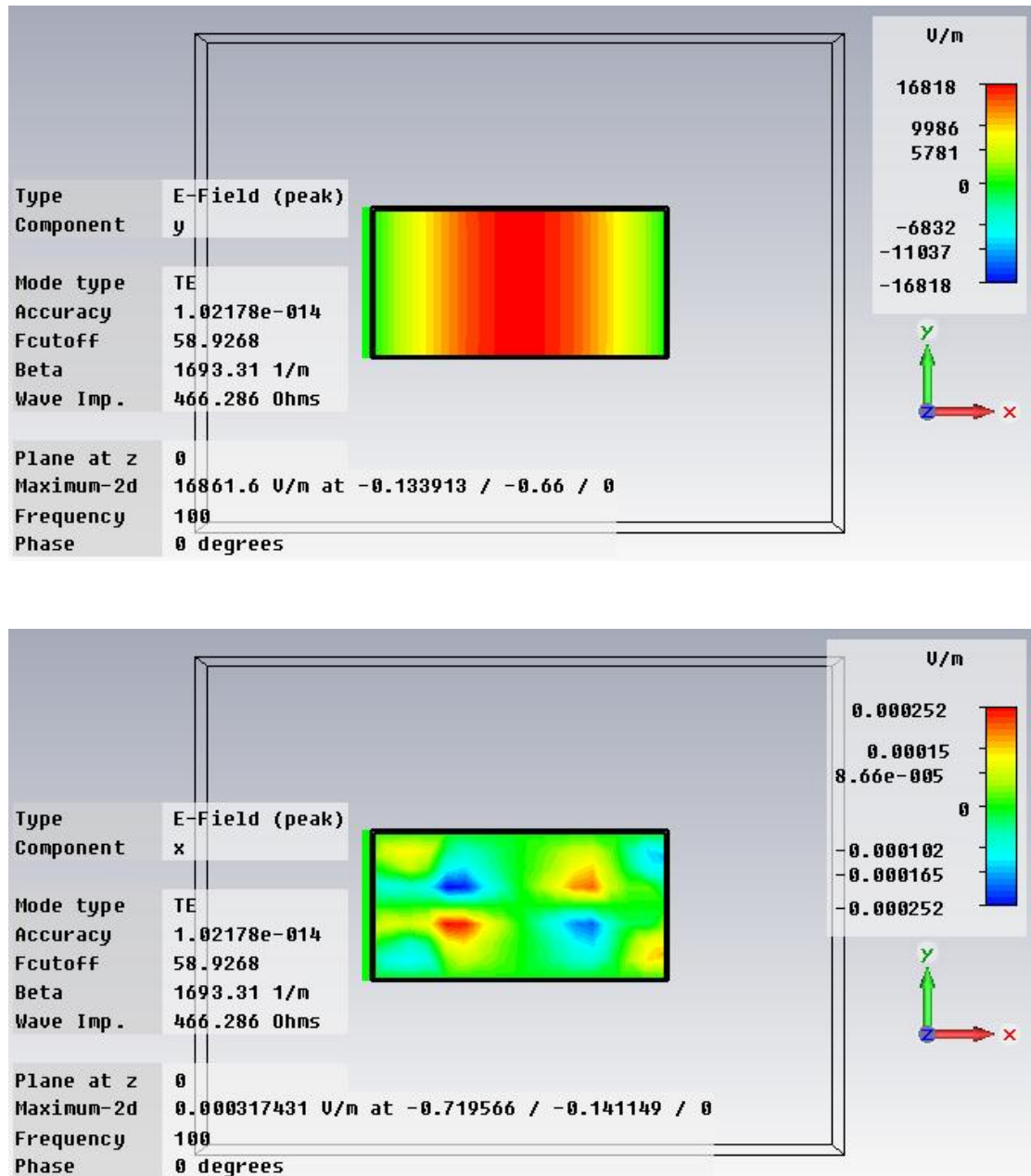


Figure 4.51 The copolar and cross-polar fields of the TE₁₀ mode excited at the input port of the rectangular waveguides. The plots are taken from CST.

In the case of the vertical arrangements the x -cuts are symmetric while it is now the y -cut for the two waveguide configuration (2WG-V) that contains the asymmetry. This can also be seen in the far field pattern at $\phi = 90^\circ$. Again a higher level of ringing in this direction is also visible.

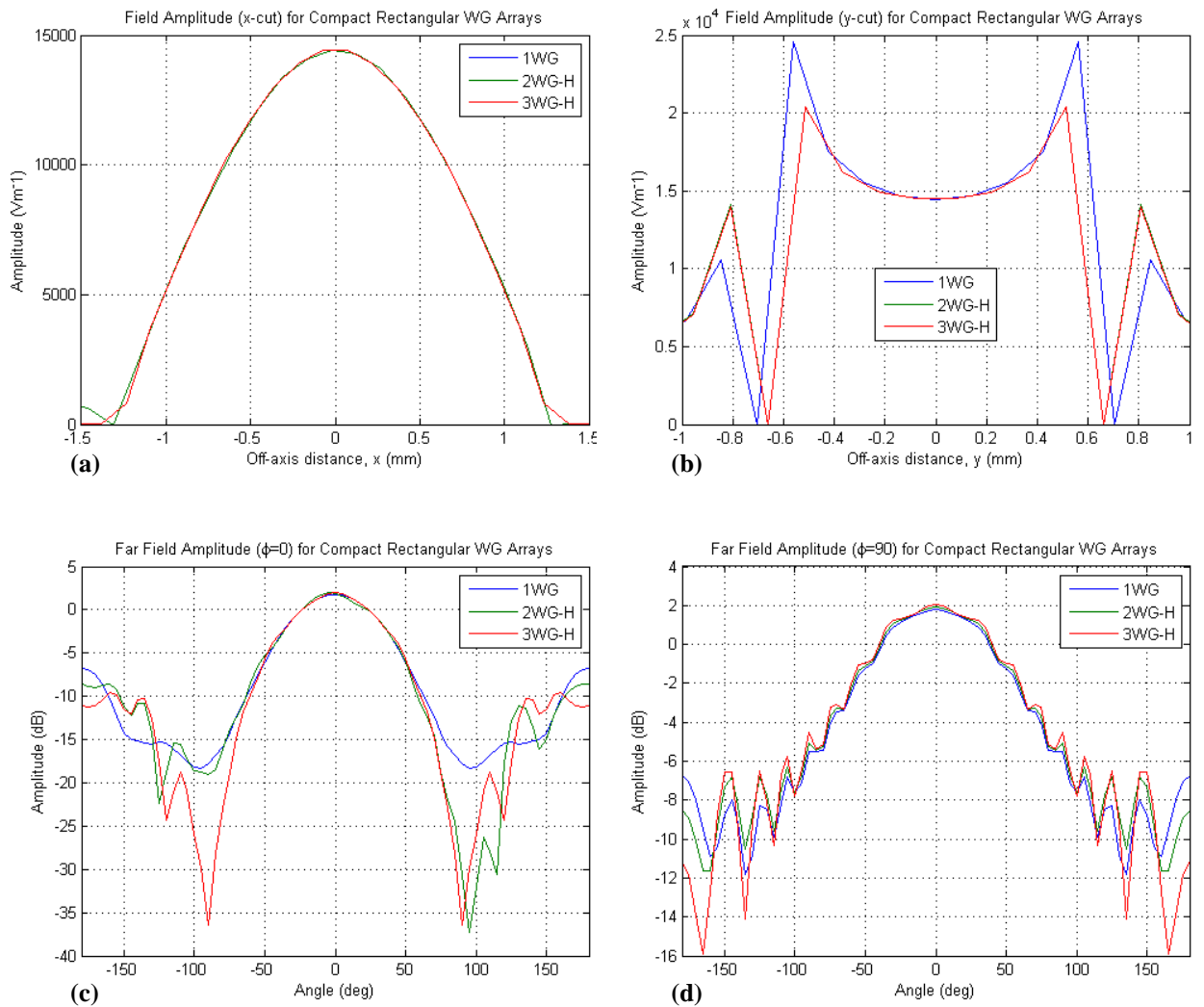


Figure 4.52 (a) Aperture field x -cut, (b) Aperture field y -cut, (c) Far field $\phi = 0^\circ$, and (d) Far field $\phi = 90^\circ$ for the rectangular waveguide horizontal configurations.

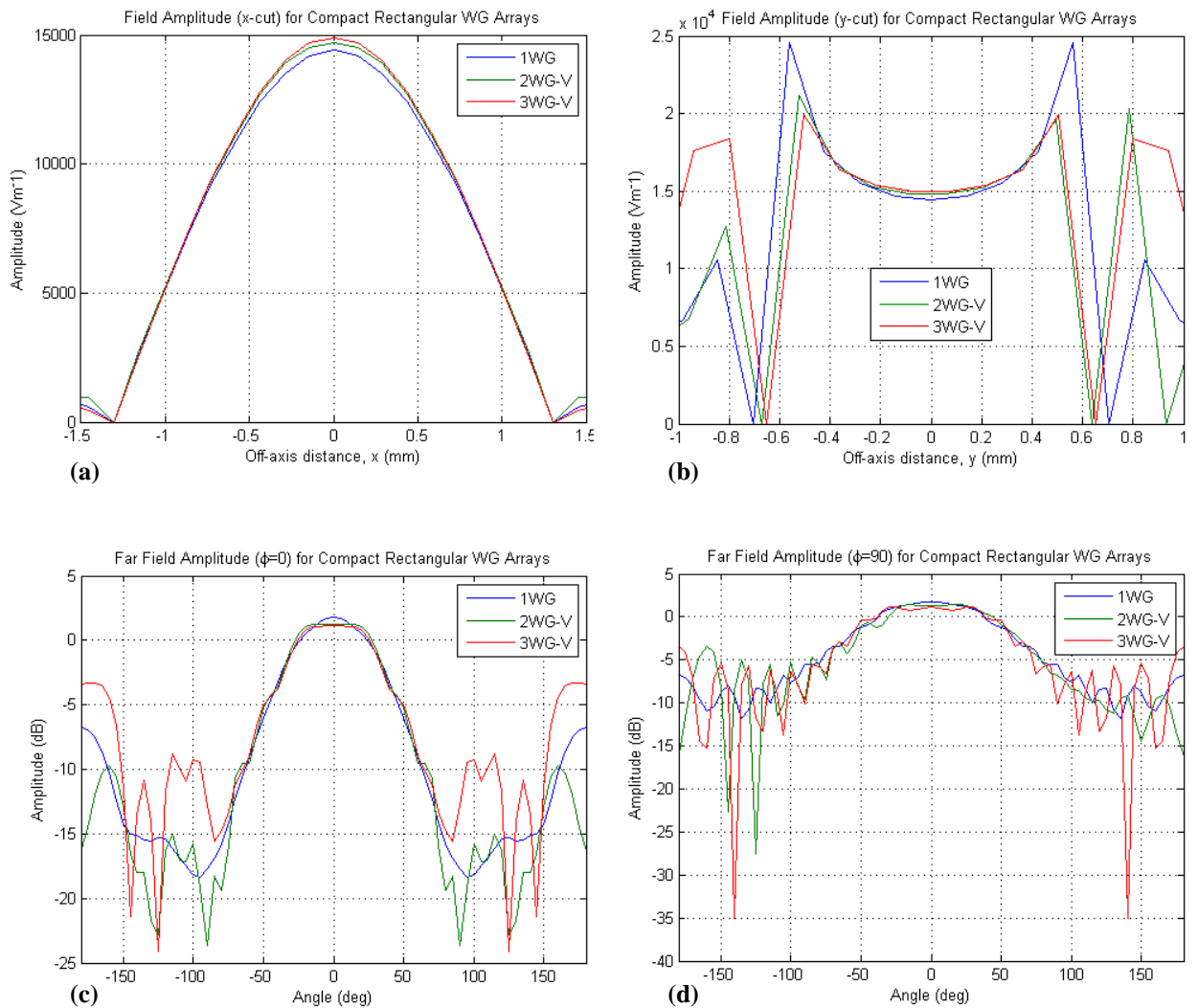


Figure 4.53 (a) Aperture field x -cut, (b) Aperture field y -cut, (c) Far field $\phi = 0^\circ$, and (d) Far field $\phi = 90^\circ$ for the rectangular waveguide vertical configurations.

Looking at both the beam patterns for both the horizontal and vertical arrangements it is the vertical ones that differ most from a single waveguide. As a further analysis, the S_{11} matrix parameters were calculated, as in the case of the circular waveguide array, for each configuration and as can be seen from Figure 4.55 the results are consistent with the beam pattern variation with the vertical arrangements varying the most from the single waveguide. This is most likely due to

the fact that the field in the y -direction remains high (or is not tapered) as far as the waveguide wall itself and therefore any waveguides placed next to this have the most effect on this field due to induced currents in the wall of the adjacent guide. As with the circular case, if the waveguides are moved further apart then the effect should be reduced and the fields should become more like those of a single rectangular waveguide. To investigate this, the two-waveguide vertical configuration (2WG-V) was altered so that the distance between the waveguides was 2mm instead of 0.1mm and the aperture and far fields were calculated. The results of this are shown in Figure 4.56. Considering first of all the x - and y -cuts of the aperture field it can be seen that the field from the 2mm separation arrangement very closely matches the main beam from the single waveguide, something which is more evident in the far field patterns. Also, the level of asymmetry in the y -direction has been reduced to be more like the single waveguide. As a final check the S_{11} parameter was calculated and as can be seen in Figure 4.57 the 2mm separation is significantly different to the case where the waveguides were separated by 0.1mm, again indicating the as the waveguides are moved apart the field becomes more like that from a single waveguide.

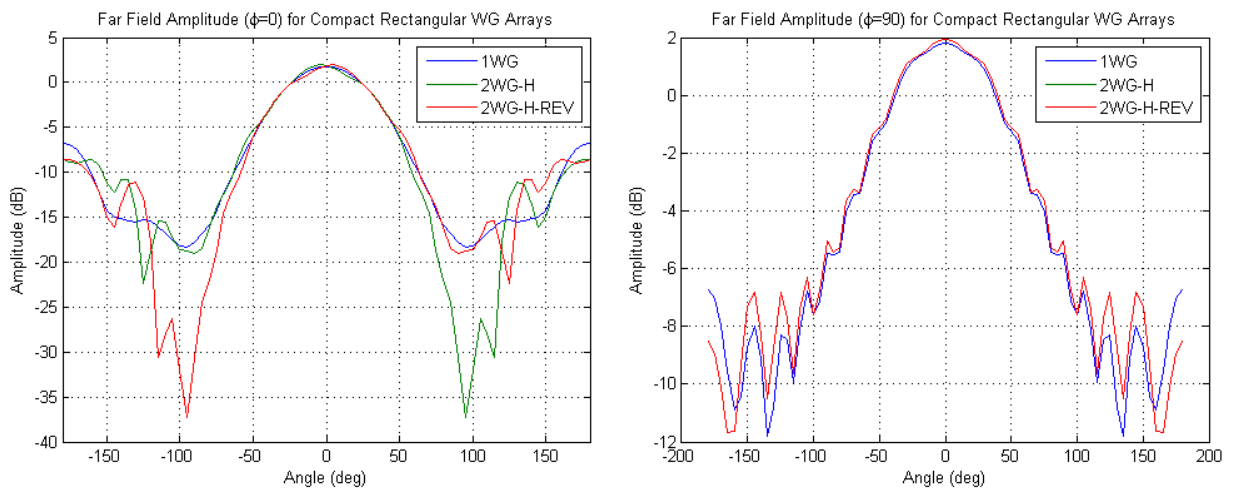


Figure 4.54 Far fields from the two-waveguide configuration 2WG-H and also a similar arrangement with the right waveguide excited (2WG-H-REV). The far field of a single circular waveguide (1WG) is also shown for comparison.

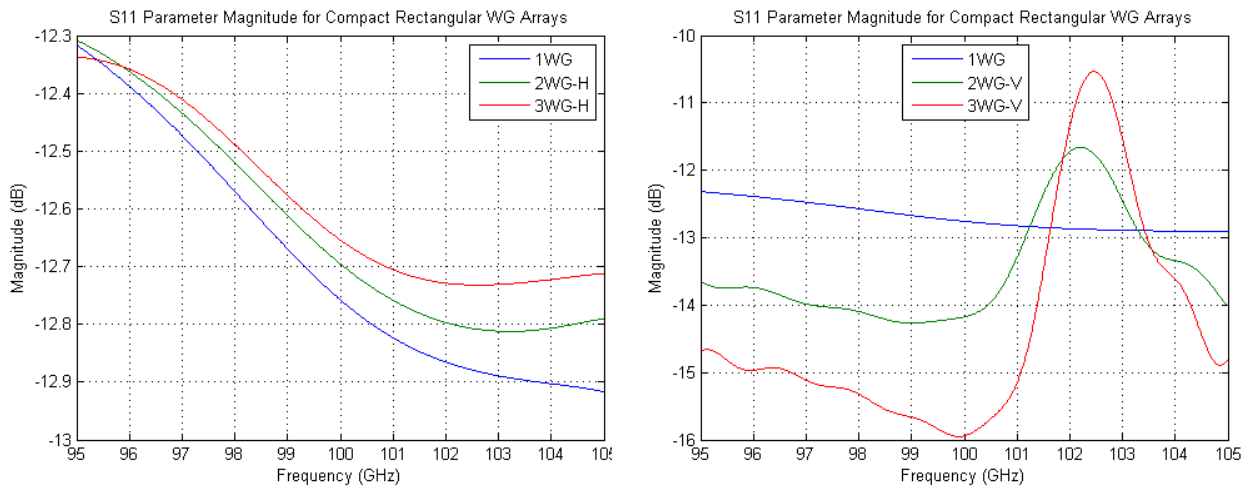


Figure 4.55 Magnitude of the S_{11} parameter for the different horizontal and vertical waveguide configurations. Note that at some frequencies reflection is found to be less the waveguide is within an array.

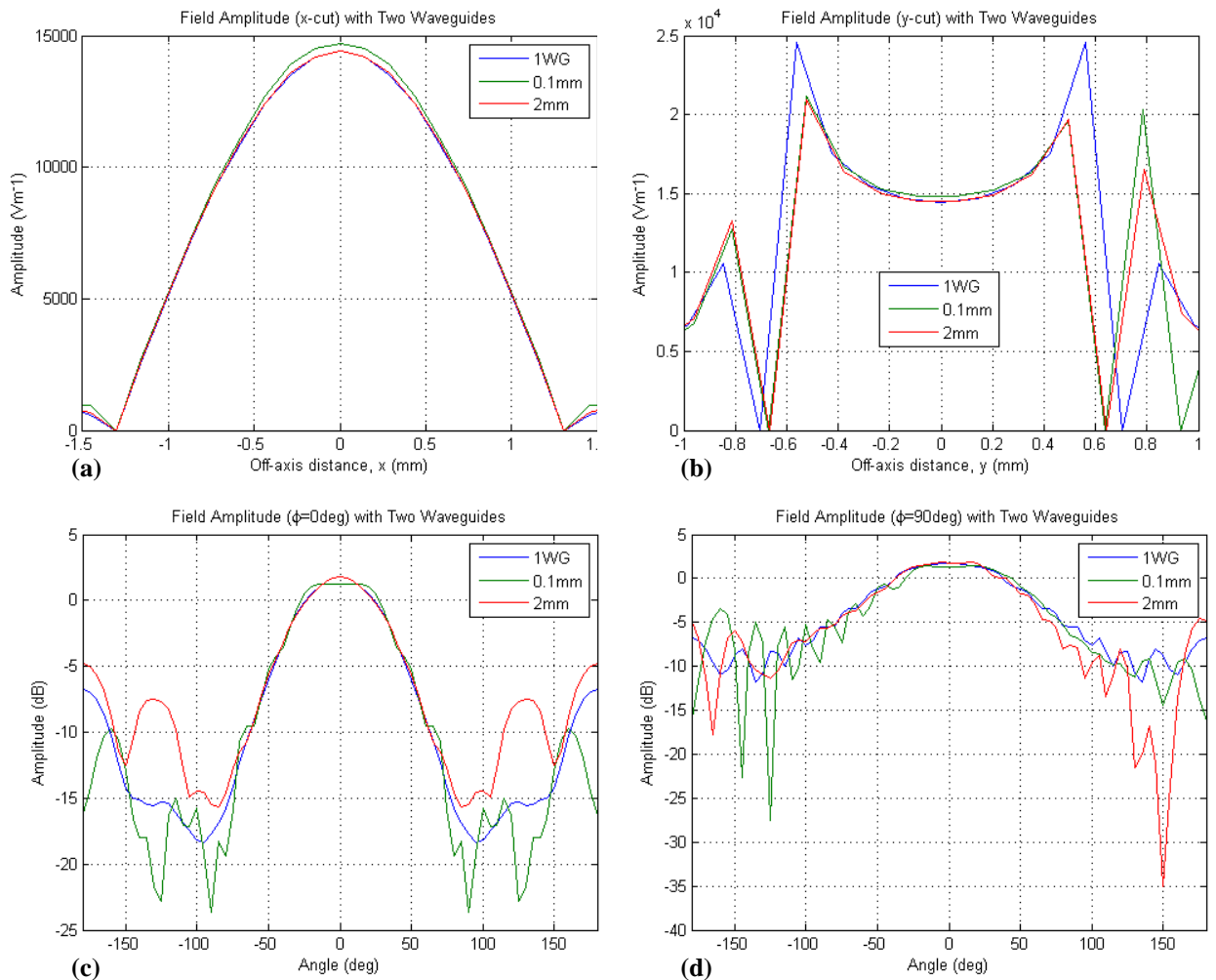


Figure 4.56 (a) Aperture field x-cut, (b) Aperture field y-cut, (c) Far field $\phi = 0^\circ$, and (d) Far field $\phi = 90^\circ$ for the rectangular waveguide arranged in a vertical configuration (2WG-V) separated by different distances.

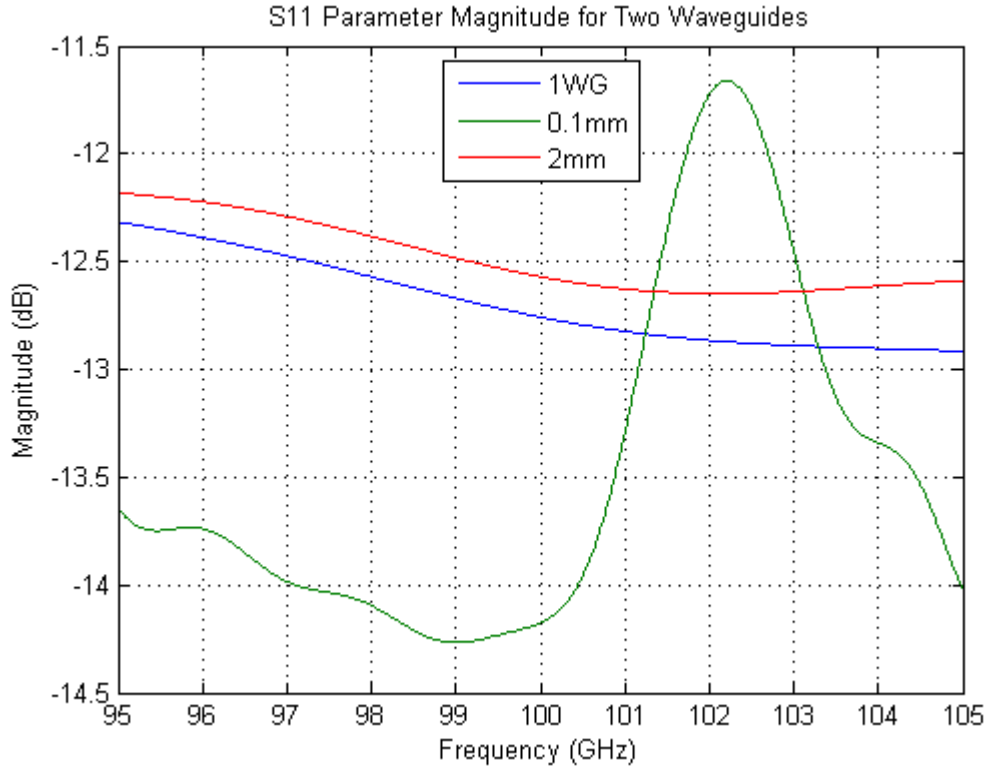


Figure 4.57 Magnitude of the S_{11} parameter for the vertical rectangular waveguide configuration 2WG-V with different separation distances.

To calculate the crosstalk between adjacent rectangular waveguides the input and output ports were configured as before for the circular waveguides, that is, port 1 was at the back of the excited waveguide while port 2 was located at the back of the non-excited waveguide, and the S_{21} parameter was calculated. Both horizontal and vertical arrays were considered. The results of this are shown in Figure 4.58 where for the waveguides arranged in a horizontal configuration (as in 2WG-H with the left waveguide excited) the S_{21} parameter has a magnitude of approximately -31.3dB at the 100GHz central frequency, while for those arranged vertically (as in 2WG-V with the bottom waveguide excited), a value of approximately -15.5dB is obtained for the same frequency. This again provides some insight as to the greater variation in the fields generated by vertically arranged waveguides as opposed to those horizontally arranged when compared to a single waveguide.

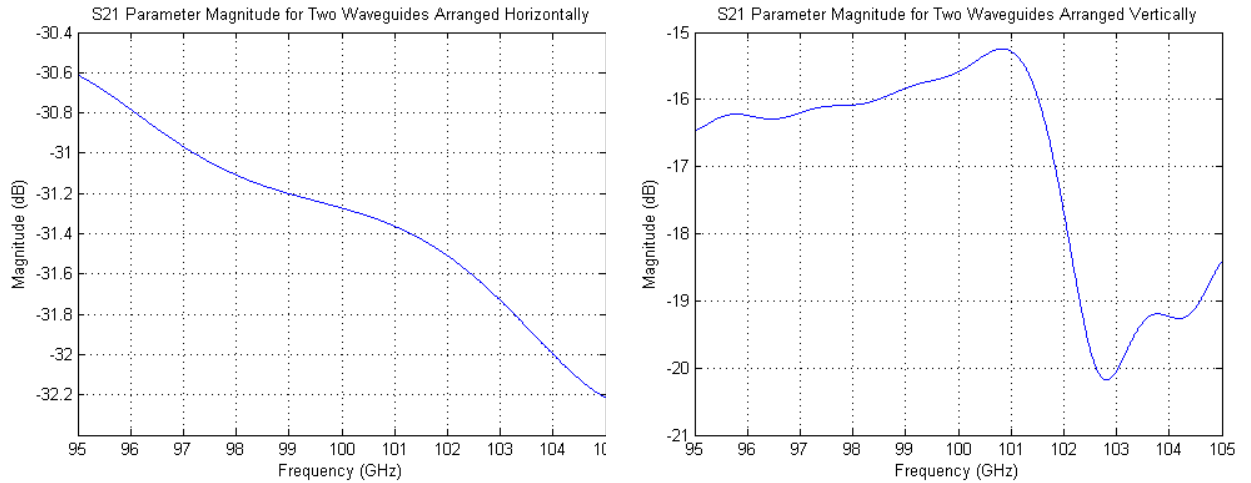


Figure 4.58 The S_{21} parameter for two rectangular waveguides aligned both horizontally (left) and vertically (right).

On examination of the far field patterns and the S parameters of the various configurations it appears that the vertical arrangements of rectangular waveguides have the most effect on the field from an individual waveguide. In the case of the S_{11} (reflection) parameter, the horizontal arrangements are very similar to each other, as well as to the single waveguide. The configurations containing vertical arrangements have similar (magnitude versus frequency) profiles to each other but quite different profiles to the single case. Although at the central frequency of 100GHz examined here the reflection is lower it rises significantly at approximately 102GHz for the vertical arrangements. The S_{21} parameter is also much greater for the rectangular waveguides arranged vertically, and these configurations also induce asymmetries into the beam patterns.

In comparison to the circular waveguide arrays the rectangular waveguide configurations in general seem to produce beam patterns with a higher sidelobe level. Also, while the crosstalk between circular waveguides in an array and the rectangular waveguides in a horizontal configuration is comparable it is much higher for vertical arrangements of rectangular waveguides. Also, the reflection coefficient for rectangular arrays is significantly higher. While the waveguide arrays presented here contained waveguides in close proximity to each other, the separation distance was also varied and it was shown that the beam patterns and S parameters became

more like those of the single waveguide, as expected if the adjacent waveguides in the array were causing the observed effects. As mentioned previously this analysis was a first approximation in the effects of adjacent waveguides on individual beam patterns. For a more detailed analysis the exact geometries of the horns used would be needed (computationally, on the PC's used here, CST could not model horns of the volume used in MBI).

In this chapter I presented an overview of both smooth-walled and corrugated conical horn antennas and the techniques used in predicting their beam patterns. The effect of using lenses on the MBI-4 smooth-walled detector horn antennas was analysed as too was changing the geometry of these horns without changing the dimensions of the lenses. It was found that a loss of 20% in coupled power occurs if the original lens designed for a horn with an aperture radius of 12.7mm is used with a horn antenna whose aperture radius is only 9.525mm (the horn slant length was also different for each horn).

The MBI-4 back-to-back conical corrugated horn antennas were also analysed in detail and the truncation effects by the cryostat windows was modelled. The mode-matching technique used to model corrugated horn antennas was discussed and extended to include scattering at rectangular-to-circular discontinuities. Finally, the effect of closely packed waveguide arrays on individual waveguide beam patterns was examined and it was found that while there is an effect it is quite small. It was also found that the effect depends on the arrangement of the array and the separation distance between the waveguides.

Chapter 5

Quasi-Optical Analysis of MBI-4

5.1 Analysis of the Fizeau Optical System Using MODAL

In this section we look at the optical design of the MBI-4 beam combiner in more detail, taking into account the four-inward facing horn antennas and producing interference patterns by modelling the exact system. We also look at truncation effects in more detail as well as mechanical tolerances and the frequency dependence of the system. Comparisons between experimental measurements and modelling are also given,

5.1.1 Defining the System in MODAL

The first step in analysing the MBI Fizeau beam combiner in MODAL was to define and create the system as a new project in the MODAL environment. To begin with, a number of reference frames were defined in terms of the global frame to allow each of the components to be positioned and orientated appropriately and also to allow easy characterisation of the polarisation directions of the feed horn antennas. The details of these frames are summarised in Figure 5.1 and Table 5.1.

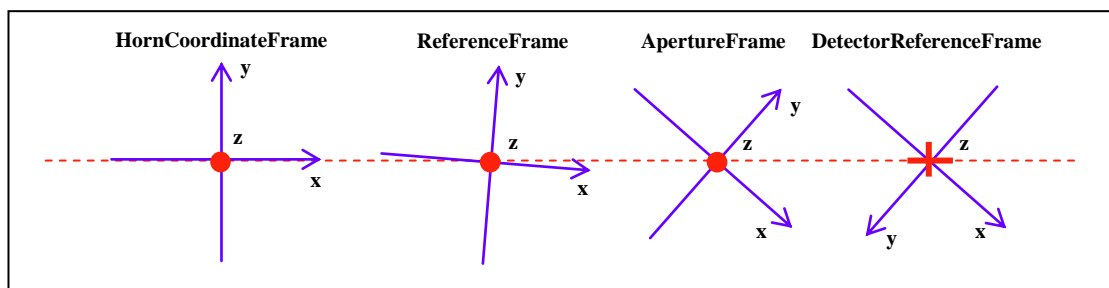


Figure 5.1 The frames used to define the optical system in MODAL.

New Frame	Transformation	Value	Original Frame
HornCoordinateFrame	n/a	n/a	Global
ReferenceFrame	z-axis rotation	-0.037181 rad	HornCoordinateFrame
ApertureFrame	z-axis rotation	-0.730141 rad	HornCoordinateFrame
DetectorReferenceFrame	z-direction translation	425 mm	HornCoordinateFrame
	x-axis rotation	π rad	HornCoordinateFrame
	z-axis rotation	-0.730141 rad	HornCoordinateFrame

Table 5.1 The reference frames used in defining the MBI system in MODAL.

The first frame created was the *HornCoordinateFrame*, which was defined as being the same as the global frame in MODAL. This frame allowed the positioning of the inward facing corrugated horn antennas as shown in Figure 5.2, where the origin of the xy -plane in the diagram corresponds to the origin of the *HornCoordinateFrame* and the coordinates and measurements are given in inches, not millimetres. The view in Figure 5.2 is from the detectors and not from the sky.

It was also necessary to take into account the polarisation directions of the source horns, which is defined as being parallel to the shortest baseline, that formed by sources 2 and 3 in Figure 5.2. Since this baseline forms an angle of approximately -0.037 radians with the horizontal, a *ReferenceFrame* was defined with its origin coinciding with that of the *HornCoordinateFrame* but with its axes being rotated around the z -axis of this frame by -0.037 radians (see Figure 5.1). This meant that the x -axis of this new frame corresponded to one polarisation direction of the horn antennas, the co-polar, while the y -axis corresponded to the other polarisation direction, the cross-polar, and these polarisation directions were defined as \hat{u} and \hat{v} vectors respectively for future reference in the MODAL project.

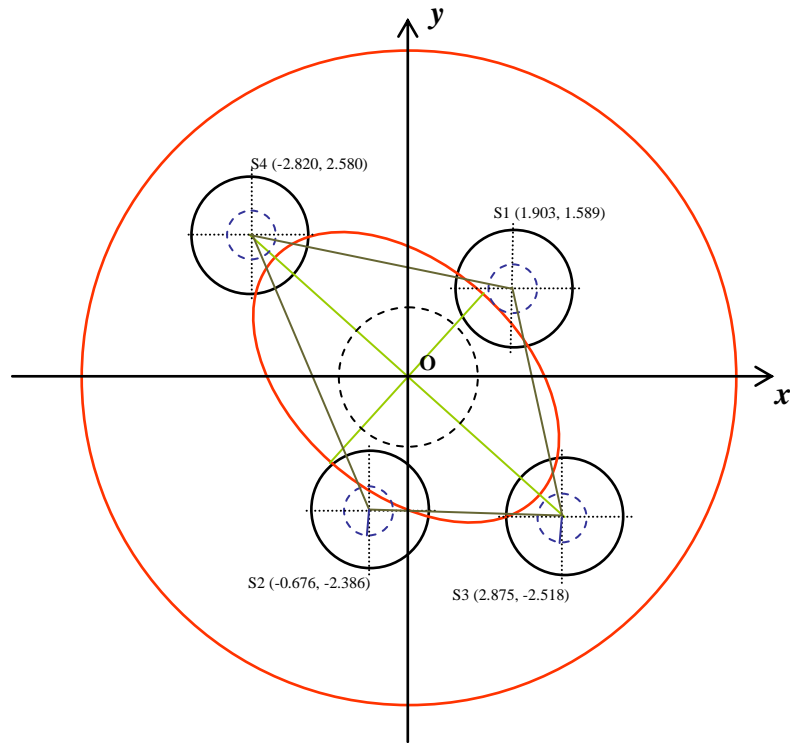


Figure 5.2 Schematic diagram showing the four inward-facing horn antennas and their coordinates (in inches) as defined in the *HornCoordinateFrame*. The primary mirror and elliptical aperture are also shown along with the secondary mirror. The view is from the detectors looking towards the sky (this is Figure 4.30 reproduced here for convenience).

Four source horn antenna frames were defined by translating the reference frame to the four horn origins shown in Figure 5.2. Throughout the analysis of the optical combiner different types of source were used and each will be described in more detail in the appropriate section. For now, the location and orientation of the frames is sufficient in describing the optical setup in MODAL.

Looking at Figure 5.3, the next surface in the system is the secondary mirror. The hyperbolic shape was defined as an aspheric surface with a radius of curvature of -61.8557mm and a conic constant of -1.3571 and its frame was defined as the *ReferenceFrame* translated a distance of 50mm in the positive z -direction of the *HornCoordinateFrame* (the choice of using the *ReferenceFrame* rather than the *HornCoordinateFrame* came from the fact that when calculating the field at the mirror in later analysis it would be more useful to have the mirror orientated in the direction of the polarisation vectors). The bounding volume for the secondary mirror

was defined as being an infinite cylinder with its axis going through the origin of the secondary mirrors frame and its radius being the same as that of the mirror, that is, a radius of 32mm.

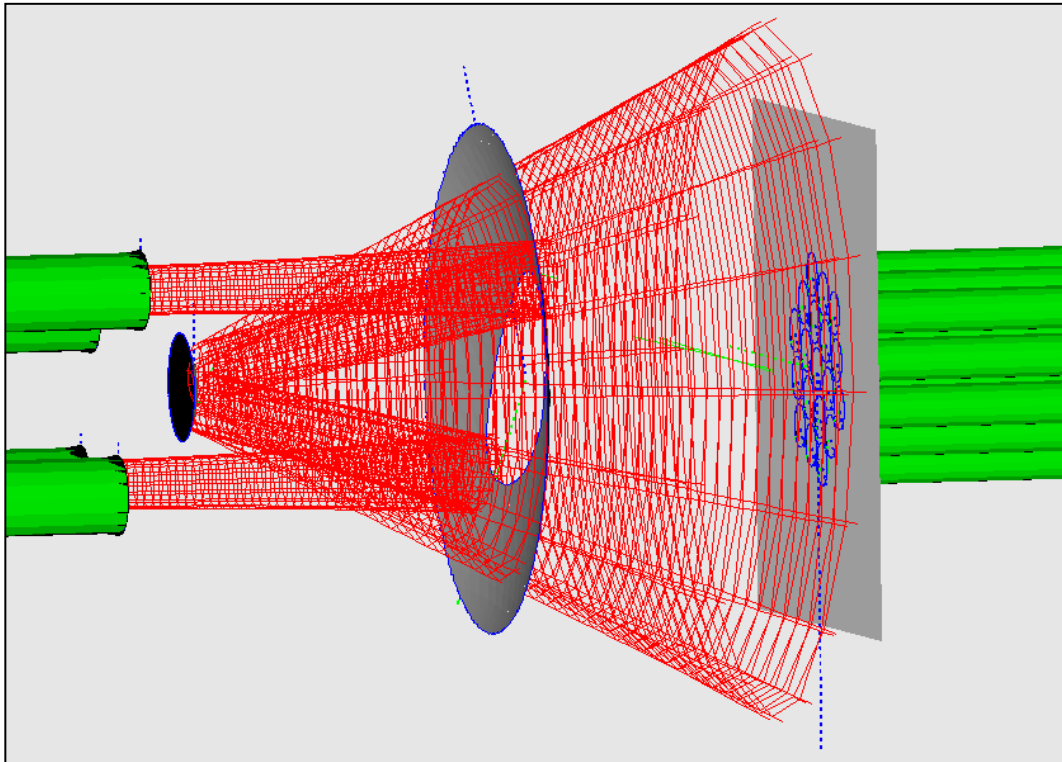


Figure 5.3 The optical system as defined in MODAL. The four inward facing horn antennas and nineteen detector horn antennas are shown as infinite cylinders because of the infinite phase front radius of curvature at the aperture of the horn.

Again, moving towards the right in Figure 5.3, the next surface encountered is that of the primary mirror, the aperture (inner rim) of which is elliptical in shape with the major axis of the ellipse being aligned along the line connecting the centres of source 3 and source 4 in Figure 5.2. To aid with the setup of this in MODAL a new frame called the *ApertureFrame* was defined as being a transformed *HornCoordinateFrame* with the transformation being a rotation around its z -axis by an angle of -0.730141 rads. Following this, the frame for the primary mirror was defined as being the *ApertureFrame* translated along the z -axis of the *HornCoordinateFrame* by 250mm, the distance from the horn apertures to the primary as described in section 3.3.3. As with the secondary mirror an aspheric

surface was used with a radius of curvature of -457.143mm and a conic constant of -1, i.e. a parabola. The overall size of the mirror and the size and shape of the aperture were set using a bounding volume, which was defined as being the difference of two geometrical objects. The first of these objects was an infinite cylinder with a diameter of 300mm centred on the frame origin. The second object was also an infinite cylinder centred on the origin, but with a different diameter in orthogonal directions (164mm in the *ApertureFrame* x -direction and 96mm in the y -direction) giving the elliptical shape required.

Moving along the z -axis through the optical system we come to the detector plane. In MBI-4 the detector array is aligned along the major axis of the elliptical aperture in the primary mirror with the centre detector horn located at the optical centre of the overall system, that is, in line with the origin of the *HornCoordinateFrame* defined earlier. This is also the centre line of both the primary and secondary mirrors and lies slightly off the midpoint of sources 3 and 4 to allow the detectors to be placed an equal distance from each of the horns in each baseline. A *DetectorReferenceFrame* was created by carrying out three transformations on the *HornCoordinateFrame*. Firstly the *HornCoordinateFrame* was rotated around its z -axis by an angle of -0.730141rads to align the x -axis of the new frame along the major axis of the aperture in the primary mirror, as with the *ApertureFrame*. Secondly, the frame was rotated around the x -axis by π radians which effectively orientated the plane so it was facing back towards the system with the positive y -axis now facing downwards. Finally, the frame was translated 425mm along the z -axis of the *HornCoordinateFrame*, placing it 175mm behind the primary mirror as desired. Figure 5.4 shows the *DetectorReferenceFrame* containing the nineteen detector horns with the grid system being used as a means of positioning and naming the horn antennas. The two vectors, \hat{n} directed along the x -axis of the frame and \hat{m} at -60° to this were given a magnitude of 1.1 inches, the separation distance between the centres of the detectors. The origin of both of these vectors coincides with the optical centre and therefore the centre detector horn antenna, with the position of each of the other horns being calculated by the vector sum $n \times \hat{n} + m \times \hat{m}$, where n and m are the grid reference numbers. The naming of each horn in the diagram can then simply refer to its position, which is (n, m) . At each

detector point in the array, both a detector polarised in the u -direction and one in the v -direction were defined, each being a smooth-walled conical horn antenna with a diameter of 1 inch. The phase front radius of curvature at the aperture of each horn was set to infinity to simulate the phase flattening lenses described in section 4.2.3.

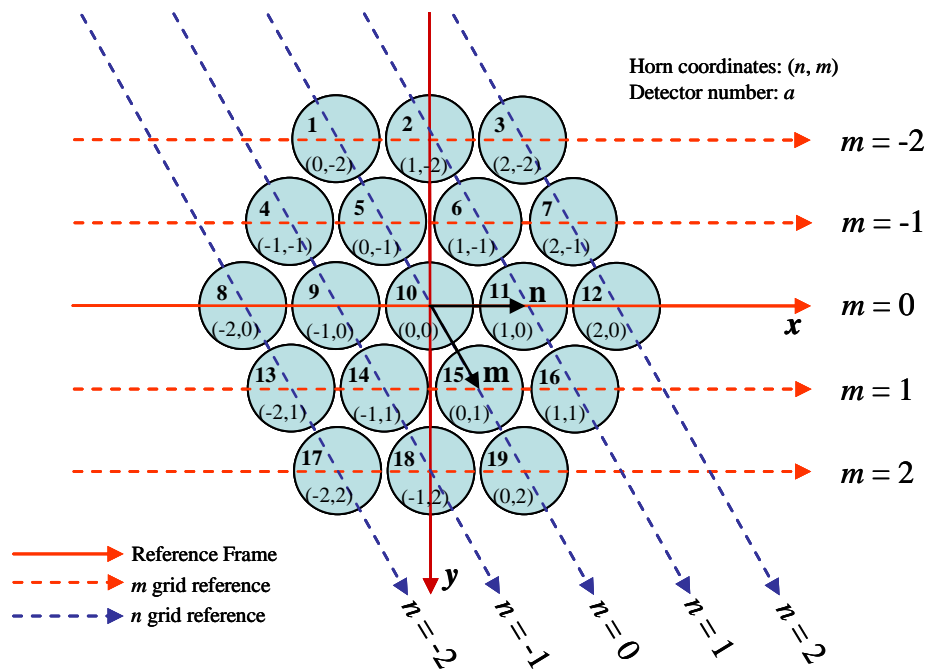


Figure 5.4 The *DetectorReferenceFrame* and grid system used to position and name the detector horn antennas. The x -axis of the frame coincides with the major axis of the elliptical aperture in the primary mirror. The view is from the detectors looking towards the optics.

With the system defined a variety of sources could be inserted for different analysis. Also, MODAL provides the user with a number of propagation techniques and in the next section we evaluate these and compare the results.

5.1.2 Evaluation of Propagation Techniques

MODAL allows the user to select one or more of three possible propagation techniques, namely Gaussian beam modes (GBM), scalar or Fresnel diffraction, and physical optics, each of which was described in detail in Chapter 2. To evaluate

these techniques the MBI-4 optical system was defined as in the previous section with inward facing corrugated conical horn antennas used as the four sources. The horns had a radius of 22.45mm and were polarised along the x -axis of the *ReferenceFrame* (\hat{u}), that is, along the direction of the shortest baseline formed by sources 2 and 3 in Figure 5.2. The initial phase of the field at the horn aperture was set to zero with a flat phase front and the power at the aperture of the horn antenna was 1W. MODAL represents the field produced by such a source as a Bessel function ($J_0(1.405r/a)$, (Figure 4.19 shows how accurate this representation is)) and propagates the fields by means of elements in the program called propagators. First the intensity of the field at the image plane was calculated for each method and the results compared. To enable this calculation the field from each source was propagated from element to element using the propagators mentioned above.

Number of Grid Points Used for Propagators			
Propagator	GBM	Scalar	Physical Optics
Source	41 x 41	81 x 81	81 x 81, 161 x 161
Sec. Transmission	41 x 41	81 x 81	81 x 81, 161 x 161
Prim. Reflect	41 x 41	81 x 81	81 x 81, 161 x 161
Sec. Reflect	41 x 41	81 x 81	81 x 81, 161 x 161
Prim. Transmission	41 x 41	81 x 81	81 x 81, 161 x 161
Image Plane	41 x 41	81 x 81	81 x 81, 161 x 161

Table 5.2 The number of grid points used for the propagators involved in propagating the field from each source to the image plane.

In evaluating the propagation techniques we wanted to see if both the Gaussian beam mode and Fresnel diffraction methods could produce a field at the image plane that displayed the overall structure of the interference pattern shown by a physical optics analysis. If this was the case, then although the fine detail achievable through physical optics may not be visible, both Gaussian beam modes and Fresnel integrals could be used as an initial design tool since they are less computationally intense.

In the case of a Gaussian beam mode analysis the horn antenna aperture field is decomposed using the appropriate mode set before it is propagated to the secondary mirror. Although the first element we require the beam to strike is the primary mirror, it will be obscured by the secondary to some extent and therefore we must take this into account by calculating the transmitted portion of the field as it propagates past the secondary mirror. This field is then propagated to the primary mirror for reflection, then to the secondary for reflection, then to the primary for transmission through the elliptical aperture and finally to the image plane. Table 5.2 shows the propagators involved in this process of transferring the field from the source to the image plane while taking all optical elements into account. The number of grid points used for each propagator is also shown for each method (there is no relationships between the number of grid points used for the different methods, these values were selected to provide an image with reasonable resolution and computational time).

For each method the power density of the interference pattern formed from a combination of both sources 2 and 3, and 3 and 4 (corresponding to the shortest and longest baselines respectively) were calculated. In Figures 5.5 and 5.6 we see the results of using a Gaussian beam mode approach with a grid size of 41×41 points at each propagation stage. The system was set up in MODAL so that the optimum mode set was chosen at each component using an SVD analysis. The axes in the figure correspond to the axes of the *ReferenceFrame*, which defines the direction of polarisation as mentioned above. The same calculations using Fresnel diffraction are shown in Figures 5.7 and 5.8 with a grid size of 81×81 points across all propagators. While the GBM analysis did provide the overall shape of the interference pattern, it lacks the detail provided by the Fresnel approach. Figures 5.9 to 5.12 show the results of the physical optics analysis and since the coupling calculations (section 5.1.3) and mechanical tolerances (section 5.1.5) were to be calculated using physical optics grid sizes of 81×81 and 161×161 were investigated. For the same number of grid points as in the scalar case we can see slightly more structure and even more so when the number of points is increased to 161×161 . On inspection of the results it appears that 81×81 points is accurate to approximately a 1% to 2% level, however, in all further physical optics analyses the 161×161 was used to ensure a higher resolution.

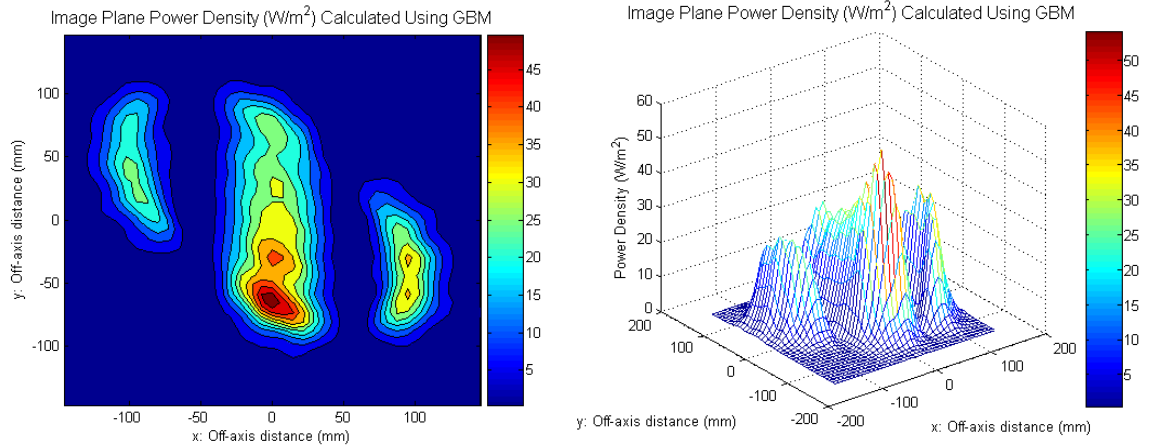


Figure 5.5 Power density of the field at the image plane calculated from a combination of Source 2 and Source 3 using Gaussian beam modes and a grid size of 41x41 points. The MODAL project was set to automatically choose the optimum numbers of orthogonal modes.

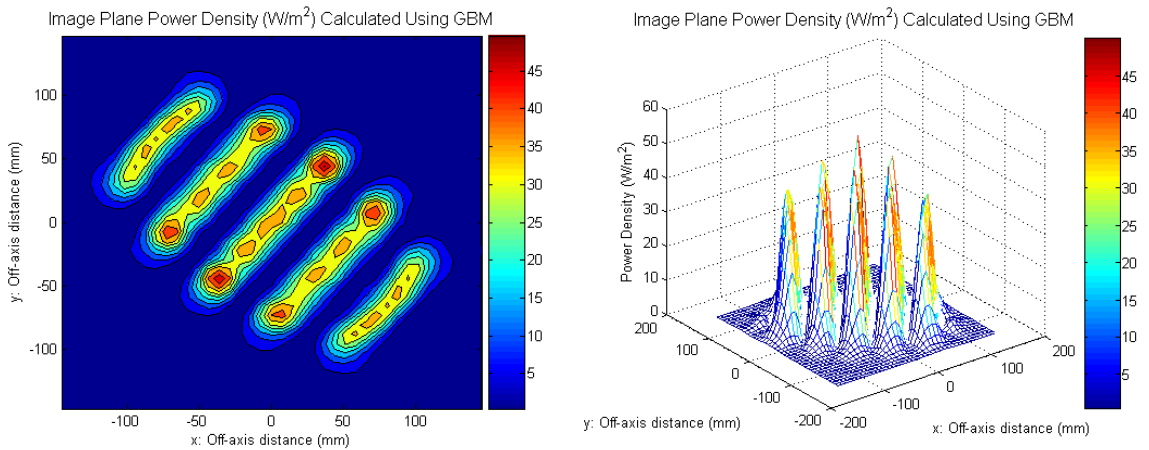


Figure 5.6 Power density of the field at the image plane calculated from a combination of Source 3 and Source 4 using Gaussian beam modes and a grid size of 41x41 points. The MODAL project was set to automatically choose the optimum numbers of orthogonal modes.

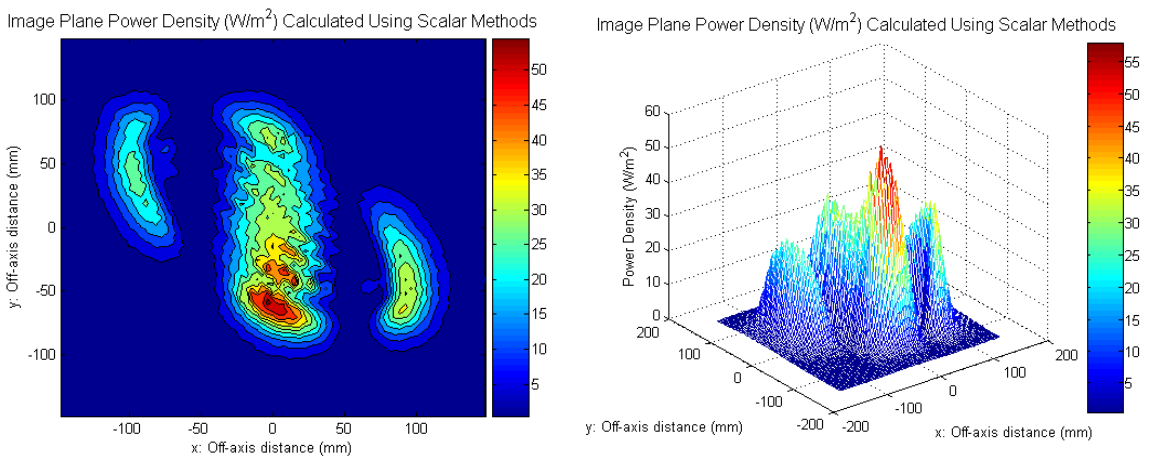


Figure 5.7 Power density of the field at the image plane calculated from a combination of Source 2 and Source 3 using Fresnel diffraction and a grid size of 81x81 points.

Image Plane Power Density (W/m^2) Calculated Using Scalar Methods

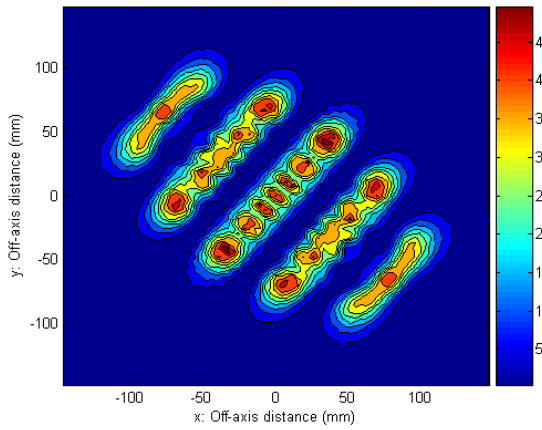


Image Plane Power Density (W/m^2) Calculated Using Scalar Methods

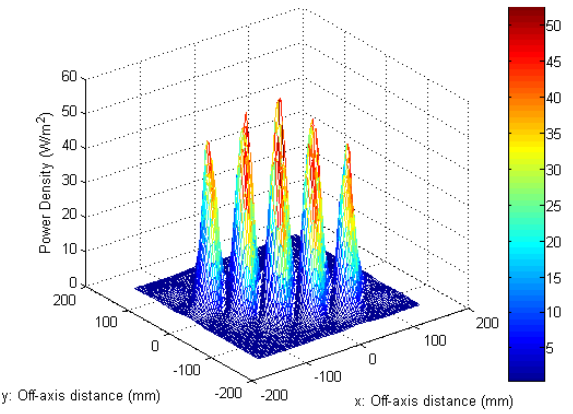


Figure 5.8 Power density of the field at the image plane calculated from a combination of Source 3 and Source 4 using Fresnel diffraction and a grid size of 81×81 points.

Image Plane Power Density (W/m^2) Calculated Using Physical Optics

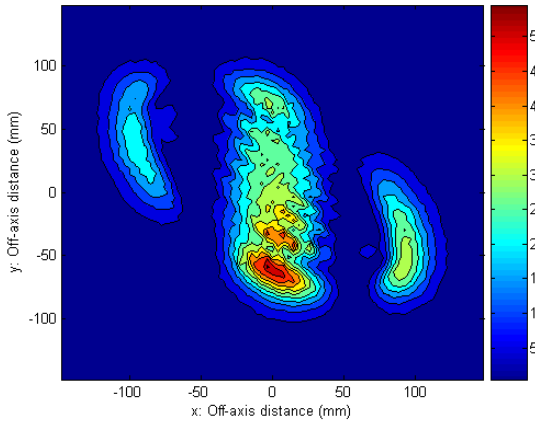


Image Plane Power Density (W/m^2) Calculated Using Physical Optics

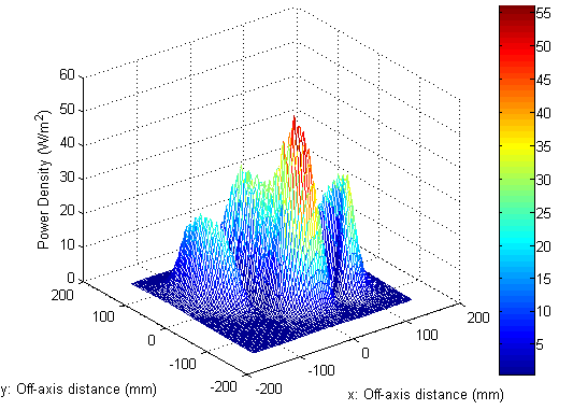


Figure 5.9 Power density of the field at the image plane calculated from a combination of Source 2 and Source 3 using physical optics and a grid size of 81×81 points.

Image Plane Power Density (W/m^2) Calculated Using Physical Optics

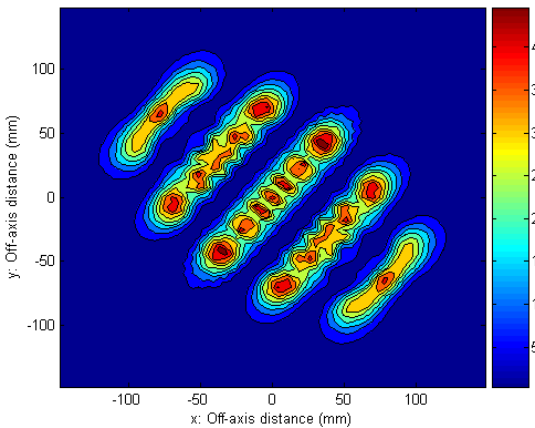


Image Plane Power Density (W/m^2) Calculated Using Physical Optics

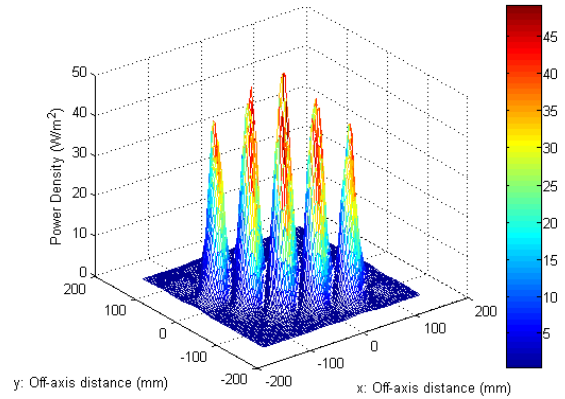


Figure 5.10 Power density of the field at the image plane calculated from a combination of Source 3 and Source 4 using physical optics and a grid size of 81×81 points.

Image Plane Power Density (W/m^2) Calculated Using Physical Optics

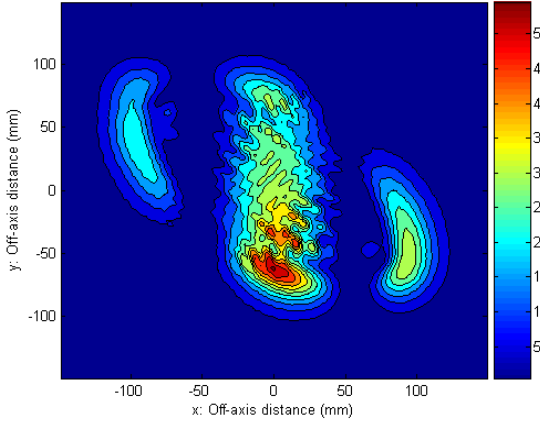


Image Plane Power Density (W/m^2) Calculated Using Physical Optics

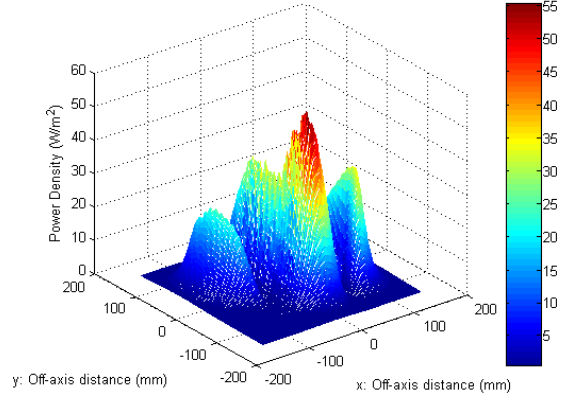


Figure 5.11 Power density of the field at the image plane calculated from a combination of Source 2 and Source 3 using physical optics and a grid size of 161x161 points.

Image Plane Power Density (W/m^2) Using Physical Optics

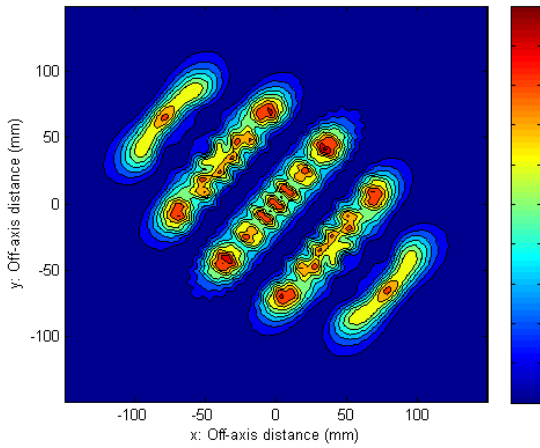


Image Plane Power Density (W/m^2) Using Physical Optics

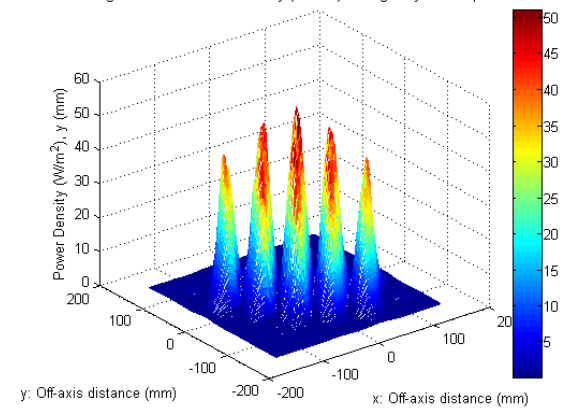


Figure 5.12 Power density of the field at the image plane calculated from a combination of Source 3 and Source 4 using physical optics and a grid size of 161x161 points.

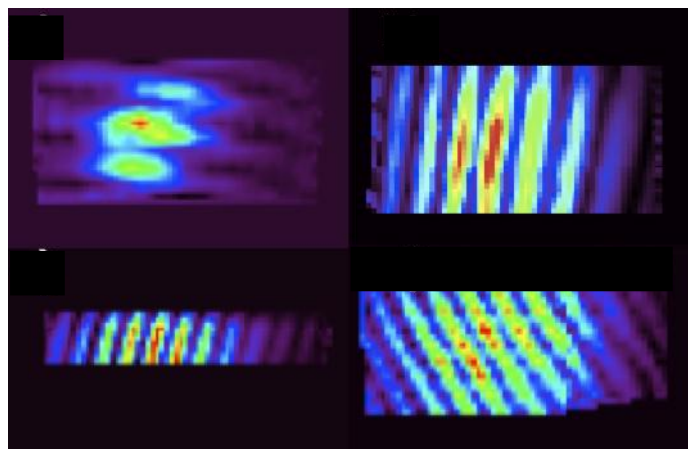


Figure 5.13 Fringes observed with the MBI-4 instrument in early 2009.

The results from Figures 5.11 and 5.12 can be compared with the fringes shown in Figure 5.13 as measured by MBI-4 during observations in early 2009. The interference patterns from measurements and simulations are shown for both a long and short baselines. It can be seen that the results are quite similar however for a fully detailed comparison the scanning strategy used during observations would also have to be taken into account in the model.

5.1.3 Calculating the System Scattering Matrix

Using MODAL we model the propagation of beams from the re-emitting (inward-facing) horn antennas onto the focal plane taking into account aberrations, diffraction, truncation and cross-polarisation effects in the beam combiner which, as illustrated by the previous figures, can be significant in systems such as MBI. As mentioned in the previous section, we can use a variety of propagation techniques for this modelling, from full vector physical optics (the same technique as the industry standard GRASP) to more approximate (although still good) and faster techniques such as Gaussian beam mode analysis. If the relative amplitude and phase for each of the four MBI re-emitting horn antennas is known, then by using these techniques the co-polar and cross-polar field amplitude and phase can be calculated at the focal plane, where they can be coupled to the detector horn antennas.

It was decided to use a scattering matrix formalism, outlined below, so that once the scattering matrix for the four horn antennas and beam combiner had been calculated it could be used to generate the field amplitude and phase at the focal plane for any combination of the input horns without having to retrace beams through the system. The coupling of the focal plane field to the detector horns in the MBI system is also included as this can be related directly to measurements. Having the scattering matrix available means it is very quick to predict the output for any given baseline or combination of baselines, since such an approach involves directly relating the output state of the system to the input state.

In the analysis on the MBI optical system presented here, the scattering matrix takes into account diffraction effects and truncation by the different optical components within the system by means of a full physical optics approach. By calculating the absolute amplitude and phase of the field at the detectors and relating this to the normalised input fields of the system the elements of the scattering matrix were generated.

In calculating the scattering matrix each source, or inward facing horn antenna, is coupled to each detector and the absolute amplitude A and phase ϕ of the field produced by the excited modes in the detector are obtained (we use the convention $Ae^{i\phi}$). This can be done for both co-polar and cross-polar fields. Having the amplitude and phase values, the scattering matrix takes the form

$$\begin{bmatrix} S_1 D_{U,(0,-2)} & S_2 D_{U,(0,-2)} & S_3 D_{U,(0,-2)} & S_4 D_{U,(0,-2)} \\ S_1 D_{V,(0,-2)} & S_2 D_{V,(0,-2)} & S_3 D_{V,(0,-2)} & S_4 D_{V,(0,-2)} \\ S_1 D_{U,(1,-2)} & S_2 D_{U,(1,-2)} & S_3 D_{U,(1,-2)} & S_4 D_{U,(1,-2)} \\ \cdot & \cdot & \cdot & \cdot \\ \cdot & \cdot & \cdot & S_4 D_{V,(n,m)} \end{bmatrix} \quad (5.1)$$

where S_a denotes Source a , $D_{U,(n,m)}$ denotes the co-polar element of detector (n, m) and $D_{V,(n,m)}$ denotes the cross-polar element of detector (n, m) . This scattering matrix is then multiplied by the input field matrix to give

$$\begin{bmatrix} S_1 D_{U,(0,-2)} & S_2 D_{U,(0,-2)} & S_3 D_{U,(0,-2)} & S_4 D_{U,(0,-2)} \\ S_1 D_{V,(0,-2)} & S_2 D_{V,(0,-2)} & S_3 D_{V,(0,-2)} & S_4 D_{V,(0,-2)} \\ S_1 D_{U,(1,-2)} & S_2 D_{U,(1,-2)} & S_3 D_{U,(1,-2)} & S_4 D_{U,(1,-2)} \\ \cdot & \cdot & \cdot & \cdot \\ \cdot & \cdot & \cdot & S_4 D_{V,(n,m)} \end{bmatrix} \begin{bmatrix} F_1 \\ F_2 \\ F_3 \\ F_4 \end{bmatrix} = \begin{bmatrix} F_{U,(0,-2)} \\ F_{V,(0,-2)} \\ \cdot \\ \cdot \\ F_{V,(n,m)} \end{bmatrix} \quad (5.2)$$

where each of the source fields F_n is again described in the form $Ae^{i\phi}$. The overall power for each detector, taking into account both the co-polar and cross-polar coupling, can then be calculated by

$$P_{Total,(n,m)} = |F_{U,(n,m)}|^2 + |F_{V,(n,m)}|^2. \quad (5.3)$$

We can easily change the source field and calculate the output at each detector for this new input. Also, by setting the input field for a particular horn antenna equal to zero we can turn on and off that source, allowing for easy field calculations resulting from different baselines.

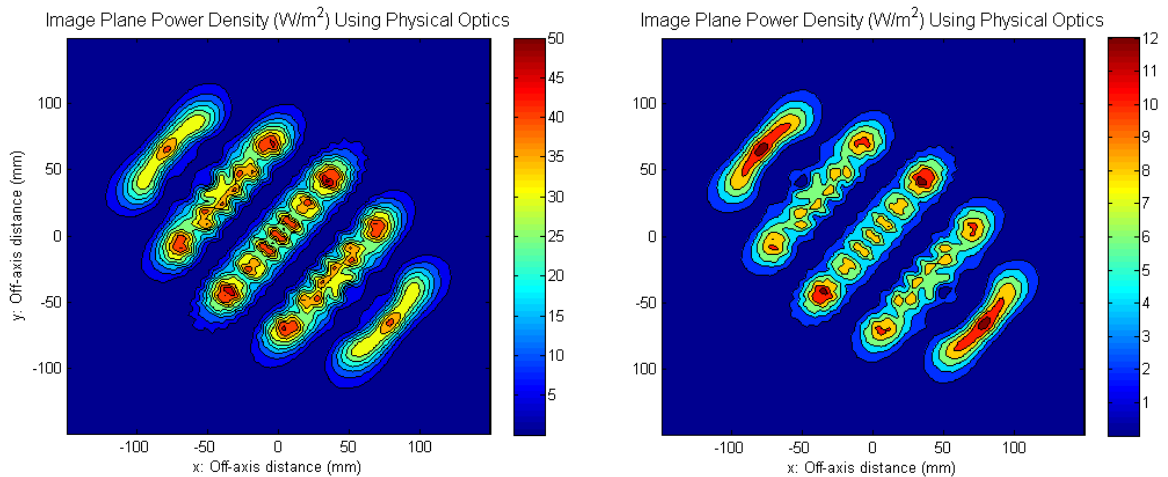


Figure 5.14 Interference pattern obtained using the real inward-facing corrugated horn antenna (left) and a corrugated horn antenna simulated by a Bessel function (right). The difference in power is because the real horn is set to 1W in the throat and not at the aperture as with the Bessel horn.

Referring back to Figure 5.2 there are four back-to-back horn antennas that pass the beam from the sky into the optical system. In our analysis we take only the inward facing horn antennas and treat them as equivalent corrugated conical horns whose field can be very well represented by a Bessel function, as demonstrated in Chapter 3. The radius of each horn was defined as 22.45mm and the phase front radius of curvature at the aperture was set to infinity, since in the real system there are phase-flattening lenses attached to the front of each antenna. The output field from the horns was propagated through the optical system described in section 5.1.1, taking into account any truncation that occurred at the primary and secondary surfaces before being coupled to the detector horn antenna array, of which the layout and numbering used in the scattering matrix calculations is shown in Figure 5.4. Figure 5.14 shows the interference pattern at the image plane produced by a model of the real inward-facing corrugated horn antenna (using the SCATTER code) used in MBI and that produced by a standard corrugated horn antenna whose aperture

field is represented by a Bessel function. It can be seen that the two are in very good agreement although there is a difference in some of the fine structure.

Within the detector array the nineteen detector horns were defined as smooth-walled conical horn antennas with a radius of 12.7mm (0.5in) which produced a field with a phase front radius of curvature of 54.3mm. However, lenses designed at NUI Maynooth (Lavelle, 2008) were attached to the apertures of each of the detector horns to flatten the phase and therefore in the modelling process the curvature of the field at the aperture of the detectors was set to infinity. Having carried out a full physical optics analysis the calculated amplitudes and phases of the elements in the scattering matrix of Equation 5.1 can be seen in Appendix A. Figures 5.15 and 5.18 show the coupling efficiencies of the four inward-facing horn antennas to the detector horns, a measure of how well the field incident on the aperture of a single detector couples to the fundamental mode in that detector. This is calculated using the equation,

$$\varepsilon = \frac{\left| \int_S \Psi_{IN} \Psi_D^* dS \right|^2}{\int_S \Psi_{IN} \Psi_{IN}^* dS \cdot \int_S \Psi_D \Psi_D^* dS} = \frac{|P_M|^2}{P_{IN} \cdot P_D} \quad (5.4)$$

where Ψ_{IN} is the incident field, Ψ_D is the detector field, S is the surface over which the coupling is calculated, P_M is the power common to both the incident and detector fields, P_{IN} is the power in the incident field over the coupling surface and P_D is the power in the detector field. In Figure 5.15 the polarisation direction of the field emitted from the four sources is parallel to the shortest baseline, that is the baseline formed by sources 2 and 3, while in Figure 5.18, the polarisation direction is perpendicular to this. In each case, both the co-polar and cross-polar fields have been calculated.

The amplitude and phase of the field coupled to the detector horns was calculated using the equations,

$$|A_{coupled}| = \frac{\left| \int_S \Psi_{IN} \Psi_D^* dS \right|}{\int_S \Psi_D \Psi_D^* dS} = \frac{|P_M|}{P_D} \quad (5.5)$$

$$\phi_{coupled} = \left(\int_S \Psi_{IN} \Psi_D^* dS \right) = \arg(P_M) \quad (5.6)$$

and since the field at the aperture of each of the inward-facing horn antennas was normalised with a power of 1W and a flat phase, that is $A = 1$ and $\phi = 0$ using the $Ae^{i\phi}$ convention, the field at the detector horns was simply equal to the amplitude and phase of the elements of the scattering matrix. From these the total power coupled to the detectors was evaluated using Equation 5.3. For each of the detectors, the total power coupled from each source is shown in Figures 5.19 and 5.20 for both polarisation directions.

Table 5.3 shows the power coupled to each of the nineteen detector horn antennas as calculated using Equation 5.3, that is, the total from both the co- and cross-polar fields (as plotted). If the power over all detectors is summed for each source and it is known that each source was normalised with an initial power of 1W, it can be seen that the coupled power is between 2% and 3% of that injected into the optical system from each source. Also, if we look again at both the coupled power and the coupling efficiencies there is a significant difference for both polarisation directions examined. This can be explained by the asymmetry in the field of the smooth-walled conical detector horn. If, for example, we consider the simple case of a single source with a polarisation direction parallel to a line of detectors at the image plane, then the detectors will measure the equivalent of a cut along the E_x field, as in part (a) of Figure 5.16. If however the polarisation direction of both the source and the detectors is rotated by 90°, measurements by the detectors will be the equivalent of a cut along the E_y field of the source, as in part (b) of Figure 5.16.

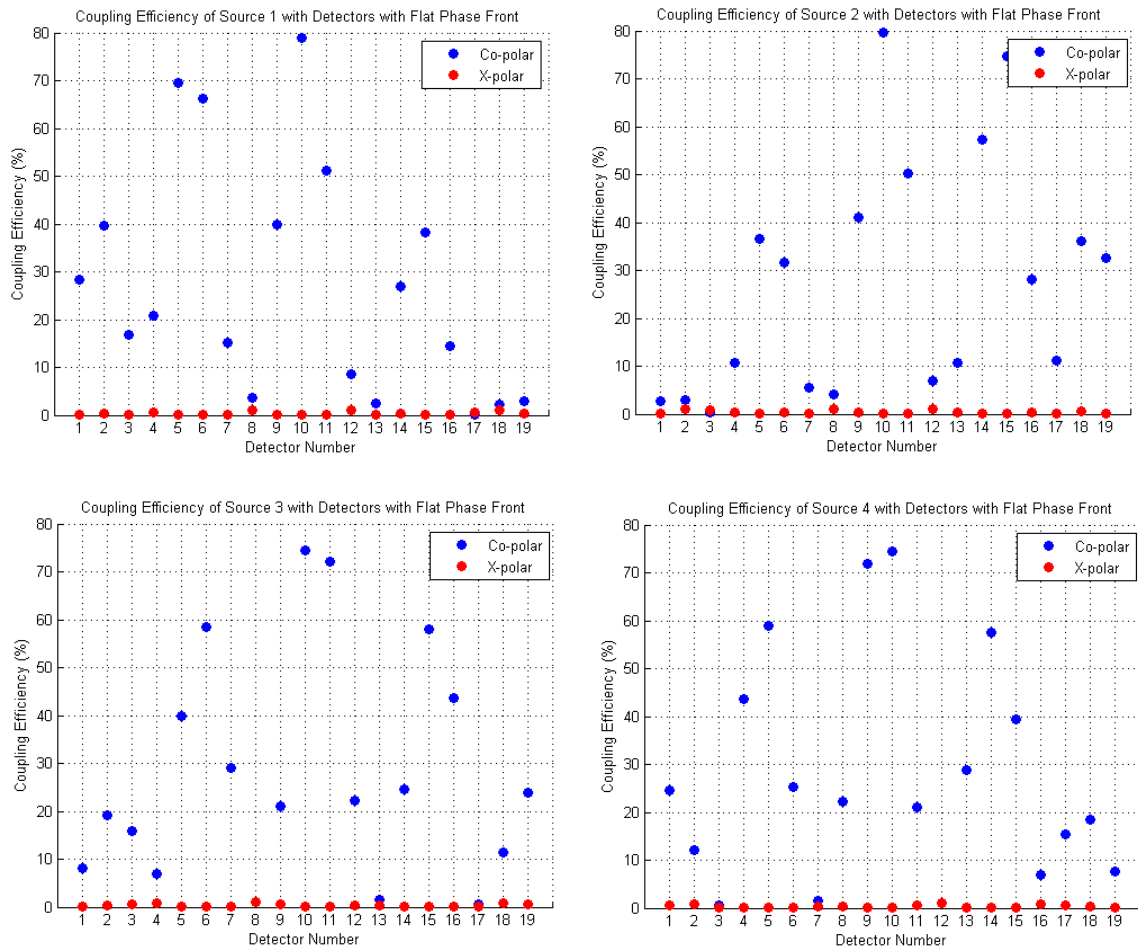


Figure 5.15 Coupling efficiencies of each inward-facing source with the detector horn antennas. The polarisation direction of the sources is parallel to the shortest baseline of the system.

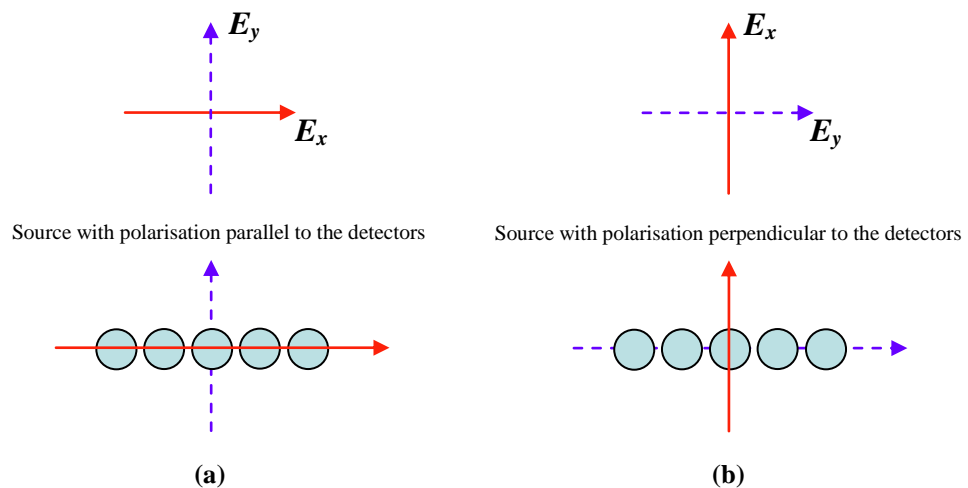


Figure 5.16 Schematic diagram showing a plane wave source polarised (a) parallel and (b) perpendicular to the line of detectors. The solid line represents the polarisation direction and in both cases the detectors are polarised in the same direction as the source.

To test this hypothesis a simple model was set up whereby the source used was a plane wave and the detector was a smooth-walled conical horn antenna from the MBI-4 system. The line of detectors was simulated by scanning the source along a single plane. A physical optics analysis was carried out and the power coupled to the detector was calculated at each point for the two orthogonal polarisation directions described above (both the source and the detectors were polarised in the same direction). The results of this can be seen in Figure 5.17 where the asymmetry in the resulting field can be seen, giving rise to the differences in both coupling efficiency and total coupled power for difference polarisation directions in MBI-4 (the plot mirrors orthogonal cuts through the conical horn beam pattern). In reality the detector array does not lie along the direction of polarisation and therefore each detector measures a combination of both the E_x and E_y fields, depending on its location in the array.

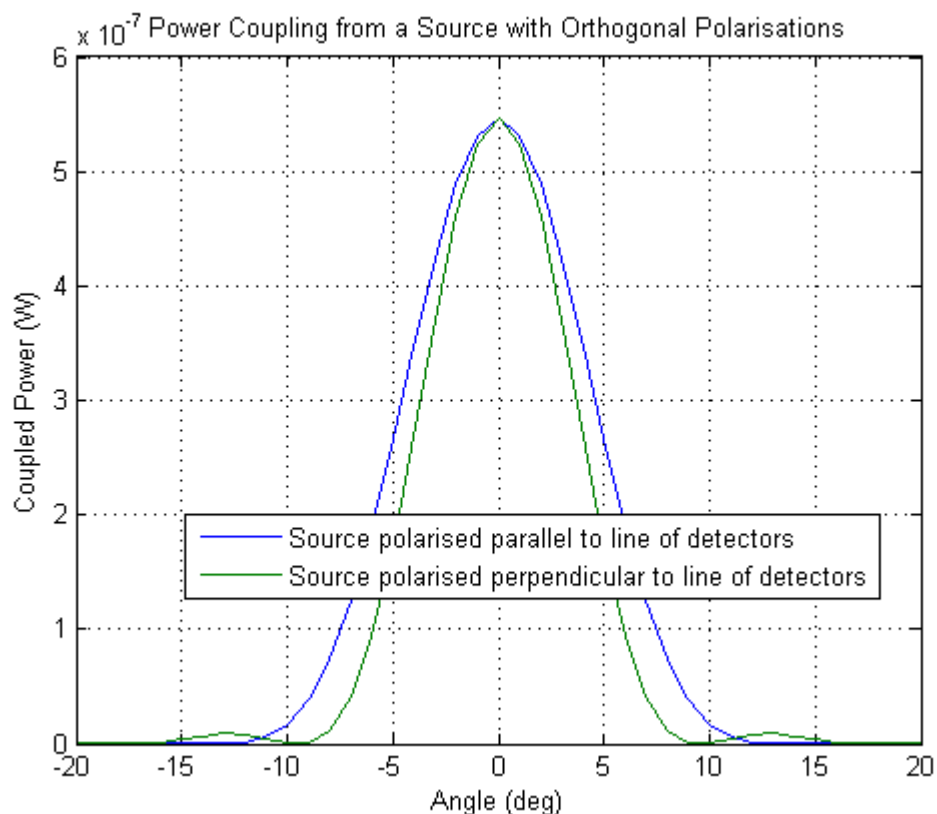


Figure 5.17 Power coupled to a smooth-walled conical horn detector for a plane wave source polarised parallel (red) and perpendicular (blue) to the line of detectors as in Figure 5.16. In both cases the detector was polarised in the same direction as the source.

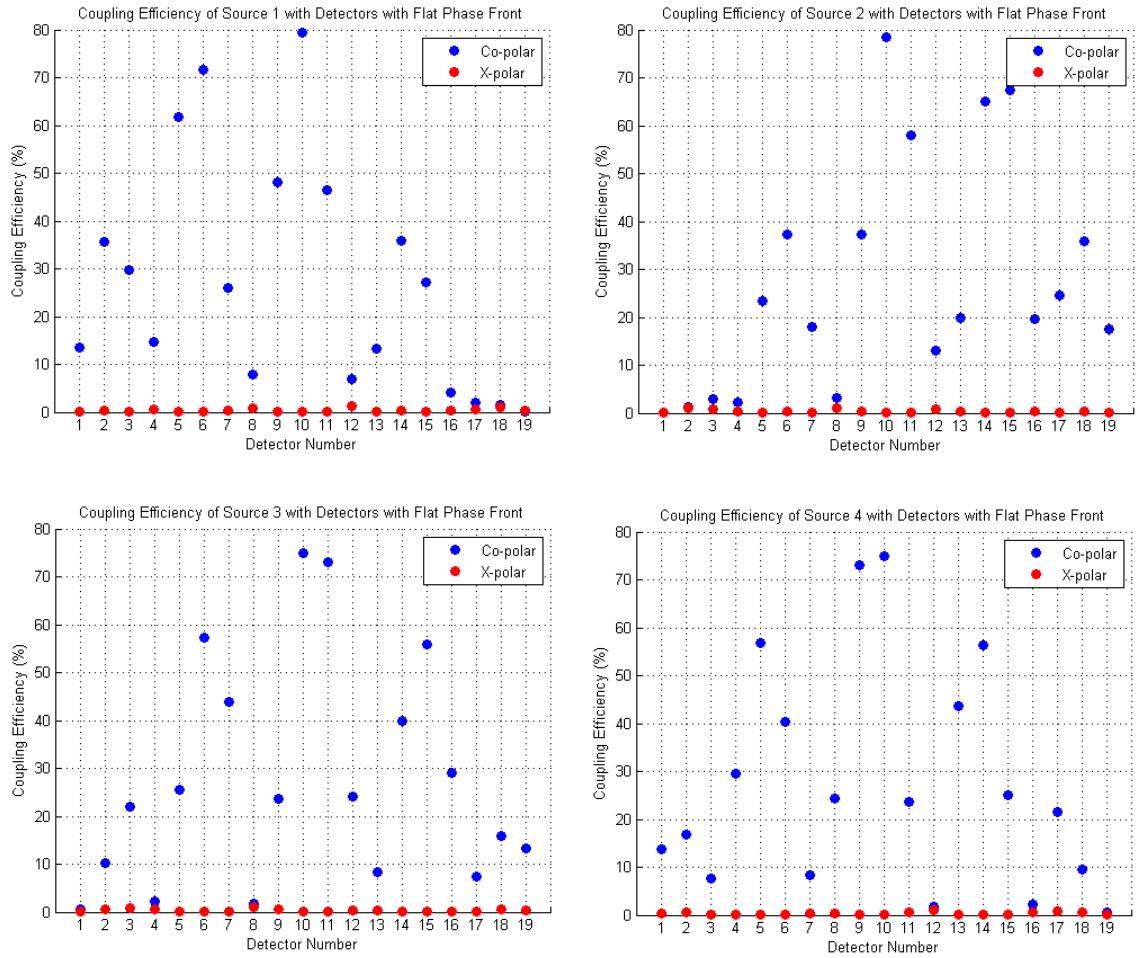


Figure 5.18 Coupling efficiencies of each inward-facing source with the detector horn antennas. The polarisation direction of the sources is perpendicular to the shortest baseline of the system.

In an ideal system the total power from the inward-facing horn antennas would be collected by the detector array, however truncation of the beam at the optical components and inefficient coupling to the smooth-walled conical horns contribute to the loss in power and must be accounted for, which is the subject of the next section (section 5.1.4). However, before looking at truncation effects it was interesting to investigate exactly what effect the detector horn phase-flattening lenses had on the overall performance of the system and hence the scattering matrix. To do this the phasefront radius of curvature of each of the smooth-walled conical horns was set to 54.3mm, the curvature the field would have in the absence of a dielectric lens. Figure 5.21 shows the coupling efficiencies of each of the four sources and the detector array with the polarisation direction of the inward-facing horns being

parallel to the shortest baseline. In Figure 5.22 the polarisation direction is perpendicular to this.

In Table 5.4 the total power from each source coupled to each of the detectors is shown for both polarisation directions. As with the case with lenses present, both polarisation directions exhibit significant differences in terms of power coupling, again due to the asymmetry in the smooth-walled conical horn field. From the table it can be seen that the total power coupled to the detector array from each of the inward-facing sources lies approximately between 1% and 2%, which is less than that obtained with detector lenses present. Although the overall coupling is quite low in both cases, having the lenses in place represents approximately a 30% increase in power coupled to the detectors, a significant and important improvement for a bolometric interferometer.

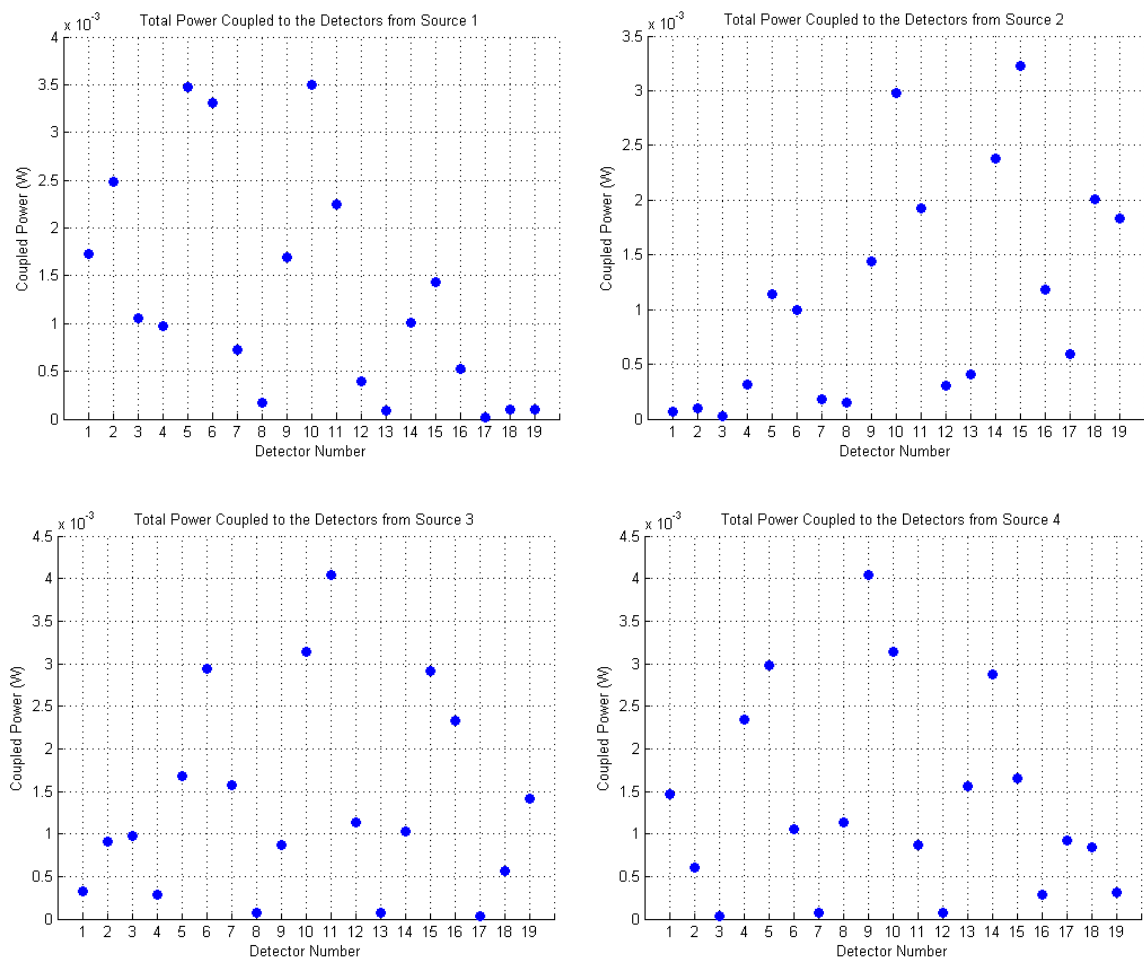


Figure 5.19 The total coupled power at each detector from each of the four inward-facing horn antennas with a polarisation direction parallel to the shortest baseline.

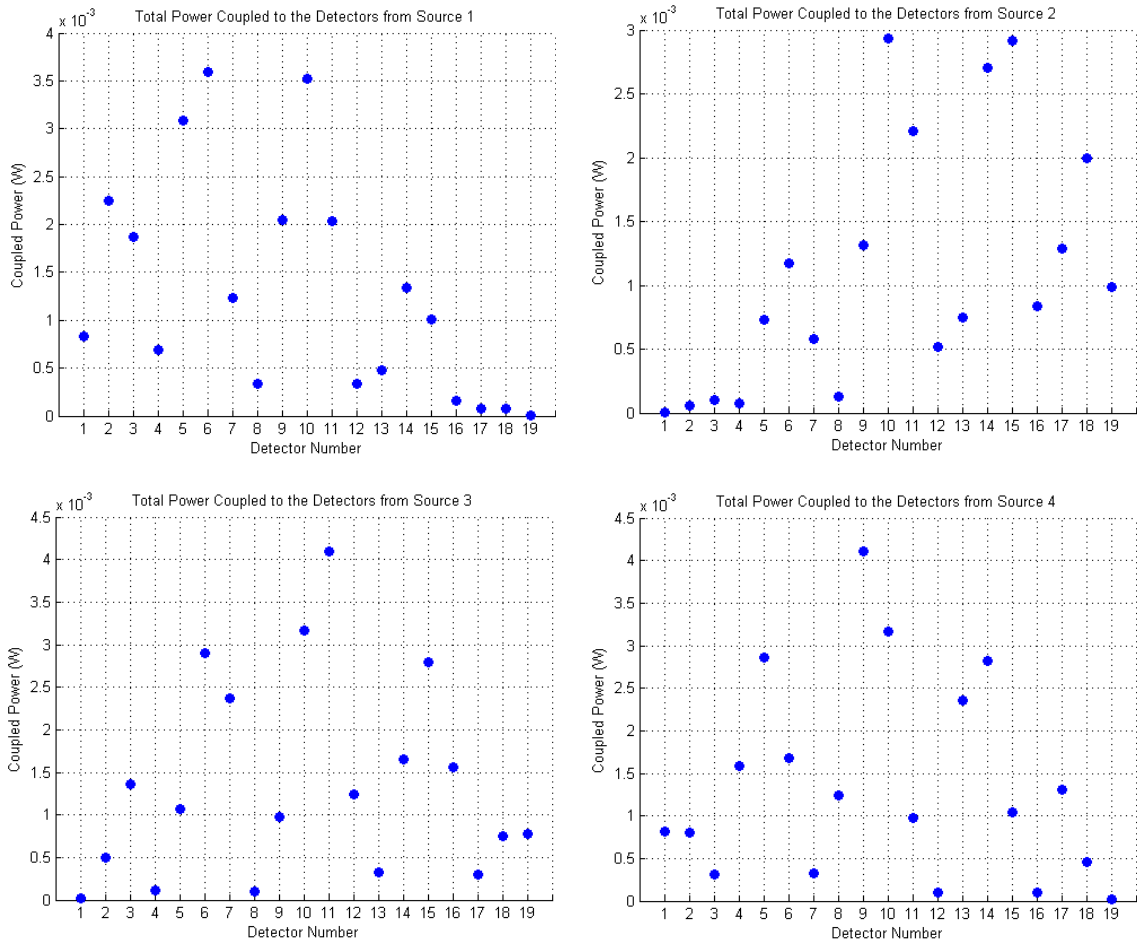


Figure 5.20 The total coupled power at each detector from each of the four inward-facing horn antennas with a polarisation direction perpendicular to the shortest baseline.

Total Power (mW) Coupled to the Detector Horn Antennas from Each of the Sources								
Detector	Parallel Polarisation				Perpendicular Polarisation			
	Source1	Source2	Source3	Source4	Source1	Source2	Source3	Source4
1	1.7295	0.0683	0.3218	1.4695	0.8307	0.0068	0.0246	0.8211
2	2.4827	0.1023	0.9031	0.5998	2.2446	0.0591	0.5003	0.7981
3	1.0587	0.0259	0.9707	0.0339	1.8735	0.0996	1.3541	0.3129
4	0.9788	0.3200	0.2914	2.3416	0.6925	0.0776	0.1107	1.5808
5	3.4778	1.1414	1.6742	2.9794	3.0829	0.7290	1.0727	2.8605
6	3.3135	0.9933	2.9468	1.0528	3.5893	1.1714	2.8962	1.6839
7	0.7213	0.1781	1.5710	0.0708	1.2275	0.5803	2.3643	0.3302
8	0.1717	0.1493	0.0691	1.1334	0.3338	0.1285	0.0948	1.2392
9	1.6975	1.4389	0.8672	4.0372	2.0489	1.3134	0.9771	4.1034
10	3.5024	2.9813	3.1459	3.1454	3.5209	2.9371	3.1680	3.1646
11	2.2450	1.9206	4.0421	0.8695	2.0399	2.2123	4.0982	0.9728

12	0.3956	0.3005	1.1370	0.0697	0.3389	0.5141	1.2360	0.0941
13	0.0916	0.4054	0.0668	1.5533	0.4798	0.7462	0.3262	2.3510
14	1.0095	2.3791	1.0259	2.8766	1.3355	2.7019	1.6583	2.8230
15	1.4296	3.2305	2.9080	1.6484	1.0124	2.9203	2.7931	1.0445
16	0.5285	1.1826	2.3317	0.2880	0.1537	0.8335	1.5649	0.1055
17	0.0185	0.5981	0.0299	0.9290	0.0752	1.2899	0.2973	1.3011
18	0.0999	2.0125	0.5598	0.8479	0.0770	1.9976	0.7477	0.4626
19	0.1012	1.8337	1.4163	0.3059	0.0097	0.9908	0.7829	0.0206
Total	25.053	21.262	26.279	26.252	24.967	21.310	26.068	26.070

Table 5.3 The power coupled to the detectors from each of the inward-facing horn antennas with polarisation parallel and perpendicular to the shortest baseline.

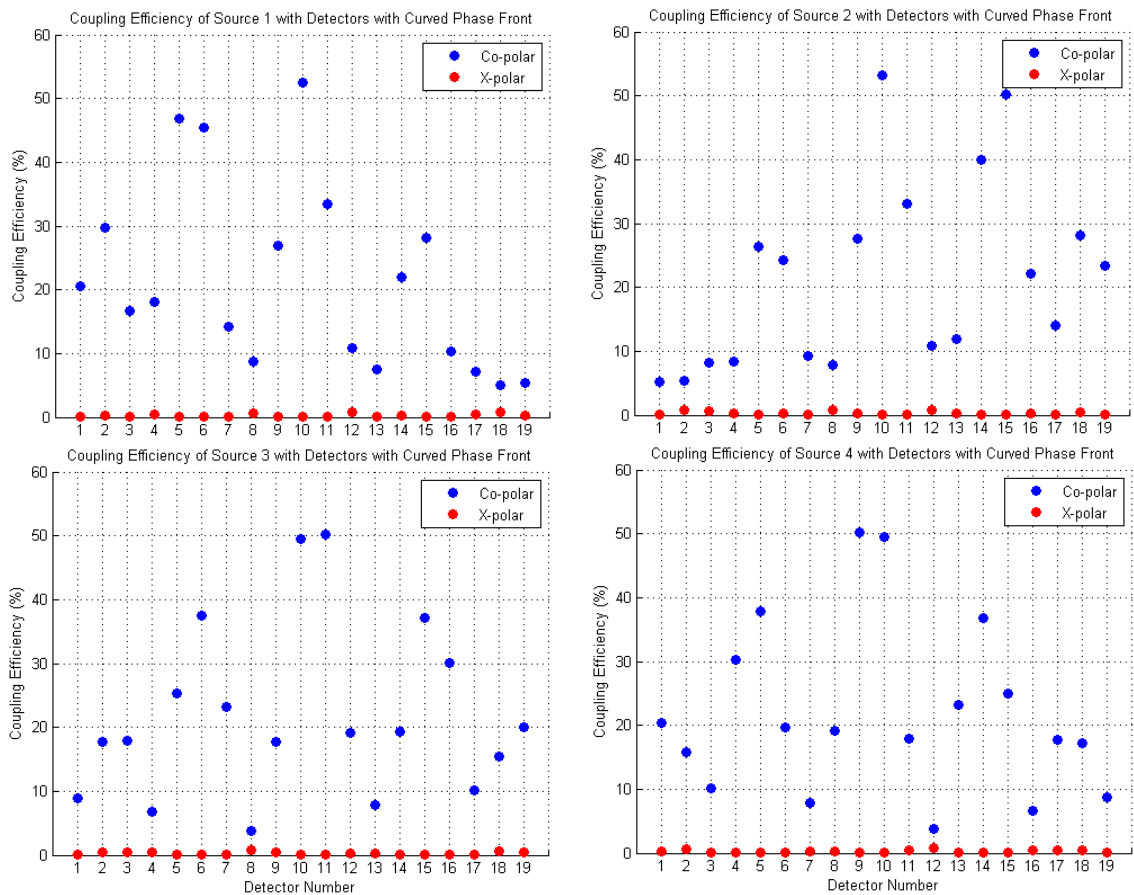


Figure 5.21 Coupling efficiencies of each inward-facing source with the detector horn antennas. The phase-flattening lenses have been removed and the polarisation direction of the sources is parallel to the shortest baseline of the system.

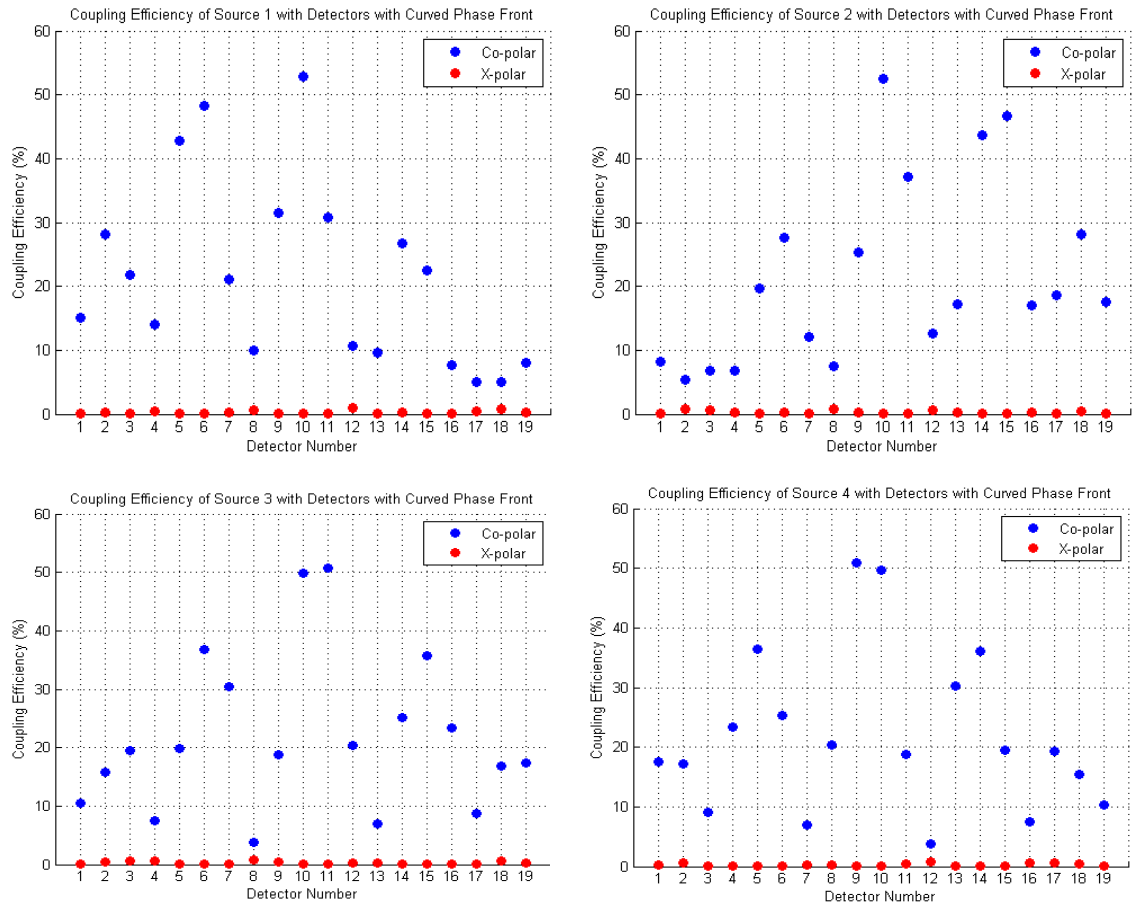


Figure 5.22 Coupling efficiencies of each inward-facing source with the detector horn antennas. The phase-flattening lenses have been removed and the polarisation direction of the sources is perpendicular to the shortest baseline of the system.

Total Power (mW) Coupled to the Detector Horn Antennas from Each of the Sources								
Detector	Parallel Polarisation				Perpendicular Polarisation			
	Source1	Source2	Source3	Source4	Source1	Source2	Source3	Source4
1	1.2580	0.1233	0.3582	1.2108	0.9267	0.1968	0.4179	1.0404
2	1.8653	0.1554	0.8394	0.7543	1.7689	0.1566	0.7461	0.8213
3	1.0456	0.2311	1.0903	0.4091	1.3716	0.1915	1.1899	0.3658
4	0.8477	0.2514	0.2778	1.6272	0.6564	0.2063	0.3061	1.2570
5	2.3406	0.8214	1.0572	1.9122	2.1395	0.6123	0.8296	1.8381
6	2.2764	0.7642	1.8916	0.8232	2.4178	0.8680	1.8583	1.0564
7	0.6747	0.2953	1.2526	0.3098	0.9933	0.3853	1.6445	0.2779
8	0.3599	0.2545	0.1541	0.9772	0.4082	0.2470	0.1494	1.0400
9	1.1514	0.9714	0.7332	2.8170	1.3447	0.8951	0.7764	2.8538

10	2.3350	1.9934	2.0908	2.0914	2.3434	1.9654	2.1048	2.1013
11	1.4670	1.2656	2.8200	0.7340	1.3505	1.4209	2.8507	0.7741
12	0.4809	0.4305	0.9805	0.1543	0.4754	0.4973	1.0372	0.1491
13	0.2696	0.4477	0.3052	1.2450	0.3498	0.6457	0.2714	1.6289
14	0.8234	1.6618	0.8066	1.8463	0.9976	1.8114	1.0446	1.8108
15	1.0500	2.1702	1.8661	1.0449	0.8418	2.0177	1.7946	0.8126
16	0.3798	0.9311	1.6155	0.2709	0.2833	0.7198	1.2499	0.3013
17	0.2215	0.7410	0.4050	1.0678	0.1574	0.9762	0.3559	1.1583
18	0.1716	1.5630	0.7215	0.7980	0.1751	1.5683	0.7822	0.7128
19	0.1724	1.3227	1.1792	0.3478	0.2549	0.9917	1.0202	0.4132
Total	19.191	16.395	20.445	20.441	19.256	16.373	20.430	20.413

Table 5.4 The power coupled to the detectors from each of the inward-facing horn antennas with polarisation parallel and perpendicular to the shortest baseline. The phase-flattening lenses have been removed from the detectors in these calculations.

5.1.4 The Effects of Truncation on the System

For this truncation analysis the configuration of the MBI system model was the same as that described in the previous section with flat fields from the inward-facing horn antennas being represented by Bessel functions and the phase-flattening lenses attached to the smooth-walled horn antennas within the detector array. Having previously calculated the power coupled to the detectors from each of the four sources it was apparent that the performance of the instrument is inhibited by truncation of the beam as it propagates through the optical system. To analyse this truncation the relative power in the beam was calculated at different points along the path of propagation, the results of which are summarised in Table 5.5 for each polarisation direction considered.

The first element that lies in the path of the beam as it propagates through the system is the secondary mirror, which as shown in Table 5.5 has almost no effect on the beam. After reflection from the primary mirror (Prim_Ref in Table 5.5) the power from sources 1 and 2 drop below 90% of the original source power while for Sources 3 and 4 approximately 92% of the power remains. This drop in power is predominantly due to truncation by the primary's elliptical aperture as shown in

Figure 5.23 for Source 1 (Appendix B shows the full range of beam plots for each of the four sources with parallel polarisation as they propagate through the optical system). Most of the power is retained as the beams are reflected off the secondary mirror and propagate towards the primary. However, a significant percent of power is not transmitted through the hole in the primary but is reflected by the primary mirror (the power profile for Source 1 with parallel polarisation at the elliptical aperture of the primary mirror is shown in Figure 5.24). At this stage the power is as low as 24% of the original power emitted from the inward-facing horn antennas. With no more obstacles in the path of the beam as it propagates towards the image plane this power is retained as the fields arrive at the detector array.

Relative Beam Power at Different Elements in the Optical System								
	Parallel Polarisation				Perpendicular Polarisation			
	Source 1	Source 2	Source 3	Source 4	Source 1	Source 2	Source 3	Source 4
Source	1.0000	1.0000	1.0000	1.0000	1.0000	1.0000	1.0000	1.0000
Sec_Tran	0.9998	0.9998	0.9999	0.9999	0.9998	0.9998	0.9999	0.9999
Prim_Ref	0.8981	0.8408	0.9242	0.9240	0.8981	0.8408	0.9242	0.9240
Sec_Ref	0.8741	0.8108	0.8944	0.8942	0.8741	0.8108	0.8944	0.8942
Prim_Tran	0.2791	0.2386	0.2973	0.2972	0.2791	0.2386	0.2973	0.2972
Image	0.2752	0.2353	0.2931	0.2930	0.2752	0.2353	0.2931	0.2930

Table 5.5 Relative (to the source) power contained in the beam at various stages of propagation through the optical system. *Source* is the power at the aperture of the inward-facing horn antenna, *Sec_Tran* represents transmission of the beam as it passes the secondary mirror, *Prim_Ref* and *Sec_Ref* refer the beam after reflection from the primary and secondary mirrors respectively, *Prim_Tran* is the portion of the beam that propagates through the aperture after reflection from the secondary mirror and *Image* represents the beam at the plane of the detector array.

In the previous section we saw that between 2% and 3% of the power from each of the inward-facing corrugated horn antennas was being coupled to the detectors. However, examination of the effects of truncation and the power retained through each propagation stage yields a value of approximately 24% to 28% of the original source power being transferred to the detector array. From this it can be deduced that the remainder of the power is being lost due to the fact that the smooth-walled conical detector horns are arranged in an array in which there are inevitably

spaces between these horns and therefore the power is not being collected. Poor coupling to the detector horn fields also contributes to this power loss. The power from each polarisation direction is also extremely similar at each element in the system, including the focal plane, which again confirms that the effects of different polarisation directions will only be evident in the coupling to the detectors.

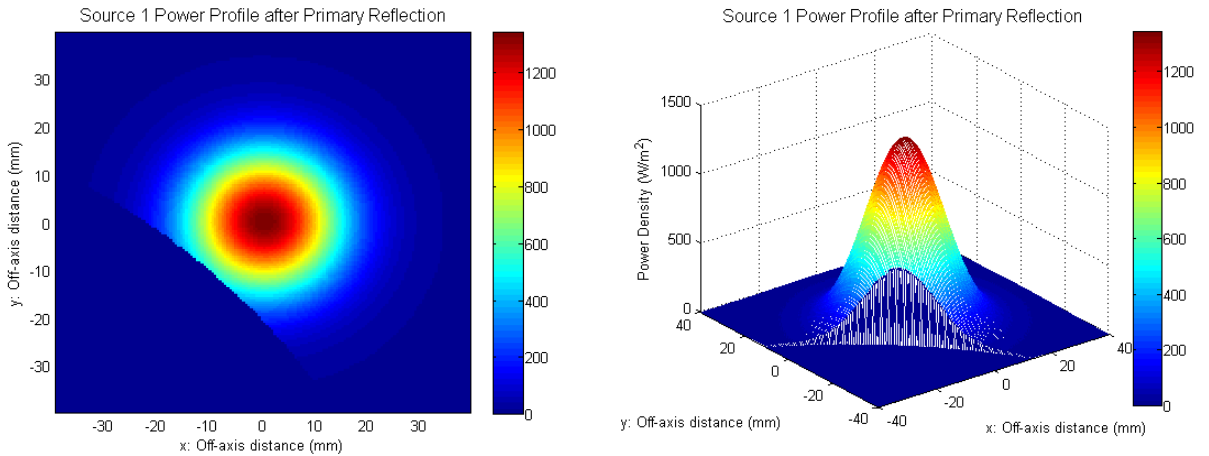


Figure 5.23 The power profile of the beam from the Source 1 inward-facing horn antenna after reflection from the primary mirror with polarisation parallel to the shortest baseline.

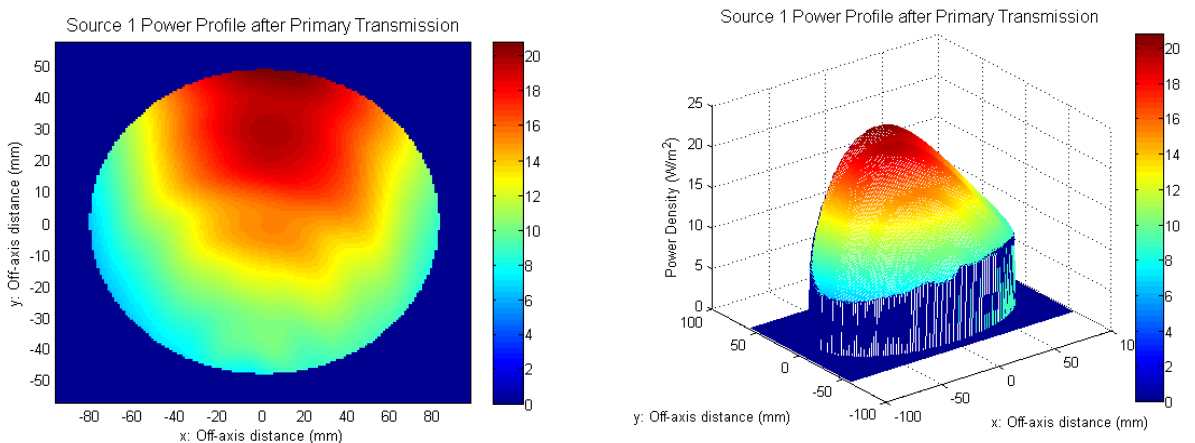


Figure 5.24 The power profile of the beam from the Source 1 inward-facing horn antenna after transmission through the aperture of the primary mirror. The frame used in the plots is that of the primary aperture.

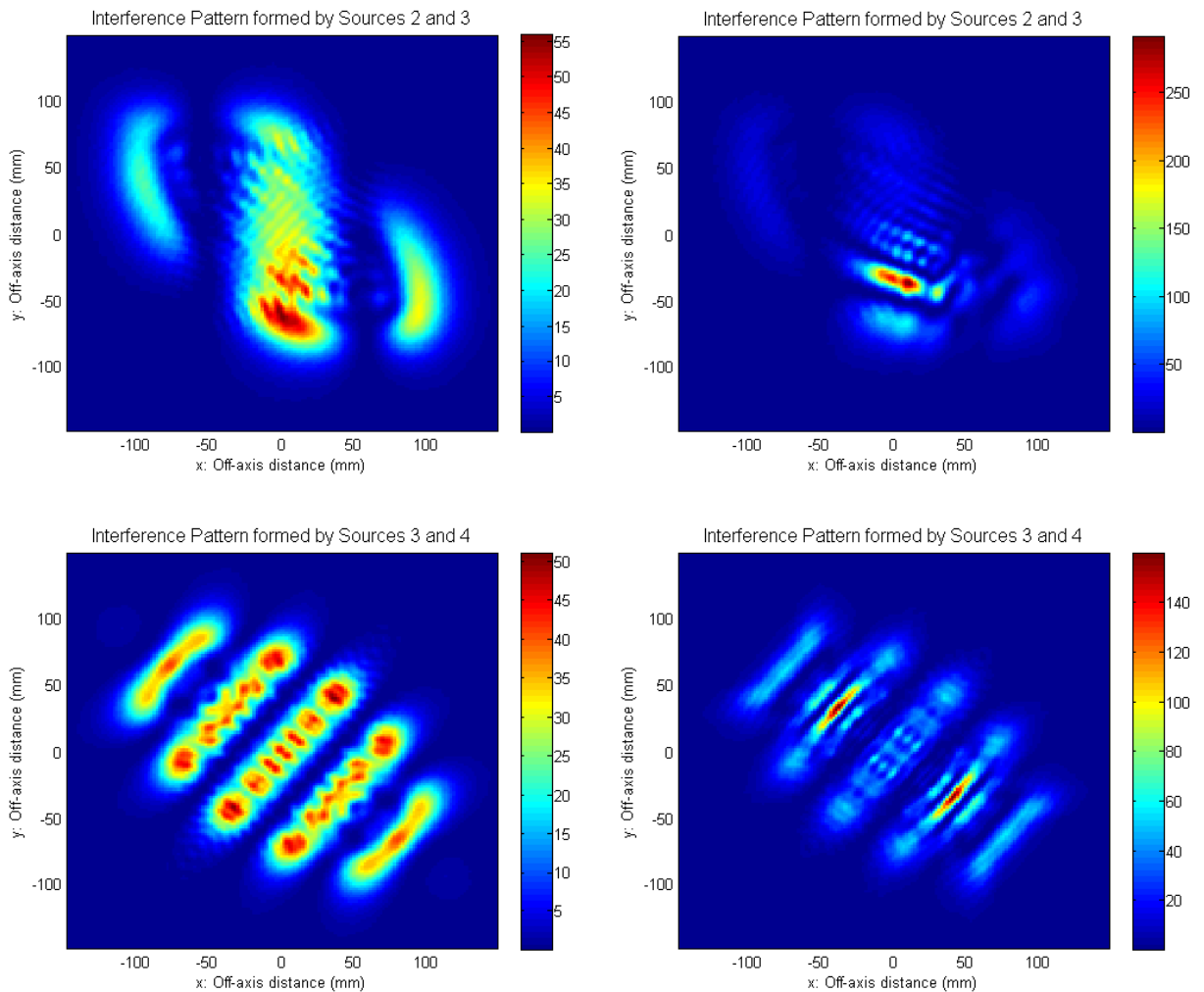


Figure 5.25 The top two images show the interference patterns generated by sources 2 and 3 with (top right) and without (top left) the beam that passes through the primary after secondary transmission taken into account. The bottom two images show the same for the longest baseline formed by sources 3 and 4.

It has been shown above that as the beam from each source is reflected from the primary mirror approximately 10% to 15% of the power is transmitted through the elliptical aperture (rather than being reflected) where it will continue to propagate to the detector array. This portion of the field will interact with that transmitted after reflection from the secondary mirror and hence have an effect on the overall field that is incident on the detector horn antennas. In Figure 5.25 we can see that the interference pattern obtained at the image plane is significantly different when this extra field is accounted for to that obtained when it is assumed that the only beam arriving at the detectors is that from the secondary mirror.

Total Power (mW) Coupled to the Detector Horn Antennas from Each of the Sources				
Polarisation Parallel to Shortest Baseline				
Detector	Source 1	Source 2	Source 3	Source 4
1	0.9778	0.0716	0.3271	1.4714
2	1.5180	0.1088	0.9217	0.5953
3	0.5179	0.0230	1.0780	0.0358
4	1.1620	0.3193	0.2887	1.1817
5	3.9958	1.0706	1.6622	2.8246
6	13.2684	0.8933	2.8325	1.0084
7	3.8296	0.1985	0.4571	0.0690
8	0.1682	0.1440	0.0694	8.4032
9	2.2641	1.5277	0.8641	4.4409
10	5.6832	5.0082	3.1402	3.1339
11	3.0760	0.8529	4.4489	0.8664
12	0.2108	1.0256	8.2609	0.0699
13	0.0901	0.2909	0.0652	0.4191
14	0.9219	0.1171	0.9822	2.8199
15	1.2078	24.4510	2.7894	1.6389
16	0.5624	7.3214	1.1074	0.2854
17	0.0212	0.9931	0.0319	1.0531
18	0.1052	2.6315	0.5645	0.8682
19	0.0986	6.2659	1.4466	0.3116
Total	39.6790	53.3145	31.3380	31.4968

Table 5.6 The power coupled to the detectors from each of the inward-facing horn antennas with polarisation parallel to the shortest baseline. The phase-flattening lenses are accounted for and the portion of the beam that passes through the primary aperture after secondary transmission is included.

Since the field at the image plane will change by taking into account the truncation effect by the primary mirror elliptical aperture, the overall scattering matrix for the system will change also. To see to what extent this occurs the coupling calculations were carried out again and hence a new scattering matrix was calculated. From this, and the fact that the inward-facing horn antennas were normalised to a known amplitude and phase, the total power coupled to each detector was again calculated. The results of these calculations are summarised in Table 5.6. Polarisation perpendicular to the shortest baseline has not been considered in this analysis.

The difference in the total power coupled to the detectors is significant when the beam passing straight through the elliptical aperture after transmission from the secondary is taken into account, with an increase of approximately 102%, 157%, 20% and 21% for each of sources 1, 2, 3 and 4 respectively compared to that obtained in the previous section. However, although the level of power being collected by the detector array has increased, it is not necessarily a desirable signal. If we look at the portions of the beam that pass through the aperture of the primary mirror after transmission from the secondary, and propagate these fields onto the detector array, as shown in Figure 5.26, it can be seen that there is very little overlap between the fields from the four sources. Phase sensitive detection could therefore be used to separate the signal that results from the interference between two sources, and that which comes directly from one. Looking at the fields arising from sources 2 and 3 we can see that the overlap is more significant than the overlap between sources 3 and 4. This should indicate that the interference pattern generated by the short baseline of sources 2 and 3 will be more affected by this signal than the long baseline of sources 3 and 4. Referring back to Figure 5.25 we can see that this is indeed the case. The field from the short baseline contains very little of the original structure while that from the long baseline remains more similar.

5.1.5 Mechanical Tolerances in MBI-4

We have seen in the previous section that truncation effects in the MBI optical system are quite significant in terms of power coupled to the bolometric detectors. In this section we examine the same parameter, coupled power, with regards to the mechanical tolerance of the components within the optical beam combiner. In particular, positioning and rotation of the detector array unit is investigated, as too is the position of both the primary and secondary mirrors.

We start by looking at the detector array which consists of a single block with nineteen conical horn antennas milled out of the surface. This means that the positions of the detectors relative to each other are fixed and therefore are not subject to a change in coupling due to mechanical misalignment. However, there is the

chance that the unit itself may not be positioned at the exact location required, mainly due to the fact that the bolometric array is suspended from the frame of the instrument using Kevlar wire (Figure 5.27) which is not rigid and therefore provides some level of flexibility in its movement. Not only is lateral movement an issue but so too is movement towards and away from the aperture of the inward-facing horn antennas, as well as rotation of the detector unit around the optical axis.

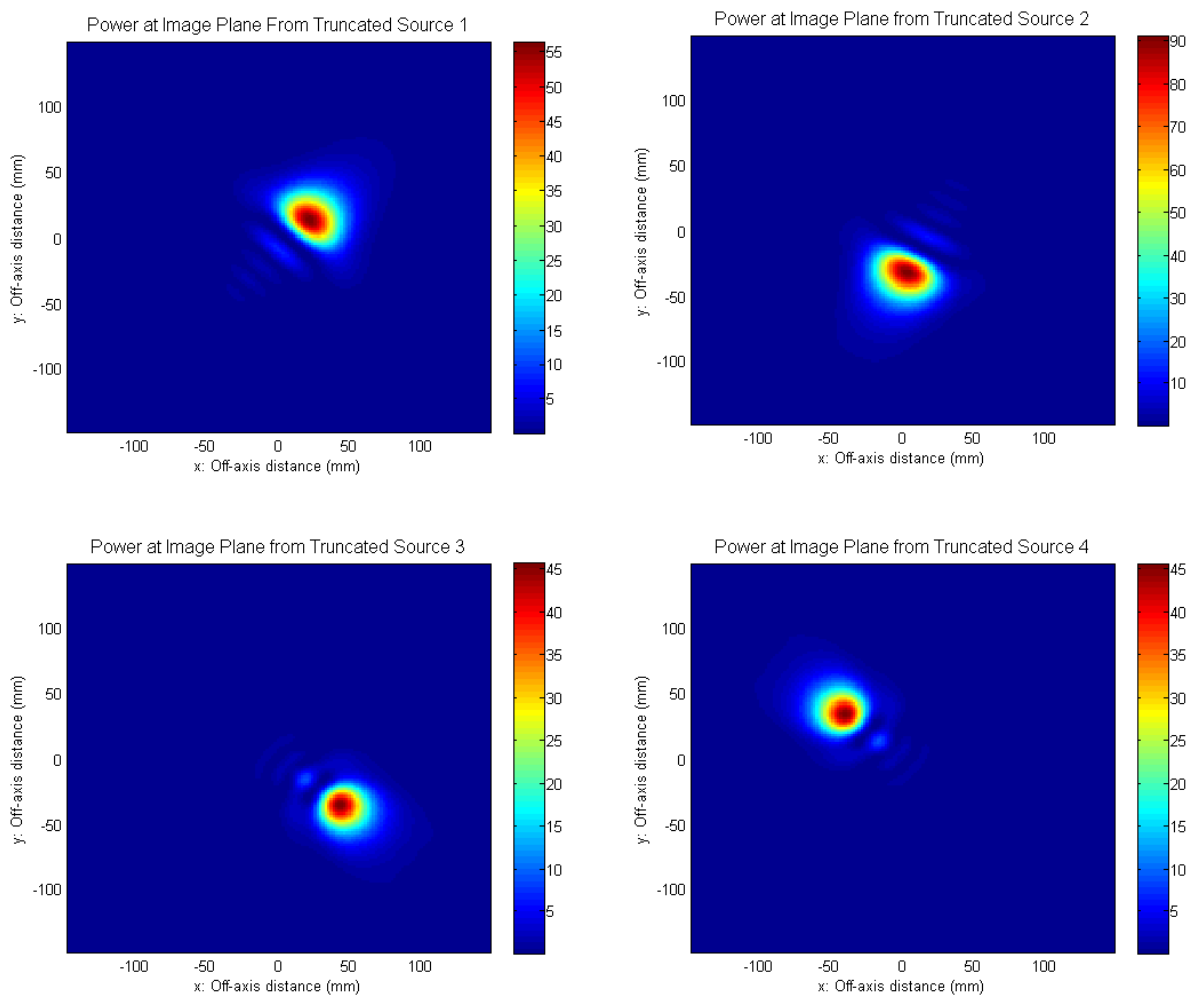


Figure 5.26 Beams at the image plane from the portions of each source that pass through the aperture of the primary mirror after transmission from the secondary.

The system was set up in MODAL as described previously with smooth-walled conical horn antennas with phase-flattening lenses as detectors. It was assumed that the portion of the field that passes through the primary mirror before reflection from the secondary could be averaged out using phase sensitive detection

as described in the previous section and therefore this was not included in the coupling calculation.

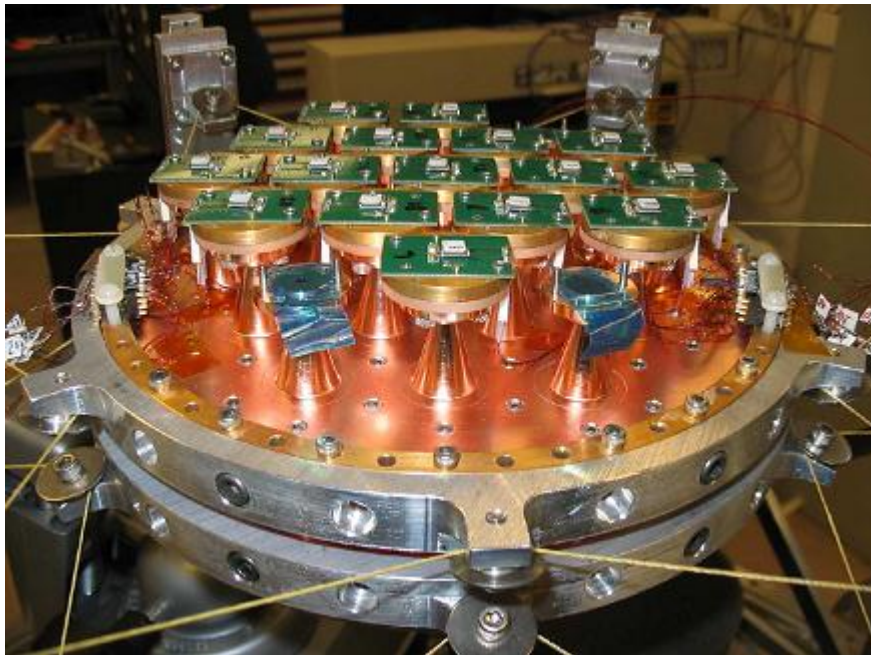


Figure 5.27 The MBI-4 instrument showing the detector array suspended from the frame by Kevlar wire.

XY Motion of the Bolometer Array

The first tolerance analysis carried out was on the effect of lateral movement in directions x and y of the detector array as shown in Figure 5.28, where the view is from the sky. The Cartesian coordinate system used was not only aligned with the bolometer array but the axes also coincided with the major and minor axes of the elliptical aperture in the primary mirror. This lateral tolerance calculation was done for a range from -2.5mm to $+2.5\text{mm}$ in 25 steps in both the x and y directions with the coupled amplitude and phase for each detector being calculated at each point in the resulting 625 point grid. Details of the coupled power for each detector are given in Appendix C and are summarised below.

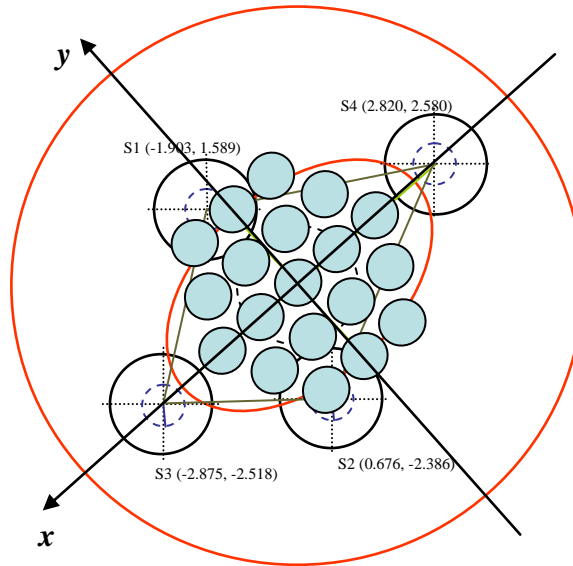


Figure 5.28 The frame used to define the movement of the bolometer array during mechanical tolerance calculations. The view shown is from the sky.

If we examine the power coupled to each detector as a function of its offset position in the x and y direction we can see from Figure 5.29 that the effect that mechanical misalignments would have on this value depends significantly on which source the detector is looking at. It should be noted that the positions of the detectors in these images are schematic and are not based on the scales of the x and y axes. The axes describe the movement of the detector ($\pm 2.5\text{mm}$) in both directions and hence produce a surface plot representing the coupled power for each one.

Examination of the coupled power in terms of the detector layout and the source to which the detector couples to shows the intensity distribution of the sources. This is also evident by looking at which detectors obtained the maximum coupled power from each source. Tables 5.7 and 5.8 show the detectors with maximum coupled power from Source 1 and Source 2 respectively, which lie approximately along the minor axis of the elliptical aperture in the primary mirror.

To get a better idea of the range of each detector's coupled power value we can study the maximum and minimum values of coupled power as the bolometer array is shifted in the x and y directions. We look at this in comparison to the centre position of the bolometer, that is, when the detectors are in the exact location they are supposed to be with no offset. This information is depicted in Figure 5.30, where we examine the effect for each of the four sources. As can be seen from the plots the

detectors with the greatest range of coupled power are 6, 14, 7 and 4 for sources 1 to 4 respectively. These detectors could be used to characterise the instrument, for example in locating the position of the detector array.

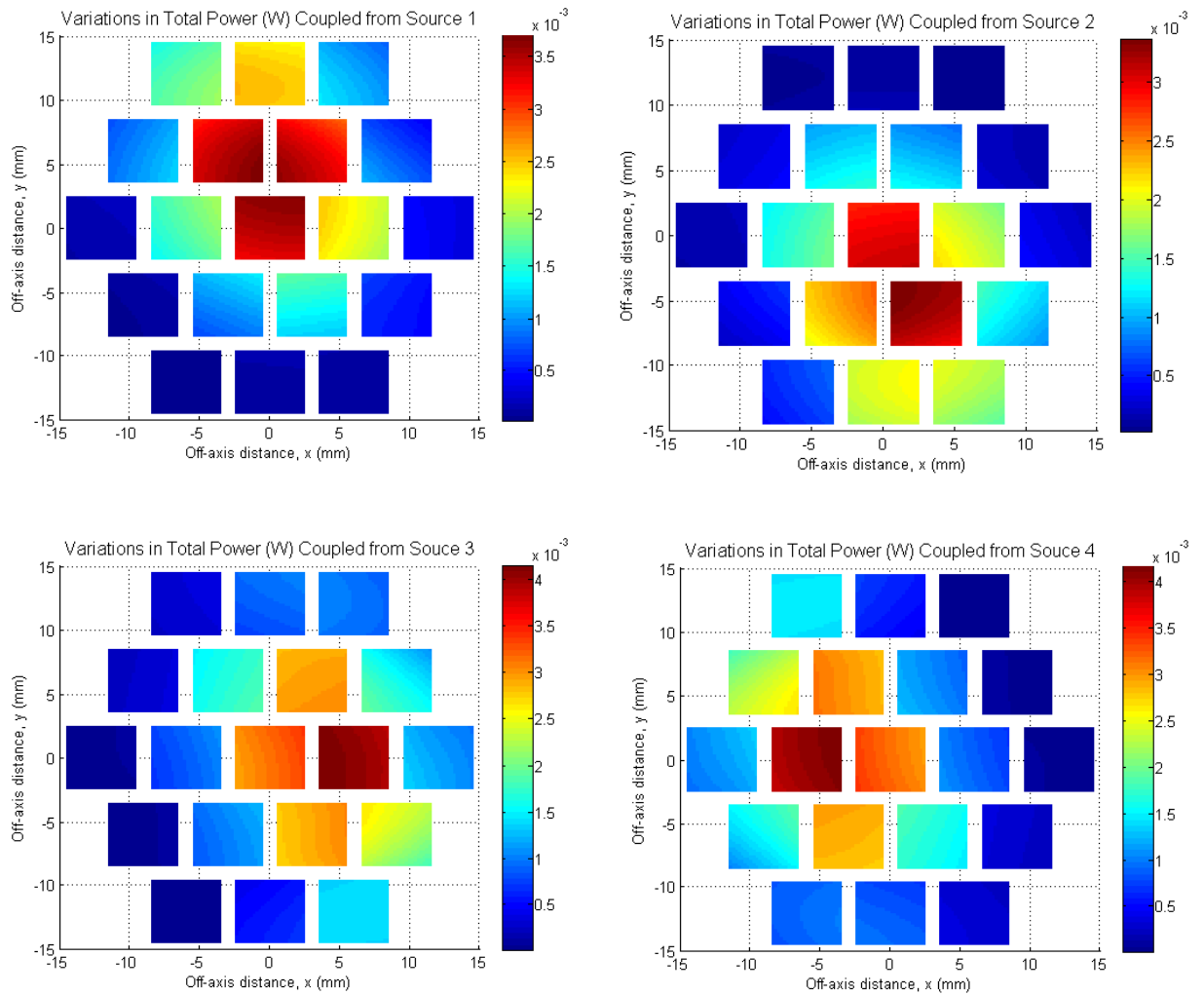


Figure 5.29 Power coupled to the detectors from sources 1 to 4 as the bolometer array moves in an xy -plane. The scales on the x and y axes show the range of movement of the detector and not its position in the array.

Top Five Maximum Values of Coupled Power from Source 1			
Detector	Power (W)	Centre Power (W)	Gain (% of Centre)
5	0.003693	0.003478	6.18
10	0.003653	0.003502	4.31
6	0.003604	0.003313	8.78
2	0.002550	0.002483	2.70
11	0.002485	0.002245	10.69

Table 5.7 The top 5 maximum values of coupled power to the detectors from Source 1. This coupled power can also be seen as a percentage gain with respect to the power coupled when the detectors are in the centre position, that is, when no mechanical offset has been accounted for.

Top Five Maximum Values of Coupled Power from Source 2			
Detector	Power (W)	Centre Power (W)	Gain (% of Centre)
15	0.003354	0.003231	3.81
10	0.003107	0.002981	4.23
14	0.002610	0.002379	9.71
11	0.002197	0.001921	14.37
18	0.002101	0.002013	4.37

Table 5.8 The top 5 maximum values of coupled power to the detectors from Source 2. This coupled power can also be seen as a percentage gain with respect to the power coupled when the detectors are in the centre position, that is, when no mechanical offset has been accounted for.

In the analysis above we have looked at the detectors with maximum and minimum coupled power and ranges and while we can get an overall picture of what is occurring from this information it is perhaps insightful to get a more detailed description of a chosen sample of detectors. Table 5.9 provides a summary of the coupling information for five detector horn antennas, which as the detector numbers show, represent a sample taken from a single quadrant of the bolometer array. The most significant variation from this selection of detectors occurs with detector 10 with Figure 5.31 showing the variation in coupled power for this detector looking at sources 1 to 4. We can also see in Figure 5.32 cuts in both the x and y directions for

the same detector and source combinations. This is an example of a detector that may be used for characterising the instrument.

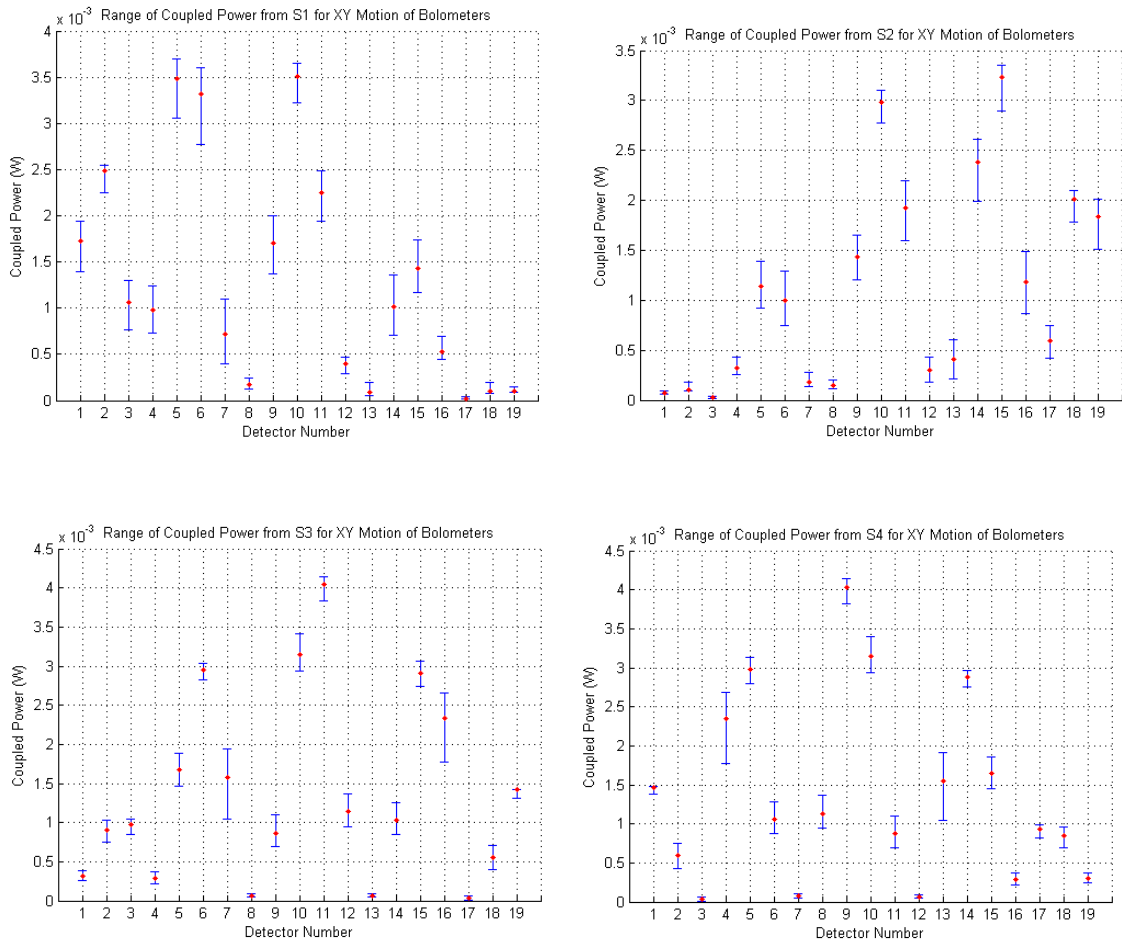


Figure 5.30 Range of power coupled to the detectors from sources 1 to 4 as the bolometer array moves in an xy -plane. The error bars represent the maximum and minimum values of coupled power.

To see the effects that the shifting bolometer array has on the interference pattern measured at the image plane we can calculate the coupled power at each detector for the combined field produced from sources 2 and 3, the shortest baseline available with MBI-4. This is shown in Figure 5.33 where the top left graph (a) represents the combined coupled power as the bolometer array is shifted in both the x and y -directions a distance of $\pm 2.5\text{mm}$, approximately 10% of the detector horn antenna radius. In the top right graph (b) we can see the combined coupled power when the detector array is at the centre position while the two bottom graphs show the same parameter for a detector position of -2.5mm (c) and $+2.5\text{mm}$ (d) in the x -direction.

Total Power Coupled to a Selection of Detectors from Each Source								
Detector Number	Max	Position		Min	Position		Range	Avg.
	(mW)	x	y	(mW)	x	y	(mW)	(mW)
Source 1								
2	2.55	-2.50	-1.25	2.24	2.50	2.50	0.305	2.447
3	1.30	-2.50	-2.50	0.76	2.50	2.50	0.533	1.045
10	3.65	2.50	2.50	3.23	-2.50	-2.50	0.428	3.480
11	2.49	-2.50	2.50	1.94	2.50	-2.50	0.541	2.230
12	0.47	-2.50	-2.50	0.30	2.50	-2.50	0.177	0.389
Source 2								
2	0.18	-2.50	-2.50	0.09	2.50	1.67	0.088	0.114
3	0.04	-2.50	2.50	0.02	2.50	-1.25	0.023	0.029
10	3.11	2.50	-2.50	2.78	-2.50	2.50	0.330	2.965
11	2.20	-2.50	-2.50	1.59	2.50	2.50	0.605	1.908
12	0.43	-2.50	-2.50	0.18	2.50	2.50	0.252	0.301
Source 3								
2	1.02	2.50	2.50	0.75	-2.50	-2.50	0.279	0.895
3	1.04	-2.50	0.42	0.84	2.50	2.50	0.194	0.954
10	3.41	2.50	2.50	2.93	-2.50	-2.50	0.482	3.157
11	4.14	-2.50	-2.50	3.83	2.50	2.50	0.309	4.023
12	1.36	-2.50	-2.50	0.95	2.50	2.50	0.418	1.137
Source 4								
2	0.75	-2.50	2.50	0.43	2.50	-2.50	0.316	0.595
3	0.06	-2.50	2.50	0.01	2.50	-2.50	0.049	0.034
10	3.40	-2.50	-2.50	2.94	2.50	2.29	0.456	3.157
11	1.10	-2.50	-2.50	0.70	2.50	2.50	0.404	0.880
12	0.09	-2.50	-2.08	0.05	2.50	2.50	0.038	0.068

Table 5.9 Details of the coupled power for a sample of five detectors from a single quadrant of the bolometer array. The coupled power is shown for all four sources and includes the range and average values.

Z and θ Motion of the Bolometer Array

The detector plane can also undergo unwanted movement in the z -direction, that is, along the optical axis. Figure 5.34 shows the effect this has on the coupled power from each source at each of the nineteen detector horn antennas. Details of the coupled power for each detector are given in Appendix C, however, as with the lateral movement, a summary of these is given below for the same selection of

detectors where a positive z -value indicates a movement away from the optical system.

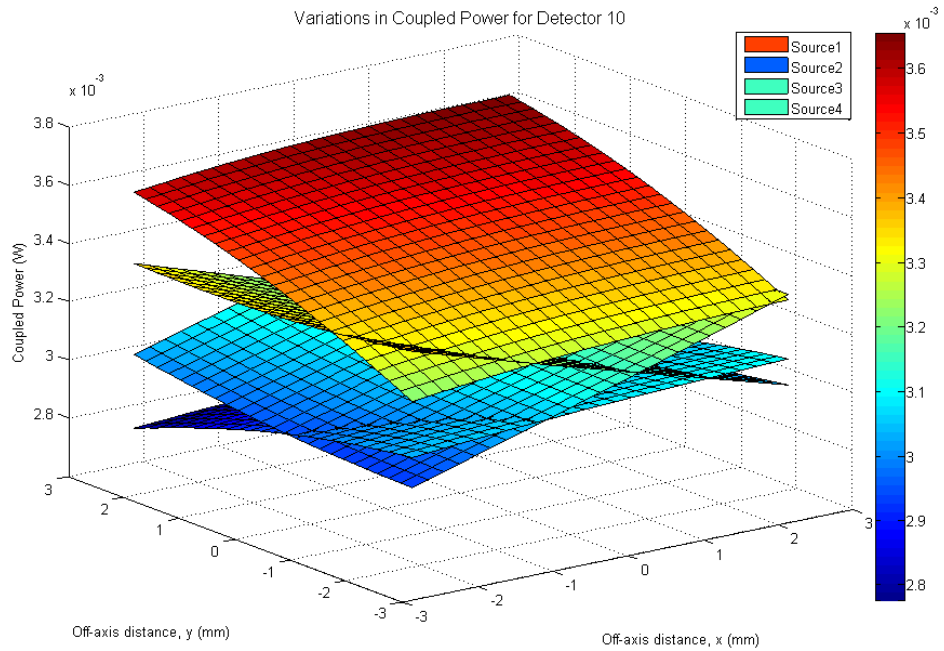


Figure 5.31 Power coupled to detector number 10 from sources 1 to 4 as the bolometer array moves in an xy -plane.

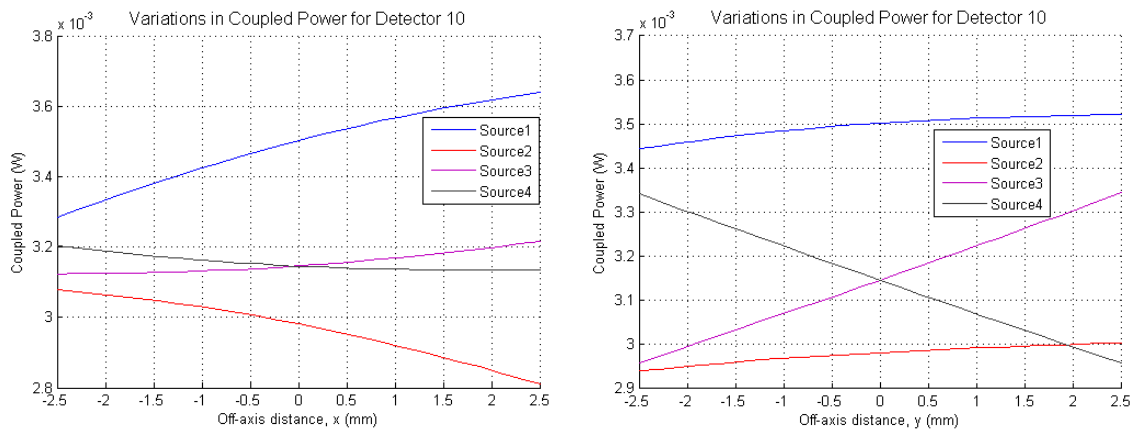


Figure 5.32 x and y cuts of power coupled to detector number 10 from sources 1 to 4 as the bolometer array moves in an xy -plane.

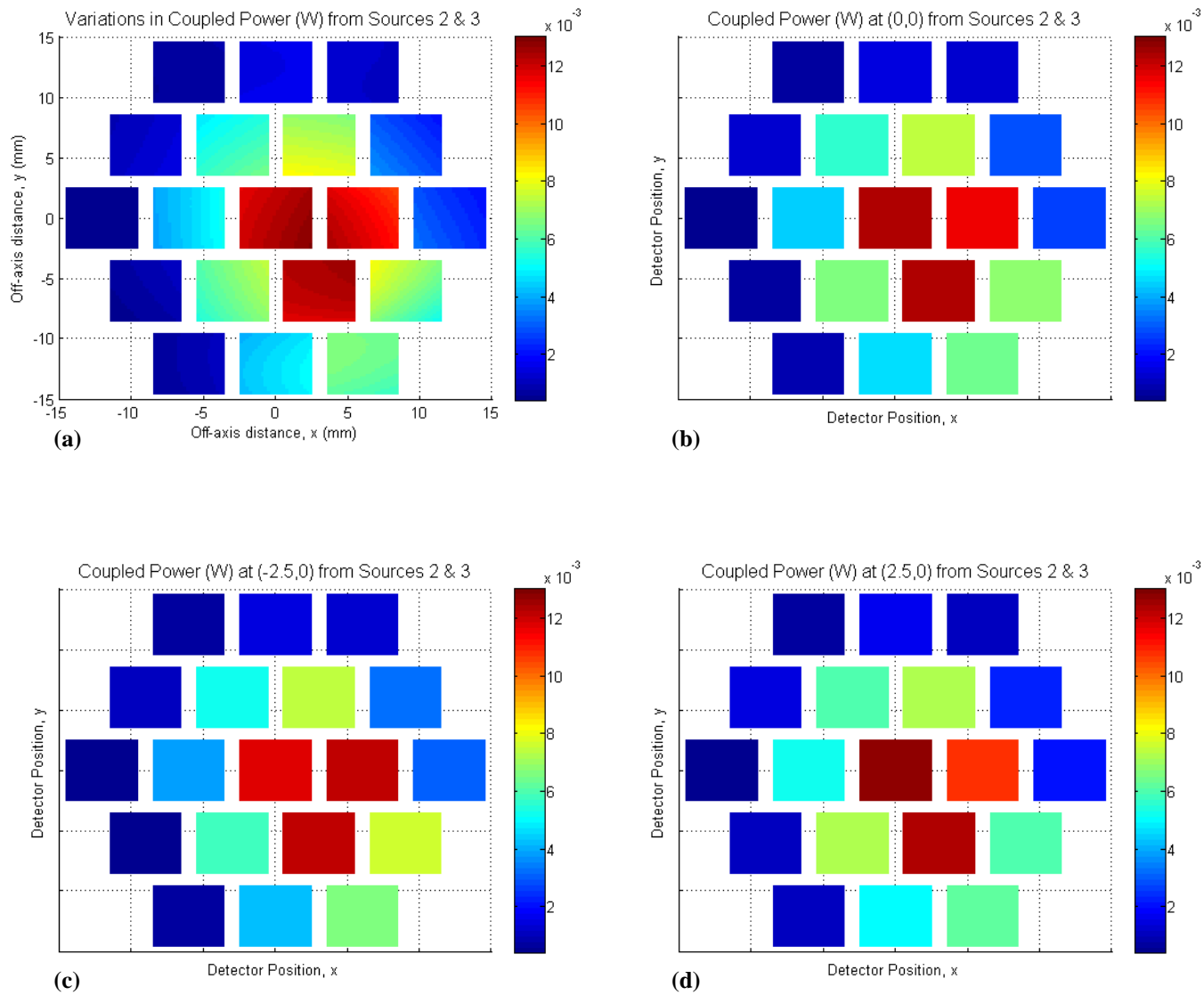


Figure 5.33 Power coupled to the detectors from a combination of sources 2 and 3. *Top left:* Coupled power as the bolometer array moves ± 2.5 mm in the x and y direction. *Top right:* Coupled power with the bolometer unit at the centre position (0, 0). *Bottom left:* Coupled power with the bolometer unit at -2.5 mm in the x -direction (-2.5, 0). *Bottom right:* Coupled power with the bolometer unit at $+2.5$ mm in the x -direction (+2.5, 0).

On analysis of the data it becomes clear that the effect of motion of the bolometer array in the z -direction is much less than that of the lateral movement. If the percentage gain is considered a change of $\leq 6\%$ is seen in all cases. These small changes are evident in Figure 5.35 where the error bars represent the maximum and minimum power coupling values. Compared with Figure 5.30 it can be seen that movement in the xy -plane has a much greater effect.

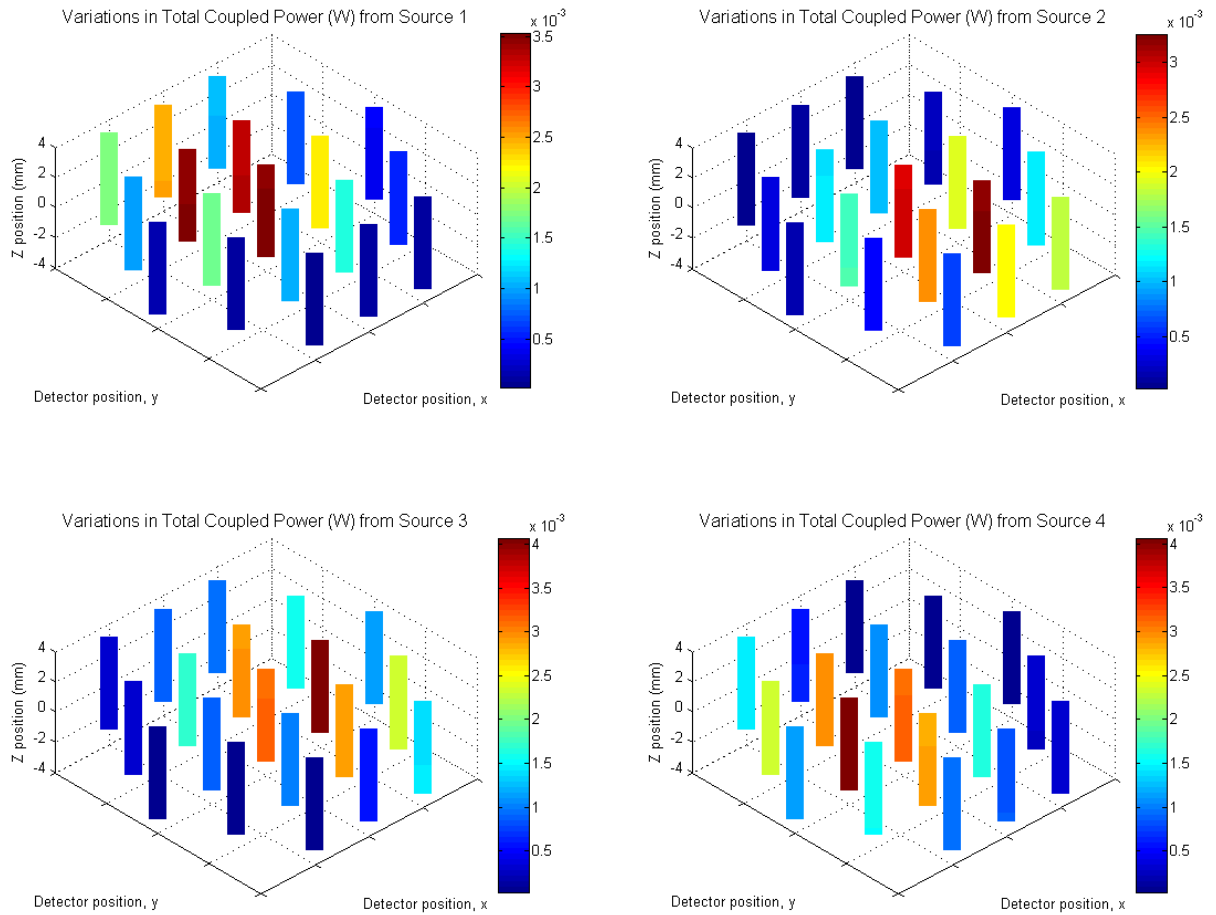


Figure 5.34 Power coupled to the detectors from sources 1 to 4 as the bolometer array moves in the z -direction. The position of the detectors is schematic with the top left detector in the xy -plane representing detector number 1.

The same analysis was carried out for rotation of the detector array around the optical (z) axis. This was done from a range of angles from -5° to 5° (a positive angle representing an anticlockwise rotation as observed from behind the detectors) in 25 steps with the coupled power to each detector from each source calculated at each step. In this type of analysis it would be expected that the greatest change in coupled power would occur at the detectors around the outside of the array since these undergo a greater range of motion during rotation. This can be seen in Figure 5.36, however, due to the position of the outer horn antennas in relation to the four sources, the coupling values are significantly lower than those at the centre regardless of their location, as seen before, and therefore the effect is only visible for certain combinations of source and detector.

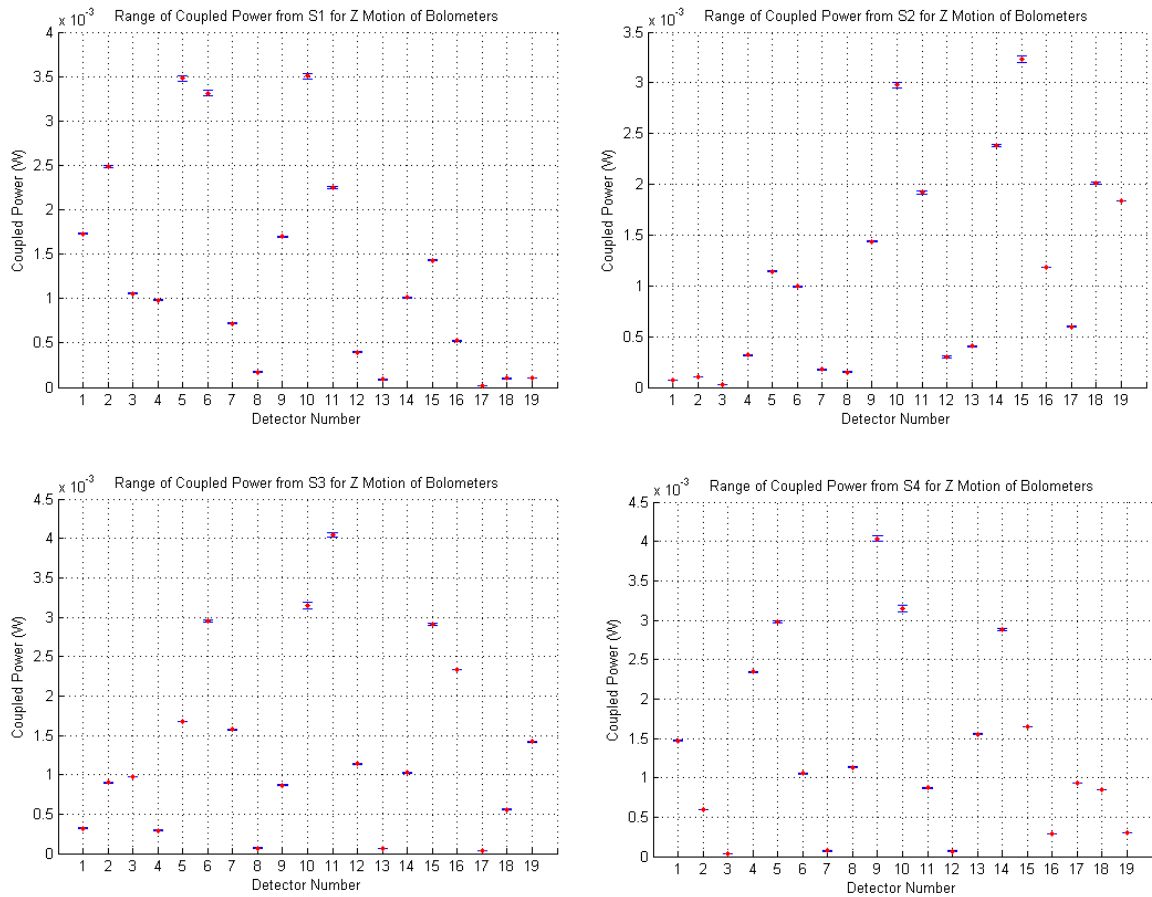


Figure 5.35 Range of power coupled to the detectors from sources 1 to 4 as the bolometer array moves in the z -direction. The error bars represent the maximum and minimum values of coupled power.

Table 5.10 shows a summary of the coupling data for the same selection of horn antennas within a single quadrant of the bolometer array (full results are provided in Appendix C). Looking at the overall data the power gained and lost as a percentage of the centre power is significantly higher with rotation of the bolometer array compared to the movement in the z -direction along the optical axis. If we consider all detectors the maximum percentage gain is 50%, 77%, 153% and 141% for source 1, 2, 3 and 4 respectively. These values are for detector 17 for sources 1 and 3, and detector 3 for source 2 and 4, both of which lie at the edge of the array, as expected. Although these percentage gains seem to be quite high the power coupled to these detectors before rotation was low and therefore a small level of power gained will appear as quite a high percentage. The power loss values, again as a

percentage of the centre power, lie in the range from 20% to 80% with the same detector/source combinations that produce the highest gain producing the highest loss. The exception to this is in the case of Source 1 where it is detector 7 that exhibits the highest percentage of power loss, again, a detector that lies on the outer edge of the unit. Figure 5.37 shows the full range of coupled power for each detectors as they view each source.

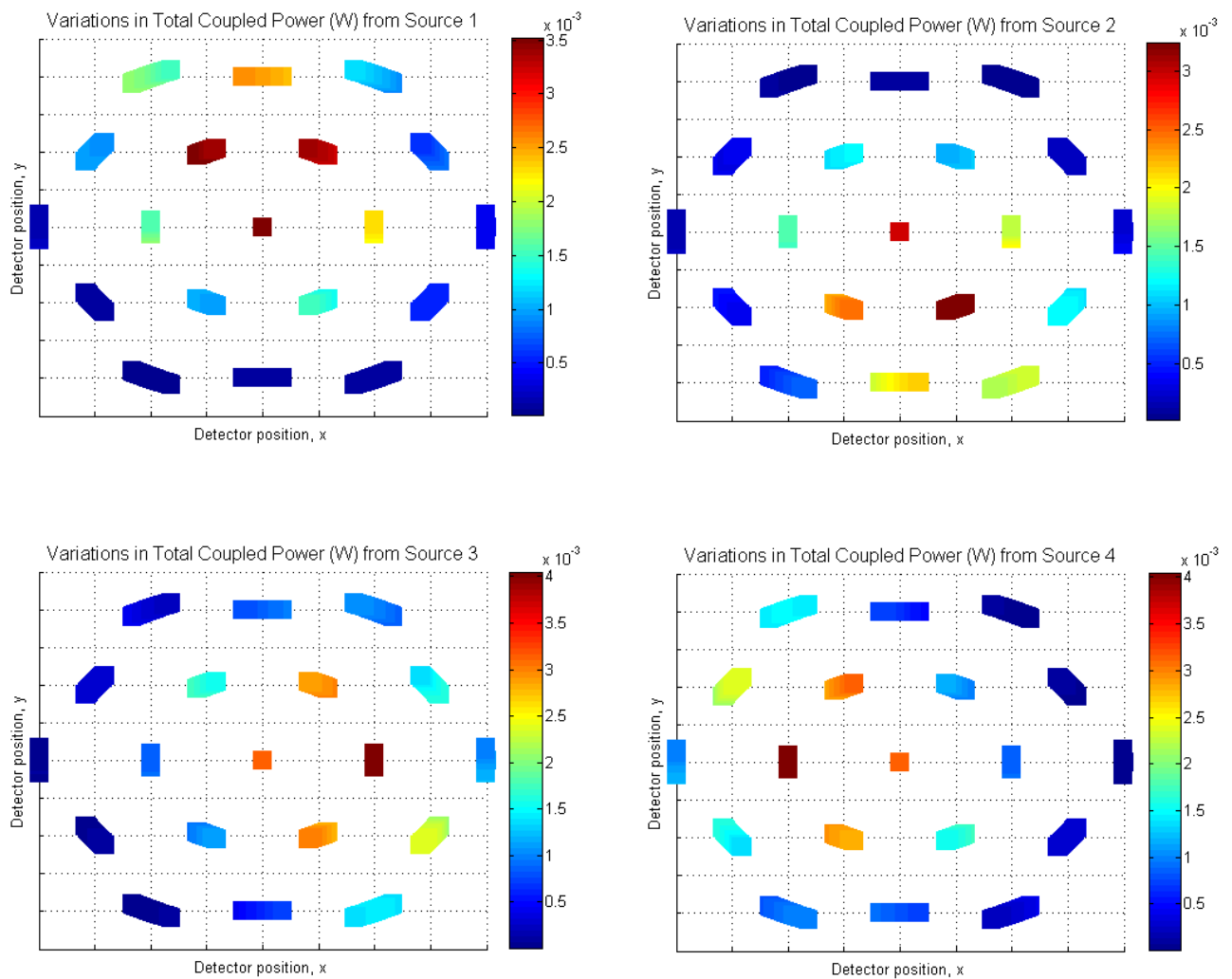


Figure 5.36 Power coupled to the detectors from sources 1 to 4 as the bolometer array rotates around the optical axis. The position of the detectors is schematic with the top left detector in the xy -plane representing detector number 1.

Total Power Coupled to a Selection of Detectors from Each Source						
Detector	Max	Position	Min	Position	Range	Average
Number	(mW)	Θ (deg)	(mW)	Θ (deg)	(mW)	(mW)
Source 1						
2	2.546	5.00	2.388	-5.00	0.158	2.478
3	1.178	5.00	0.894	-5.00	0.284	1.049
10	3.502	-5.00	3.502	-5.00	0.000	3.502
11	2.280	5.00	2.158	-5.00	0.122	2.235
12	0.399	-5.00	0.374	5.00	0.025	0.392
Source 2						
2	0.106	5.00	0.099	-5.00	0.007	0.102
3	0.046	5.00	0.019	-5.00	0.027	0.028
10	2.981	-5.00	2.981	-5.00	0.000	2.981
11	2.024	-5.00	1.781	5.00	0.243	1.914
12	0.386	-5.00	0.250	5.00	0.136	0.307
Source 3						
2	0.984	-5.00	0.800	5.00	0.184	0.899
3	1.057	5.00	0.839	-5.00	0.219	0.963
10	3.146	-5.00	3.146	-5.00	0.000	3.146
11	4.050	-4.17	3.999	5.00	0.050	4.035
12	1.214	-5.00	0.973	5.00	0.240	1.119
Source 4						
2	0.762	5.00	0.457	-5.00	0.305	0.604
3	0.082	5.00	0.008	-5.00	0.075	0.038
10	3.145	-5.00	3.145	-5.00	0.000	3.145
11	0.928	-5.00	0.849	5.00	0.079	0.877
12	0.071	-1.25	0.053	5.00	0.017	0.065

Table 5.10 Details of the coupled power for a sample of five detectors from a single quadrant of the bolometer array. The coupled power is shown for all four sources and includes the range and average values.

XY Motion of the Mirror System

Having considered tolerance issues in terms of the position of the bolometer array the next most critical components with regards to mechanical tolerances are the

primary and secondary mirrors. These mirrors are mounted on the same frame and are therefore considered as a single unit. To begin with, the mirror unit was shifted in both the x and y -directions with regard to the horn coordinate frame (see Figure 5.2) and as with the detector array the coupled power was calculated at each point in the grid resulting from a motion of $\pm 0.5\text{mm}$ in each direction. Figure 5.38 below shows the results of this analysis. As with the bolometer scan, the positioning of the detectors in each diagram is schematic and the axes represent the range of movement of the mirror system that took place. Since the tolerance value in this case was much smaller than that of detector unit it can be seen that the effect on the coupled power is not as dramatic, as expected.

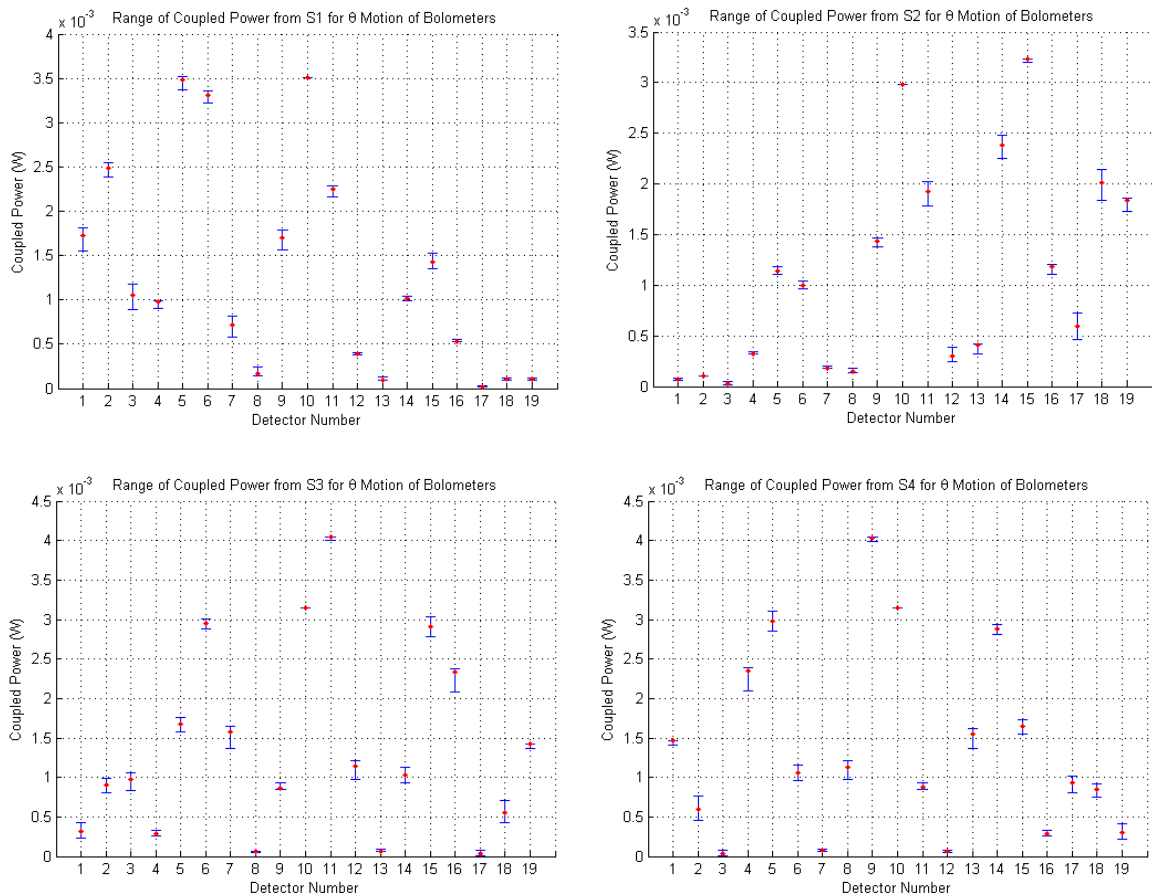


Figure 5.37 Range of power coupled to the detectors from sources 1 to 4 as the bolometer array rotates around the optical axis. The error bars represent the maximum and minimum values of coupled power.

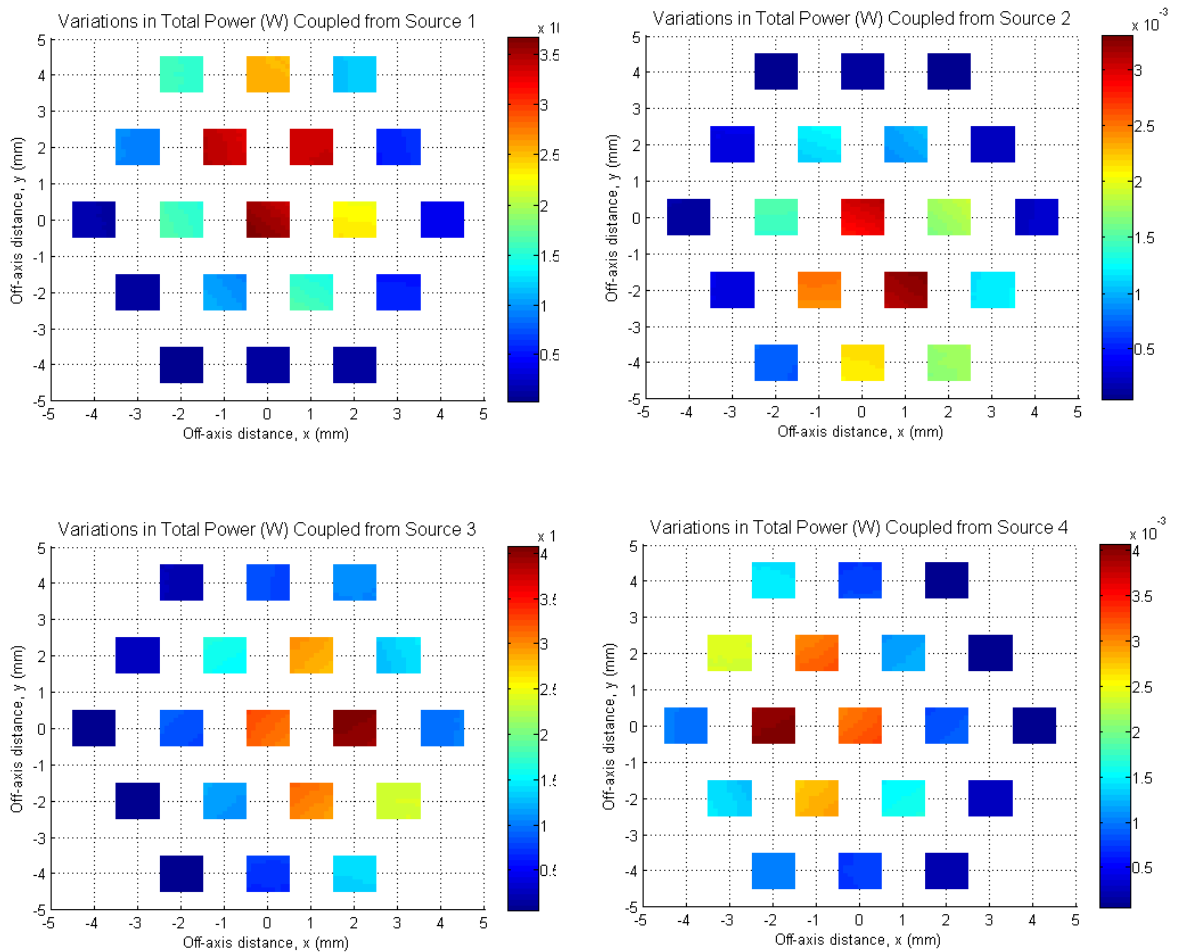


Figure 5.38 Power coupled to the detectors from sources 1 to 4 as the mirror system (primary and secondary) moves in an xy -plane. The scales on the x and y axes show the range of movement of the detector and not its position in the array.

On further examination of the data (Appendix C) we see that the detectors with the greatest range of coupled power are 10, 10, 7 and 13 for sources 1 to 4 respectively, as is evident from the plots in Figure 5.39 where the error bars represent the maximum and minimum coupled power values and the point represents the centre value. Again the detectors with the greatest range of coupled power could be used to locate the position of the mirrors within the instrument.

As with the analysis of bolometer array movement a selection of five detector horn antennas from a single quadrant of the array was chosen for further analysis.

Table 5.11 shows a summary of the data for these detector horns. The effect of this movement is small for most of the detector array but as with the movement of the

bolometer unit it is detector 10 that is most affected, the detector at the centre of the array. Figure 5.40 shows the change in coupled power for detector 10 as the mirror system is moved laterally in the xy -plane.

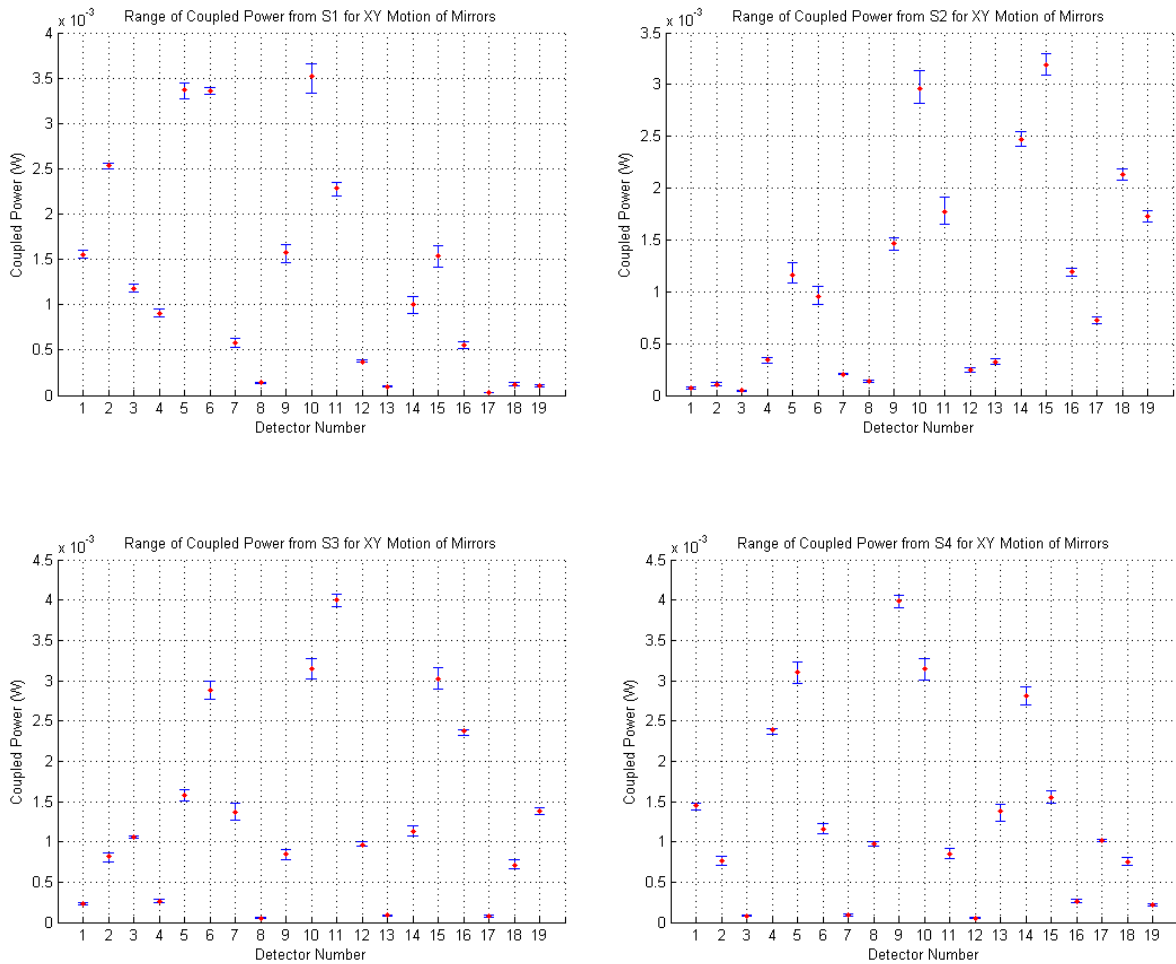


Figure 5.39 Range of power coupled to the detectors from sources 1 to 4 as the mirror system (primary and secondary) moves in an xy -plane. The error bars represent the maximum and minimum values of coupled power.

Z Motion of the Mirror System

As well as lateral movement of the mirrors within the instrument there is also the possibility of movement in the z -direction along the optical axis, that is, to (negative z value) and from (positive z value) the inward facing horn antennas. The mechanical tolerance in this direction is within ± 2.5 mm (Korotkov, 2010) and

Total Power Coupled to a Selection of Detectors from Each Source								
Detector	Max	Position		Min	Position		Range	Avg.
Number	(mW)	x	y	(mW)	x	y	(mW)	(mW)
Source 1								
2	2.57	0.06	-0.50	2.48	0.00	0.00	0.083	2.535
3	1.22	0.50	-0.06	1.06	0.00	0.00	0.162	1.177
10	3.66	-0.50	-0.50	3.34	0.50	0.50	0.321	3.499
11	2.35	-0.39	-0.50	2.20	0.50	0.50	0.151	2.280
12	0.40	0.00	0.00	0.36	-0.17	0.50	0.033	0.375
Source 2								
2	0.13	0.50	0.50	0.01	-0.50	-0.50	0.031	0.108
3	0.05	-0.28	-0.50	0.03	0.00	0.00	0.023	0.046
10	3.14	0.50	0.50	2.82	-0.50	-0.50	0.319	2.980
11	1.92	0.00	0.00	1.66	-0.50	-0.50	0.266	1.781
12	0.30	0.00	0.00	0.23	-0.50	0.50	0.073	0.251
Source 3								
2	0.90	0.00	0.00	0.75	0.50	0.28	0.150	0.806
3	1.07	-0.06	0.39	0.97	0.00	0.00	0.097	1.058
10	3.28	-0.50	0.50	3.02	0.50	-0.50	0.262	3.143
11	4.07	-0.50	0.50	3.92	0.50	-0.50	0.144	3.997
12	1.14	0.00	0.00	0.95	-0.50	-0.50	0.191	0.974
Source 4								
2	0.82	-0.06	-0.50	0.60	0.00	0.00	0.224	0.764
3	0.09	0.50	-0.50	0.03	0.00	0.00	0.059	0.082
10	3.28	0.50	-0.50	3.01	-0.50	0.50	0.263	3.145
11	0.91	0.50	-0.50	0.79	-0.50	0.50	0.125	0.849
12	0.07	0.00	0.00	0.05	-0.50	0.39	0.020	0.054

Table 5.11 Details of the coupled power for a sample of five detectors from a single quadrant of the bolometer array. The coupled power is shown for all four sources and includes the range and average values.

therefore both the primary and secondary mirrors were shifted by this amount as a single unit and the power coupled to the detectors calculated. It can be seen from Figure 5.41 that the effect this movement has on individual detectors is minimal with very little variation in power occurring. On analysis of the data (Appendix C) we can see that the maximum gain in power as a percentage of the centre power is approximately 7% which occurs with source 4 and detector 7, while the maximum

power loss, again as a percentage of the centre power, is just above 5% and occurs with source 1 and detector 13. As with the movement of the detector array in the z -direction the effect is much less than the lateral movement and this is again evident in Figure 5.42 which shows the range of coupled power for each source and each detector.

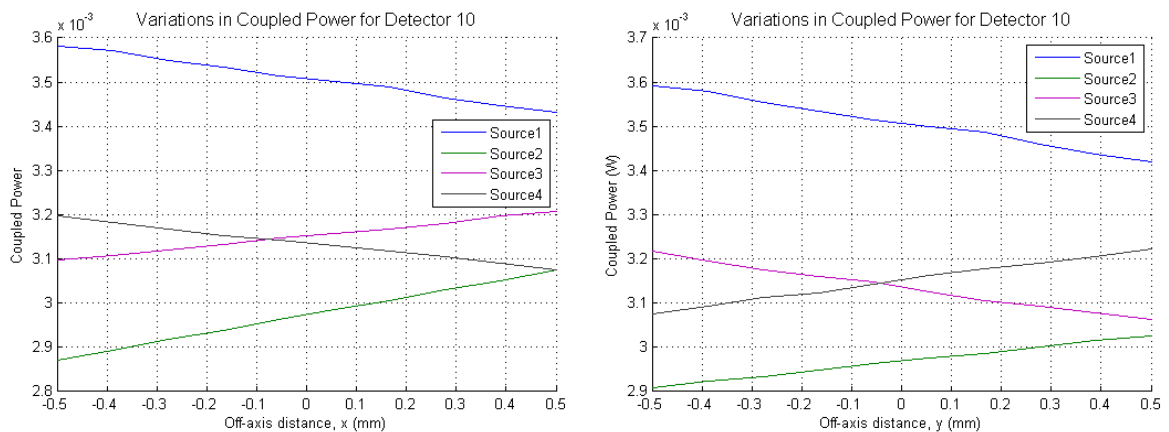


Figure 5.40 x and y cuts of power coupled to detector number 10 from sources 1 to 4 as the mirror system (primary and secondary) moves in an xy -plane.

While details of the coupled power for each detector are given in Appendix C, a summary for the selection of five detector horn antennas as used before is given in Table 5.12. The table shows the maximum and minimum values of coupled power for each of the five detectors along with the offset position along the z -axis at which this power occurs. The range and average power values are also shown.

Thermal Contraction of the Mirror System

The final mechanical tolerance considered was the thermal contraction of the primary and secondary mirror system within the cold cryostat. Until now both mirrors have been moved as a single unit since they are both mounted on the same frame, however, it is possible for frame to contract therefore causing the mirrors to move with respect to each other. In this analysis the secondary mirror was moved a distance of 0.5mm along the z -axis of the optical system, that is, 0.5mm towards the

detector array. In a similar manner, the primary mirror was moved the same distance in the negative z -direction towards the inward-facing horn antennas. Both movements resulted in a total mirror contraction of 1mm with the power coupled to each detector from each source being calculated (Appendix C) with this effect taken into account. The results of this analysis can be seen in Figure 5.43.

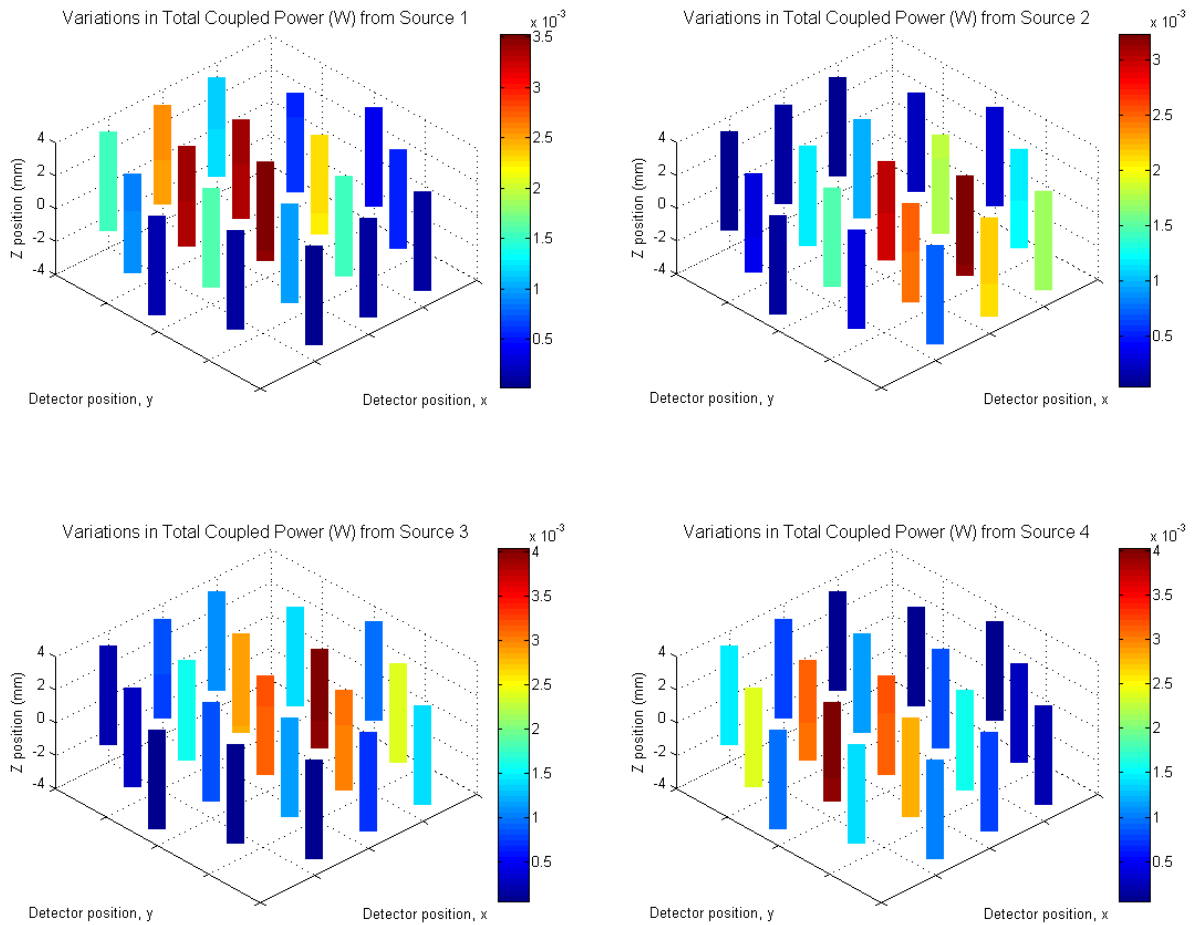


Figure 5.41 Power coupled to the detectors from sources 1 to 4 as the mirror system (primary and secondary) moves in the z -direction. The position of the detectors is schematic with the top left detector in the xy -plane representing detector number 1.

As seen from the scatter plots the results of this thermal contraction of the mirrors relative to each other is minimal and it does not cause any significant effect on the power coupled to the detectors.

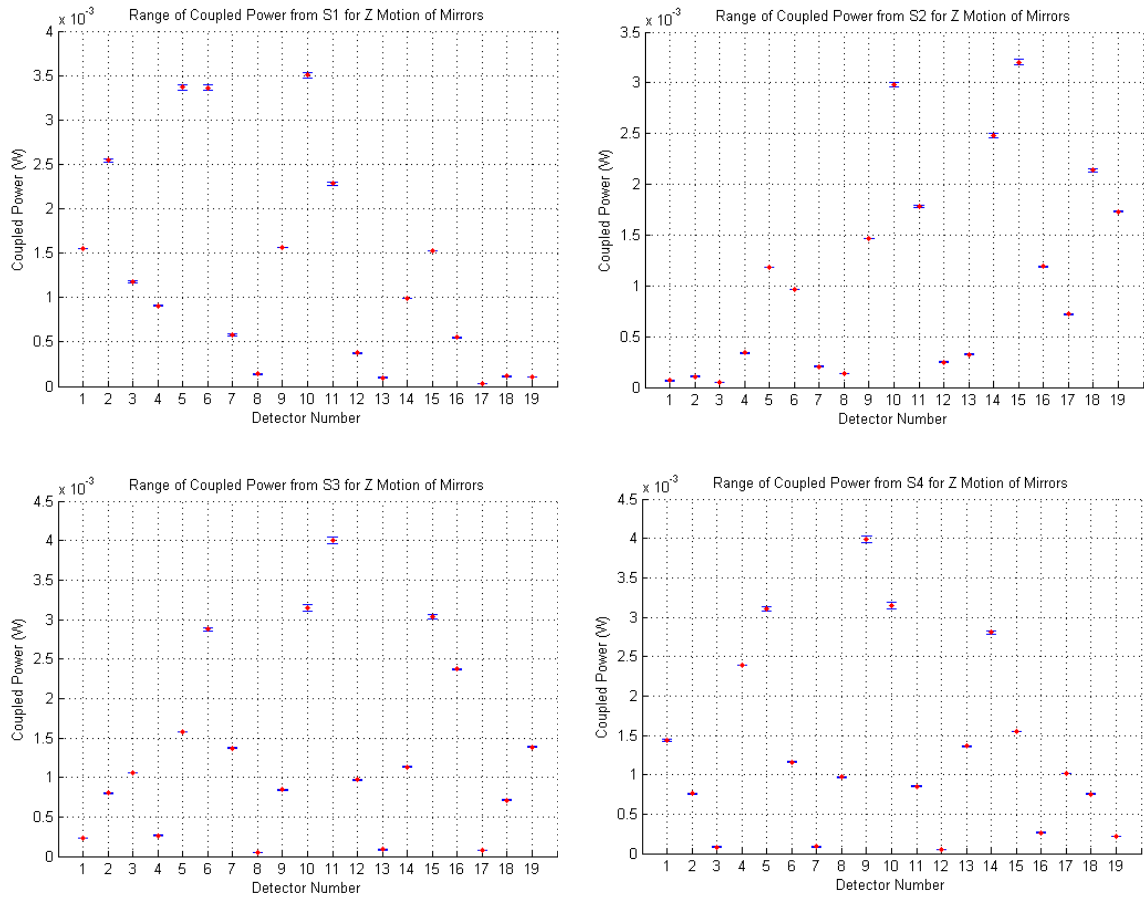


Figure 5.42 Range of power coupled to the detectors from sources 1 to 4 as the mirror system (primary and secondary) moves in the z -direction. The error bars represent the maximum and minimum values of coupled power.

5.1.6 Frequency Dependence of the Instrument

The MBI-4 optical band is defined by filters and it operates at a central frequency of 90GHz (Korotkov *et al.*, 2006). The analysis presented so far in this thesis has assumed this single frequency value, however, to fully understand the operation of the instrument it is essential to investigate and analyse the effect of wide-band operation on the overall performance. To do this, a physical optics analysis was carried out whereby the power coupled to the detectors was calculated at a range of frequencies lying between 80GHz and 100GHz. While the full results are available in Appendix D Figure 5.44 shows the variations in power coupled for

five frequencies between these limits, i.e. 80GHz, 85GHz, 90GHz, 95GHz and 100GHz. Table 5.13 also shows a summary of the results from the five detectors used in the previous analysis.

Total Power Coupled to a Selection of Detectors from Each Source						
Detector	Max	Position	Min	Position	Range	Average
Number	(mW)	z	(mW)	z	(mW)	(mW)
Source 1						
2	2.566	2.50	2.525	-2.50	0.041	2.546
3	1.186	-2.50	1.170	2.50	0.016	1.178
10	3.533	2.50	3.471	-2.50	0.062	3.502
11	2.294	2.50	2.267	-2.50	0.027	2.280
12	0.381	-2.50	0.367	2.50	0.013	0.374
Source 2						
2	0.111	-2.50	0.102	2.50	0.009	0.106
3	0.046	2.50	0.045	-2.50	0.001	0.046
10	3.007	2.50	2.956	-2.50	0.052	2.981
11	1.790	2.50	1.772	-2.50	0.018	1.781
12	0.256	-2.50	0.245	2.50	0.011	0.250
Source 3						
2	0.808	2.50	0.792	-2.50	0.016	0.800
3	1.058	1.46	1.056	-2.50	0.001	1.057
10	3.186	2.50	3.109	-2.50	0.077	3.146
11	4.044	2.50	3.955	-2.50	0.089	3.999
12	0.980	-2.50	0.966	2.50	0.014	0.973
Source 4						
2	0.769	2.50	0.755	-2.50	0.014	0.762
3	0.085	-2.50	0.080	2.50	0.005	0.082
10	3.186	2.50	3.108	-2.50	0.078	3.146
11	0.856	-2.50	0.842	2.50	0.014	0.849
12	0.055	-2.50	0.052	2.50	0.003	0.053

Table 5.12 Details of the coupled power for a sample of five detectors from a single quadrant of the bolometer array. The coupled power is shown for all four sources and includes the range and average values.

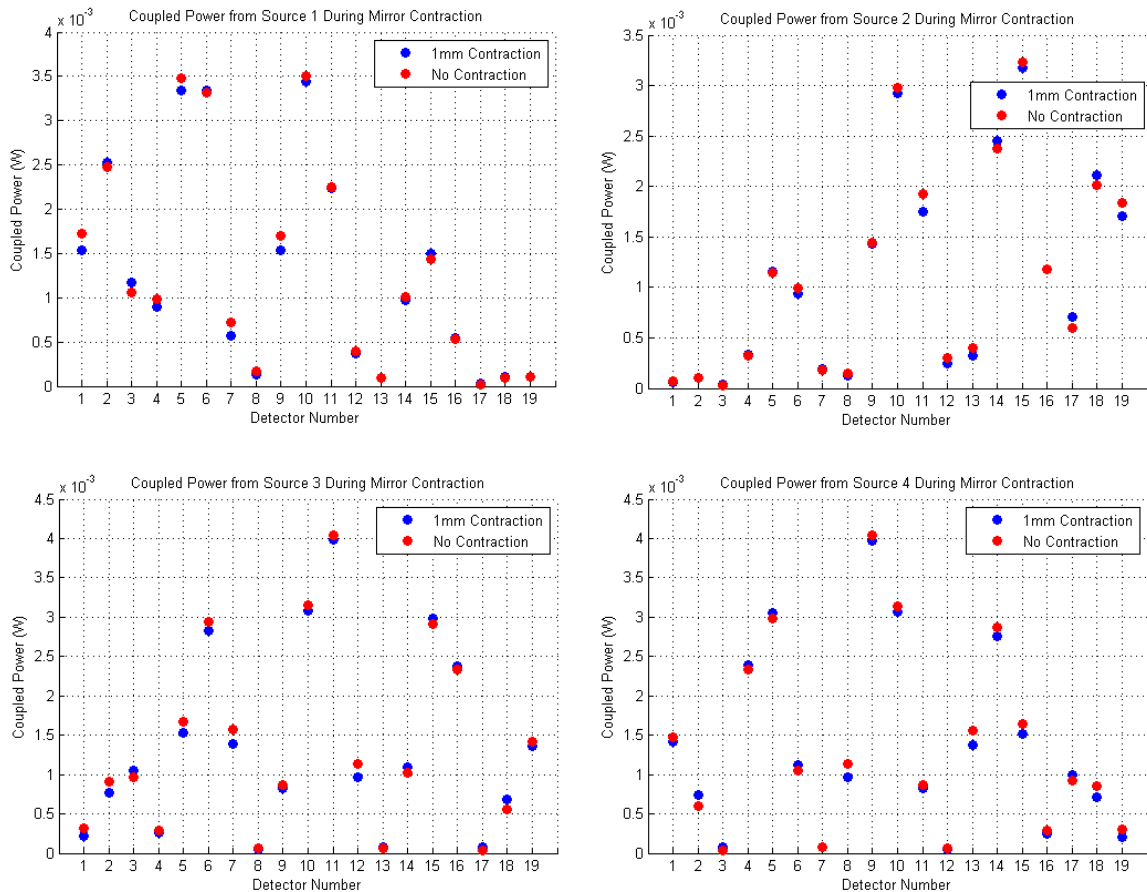


Figure 5.43 Power coupled to the detectors from sources 1 to 4 as the mirror system (primary and secondary) contracts by 1mm. Also shown is the coupled power with no contraction taken into account.

From the data it can be seen that the range of coupled power goes from a minimum of 0.041mW for source 1 detector 17 to a maximum of 1.282mW for source 1 detector 10 as the frequency varies from 80GHz to 100GHz. In terms of power coupled to the detectors the maximum lies at approximately 4.4mW for source 3 detector 11 at 100GHz and the minimum at 0.008mW for both source 3 detector 17 at 97GHz and source 4 detector 3, also at 97GHz.

In summary, a number of simulations were carried out to determine the effect of mechanical tolerances within the MBI-4 instrument. It was found that movement of the bolometer array in the xy -direction had the most significant effect on the power coupled from the telescope beam to the detector horn antennas. While rotation and lateral movement of the detector unit did show some changes in coupled

power, the effect was quite small. This was also the case for the mechanical tolerances of the mirror system. The frequency dependence of the instrument was also examined where again it was shown that there are some changes in coupled power.

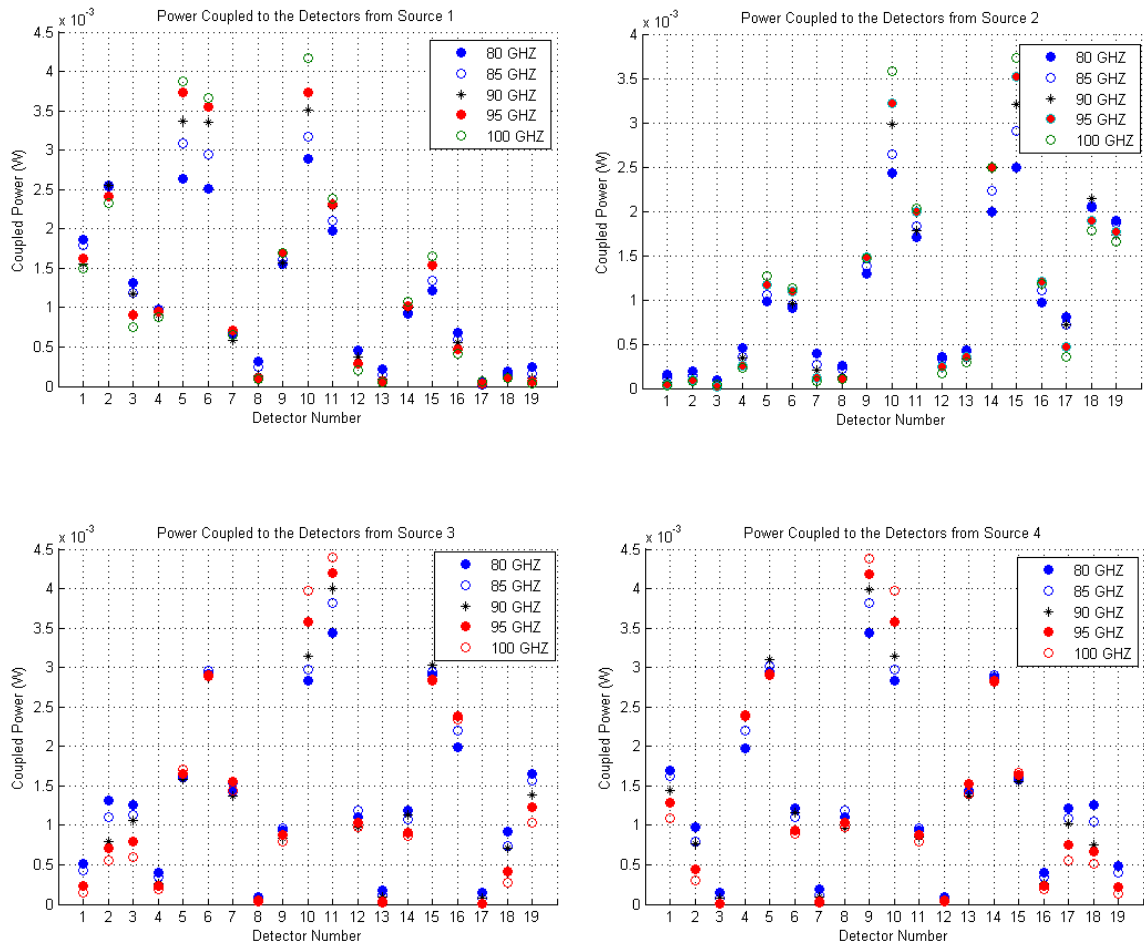


Figure 5.44 Power coupled to the detectors from sources 1 to 4 as frequency varies between 80GHz and 100GHz in steps of 5GHz.

5.1.7 Simulating Lab Measurements

In August 2010 the beam patterns from individual sources were measured at Brown University. This was done by sequentially removing the sky-facing corrugated horn antennas from the instrument and replacing each one with a Gunn oscillator directly at the input waveguide and before the phase shifters. The beam

then propagated through the optics of the beam combiner before being measured at the focal plane by a room temperature detector on an *x-y* stage scanned over an area covering seven inches square. The results from these measurements are given in Figure 5.45 where the focal plane beam patterns for each of the four source horns are shown.

Total Power Coupled to a Selection of Detectors from Each Source						
Detector	Max	Freq	Min	Freq	Range	Average
Number	(mW)	(GHz)	(mW)	(GHz)	(mW)	(mW)
Source 1						
2	2.553	83	2.329	100	2.555	2.473
3	1.238	83	0.746	100	1.313	1.049
10	3.875	97	2.891	80	4.170	3.485
11	2.346	97	1.979	80	2.382	2.211
12	0.455	81	0.208	100	0.456	0.365
Source 2						
2	0.173	83	0.085	99	0.199	0.122
3	0.063	83	0.022	93	0.091	0.041
10	3.344	97	2.433	80	3.579	2.960
11	2.016	97	1.711	80	2.033	1.899
12	0.342	83	0.173	100	0.362	0.282
Source 3						
2	1.194	83	0.550	100	1.314	0.910
3	1.188	83	0.601	100	1.253	0.961
10	3.731	97	2.828	80	3.968	3.269
11	4.262	97	3.435	80	4.388	3.988
12	1.181	87	0.973	90	1.189	1.096
Source 4						
2	0.865	83	0.306	100	0.973	0.626
3	0.109	83	0.008	97	0.152	0.054
10	3.731	97	2.831	80	3.970	3.270
11	0.953	86	0.800	100	0.970	0.895
12	0.091	83	0.035	99	0.091	0.065

Table 5.13 Details of the coupled power for a sample of five detectors from a single quadrant of the bolometer array. The coupled power is shown for all four sources and includes the range and average values.

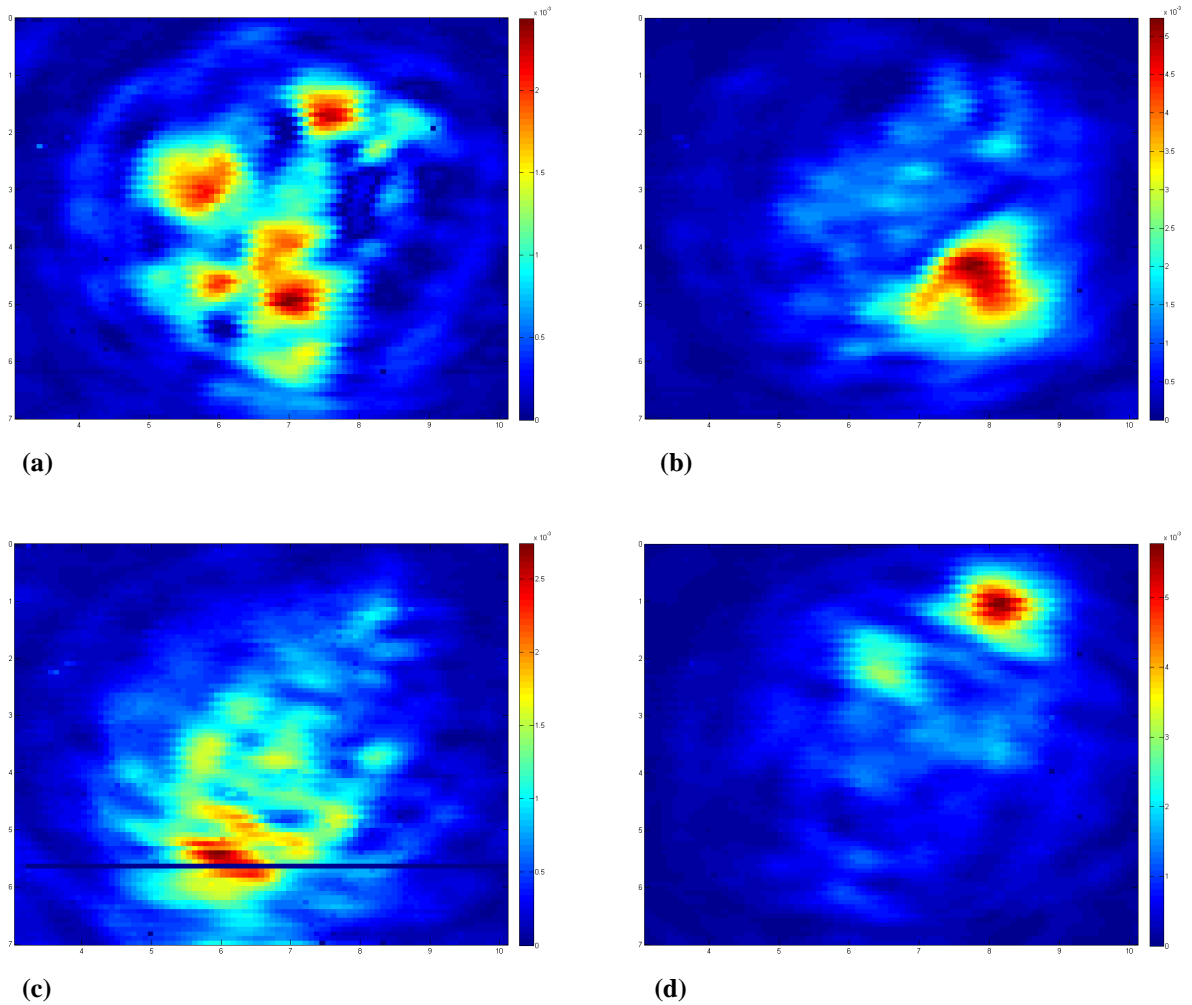


Figure 5.45 Measurements of beam patterns on the focal plane from individual sources of MBI-4. (a) shows the beam obtained from source 1, (b) shows the beam obtained from source 2, (c) shows the beam obtained from source 3 and (d) shows the beam obtained from source 4.

As a comparison the same system was setup in MODAL where each Gunn oscillator and optics-facing corrugated horn antenna was represented by a Bessel function with a single polarisation direction as in the previous analysis. Each source was propagated through the beam combiner separately using physical optics and the field on the focal plane was calculated. Figure 5.46 shows the results of this analysis, which were confirmed by simulations carried out in both GRASP and Zemax. Looking at the results from the measurements and the simulations it can be seen that they are significantly different. In the measurements the fields are heavily concentrated in individual quadrants (with the exception of source 1) depending on the position of the source used, while in the models the beam pattern is more

extended over the area of the truncating elliptical aperture in the primary mirror. As a further investigation the portion of the beam that is truncated by this aperture after transmission by the secondary mirror was taken into account and the focal plane beam patterns calculated. The results are shown in Figure 5.47.

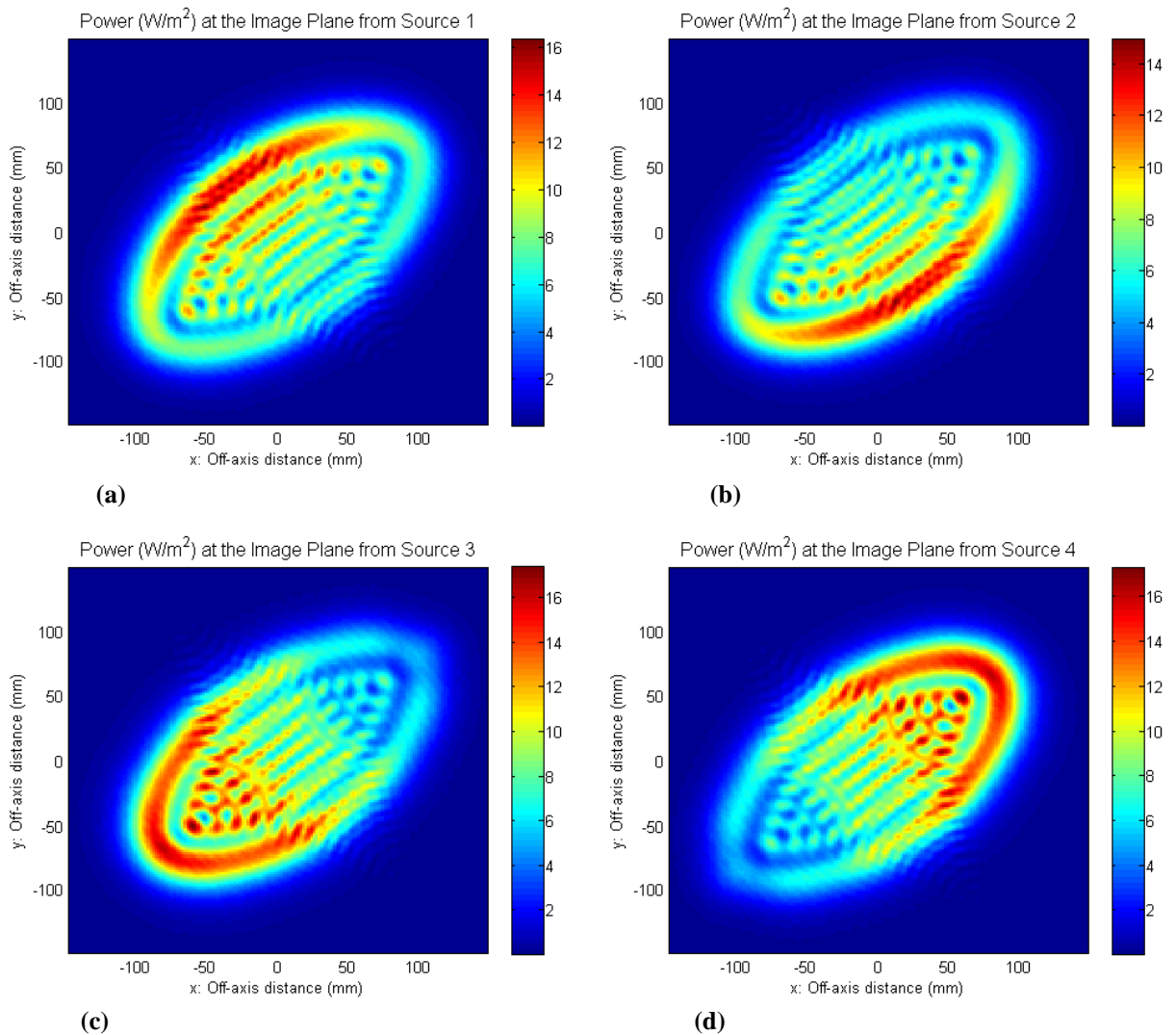


Figure 5.46 Modelling of beam patterns on the focal plane from individual sources of MBI-4. (a) shows the beam obtained from source 1, (b) shows the beam obtained from source 2, (c) shows the beam obtained from source 3 and (d) shows the beam obtained from source 4.

Taking this truncation into account does show beam patterns that are more similar to those obtained through the measurements, with most of the power focused in a single quadrant. This can be explained by the truncation analysis carried out in section 5.1.4 where it was shown that the power going through the elliptical aperture in the primary after transmission from the secondary was far greater than the power in the

beam passing through the same aperture after reflecting off the secondary mirror. Other factors that may explain some of the differences between the results from the measurements and those from the simulations are the number of sample points used over the focal plane (161 points over 200mm for the simulations and 89 points over approximately 180mm for the measurements) and the physical size of the detector. This is something that can be further analysed in the future.

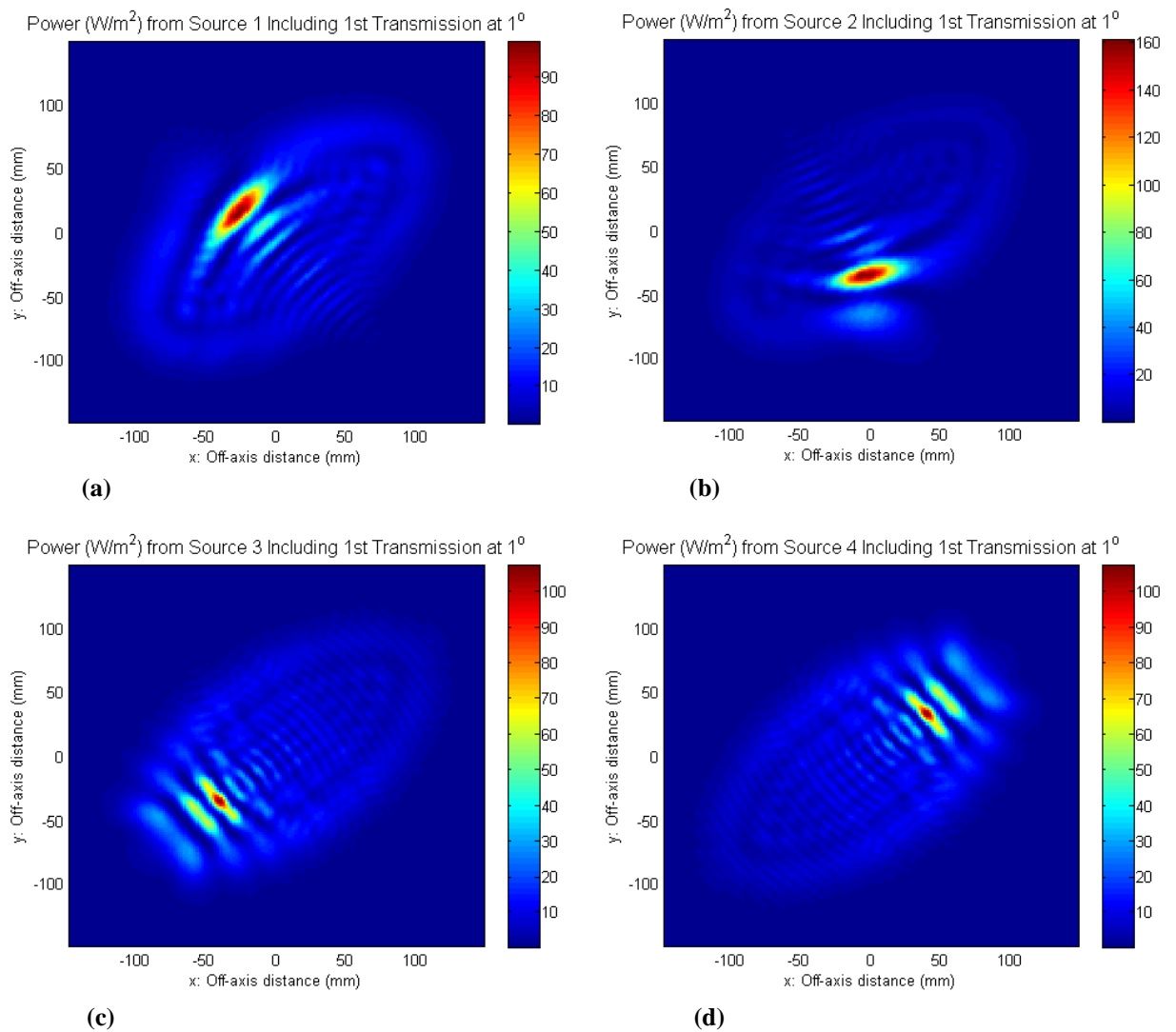


Figure 5.47 Modelling of beam patterns on the focal plane from individual sources of MBI-4. The truncation of the beam by the elliptical primary aperture after transmission at the secondary mirror has been accounted for. (a) shows the beam obtained from source 1, (b) shows the beam obtained from source 2, (c) shows the beam obtained from source 3 and (d) shows the beam obtained from source 4.

5.2 Conclusions

The MBI-4 system was modelled in MODAL to allow a full physical optics analysis to be carried out. In fact different propagation techniques were evaluated where it was shown that both a Gaussian beam mode and a Fresnel diffraction approach produced the general structure of the interference pattern on the image plane and therefore could be used as an initial design tool. The physical optics method provided a much more detailed image showing the fine structure of the interference patterns. These were compared to experimental measurements taken by MBI-4 in 2009 and there was quite a high level of agreement, however the scanning strategy of the observations was not taken into account in the model.

A scatter matrix was calculated for the optical beam combiner by coupling the field from each of the four sources to each detector in the bolometer array. This was done for two orthogonal polarisation directions and it was shown that due to the asymmetric aperture field of the smooth-walled conical detector horns the coupling efficiencies and therefore the coupled power depended on the direction of polarisation of the source. The effect is significant, however, if the coupled power is summed over all detectors both polarisations are very similar. The use of lenses on the detector horn antennas was also investigated where it was found that an increase of approximately 30% in coupled power is obtained if the lenses are present.

The power coupled to the detectors from each of the sources was found to be very low so a truncation analysis was carried out. It was shown that the elliptical aperture in the primary mirror after reflection from the secondary mirror was the plane at which most of the power in the beam was being lost. Also taken into account was the portion of the beam that passes through this aperture after transmission at the secondary mirror and the effect this has on the interference pattern at the image plane. While the power at the image plane from each of the sources was between 23% and 30% the power coupled to the detectors was much lower.

Mechanical tolerances of both the detector array and the mirrors was also investigated and it was found that xy -motion of the detector array had the most effect

on coupled power. However, by choosing an appropriate source and detector combination this could be used to characterise the instrument and determine the position of the detector array. Movement and rotation of the detectors in the z and θ direction, as well as xy and z motion of the mirrors, and mirror contraction, was found to have only a small effect on the performance of the instrument. An analysis of different bandwidth frequencies (as outlined in the systematic effects of interferometers in Table 1.4) was also carried out and the results are summarised.

Finally, a simulation of lab measurements carried out at Brown University using MBI-4 was carried out. The field from each of the four inward-facing horn antennas (generated using a Gunn oscillator) was propagated through the optical system to the focal plane where a single detector was placed on an xy -stage and scanned over a certain area. The same arrangement was modelled in MODAL and the results were confirmed using calculations in both Zemax and GRASP. While the measurements and modelling did not fully agree both showed that the field was focused on a single quadrant of the image plane, most likely due to the truncation of the beam by the elliptical aperture in the primary mirror. Other factors that need to be accounted for in future work are the resolution of the scan and the physical size of the detector used.

While MBI-4 has been used to prove the concept of bolometric interferometry it was designed around a number of constraints. However, MBI has now merged with BRAIN to form a new instrument called QUBIC (Q U Bolometric Interferometer for Cosmology) where the constraints on the optical system are not as rigid. The design and analysis of the optics used in this instrument are described in the Chapter 6.

Chapter 6

Quasi-Optical Design and Analysis of QUBIC

6.1 Introduction

In this Chapter we look at a very brief analysis of the QUBIC instrument, a system that has evolved from the success of the bolometric interferometry carried out by MBI-4 and the work carried out by the BRAIN (Background RAdiation INterferometer) pathfinder, another bolometric interferometer, that was stationed in Antarctica (Piccirillo, 2003). To reduce the impact of atmospheric emission (Hanany and Rosenkranz, 2003) the Concordia station in Dome-C was chosen as the best site for BRAIN observations. This station is a French–Italian base placed on the Antarctic plateau at ~1100km from both Mario Zucchelli and Dumont D’Urville stations where low humidity and absence of wind create the best conditions for astrophysical observations (Polenta *et al.*, 2007). A pathfinder for the instrument was built and brought to the observation site with the aim of testing the cryogenic system. Short observations of atmospheric emission were made for a few elevations and the acquired data fit very well to the secant law as expected for atmospherical emission. Measurements repeated at different azimuth and during different days would be needed to obtain a statistically significant estimation of the transparency of the atmosphere at the operating frequency of 145GHz. The BRAIN pathfinder proved the concept of cryogenics needed for measurements of the CMB at Dome-C, much the same as the MBI-4 instrument was built as a prototype to test the concept of bolometric interferometry.

In 2008 it was decided by both groups, the MBI team and the BRAIN team, to collaborate on a project, one that would use the findings of both MBI-4 and the BRAIN pathfinder to design and create one state-of-the-art bolometric interferometer known as the Q U Bolometric Interferometer for Cosmology (QUBIC). In this

Chapter we look at the QUBIC instrument and in particular the design and analysis of the optical system.

6.2 Science and Challenges with QUBIC

The scientific objective of the QUBIC instrument is very similar to that of MBI and BRAIN, that is, to generate a complete polarisation map of the cosmic microwave background, and in particular to measure the B -type polarisation generated by gravitational wave perturbations. Since linear perturbation theory tells us that a scalar field (such as a density perturbation) cannot couple to the pseudoscalar B -component of the CMB polarisation, the B -component is predicted to be an order of magnitude smaller than the E -component on all angular scales. It was seen earlier that on large angular scales, the B -component of the CMB polarisation may be dominated by the stochastic background of gravitational waves produced during inflation, while on smaller angular scales a different source of B modes appears, the conversion of E -type perturbations into B modes by gravitational lensing. Although detection of the lensing signal would not have the same revolutionary importance as detection of the tensor signal, it would provide powerful corroborative evidence of our understanding of the physics of CMB polarisation.

Due to the extremely small amplitude of the B -mode signal its detection will pose formidable although not insurmountable challenges. The sensitivity required should be achievable by observing for approximately one year with around 10^3 detectors, however, foregrounds and systematic effects will prove to be the most difficult challenges. With regards to foregrounds, known sources of polarised foreground emission such as galactic dust and synchrotron radiation are expected to be larger than the cosmological signal. However, the experience of past experiments such as WMAP suggest that it will be possible to characterise and remove these unwanted foreground signals from the data.

Systematic errors are the other chief challenge and any experiment hoping to characterise the CMB B mode polarisation will require unprecedented control of

systematic effects. In the past, interferometry has proved to be a powerful technique for reducing systematic errors in CMB experiments and the QUBIC team believe that the potential for improved control of the systematics in a bolometric interferometer is one of the main reasons for exploring this option for characterising the CMB B modes.

With such sensitivity and characterisation of systematic effects required it is essential that the system as a whole is fully understood. The author and the THz Optics group at NUI Maynooth are involved in the design and modelling of the optical system which plays a vital role in the successful operation of the instrument.

6.3 The QUBIC Instrument

QUBIC will be composed of six interferometer modules operating at three different frequencies, 97GHz, 150GHz and 220GHz, with a 25% bandwidth for optical sensitivity. This will provide a good check against contamination from foregrounds. Each of these modules will contain an array of 144 receiver horn antennas whose signals will be split into orthogonal polarisations and re-emitted by secondary horns before being combined using an optical beam combiner located inside each of the six cryostats. The primary horn antennas will be single-moded corrugated horns which are well understood and have low cross-polarisation and low sidelobe levels, as shown in Chapter 3. They are quite easy to manufacture at the QUBIC operating frequencies. The interference fringes produced at the focal plane will be imaged using a 900-element array cooled down to 100mK. This will allow the reconstruction of the four Stokes parameters described previously.

The QUBIC cryogenic system will also be modular with each cryostat cooling a single array. Pulse-tube (PT) refrigerators will be used as the main coolers due to the difficulty of providing liquid helium to Dome-C, where QUBIC will be located, during the winter. For the lowest temperature stages ^3He fridges or dilution fridges will be used. Such a cryogenic system has been operated successfully during two summer campaigns with the BRAIN instrument. The BRAIN experiment found that the disadvantages of the PT solution with respect to the standard operation with

liquid helium are the amount of power required (approximately 7KW) and low level vibrations of the 2K flange of the PT by the He pressure pulses. However, both of these issues were overcome. Other issues to be considered with regards to the cryogenics are the large physical size of the windows and filters, which have stringent requirements due to radiative heat loads, and the range of zenith angles that can be achieved since the PT must be kept as vertical as possible. Both of these issues can be overcome but increase the level of complexity of the system (QUBIC White Paper, 2009).

6.4 Design and Analysis of the Beam Combiner

Like MBI, QUBIC will make use of a quasi-optical beam combiner and in this section we look at the possible configurations of the combiner to be implemented in QUBIC. Systems containing both mirrors and lenses are considered. Mirrors can be characterised extremely well but introduce aberrations into the system and although lenses do not have this effect they are difficult to model accurately. We begin by looking at the constraints placed on the design of the optical system.

6.4.1 Optical System Design Constraints

The combining of signals from the receiver horn antennas will be done by means of an optical beam combiner where the fields radiated from back-to-back horn antennas will be transferred to the image plane by a Fizeau system. At present, the QUBIC optical system must satisfy the following requirements (QUBIC White Paper, 2009):

- The combiner must be a focusing system so that rays launched at a given angle from the re-emitting horn array are focused to a single point on the focal plane. In this way equivalent baselines will produce identical fringe patterns.

- The limit on the total number of bolometers that can be produced, together with the sampling requirement for at least two bolometers per fringe (Nyquist criteria) means that the equivalent focal length of the combiner must range from 200mm to 300mm. Since the back-to-back horn array size is approximately 240mm by 240mm the combiner will be a very fast system (have a small F/#).
- Mirrors or lenses can be used within the combiner with the choice being between an on-axis lens system and an off-axis mirror system that can avoid the shadowing of any baselines. On-axis mirrors are not being considered due to the high levels of truncation they exhibit. The benefit of using mirrors is that they can be extremely well characterised using physical optics, however off-axis systems will introduce aberrations.
- The fringe pattern produced by equivalent baselines should be the same. In order to prevent signal leakage from the unpolarised to polarised signal, the power coupled to any given detector should not vary by more than 1% between these baselines. This is a significant challenge given the very small F/# and is a severe limitation on the aberrations that can be tolerated.
- The beam from the re-emitting horns will have a FWHM of approximately 14°. The system must therefore not only have a short focal length but a wide field of view.
- The system has to be compact enough to fit within a cryostat of about 1m³.

Since this system is still evolving these constraints are relatively new and were not present during the initial optics design phase. In the next section we consider the first mirror configuration which was initially proposed by Spinelli (2010) in the very early stages of the project. A design by Bennett (2011) carried out at NUIM as part of the work for a Ph.D. (Bennett, 2011) is also examined.

6.4.2 Physical Optics Analysis of the Mirror Configurations

The first system described here was proposed by Spinelli (2010) and consists of an off-axis Gregorian system with a parabolic primary mirror and elliptical

secondary mirror. The system was modelled using MODAL as shown in Figure 6.1 using a series of reference points and frames similar to the MBI-4 model. In this system, designed using ray tracing, the re-emitting horns were positioned 400mm from the point at which the on-axis ray strikes the primary mirror as shown. In terms of beams rather than rays this source position corresponds to the location of the beam waist at which the radius of curvature is infinite. In this initial design the horn antennas feeding the optics were 13.1mm in diameter and produced a beam with a FWHM opening angle of 21 degrees. The FWHM was converted to a divergence angle at a radius of $1/e$ (the asymptotic beam growth angle, θ_0) using the equation,

$$\theta_{fwhm} = 1.18\theta_0 \quad (6.1)$$

where θ_0 is related to the beam waist radius by

$$w_0 = \frac{\lambda}{\pi\theta_0} \quad (6.2)$$

where in this case the wavelength, λ , was 3.12mm. A corrugated horn antenna will produce a beam that has a beam radius of $w=0.644a$ at the aperture of the horn where a is the horn radius (aperture = 13.1mm/2). The distance the beam propagates from the waist position to the horn aperture was then calculated as

$$z = \frac{\pi w_0}{\lambda} \left[w^2 - w_0^2 \right]^{0.5}. \quad (6.3)$$

By knowing the propagation distance and the beam waist radius the radius of curvature at the aperture of the horn antenna was calculated using:

$$R = z \left[1 + \left(\frac{\pi w_0^2}{\lambda z} \right)^2 \right]. \quad (6.4)$$

A summary of the results from these calculations is given in Table 6.1. The horn aperture was placed $z=8.54\text{mm}$ in front of the known beam waist location (400mm from the primary mirror).

Horn Antenna Parameters	
Horn Antenna Diameter	13.1mm
Full Width Half Maximum Angle	21 deg
Beam Waist Radius	3.2mm
Distance from Waist to Horn Aperture	8.54mm
Radius of Curvature at Horn Aperture	21mm

Table 6.1 Parameters of the horn antennas used in the off-axis Gregorian system.

The frame of the primary mirror was positioned with its origin located at the point at which the centre ray from an on-axis source strikes the mirror (Figure 6.1). This was 400mm from the beam waist position or from the focus if thinking in terms of rays. The centre of the mirror (aperture) was then positioned at the origin of this frame. To create the surface shape of the mirror the focal point, the vertex direction (the direction from the focal point to the vertex) and the centre of the section of mirror that was being used, which is defined by the bounding volume, were defined. In this case the bounding volume was described in MODAL as an infinite cylinder with its axis of symmetry along direction of the primary ray with a diameter of 400mm.

The secondary mirror was set up in a similar way to the primary with its frame established by defining the origin and two vectors, the vectors being the z -axis and the x -axis, which had the same direction as those defining the source 1 (S1) in Figure 6.1. As with the primary mirror, the secondary was positioned by placing the centre of the section at the origin of frame and defining the location of three points: the two foci and a point on the surface, which is the same as the centre. Again, the bounding volume was an infinite cylinder, this time with a diameter of 380mm as per the initial design. A frame for the image plane was defined by translating the

secondary frame a distance of 400mm along the z -axis. The image plane was centred on the origin of this frame and consisted of a simple square surface with a side length of 200mm.

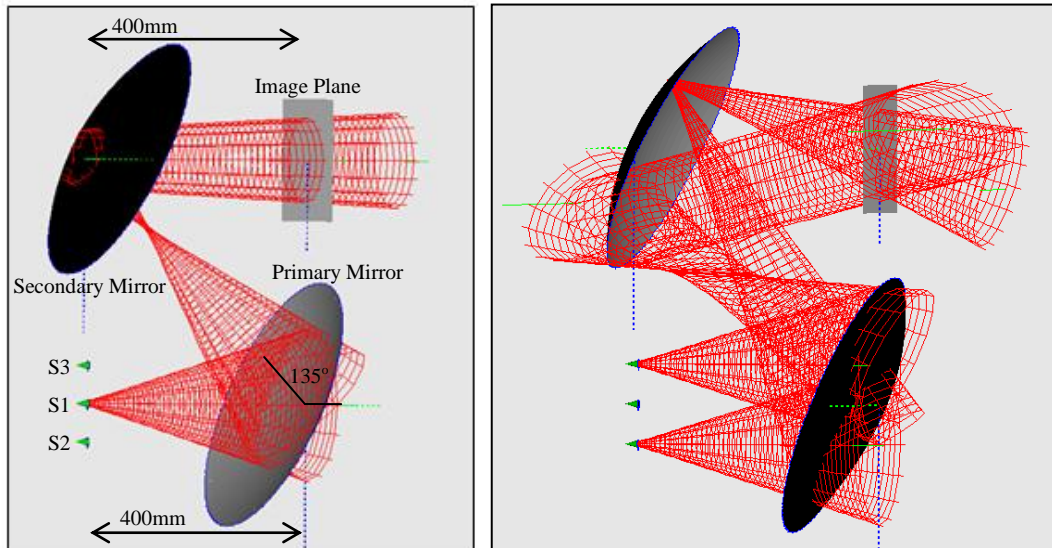


Figure 6.1 QUBIC Gregorian optical system as modelled in MODAL. In the image on the left a single beam from source 1 is propagated through the system while in the image on the right beams from sources 2 and 3 are propagated through the optical system.

As a first analysis the beam from a single on-axis horn antenna was propagated through the optical system using a physical optics approach. The power density at each element was calculated and the results of this are shown in Figure 6.2 (a). Two other horn antennas, separated by a baseline of 125mm, were placed along the same axis as the single horn (S2 and S3 in Figure 6.1). The power density for each of these horns was calculated in the same way and is also shown in Figure 6.2. The interference pattern produced by sources 2 and 3 was calculated and is given in Figure 6.3 where it can be seen that the fringes are quite distorted, as is the phase for the same baseline (also shown in Figure 6.3). Because of these distortions equivalent baselines will not produce identical fringe patterns.

The above system was also analysed for four equivalent 40mm baselines as shown in Figure 6.4. The first of these is centred on the origin and lies along the y -

axis, the second represents a shift along the y -axis, the third a shift along the x -axis and finally the fourth baseline is horizontal and also shifted off-axis. The resulting fringe patterns at the image plane can be seen in Figure 6.5. Baselines 1 to 3 are equivalent and in a perfect imaging system would produce identical fringe patterns.

Parameters of the Gregorian Optical System	
Distance from horn waist to primary mirror	400mm
Beam bending angle	135 degrees
Distance from primary mirror to secondary mirror	565.68mm
Distance from secondary mirror to image plane	400mm
Primary mirror shape	Parabolic
Primary mirror diameter	400mm
Secondary mirror shape	Elliptical
Secondary mirror diameter	380mm
Image plane width	200mm

Table 6.2 Parameters of the off-axis Gregorian optical system.

The results of this analysis show that within this system truncation of the beam is not really a problem, even for the 125mm baseline examined above, however beam distortion is quite significant. The fringe pattern is curved due to amplitude distortion caused by the optical system. When the beam spreads over the primary reflector, different regions of the field experience a different equivalent focal length causing an asymmetry in the beam. In terms of Gaussian beam modes this is equivalent to scattering the power into higher order modes and shifting the peak of the beam off centre. While the secondary mirror can be designed to compensate for this effect the overall asymmetry introduced in the system depends on the phase slippage between the modes. The less variation in phase slippage as the field propagates between the mirrors the better the compensation will be. However, in the above Gregorian system it can be seen that the beam passes through a waist position between the primary and secondary mirrors, meaning the phase slippage is varying significantly causing a high level of curvature in the fringe pattern.

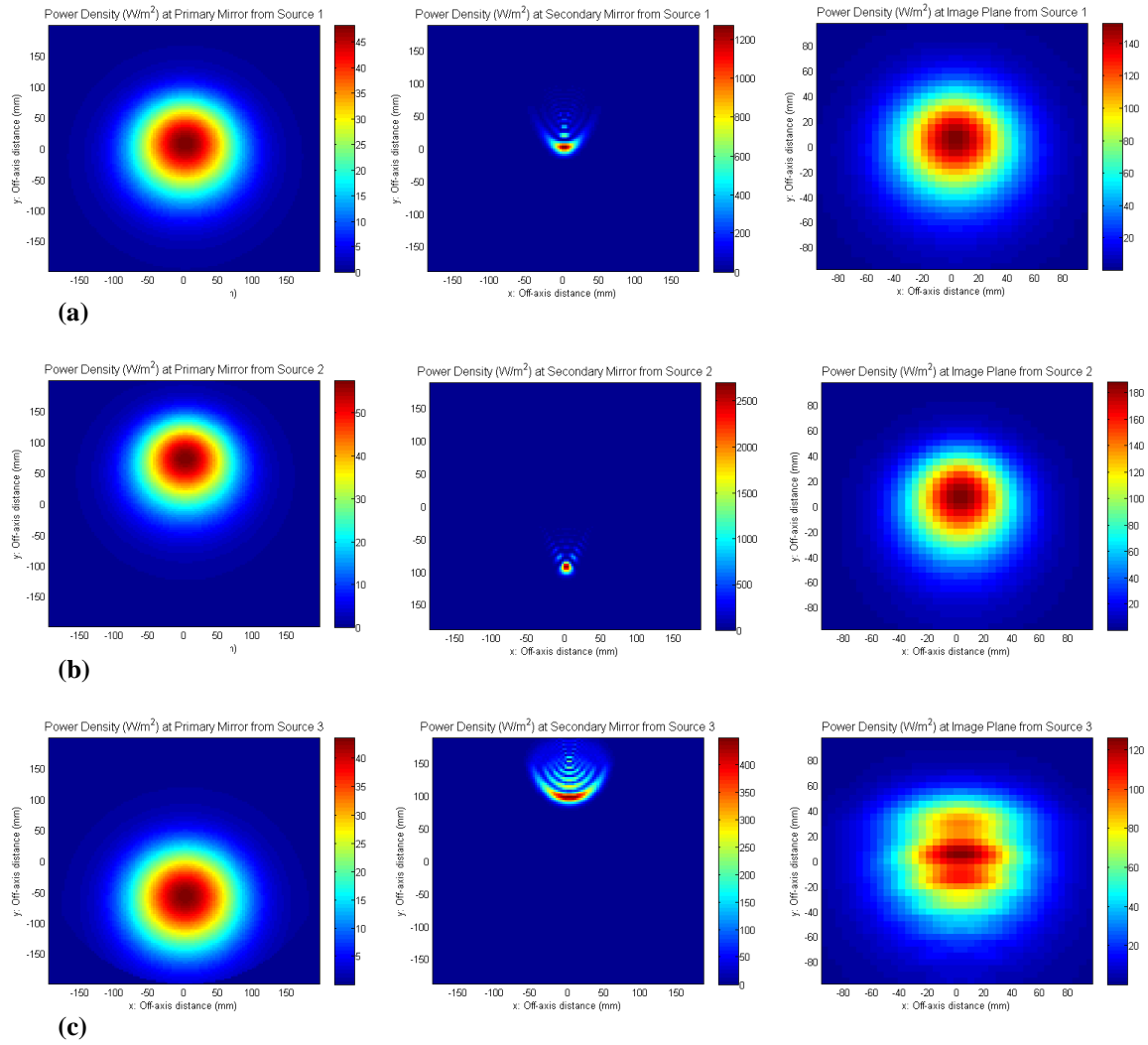


Figure 6.2 The power density of source 1 at the primary mirror, secondary mirror and the image plane of the Gregorian system is shown in (a). Parts (b) and (c) show the same plots for sources 2 and 3 respectively.

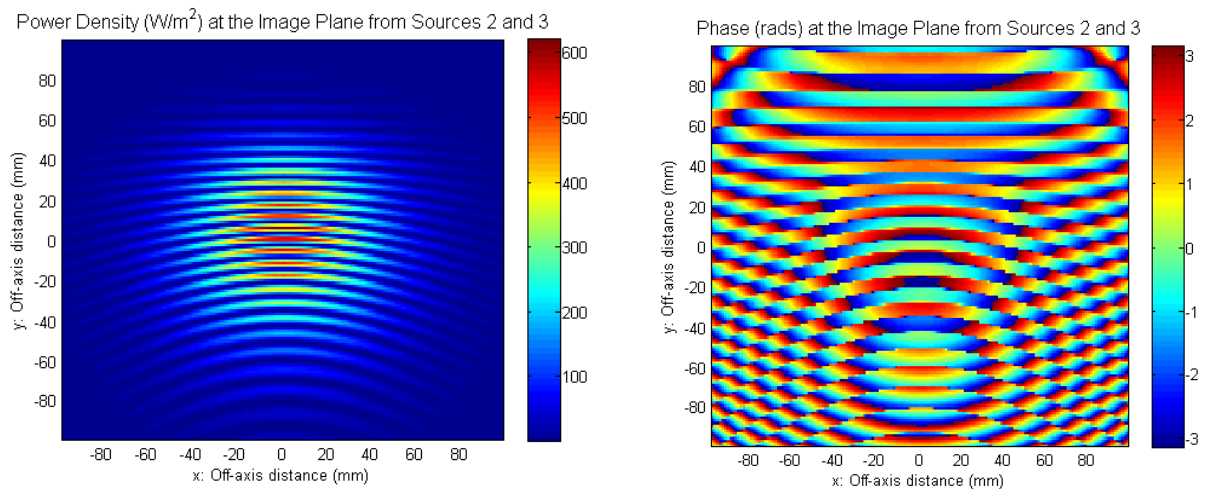


Figure 6.3 The interference fringe pattern produced by sources 2 and 3 of the off-axis Gregorian system using physical optics. The image on the left shows the power density while the phase is shown in the image on the right

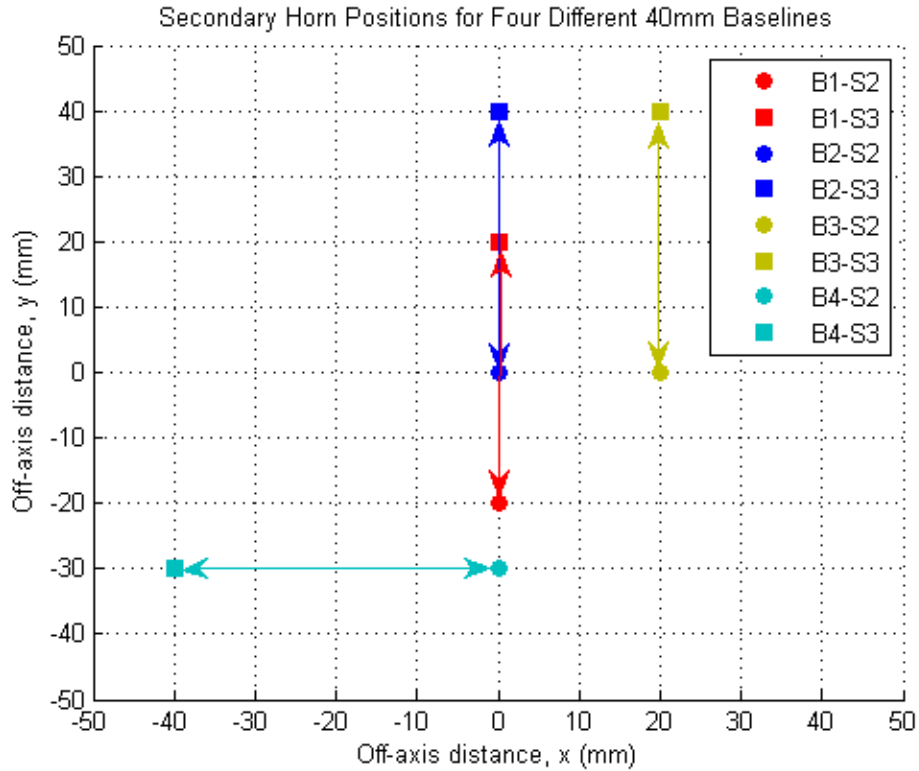


Figure 6.4 Four equivalent baselines of 40mm that were analysed using physical optics. B_m-S_n represents baseline m and source n .

If the curvature of the fringes is known and is the same for all equivalent baselines it will average out when the baselines are added. However, if the curvature varies between equivalent baselines it will cause unwanted smearing of the signal when all baselines are combined. While on first inspection of Figure 6.5 equivalent baselines seem to produce the same fringe pattern, the x - and y -cuts shown in Figure 6.6 for baselines 1 and 3 show that actually the fringe patterns are significantly different and that equivalent baselines within the Gregorian system so not produce the same fringe patterns.

To eliminate the curvature seen in the interference pattern a new dual reflector system was proposed by Bennett (2011). The optics were arranged in a general crossed Cassegrain (GCC) configuration with a parabolic primary mirror (diameter = 180mm) and a hyperbolic secondary mirror (diameter = 380mm), and were optimised using the Dragone condition to minimise astigmatism and cross polarisation levels.

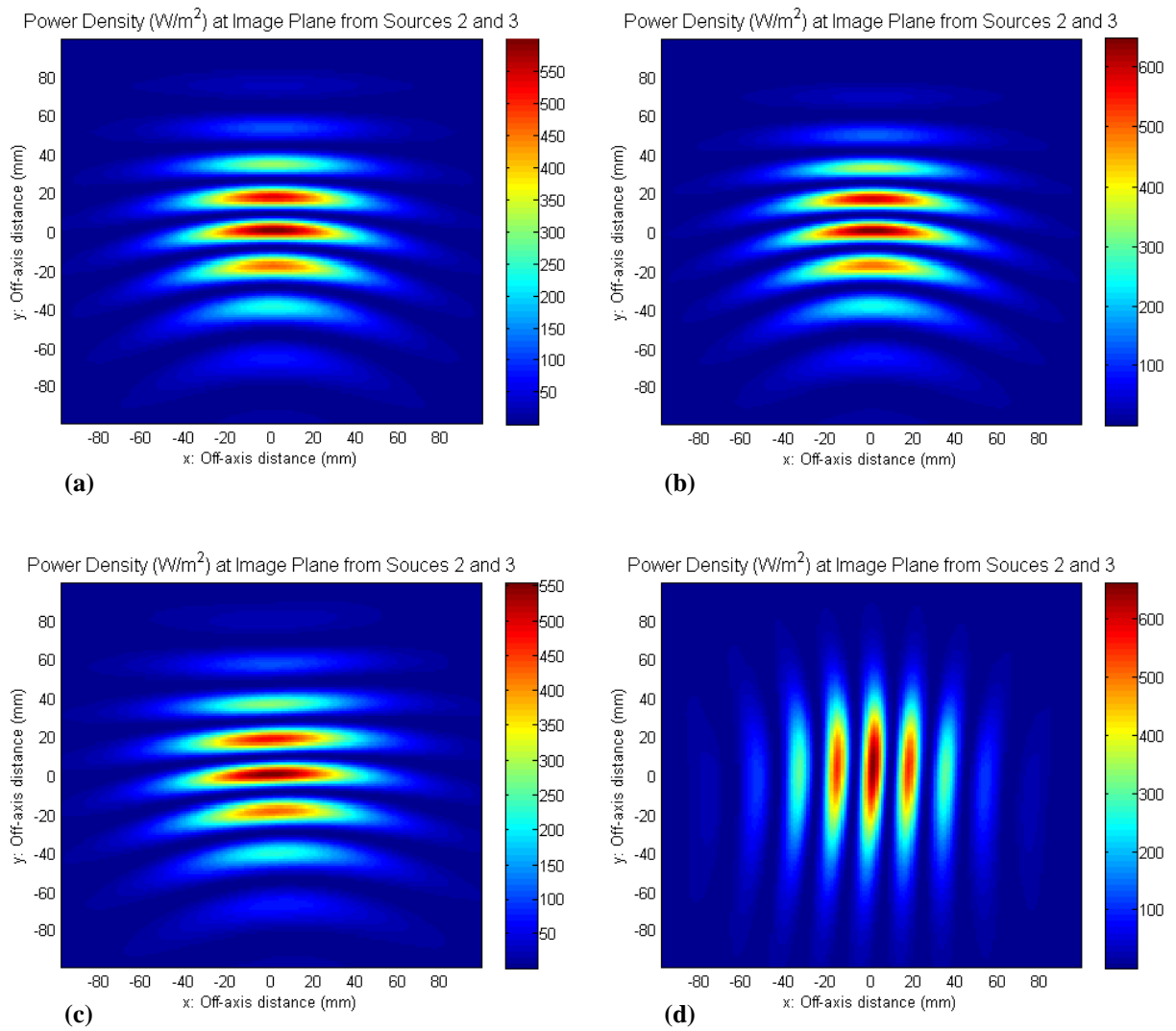


Figure 6.5 Interference fringe patterns at the image plane of the Gregorian system from (a) baseline 1, (b) baseline 2, (c) baseline 3 and (d) baseline 4.

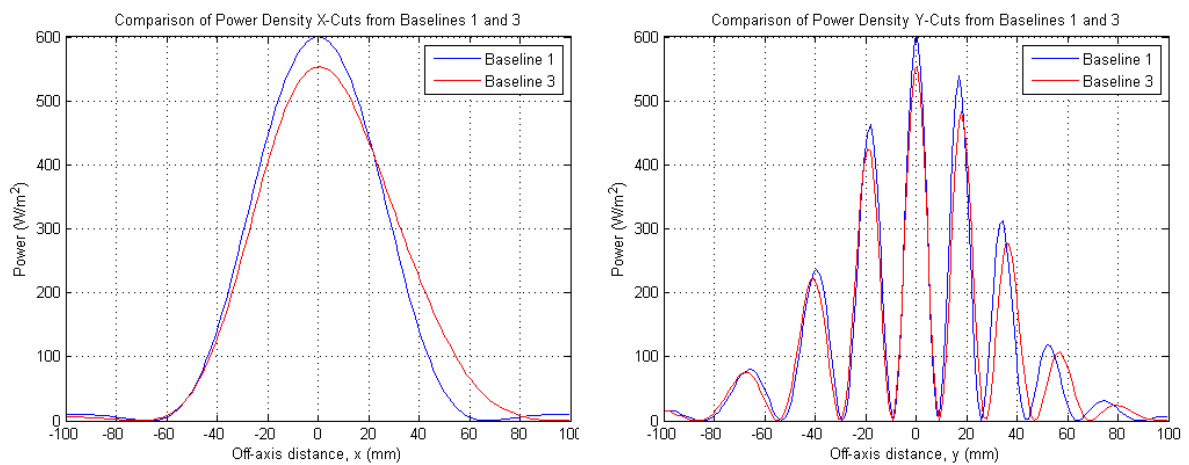


Figure 6.6 An x -cut (left) and y -cut (right) across the fringe patterns produced at the image plane of the Gregorian system by baselines 1 and 3.

The primary mirror was defined by three parameters, the frame, the focal point and the direction from the focal point to the vertex. Considering Figure 6.7, the vertical distance d_1 from the vertex of the primary mirror to the point at which the on-axis beam struck the mirror was 638.575mm. The distance d_2 from the source waist position to the vertex was 400mm. Using the equation for a parabola in terms of its focal length ($y = x^2/4f$) the distance d_3 was found and also the distance d_4 from the waist to the point at which the beam hits the mirror. The primary mirror frame mentioned above was therefore defined as being translated approximately 215.98mm from the waist position. The coordinates of the focal point were defined as $(x, y, z) = (0, 638.575, -153.975)$ and the vertex direction the z -axis of the global frame.

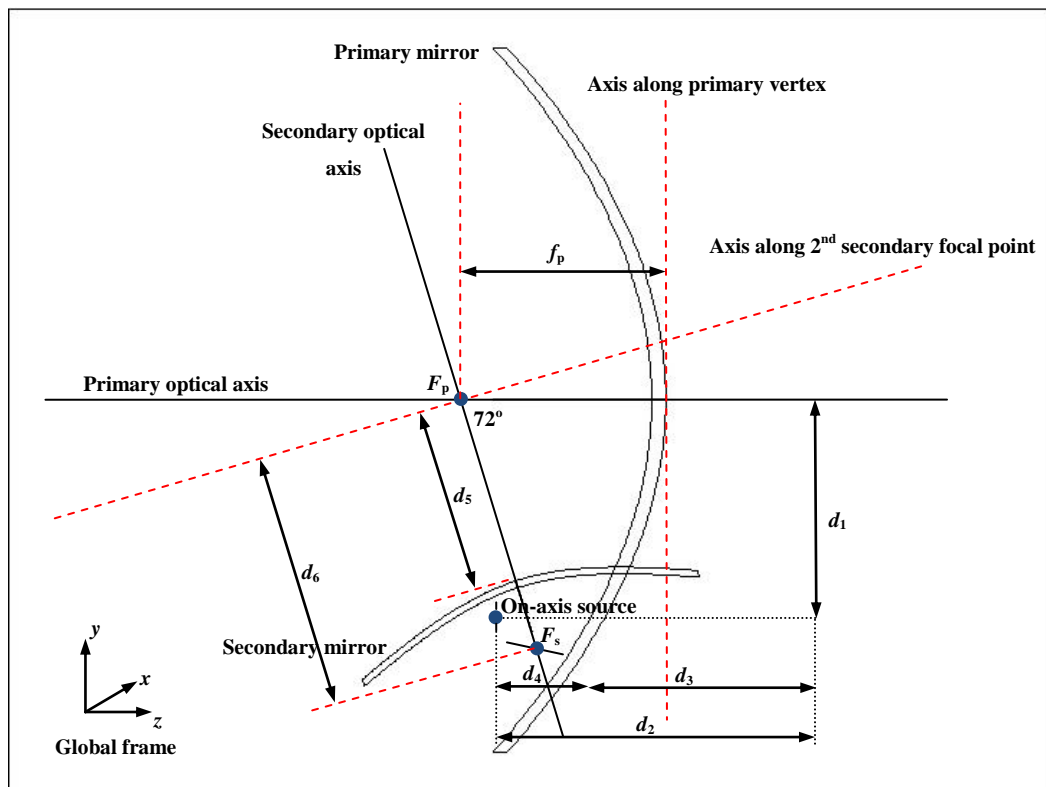


Figure 6.7 Design parameters of the general crossed Cassegrain system proposed for the QUBIC instrument. The mirrors are oversized in this image to show the shape of the conic section and the axes of the mirrors. The orientation of the global frame is also shown, however its origin is 10mm behind the on-axis source waist position.

In the case of the secondary mirror, its radius of curvature (ROC) and conic constant (k) were known and therefore its eccentricity, e , could be calculated (since

$k = e^2$). The focal point of the primary mirror coincided with one of the focal points of the hyperbolic secondary mirror allowing the distance d_5 to be calculated ($d_5 = ROC/(1 - e^2)$), and therefore the distance from the point focal point (F_p) to the second focal point of the secondary mirror (F_s), since $d_6 = d_5 \times e$. The direction of the secondary optical axis was known to be at an angle of -72 degrees to the primary optical axis.

The optical axis of the image plane was defined at an angle of 31 degrees to the secondary optical axis with its frame centre coinciding with the secondary focal point. It had a width of 150mm in both directions. The design parameters are summarised in Table 6.3. A ray tracing diagram for a long baseline is given in Figure 6.8 (Bennett, 2011) while the system, as modelled in MODAL, is shown in Figure 6.9. In Figure 6.9 it can be seen that the beams from the secondary mirror remain approximately collimated as they propagate to the image plane, ensuring a lower level of distortion compared with that seen in the Gregorian system analysed above.

Design Parameters of the General Crossed Cassegrain System	
Distance from primary vertex to on-axis horn antenna (d_1)	638.575mm
Distance from on-axis source waist to primary vertex (d_2)	400mm
Distance from primary mirror surface to primary vertex (d_3)	184.02mm
Distance from on-axis source waist to primary mirror (d_4)	215.98mm
Distance from primary focal point to secondary vertex (d_5)	560.9mm
Distance from primary focal point to secondary focal point (d_6)	775mm
Primary mirror type	Parabolic
Secondary mirror type	Hyperbolic
Primary mirror focal length (f_p)	553.975mm
Secondary mirror focal length (f_s)	387.5mm
Primary mirror diameter	180mm
Secondary mirror diameter	380mm
Image plane width	150mm

Table 6.3 Design parameters of the general crossed Cassegrain design as modelled in MODAL.

The corrugated conical horn antennas feeding the optics were 11.6mm in diameter and produced a beam with a FWHM opening angle of 14 degrees. Similar calculations to those carried out for the Gregorian system feed horns using equations 6.1 to 6.4 were done for this system and the results of these are summarised in Table 6.4. As shown in Figure 6.9 three horn feeds were considered, one on-axis (S1) and two off-axis horn antennas (S2 and S3), equivalent to baseline 1 described in Figure 6.4. Figure 6.10 shows the power in the beam from each of these as they pass through the optical system as calculated using physical optics while Figure 6.11 shows the power and phase of the interference pattern resulting from the combining of sources 2 and 3 at the image plane. A similar analysis was carried out using GRASP (Bennett, 2011) and the results were in good agreement with those calculated using MODAL. As with the Gregorian system truncation by the optical system is not significant and in this case the amplitude distortion has been greatly reduced to produce straight fringes. This is also evident from the phase pattern where it can be seen to be similar to a step function.

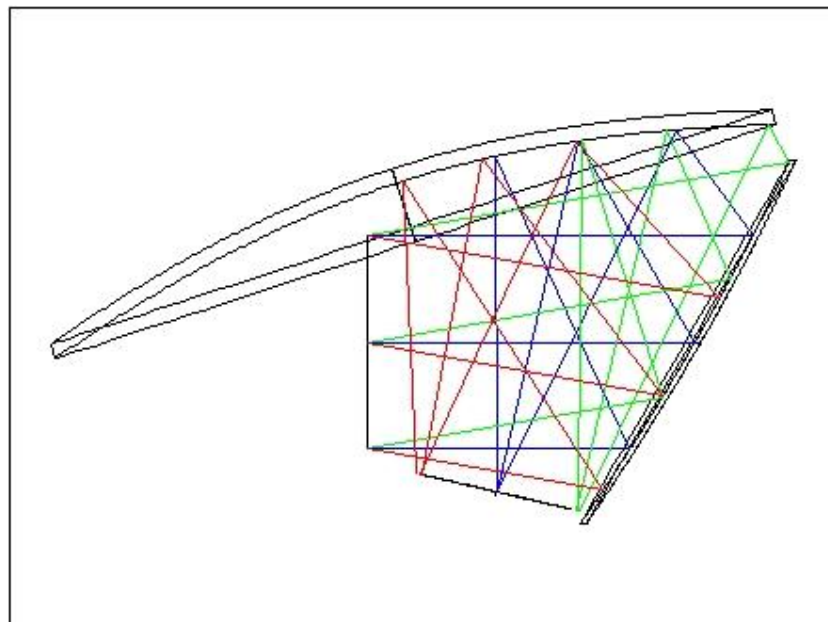


Figure 6.8 Ray tracing diagram of the general crossed Cassegrain proposed for QUBIC (Bennett, 2011).

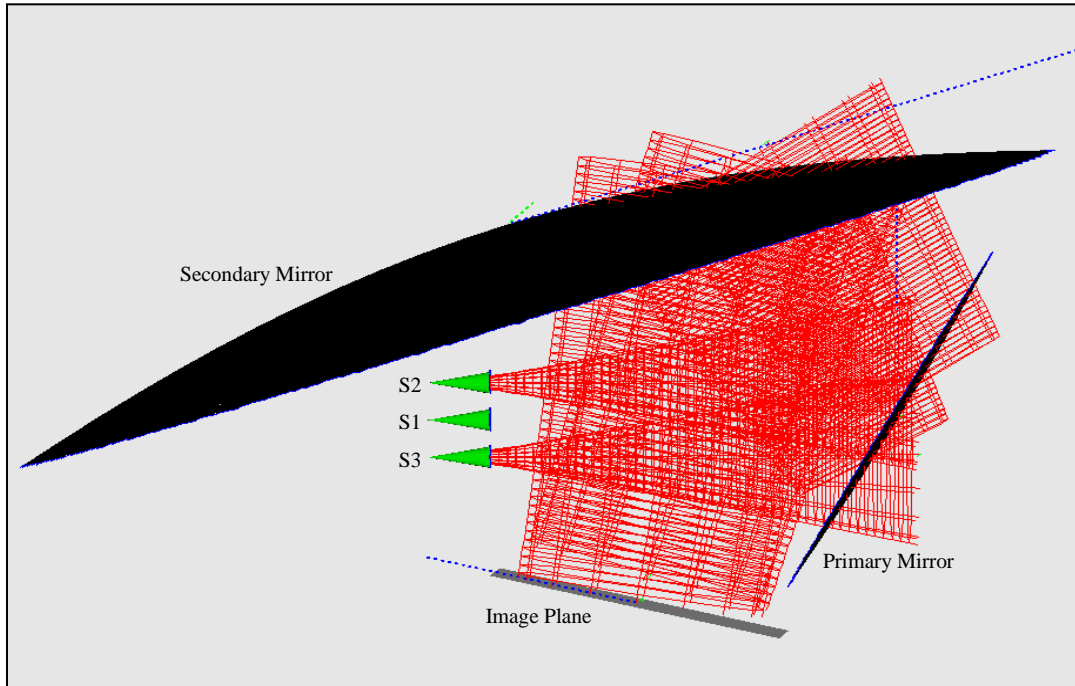


Figure 6.9 The general crossed Cassegrain system as modelled in MODAL. As can be seen the secondary mirror could be reduced in size without any significant truncation.

Horn Antenna Parameters	
Horn Antenna Diameter	11.6mm
Full Width Half Maximum Angle	14 deg
Beam Waist Radius	3mm
Distance from Waist to Horn Aperture	10mm
Radius of Curvature at Horn Aperture	32mm

Table 6.4 Horn antenna parameters as implanted in the general crossed Cassegrain design.

The three other baselines described above (Figure 6.4) were also analysed and the resulting fringe patterns can be seen in Figure 6.12. As expected, the equivalent baselines examined produced almost identical interference fringe patterns and the results were consistent with those produced by GRASP.

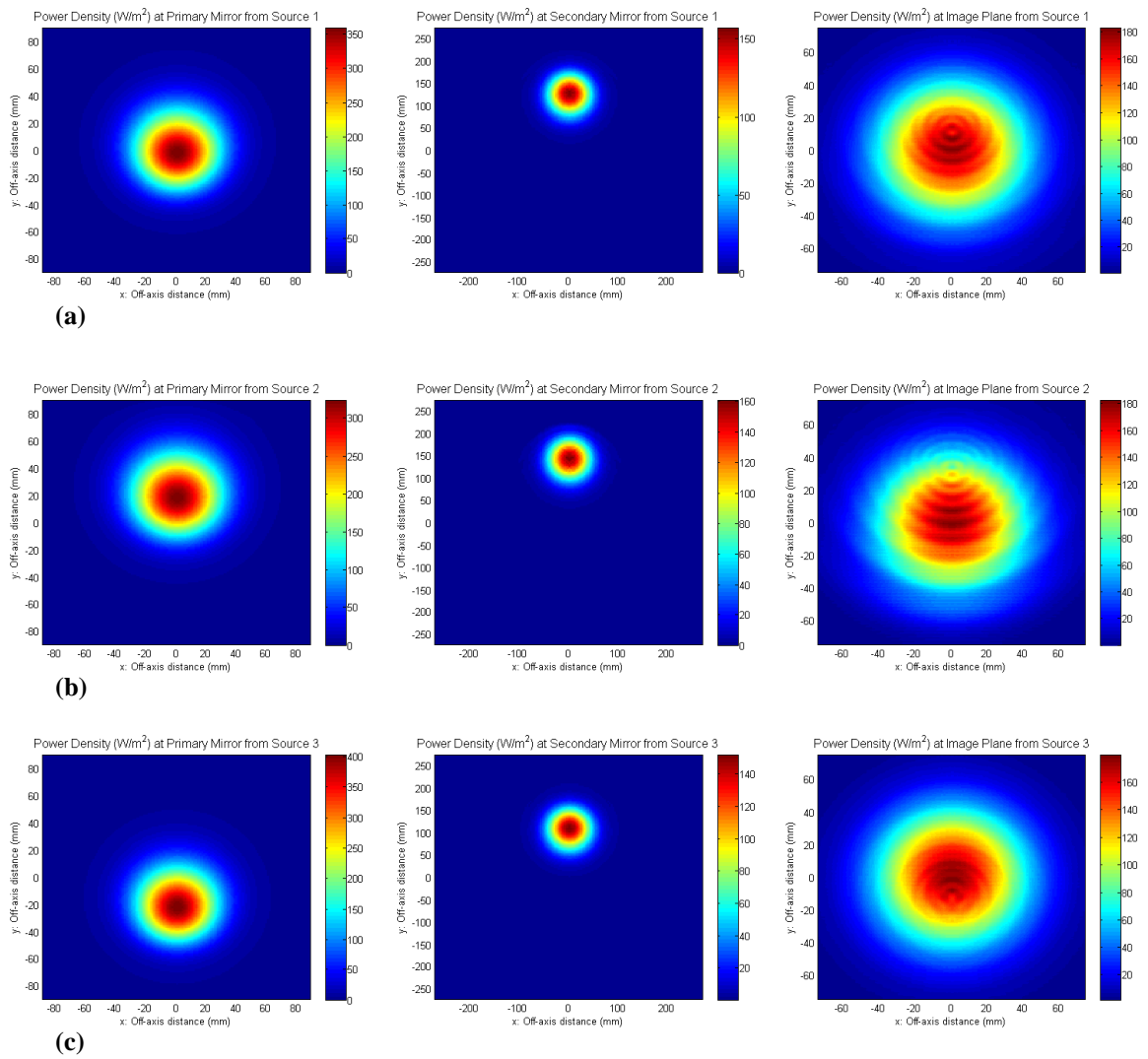


Figure 6.10 The power density of source 1 at the primary mirror, secondary mirror and the image plane of the general crossed Cassegrain system is shown in (a). Parts (b) and (c) show the same plots for sources 2 and 3 respectively.

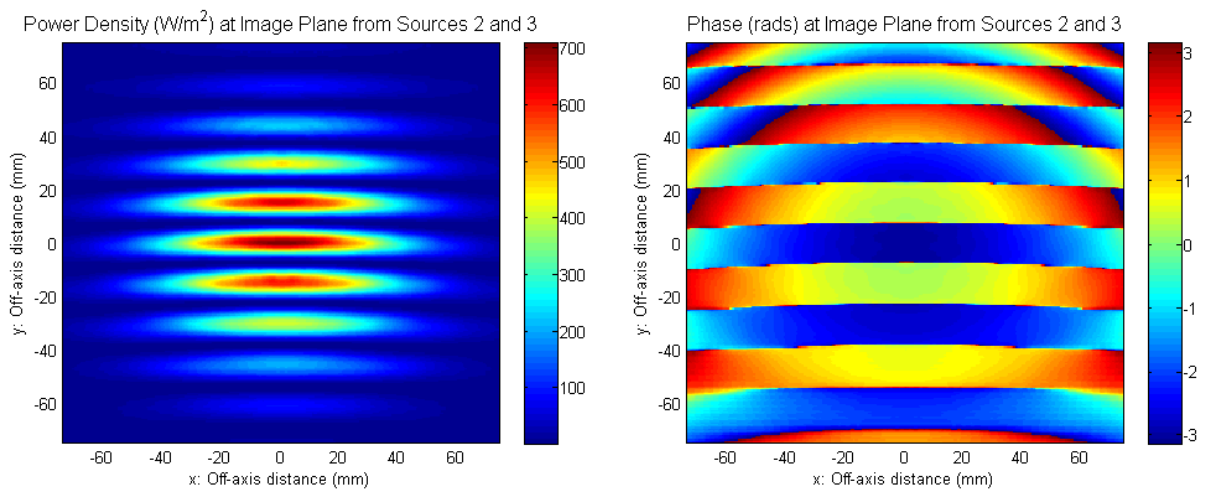


Figure 6.11 The interference fringe pattern produced by sources 2 and 3 of the general crossed Cassegrain system using physical optics. The image on the left shows the power density while the phase is shown in the image on the right.

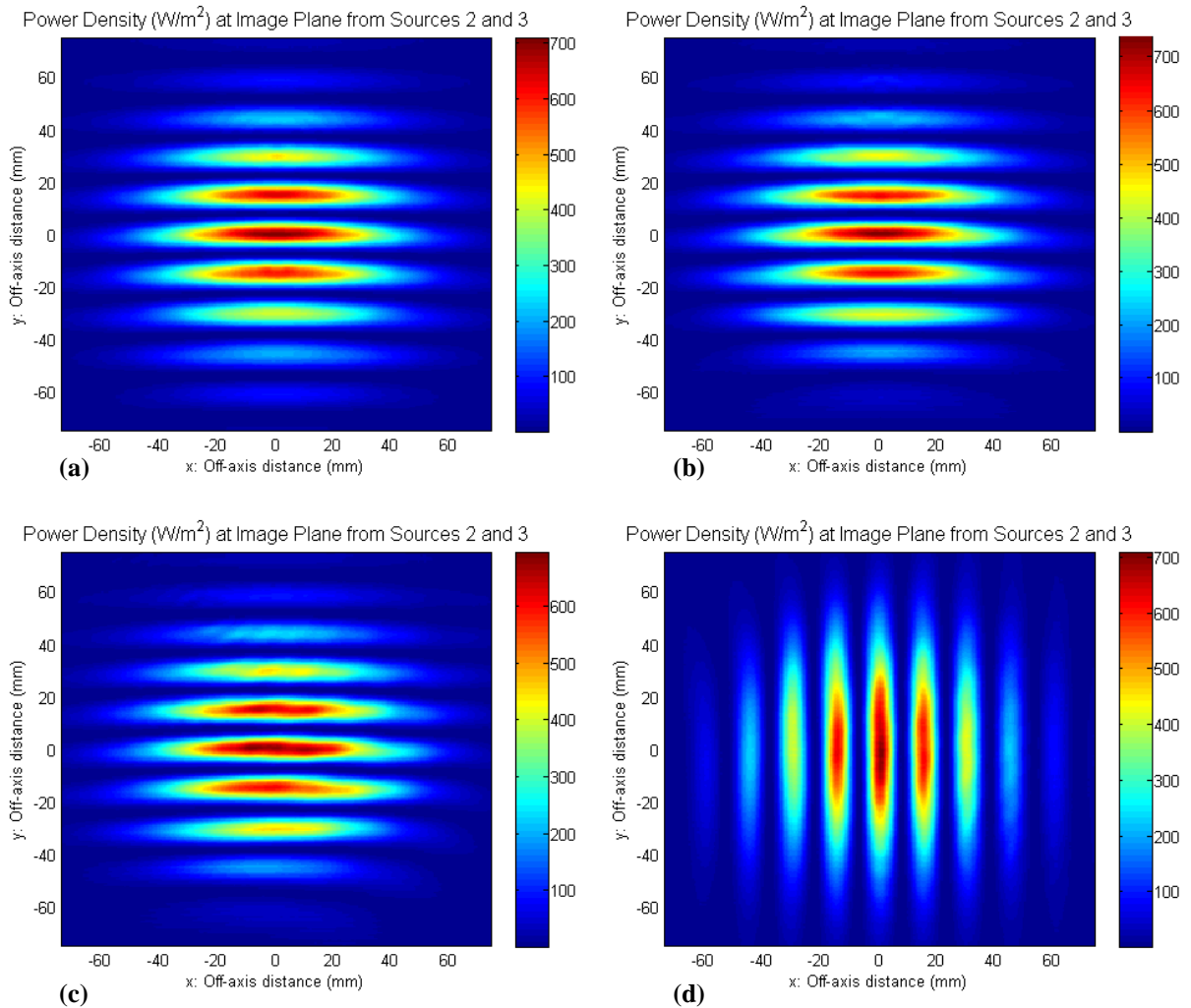


Figure 6.12 Interference fringe patterns at the image plane of the general crossed Cassegrain system from (a) baseline 1 (as in Figure 6.11 but shown here for comparison), (b) baseline 2, (c) baseline 3 and (d) baseline 4.

6.4.3 The Implementation of Lenses

The final system analysed in this chapter is one containing lenses. While the two systems described so far both contained mirrors, elements whose properties are very well known and can be simulated very accurately using physical optics (with existing commercially available software such as GRASP), the system presented here contains lenses, which are more difficult to model. While ray tracing is an extremely useful tool for modelling optical elements, as was seen in Chapter 3, such an approach is only useful in the limit of extremely short wavelengths and therefore

diffraction effects are neglected. However, physical optics can be applied to lenses and MODAL has the ability to model these elements by means of a series of reflections from the lens surfaces. The field undergoes a series of propagations and reflections within the lens until the total power being reflecting is extremely small, therefore assuring that the transmitted power is accurate.

Cross systems such as the one just described may suffer from stray-light problems and so on-axis designs using lenses were also considered. The details of the system presented here and designed by Bennett (2011) are given in Table 6.5 and an image of the system as implemented in MODAL is shown in Figure 6.13. To define the system in MODAL the radius of curvature and conic constant of each lens surface is entered as well the lens location, centre thickness and refractive index. The sources were defined as corrugated horn antennas with a slant length of 50mm and an aperture radius of 4.767mm giving a beam radius of 3.07mm ($=0.644a$) at the aperture of the horn. An initial analysis was carried out by passing the field from each of the two horn antennas (S2 and S3 in Figure 6.13), placed 20mm each side of the optical axis (baseline 1), through the optical system and propagating them to the image plane. The results from this are shown in Figure 6.14.

The power at each element in the system as a fraction of the source power was calculated. Having propagated through lens 1 both sources 2 and 3 contained 92% of the original source power (1W). After lens 2 the power, again in both sources, was 84% of the source power and at the image plane the power was 81% in both sources. It was expected that sources 1 and 2 would not only have mirrored beam patterns as seen in Figure 6.13 but also the same power characteristics since the lenses are rotationally symmetric and the here we considered a baseline that was centred on the optical axis.

The fringe pattern for this baseline and the three other baselines analysed in the mirror systems were also considered with the power density calculated using physical optics shown in Figure 6.15. As with the general crossed Cassegrain reflector system the fringes produced by this system are straight and similar in power distribution for all equivalent baselines examined.

Lens System Design Parameters	
Distance from waist to surface 1 of lens 1	135.85mm
Centre thickness of lens 1	100mm
Diameter of lens 1	240mm
Refractive index of lens 1	1.5
Radius of curvature of lens 1 surface 1	596.82mm
Conic constant of lens 1 surface 1	-1
Radius of curvature of lens 1 surface 2	-389.44
Conic constant of lens 1 surface 2	-1
Distance from waist to surface 1 of lens 2	399.99mm
Centre thickness of lens 2	100mm
Diameter of lens 2	240mm
Refractive index of lens 2	1.5
Radius of curvature of lens 2 surface 1	389.44
Conic constant of lens 2 surface 1	-1
Radius of curvature of lens 2 surface 2	-596.82
Conic constant of lens 2 surface 2	-1

Table 6.5 Design parameters of a proposed lens system for the QUBIC beam combiner.

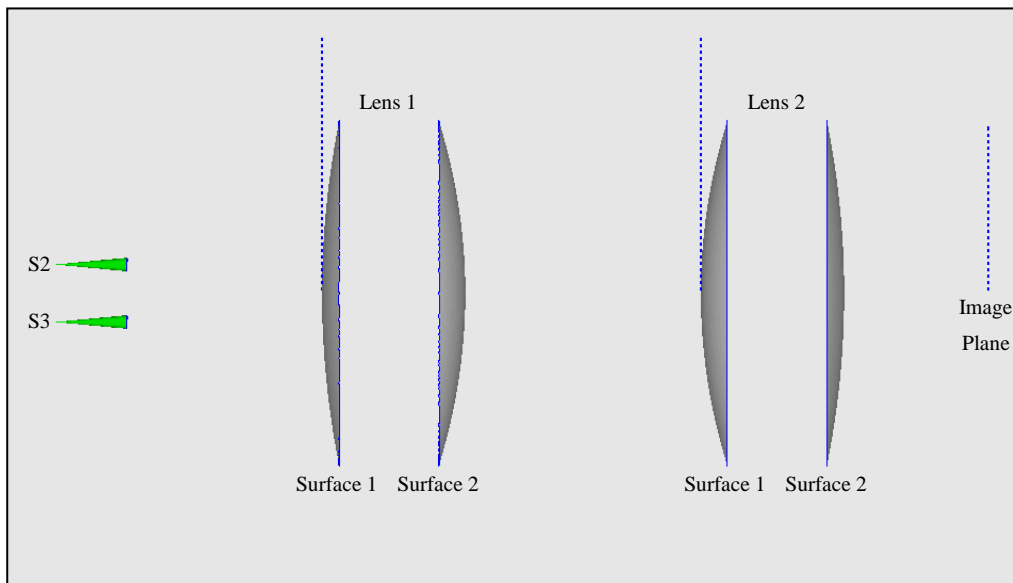


Figure 6.13 The QUBIC lens system as modelled in MODAL. The sources are labelled S2 and S3 to coincide with the convention used in the dual reflector systems.

6.5 Conclusions and Future Work

In this section three optical systems were considered for the beam combiner of the QUBIC instrument. Two of the systems described were composed of reflectors while the final system contained lenses to focus the beam on the image plane. In the case of the dual reflector systems, it was shown that the off-axis Gregorian system introduced amplitude distortion into to beam and therefore the interference fringes at the image plane were found to be curved. However, by implementing a general crossed Cassegrain configuration, the beams propagating to the image plane from the secondary mirror were approximately collimated, therefore eliminating the distortion found in the previous system. A physical optics analysis was also carried out on the lens system and again it was seen that the fringes produced at the image plane were straight. The analysis of each system was carried out for four equivalent 40mm baselines and showed that the interference patterns from these were in very good agreement. The ability to model a lens system with full vector physical optics, an option not yet available with commercial software, will be very important in the design phases of QUBIC.

One method that is being considered for calibration of QUBIC is the measurement and reconstruction of the scattering matrix describing the instrument. The scattering matrix approach, as discussed in detail in Chapter 4 (as applied to MBI), allows tracking of the response of each bolometer in the detector array to the field amplitudes of the sky-facing horn antennas and therefore the interference fringes on the sky. The scattering matrix elements at a single operating frequency can be measured as the response of a calibrated bolometer to a linearly polarised monochromatic source of know amplitude. It is noted in the QUBIC White Paper (2009) that the scattering matrix approach should rely on a detailed model of the system, which in turn, must be verified at different frequencies within the bandwidth. While not carried out for this thesis this detailed modelling is something that could be done in the future using a physical optics approach as was done for MBI-4 in Chapter 5.

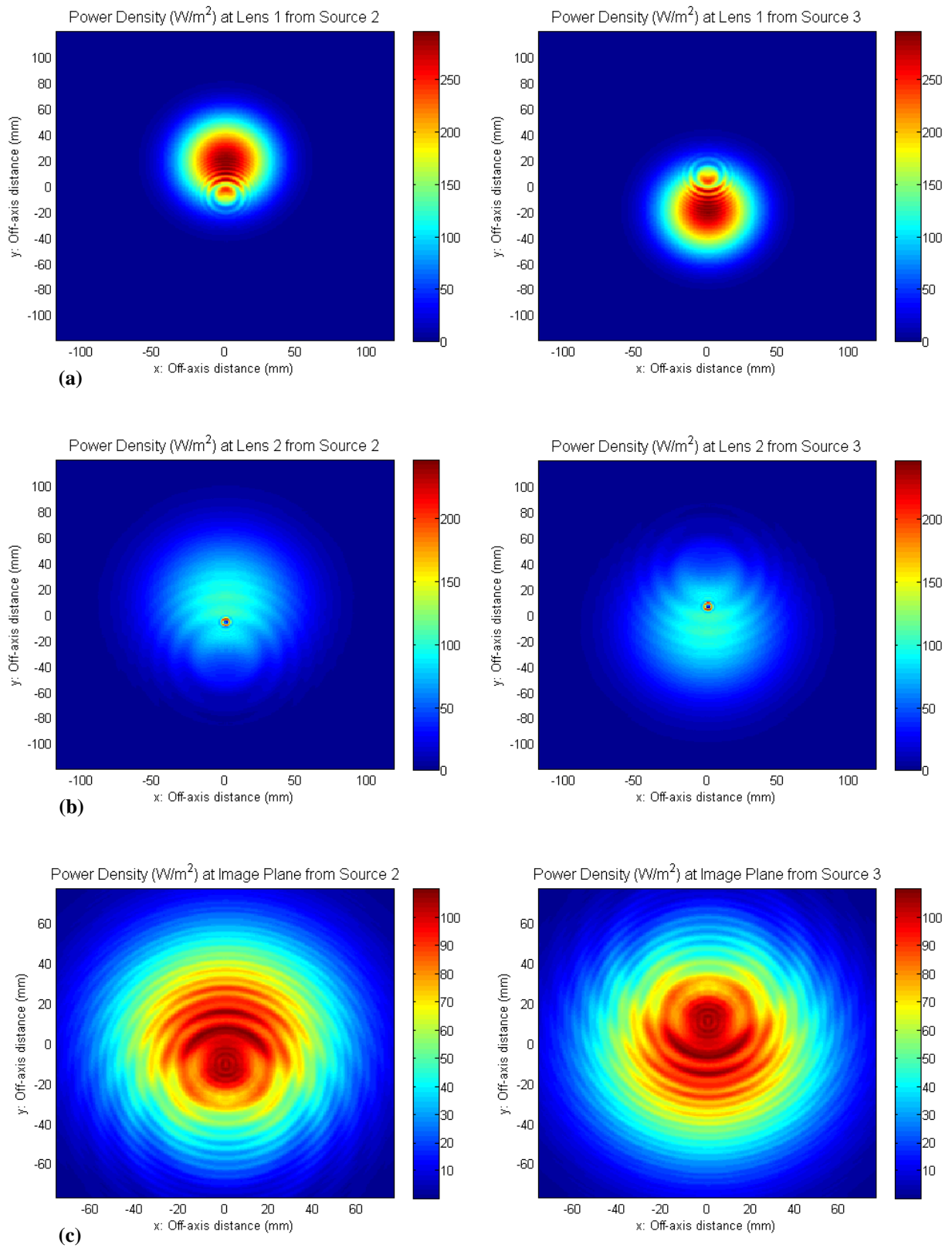


Figure 6.14 The power density of sources 1 and 2 at lens 1 is shown in (a). Parts (b) and (c) show the same plots for lens 2 and the image plane respectively.

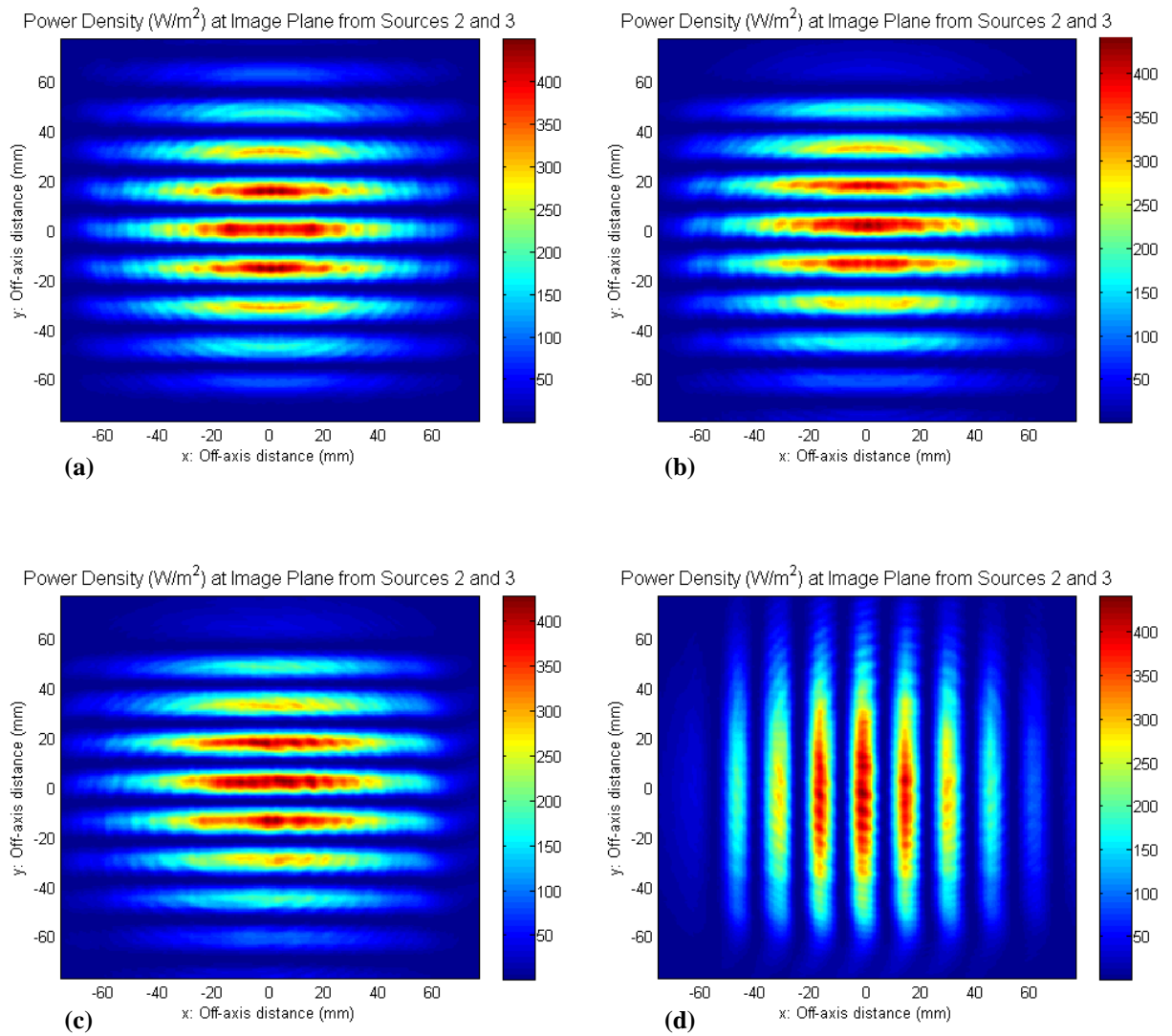


Figure 6.15 Interference fringe patterns at the image plane of the lens system from (a) baseline 1, (b) baseline 2, (c) baseline 3 and (d) baseline 4.

Chapter 7

Summary and Conclusions

This subject area of this thesis was concerned with the design and analysis of bolometric interferometers for measuring the polarisation of the CMB, with a particular emphasis on both the MBI-4 and QUBIC instruments. The difficulty and importance of measuring CMB modes was the motivation behind the accurate optical characterisation that forms the basis for much of the work carried out.

Chapter 1 of this thesis gave an overview of the CMB and the science that can be carried out with accurate measurements of its temperature and polarisation signals. The importance of these measurements is indicated by the number of experiments dedicated to this area of astronomy. The MBI-4 and QUBIC instruments both take advantage of bolometric interferometry techniques to measure polarisation signals and therefore an outline of the theory of both interferometry and polarisation was given, as well as a discussion on the instruments themselves and the systematic effects they are subject to.

To carry out the detailed analysis required to characterise these instruments a number of techniques were applied. In Chapter 2 these techniques were described in detail. I began with a description of geometrical optics, a technique that neglects diffraction effects due to the nature of the rays used. It was shown that while this technique is valuable for the initial design of an optical system, further methods are required for a more detailed analysis. Two other techniques were outlined, Fresnel integration and GBM, both of which are scalar methods and make good predictions of diffraction effects within the optical system. It was shown through examples that while both the Fresnel integral and GBM methods provide a powerful analysis tool, the GBM approach is much more efficient due to the nature of the integration required to model the electromagnetic field. In the Fresnel case the integral must be carried out at each element while for GBM integration (neglecting effects such as truncation) of the field is only required on a single plane.

Finally in Chapter 2, the physical optics method was described. This approach provides a full vector description of the field and provides a very accurate tool for modelling optical systems. An example was given and compared to the Fresnel and GBM methods where it could be seen that while the overall structure of the predicted beam was similar, for a very accurate model physical optics must be used. The techniques described in Chapter 2 were made possible through a combination of both in-house software and commercially available packages. A description of these packages was provided with a focus on MODAL, the one used most extensively throughout this work.

Chapter 3 described in detail the MBI-4 instrument, including the observing strategy, detectors and signal processing, cryogenics and the optical system. This was followed by a description of the design process for the MBI-4 optical beam combiner. An initial design was carried out using geometrical optics which provided details about the required focal lengths of the mirrors to get the correct beam sampling at the image plane. Before deciding on a final design for the optics a diffraction analysis was carried out, which indicated that the system would perform better if the beam waist was located at the aperture of the inward-facing back-to-back horn antenna. By doing this it was shown that the beam would not diffract as much and would remain more collimated as it propagated towards the optics. The phase radius of curvature was calculated as a function of distance from the waist position to the primary mirror and the beam radii at different elements were calculated as a function of distance from the waist position to the secondary mirror. Both of these were carried out using a GBM approach. With the calculated information a design was chosen that provided a beam with a relatively large phase radius of curvature at the image plane (to allow for good coupling to the detector array) and suitable beam widths at each of the mirrors to prevent excessive blockage and truncation as much as was possible. It was also important that the final design would fit within the dimensions of the cryostat, which was already built. The layout of the horn antennas feeding the system was such that an elliptical aperture was chosen for the hole in the primary mirror.

Having considered the design of the optical beam combiner in Chapter 3, a more detailed look at the horn antennas within the system was carried out in Chapter 4. I began by describing the geometry and performance of smooth-walled conical horn antennas, the type used as detector feeds in MBI-4. Examples of both aperture and far field beam patterns were given and the implications of the results discussed. The author was involved in the implemented of this type of antenna into the MODAL code and so a comparison of both fields generated by MODAL and those from in-house software are compared for verification.

To obtain greater coupling between the telescope field and the detector horn antennas of MBI-4, the smooth-walled conical horn antennas are fitted with phase-flattening lenses. In lab measurements the use of smaller horn antennas was considered to improve sampling, but with the original lenses. The effect of this was analysed by calculating the coupling efficiency for the new horn with the original phase-flattening lens and also for the new horn with a new lens design. It was shown that a loss in power coupling of approximately 25% would occur if the original lens was used with the new smaller horn antenna. This analysis was carried out for on- and off-axis detectors.

The next element of Chapter 4 was a discussion on corrugated horn antennas, their geometry and their performance. Examples of aperture and far fields, both co- and cross-polar, were given and the results discussed. It was shown that the asymmetry in the field produced by the smooth-walled horn was greatly reduced and so too was the side-lobe level since the field was not truncated so severely. A program called SCATTER was used to generate the fields from corrugated horns with a very specific geometry. This code makes use of scattering matrices (as well as mode-matching) and this techniques is outlined in some detail, since it also applied to the MBI-4 optical system analysis carried out in Chapter 5. The SCATTER code, which was implemented in MODAL was used to generate the field produced by the back-to-back corrugated horn antennas in MBI-4 and it was ensured that the structure was single-moded by changing the geometry of the horn to include a single-moded section of cylindrical waveguide between the two horns. Truncation of the beam by the cryostat windows was also modelled where it was found that it

could be significant, depending on the exact distance from the horn to the truncating aperture, and should be taken into account.

Measurements taken in 2008, with which the author was involved, by the MBI-4 instrument showed beam patterns from the back-to-back horn antennas as being asymmetric, something was unexpected from single-moded structures. The system was modelled by the author which showed that while the beams were symmetric when the horn antennas were illuminated by a plane wave propagating parallel to the axis of the horn, when illumination at off-axis angles the asymmetry found in the experimental measurements was evident, indicating that at off-axis angles the back-to-back horn antennas became multi-moded. These modes were analysed in terms of their amplitude and phase relative to the scanning angle and their composition in terms of TE and TM waveguide modes was examined by means of SVD. Further investigation found that the higher order modes could be removed by means of a single-moded cylindrical waveguide section.

The SCATTER code uses a mode match-matching technique to calculate power scattered between modes at discontinuities with a horn antenna structure. This code was initially written for conical horns but was extended at NUIM to model rectangular horn antennas. In Chapter 4 the author describes how this code could be further extended to include rectangular-to-circular transitions so that a complete back-to-back structure in MBI-4 could be modelled. The mode-matching technique is discussed and an example of a rectangular-to-circular junction is provided. The same system is also modelled using commercially available software for comparison, however, since the techniques used are very different it is difficult to compare like with like. The actual structures used are rather large for commercially available software. Future work in this area should include expanding the number of modes used in the mode-matching method which should provide a more accurate representation of the field.

Finally in Chapter 4 I presented work carried out on the analysis of closely-packed waveguide array (as a model for the MBI-4 detector array). The effect that the neighbouring waveguides have on the beam pattern of an individual waveguide is examined for both circular and rectangular waveguides in various configurations. It

was shown that the effect is quite small and can be removed by separating the waveguides sufficiently. Also, waveguides at the edges of arrays are more likely to suffer from beam distortion due to the asymmetry of the array, while the effect is removed for waveguides at the centre which are completely surrounded.

In Chapter 5 the optical beam combiner in MBI-4 was examined in detail. While different propagation techniques were compared at the beginning it was physical optics that was used in this analysis. The power coupled from each of the back-to-back horn antennas to each detector was calculated, forming the elements of the scattering matrix describing the system. This matrix linked the input field to the detector array in such a way that by changing the input field, the field at the detectors can be calculated relatively easily. The system was analysed for two orthogonal polarisation directions which showed a significant difference in coupled power. It was explained how this was due to the asymmetry in beam pattern of the smooth-walled conical detector horn antenna. The input polarisation direction of the horn antenna therefore needs to be accurately defined in any experimental tests. The effect of flattening the phase radius of curvature at the front of the detector horns was also examined here and it was found that with lenses present the power coupled to the detectors was increased by approximately 30%.

Truncation effects in the system were modelled and it was calculated that between 23% and 30% of the initial power from the inward-facing horn antennas was propagated to the image plane. The most significant truncation occurred as the beam propagated through the elliptical aperture of the primary mirror after reflection from the secondary mirror. It was also seen that between 8% and 15% of the power passes through the elliptical aperture as the beam is reflected from the primary mirror, which was shown to have a significant effect on the interference pattern, particularly for the short baselines. Chapter 5 also examined mechanical tolerances and systematic effects within the system. Axial, lateral and rotational movement were all analysed and it was found that the xy -movement of the detector array produced the greatest effect in terms of power coupled to the bolometers. The last section discussed in Chapter 5 involved simulating lab measurements carried out with the MBI-4 instrument. The field from each of the four back-to-back horns fed with a Gunn oscillator was measured at the image plane and the same system was

modelled in MODAL. The beams from the measurements appeared to be focused in individual quadrant and this was evident in the simulations if the portion of the field that passed through the primary elliptical aperture on first pass was taken into account. Factors that need to be accounted for in future work are the resolution of the scan and the physical size of the detector used in the measurements.

The final chapter in this thesis dealt with the QUBIC instrument, and in particular the optical beam combiner. Three optical system were modelled, two containing mirrors and one containing lenses. For each of the three systems a physical optics analysis was carried out and the fringes at the image plane were produced. It was shown that in the first mirror system the fringes were curved due to amplitude distortion introduced by the system. In the second design, a general crossed Cassegrain system, the beams were approximately collimated as they propagated to the image plane and the distortion was removed, producing straight fringes. In general, the curved fringes were not problematic as long as they could be characterised. The problem with the Gregorian system that produced such fringes was that equivalent baselines did not produce the same fringes, meaning that when different equivalent baselines are combined the fringes pattern would be averaged out. It was shown that the lens system also produced straight fringes by means of a physical optics analysis, something which at present cannot be done using commercially available software.

The main area of future work lies in the rectangular-to-circular mode-matching code, which could be extended to include a higher number of modes and therefore produce a more accurate representation of the field. This code could also be implemented into MODAL to allow the user build a structure using a combination of circular and rectangular segments and transitions between the two. Also, further analysis on a final design for the QUBIC instrument is required to fully understand its performance, similar to the work carried out and presented in this thesis for MBI-4.

References

Albrecht, A. and Steinhardt, P. J., “Cosmology For Grand Unified Theories With Radiatively Induced Symmetry Breaking”, *Phys. Rev. Lett.*, Vol. 48, p. 1220, 1982.

Ali, S., Ade, P. A. R., Bock, J. J., Novak, G., Piccirillo, L, Timbie, P., Tucker, G. S., “The Millimeter-Wave Bolometric Interferometer”, *Proceedings of the Second Workshop on New Concepts for Far-Infrared and Submillimeter Space Astronomy*”, p. 309, 2003.

Alpher, R. A., Bethe, H. and Gamow, G., “The Origin of Chemical Elements,” *Physical Review*, Vol. 73, No. 7, p. 803-804, 1948.

Alpher, R. A., Herman, R. C., “Early Work on ‘Big-Bang’ Cosmology and the Cosmic Blackbody Radiation”, *Proceedings of the American Philosophical Society*, Vol. 119, No. 5, p. 325-348, 1975.

Baker, J. C., Grainge, K., Hobson, M. P., Jones, M. E., Kneissl, R., Lasenby, A. N., O’Sullivan, C. M. M., Pooley, G., Richa, G., Saunders, R., Scott, P. F., Waldram, E. M., “Detection of Cosmic Microwave Background Structure in a Second Field with the Cosmic Anisotropy Telescope”, *Astrophysical Journal.*, Vol. 308, p. 1173-1178, 1999.

Balanis, C.A., “Antenna Theory: Analysis and Design”, Second Edition, John Wiley & Sons Inc., Toronto, 1997.

Baranne, A., Launay, F., “Cassegrain: A Famous Unknown of Instrument Astronomy”, *Journal of Optics*, Vol. 28, No. 4, p. 158-192, 1997.

Bennett, C. L., Smoot, G. F., Janssen, M., Gulkis, S., Kogut, A., Hinshaw, G., “COBE Differential Microwave Radiometers - Calibration Techniques”, *Astrophysical Journal*, Vol. 391, No. 2, p. 466-482, 1992.

Bennett, C. L., Halpern, M., Hinshaw, G., Jarosik, N., Kogut, A., Limon, M., Meyer, S. S., Page, L., Spergel, D. N., Tucker, G. S., Wollack, E., Wright, E. L., Barnes, C., Greason, M. R., Hill, R. S., Komatsu, E., Nolta, M. R., Odegard, N., Peiris, H. V., Verde, L., Weiland, J. L., “First-Year Wilkinson Microwave Anisotropy Probe (WMAP) Observations: Preliminary Maps and Basic Results”, *Astrophysical Journal*, Vol. 148, 2003a.

Bennett, C. L., Hill, R. S., Hinshaw, G., Nolta, M. R., Odegard, N., Page, L., Spergel, D. N., Weiland, J. L., Wright, E. L., Halpern, M., Jarosik, N., Kogut, A., Limon, M., Meyer, S. S., Tucker, G. S., Wollack, E., “First-Year Wilkinson Microwave Anisotropy Probe (WMAP) Observations: Foreground Emission”, *Astrophysical Journal Supplement Series*, Vol. 148, p. 97–117, 2003b.

Bennett, D., Ph.D. thesis, National University of Ireland, Maynooth, Ireland, 2011 (in preparation).

Björck, A., “Numerical Methods for Least Squares Problems”, Society for Industrial and Applied Mathematics, Philadelphia, 1996.

BLAST website: <http://www.blastexperiment.info/index.php>

Boker, T., Allen, J.A., “Imaging and Nulling with the Space Interferometer Mission”, *Astrophysical Journal Supplement Series*, Vol. 125, p. 123, 1999.

Born, M., Wolf, E., “Principles of Optics”, Seventh (expanded) Edition, Cambridge University Press, England, 1999.

Brown, M. L., Ade, P., Bock, J., Bowden, M., Cahill, G., Castro, P. G., Church, S., Culverhouse, T., Friedman, R. B., Ganga, K., Gear, W. K., Gupta, S., Hinderks, J., Kovac, J., Lange, A. E., Leitch, E., Melhuish, S. J., Memari, Y., Murphy, J. A., Orlando, A., O’Sullivan, C., Piccirillo, L., Pryke, C., Rajguru, N., Rusholme, B., Schwarz, R., Taylor, A. N., Thompson, K. L., Turner, A. H., Wu, E. Y., S., Zemcov, M., “Improbable Measurements of the Temperature and Polarization of the Cosmic

Microwave Background from QUaD”, *Astrophysical Journal*, Vol. 705, p. 978–999, 2009.

Bunn, E.F., “Separating E from B”, *New Astronomy Reviews*, Vol. 47, p. 987, 2003.

Bunn, E.F., “Systematic Errors in Cosmic Microwave Background Interferometry”, *Physical Review*, D75:083517, 2007.

Caltech Astronomy Department website: <http://www.astro.caltech.edu>

Carlstrom, J. E., Kovac, J., Leitch, E. M., Pryke, C., “Status of CMB Polarization Measurements from DASI and other Experiments”, *New Astronomy Review*, Vol. 47, p. 953–966, 2003.

Cartwright, J. K., Pearson, T. J., Readhead, A. C. S., Shepard, M. C., Sievers, J. L., Taylor, G. B., “Limits on the Polarization of the Cosmic Microwave Background Radiation at Multipoles up to $l \approx 2000$ ”, *Astrophysical Journal*, Vol. 623, p. 11-16, 2005.

Charlassier, R., Hamilton, J. -Ch., Bréelle, É., Ghribi, A., Giraud-Héraud, Y., Kaplan, J., Piat, M., Prêle, “An Efficient Phase-Shifting Scheme for Bolometric Additive Interferometry”, *Astronomy and Astrophysics*, 2008.

Chicago University Department of Astronomy and Astrophysics website: <http://astro.uchicago.edu>

Church, S. E., “Predicting Residual Levels of Atmospheric Sky Noise in Ground-Based Observations of the Cosmic Background Radiation”, *MNRAS*, Vol. 272, p. 551, 1995.

Coles, P., Lucchin, F., “Cosmology, The Origin and Evolution of Cosmic Structure”, Wiley Publishing, 1995.

Colgan, R., “Electromagnetic and Quasi-Optical Modelling of Horn Antennas for Far IR Space Applications”, Ph.D. thesis, National University of Ireland, Maynooth, Ireland, 2001.

Collett, E., “Field Guide to Polarization”, The Society of Photo-Optical Instrumentation Engineers, Washington, USA, 2005.

Collin, R. E., Zucker, F. J., “Antenna Theory”, McGraw-Hill, New York, 1969.

Curran, G. S., “Quasi-Optical Design of the HIFI Instrument for the Herschel Space Observatory”, M.Sc. thesis, National University of Ireland, Maynooth, Ireland, 2002.

DARWIN website: <http://sci.esa.int/science-e/www/area/index.cfm?fareaid=28>

Dickenson, C., Battye, R. A., Cleary, K., Davies, R. D., Davis, R. J., Genova-Santos, R., Grainge, K., Gutierrez, C. M., Hafez, Y. A., Hobson, M. P., Jones, M. E., Kneissl, R., Lancaster, K., Lasenby, A., Leahy, J. P., Maisinger, K., Odman, C., Pooley, G., Rajguru, N., Rebola, R., Rubino-Martin, J., A., Saunders, R. D. E., Savage, R. S., Scaife, A., Scott, P. F., Slosar, A., Molina, P. S., Taylor, A. C., Titterton, D., Waldram, E., Watson, R. A., Wilkinson, A., “High Sensitivity Measurements of the CMB Power Spectrum with the Extended Very Small Array”, *Astrophysical Journal*, Vol. 353, p. 732-746, 2004.

Doherty, S., Trappe, N., “A Modal Approach to the Modelling of Rectangular Detector Horns and Cavities at THz Frequencies”, submitted to SPIE Photonics West Conference Proceedings, 2011.

ESA’s PLANCK Satellite website:

<http://sci.esa.int/sciencee/www/area/index.cfm?fareaid=17>

Farese, P. C., Dall’Oglio, G., Gundersen, J. O., Keating, B. G., Klawikowski, S., Knox, L., Levy, A., Lubin, P. M., O’Dell, C. W., Peel, A., Piccirillo, L., Ruhl, J., Timbie, P. T., “COMPASS: An Upper Limit on Cosmic Microwave Background

Polarization at an Angular Scale of $20''$ ”, *Astrophysical Journal*, Vol. 610, p. 625-634, 2004.

Fitzgerald, A. J., Wallace, V. P., Jimenez-Linan, M., Bobrow, L., Pye, R. J., Purushotham, A. D., Arnone, D. D., “Terahertz Pulsed Imaging of Human Breast Tumors”, *Radiology*, Vol. 239, No. 2, p. 533-540, 2006.

Gleeson, E., “Single and Multi-moded Corrugated Horn Design for Cosmic Microwave Background Experiments”, Ph.D. thesis, National University of Ireland, Maynooth, Ireland, 2004.

Goldsmith, P.F, “Quasi-optical Techniques and Millimeter and Submillimeter Wavelengths”, *Infrared and Millimeter Waves*, Vol. 8, p. 227, 1982.

Goldsmith, P.F, “Quasioptical Systems: Gaussian Beam Quasioptical Propagation and Applications”, IEEE Press, New York, 1998.

Golub, B., Van Loan, C., “Matrix Computations”, John Hopkins University Press, Baltimore, MD, 1996.

Goodman, J.W., “Introduction to Fourier Optics”, McGraw-Hill, New York, 1968.

Goubau, G., “Optical and Quasi-Optical Transmission Schemes”, *Millimetre and Submillimetre Waves*, Ilffe, 1969.

Gradshteyn, I.S., Ryzhik, I.M., “Tables of Integrals, Series and Products”, Academic Press Inc., Orlando, 1980.

Gradziel, M. L., O’Sullivan, C., Murphy, J. A., Cahill, G., Curran, G. S., Pryke, C., Gear, W., Church, S., “Modeling of the Optical Performance of Millimeter-Wave Instruments using MODAL”, *Proc. SPIE*, Vol. 6472, 64720D, 2008.

Guth, A. H., “Inflationary Universe: A Possible Solution to the Horizon and Flatness Problems”, *Physical Review D*, Vol. 23, Issue 2, p. 347-356, 1981.

Guth, A. H., Pi, S-Y., "Fluctuations in the New Inflationary Universe", Physical Review Letters, Vol. 49, p. 1110-1113, 1982.

Hallym University Dept of Physics website: <http://www.hallym.ac.kr/~physics>

Halverson, N. W., Leitch, E. M., Pryke, C., Kovac, J., Carlstrom, J. E., Holzzapfel, W. L., Dragovan, M., Cartwright, J. K., Mason, B. S., Padin, S., Pearson, T. J., Readhead, A. C. S., Shepherd, M. C., "Degree Angular Scale Interferometer First Results: A Measurement of the Cosmic Microwave Background Angular Power Spectrum" Astrophysical Journal, Vol. 568, p. 38, 2002.

Hamilton, J.-Ch., Charlassier, R., Cressiot, C., Kaplan, J., Piat, M., Rosset, C., "Sensitivity of a Bolometric Interferometer to the CMB Power Spectrum", Astronomy and Astrophysics, Vol. 491, p. 923-927, 2008.

Hanany, S., Rosenkranz, P., "Polarisation of the Atmosphere as a Foreground for Cosmic Microwave Background Polarisation Experiments", New Astronomy Reviews, Vol. 47, Issue 11-12, p. 1159-1165, 2003.

Harrington, R. F., "Matrix methods for Field Problems," Proc. IEEE, Vol. 55, pp. 136-49, 1967.

Harrington, R. F., "Field Computation by Moment Methods", Wiley IEEE Press, 1993.

Hauser, M., Arendt, R., Kelsall, T., Dwek, E., Odegard, N., Weiland, J., Freudenreich, H., Reach, W., Silverberg, R., Moseley, S., Pei, Y., Lubin, P., Mather, J., Shafer, R., Smoot, G., Weiss, R., Wilkinson, D., Wright, E., "The COBE Diffuse Infrared Background Experiment Search for the Cosmic Infrared Background. I. Limits and Detections", Astrophysical Journal, Vol. 508, pp. 25-43, 1998.

Hecht, E., "Note on an Operational Definition of the Stokes Parameters", American Journal of Physics, Vol. 38, p. 1156, 1970.

Hecht, E., "Optics", Third Edition, Addison-Wesley, US, 1998.

Heanue, M., "Submillimetre-Wave Local Oscillator Multiplexing Using Phase Gratings", M.Sc. thesis, St. Patrick's College, Maynooth, Ireland, 1995.

Hildebrand, R. H., Dotson, J. L., Dowell, C. D., Schleuning, D. A., Vaillancourt, J. E., "The Far-Infrared Polarisation Spectrum: First Results and Analysis", *Astrophysical Journal*, Vol. 516, p. 834-842, 1999.

Hinderks, J. R., "QUaD: A Millimeter-Wave Polarimeter for Observation of the Cosmic Microwave Background Radiation", Ph.D. thesis, Stanford University, 2005.

Holliday, K., "Introductory Astronomy", John Wiley & Sons Inc., Chichester, 1999.

Hu, W., White, M., "CMB Anisotropies: Total Angular Momentum Method", *Physical Review*, D56, pp. 596-615, 1997.

Hu, W., White, M., "The Cosmic Symphony", *Scientific American*, p. 44-53, 2004.

Hu, W., Hedman, M. M., Zaldarriaga, M., "Benchmark Parameters for CMB Polarization Experiments", *Physical Review*, D67:043004, 2003.

Hyland, P.O., "The Millimeter-Wave Bolometric Interferometer", Ph.D. thesis, University of Wisconsin-Madison, 2008.

Institute for Astronomy at the University of Hawaii website:
<http://www.ifa.hawaii.edu>

Jones, W. C., Ade, P. A. R., Bock, J. J., Bond, J. R., Borrill, J., Boscaleri, A., Cabella, P., Contaldi, C. R., Crill, B. P., De Bernardis, P., De Gasperis, G., De Oliveira-Costa, A., De Troia, G., Di Stefano, G., Hivon, E., Jaffe, A. H., Kisner, T. S., Lange, A. E., MacTavish, C. J., Masi, S., Mausekopf, P. D., Melchiorri, A., Montroy, T. E., Natoli, P., Netterfield, C. B., Pascale, E., Piacentini, F., Pogosyan, D., Polenta, G., Prunet, S., Ricciardi, S., Romeo, G.,

Ruhl, J. E., Santini, P., Tegmark, M., Veneziani, M., Vittorio, N., “A Measurement of the Angular Power Spectrum of the CMB Temperature Anisotropy from the 2003 Flight of BOOMERANG”, *Astrophysical Journal*, Vol. 647, Issue 2, p. 823-832, 2006.

Kaplan, J., Delabrouille, J., “Some Sources of Systematic Errors on CMB Polarized Measurements with Bolometers”, *Astrophysical Polarized Backgrounds: Workshop on Astrophysical Polarized Backgrounds*, American Institute of Physics Conference Proceedings, Vol. 609, p. 209, 2002.

Keller, J., “A Geometrical Theory of Diffraction”, *Proceedings of Symposia in Applied Mathematics*, Vol. 8, p. 27-52, 1958.

Knox, L., Song, Y.-S., “Limit on the Detectability of the Energy Scale of Inflation”, *Physical Review Letters*, Vol. 89, 2002.

Korotkov, A., Kim, J., Tucker, G. S., Gault, A. C., Hyland, P. O., Malu, S. S., Timbie, P. T., Bunn, E., Bierman, E., Keating, B., Murphy, J. A., O’Sullivan, C., Ade, P. A. R., Calderon, C., Piccirillo, L., “The Millimeter-Wave Bolometric Interferometer”, *Proc. SPIE*, Vol. 6275, 2006.

Korotkov, A., Private communication, 2010.

Kovac, J., Leitch, E. M., Pryke, C., Carlstrom, J. E., Halverson, N. W., Holzzapfel, W. L., “Detection of Polarization in the Cosmic Microwave Background using DASI”, *Nature*, Vol. 420, p. 772-787, 2002.

Lavelle, J., “The Design and Optimisation of Quasioptical Telescopes”, Ph.D. thesis, National University of Ireland, Maynooth, Ireland, 2008.

Lawrence Berkley National Laboratory Website: <http://www.lbl.gov>

Leitch, E. M., Kovac, J. M., Halverson, N. W., Carlstrom, J. E., Pryke, C., Smith, M. W. E., “DASI Three-Year Cosmic Microwave Background Polarization Results”, *Astrophysical Journal*, Vol. 624, p. 10-20, 2005.

Lesurf, J.C.G., “Millimetre-Wave Optics, Devices and Systems”, Institute of Physics Press, 1993.

Lewis, A., Challinor, A., Turok, N., “Analysis of CMB Polarization on an Incomplete Sky”, *Physical Review*, D65:023505, 2002.

Linde, A., “A New Inflationary Universe Scenario: A Possible Solution of the Horizon, Flatness, Homogeneity, Isotropy and Primordial Monopole Problems”, *Physical Letters B*, Vol. 108, p. 389. 1982.

Lineweaver, C. H., “What is the Universe Made Of? How Old Is It?”, *Astrophysical Journal*, 9911294, 1999.

Luukanen, A., Grönberg, L., Grönholm, M., Lappalainen, P., Leivo, M., Rautiainen, A., Tamminen, A., Ala-Laurinaho, J., Dietlein, C. R., Grossman, E. N., “Real-Time Passive Terahertz Imaging System for Standoff Concealed Weapons Imaging”, *Passive Millimeter-Wave Imaging Technology XIII Proceedings*, Vol. 7670, 2010.

Malu, S. S., Timbie, P. T., “Broadband Fizeau Interferometers for Astrophysics”, *Astronomy and Astrophysics*, App 35, 2010.

Mather, J. C., Cheng, E. S., Eplee, R. E., Isaacman, R. B., Meyer, S. S., Shafer, R. A., Weiss, R., Wright, E. L., Bennett, C. L., Boggess, N. W., Dwek, E., Gulkis, S., Hauser, M. G., Janssen, M., Kelsall, T., Lubin, P. M., Moseley, S. H., Murdock, T. L., Silverberg, R. F., Smoot, G. F., Wilkinson, D. T., “A Preliminary Measurement of the Cosmic Microwave Background Spectrum by the Cosmic Background Explorer (COBE) Satellite”, *Astrophysical Journal*, Vol. 354, p. L37-L40, 1990.

Mather, J. C., Cheng, E. S., Cottingham, D. A., Eplee, R. E., Jr., Fixsen, D. J., Hewagama, T., Isaacman, R. B., Jensen, K. A., Meyer, S. S., Noerdlinger, P. D.,

Read, S. M., Rosen, L. P., Shafer, R. A., Wright, E. L., Bennett, C. L., Boggess, N. W., Hauser, M. G., Kelsall, T., Moseley, S. H., Jr., Silverberg, R. F., Smoot, G. F., Weiss, R., Wilkinson, D. T., "Measurement of the Cosmic Microwave Background Spectrum by the COBE FIRAS Instrument", *The Astrophysical Journal*, Part 1, Vol. 420, No. 2, p. 439-444, 1994.

Mather, J. C., Fixsen, D. J., Shafer, R. A., Mosier, C., Wilkinson, D. T., "Calibrator Design for the COBE Far-Infrared Absolute Spectrophotometer (FIRAS)", *The Astrophysical Journal*, Vol. 512, p. 511-520, 1999.

MathWorks Matlab website: <http://www.mathworks.com/products/matlab>

Marcuvitz, N., "Waveguide Handbook", Peter Peregrinus Ltd., London, England, 1993.

Martin, D.H., Lesurf, J.C.G., "Sub-millimetre-wave optics", *Infrared Physics*, Vol. 18, p. 405 – 412, 1978.

Martin D., Bowen J. "Long wave optics", *IEEE Trans. Microwave Theory Tech.*, Vol. 41, p. 1676 - 1689, 1993.

Masterman, P.H., Clarricoats, P.J.B., "Computer Field Matching Solution of Waveguide Transverse Discontinuities", *Proc. IEEE*, Vol. 118, p. 51 – 63, 1971.

McAuley, I., Young, L., Gradziel, M., Lanigan, W., O'Sullivan, C., Murphy, J. A., Mahon, R., May, R., Trappe, N., "Millimetre-Wave and Terahertz Imaging Systems with Biomedical Applications", *Proceedings of IRMMW-THz*, p. 371, 2006.

Mogensen, M., Jemec, G. B. E., "Diagnosis of Nonmelanome Skin Cancer/Keratinocyte Carcinoma: A Review of Diagnostic Accuracy of Nonmelenoma Skin Cancer Diagnostic Tests and Technologies", *Dermatological Surgery*, Vol. 33, Issue 10, p. 1158-1174, 2007.

Murphy, J.A., “Aperture Efficiencies of Large Axisymmetric Reflector Antennas Fed by Conical Horns”, IEEE Trans. On Antennas and Propagation, Vol. 40, No. 4, p. 570–575, 1988.

Murphy, J.A, Egan A., “Examples of Fresnel diffraction using Gaussian modes”, European. Journal of Physics, Vol. 14, p. 121-127, 1993.

Murphy, J. A., Colgan, R., O’Sullivan, C., Maffei, B., Ade, P., “Radiation Patterns of Multi-Moded Corrugated Horns for Far-IR Space Applications”, Journal of Infrared Physics and Technology, Vol. 42, p. 515-528, 2001.

NASA’s Legacy Archive for Microwave Background Data Analysis web site:
<http://lambda.gsfc.nasa.gov>

NASA’s WMAP website: <http://map.gsfc.nasa.gov>

Netterfield, C. B., Ade, P. A. R., Bock, J. J., Bond, J. R., Borrill, J., Boscaleri, A., Coble, K., Contaldi, C. R., Crill, B. P., De Bernardis, P., Farese, P., Ganga, K., Giacometti, M., Hivon, E., Hristov, V. V., Iacoangeli, A., Jaffe, A. H., Jones, W. C., Lange, A. E., Martinis, L., Masi, S., Mason, P., Mouskops, P. D., Melchiorri, A., Montroy, T., Pascale, E., Piacentini, F., Pogosyan, D., Pongetti, F., Prunet, S., Romeo, G., Ruhl, J. E., Scaramuzzi, F., “A Measurement by BOOMERANG of Multiple Peaks in the Angular Power Spectrum of the Cosmic Microwave Background”, Astrophysical Journal, Vol. 571, p. 604-614, 2002.

Newton, I., “Opticks or A Treatise of the Reflections, Refractions, Inflections & Colours of Light”, General Publishing Company Inc., Toronto, 1979.

Nolta, M. R., Dunkley, J., Hill, R. S., Hinshaw, G., Komatsu, E., Larson, D., Page, L., Spergel, D. N., Bennett, C. L., Gold, B., Jarosik, N., Odegard, N., Weiland, J. L., Wollack, E., Halpern, M., Kogut, A., Limon, M., Meyer, S. S., Tucker, G. S., Wright, E. L., “Five-Year Wilkinson Microwave Anisotropy Probe (WMAP) Observations: Angular Power Spectra” Astrophysical Journal Supplement, Vol. 180, p. 296-305, 2009.

Olver, A.D., Clarricoats, P.J.B., Kishk, A.A., Shafi, L., “Microwave Horns and Feeds”, IEEE Press, New York, 1994.

O'Sullivan, C., Cahill, G., Murphy, J. A., Gear, W. K., Harris, J., Ade, P. A. R., Church, S. E., Thompson, K. L., Pryke, C., Bock, J., Bowden, M., Brown, M. L., Carlstrom, J. E., Castro, P. G., Culverhouse, T., Friedman, R. B., Ganga, K. M., Haynes, V., Hinderks, J. R., Kovak, J., Lange, A. E., Leitch, E. M., Mallie, O. E., Melhuish, S. J., Orlando, A., Piccirillo, L., Pisano, G., Rajguru, N., Rusholme, B. A., Schwarz, R., Taylor, A. N., Wu, E. Y. S., Zemcov, M., “The Quasi-Optical Design of the QUaD Telescope”, *Infrared Physics & Technology*, Vol. 51, Issue 4, p. 277-286, 2008.

Park, C-G., Ng, K-W., Park, C., Liu, G-C., Umetsu, K., “Observational Strategies of CMB Temperature and Polarization Interferometry Experiments”, *Astrophysical Journal*, Vol. 589, p. 67-81, 2003.

Park, C-G., Ng, K-W., “E/B Separation in CMB Interferometry”, *Astrophysical Journal*, Vol. 609, p. 15, 2004.

Penzias, A. A., Wilson, R. W., “A Measurement of Excess Antenna Temperature at 4080Mc/s”, *Astrophysical Journal*, Vol. 142, p. 419-421, 1965.

Piccirillo, L., Ade, P.A.R., Bock, J.J., Bowden, M., Church, S.E., Ganga, K., Gear, W.K., Hinderks, J., Keating, B.G., Lange, A.E., Maffei, B., Mallié, O., Melhuish, S.J., Murphy, J.A., Pisano, G., Rusholme, B., Taylor, A., Thompson, K., “QUEST – A 2.6m Millimeter-Wave Telescope for CMB Polarization Studies”, *Astrophysical Polarized Backgrounds*, Bologna, Italy, 2001.

Piccirillo, L., “A Large Angular Scale CMB Polarization Experiment for Dome-C”, *Mem. S.A.It. Suppl. Vol. 2*, p. 200, 2003.

Pickwell, E., Wallace, V. P., “Biomedical Applications of Terahertz Technology”, *Journal of Physics D: Applied Physics*, Vol. 39, No. 17, p. R301-R310, 2006.

Pickwell, E., Cole, B. E., Fitzgerald, A. J., Pepper, M., Wallace, V. P., “In Vivo Study of Human Skin Using Pulsed Terahertz Radiation”, *Physics in Medicine and Biology*, Vol. 49, p. 1595-1607, 2004.

Polenta, G., Ade, P. A. R., Bartlett, J., Bréelle, E., Conversi, L., De Bernardis, P., Dufour, C., Gervasi, M., Giard, M., Giordano, C., Giraud-Heraud, Y., Maffei, B., Masi, S., Nati, F., Orlando, A., Peterzen, S., Piacentini, F., Piat, M., Piccirillo, L., Pisano, G., Pons, R., Rosset, C., Savini, G., Tartart, A., Veneziani, M., Zannoni, M., “The BRAIN CMB Polarization Experiment”, *New Astronomy Reviews*, Vol. 51, Issues 3-4, p. 256-259, 2007.

Pozar, D. M., “*Microwave Engineering*”, Second Edition, John Wiley & Sons Inc., Toronto, 1998.

Prantzos, N., “Fast Track to Cosmic Splendour”, *Physics World*, p. 43-44, 2000.

QUBIC White Paper, QUBIC Collaboration, April 2009.

Ray, T.P., Beckwith, S.V.W., “*Star Formation and Techniques in Infrared and mm-Wave Astronomy*”, EADN Predoctoral Astrophysics School V, Springer-Verlag, 1992.

Readhead, A. C. S., Mason, B. S., Contaldi, C. R., Pearson, T. J., Bond, J. R., Myers, S. T., Padin, S., Sievers, J. L., Cartwright, J. K., Shepherd, M. C., Pogosyan, D., Prunet, S., Altamirano, P., Bustos, R., Bronfman, L., Casassus, S., Holzappel, W. L., May, J., Pen, U.-L., Torres, S., Udomprasert, P. S., “Extended Mosaic Observations with the Cosmic Background Imager”, *Astrophysical Journal*, Vol. 609, Issue 2, p. 498-512, 2004a

Readhead, A. C. S., Myers, S. T., Pearson, T. J., Sievers, J. L., Mason, B. S., Contaldi, C. R., Bond, J. R., Bustos, R., Altamirano, P., Achermann, C., Bronfman, L., Carlstrom, J. E., Cartwright, J. K., Casassus, S., Dickinson, C., Holzappel, W. L., Kovac, J. M., Leitch, E. M., May, J., Padin, S., Pogosyan, D., Pospieszalski, M., Pryke, C., Reeves, R., Shepherd, M. C., Torres, S., “Polarization Observations with

the Cosmic Background Imager”, *Astrophysical Journal*, Vol. 306, Issue 2, p. 836-844, 2004b.

Reichardt, C. L., Ade P. A. R., Bock, J. J., Bond, J. R., Brevik, J. A., Contaldi, C. R., Daub, M. D., Dempsey, J. T., Goldstein, J. H., Holzappel, W. L., Kuo, C. L., Lange, A. E., Lueker, M., Newcomb, M., Peterson, J. B., Ruhl, J., Runyan, M. C., Staniszewski, Z., “High Resolution CMB Power Spectrum from the Complete ACBAR Data Set”, *Astrophysical Journal*, Vol. 694, p. 1200-1219, 2009.

Rohlfs, K., Wilson, T. L., “Tools of Radio Astronomy”, 2nd ed., Springer, New York, 1996.

Rusholme, B., Ade, P., Bowden, M., Bock, J., Church, S., Ganga, K., Gear, W., Hinderks, J., Keating, B., Lange, A., Melhuish, S., Murphy, J. A., O’Sullivan, C., Piccirillo, L., Taylor, A., “QUEST: A Ground Based MM-Wave Telescope for CMB Polarisation Studies”, *Carnegie Centennial Symposium proceedings*, 2002.

Shurcliff, W.A., Ballard, S.S., “Polarised Light”, D. Van Nostrand Company Inc., New Jersey, USA, 1964.

Siegman, A.E., “Lasers”, University Science Books, California, 1986.

Siegel, P. H., “Terahertz Technology”, *IEEE transactions on microwave theory and techniques*, Vol. 50, No. 3, 2002.

Silver, S., “Microwave Antenna Theory and Design”, Peter Peregrinus Ltd., London, England, 1997.

Simmons, A.J., Kay, A.F., “The Scalar Feed – A High Performance Feed for Paraboloid Reflectors, Design and Construction of Large Steerable Aerials”, *IEE Conf. Publ. Vol. 21*, p. 213 – 217, 1966.

Smith, F.G., King, T.A., “Optics and Photonics – An Introduction”, John Wiley & Sons Ltd., Chichester, England, 2000.

Smoot, G. F., Bennett, C. L., Kogut, A., Wright, E. L., Aymon, J., Bogges, N. W., Cheng, E. S., de Amici, G., Gulkis, S., Hauser, M. G., Hinshaw, G., Jackson, P. D., Janssen, M., Kaita, E., Kelsall, T., Keegstra, P., Lineweaver, C., Loewenstein, K., Lubin, P., Mather, J., Meyer, S. S., Moseley, S. H., Murdock, T., Rokke, L., Silverberg, R. F., Tenorio, L., Weiss, R., Wilkinson, D. T., “Structure in the COBE Differential Microwave First-Year Maps”, *Astrophysical Journal Letters*, Vol. 396, p. 1, 1992.

Smoot, G. F., Scott, D., “The Cosmic Background Radiation”, *Review of Particle Properties*, *European Physics Journal*, Vol. C3, p. 127-131, 1998.

Spergel, D. N., Verde, L., Peiris, H. V., Komatsu, E., Nolta, M. R., Bennett, C. L., Halpern, M., Hinshaw, G., Jarosik, N., Kogut, A., Limon, M., Meyer, S. S., Page, L., Tucker, G. S., Weiland, J. L., Wollack, E. L., Wright, E. L., “First Year Wilkinson Microwave Anisotropy Probe (WMAP) Observations: Determination of Cosmological Parameters”, *Astrophysical Journal Supplement Series*, Vol. 148, p. 175–194, 2003.

Spergel, D. N., Bean, R., Doré, O., Nolta, M. R., Bennett, C. L., Dunkley, J., Hinshaw, G., Jarosik, N., Komatsu, E., Page, L., Peiris, H. V., Verde, L., Halpern, M., Hill, R. S., Kogut, A., Limon, M., Meyer, S. S., Odegard, N., Tucker, G. S., Weiland, J. L., Wollack, E., Wright, E. L., “Wilkinson Microwave Anisotropy Probe (WMAP) Three Year Results: Implications for Cosmology”, *Astrophysical Journal Supplement Series*, Vol. 170, p. 377, 2008.

Spinelli, S., “The Use of Optical Coherence for CMB Devoted Instrumentation Development”, Ph.D. thesis, *Universita degli Studi di Milano – Bicocca*, Italy, 2010.

Stanford University QUaD website: <http://www.stanford.edu/~schurch/quad.html>

Starobinski, A. A., “A New Type of Isotropic Cosmological Models without Singularity”, *Physics Letters B*, Issue 1, pp. 99-102, 1980.

Tauber, J. A., “The Planck Mission”, New Cosmological Data and the Values of the Fundamental Parameters, Proceedings of IAU Symposium #201, Astronomical Society of the Pacific (ASP), p. 86, 2005.

Thompson, A. R., Moran, J. M., Swenson Jr., G. W., “Interferometry and Synthesis in Radio Astronomy”, Krieger Publishing Company, Malabar, Florida, 1998.

TICRA’s GRASP website:

<http://www.ticra.com/what-we-do/software-descriptions/grasp>

Timbie, P. T., Tucker, G. S., “Adding Interferometry for CMBPol”, J. Phys.: Conf. Ser., Vol. 155, 012003, 2008.

Tolansky, S., “An Introduction to Interferometry”, Second Edition, John Wiley & Sons Ltd., 1973.

Trappe, N., “Quasi-optical Analysis of the HIFI Instrument for the Herschel Space Observatory”, Ph.D. thesis, National University of Ireland, Maynooth, Ireland, 2002.

Tucker G.S., Korotkov, A. L., Gault, A. C., Hyland, P. O., Malu, S., Timbie, P. T., Bunn, E. F., Keating, B. G., Bierman, E., O’Sullivan, C., Ade, P. A. R., Piccirillo, L., “The Millimeter-Wave Bolometric Interferometer (MBI)”, in Proceedings of SPIE Vol. 7020, Millimeter and Submillimeter Detectors and instrumentation for Astronomy IV, Duncan, W. D., Holland, W. S., Withington, S., Zmuidzinas, J., eds., 70201M, Marseille, France, 2008.

Tucker, G. S., Timbie, P. T., “Millimeter-Wave Bolometric Interferometer - NASA Proposal”, 2008.

Tucker, G. S., Timbie, P. T., “Millimeter-Wave Bolometric Interferometer - NASA Proposal”, 2009.

Turner, M. S., “Cosmology: Going Beyond the Big Bang”, *Physics World*, Sept. 1996.

Verschuur, G.L., Kellermann, K., “Galactic and Extragalactic Radio Astronomy”, Springer-Verlag, New York, 1988.

Wang, Y., Zhang, L., Deng, C., Li, W., Zhong, H., Zhang, C., “Feature Extraction and Identification of Explosive Materials in Reflective Terahertz Spectroscopic Imaging System”, *Proceedings of 2008 International Conference on Optical Instruments and Technology: Microelectronic and Optoelectronic Devices and Integration*, Vol. 7158, 2009.

Wexler, A., “Solution of Waveguide Discontinuities by Modal Analysis”, *IEEE Trans.*, MTT-15, p. 508–517, 1967.

White, M., Cohn, J. D., “The Theory of Anisotropies in the Cosmic Microwave Background”, *American Journal of Physics*, Vol. 70, p. 106-118, 2002.

White, D. R., “The Development of Efficient CAD Software for Terahertz Optical Design and Analysis”, Ph.D. thesis, National University of Ireland, Maynooth, Ireland, 2006.

Wolfram Mathematica website: <http://www.wolfram.com/mathematica>

Wylde, R.J., “Millimetre Wave Gaussian Beam Mode Optics and Corrugated Feed Horns”, *IEEE Proc.* Vol. 131, p. 158–262, 1984.

Zaldarriaga, M., “Nature of the E-B decomposition of the CMB Polarization”, *Physical Review D*, Vol. 64, p. 103001-1 – 103001-8, 2001.

ZAX Millimeter Wave Corporation website: www.millimeterwave.com

ZEMAX website: <http://www.zemax.com>

Zmuidzinas, J., “Cramér-Rao Sensitivity Limits for Astronomical Instruments: Implications for Interferometer Design”, *Optical Society of America Journal A*, Vol. 20, p. 218-233.

Appendix A

Scatter Matrix Elements

Coupled Amplitude and Phase from Each Source to Each Detector								
Detector	S1 A	S1 ϕ	S2 A	S2 ϕ	S3 A	S3 ϕ	S4 A	S4 ϕ
Co-Polar Component								
1	0.0416	-1.7722	0.0080	0.2658	0.0179	0.8887	0.0379	-1.9420
2	0.0496	0.0849	0.0088	2.8120	0.0297	-2.0172	0.0236	-2.0219
3	0.0324	-1.4048	0.0026	1.1097	0.0307	-1.9462	0.0053	0.7811
4	0.0308	-0.9572	0.0176	2.9146	0.0162	2.0285	0.0484	0.8591
5	0.0590	2.7029	0.0338	0.6933	0.0409	0.9280	0.0545	2.5713
6	0.0575	2.8758	0.0314	1.2308	0.0543	2.5748	0.0324	0.9301
7	0.0267	-0.3657	0.0133	-1.8821	0.0396	0.9128	0.0077	2.1866
8	0.0116	2.5506	0.0110	1.8591	0.0056	-0.1751	0.0333	-0.0809
9	0.0411	1.6726	0.0378	1.3374	0.0290	0.1093	0.0635	-2.8396
10	0.0592	-2.7068	0.0546	-2.6999	0.0561	-2.7423	0.0561	-2.7428
11	0.0473	1.9624	0.0438	2.3038	0.0636	-2.8397	0.0291	0.1086
12	0.0187	3.1291	0.0162	-2.4108	0.0334	-0.0826	0.0056	-0.1865
13	0.0095	-2.7764	0.0199	-1.3834	0.0075	2.1573	0.0394	0.8751
14	0.0316	0.8389	0.0488	2.4716	0.0320	0.9009	0.0536	2.5414
15	0.0377	0.9574	0.0568	2.9548	0.0538	2.5379	0.0406	0.8957
16	0.0228	-2.4823	0.0341	-0.0525	0.0483	0.8224	0.0161	1.9929
17	0.0005	2.7298	0.0243	-2.1899	0.0049	0.6878	0.0300	-2.0247
18	0.0082	2.7644	0.0445	-0.0657	0.0228	-2.0927	0.0288	-2.0863
19	0.0096	0.8240	0.0428	-1.2769	0.0372	-2.0178	0.0175	0.8153
Cross-Polar Component								
1	0.0002	2.4617	0.0021	-2.8374	0.0009	-0.0103	0.0057	1.1899
2	0.0050	-3.0865	0.0051	-0.6140	0.0043	1.3934	0.0065	1.2220
3	0.0035	1.5826	0.0044	-1.8545	0.0055	1.2562	0.0025	-2.0660
4	0.0054	-1.2934	0.0031	2.7640	0.0053	1.8228	0.0009	0.2449
5	0.0002	0.0231	0.0015	-2.3675	0.0018	0.9736	0.0029	-0.9251
6	0.0016	-0.3456	0.0027	-1.9929	0.0017	-0.9879	0.0006	-2.7385
7	0.0030	-0.8430	0.0007	-1.4376	0.0002	-0.2063	0.0034	1.8011
8	0.0060	2.1315	0.0053	1.5377	0.0062	-0.8777	0.0046	-0.5854
9	0.0027	1.6238	0.0029	1.2459	0.0049	-0.0984	0.0013	-3.0489
10	0.0003	-0.7336	0.0002	-1.4092	0.0006	2.9140	0.0006	2.9153
11	0.0022	1.9855	0.0018	2.3448	0.0013	-3.0456	0.0049	-0.0985
12	0.0067	2.8000	0.0062	-2.7511	0.0046	-0.5873	0.0062	-0.8792
13	0.0010	-3.0383	0.0032	-1.8501	0.0033	1.7623	0.0001	-0.2804
14	0.0031	-2.3993	0.0011	-0.8577	0.0006	-2.7636	0.0017	-1.0210
15	0.0025	-2.1831	0.0011	-0.2903	0.0029	-0.9631	0.0018	0.9336
16	0.0025	-2.5139	0.0043	-0.4116	0.0008	0.2463	0.0053	1.7850
17	0.0043	-2.6940	0.0027	0.8416	0.0025	-2.1407	0.0055	1.1910
18	0.0057	-0.7582	0.0054	3.0503	0.0065	1.1529	0.0043	1.3186
19	0.0031	-2.3983	0.0016	1.8731	0.0057	1.1193	0.0008	-0.1254

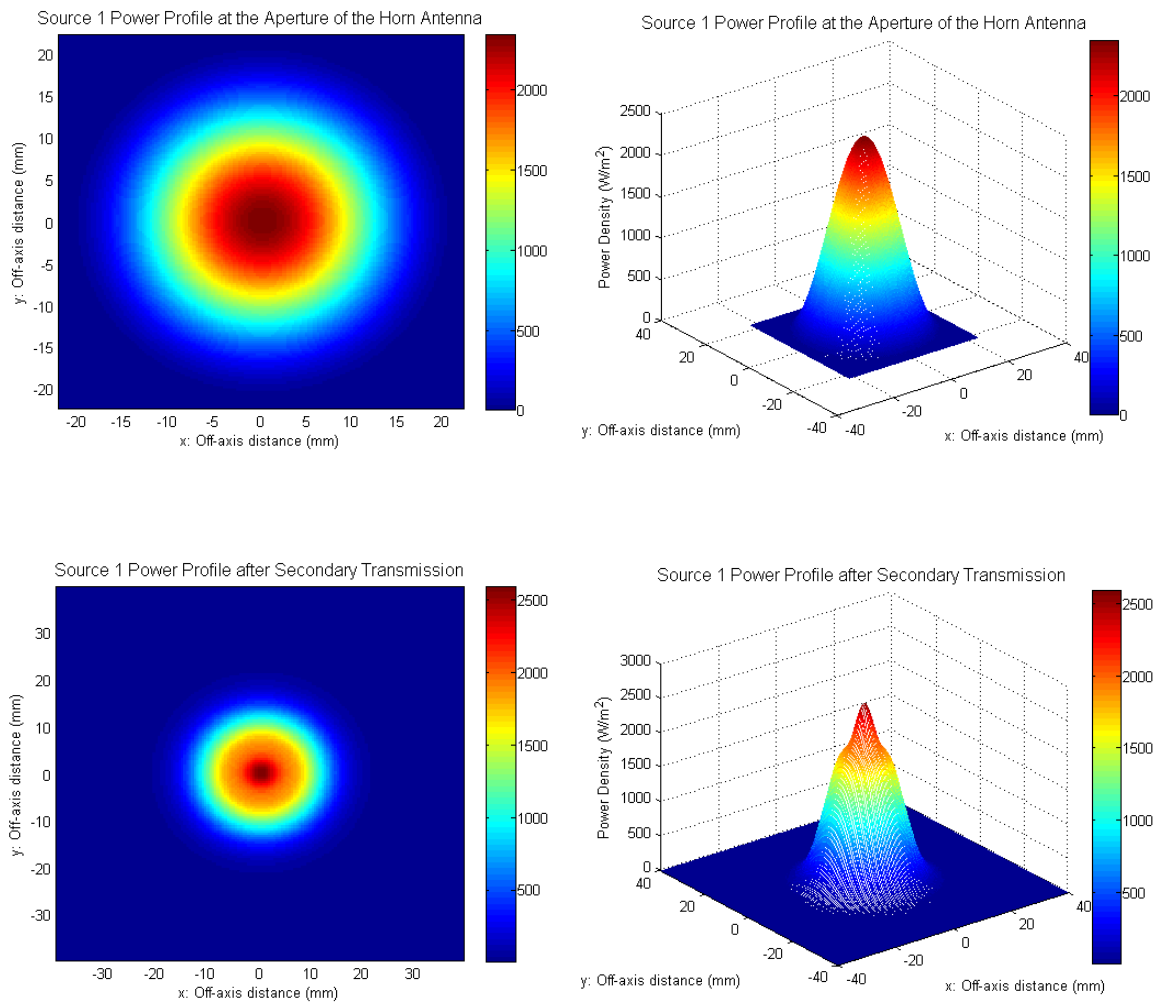
S_n represents source n , A is the amplitude and ϕ is the phase.

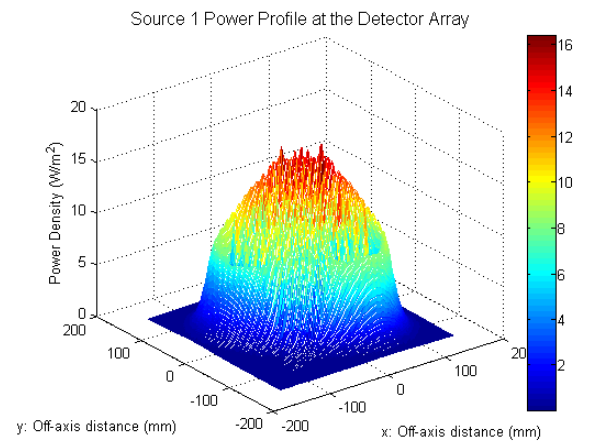
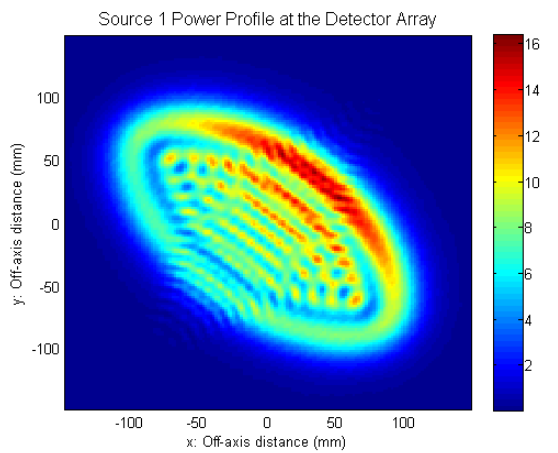
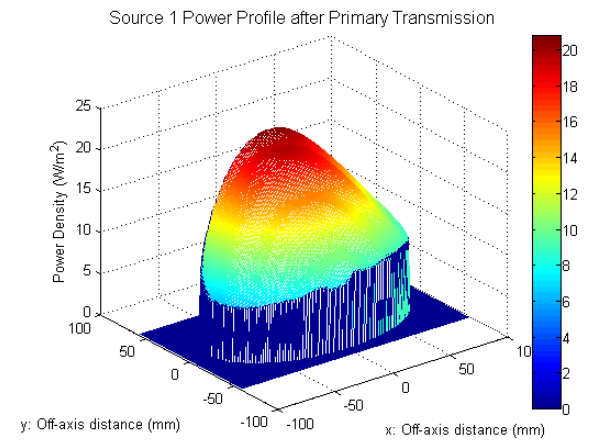
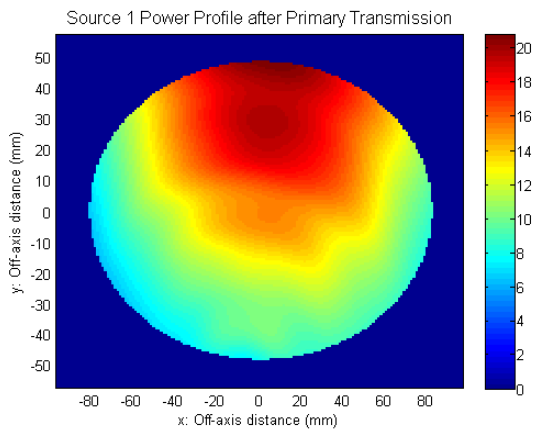
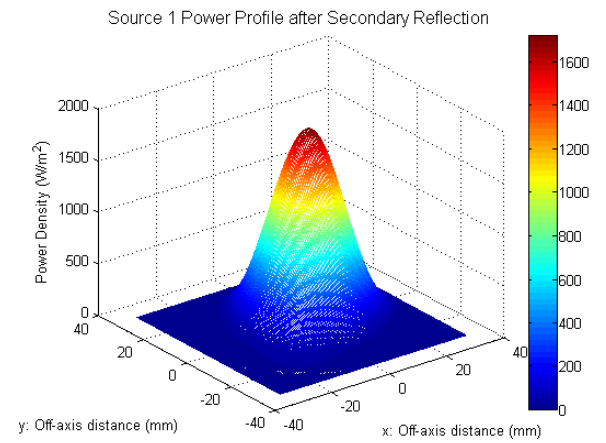
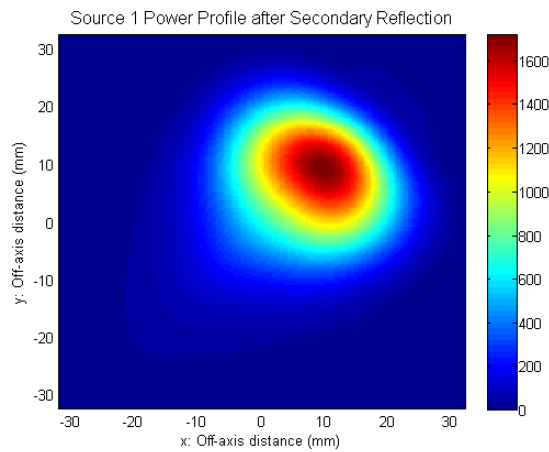
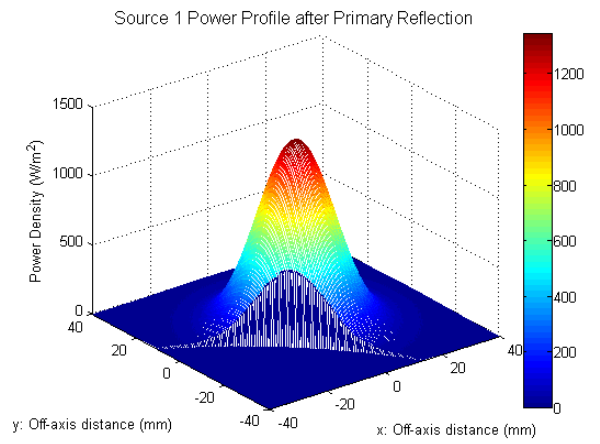
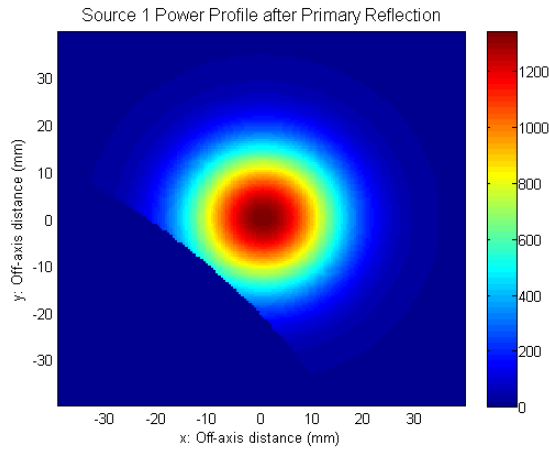
Appendix B

Beam Power Profiles

Below are the power profiles for each of the MBI-4 inward-facing horn antennas as the beam propagates through the optical beam combiner. The calculations were carried out with each source having a polarization direction both parallel and perpendicular to the shortest baseline, however only the parallel case is shown here since the results are very similar.

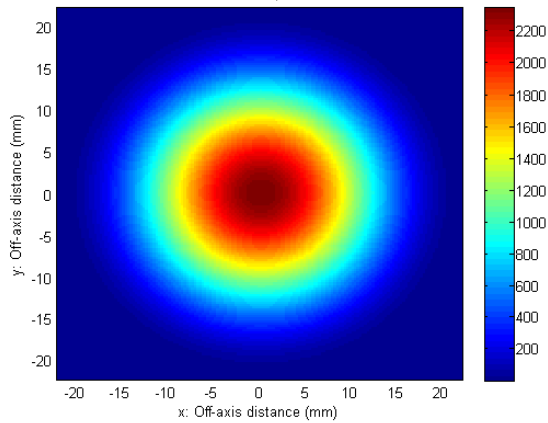
Source 1 Power Profiles



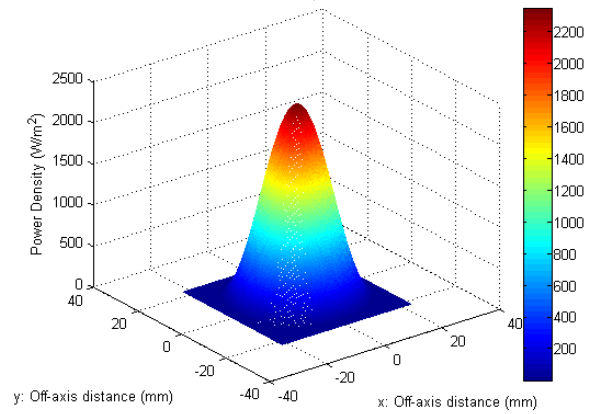


Source 2 Power Profiles

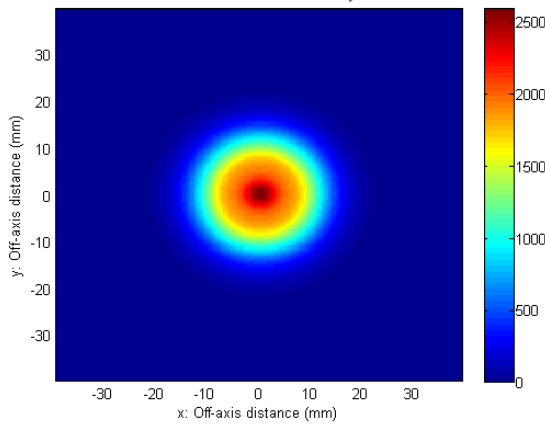
Source 2 Power Profile at the Aperture of the Horn Antenna



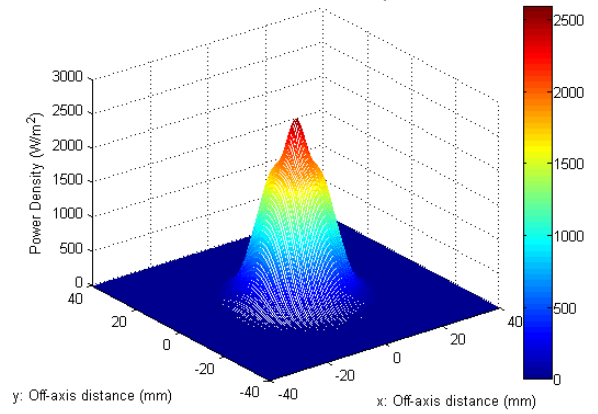
Source 2 Power Profile at the Aperture of the Horn Antenna



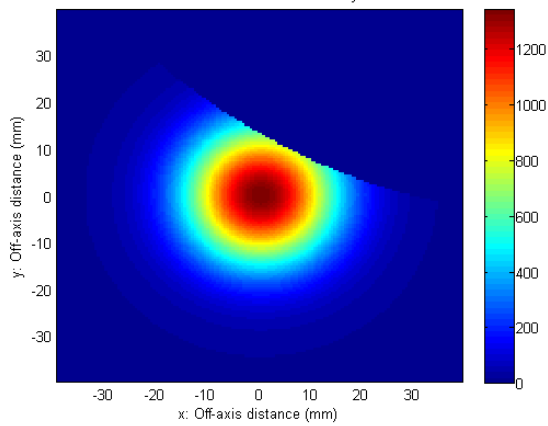
Source 2 Power Profile after Secondary Transmission



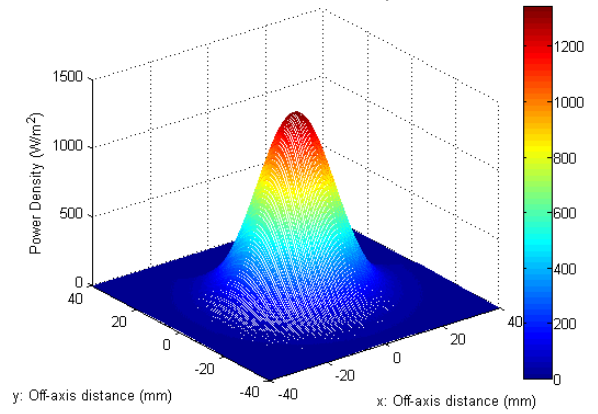
Source 2 Power Profile after Secondary Transmission



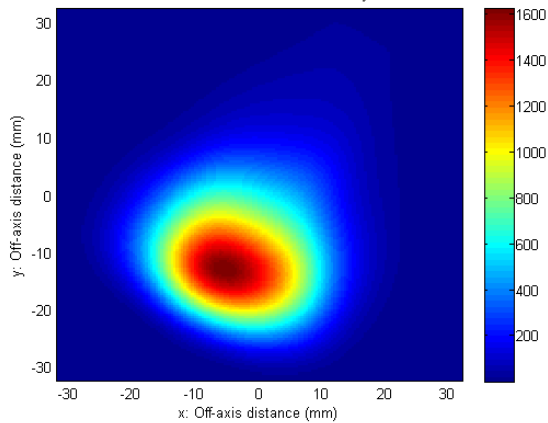
Source 2 Power Profile after Primary Reflection



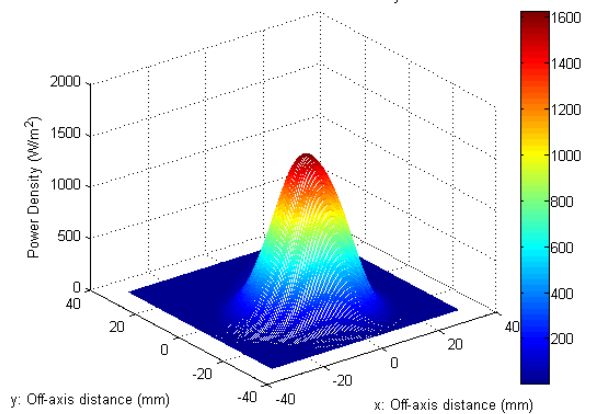
Source 2 Power Profile after Primary Reflection

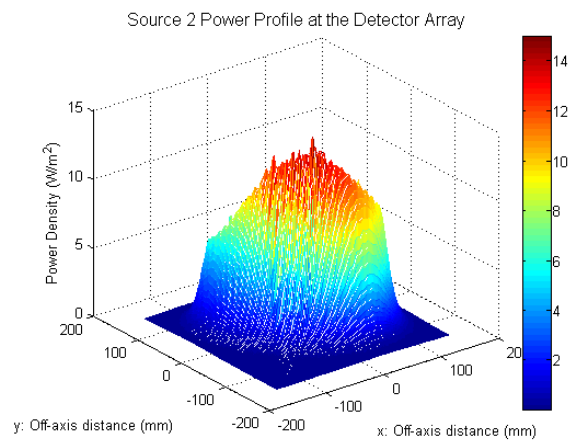
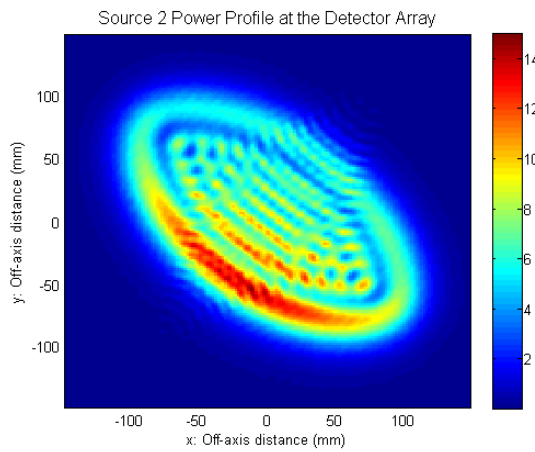
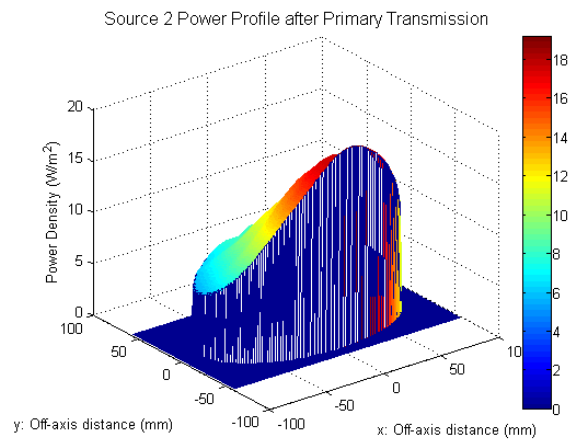
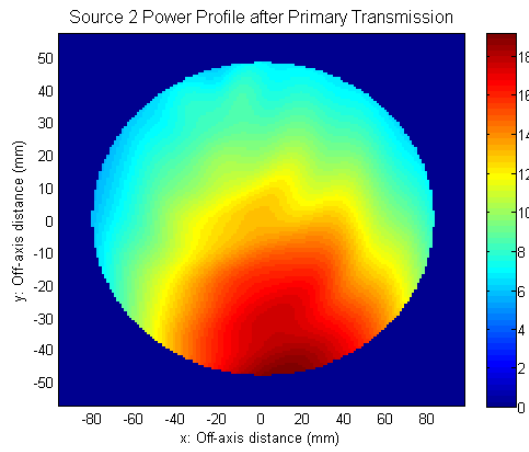


Source 2 Power Profile after Secondary Reflection

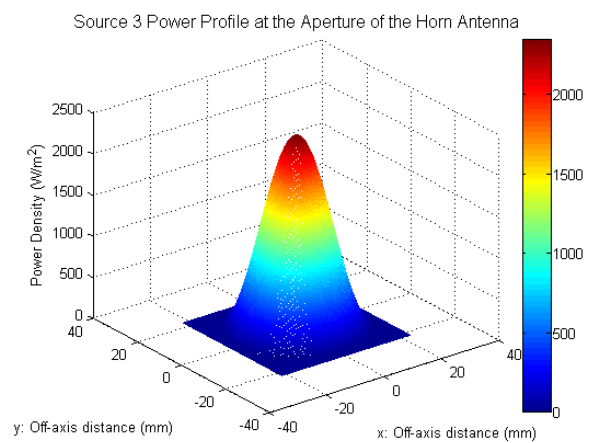
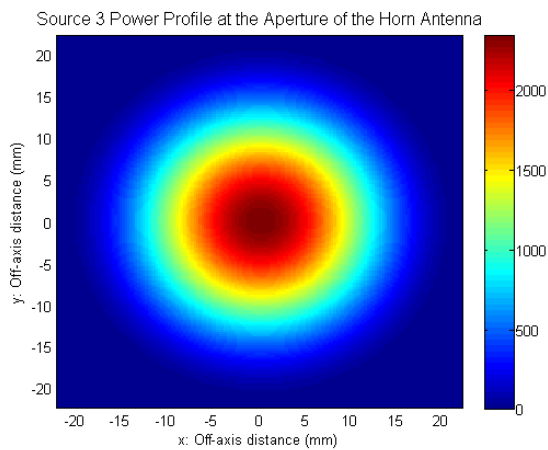


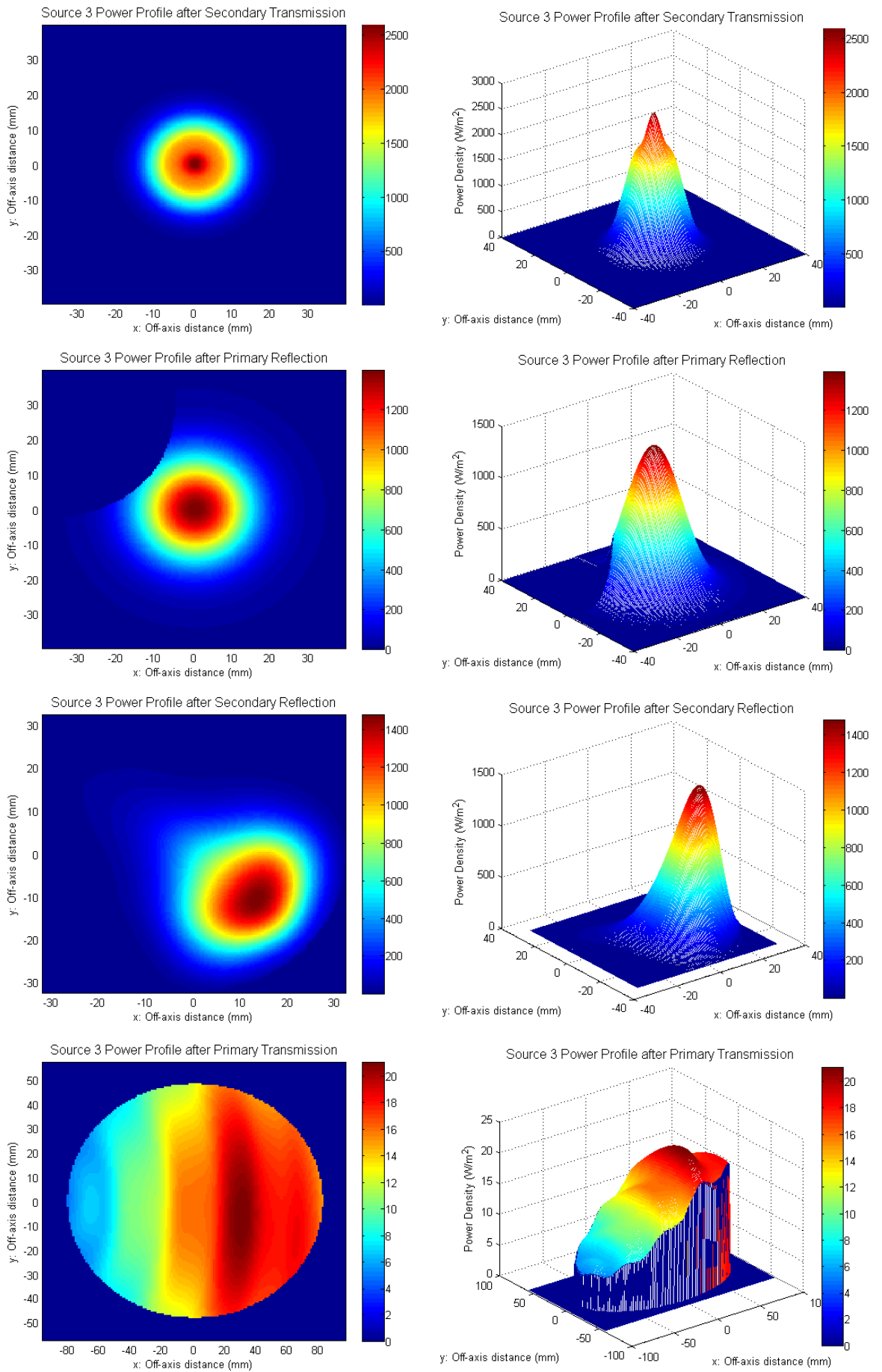
Source 2 Power Profile after Secondary Reflection

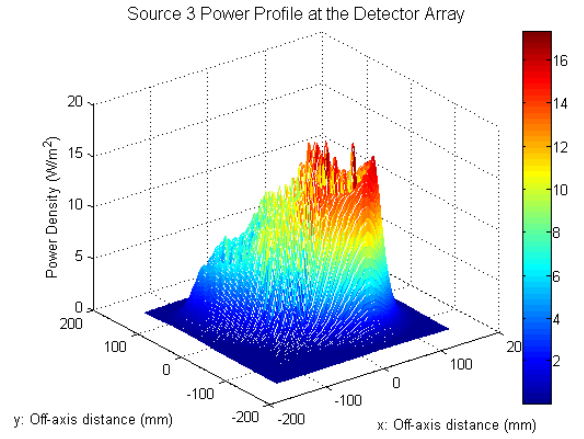
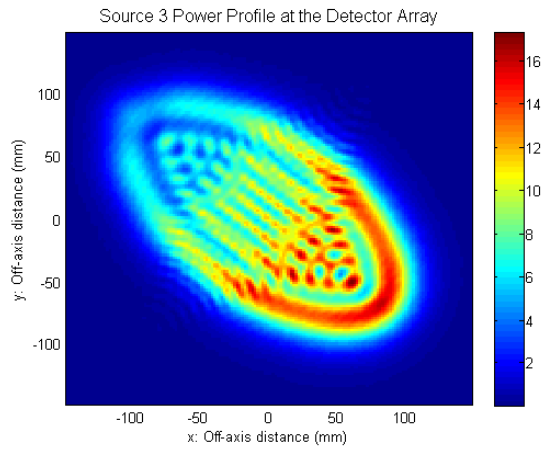




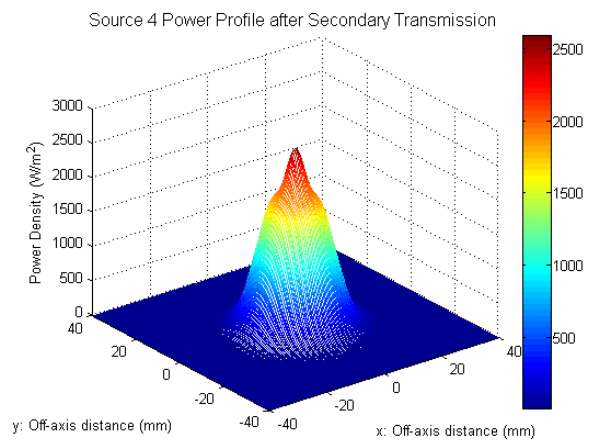
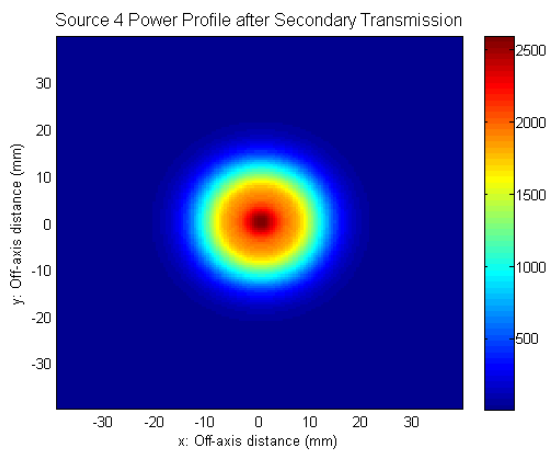
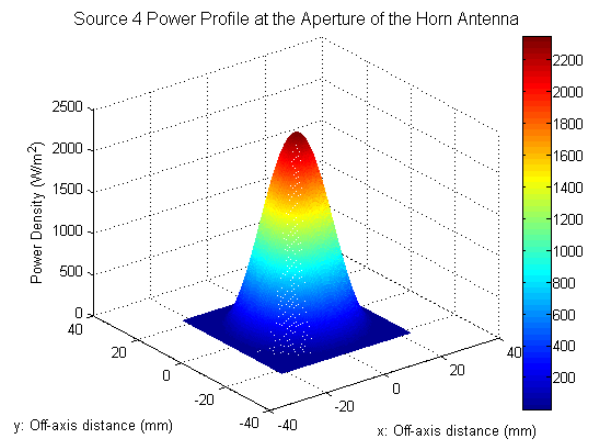
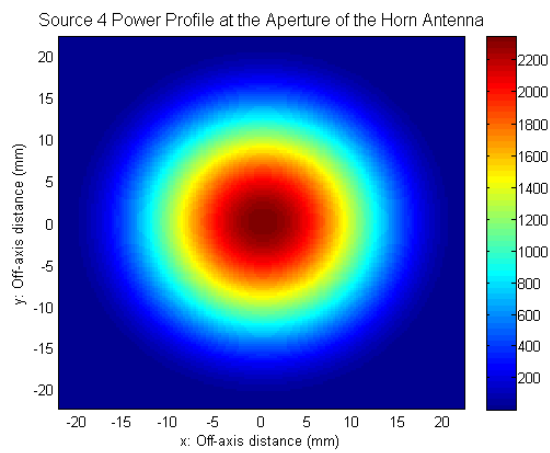
Source 3 Power Profiles

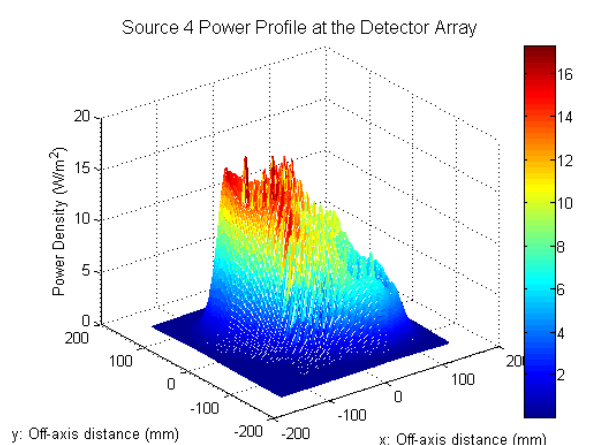
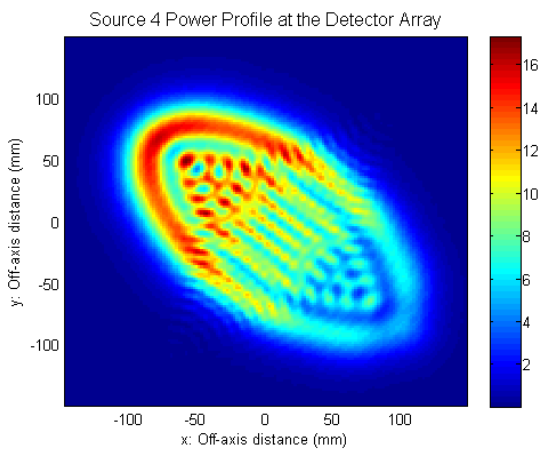
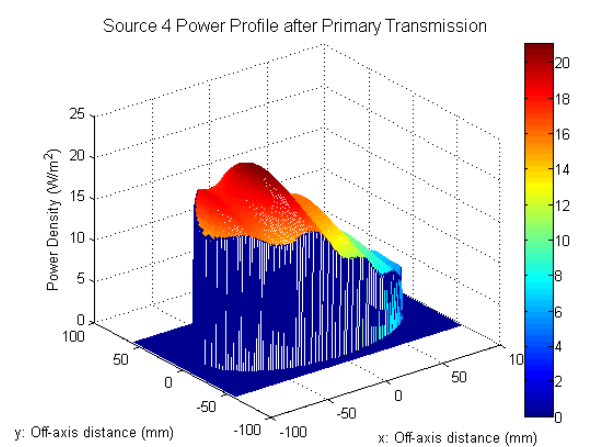
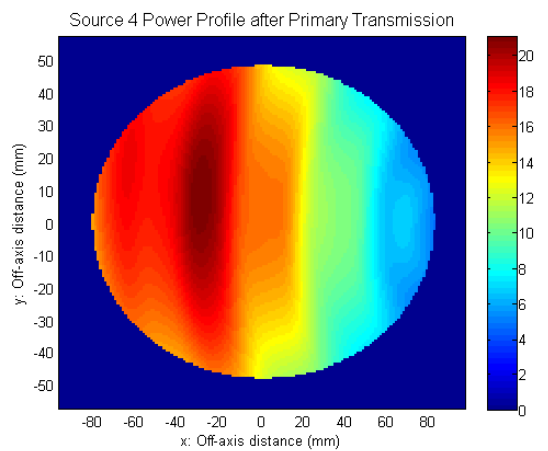
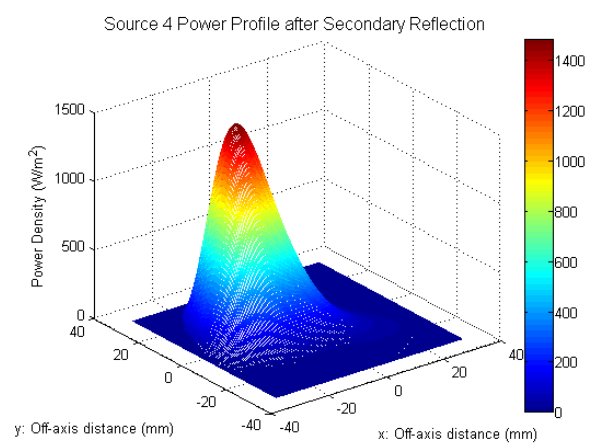
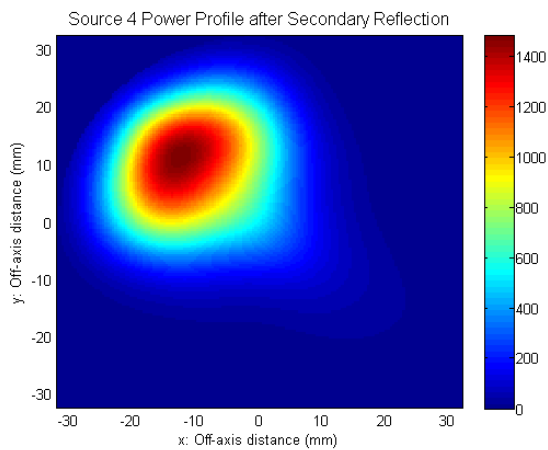
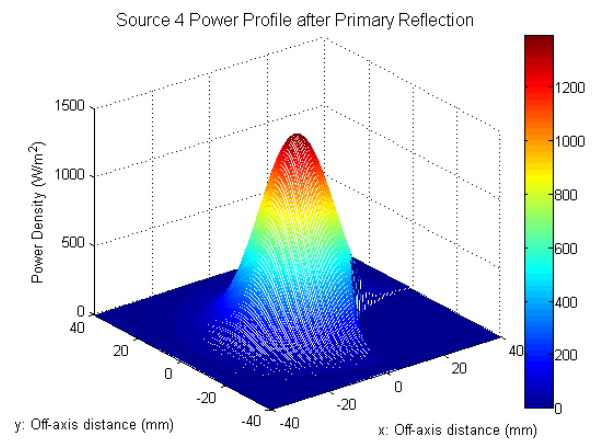
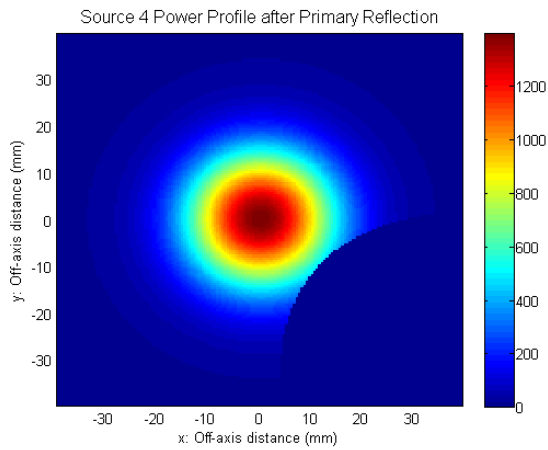






Source 4 Power Profiles





Appendix C

Mechanical Tolerance Data

- *Max* represents the maximum power coupled to that detector during the movement of the element indicated.
- *Min* represents the minimum power coupled to that detector during the movement of the element indicated.
- *Cen.* represents the power coupled to that detector when the element is centered.
- *Range* represents the range of coupled power during the movement of the element indicated.

Summary of the Power Coupled to the Detectors During XY-Movement of the Bolometer Array								
Detector	Max (mW)	x (mm)	y (mm)	Min (mW)	x (mm)	y (mm)	Cen. (mW)	Range (mW)
Source 1								
1	1.9450	2.5	-2.5	1.4000	-2.5	2.5	1.7290	0.5450
2	2.5500	-2.5	-1.3	2.2440	2.5	2.5	2.4830	0.3050
3	1.2960	-2.5	-2.5	0.7630	2.5	2.5	1.0590	0.5330
4	1.2420	2.5	-2.5	0.7270	-2.5	2.5	0.9790	0.5140
5	3.6930	2.5	-2.3	3.0590	-2.5	2.5	3.4780	0.6340
6	3.6040	-2.5	-2.5	2.7710	2.5	2.5	3.3130	0.8340
7	1.0930	-2.5	-2.5	0.3930	2.5	2.5	0.7210	0.7010
8	0.2470	2.5	2.5	0.1230	-2.5	-2.5	0.1720	0.1240
9	1.9990	2.5	2.5	1.3700	-2.5	-2.5	1.6980	0.6290
10	3.6530	2.5	2.5	3.2250	-2.5	-2.5	3.5020	0.4280
11	2.4850	-2.5	2.5	1.9440	2.5	-2.5	2.2450	0.5410
12	0.4730	-2.5	-2.5	0.2960	2.5	-2.5	0.3960	0.1770
13	0.1900	2.5	2.5	0.0570	-2.5	-2.1	0.0920	0.1340
14	1.3550	2.5	2.5	0.7110	-2.5	-2.5	1.0090	0.6440
15	1.7350	-2.5	2.5	1.1670	2.5	-2.5	1.4300	0.5680
16	0.6910	-2.5	2.5	0.4430	2.5	-1.5	0.5280	0.2470
17	0.0370	2.5	2.5	0.0170	-2.5	-0.6	0.0180	0.0200

18	0.1980	2.5	2.5	0.0780	-2.5	-1.9	0.1000	0.1210
19	0.1460	-2.5	2.5	0.0940	2.5	0.4	0.1010	0.0520
Source 2								
1	0.0960	2.5	-2.5	0.0620	-2.5	-0.4	0.0680	0.0340
2	0.1770	-2.5	-2.5	0.0890	2.5	1.7	0.1020	0.0880
3	0.0430	-2.5	2.5	0.0200	2.5	-1.3	0.0260	0.0230
4	0.4320	2.5	-2.5	0.2520	-2.5	2.5	0.3200	0.1800
5	1.3920	2.5	-2.5	0.9210	-2.5	2.5	1.1410	0.4700
6	1.2940	-2.5	-2.5	0.7440	2.5	2.5	0.9930	0.5500
7	0.2820	-2.5	-2.5	0.1370	2.5	0.4	0.1780	0.1450
8	0.2060	2.5	2.5	0.1200	-2.5	-2.5	0.1490	0.0860
9	1.6490	2.5	-2.3	1.2090	-2.5	2.5	1.4390	0.4400
10	3.1070	2.5	-2.5	2.7760	-2.5	2.5	2.9810	0.3300
11	2.1970	-2.5	-2.5	1.5920	2.5	2.5	1.9210	0.6050
12	0.4280	-2.5	-2.5	0.1760	2.5	2.5	0.3000	0.2520
13	0.6070	2.5	2.5	0.2150	-2.5	-2.5	0.4050	0.3920
14	2.6100	2.5	2.1	1.9870	-2.5	-2.5	2.3790	0.6240
15	3.3540	-2.5	1.7	2.8990	2.5	-2.5	3.2310	0.4550
16	1.4930	-2.5	2.5	0.8710	2.5	-2.5	1.1830	0.6230
17	0.7430	2.5	2.5	0.4200	-2.5	-2.5	0.5980	0.3230
18	2.1010	2.5	0.8	1.7790	-2.5	-2.5	2.0130	0.3210
19	2.0110	-2.5	2.3	1.5140	2.5	-2.5	1.8340	0.4970
Source 3								
1	0.3920	2.5	2.5	0.2530	-2.5	-2.5	0.3220	0.1400
2	1.0230	2.5	2.5	0.7450	-2.5	-2.5	0.9030	0.2790
3	1.0370	-2.5	0.4	0.8430	2.5	2.5	0.9710	0.1940
4	0.3730	2.5	-2.5	0.2220	-2.5	2.5	0.2910	0.1510
5	1.8830	2.5	-2.5	1.4700	-2.5	2.5	1.6740	0.4130
6	3.0350	2.5	-2.5	2.8210	-2.5	2.5	2.9470	0.2140
7	1.9460	-2.5	-2.5	1.0430	2.5	2.5	1.5710	0.9030
8	0.0850	2.5	1.9	0.0480	-2.5	-2.5	0.0690	0.0370
9	1.1040	2.5	2.5	0.6920	-2.5	-2.5	0.8670	0.4120
10	3.4120	2.5	2.5	2.9300	-2.5	-2.5	3.1460	0.4820
11	4.1380	-2.5	-2.5	3.8290	2.5	2.5	4.0420	0.3090
12	1.3640	-2.5	-2.5	0.9460	2.5	2.5	1.1370	0.4180
13	0.0970	2.5	2.5	0.0490	-2.5	-2.5	0.0670	0.0470
14	1.2560	2.5	2.5	0.8470	-2.5	-2.5	1.0260	0.4080
15	3.0680	2.5	2.5	2.7370	-2.5	-2.5	2.9080	0.3310

16	2.6570	-2.5	2.5	1.7780	2.5	-2.5	2.3320	0.8790
17	0.0570	2.5	-2.5	0.0110	-2.5	2.5	0.0300	0.0460
18	0.7060	2.5	-2.5	0.4010	-2.5	2.5	0.5600	0.3050
19	1.4230	2.1	0.2	1.3140	-2.5	2.5	1.4160	0.1080
Source 4								
1	1.4730	-1.9	-0.4	1.3760	2.5	-2.5	1.4700	0.0970
2	0.7480	-2.5	2.5	0.4320	2.5	-2.5	0.6000	0.3160
3	0.0620	-2.5	2.5	0.0130	2.5	-2.5	0.0340	0.0490
4	2.6840	2.5	-2.5	1.7730	-2.5	2.5	2.3420	0.9110
5	3.1350	-2.5	-2.5	2.8010	2.5	2.5	2.9790	0.3340
6	1.2780	-2.5	-2.5	0.8740	2.5	2.5	1.0530	0.4040
7	0.1010	-2.5	-2.5	0.0520	2.5	2.5	0.0710	0.0500
8	1.3610	2.5	2.5	0.9420	-2.5	-2.5	1.1330	0.4190
9	4.1420	2.5	2.5	3.8200	-2.5	-2.5	4.0370	0.3220
10	3.3970	-2.5	-2.5	2.9410	2.5	2.3	3.1450	0.4560
11	1.1020	-2.5	-2.5	0.6980	2.5	2.5	0.8700	0.4040
12	0.0860	-2.5	-2.1	0.0480	2.5	2.5	0.0700	0.0380
13	1.9110	2.5	2.5	1.0410	-2.5	-2.5	1.5530	0.8700
14	2.9690	-2.5	2.5	2.7570	2.5	-2.5	2.8770	0.2110
15	1.8590	-2.5	2.5	1.4450	2.5	-2.5	1.6480	0.4140
16	0.3700	-2.5	2.5	0.2200	2.5	-2.5	0.2880	0.1500
17	0.9920	2.5	-0.8	0.8140	-2.5	-2.5	0.9290	0.1780
18	0.9670	-2.5	-2.5	0.6980	2.5	2.5	0.8480	0.2690
19	0.3750	-2.5	-2.5	0.2390	2.5	2.5	0.3060	0.1360

Summary of the Power Coupled to the Detectors During Z-Movement of the Bolometer Array						
Detector	Max (mW)	z (mm)	Min (mW)	z (mm)	Cen. (mW)	Range (mW)
Source 1						
1	1.734	2.5	1.725	-2.5	1.729	0.010
2	2.494	-2.5	2.471	2.5	2.483	0.022
3	1.067	2.5	1.050	-2.5	1.059	0.017
4	0.985	2.5	0.972	-2.5	0.979	0.012
5	3.506	-2.5	3.449	2.5	3.478	0.057
6	3.340	-2.5	3.286	2.5	3.313	0.053
7	0.728	2.5	0.715	-2.5	0.721	0.013

8	0.178	2.5	0.166	-2.5	0.172	0.012
9	1.703	-2.5	1.691	2.5	1.698	0.012
10	3.533	-2.5	3.470	2.5	3.502	0.063
11	2.258	-2.5	2.231	2.5	2.245	0.026
12	0.404	2.5	0.387	-2.5	0.396	0.017
13	0.096	2.5	0.087	-2.5	0.092	0.009
14	1.012	2.5	1.007	-2.5	1.009	0.004
15	1.433	-2.5	1.427	2.5	1.430	0.006
16	0.534	2.5	0.523	-2.5	0.528	0.011
17	0.019	2.5	0.018	-0.2	0.018	0.000
18	0.105	2.5	0.096	-2.5	0.100	0.009
19	0.102	2.5	0.100	-2.5	0.101	0.002
Source 2						
1	0.070	2.5	0.067	-2.5	0.068	0.003
2	0.106	2.5	0.099	-2.5	0.102	0.007
3	0.026	2.5	0.026	-1.5	0.026	0.000
4	0.325	2.5	0.315	-2.5	0.320	0.010
5	1.146	-2.5	1.137	2.5	1.141	0.008
6	0.995	-2.5	0.992	2.5	0.993	0.003
7	0.183	2.5	0.174	-2.5	0.178	0.009
8	0.154	2.5	0.145	-2.5	0.149	0.008
9	1.444	-2.5	1.433	2.5	1.439	0.011
10	3.009	-2.5	2.954	2.5	2.981	0.055
11	1.934	-2.5	1.906	2.5	1.921	0.028
12	0.308	2.5	0.293	-2.5	0.300	0.016
13	0.413	2.5	0.397	-2.5	0.405	0.016
14	2.389	-2.5	2.369	2.5	2.379	0.020
15	3.262	-2.5	3.200	2.5	3.231	0.062
16	1.184	2.5	1.181	-2.5	1.183	0.003
17	0.606	2.5	0.590	-2.5	0.598	0.017
18	2.023	-2.5	2.001	2.5	2.013	0.022
19	1.834	-0.8	1.833	2.5	1.834	0.001
Source 3						
1	0.323	2.5	0.320	-2.5	0.322	0.003
2	0.909	-2.5	0.897	2.5	0.903	0.012
3	0.974	-2.5	0.968	2.5	0.971	0.006
4	0.298	2.5	0.285	-2.5	0.291	0.012
5	1.675	-2.5	1.672	2.5	1.674	0.003

6	2.961	-2.5	2.932	2.5	2.947	0.028
7	1.579	2.5	1.563	-2.5	1.571	0.016
8	0.072	2.5	0.067	-2.5	0.069	0.005
9	0.874	2.5	0.861	-2.5	0.867	0.012
10	3.183	-2.5	3.112	2.5	3.146	0.071
11	4.072	-2.5	4.012	2.5	4.042	0.061
12	1.148	2.5	1.126	-2.5	1.137	0.022
13	0.070	2.5	0.064	-2.5	0.067	0.006
14	1.033	2.5	1.017	-2.5	1.026	0.016
15	2.921	-2.5	2.895	2.5	2.908	0.027
16	2.332	-2.3	2.331	2.5	2.332	0.001
17	0.031	2.5	0.029	-2.5	0.030	0.003
18	0.562	-2.5	0.557	2.5	0.560	0.005
19	1.425	-2.5	1.408	2.5	1.416	0.017
Source 4						
1	1.478	-2.5	1.461	2.5	1.470	0.017
2	0.603	-2.5	0.597	2.5	0.600	0.005
3	0.035	2.5	0.033	-2.5	0.034	0.003
4	2.342	-2.5	2.340	2.5	2.342	0.002
5	2.993	-2.5	2.966	2.5	2.979	0.027
6	1.061	2.5	1.043	-2.5	1.053	0.017
7	0.074	2.5	0.068	-2.5	0.071	0.007
8	1.144	2.5	1.122	-2.5	1.133	0.022
9	4.067	-2.5	4.007	2.5	4.037	0.060
10	3.183	-2.5	3.111	2.5	3.145	0.072
11	0.876	2.5	0.864	-2.5	0.870	0.012
12	0.072	2.5	0.067	-2.5	0.070	0.005
13	1.562	2.5	1.545	-2.5	1.553	0.017
14	2.890	-2.5	2.862	2.5	2.877	0.028
15	1.649	-2.5	1.646	2.5	1.648	0.003
16	0.294	2.5	0.282	-2.5	0.288	0.012
17	0.932	-2.5	0.926	2.5	0.929	0.006
18	0.853	-2.5	0.842	2.5	0.848	0.011
19	0.307	2.5	0.305	-2.5	0.306	0.003

**Summary of the Power Coupled to the Detectors During θ -
Movement of the Bolometer Array**

Detector	Max (mW)	θ (deg)	Min (mW)	θ (deg)	Cent. (mW)	Range (mW)
Source 1						
1	1.813	-5.0	1.550	5.0	1.729	0.262
2	2.546	5.0	2.388	-5.0	2.483	0.158
3	1.178	5.0	0.894	-5.0	1.059	0.284
4	0.986	-2.5	0.906	5.0	0.979	0.080
5	3.524	-5.0	3.368	5.0	3.478	0.156
6	3.360	5.0	3.223	-5.0	3.313	0.137
7	0.822	-5.0	0.580	5.0	0.721	0.242
8	0.248	-5.0	0.140	5.0	0.172	0.108
9	1.787	-5.0	1.567	5.0	1.698	0.220
10	3.502	-5.0	3.502	-5.0	3.502	0.000
11	2.280	5.0	2.158	-5.0	2.245	0.122
12	0.399	-5.0	0.374	5.0	0.396	0.025
13	0.132	-5.0	0.088	2.1	0.092	0.045
14	1.038	-5.0	0.996	5.0	1.009	0.043
15	1.531	5.0	1.348	-5.0	1.430	0.183
16	0.553	-5.0	0.528	0.0	0.528	0.025
17	0.027	5.0	0.018	-0.4	0.018	0.008
18	0.115	5.0	0.090	-5.0	0.100	0.025
19	0.117	-5.0	0.099	2.1	0.101	0.019
Source 2						
1	0.086	-5.0	0.065	2.9	0.068	0.021
2	0.106	5.0	0.099	-5.0	0.102	0.007
3	0.046	5.0	0.019	-5.0	0.026	0.027
4	0.342	5.0	0.319	-1.3	0.320	0.024
5	1.178	5.0	1.103	-5.0	1.141	0.075
6	1.041	-5.0	0.961	5.0	0.993	0.081
7	0.205	5.0	0.177	-1.3	0.178	0.028
8	0.180	-5.0	0.134	4.2	0.149	0.045
9	1.466	5.0	1.377	-5.0	1.439	0.089
10	2.981	-5.0	2.981	-5.0	2.981	0.000
11	2.024	-5.0	1.781	5.0	1.921	0.243
12	0.386	-5.0	0.250	5.0	0.300	0.136
13	0.425	-3.3	0.326	5.0	0.405	0.099

14	2.481	5.0	2.257	-5.0	2.379	0.225
15	3.236	-3.3	3.204	5.0	3.231	0.032
16	1.200	2.9	1.104	-5.0	1.183	0.096
17	0.722	5.0	0.461	-5.0	0.598	0.261
18	2.141	5.0	1.838	-5.0	2.013	0.303
19	1.855	-3.8	1.730	5.0	1.834	0.126
Source 3						
1	0.431	-5.0	0.229	5.0	0.322	0.202
2	0.984	-5.0	0.800	5.0	0.903	0.184
3	1.057	5.0	0.839	-5.0	0.971	0.219
4	0.327	-5.0	0.266	5.0	0.291	0.061
5	1.764	-5.0	1.577	5.0	1.674	0.187
6	3.000	-5.0	2.878	5.0	2.947	0.123
7	1.648	-5.0	1.373	5.0	1.571	0.275
8	0.070	-0.8	0.053	5.0	0.069	0.016
9	0.929	-5.0	0.842	5.0	0.867	0.087
10	3.146	-5.0	3.146	-5.0	3.146	0.000
11	4.050	-4.2	3.999	5.0	4.042	0.050
12	1.214	-5.0	0.973	5.0	1.137	0.240
13	0.084	5.0	0.059	-3.8	0.067	0.026
14	1.133	5.0	0.933	-5.0	1.026	0.200
15	3.032	5.0	2.778	-5.0	2.908	0.254
16	2.379	3.8	2.087	-5.0	2.332	0.292
17	0.076	5.0	0.006	-5.0	0.030	0.069
18	0.713	5.0	0.426	-5.0	0.560	0.288
19	1.418	0.8	1.365	-5.0	1.416	0.053
Source 4						
1	1.471	0.8	1.416	-5.0	1.470	0.055
2	0.762	5.0	0.457	-5.0	0.600	0.305
3	0.082	5.0	0.008	-5.0	0.034	0.075
4	2.395	3.8	2.090	-5.0	2.342	0.306
5	3.103	5.0	2.848	-5.0	2.979	0.255
6	1.163	5.0	0.956	-5.0	1.053	0.207
7	0.087	5.0	0.062	-4.2	0.071	0.026
8	1.212	-5.0	0.969	5.0	1.133	0.243
9	4.049	-5.0	3.989	5.0	4.037	0.060
10	3.145	-5.0	3.145	-5.0	3.145	0.000
11	0.928	-5.0	0.849	5.0	0.870	0.079

12	0.071	-1.3	0.053	5.0	0.070	0.017
13	1.622	-5.0	1.366	5.0	1.553	0.256
14	2.930	-5.0	2.810	5.0	2.877	0.120
15	1.735	-5.0	1.554	5.0	1.648	0.182
16	0.324	-5.0	0.263	5.0	0.288	0.061
17	1.015	5.0	0.801	-5.0	0.929	0.214
18	0.923	-5.0	0.752	5.0	0.848	0.172
19	0.411	-5.0	0.216	5.0	0.306	0.195

Summary of the Power Coupled to the Detectors During XY-Movement of the Mirror System (Primary and Secondary Combined)								
Detector	Max	x	y	Min	x	y	Cen.	Range
	(mW)	(mm)	(mm)	(mW)	(mm)	(mm)	(mW)	(mW)
Source 1								
1	1.7290	0.0	0.0	1.5080	0.5	0.4	1.7290	0.2210
2	2.5660	0.1	-0.5	2.4830	0.0	0.0	2.4830	0.0830
3	1.2210	0.5	-0.1	1.0590	0.0	0.0	1.0590	0.1620
4	0.9790	0.0	0.0	0.8680	0.5	-0.1	0.9790	0.1110
5	3.4780	0.0	0.0	3.2680	0.5	0.5	3.4780	0.2100
6	3.3980	0.5	-0.5	3.3130	0.0	0.0	3.3130	0.0850
7	0.7210	0.0	0.0	0.5300	-0.5	-0.3	0.7210	0.1910
8	0.1720	0.0	0.0	0.1330	0.5	0.5	0.1720	0.0390
9	1.6980	0.0	0.0	1.4690	0.5	0.5	1.6980	0.2290
10	3.6570	-0.5	-0.5	3.3360	0.5	0.5	3.5020	0.3210
11	2.3530	-0.4	-0.5	2.2020	0.5	0.5	2.2450	0.1510
12	0.3960	0.0	0.0	0.3630	-0.2	0.5	0.3960	0.0330
13	0.1030	-0.5	0.5	0.0900	0.5	-0.5	0.0920	0.0130
14	1.0950	-0.5	-0.5	0.9040	0.5	0.5	1.0090	0.1910
15	1.6510	-0.5	-0.5	1.4150	0.5	0.5	1.4300	0.2360
16	0.5920	-0.4	-0.5	0.5130	0.5	0.5	0.5280	0.0790
17	0.0290	0.3	0.5	0.0180	0.0	0.0	0.0180	0.0110
18	0.1380	-0.5	-0.5	0.1000	0.0	0.0	0.1000	0.0380
19	0.1230	-0.5	-0.5	0.0910	0.5	0.5	0.1010	0.0320
Source 2								
1	0.0790	0.5	0.5	0.0580	-0.5	-0.5	0.0680	0.0210

2	0.1260	0.5	0.5	0.0950	-0.5	-0.5	0.1020	0.0310
3	0.0490	-0.3	-0.5	0.0260	0.0	0.0	0.0260	0.0230
4	0.3680	0.5	0.5	0.3160	-0.1	-0.5	0.3200	0.0520
5	1.2760	0.5	0.5	1.0860	-0.5	-0.5	1.1410	0.1900
6	1.0570	0.5	0.5	0.8750	-0.5	-0.5	0.9930	0.1820
7	0.2140	0.2	0.5	0.1780	0.0	0.0	0.1780	0.0360
8	0.1500	-0.5	0.5	0.1270	0.3	-0.5	0.1490	0.0230
9	1.5240	-0.2	0.5	1.4060	0.5	-0.5	1.4390	0.1180
10	3.1390	0.5	0.5	2.8200	-0.5	-0.5	2.9810	0.3190
11	1.9210	0.0	0.0	1.6550	-0.5	-0.5	1.9210	0.2660
12	0.3000	0.0	0.0	0.2270	-0.5	0.5	0.3000	0.0730
13	0.4050	0.0	0.0	0.2990	0.5	0.3	0.4050	0.1060
14	2.5490	-0.2	0.5	2.3790	0.0	0.0	2.3790	0.1700
15	3.3030	0.5	0.5	3.0910	-0.5	-0.5	3.2310	0.2120
16	1.2280	0.5	-0.5	1.1450	-0.5	0.5	1.1830	0.0830
17	0.7570	-0.5	0.4	0.5980	0.0	0.0	0.5980	0.1590
18	2.1850	-0.1	0.5	2.0130	0.0	0.0	2.0130	0.1720
19	1.8340	0.0	0.0	1.6720	-0.5	-0.4	1.8340	0.1620

Source 3

1	0.3220	0.0	0.0	0.2100	0.5	-0.5	0.3220	0.1120
2	0.9030	0.0	0.0	0.7530	0.5	0.3	0.9030	0.1500
3	1.0680	-0.1	0.4	0.9710	0.0	0.0	0.9710	0.0970
4	0.2910	0.0	0.0	0.2430	0.5	-0.5	0.2910	0.0480
5	1.6740	0.0	0.0	1.5020	0.5	-0.5	1.6740	0.1720
6	2.9870	-0.5	0.5	2.7720	0.5	-0.5	2.9470	0.2150
7	1.5710	0.0	0.0	1.2620	-0.5	-0.5	1.5710	0.3090
8	0.0690	0.0	0.0	0.0500	0.5	-0.4	0.0690	0.0190
9	0.9060	-0.5	0.5	0.7800	0.5	-0.5	0.8670	0.1260
10	3.2780	-0.5	0.5	3.0160	0.5	-0.5	3.1460	0.2620
11	4.0660	-0.5	0.5	3.9220	0.5	-0.5	4.0420	0.1440
12	1.1370	0.0	0.0	0.9460	-0.5	-0.5	1.1370	0.1910
13	0.0960	-0.5	0.5	0.0670	0.0	0.0	0.0670	0.0290
14	1.1940	-0.5	0.5	1.0260	0.0	0.0	1.0260	0.1680
15	3.1550	-0.5	0.5	2.8970	0.5	-0.5	2.9080	0.2580
16	2.3850	0.5	-0.2	2.3180	-0.5	0.5	2.3320	0.0670
17	0.0850	-0.5	0.5	0.0300	0.0	0.0	0.0300	0.0550
18	0.7730	0.1	0.5	0.5600	0.0	0.0	0.5600	0.2130
19	1.4260	0.3	0.5	1.3420	-0.3	-0.5	1.4160	0.0840

Source 4								
1	1.4810	-0.3	-0.5	1.3990	0.3	0.5	1.4700	0.0820
2	0.8240	-0.1	-0.5	0.6000	0.0	0.0	0.6000	0.2240
3	0.0930	0.5	-0.5	0.0340	0.0	0.0	0.0340	0.0590
4	2.4070	-0.5	0.2	2.3340	0.5	-0.5	2.3420	0.0730
5	3.2270	0.5	-0.5	2.9660	-0.5	0.5	2.9790	0.2610
6	1.2250	0.5	-0.5	1.0530	0.0	0.0	1.0530	0.1720
7	0.0990	0.5	-0.5	0.0710	0.0	0.0	0.0710	0.0280
8	1.1330	0.0	0.0	0.9410	0.5	0.5	1.1330	0.1920
9	4.0570	0.5	-0.5	3.9110	-0.5	0.5	4.0370	0.1460
10	3.2770	0.5	-0.5	3.0140	-0.5	0.5	3.1450	0.2630
11	0.9120	0.5	-0.5	0.7870	-0.5	0.5	0.8700	0.1250
12	0.0700	0.0	0.0	0.0500	-0.5	0.4	0.0700	0.0200
13	1.5530	0.0	0.0	1.2560	0.5	0.5	1.5530	0.2970
14	2.9170	0.5	-0.5	2.7050	-0.5	0.5	2.8770	0.2120
15	1.6480	0.0	0.0	1.4790	-0.5	0.5	1.6480	0.1690
16	0.2880	0.0	0.0	0.2400	-0.5	0.5	0.2880	0.0480
17	1.0260	0.5	-0.4	0.9290	0.0	0.0	0.9290	0.0970
18	0.8480	0.0	0.0	0.7080	-0.5	-0.5	0.8480	0.1400
19	0.3060	0.0	0.0	0.1990	-0.5	0.5	0.3060	0.1070

Summary of the Power Coupled to the Detectors During Z-Movement of the Mirror System (Primary and Secondary Combined)						
Detector	Max (mW)	z (mm)	Min (mW)	z (mm)	Cen. (mW)	Range (mW)
Source 1						
1	1.5540	2.5	1.5460	-2.5	1.5500	0.0070
2	2.5660	2.5	2.5250	-2.5	2.5460	0.0410
3	1.1860	-2.5	1.1700	2.5	1.1780	0.0160
4	0.9130	-2.5	0.8990	2.5	0.9060	0.0140
5	3.4010	2.5	3.3350	-2.5	3.3680	0.0670
6	3.3910	2.5	3.3280	-2.5	3.3600	0.0630
7	0.5860	-2.5	0.5730	2.5	0.5800	0.0130
8	0.1430	-2.5	0.1360	2.5	0.1400	0.0070

9	1.5680	2.5	1.5660	-2.5	1.5670	0.0020
10	3.5330	2.5	3.4710	-2.5	3.5020	0.0620
11	2.2940	2.5	2.2670	-2.5	2.2800	0.0270
12	0.3810	-2.5	0.3670	2.5	0.3740	0.0130
13	0.1020	-2.5	0.0920	2.5	0.0970	0.0100
14	0.9970	-2.5	0.9950	2.5	0.9960	0.0020
15	1.5320	-2.5	1.5290	2.5	1.5310	0.0020
16	0.5560	-2.5	0.5460	2.5	0.5510	0.0110
17	0.0280	2.5	0.0260	-2.5	0.0270	0.0010
18	0.1200	-2.5	0.1100	2.5	0.1150	0.0100
19	0.1120	-2.5	0.1010	2.5	0.1060	0.0110
Source 2						
1	0.0700	-2.5	0.0640	2.5	0.0670	0.0060
2	0.1110	-2.5	0.1020	2.5	0.1060	0.0090
3	0.0460	2.5	0.0450	-2.5	0.0460	0.0010
4	0.3490	-2.5	0.3360	2.5	0.3420	0.0130
5	1.1800	-2.5	1.1780	2.5	1.1780	0.0020
6	0.9620	2.5	0.9610	-0.8	0.9610	0.0010
7	0.2120	-2.5	0.1980	2.5	0.2050	0.0130
8	0.1380	-2.5	0.1320	2.5	0.1350	0.0060
9	1.4700	2.5	1.4620	-2.5	1.4660	0.0080
10	3.0070	2.5	2.9560	-2.5	2.9810	0.0520
11	1.7900	2.5	1.7720	-2.5	1.7810	0.0180
12	0.2560	-2.5	0.2450	2.5	0.2500	0.0110
13	0.3310	-2.5	0.3200	2.5	0.3260	0.0110
14	2.4990	2.5	2.4630	-2.5	2.4810	0.0360
15	3.2330	2.5	3.1760	-2.5	3.2040	0.0560
16	1.1970	-2.5	1.1850	2.5	1.1910	0.0130
17	0.7280	-2.5	0.7150	2.5	0.7220	0.0140
18	2.1580	2.5	2.1240	-2.5	2.1410	0.0350
19	1.7360	2.5	1.7240	-2.5	1.7300	0.0130
Source 3						
1	0.2300	-2.5	0.2270	2.5	0.2290	0.0040
2	0.8080	2.5	0.7920	-2.5	0.8000	0.0160
3	1.0580	1.5	1.0560	-2.5	1.0570	0.0010
4	0.2730	-2.5	0.2600	2.5	0.2660	0.0130
5	1.5800	2.5	1.5750	-2.5	1.5770	0.0050
6	2.8980	2.5	2.8560	-2.5	2.8780	0.0420

7	1.3790	-2.5	1.3670	2.5	1.3730	0.0120
8	0.0550	-2.5	0.0520	2.5	0.0530	0.0030
9	0.8500	-2.5	0.8360	2.5	0.8420	0.0140
10	3.1860	2.5	3.1090	-2.5	3.1460	0.0770
11	4.0440	2.5	3.9550	-2.5	3.9990	0.0890
12	0.9800	-2.5	0.9660	2.5	0.9730	0.0140
13	0.0890	-2.5	0.0800	2.5	0.0840	0.0100
14	1.1410	-2.5	1.1250	2.5	1.1330	0.0160
15	3.0570	2.5	3.0070	-2.5	3.0320	0.0500
16	2.3770	-2.5	2.3670	2.5	2.3720	0.0100
17	0.0780	-2.5	0.0730	2.5	0.0760	0.0050
18	0.7200	2.5	0.7060	-2.5	0.7130	0.0140
19	1.3980	2.5	1.3750	-2.5	1.3870	0.0230
Source 4						
1	1.4530	2.5	1.4300	-2.5	1.4410	0.0230
2	0.7690	2.5	0.7550	-2.5	0.7620	0.0140
3	0.0850	-2.5	0.0800	2.5	0.0820	0.0050
4	2.3960	-2.5	2.3860	2.5	2.3910	0.0100
5	3.1280	2.5	3.0780	-2.5	3.1030	0.0510
6	1.1710	-2.5	1.1550	2.5	1.1630	0.0160
7	0.0930	-2.5	0.0830	2.5	0.0870	0.0100
8	0.9760	-2.5	0.9620	2.5	0.9690	0.0140
9	4.0330	2.5	3.9460	-2.5	3.9890	0.0870
10	3.1860	2.5	3.1080	-2.5	3.1450	0.0780
11	0.8560	-2.5	0.8420	2.5	0.8490	0.0140
12	0.0550	-2.5	0.0520	2.5	0.0530	0.0030
13	1.3720	-2.5	1.3590	2.5	1.3660	0.0120
14	2.8300	2.5	2.7890	-2.5	2.8100	0.0410
15	1.5560	2.5	1.5510	-2.5	1.5540	0.0050
16	0.2700	-2.5	0.2570	2.5	0.2630	0.0130
17	1.0160	2.5	1.0130	-2.5	1.0150	0.0020
18	0.7590	2.5	0.7440	-2.5	0.7520	0.0150
19	0.2180	-2.5	0.2140	2.5	0.2160	0.0040

Summary of the Power Coupled to the Detectors For a 1mm Mirror Contraction

Detector	S1 Co	S1 X	S2 Co	S2 X	S3 Co	S3 X	S4 Co	S4 X
1	1.5203	0.0017	0.0624	0.0019	0.2134	0.0017	1.3900	0.0201
2	2.4840	0.0211	0.0811	0.0215	0.7467	0.0135	0.6841	0.0448
3	1.1454	0.0193	0.0187	0.0230	1.0010	0.0351	0.0651	0.0115
4	0.8576	0.0294	0.3193	0.0111	0.2209	0.0332	2.3669	0.0031
5	3.3100	0.0001	1.1423	0.0014	1.5173	0.0061	3.0278	0.0062
6	3.3084	0.0032	0.9243	0.0081	2.8037	0.0034	1.1175	0.0015
7	0.5674	0.0043	0.1937	0.0003	1.3724	0.0009	0.0758	0.0072
8	0.1041	0.0292	0.1005	0.0295	0.0197	0.0309	0.9286	0.0257
9	1.5209	0.0054	1.4167	0.0078	0.7910	0.0221	3.9401	0.0014
10	3.4177	0.0001	2.8987	0.0000	3.0506	0.0004	3.0501	0.0004
11	2.2216	0.0043	1.7365	0.0024	3.9505	0.0014	0.7976	0.0222
12	0.3226	0.0404	0.2214	0.0243	0.9319	0.0265	0.0199	0.0308
13	0.0905	0.0000	0.3128	0.0055	0.0730	0.0069	1.3643	0.0010
14	0.9561	0.0110	2.4304	0.0021	1.0882	0.0015	2.7362	0.0035
15	1.4853	0.0049	3.1507	0.0006	2.9576	0.0062	1.4953	0.0060
16	0.5274	0.0090	1.1538	0.0174	2.3481	0.0030	0.2189	0.0328
17	0.0024	0.0226	0.6937	0.0136	0.0586	0.0115	0.9580	0.0353
18	0.0824	0.0295	2.0722	0.0271	0.6367	0.0444	0.6996	0.0138
19	0.0974	0.0055	1.6983	0.0002	1.3362	0.0205	0.2019	0.0016

S_n Co represents source *n* co-polar component.

S_n X represents source *n* cross-polar component.

Appendix D

Frequency Dependence Data

- *Range* represents the range of coupled power over all frequencies.
- *Avg.* represents the average of coupled power over all frequencies.

Summary of the Power Coupled (mW) to the Detectors at Varying Operating Frequencies from Each Source								
Source 1								
Detector	80GHz	81GHz	82GHz	83GHz	84GHz	85GHz	86GHz	87GHz
1	1.858	1.845	1.832	1.819	1.808	1.798	1.789	1.778
2	2.556	2.557	2.557	2.553	2.547	2.539	2.530	2.521
3	1.313	1.290	1.265	1.238	1.212	1.186	1.162	1.137
4	0.959	0.967	0.973	0.977	0.978	0.978	0.978	0.979
5	2.641	2.735	2.829	2.920	3.008	3.091	3.171	3.250
6	2.514	2.605	2.696	2.782	2.864	2.941	3.016	3.090
7	0.672	0.683	0.691	0.698	0.703	0.708	0.711	0.714
8	0.310	0.300	0.288	0.275	0.262	0.248	0.234	0.219
9	1.560	1.580	1.594	1.604	1.610	1.617	1.627	1.642
10	2.891	2.966	3.028	3.077	3.122	3.169	3.225	3.290
11	1.979	1.998	2.018	2.040	2.066	2.096	2.130	2.164
12	0.455	0.455	0.456	0.456	0.455	0.453	0.447	0.439
13	0.223	0.203	0.187	0.173	0.161	0.149	0.138	0.126
14	0.920	0.903	0.895	0.899	0.914	0.937	0.962	0.985
15	1.214	1.221	1.240	1.268	1.303	1.338	1.370	1.395
16	0.685	0.662	0.644	0.626	0.610	0.594	0.580	0.566
17	0.052	0.045	0.040	0.035	0.031	0.027	0.024	0.021
18	0.188	0.179	0.172	0.164	0.156	0.146	0.136	0.125
19	0.240	0.227	0.213	0.197	0.181	0.164	0.148	0.134
Detector	88GHz	89GHz	90GHz	91GHz	92GHz	93GHz	94GHz	95GHz
1	1.764	1.748	1.550	1.710	1.690	1.670	1.648	1.626
2	2.509	2.497	2.546	2.468	2.453	2.439	2.426	2.412
3	1.113	1.087	1.178	1.027	0.995	0.962	0.931	0.900
4	0.980	0.980	0.906	0.976	0.972	0.965	0.957	0.946

5	3.328	3.404	3.368	3.546	3.607	3.658	3.701	3.735
6	3.165	3.241	3.360	3.380	3.437	3.485	3.525	3.558
7	0.716	0.719	0.580	0.723	0.724	0.722	0.718	0.712
8	0.203	0.188	0.140	0.156	0.142	0.128	0.117	0.107
9	1.660	1.680	1.567	1.709	1.713	1.710	1.704	1.698
10	3.363	3.435	3.502	3.560	3.607	3.648	3.689	3.738
11	2.196	2.223	2.280	2.262	2.277	2.291	2.304	2.318
12	0.427	0.413	0.374	0.376	0.355	0.333	0.310	0.289
13	0.114	0.103	0.097	0.081	0.073	0.066	0.061	0.058
14	1.001	1.009	0.996	1.006	1.003	1.005	1.013	1.026
15	1.411	1.421	1.531	1.440	1.457	1.481	1.511	1.544
16	0.553	0.540	0.551	0.517	0.506	0.496	0.485	0.475
17	0.019	0.018	0.027	0.020	0.022	0.026	0.029	0.034
18	0.115	0.106	0.115	0.096	0.096	0.098	0.101	0.103
19	0.121	0.111	0.106	0.093	0.084	0.076	0.069	0.062
Detector	96GHz	97GHz	98GHz	99GHz	100GHz	Range	Avg.	
1	1.603	1.578	1.553	1.526	1.500	0.359	1.700	
2	2.398	2.383	2.367	2.349	2.329	0.228	2.473	
3	0.870	0.840	0.809	0.778	0.746	0.567	1.049	
4	0.935	0.923	0.911	0.898	0.884	0.096	0.953	
5	3.765	3.791	3.817	3.843	3.870	1.230	3.385	
6	3.586	3.611	3.632	3.650	3.666	1.152	3.229	
7	0.702	0.690	0.677	0.663	0.649	0.144	0.694	
8	0.100	0.095	0.091	0.089	0.088	0.222	0.180	
9	1.693	1.691	1.693	1.696	1.701	0.152	1.655	
10	3.799	3.875	3.966	4.067	4.173	1.282	3.485	
11	2.332	2.346	2.360	2.373	2.384	0.405	2.211	
12	0.269	0.250	0.234	0.220	0.208	0.249	0.365	
13	0.056	0.054	0.054	0.052	0.051	0.172	0.109	
14	1.043	1.059	1.071	1.076	1.074	0.181	0.990	
15	1.578	1.607	1.629	1.642	1.646	0.432	1.440	
16	0.464	0.452	0.441	0.430	0.419	0.266	0.538	
17	0.038	0.043	0.048	0.053	0.059	0.041	0.034	
18	0.105	0.105	0.104	0.103	0.102	0.092	0.124	
19	0.055	0.049	0.045	0.041	0.039	0.201	0.117	
Source 2								
Detector	80GHz	81GHz	82GHz	83GHz	84GHz	85GHz	86GHz	87GHz
1	0.159	0.147	0.138	0.130	0.124	0.118	0.110	0.101
2	0.199	0.192	0.184	0.173	0.161	0.148	0.135	0.123

3	0.091	0.080	0.071	0.063	0.055	0.048	0.042	0.037
4	0.450	0.434	0.414	0.394	0.376	0.362	0.351	0.342
5	0.983	0.982	0.987	1.002	1.024	1.052	1.080	1.106
6	0.904	0.905	0.912	0.922	0.933	0.943	0.951	0.958
7	0.397	0.372	0.346	0.319	0.293	0.269	0.248	0.228
8	0.260	0.256	0.249	0.241	0.231	0.218	0.205	0.190
9	1.297	1.323	1.344	1.358	1.368	1.375	1.382	1.391
10	2.433	2.472	2.506	2.542	2.585	2.638	2.701	2.772
11	1.711	1.731	1.754	1.780	1.808	1.836	1.860	1.880
12	0.362	0.354	0.348	0.342	0.337	0.332	0.327	0.322
13	0.437	0.433	0.429	0.426	0.424	0.423	0.421	0.419
14	1.988	2.041	2.094	2.144	2.189	2.228	2.262	2.293
15	2.498	2.600	2.693	2.775	2.847	2.910	2.971	3.032
16	0.973	1.001	1.028	1.055	1.080	1.103	1.124	1.142
17	0.808	0.791	0.774	0.756	0.736	0.714	0.691	0.668
18	2.041	2.048	2.053	2.056	2.055	2.050	2.044	2.038
19	1.888	1.891	1.891	1.886	1.878	1.869	1.861	1.855
Detector	88GHz	89GHz	90GHz	91GHz	92GHz	93GHz	94GHz	95GHz
1	0.090	0.079	0.067	0.059	0.051	0.045	0.041	0.038
2	0.114	0.107	0.106	0.100	0.098	0.096	0.094	0.092
3	0.033	0.029	0.046	0.024	0.022	0.022	0.022	0.023
4	0.335	0.328	0.342	0.310	0.299	0.286	0.274	0.262
5	1.125	1.137	1.178	1.142	1.141	1.143	1.151	1.166
6	0.967	0.978	0.961	1.012	1.034	1.056	1.077	1.096
7	0.210	0.193	0.205	0.164	0.151	0.138	0.127	0.116
8	0.176	0.162	0.135	0.138	0.128	0.120	0.114	0.109
9	1.403	1.420	1.466	1.457	1.472	1.480	1.482	1.479
10	2.845	2.917	2.981	3.037	3.085	3.127	3.170	3.219
11	1.896	1.909	1.781	1.933	1.948	1.963	1.978	1.993
12	0.316	0.309	0.250	0.291	0.279	0.267	0.254	0.240
13	0.416	0.412	0.326	0.397	0.387	0.375	0.364	0.351
14	2.322	2.350	2.481	2.408	2.436	2.462	2.483	2.497
15	3.097	3.163	3.204	3.296	3.357	3.413	3.465	3.513
16	1.158	1.172	1.191	1.191	1.197	1.200	1.201	1.200
17	0.645	0.622	0.722	0.574	0.549	0.524	0.499	0.473
18	2.031	2.024	2.141	1.996	1.975	1.950	1.924	1.899
19	1.849	1.843	1.730	1.823	1.810	1.797	1.784	1.770
Detector	96GHz	97GHz	98GHz	99GHz	100GHz	Range	Avg.	
1	0.036	0.034	0.032	0.030	0.027	0.131	0.079	

2	0.090	0.087	0.086	0.085	0.085	0.114	0.122	
3	0.025	0.028	0.031	0.034	0.038	0.069	0.041	
4	0.252	0.244	0.238	0.234	0.230	0.220	0.322	
5	1.188	1.214	1.238	1.257	1.266	0.284	1.122	
6	1.112	1.123	1.130	1.132	1.131	0.228	1.011	
7	0.107	0.098	0.091	0.086	0.081	0.316	0.202	
8	0.106	0.104	0.103	0.102	0.101	0.158	0.164	
9	1.474	1.469	1.467	1.469	1.475	0.185	1.422	
10	3.276	3.344	3.421	3.501	3.581	1.148	2.960	
11	2.005	2.016	2.024	2.030	2.034	0.323	1.899	
12	0.226	0.211	0.198	0.185	0.173	0.189	0.282	
13	0.339	0.327	0.316	0.304	0.292	0.145	0.382	
14	2.504	2.504	2.500	2.494	2.488	0.516	2.341	
15	3.559	3.603	3.646	3.691	3.735	1.236	3.194	
16	1.197	1.193	1.188	1.183	1.177	0.229	1.141	
17	0.448	0.425	0.402	0.379	0.356	0.452	0.598	
18	1.876	1.855	1.834	1.810	1.784	0.357	1.975	
19	1.753	1.733	1.708	1.680	1.650	0.241	1.807	

Source 3

Detector	80GHz	81GHz	82GHz	83GHz	84GHz	85GHz	86GHz	87GHz
1	0.509	0.493	0.477	0.460	0.442	0.423	0.402	0.381
2	1.314	1.275	1.235	1.194	1.152	1.110	1.067	1.026
3	1.253	1.236	1.214	1.188	1.161	1.132	1.102	1.070
4	0.406	0.392	0.378	0.366	0.357	0.350	0.343	0.333
5	1.620	1.620	1.615	1.607	1.602	1.604	1.616	1.634
6	2.920	2.944	2.958	2.964	2.964	2.960	2.957	2.955
7	1.434	1.461	1.484	1.506	1.524	1.538	1.548	1.555
8	0.090	0.090	0.090	0.089	0.087	0.084	0.080	0.077
9	0.930	0.935	0.948	0.961	0.969	0.966	0.951	0.927
10	2.828	2.834	2.853	2.886	2.928	2.972	3.010	3.041
11	3.435	3.513	3.590	3.669	3.747	3.820	3.883	3.935
12	1.111	1.140	1.163	1.179	1.188	1.190	1.188	1.181
13	0.180	0.164	0.149	0.134	0.122	0.113	0.104	0.095
14	1.194	1.176	1.153	1.126	1.100	1.079	1.066	1.058
15	2.909	2.939	2.958	2.965	2.961	2.952	2.941	2.932
16	1.986	2.040	2.087	2.130	2.167	2.200	2.229	2.257
17	0.143	0.128	0.114	0.101	0.089	0.077	0.066	0.055
18	0.926	0.888	0.852	0.817	0.781	0.745	0.707	0.668
19	1.650	1.645	1.635	1.620	1.599	1.574	1.545	1.514

Detector	88GHz	89GHz	90GHz	91GHz	92GHz	93GHz	94GHz	95GHz
1	0.360	0.340	0.229	0.304	0.287	0.268	0.250	0.231
2	0.985	0.944	0.800	0.863	0.824	0.787	0.751	0.716
3	1.038	1.005	1.057	0.936	0.901	0.866	0.830	0.793
4	0.321	0.307	0.266	0.276	0.261	0.248	0.238	0.229
5	1.653	1.668	1.577	1.672	1.665	1.658	1.655	1.659
6	2.954	2.952	2.878	2.938	2.928	2.918	2.910	2.904
7	1.561	1.567	1.373	1.574	1.575	1.573	1.566	1.554
8	0.074	0.071	0.053	0.066	0.063	0.058	0.052	0.046
9	0.901	0.879	0.842	0.866	0.872	0.879	0.883	0.878
10	3.067	3.100	3.146	3.211	3.294	3.388	3.483	3.573
11	3.977	4.011	3.999	4.071	4.100	4.129	4.160	4.192
12	1.170	1.155	0.973	1.117	1.096	1.075	1.055	1.037
13	0.086	0.076	0.084	0.058	0.050	0.044	0.039	0.035
14	1.052	1.042	1.133	1.002	0.974	0.946	0.923	0.908
15	2.925	2.918	3.032	2.895	2.879	2.863	2.850	2.841
16	2.285	2.310	2.372	2.350	2.364	2.373	2.378	2.379
17	0.045	0.037	0.076	0.024	0.019	0.015	0.012	0.010
18	0.630	0.594	0.713	0.528	0.498	0.469	0.440	0.411
19	1.482	1.449	1.387	1.382	1.347	1.310	1.273	1.234
Detector	96GHz	97GHz	98GHz	99GHz	100GHz	Range	Avg.	
1	0.212	0.195	0.179	0.164	0.149	0.360	0.322	
2	0.682	0.647	0.613	0.581	0.550	0.765	0.910	
3	0.756	0.717	0.678	0.639	0.601	0.653	0.961	
4	0.221	0.214	0.206	0.196	0.186	0.220	0.290	
5	1.669	1.683	1.695	1.703	1.704	0.126	1.647	
6	2.900	2.896	2.893	2.892	2.894	0.087	2.928	
7	1.537	1.518	1.494	1.467	1.437	0.202	1.516	
8	0.041	0.037	0.035	0.035	0.036	0.055	0.065	
9	0.865	0.846	0.826	0.808	0.796	0.173	0.892	
10	3.655	3.731	3.805	3.884	3.970	1.143	3.269	
11	4.226	4.262	4.300	4.344	4.391	0.957	3.988	
12	1.022	1.009	0.997	0.986	0.976	0.217	1.096	
13	0.032	0.030	0.027	0.024	0.023	0.158	0.080	
14	0.899	0.895	0.890	0.881	0.868	0.326	1.017	
15	2.836	2.834	2.832	2.831	2.831	0.201	2.901	
16	2.376	2.371	2.363	2.352	2.340	0.393	2.272	
17	0.008	0.008	0.009	0.010	0.012	0.135	0.050	
18	0.381	0.353	0.327	0.303	0.280	0.645	0.586	

19	1.195	1.156	1.116	1.075	1.034	0.616	1.392	
Source 4								
Detector	80GHz	81GHz	82GHz	83GHz	84GHz	85GHz	86GHz	87GHz
1	1.688	1.685	1.676	1.661	1.642	1.619	1.592	1.562
2	0.973	0.936	0.900	0.865	0.829	0.791	0.751	0.711
3	0.152	0.137	0.123	0.109	0.096	0.084	0.072	0.061
4	1.980	2.034	2.082	2.126	2.164	2.198	2.229	2.260
5	2.952	2.986	3.008	3.017	3.017	3.010	3.003	2.998
6	1.223	1.205	1.180	1.153	1.128	1.108	1.096	1.088
7	0.184	0.168	0.152	0.139	0.127	0.118	0.109	0.100
8	1.105	1.134	1.157	1.173	1.182	1.185	1.183	1.176
9	3.432	3.511	3.588	3.666	3.744	3.816	3.880	3.931
10	2.831	2.837	2.855	2.887	2.929	2.973	3.011	3.041
11	0.932	0.937	0.950	0.963	0.971	0.968	0.953	0.929
12	0.091	0.091	0.091	0.091	0.088	0.085	0.081	0.077
13	1.435	1.461	1.484	1.504	1.521	1.533	1.541	1.546
14	2.874	2.894	2.906	2.910	2.907	2.900	2.894	2.889
15	1.593	1.595	1.590	1.583	1.577	1.579	1.589	1.607
16	0.405	0.390	0.376	0.363	0.353	0.345	0.337	0.328
17	1.223	1.205	1.182	1.155	1.127	1.096	1.065	1.031
18	1.254	1.214	1.174	1.133	1.091	1.049	1.007	0.967
19	0.488	0.472	0.457	0.441	0.424	0.405	0.385	0.365
Detector	88GHz	89GHz	90GHz	91GHz	92GHz	93GHz	94GHz	95GHz
1	1.532	1.501	1.441	1.437	1.403	1.367	1.331	1.293
2	0.672	0.635	0.762	0.567	0.536	0.505	0.474	0.443
3	0.050	0.042	0.082	0.027	0.022	0.017	0.013	0.011
4	2.289	2.317	2.391	2.362	2.379	2.391	2.399	2.402
5	2.993	2.988	3.103	2.966	2.950	2.934	2.921	2.912
6	1.082	1.071	1.163	1.027	0.998	0.969	0.947	0.932
7	0.091	0.081	0.087	0.061	0.053	0.047	0.042	0.038
8	1.166	1.151	0.969	1.113	1.093	1.072	1.052	1.034
9	3.972	4.007	3.989	4.066	4.094	4.123	4.154	4.185
10	3.067	3.099	3.145	3.211	3.294	3.387	3.483	3.574
11	0.903	0.881	0.849	0.868	0.875	0.883	0.886	0.882
12	0.074	0.072	0.053	0.067	0.063	0.058	0.052	0.047
13	1.549	1.552	1.366	1.554	1.552	1.548	1.538	1.524
14	2.886	2.883	2.810	2.868	2.857	2.847	2.839	2.834
15	1.625	1.641	1.554	1.648	1.641	1.634	1.629	1.632
16	0.317	0.303	0.263	0.273	0.258	0.245	0.234	0.225

17	0.998	0.964	1.015	0.894	0.858	0.823	0.787	0.750
18	0.927	0.887	0.752	0.809	0.772	0.736	0.702	0.669
19	0.344	0.324	0.216	0.288	0.271	0.253	0.235	0.217
Detector	96GHz	97GHz	98GHz	99GHz	100GHz	Range	Avg.	
1	1.255	1.216	1.176	1.135	1.093	0.595	1.443	
2	0.413	0.383	0.355	0.330	0.306	0.667	0.626	
3	0.009	0.008	0.008	0.009	0.011	0.144	0.054	
4	2.402	2.400	2.395	2.388	2.378	0.422	2.284	
5	2.908	2.904	2.902	2.899	2.897	0.206	2.965	
6	0.925	0.920	0.915	0.905	0.891	0.333	1.044	
7	0.035	0.031	0.028	0.026	0.023	0.160	0.083	
8	1.019	1.005	0.993	0.982	0.972	0.216	1.091	
9	4.219	4.254	4.293	4.335	4.383	0.951	3.983	
10	3.656	3.731	3.806	3.885	3.973	1.141	3.270	
11	0.869	0.850	0.829	0.812	0.800	0.171	0.895	
12	0.041	0.038	0.035	0.035	0.036	0.056	0.065	
13	1.506	1.484	1.459	1.430	1.399	0.188	1.499	
14	2.830	2.826	2.824	2.823	2.826	0.100	2.863	
15	1.640	1.652	1.664	1.671	1.673	0.119	1.620	
16	0.218	0.210	0.202	0.193	0.183	0.222	0.287	
17	0.713	0.675	0.636	0.598	0.561	0.662	0.922	
18	0.636	0.603	0.570	0.539	0.510	0.744	0.857	
19	0.199	0.182	0.166	0.151	0.137	0.351	0.306	